Caractériser le milieu interstellaire : un clé pour comprendre l'Univers

Jérôme Pety

▶ **To cite this version:**

Jérôme Pety. Caractériser le milieu interstellaire : un clé pour comprendre l'Univers. Astrophysique galactique [astro-ph.GA]. Université Pierre et Marie Curie - Paris VI, 2012. tel-00726959

HAL Id: tel-00726959

https://theses.hal.science/tel-00726959

Submitted on 31 Aug 2012

HAL is a multi-disciplinary open access archive for the deposit and dissemination of scientific research documents, whether they are published or not. The documents may come from teaching and research institutions in France or abroad, or from public or private research centers.

L'archive ouverte pluridisciplinaire **HAL**, est destinée au dépôt et à la diffusion de documents scientifiques de niveau recherche, publiés ou non, émanant des établissements d'enseignement et de recherche français ou étrangers, des laboratoires publics ou privés.

UNIVERSITÉ PIERRE ET MARIE CURIE

HABILITATION À DIRIGER DES RECHERCHES

présentée par

Jérôme PETY

Caractériser le milieu interstellaire : une clé pour comprendre l'Univers

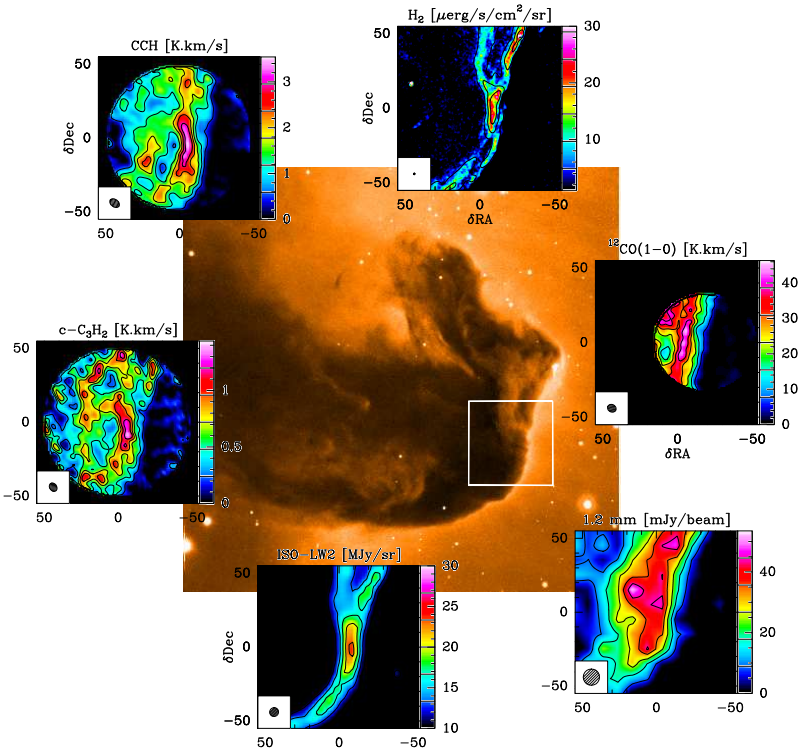

Soutenue le 6 juin 2012 devant la commission d'examen :

M.	Pierre COX	Examinateur
M.	Thierry FORVEILLE	Rapporteur
Mme	Maryvonne GERIN	Examinatrice
M.	Martin GIARD	Rapporteur
Mme	Christine JOBLIN	Examinatrice
M.	Harvey S. LISZT	Examinateur
Mme	Caroline TERQUEM	Présidente
M.	Alwyn WOOTTEN	Rapporteur

IRAM, 300 rue de la Piscine, F-38406 Saint Martin d'Hères Cedex
& LERMA, Observatoire de Paris, UMR 8112, 61 avenue de l'Observatoire, 75014 Paris

Becoming a scientist requires a whole community.
Thanks to all.

Table des matières

1 Rapport de soutenance **7**

2 Curriculum vitae **9**
2.1 Thèmes de recherche 9
2.2 Tâches de service 9
2.3 Gestion et administration de la recherche 9
2.4 Participation à d'autres contrats de recherche 10
2.5 Enseignement 10
2.6 Encadrement 10
2.7 Animation et diffusion de la culture scientifique 11
2.8 Parcours 12

3 Introduction **15**

4 Caractériser observationnellement la transition HI $\rightarrow$ H_2 **17**
4.1 Etudes en absorption derrière une source continuum 18
4.2 Etudes directes en émission 19
4.3 Combiner les deux approches 19
4.4 La luminosity CO par molécule H_2 20
4.5 Intermittency of interstellar turbulence : extreme velocity-shears and CO emission on milliparsec scale 22
4.6 The CO luminosity and CO-H_2 conversion factor of diffuse ISM : does CO emission trace dense molecular gas ? 36
4.7 Imaging diffuse clouds : Bright and dark gas mapped in CO 46

5 La Tête de Cheval : une référence observationnelle pour les modèles chimiques **69**
5.1 Les modèles photochimiques et la Tête de Cheval 69
5.2 Une physique bien contrainte et une chimie riche 70
5.3 Perspectives : des relevés de raies sensibles et non-biaisés 73
5.4 Are PAHs precursors of small hydrocarbons in photo-dissociation regions ? The Horsehead case 75
5.5 Low sulfur depletion in the Horsehead PDR 90
5.6 Deuterium fractionation in the Horsehead edge 110
5.7 The ionization fraction gradient across the Horsehead edge : an archetype for molecular clouds 114

5.8 HCO mapping of the Horsehead : tracing the illuminated dense molecular cloud surfaces . . . 127
5.9 H_2CO in the Horsehead PDR : photo-desorption of dust grain ice mantles . . . 136

6 Le projet SCHISM, financé par l'Agence Nationale de la Recherche 145
6.1 Résumé . . . 145
6.2 Dossier . . . 147

7 Spectro-imagerie grand-champ en radio-astronomie (sub)-millimétrique 159
7.1 Mode télescope unique . . . 159
7.2 Mode interférométrique . . . 160
7.3 Le futur de la radio-astronomie (sub-)millimétrique . . . 162
7.4 CLASS evolution : I. Improved OTF support . . . 164
7.5 Weeds : a CLASS extension for the analysis of millimeter and submillimeter spectral surveys . . . 169
7.6 IRA-M30m EMIR time/sensitivity estimator . . . 174
7.7 IRAM-30m HERA time/sensitivity estimator . . . 178
7.8 Impact of ACA on the wide-field imaging capabilities of ALMA . . . 180
7.9 Wide-field imaging of ALMA with the ALMA Compact Array : Imaging simulations . . . 190
7.10 Revisiting the theory of interferometric wide-field synthesis . . . 198
7.11 WIFISYN : The GILDAS implementation of a new wide-field synthesis algorithm 219

8 Gestion des logiciels `GILDAS` 225
8.1 Présentation et contexte . . . 225
8.2 Assurer la continuité et la professionnalisation . . . 226
8.3 Perspectives . . . 227
8.4 Preparing GILDAS for large datasets : I. GREG 2011 . . . 228

9 Action Spécifique ALMA (administration de la recherche) 235
9.1 Statut du projet ALMA . . . 235
9.2 Objectifs de l'action spécifique . . . 235
9.3 Activités 2008-2011 . . . 236
9.4 Quel avenir pour l'ASA ? . . . 238
9.5 Contribution de l'Action Spécifique ALMA à l'exercice de prospective 2009 . . . 239
9.6 Besoins en services d'observation ALMA pour la période 2011-2014 . . . 242

Articles publiés dans des revues à comité de lecture 245

Mémos IRAM et ALMA 249

Actes de colloques nationaux et internationaux 251

Rapport après soutenance

Habilitation à Diriger des Recherches de Jérôme Pety,
présentée le 6 juin 2012

Dans son mémoire intitulé "Caractériser le milieu interstellaire: une clé pour comprendre l'univers", présenté par écrit et en séminaire, Jérôme Pety fait le point sur un domaine de recherche très actuel et actif auquel il a apporté une contribution très importante. Les trois rapporteurs qui ont examiné son mémoire écrit ont conclu à la pleine recevabilité de celui–ci, sous réserve de la présentation orale.

A l'issue de cette présentation, le jury considère que Jérôme Pety a atteint le niveau d'un chercheur accompli, bénéficiant d'une reconnaissance internationale, auteur de travaux originaux couvrant un large spectre, de l'instrumentation logicielle à la recherche observationnelle.

L'expertise de Jérôme Pety est reconnue dans un domaine extrêmement vaste. Ses recherches observationnelles sur la physico–chimie du milieu interstellaire ont donné des résultats souvent inattendus car contraires aux prédictions des modèles. Ses études font ainsi progresser très significativement la compréhension de la chimie interstellaire. L'activité d'instrumentation logicielle de Jérôme Pety, qui concerne le développement de logiciels d'analyse de données d'une part et de nouvelles fonctionalités de spectro–imagerie grand champ en radioastronomie d'autre part, a une portée internationale et est indispensable à la communauté des radioastronomes. Jérôme Pety fait preuve dans ces développements d'un esprit tout à fait novateur.

Enfin, le jury souligne le fait que Jérôme Pety a d'importantes responsabilités dans la gestion de la recherche, et qu'il a déjà co–encadré avec beaucoup d'enthousiasme et de succés des thèses de doctorat et des post–doctorants. Il a un talent certain pour gérer des groupes et faire travailler ensemble des chercheurs et des ingénieurs.

Il ne fait aucun doute que Jérôme Pety a acquis une grande expérience dans un domaine qu'il a largement contribué à développer. Il a démontré qu'il a la stature d'un directeur de recherches, apte à créer une école ainsi qu'à stimuler des coopérations internationales largement engagées. Par conséquent, le jury à l'unanimité décerne à Jérôme Pety l'Habilitation à Diriger des Recherches.

Caroline Terquem
Professeur UPMC

Chapitre 2

Curriculum vitae

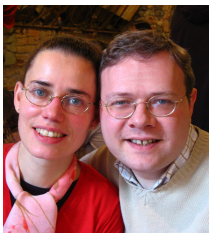

Jérôme PETY
Marié, deux enfants.
Astronome-adjoint à l'Obs. de Paris,
détaché à l'IRAM (Grenoble).

2.1 Thèmes de recherche

- Physique et chimie du milieu interstellaire (gaz diffus et régions de photo-dissociation).
- Spectro-imagerie grand-champ en radio-astronomie (sub)-millimétrique.

2.2 Tâches de service

2003–Présent — RESPONSABLE DES LOGICIELS GILDAS
Temps passé : 70% jusque 2006, 50% depuis.
GILDAS est la suite des logiciels de réduction et d'analyse des données produites par les instruments de l'IRAM : l'interféromètre du Plateau de Bure (France) et le 30m à Pico Veleta (Espagne).

2.3 Gestion et administration de la recherche

2012–2016 — LEADER DU PACKAGE SCIENCE SOFTWARE POUR LE PROJET NOEMA
Définition et suivi du planning des développements logiciels. Participation au développement des spécifications instrumentales.

2009–2013 — COORDINATEUR DU PROJET DE RECHERCHE ANR : SCHISM
Structure and Chemistry of the Inter-Stellar Medium.
Partenaires : IRAM, LERMA-LRA and LUTH-ISM.
Budget demandé et alloué : 488 438 euros

2008– Présent — DIRECTEUR DE L'ACTION SPÉCIFIQUE ALMA
Réflexion sur les besoins en services d'observation ALMA pour la période 2011-2014. Représentation du conseil scientifique à la commission spécialisée Astronomie-Astrophysique du CNRS et à l'exercice de prospective 2009-2010 de l'astronomie.

2.4 Participation à d'autres contrats de recherche

2010–2012 — CHERCHEUR EXTÉRIEUR DANS LE CONTRAT ESPAGNOL MICINN "ASTROFISICA MOLECULAR : UNA NUEVA VISION DEL UNIVERSO EN LA ERA DE HERSCHEL Y ALMA", PI : J.R. GOICOECHEA.
AYA2009-07304

2.5 Enseignement

2009, 2011 — ECOLES DE RADIO-ASTRONOMIE MILLIMÉTRIQUE DE L'IRAM
Cours 1 : Présentation de GILDAS.
Cours 2 : Démonstration de la réduction de données avec CLASS.
Cours 3 : Stratégies d'observations hétérodynes.
Cours 4 : La PDR de la Tête de Cheval.
TP : Encadrement de groupes qui ont cartographié le milieu interstellaire (la PDR de NGC7023 ou de l'environnement de la region HII W49 en CO).

2002, 2004, 2006, 2008, 2010 — ECOLES D'INTERFÉROMÉTRIE MILLIMÉTRIQUE DE L'IRAM
Cours 1 : Une visite guidée de l'interférométrie millimétrique.
Cours 2 : L'imagerie et la déconvolution.
Cours 3 : Présentation de GILDAS.
TP : Co-organisation des TP de calibration et d'imagerie.

2.6 Encadrement

2011–2012 — SÉJOUR POST-DOCTORAL DE P. GRATIER.
Financé par le programme ANR SCHISM pour travailler sur la structure et la chimie du milieu interstellaire.

2011 — TRAVAIL DE M. LONJARET ET J.-C. ROCHE, INGÉNIEURS DE RECHERCHE.
Financés par un contrat européen du 6ème PCRD (ALMA Enhancement) pour travailler sur l'imagerie grand-champ d'ALMA.

2010–2013 — THÈSE DE V. GUZMAN.
Co-direction avec M. Gerin et J.R. Goicoechea. « Etude de la nébuleuse de la Tête de Cheval. » Financée par une bourse chilienne, complétée par l'IRAM pour la durée de sa thèse.

2008 STAGE DE MASTER 2 DE J. MONTILLAUD.
Co-direction avec M. Gerin. « Etude de l'émission de CN, HCN et HNC dans la nébuleuse de la Tête de Cheval. » J. Montillaud a continué en thèse avec C. Joblin à Toulouse pour des raisons personnelles.

2007–2011 SÉJOUR POST-DOCTORAL DE N. RODRIGUEZ-FERNANDEZ.
Co-direction avec F. Gueth. Financé par un contrat européen du 6ème PCRD (ALMA Enhancement) pour travailler sur l'imagerie grand-champ d'ALMA.

2007–Présent TRAVAIL D'E. REYNIER, INGÉNIEUR DE RECHERCHE
Financé par l'IRAM pour moderniser les services généraux de `GILDAS`, puis pour mettre en place un niveau système de soumission et de gestion des projets scientifiques.

2006–Présent TRAVAIL DE S. BARDEAU, INGÉNIEUR DE RECHERCHE
Co-direction avec S. Guilloteau jusqu'en 2008. Financé par un contrat CNRS de 2006 à 2008 (1 an à l'Observatoire de Bordeaux et 2 ans à l'IRAM), S. Bardeau a mis au point l'interfaçage de `GILDAS` avec `python`.
Depuis 2009, S.Bardeau a un contrat avec l'IRAM pour travailler à mi-temps sur le coeur de `GILDAS` et à mi-temps sur `CLASS`, le logiciel de réduction des données spectroscopiques (en remplacement de P. Hily-Blant, voir ci-dessous).

2006–2007 SÉJOUR POST-DOCTORAL DE V. PIÉTU.
Co-direction avec F. Gueth. Financé par l'IRAM pour travailler sur le logiciel d'étalonnage des données interférométriques, `CLIC` de `GILDAS`. V. Piétu a obtenu un CDI de l'IRAM en 2008 comme responsable de `CLIC`.

2005–2007 SÉJOUR POST-DOCTORAL DE P. HILY-BLANT.
Financé par l'IRAM pour travailler sur `CLASS`. P. Hily-Blant a obtenu un poste de maître de conférence à l'université Joseph Fourier de Grenoble début 2008.

2.7 Animation et diffusion de la culture scientifique

Juin 2012 ATELIER PCMI-ASA AUX JOURNÉES DE LA SF2A
"Analyse, réduction et visualisation de données de spectro-imagerie".

Dec. 2011 JOURNÉES ASA À GRENOBLE ($\sim$ 60 SCIENTIFIQUES)
"ALMA early science cycle 0 : et après ?", en collaboration avec le GDR spectroscopie.

2011 CONTACTS AVEC PLUSIEURS JOURNALISTES SUR ALMA
Voir par exemple l'article "ALMA en éveil" dans la Libre Belgique.

Nov. 2010 ARTICLE "ALMA, L'OBSERVATOIRE GÉANT" DANS LA REVUE *L'Astronomie* ÉDITÉE PAR LA SOCIÉTÉ FRANÇAISE D'ASTRONOMIE.
Rédaction et iconographie.

Juin 2010 ATELIER ASA À LA SEMAINE DE L'ASTROPHYSIQUE FRANÇAISE
"ALMA Early Science".

Nov. 2009 COMMUNIQUÉ DE PRESSE CNRS SUR LES PREMIÈRES FRANGES D'ALMA
Participation à la rédaction.

Avril 2009 JOURNÉES ASA À GRENOBLE
Organisation de l'atelier où ~ 100 scientifiques sont venus discuter pendant 2 jours de la manière dont ils voulaient se préparer scientifiquement aux premiers appels à proposition d'ALMA.

Juillet 2007 CHRONIQUE CUTTING EDGE DE LA REVUE ANGLAISE *Astronomy Now*
Sujet : "The Horsehead's heavy hydrogen". Interaction avec le chroniqueur et relecture.

Nov. 2006 COLLOQUE PCMI À GRENOBLE
Participation au comité d'organisation scientifique.

Février 2005 COMMUNIQUÉ DE PRESSE JOINT *A&A* ET CNRS
Sujet : "Hydrocarbons in the Horsehead mane". Rédaction du communiqué. Information reprise dans le *Nouvel Obs.*, *Ciel & Espace*, *Le Monde*, et sur de nombreux sites internet d'information scientifique.

2.8 Parcours

2006–Présent INSTITUT DE RADIO ASTRONOMIE MILLIMÉTRIQUE/OBSERVATOIRE DE PARIS
Astronome-adjoint à l'Obs. de Paris, détaché à l'IRAM (Grenoble).

2003–2005 OBSERVATOIRE DE PARIS/INSTITUT DE RADIO ASTRONOMIE MILLIMÉTRIQUE
Astronome-adjoint à l'Obs. de Paris, en mission longue à l'IRAM (Grenoble).

2001–2002 INSTITUT DE RADIO ASTRONOMIE MILLIMÉTRIQUE
Séjour post-doctoral à Grenoble.

2000 UNIVERSITÉ PARIS VI
ATER.

1997–1999 ÉCOLE NORMALE SUPÉRIEURE/OBSERVATOIRE DE PARIS
Thèse d'astrophysique soutenue le 4 octobre 1999.

1995–1996 CALIFORNIA INSTITUTE OF TECHNOLOGY
Service militaire en tant que coopérant scientifique.

1994 UNIVERSITÉ PARIS VI
DEA d'astrophysique.

1992–1993 ÉCOLE NORMALE SUPÉRIEURE/UNIVERSITÉ PARIS VI
Magistère Interuniversitaire de Physique.

1989–1991 CLASSES PRÉPARATOIRES EFFECTUÉES AU LYCÉE FAIDHERBES, LILLE.
Admis à l'École Normale Supérieure (Ulm).

1988 BACCALAURÉAT SÉRIE C OBTENU DANS L'ACADÉMIE DE LILLE.

Copyright: IRAM/PdBI

Chapitre 3

Introduction

Les molécules sont de loin les traceurs les plus riches de la matière diffuse dans l'univers, des galaxies à grand z aux disques proto-planétaires. Leurs degrés de liberté internes et externes gardent en effet la signature des conditions physiques de l'environnement où elles évoluent. Pour bénéficier pleinement des diagnostics fondés sur les raies moléculaires, leurs processus de formation et de destruction doivent être compris *quantitativement* et pas seulement qualitativement. C'est une véritable gageure étant donné les conditions physiques extrêmes (faible densité, basse température, éclairement UV souvent important) et la dynamique complexe (turbulence magnéto-hydrodynamique) du milieu.

Mes travaux cherchent à définir, à réaliser et à interpréter les observations originales, souvent à la limite des capacités instrumentales actuelles en radio-astronomie (sub)-millimétrique. Ces observations permettent des avancées significatives dans la compréhension des processus physiques et chimiques à l'œuvre dans le milieu interstellaire galactique ou extra-galactique, de la naissance des étoiles à leur mort. J'ai ainsi été amené à participer à des études variées : détection puis cartographie des raies de CO et CI dans des QSO à grand redshift (2.58 et 4.12) [A30, A31, A34], caractérisation des courants de refroidissement dans le cœur de l'amas de galaxies Persée [A17], étude de la morphologie des vents d'une AGB [A20], caractérisation de la physique et de la chimie de proto-étoiles [A14, A19, A22, A23, A24, A26, A3]. Ces études se font à l'interface de PCMI et des PNCG et PNPS.

Plutôt qu'une description exhaustive de l'ensemble de mes travaux, j'ai choisi de présenter ici ceux qui m'ont continuement occupé durant les dix dernières années et qui cherchent à caractériser la structure et la chimie du milieu interstellaire local. La partie 4 décrit les efforts que j'ai entrepris pour contraindre la composition et la formation des nuages moléculaires géants. La partie 5 montre que la nébuleuse de la Tête de Cheval est non seulement un objet emblématique de l'astronomie, mais surtout un fantastique laboratoire pour tester la physique et la chimie du milieu interstellaire. Comprendre les diagnostics physiques et chimiques localement est d'autant plus important que les progrès récents en radio-astronomie (spectromètres à haute résolution sur de très larges bandes passantes, échantillonnage du plan focal par des multi-pixels, haute résolution angulaire à l'aide des interféromètres) permettent l'observation de traceurs chimiques dans de nouveaux environnements extrêmes comme les disques proto-planétaires ou les galaxies locales et à haut redshift. Dans la mesure du possible, j'essaie de mettre à disposition de la communauté les outils nouveaux développés pour réaliser ces études. Par exemple, la partie 7 présente les algorithmes et les logiciels qu'il a fallu (qu'il faut) créer ou modifier pour permettre

de faire efficacement de l'imagerie grand-champ en radio-astronomie (sub)-millimétrique.

Les deux parties suivantes de ce dossier détaillent deux autres activités dont l'impact sur les communautés française et internationale est important, même si cela ne se traduit pas en nombre de citations d'articles. Qui plus est, ces activités occupent une large fraction de mon temps depuis que je suis devenu astronome-adjoint fin 2002. Il s'agit d'une part de gérer les logiciels GILDAS (cf. partie 8) : non seulement tous les résultats obtenus avec les instruments de l'IRAM (30m à Pico Veleta et interféromètre du Plateau de Bure) sont réduits à l'aide de GILDAS, mais certains de ces logiciels (par exemple CLASS) sont utilisés dans de nombreux autres observatoires de radio-astronomie dans le monde (par exemple l'instrument HIFI d'Herschel). D'autre part, je suis directeur de l'Action Spécifique ALMA depuis janvier 2008. Le premier objectif de l'ASA est de préparer la communauté française à la compétition accrue sur ALMA, de façon à obtenir un retour scientifique à la hauteur des investissements français dès les premiers appels à propositions[1] (cf. partie 9).

Enfin, je coordonne le projet ANR SCHISM (Structure and Chemistry of the Interstellar Medium) depuis le 1er septembre 2009 pour une durée de 4 ans (cf. partie 6). Ce projet explore le couplage de la chimie en phase gazeuse à celle à la surface des grains, et le couplage de la chimie avec la turbulence magnéto-hydrodynamique (MHD) (phénomènes de transport, structures dissipatives, chocs). Sa pertinence vient du lien fort entre développements numériques pointus et observations utilisant les instruments les plus performants du domaine : le satellite Herschel et les interféromètres millimétriques (Plateau de Bure et ALMA). Dans ce cadre, j'encadre en thèse Viviana Guzman en co-direction avec M. Gerin et J. Goicoechea.

L'ensemble de ces activités se fait en collaborations nationales et internationales. En ce qui concerne la recherche, il faut retenir plus particulièrement le groupe de M. Gerin et E. Falgarone au LERMA, celui de S. Guilloteau au LAB, H. Liszt du NRAO (USA), R. Lucas du JAO (Joint ALMA office au Chili), J.R. Goicoechea (CSIC, Espagne). Il faut ajouter plus récemment le groupe PDR de Meudon (F. Le Petit et al., LUTH) qui est l'un des trois partenaires de l'ANR SCHISM, ainsi que S. Maret et P. Hily-Blant de l'IPAG pour l'interfaçage des bases de données spectroscopiques (par exemple CDMS et/ou JPL) à GILDAS [A4]. Mes activités IRAM et ALMA me donnent aussi l'occasion d'être en contact avec la plupart des grands observatoires de radio-astronomie du monde. J'apprécie particulièrement le travail en équipe, tant avec des chercheurs confirmés qu'avec de jeunes chercheurs ou ingénieurs. A l'IRAM, j'encadre ainsi régulièrement des post-docs et des ingénieurs logiciels. En 2008, j'ai aussi suivi une formation de chef de projet au CNRS pour améliorer mes capacités de gestion.

Je suis actuellement astronome-adjoint à l'Observatoire de Paris, détaché à l'IRAM. Dans cette position particulière, je participe au lien entre la communauté française et l'IRAM, un des acteurs majeurs de la radio-astronomie aujourd'hui. Je souhaite continuer à jouer un rôle dans la mise en service scientifique d'ALMA et dans la réalisation du projet NOEMA d'extension du Plateau de Bure pour un budget total de 33 Meuros[2].

[1] La date limite du premier appel pour le cycle 0 de la phase dite "early science" (avec 16 antennes disponibles) était fin juin 2011. La date limite pour le prochain appel (lorsque 32 antennes seront disponibles) sera probablement début juillet 2012.

[2] Ce projet a été classé 1ère priorité dans la catégorie des projets à budget moyen par l'exercice de prospective 2009-2010 de l'INSU, puis il a été sélectionné comme projet EQUIPEX à hauteur de 10 Meuros en 2011.

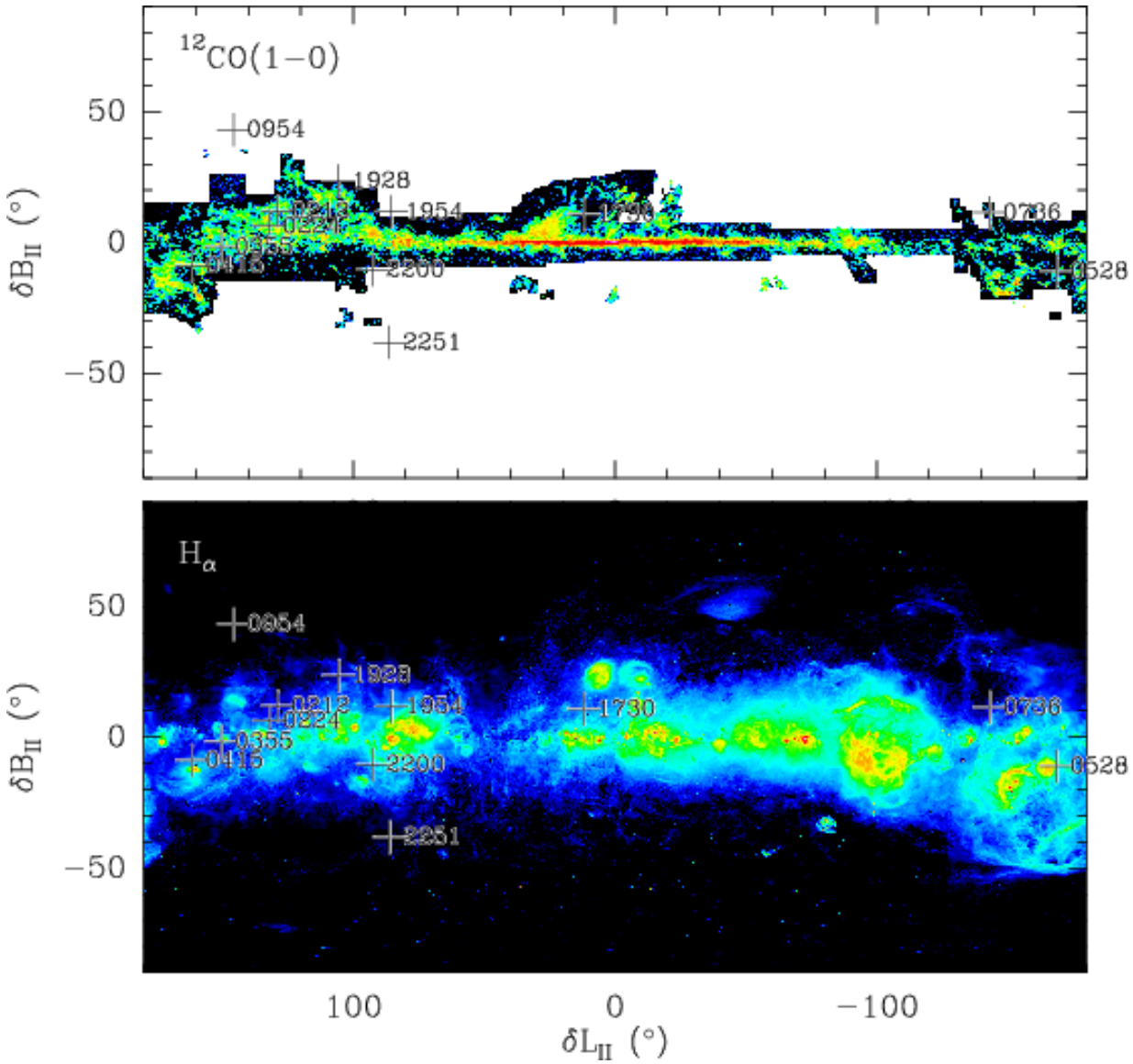

Copyright: Tom Dame (Top) & Douglas P. Finkbeiner (Bottom)

Chapitre 4

Caractériser observationnellement la transition HI → H_2

Sur le long chemin qui conduit des phases ionisées, chaudes et peu denses du milieu interstellaire, jusqu'à la formation des étoiles et des systèmes planétaires associés, la formation des nuages moléculaires géants est encore mal comprise aujourd'hui. L'incompréhension de cette étape clé est due aux difficultés intrinsèques à caractériser observationnellement la transition HI → H_2 : 1) au contraire de nombreux autres objets astrophysiques (par exemple galaxies vues de face, proto-étoiles, étoiles, planètes), la géométrie du milieu interstellaire est mal contrainte,

les différentes phases étant imbriquées les unes dans les autres ; 2) le milieu est très turbulent ; 3) alors que l'hydrogène ionisé et neutre peut être directement caractérisé par les raies Hα et HI à 21 cm, l'hydrogène moléculaire froid est invisible car H_2 n'a pas de raies dipolaires, comme toute molécule symétrique. Les points 1 et 2 impliquent une approche statistique. Le point 3 implique une caractérisation du gaz moléculaire par des traceurs minoritaires, typiquement CO, qui sont affectés par une chimie propre, dont il faut tenir compte. Il y a donc besoin de diagnostiques physiques et chimiques clairs pour progresser.

Les nuages moléculaires géants ont été définis observationnellement comme étant les régions du ciel détectées en ^{12}CO J=1–0 avec des antennes de petite taille (typiquement 1m de diamètre) : ils ont une masse et une taille typique de $10^6\,\mathrm{M}_\odot$ et 20 pc, ce qui donne une densité moyenne de $600\,\mathrm{H}_2\,\mathrm{cm}^{-3}$. Pour mieux comprendre la composition et la formation des nuages moléculaires géants, il faut faire appel à un autre classement observationnel basé sur l'extinction visuelle et l'émission HI :

Les nuages diffus sont définis par leur émission HI et ils ont une extinction visuelle faible ($A_\mathrm{v} \leq 1\,\mathrm{mag}$). Le gaz de ces nuages diffus est neutre, tiède (60 K) et peu dense ($10^2\,\mathrm{cm}^{-3}$). Il voit son hydrogène atomique se transformer en hydrogène moléculaire alors que son carbone est sous forme neutre ou ionisée ($N_\mathrm{CO} <$ quelques $10^{16}\,\mathrm{cm}^{-2}$ et $N_\mathrm{C} \sim 3.10^{17}\,\mathrm{cm}^{-2}$). Le gaz est soumis au champ UV typique inter-étoiles, ce qui devrait empêcher le développement d'une chimie même rudimentaire.

Les nuages sombres sont traditionnellement identifiés par leur forte extinction visuelle ($A_\mathrm{v} > 6\,\mathrm{mag}$, typiquement 10) et par leur émission CO. Le gaz des nuages sombres est neutre, froid (10 K), dense ($10^4\,\mathrm{cm}^{-3}$). Le gaz moléculaire est constitué d'hydrogène moléculaire et tout son carbone se trouve dans CO. Le gaz est bien protégé du champ de rayonnement UV, ce qui permet le développement d'une chimie complexe.

Les nuages translucents ont une extinction visuelle comprise entre 2 et 5. Ils forment la transition entre nuages diffus et nuages sombres.

Nous verrons par la suite que cette distinction par l'extinction visuelle n'est pas aussi simple. Il y a deux moyens complémentaires de caractériser observationnellement la transition du gaz diffus au gaz sombre.

4.1 Etudes en absorption derrière une source continuum

Le milieu interstellaire a été découvert en 1907 par l'étude de raies atomiques en absorption (NaI et CaII) devant le continuum visible d'étoiles. Les premières molécules (CN, CH et CH^+) ont aussi été détectées en absorption dans les années 1937–1940. Les raies en absorption UV de CO et H_2 ont été détectées en 1970–1971 avant d'être étudiées plus systématiquement par le satellite Copernicus. Cette méthode, qui est encore très utilisée de nos jours (cf. le satellite FUSE ou quelques programmes utilisant le dernier spectrographe UV du HST : COS), met justement en évidence les nuages diffus. Mais il est difficile de savoir si les propriétés mesurées sont celles du gaz diffus ou si elles sont dues à l'interaction entre l'étoile à l'origine du continuum visible ou UV et le gaz instellaire comme nous l'avons montré avec P. Boissé (professeur à l'UPMC) dans le cas de la ligne de visée menant à HD34078 [A10]. L'avantage majeur de cette technique est qu'elle permet une mesure directe et donc très précise de la densité de colonne de l'espèce

absorbante, indépendamment de tout transfert de rayonnement (un photon continuum absorbé égale une molécule absorbante).

H. Liszt (NRAO, USA) et R. Lucas (Joint ALMA Office, Chili) ont donc adapté cette méthode en radio-astronomie millimétrique avec l'étude de l'absorption par le gaz galactique de l'émission continuum brillante de quelques dizaines de quasars extragalactiques, assurant une mesure non-biaisée (par la source continuum) des propriétés du gaz diffus. Ce travail, que j'ai rejoint en 2003, a conduit à de nombreuses surprises, parmi lesquelles une importante (mais néanmoins limitée) chimie polyatomique : détection de HCO^+, CCH, C_3H_2, CN, HCN, HNC, H_2CO, NH_3 [A27, et références citées dans cet article] ; non-détection de CH_3OH et HC_5N [A16]. Cette chimie a parfois lieu dans des régions incapables d'exciter CO à des niveaux d'émission détectables. Les modèles standards de la chimie des nuages diffus prévoit des abondances chimiques inférieures d'au moins un ordre de grandeur à ce qui est observé. Les profils de raies ne montrent pas de traces évidentes de processus énergétiques (des chocs par exemple), qui permettraient d'activer une chimie chaude. En résumé, nous avons vu une chimie extraordinaire dans le gaz diffus, mais les données ne donnent pas encore de suggestions claires qui puissent l'expliquer. L'étape suivante est la recherche en émission de la structure du gaz par observation des nuages porteurs. Un des buts majeurs de ce travail est de comprendre si la cinématique des raies signale le dépôt d'énergie en quantité suffisante pour provoquer la chimie observée en absorption.

4.2 Etudes directes en émission

Pour former des nuages moléculaires géants, il faut dissiper localement l'énergie turbulente et magnétique responsable du support des nuages diffus contre l'effondrement gravitationnel. Bien que ces processus de dissipation soient mal connus, ils sont une source potentielle d'énergie pour provoquer la chimie du milieu diffus [A36]. Durant mon service militaire et ma thèse, j'ai mis au point avec D. Lis (Caltech, USA) et E. Falgarone (LERMA) des outils d'étude de la cinématique des raies de CO, permettant de caractériser la dissipation de la turbulence [A33, A38, A39]. Les résultats de ces outils statistiques sont d'autant plus probants que la taille de l'échantillon étudié est plus grande. Deux possibilités s'offrent dans le cadre du milieu interstellaire. Soit on augmente la taille de la région étudiée à résolution constante : la limite vient du risque d'étudier des régions soumises à des conditions physiques différentes. Soit on augmente la résolution à taille de région fixée : il est alors naturel de faire de l'imagerie grand-champ avec des interféromètres. Avec P. Hily-Blant et E. Falgarone, nous avons réalisé les deux options dans la même région du ciel appelée Polaris [A9, A18]. Les données du Plateau de Bure nous ont permis en particulier de mettre en évidence de nouvelles structures CO à très petite échelle (milli-parsec) : il s'agit de gradients d'émission très aigus à la fois spatialement et en vitesse, aux bords de régions où l'émission CO est relativement continue. Les gradients de vitesse locaux, jusque $780\,\mathrm{km\,s^{-1}\ pc^{-1}}$, sont les plus grands jamais mesurés dans une région sans formation active d'étoile. Une interprétation possible est que ces structures sont un lieu de dissipation de l'énergie turbulente à l'origine du CO vu en émission.

4.3 Combiner les deux approches

Depuis 2006, j'améliore avec H. Liszt et R. Lucas notre compréhension de la transition du gaz diffus au gaz sombre en combinant les deux approches sur les mêmes régions du ciel. Ce qui rend vraiment fructueux cet exercice est que les échelles spatiales échantillonnées par les deux méthodes dans le plan du ciel sont très différentes. La figure 4.1 montre par exemple le rougissement mesuré à une résolution angulaire de 6 minutes d'arc en fonction de la profondeur optique en HI mesurée en absorption devant des sources continuum qui ne sont pas résolues (sauf exception) à 1 seconde d'arc avec l'interféromètre du VLA. L'excellente corrélation (coefficient de corrélation égal à 0.9) entre ces deux grandeurs mesurées à des résolutions très différentes ne peut s'expliquer que de deux manières : soit le gaz HI ne présente pas de structures, soit le gaz HI absorbant est bien mélangé avec l'ensemble du gaz (atomique et moléculaire) tracé par l'extinction visuelle [A6]. Ainsi, nous nous demandons 1) quelle est la nature du nuage qui « héberge » la ligne de visée étudiée en absorption et 2) si les propriétés déduites par les études en absorption sont représentatives des caractéristiques de ce nuage hôte.

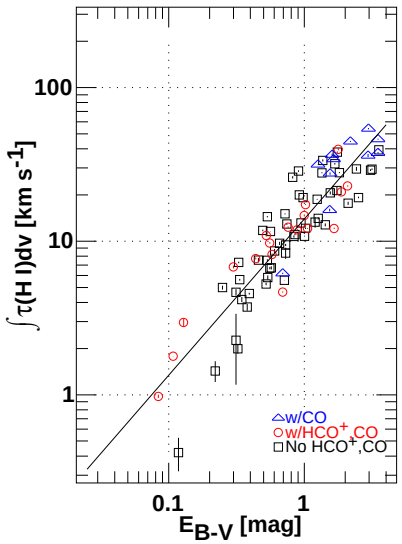

FIG. 4.1 – Absorption par l'hydrogène atomique (résolution angulaire: $< 1''$) en fonction du rougissement total mesuré dans la même direction (résolution angulaire: $\sim 6'$, Schlegel et al. 1998).

Nous avons par exemple analysé une carte de 7° de champ de vue à une résolution de $3'$ obtenue avec le télescope de NANTEN autour de la ligne de visée conduisant à l'étoile ζOph, ligne de visée archétype des études du milieu diffus en optique [A11]. Nous avons montré que l'étoile est occultée par un seul nuage hôte qui a une structure cinématique complexe et nullement par deux nuages distincts comme les études en absorption le laissaient supposer : les études en absorption ne capturent donc qu'une partie aléatoire des propriétés du nuage hôte. Ainsi, seule une étude statistique d'un grand nombre de lignes de visée observées en absorption permet de déduire le comportement intrinsèque du gaz diffus.

Nous avons aussi obtenu avec l'interféromètre du Plateau de Bure une carte de l'émission de ^{12}CO J=1–0 dans la direction du quasar NRAO150 sur un champ de vue de $100'' \times 100''$ à une résolution de $4''$ [A15]. Alors que les raies d'émission de ^{12}CO J=1–0 font typiquement 2-3 K à une résolution spatiale de l'ordre de la minute d'arc, nous avons obtenu ici des brillances maximum de 12-13 K parfois à moins de $6''$ de la direction de NRAO150. La présence de points brillants aussi proches d'une ligne de visée diffuse est une réelle surprise car il n'est pas intuitif *a priori* d'associer une faible extinction visuelle ($A_v \sim 1$ mag) à une forte émission en CO.

4.4 La luminosity CO par molécule H_2

Pendant les trois dernières années, nous avons imagé en ^{12}CO J=1–0 les nuages hôtes d'environ une dizaine d'autres lignes de visées à différentes latitudes galactiques avec le 30m de l'IRAM et le 12m de l'Arizona Radio Observatory. Nous échantillonnons ainsi deux types de

lignes de visée : 1) des lignes de visée diffuses ($A_{\rm v} \leq 1$) ; et 2) des lignes de visée classiquement appelées sombres ($A_{\rm v} \geq 6$). Les lignes de visées dites sombres se trouvent dans le plan de la Galaxie : elles sont en fait composées d'un ensemble de nuages diffus, chaque nuage ayant une extinction visuelle typique de 1. Par ailleurs, on observe des brillances de l'ordre de 10 K dès qu'on fait des cartes en émission, quelle que soit la latitude ou l'extinction visuelle. Ainsi, des lignes de visée dont on croit habituellement qu'elles font partie de nuages moléculaires géants sont en fait composées de gaz diffus [A6]. C'est possible car deux régimes physiques bien séparés produisent le même genre de brillance en ^{12}CO J=1–0 (typiquement 10 K) : d'une part, le gaz diffus à cause d'une excitation subthermale dans un gaz tiède ($30 - 60$ K) et à faible densité ($< 300 - 500\,{\rm cm}^{-3}$) ; d'autre part, le gaz moléculaire thermalisé à basse température (< 20 K) et à haute densité ($> 10^4\,{\rm cm}^{-3}$). Nous mettons ainsi en évidence aussi bien du gaz qui n'émet pas en CO (gaz sombre) que du gaz qui émet plus de CO que son contenu en hydrogène ne le laisse supposer (gaz surbrillant) [A1]. Le facteur de conversion CO-H_2 reste néanmoins typique parce que les luminosités CO par molécule de H_2 et les facteurs de couverture en surface du CO sombre ou surbrillant se compensent en moyenne.

Ces résultats sont d'une grande importance pour la compréhension 1) du gaz sombre détecté par FERMI (Abdo et Fermi/LAT collaboration, ApJ 2010, 710, 133) et PLANCK (Planck Collaboration, 2011, ArXiv e-prints 1101.2029), et 2) de l'utilisation du facteur $X_{\rm CO} = N_{\rm H_2}/W_{\rm CO}$ ($W_{\rm CO}$ étant l'aire intégrée de l'émission CO) dans l'indicateur d'efficacité de la formation des étoiles dans les galaxies extérieures ($L_{\rm FIR}/M_{\rm H_2}$). Cette problématique est au cœur de plusieurs conférences internationales sur le milieu interstellaire. Cela a par exemple permis de mettre en évidence la contradiction entre nos mesures [C5, C1] et le résultats de modèles récents (Glover et al. 2010, MNRAS, 404, 2-29). Cette contradiction provient d'une chimie inadaptée au milieu diffus dans les modèles utilisés (Shetty et al. 2011, MNRAS, 412, 1686).

A&A 507, 355–368 (2009)
DOI: 10.1051/0004-6361/200810963
© ESO 2009

Astronomy & Astrophysics

Intermittency of interstellar turbulence: extreme velocity-shears and CO emission on milliparsec scale⋆

E. Falgarone[1], J. Pety[1,2], and P. Hily-Blant[3]

[1] LERMA/LRA, CNRS, UMR 8112, École Normale Supérieure & Observatoire de Paris, 24 rue Lhomond, 75005 Paris, France
e-mail: falgarone@lra.ens.fr
[2] Institut de Radio Astronomie Millimétrique, 300 rue de la Piscine, 38406 Saint-Martin-d'Hères, France
e-mail: pety@iram.fr
[3] LAOG, CNRS UMR 5571, Université Joseph Fourier, BP53, 38041 Grenoble, France
e-mail: pierre.hilyblant@obs.ujf-grenoble.fr

Received 13 September 2008 / Accepted 29 September 2009

ABSTRACT

Aims. The condensation of diffuse gas into molecular clouds and dense cores occurs at a rate driven largely by turbulent dissipation. This process still has to be caught in action and characterized.
Methods. We observed a mosaic of 13 fields with the IRAM-PdB interferometer (PdBI) to search for small-scale structure in the ^{12}CO(1−0) line emission of the turbulent and translucent environment of a low-mass dense core in the Polaris Flare. The large size of the mosaic ($1' \times 2'$) compared to the resolution ($4''$) is unprecedented in the study of the small-scale structure of diffuse molecular gas.
Results. The interferometer data uncover eight weak and elongated structures with thicknesses as small as ≈3 mpc (600 AU) and lengths up to 70 mpc, close to the size of the mosaic. These are not filaments because once merged with short-spacings data, the PdBI-structures appear to be the sharp edges, in space and velocity-space, of larger-scale structures. Six out of eight form quasi-parallel pairs at different velocities and different position angles. This cannot be the result of chance alignment. The velocity-shears estimated for the three pairs include the highest values ever measured in regions that do not form stars (up to 780 km s^{-1} pc^{-1}). The CO column density of the PdBI-structures is in the range N(CO) = 10^{14} to 10^{15} cm^{-2} and their H_2 density, estimated in several ways, does not exceed a few 10^3 cm^{-3}. Because the larger scale structures have sharp edges (with little or no overlap for those that are pairs), they have to be thin layers of CO emission. We call them SEE(D)S for sharp-edged extended (double) structures. These edges mark a transition, on the milliparsec scale, between a CO-rich component and a gas undetected in the ^{12}CO(1−0) line because of its low CO abundance, presumably the cold neutral medium.
Conclusions. We propose that these SEE(D)S are the first directly-detected manifestations of the intermittency of interstellar turbulence. The large velocity-shears reveal an intense straining field, responsible for a local dissipation rate several orders of magnitude above average, possibly at the origin of the thin CO layers.

Key words. ISM: evolution – ISM: kinematics and dynamics – ISM: molecules – ISM: structure – ISM: general – turbulence

1. Introduction

Turbulence in the interstellar medium (ISM) remains a puzzle in spite of dedicated efforts on observational and numerical grounds. This is because it is compressible, magnetized, and multi-phase, but also because of the huge range of scales separating those of injection and dissipation of energy. Moreover, because turbulence and magnetic fields are the main support of molecular clouds against their self-gravity, turbulent dissipation is a key process among all those eventually leading to star formation (see the reviews of Elmegreen & Scalo 2004; Scalo & Elmegreen 2004).

In molecular clouds, turbulence is observed to be highly supersonic with respect to the cold gas. It is thus anticipated to dissipate in shocks in a cloud-crossing time (i.e. ≈ a few 10 Myr for giant molecular clouds of 100 pc with internal velocity dispersion of a few km s^{-1}). Magnetic fields do not significantly slow the dissipation down (Mac Low et al. 1998). Actually, this is the basis of the turbulent models of star formation (Mac Low & Klessen 2004) – one of the two current scenarii of low-mass star formation – in which self-gravitating entities form in the shock-compressed layers of supersonic turbulence.

However, while it is unquestionable that the ISM is regularly swept by large-scale shock-waves triggered by supernovae explosions that partly feed the interstellar turbulent cascade (Joung & Mac Low 2006; de Avillez & Breitschwerdt 2007), the smallest scales, barely subparsec in these simulations, are still orders of magnitude above the smallest observed structures and are unlikely to provide a proper description of the actual dissipation processes. Whether turbulent dissipation occurs primarily in compressive (curl-free) or in solenoidal (divergence-free) modes in the interstellar medium has therefore to be considered as an open issue.

An ideal target to study turbulent dissipation is the diffuse molecular gas because it is the component in which dense cores form, with less turbulent energy density than their environment. The word "diffuse" here comprises all material in the neutral ISM at large that is not in dense cores i.e. whose total hydrogen column density is less than a few 10^{21} cm^{-2}. This

⋆ Based on observations obtained with the IRAM Plateau de Bure interferometer and 30m telescope. IRAM is supported by INSU/CNRS (France), MPG (Germany), and IGN (Spain).

includes the mixture of cold and warm neutral medium (CNM and WNM), the edges of molecular cloud complexes (also called translucent gas), and the high latitude clouds. Diffuse gas builds up a major mass fraction of the ISM. Actually, on the 30 pc scale, Goldsmith et al. (2008) find that half the mass of the Taurus-Auriga-Perseus complex lies in regions having H_2 column density below 2.1×10^{21} cm^{-2}.

Turbulent dissipation may also provide clues to the "outstanding mysteries" raised by observations of diffuse molecular gas (see the review of Snow & McCall 2006): the ubiquitous small scale structure, down to AU-scales (Heiles 2007), the remarkable molecular richness found in this hostile medium, weakly shielded from UV radiation (e.g. Liszt & Lucas 1998; Gredel et al. 2002), the bright emission in the H_2 pure rotational lines exceeding the predictions of photon-dominated region (PDR) models (Falgarone et al. 2005; Lacour et al. 2005), the ^{12}CO small-scale structures with a broad range of temperatures, H_2 densities and linewidths that preclude a single interpretation in terms of cold dense clumps (Ingalls et al. 2000, 2007; Heithausen 2004, 2006; Sakamoto & Sunada 2003).

The present paper extends the investigation of turbulence down to the mpc-scale in the translucent environment of a low-mass dense core of the Polaris Flare. Over the years, this investigation has progressed along three complementary directions:

(i) A two-point statistical analysis of the velocity field traced by the ^{12}CO line emission, and conducted on maps of increasing size. Using numerical simulations of mildly compressible turbulence, Lis et al. (1996) and Pety & Falgarone (2003) first proposed that the non-Gaussian probability distribution functions (*pdf*s) of line centroid velocity increments (CVI) be the signatures of the space-time intermittency of turbulence[1] because the extrema of CVI (E-CVI) trace extrema of the line-of-sight average of the modulus of the plane-of-the-sky (*pos*) vorticity. Statistical analysis conducted on parsec-scale maps in two nearby molecular clouds have revealed that these extrema form parsec-scale coherent structures (Hily-Blant et al. 2008; Hily-Blant & Falgarone 2009, resp. Paper III, HF09).

(ii) A detailed analysis (density, temperature, molecular abundances) of these coherent structures, based on their molecular line emission. The gas there is more optically thin in the ^{12}CO lines, warmer and more dilute than the bulk of the gas (Hily-Blant & Falgarone 2007, hereafter Paper II), and large HCO^+ abundances, unexpected in an environment weakly shielded from UV radiation, have been detected there (Falgarone et al. 2006, Paper I).

(iii) Chemical models of non-equilibrium warm chemistry triggered by bursts of turbulent dissipation (Joulain et al. 1998). The most recent progresses along those lines include the chemical models of turbulent dissipation regions (TDRs) by Godard et al. (2009) and their successful comparison to several data sets, among which new submillimeter detections of $^{13}CH^+(1-0)$ (Falgarone et al., in preparation).

[1] Intermittency here refers to the empirical property of high Reynolds number turbulence to present an excess of rare events compared to Gaussian statistics, this excess being increasingly large as velocity fluctuations at smaller and smaller scales are considered (see the review of Anselmet et al. 2001). Although the origin of intermittency is still an open issue (but see Mordant et al. 2002; Chevillard et al. 2005; Arnéodo et al. 2008), it is quantitatively characterized by the anomalous scaling of the high-order structure functions of the velocity and the shape of non-Gaussian *pdf*s of quantities involving velocity derivatives (e.g. Frisch 1995).

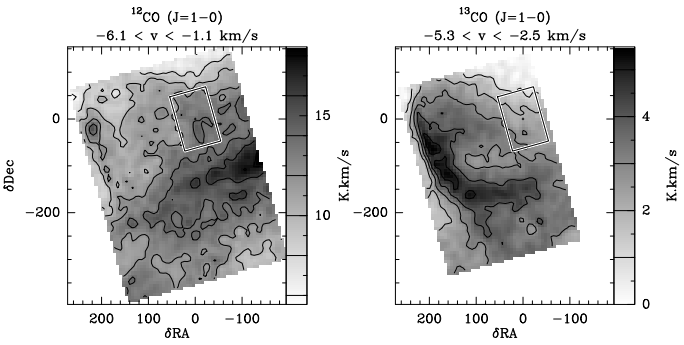

Fig. 1. The location of the 13-field mosaic observed at the Plateau de Bure interferometer (centered at RA = 01:55:12.26 and Dec = 87:41:56.30) is shown as the box on top of the integrated emission of the ^{12}CO and ^{13}CO (J = 1–0) maps obtained at the IRAM-30m. This is a place of low, almost featureless, CO line brightness. The arc-like structure visible in ^{13}CO traces the outer layers of the low-mass dense core. Contour levels are shown in the wedges.

The ^{12}CO(J = 2–1) observations of the Polaris Flare with unprecedented angular resolution and dynamic range are the first to evidence the association between extrema of CVI and observed velocity-shears[2] (HF09). No shock signature (density and/or temperature enhancement, SiO detection) has been found in the coherent structure of E-CVI identified in the Polaris Flare (Hily-Blant and Falgarone, in preparation). All the above suggest (but does not prove yet) that the coherent structures carrying the statistical properties of intermittency are regions of intense velocity-shears where dissipation of turbulence is concentrated.

The ^{12}CO(1–0) observations reported in this paper have been performed in a field located on one branch of the Polaris Flare E-CVI structure, in the translucent and featureless environment of a dense core (Fig. 1). The outline of the paper is the following: the observations and data reduction are described in Sect. 2. The observational results are given in Sect. 3. The characterization of the emitting gas is made in Sect. 4 and we discuss, in Sect. 5, the possible origin and nature of the CO structures that we have discovered. Section 6 puts our results in the broad perspective provided by other data sets and Sect. 7 compares them to chemical model predictions and numerical simulations of turbulence. The conclusions are given in Sect. 8.

2. IRAM Plateau de Bure Interferometer observations

We used the IRAM Plateau de Bure Interferometer (PdBI) to image, at high angular resolution and in the ^{12}CO (J = 1–0) line, a region of $\sim 1' \times 2'$ in the translucent environment of a dense core in the Polaris Flare (Heithausen 1999; Heithausen et al. 2002). The location of the target field is shown in Fig. 1 as a rectangle on larger scale, single-dish maps of integrated ^{12}CO(J = 1–0) and ^{13}CO(J = 1–0) emission from (Falgarone et al. 1998, hereafter F98). The average column density in this region ($\sim 10^{21}$ cm^{-2}) is about 100 times smaller than in the central parts of the dense core ($\sim 10^{23}$ cm^{-2}), 3 arcmin westwards. The average integrated ^{13}CO intensity over the mosaic area is weak $W(^{13}\mathrm{CO}) = 2$ K km s^{-1}.

[2] We use velocity-shear rather than velocity-gradient because the observations provide cross-derivatives of the velocity field, i.e. the displacement measured in the plane-of-the-sky (*pos*) is perpendicular to the line-of-sight velocity.

Table 1. Observation parameters. The projection center of all the data displayed in this paper is: $\alpha_{2000} = 01^h55^m12.26^s$, $\delta_{2000} = 87°41'56.30''$.

Molecule	Transition	Frequency GHz	Instrument	Config.	Beam arcsec	PA °	Vel. Resol. km s^{-1}	Int. Time hours	Noise K
^{12}CO	($J = 1–0$)	115.271195	PdBI	C&D	4.4×4.2	80	0.1	65.2/180[a]	0.23[b]
		115.271195	30m	—	21.3	0	0.1	—/—	0.40
^{13}CO	($J = 1–0$)	110.201354	30m	—	22.3	0	0.1	—/—	0.19

[a] Two values are given for the integration time: the 5 antennae array equivalent on-source time and the telescope time.
[b] The noise value quoted here is the noise at the mosaic phase center.

2.1. Observations

The observations dedicated to this project were carried out in 1998 and 1999 with the IRAM interferometer at Plateau de Bure in the C and D configurations (baseline lengths from 24 m to 161 m). One correlator band of 10 MHz was centered on the ^{12}CO ($J = 1–0$) frequency to cover a ~23 km s^{-1} bandwidth with a channel spacing of 39 kHz, i.e. ~0.1 km s^{-1}. Four additional correlator bands of 160 MHz were used to measure the 2.6 mm continuum over the 500 MHz instantaneous IF-bandwidth then available.

We observed a 13-field mosaic centered on $\alpha_{2000} = 01^h55^m12.26^s$, $\delta_{2000} = 87°41'56.30''$. The field positions followed a compact hexagonal pattern to ensure Nyquist sampling in all directions and an almost uniform noise over a large fraction of the mosaic area (see Fig. A.1 of Appendix A). The imaged field-of-view is about a rectangle of dimension of $85'' \times 130''$ oriented at a position-angle of 15° (because the (RA, Dec) PdBI field was selected in maps made in (l, b) coordinates).

Polaris being a circumpolar source, this project was a good time-filler. It was thus observed at 22 different occasions, giving a total of about 180 hours of *telescope* time with most often 3 or 4 antennas and rarely 5 antennas. Taking into account the time for calibration and data filtering this translates into *on-source* integration time of useful data of 65.2 h for a full 5-antenna array. The typical 2.6 mm resolution of these data is 4.3″. The data used to produce the missing short-spacings are those of the IRAM key-program, fully described in F98 (see also Table 1).

2.2. Data reduction

The data processing was done with the GILDASf[3] software suite (Pety 2005). Standard calibration methods implemented in the GILDAS/CLIC program were applied using close bright quasars as calibrators. The calibrated *uv* tables were processed through an Hanning filter which spectrally smoothed the data (to increase the intensity signal-to-noise ratio) while keeping the same velocity/frequency channel spacing.

All other processing took place into the GILDAS/MAPPING software. Following Gueth et al. (1996), the single-dish map from the IRAM-30m key program were used to create the short-spacing visibilities not sampled at the Plateau de Bure. These were then merged with the interferometric observations. Two different sets of *uv* tables (i.e. with and without short-spacings) were then imaged using the same method. Each mosaic field was imaged and a dirty mosaic was built combining those fields in the following optimal way in terms of signal-to-noise ratio (Gueth 2001)

$$J(\alpha,\delta) = \sum_i \frac{B_i(\alpha,\delta)}{\sigma_i^2} F_i(\alpha,\delta) \Big/ \sum_i \frac{B_i(\alpha,\delta)^2}{\sigma_i^2}.$$

[3] See http://www.iram.fr/IRAMFR/GILDAS for more information about the GILDAS softwares.

In this equation, $J(\alpha,\delta)$ is the brightness distribution in the dirty mosaic image, B_i are the response functions of the i primary antenna beams, F_i are the brightness distributions of the individual dirty maps and σ_i are the corresponding noise values. As may be seen in this expression, the dirty intensity distribution is corrected for primary beam attenuation, which makes the noise level spatially heterogeneous. In particular, noise strongly increases near the edges of the field of view. To limit this effect, both the primary beams used in the above formula and the resulting dirty mosaics are truncated. The standard level of truncation is set at 20% of the maximum in MAPPING.

Deconvolution methods were different for both data sets (i.e. with and without short-spacings). The dirty image of the PdBI-only data was deconvolved using the standard Clark CLEAN algorithm. One spatial support per channel map was defined by selecting positive regions on the first clean image which was obtained without any constraint. This geometrical constraint was then used in a second deconvolution. While it can bias the result, this two-step process is needed when deconvolving interferometric observations of extended sources without short-spacings. Indeed, the lack of short-spacings implies (among other things) a zero valued integral of the dirty beam and dirty image, which in turn perturbs the CLEAN convergence when the source is extended because the algorithm searches as many positive as negative CLEAN components. The only way around is to guide the deconvolution by the definition of a support where the signal is detected. On the other hand, the deconvolution of the combined short-spacings and interferometric *uv* visibilities can process blindly (i.e. without the possible bias of defining a support where to search for CLEAN components). This is what has been done and the good correlation of the structures seen in the deconvolved images of the data with and without short-spacings (see Figs. 4 and 5) gives us confidence in our deconvolution of the PdBI-only data.

The two resulting data cubes (with and without short-spacings) were then scaled from Jy/beam to T_{mb} temperature scale using the synthesized beam size (see Table 1). Final noise rms measured at the centered of the mosaic is about 0.23 K in both data cubes.

3. Observational results

3.1. PdBI structures: sharp edges of extended structures

At the adopted cloud distance of $d = 150$ pc, 1″ corresponds to 0.75 mpc or 150 AU, so that the spatial resolution of the PdBI data is 3.2 mpc or 660 AU.

The integrated emission detected with the PdBI is displayed in Fig. 2 (left panel), with the corresponding signal-to-noise ratio (right panel). The integrated emission covers most of the mosaic area. This is no longer true when this emission is displayed in velocity slices (Fig. 3, top panels). Several distinct structures are detected in addition to the bright CO peak, at

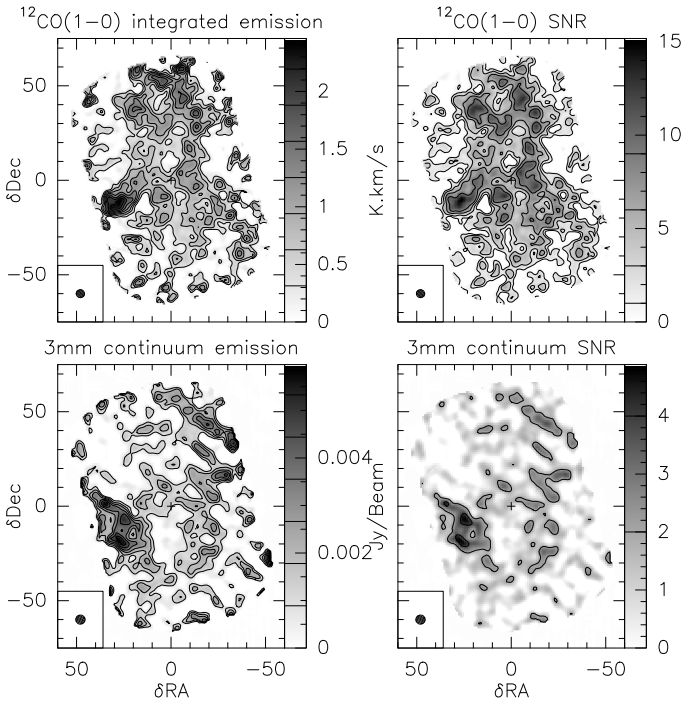

Fig. 2. Map of integrated emission of the PdBI data (*top left*), and signal-to-noise ratio (*top right*) for the ^{12}CO (J = 1−0) line. Same for the 3 mm continuum emission (*bottom panels*). The synthesized beam is shown in the bottom left inserts.

velocities [−3.1, −2.3] km s^{-1}. Most are weak (the first level in the PdBI channel maps of Fig. 3 is 3σ) but they extend over many contiguous synthesized beams (10 to 30).

The PdBI data merged with the short-spacings provided by the 30m telescope and the ^{12}CO(1−0) emission detected by the IRAM-30m telescope are displayed in the same velocity-slices, for comparison, in Fig. 3, central and bottom panels respectively. Most of the structures seen by the PdBI lie at the edge in space and in velocity space of extended emission present in the single-dish channel maps. This property is most visible for the two structures in the north-west of the mosaic over [−4.8, −4.4] km s^{-1} and [−2, −1.2] km s^{-1}, and in the central region at v = −2.8 km s^{-1}. It is even better seen by comparing the single-dish maps before and after combination with the PdBI data. The single-dish maps are changed in two-ways: the structures exhibit sharper, more coherent boundaries and these boundaries extend further in velocity-space (e.g. channels −4.7 and −2.3 km s^{-1}). In a given channel of width Δv_c, the size of the detected structures in the CO emission Δx_c is inversely proportional to the velocity-shear, $\Delta x_c = \Delta v_c/(\partial v_{LSR}/\partial x_{pos})$. Hence, the detection of small-scale structures at the edge of the velocity coverage of larger-scale structures may be favored by an increase of the velocity shear at these edges.

The fact that these structures appear both in PdBI-only data and in combined (PdBI+30m) data gives confidence in their reality, independently of the deconvolution techniques.

In summary, the interferometer is sensitive by construction to small-scale (i.e. sharp) variations of the space-velocity CO distribution. It happens that the sharp structures detected by the interferometer lie at the edge in space and velocity of regions of shallow CO emission that extend over at least arcminutes, as displayed in the 30m channel maps. The PdBI-structures are therefore the sharp edges of extended structures.

3.2. Observed characteristics of the PdBI structures

We have identified eight structures in the space-velocity ^{12}CO(J = 1−0) PdBI data cube that are well separated from one another in direction and in velocity. They are shown in Fig. 4, each drawn over its proper velocity range. The right panels show the PdBI data combined with 30m data over the same velocity ranges to further illustrate that the PdBI filtering emphasizes the sharpness of the edge of the space-velocity structures. Figure 4 also shows that the single-dish structures cover a large fraction of the mosaic area. For instance, in the case of structure #1, the single-dish structure extends over the whole southern half of the mosaic, while for structure #5 it almost covers the northern half.

The observed properties of the 8 PdBI structures are given in Table 2. The peak ^{12}CO(J = 1−0) temperature is that detected by the PdBI, therefore the excess above the extended background, resolved out by the PdBI. The size $\theta_{1/2}$ is the half-power thickness of the elongated structures, deconvolved from the beam size. The projected thickness, in mpc, is called $l_\perp$ by opposition to the unknown depth along the line-of-sight (*los*), called $l_\parallel$. The position-angle PA is that of the direction defined, within ±10°, by the three brightest pixels of each structure. When they are not aligned, as in the case of #8, we determine a direction with the meaning of a least-square fit. It corresponds to an average PA over the detected structure that does not take into account the substructure visible in Fig. 6 for instance. Because of their different velocity width and CO line temperature, the CO integrated brightness of the eight structures varies by a factor 25.

Most of the PdBI-structures are elongated and straight with different position-angles in the sky. Interestingly, they do not shadow each other in space and in velocity space (i.e. each fills only a small area of the mosaic in a small velocity interval, and the positions and areas of the detected structures are different). Their cumulative surface filling factor in the mosaic field is large, $f_S \approx 0.5$ (Fig. 2), i.e. $f_S = 0.6$ for the structures detected at more than 1-sigma and $f_S = 0.3$ for 3-sigma detections. However, the fraction of the single-dish power (integrated over the mosaic) seen by the PdBI in the ^{12}CO(1−0) line is low. It depends on the velocity interval: it varies between 2% in the ^{12}CO line-core (defined as the velocity range, [−5.0, −3.5] km s^{-1}, over which the single-dish ^{13}CO/^{12}CO is the largest, see F98), and 6% in the line-wings. Figure 5 displays the emission profile of the 8 PdBI-structures with the single-dish ^{12}CO and ^{13}CO(J = 1−0) emissions over the same area (defined by the polygons of Fig. 4).

Last, the PdBI-structures cover the full velocity range of the single-dish CO line (see bottom panel of Fig. 5) including the far line-wings (e.g. structure #2 at −5.5 km s^{-1}). Note however that the spectrum integrated over the whole mosaic peaks at −3 km s^{-1}, in the wing of the single-dish ^{12}CO line while its minimum, around −4.5 km s^{-1}, coincides with the peak of the single-dish ^{13}CO line (i.e. line core). The broad velocity distribution of the PdBI-structures within the single-dish line coverage ensures that they are not artefacts of radiative transfer. If they were, they would appear preferentially at extreme velocities because CO photons escape probability is larger there. There may be a small effect since the power fraction in the line-wings is slightly larger than in the line-core, but these fractions are a few percent in each case. The structures found are therefore real edges in space and velocity-space of larger structures.

In this respect, it is interesting to place each PdBI-structure in its ^{12}CO(1−0) larger-scale environment at the appropriate velocity (Fig. 8). The PdBI-structures, marked as polygons, lie at the edge of structures that extend beyond the field of the mosaic,

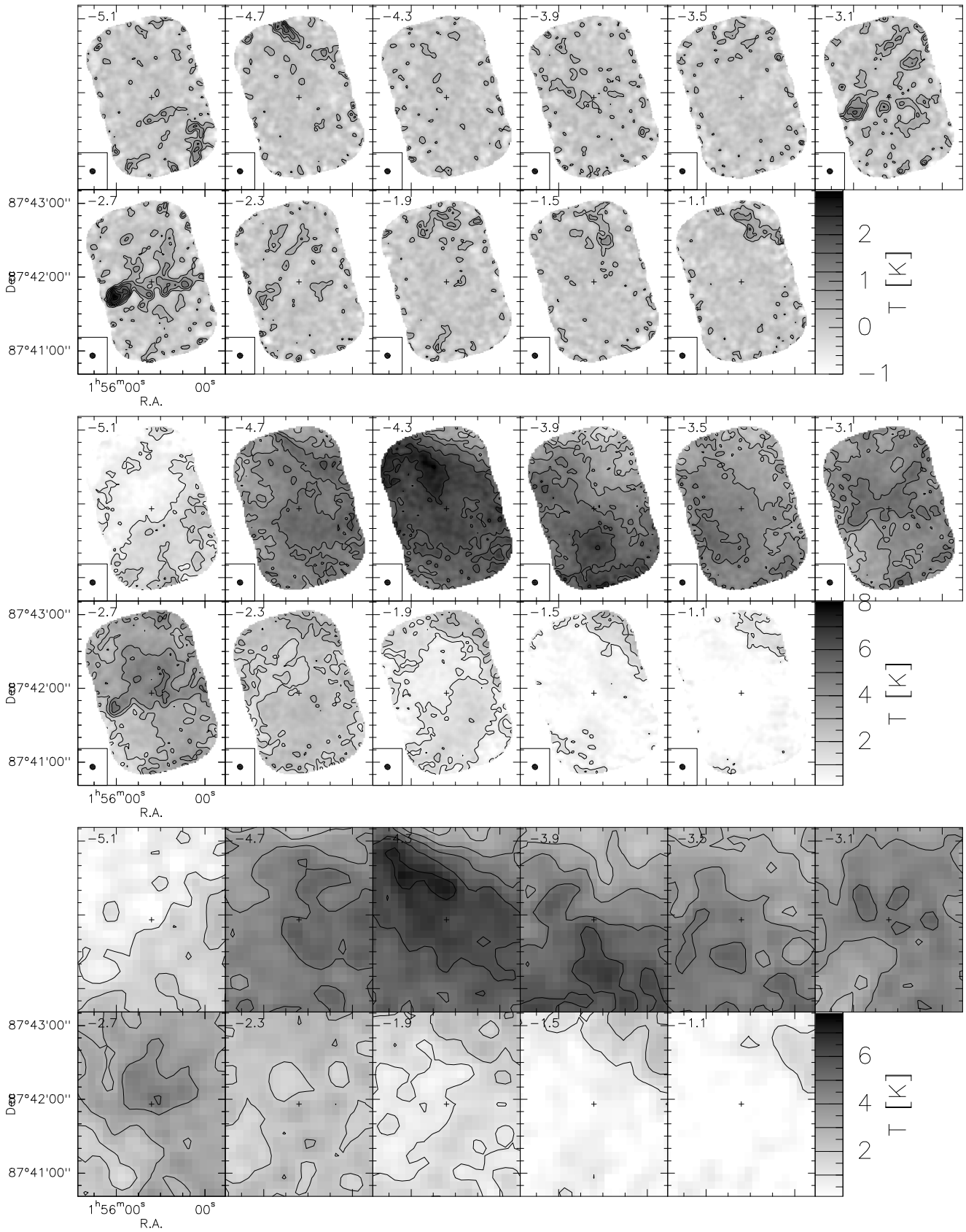

Fig. 3. *From top to bottom*, maps of the PdBI, PdBI+30m and 30m of ^{12}CO(1−0) emission integrated over the same velocity slices of 0.3 km s^{-1} centered as indicated.

up to ∼300″ or 0.2 pc. In the case of structures #3, #4 and #5, the orientation of the edges of the large-scale patterns is more visible in the ^{13}CO(1−0) maps (Fig. 9), likely because of the ^{12}CO(1−0) optical depth. This coincidence strongly suggests that the

Table 2. Spatial and kinematic characteristics of the ^{12}CO PdBI-only structures.

Structure	$v_{\rm min}$	$v_{\rm max}$	$\Delta v_{1/2}$	$T_{\rm peak}$	W(CO)	$\theta_{1/2}$	$l_\perp$ [a]	PA	$n_{\rm H_2}^{\rm max}$ [b]
	km s^{-1}	km s^{-1}	km s^{-1}	K	K km s^{-1}	arcsec	mpc	$^\circ$	cm^{-3}
1	–5.7	–5.2	0.1	0.6	0.06	4	3.0	109	1000
2	–5.6	–5.4	0.2	1.8	0.36	10	7.5	173	2400
3	–5.2	–4.8	0.2	2.4	0.48	9	6.8	62	3200
4	–4.3	–4.1	0.1	1.2	0.12	8	6.0	59	1000
5	–3.4	–2.6	0.4	4	1.6	12	9.0	91	8900
6	–3.4	–2.6	0.25	1.2	0.3	10	7.5	161	2000
7	–3.2	–3.0	0.15	1.2	0.18	15	11.3	173	800
8	–1.7	–1.3	0.15	1.2	0.18	9	6.8	59	1200

[a] Projected thickness of the filamentary structures deconvolved from beam size; [b] upper limit because computed as $n_{\rm H_2} = N({\rm H_2})/l_\perp$ instead of using $l_\parallel$ with $N({\rm H_2})$ derived from W(CO) (see text).

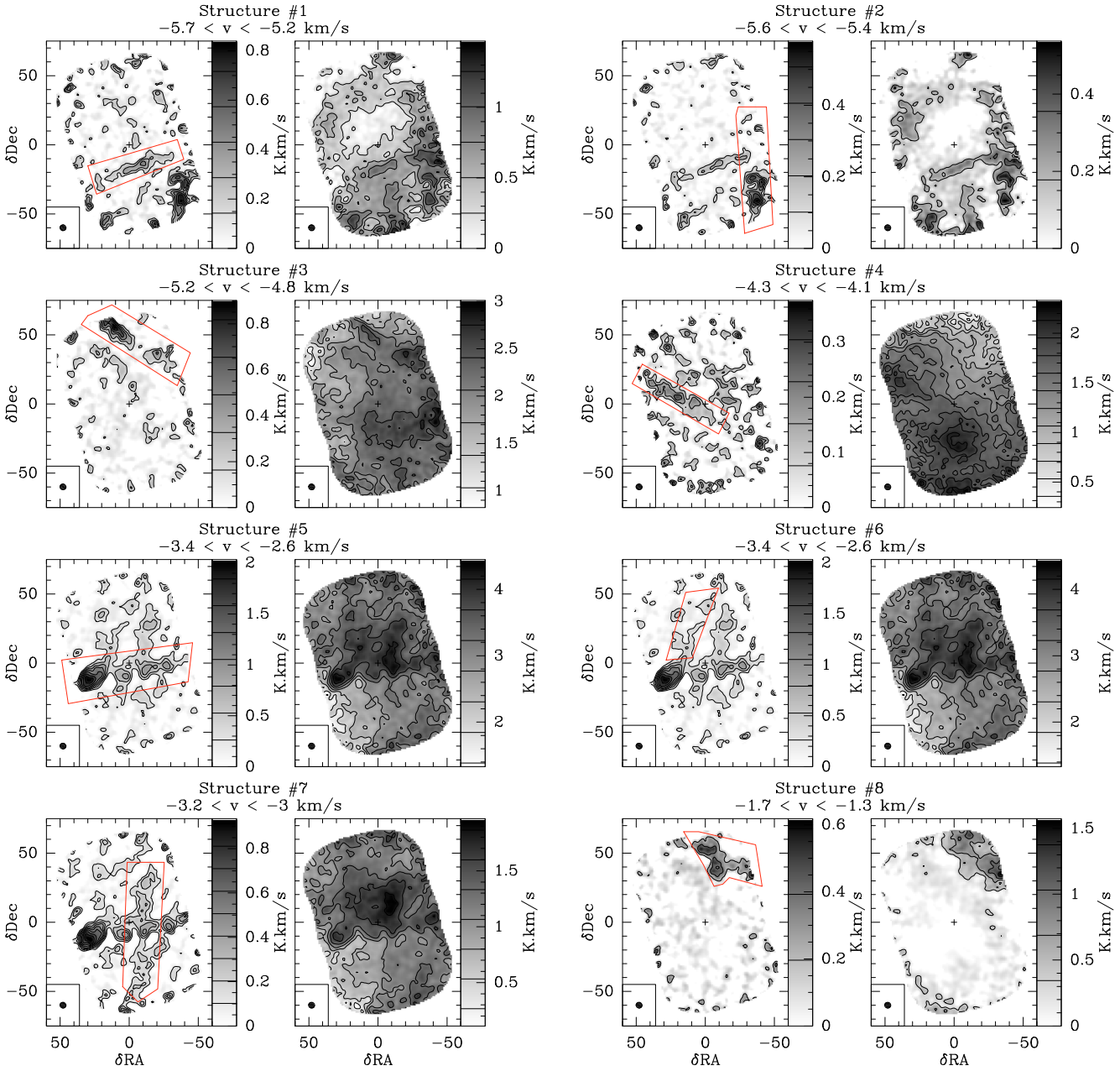

Fig. 4. The 8 structures described in Table 1. *Left panels*: PdBI-only ^{12}CO(1−0) emission integrated over the indicated velocity interval appropriate to each structure. *Right panels*: same for the combined PdBI+30m mission. The polygons show the area over which the CO spectra of Fig. 5 are computed.

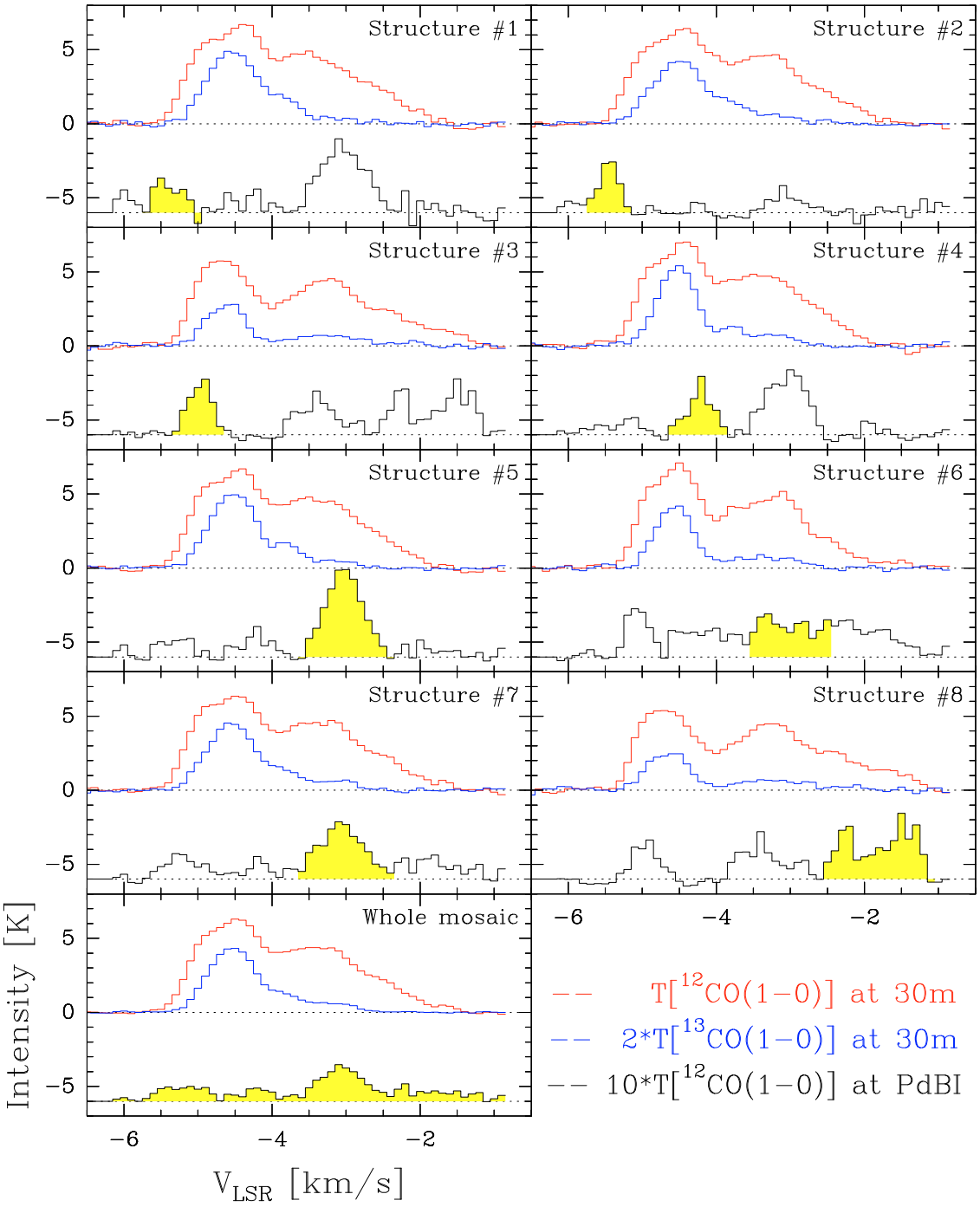

Fig. 5. Comparison of spectra integrated over either the polygons defined in Fig. 4 and the whole mosaic. The ^{12}CO and ^{13}CO (J = 1–0) single-dish spectra are shown resp. in light and darker grey, while the PdBI only ^{12}CO (J = 1–0) spectra is shown in black. ^{13}CO amplitude have been multiplied by a factor of two and PdBI only ^{12}CO amplitude by a factor of 10. Note that *i)* only a small fraction of the single-dish flux is recovered at PdBI and *ii)* the centroid velocities of the small-scale structures are all, but one, outside that of the ^{13}CO peak.

orientation of the PdBI-structures is not only real but also rooted in the larger-scale environment.

3.3. Pairs of parallel structures

One of the most challenging finding of this study is the fact that among the eight elongated PdBI-structures, six form 3 close pairs (separated by less than 20″ in projection) of structures parallel within ±10° (Table 2 and Fig. 4). These are the pairs of structures [#3, #8], [#1, #5] and [#6, #7]. The average position-angles of each pair $\overline{\mathrm{PA}}$ = 60, 100 and 168° are all different. Since the structures (at least in the two first pairs) are at different velocities, they are not due to artefacts of the deconvolution process.

The probability of a chance association of these three pairs in the field of the mosaic is estimated to be at most 4×10^{-9}. It is the cube of the probability of having one close pair of parallel structures. The latter is the product of the probability, equal to 5.4×10^{-3}, that two, out of eight, randomly oriented straight structures be aligned within ±10° of each other (i.e. be together in a

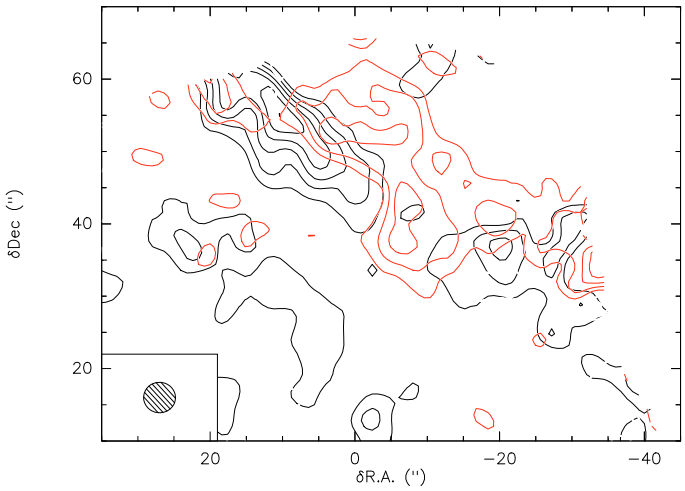

Fig. 6. Structures #3 at -5 km s^{-1} and #8 at -1.5 km s^{-1} overplotted (resp. black and red contours) to display their close spatial correlation.

solid angle $\Delta\Omega = 0.1$ sr), by that (ranging between 0.2 and 0.3 depending on the orientation of the pair) to be separated in projection by less than 20″ in a mosaic of $1' \times 2'$. The probability of a chance association is only slightly underestimated if one considers the structure #8 that is not straight, strictly speaking.

Since the probability of a chance association of the observed pairs is so low, we infer that the pairs are real associations. This physical connexion is supported by the detail of the spatial distribution of the ^{12}CO emission integrated over the two velocity ranges of structures #3 and #8 in Fig. 6: the hole, in the low-velocity emission is filled in by high-velocity emission, while a common average orientation exists over $\sim 1'$ for the pair.

Two position-velocity cuts (Fig. 7) across the pair [#3, #8] further illustrate what is meant by sharp edges and real association. The cut across the PdBI-only data cube (left panel) shows two CO peaks centered at offset positions 40″ (resp. 46″) and velocities -4.9 km s^{-1} (resp. -1.6 km s^{-1}) for the low- and high-velocity component respectively. These resolved peaks are located exactly at the terminal pixels of the larger-scale structures visible at the same velocities in the cut across the PdBI+30m data cube (right panel). On this cut, the low-velocity component may be followed over all offsets below ≈46″, while the high-velocity component is visible at all offsets above ≈40″. This cut also illustrates a clear difference between the two velocity components: the velocity of structure #3 (peak at -5 km s^{-1} in the PdBI spectrum of Fig. 5) falls within the velocity coverage of the bright extended gas (^{12}CO and ^{13}CO line core in the single-dish spectra) while that of structure #8 (peak at -1.5 km s^{-1} in the PdBI spectrum of Fig. 5) is not blended with any other emission in that extreme velocity range and appears as a weak emission in the single-dish spectrum (i.e. a line-wing). Such blendings in space and velocity projections with extended components resolved out by the PdBI observations (Fig. 7, right panel) explain why such pairs of structures are so difficult to recognize in single-dish observations or low sensitivity interferometric observations.

The PdBI-structures cannot therefore be understood as isolated entities. Not only are they the sharp edges of larger CO-structures seen in the single-dish maps but also 6 out of 8 of these edges are paired. In the following, we will call the CO extended structures bounded by sharp edges either sharp-edged extended structures (SEES) or sharp-edged extended double structures (SEEDS) when they belong to a pair, to emphasize this essential property.

3.4. Velocity shears

The pairs being real associations, we ascribe a velocity-shear to each of them. The projected separation $\delta l_\perp$ and velocity difference $\delta v_{\rm LSR}$ between the low- and high-velocity components of each pair provide a measure of the velocity-shear $\delta v_{\rm LSR}/\delta l_\perp$. We cannot determine whether this measure is a lower or upper limit of the true velocity-shears because of the projection effects: both the separation measured in the *pos* and the velocity difference are lower limits.

The results are given in Table 4. The method used is illustrated in Fig. 7 (left panel) for the pair [#3, #8]: the projected separation between the low- and high-velocity components is 6″ or 4.5 mpc while the velocity separation is 3.5 km s^{-1}, hence a velocity-shear of 777 km s^{-1} pc^{-1}, the largest ever measured in CO emission in a molecular cloud devoid of star formation activity. These values correspond to an average over several positions along the shear direction, including those where the two velocity components partially overlap. The separation is therefore slightly underestimated by the averaging. Note that one pair only, [#6, #7], has a very small velocity-shear, probably because, in that case, the two velocity components involved in the shear are mostly in the *pos*. A rate-of-strain, defined as $a = \frac{1}{2}\delta v_{\rm LSR}/\delta l_\perp$, and timescale $\tau = a^{-1}$, are also given to help comparison with chemical models (Sect. 7). The large observed velocity-shears translate into timescales as short as a few 10^3 yr, if the Lagrangian and Eulerian views of the fluid can be exchanged (see Mordant et al. 2002).

3.5. The SEE(D)S are layers of CO emission

The small-scale structures detected by the PdBI have properties never seen before because the present observations are most sensitive and the field of view is large in comparison to the resolution: (1) they are not clumps, but elongated structures, only bounded by the limited size of the mosaic; (2) they all mark a sharp fall-off of the CO emission in selected velocity ranges: they are not isolated filaments, but the sharp edges (3 to 11 mpc in projection), simultaneously in space and velocity-space, of larger structures, the SEE(D)S, extending beyond the mosaic ($l > 0.2$ pc); (3) six of these form three pairs of parallel structures at different velocities, with a small projected separation and the velocity-shears estimated for two of these pairs, several 100 km s^{-1} pc^{-1}, are the largest ever measured in non-star forming clouds.

If the SEE(D)S were CO-emitting volumes (i.e. 3-dimensional structures in space) of characteristic dimension l, their edges would be surfaces commensurate with l^2. In projection, these edges would appear as surfaces, also commensurate with l^2 for a random viewing angle. Only if these surfaces were plane and viewed edge-on (within ±5 deg for a projected size less than one tenth of their real size) would these edges appear as thin elongated structures. We rule this out on statistical grounds: the mere fact that we detect 8 sharp CO-edges in the small field-of-view of the PdBI observations suggests that it is not a rare configuration and that the eight sharp CO-edges are seen from random viewing angles. We thus infer that the SEE(D)S are CO-layers, rather than volumes and that their thickness is ∼10 mpc or less, on the order of the width of the PdBI-structures.

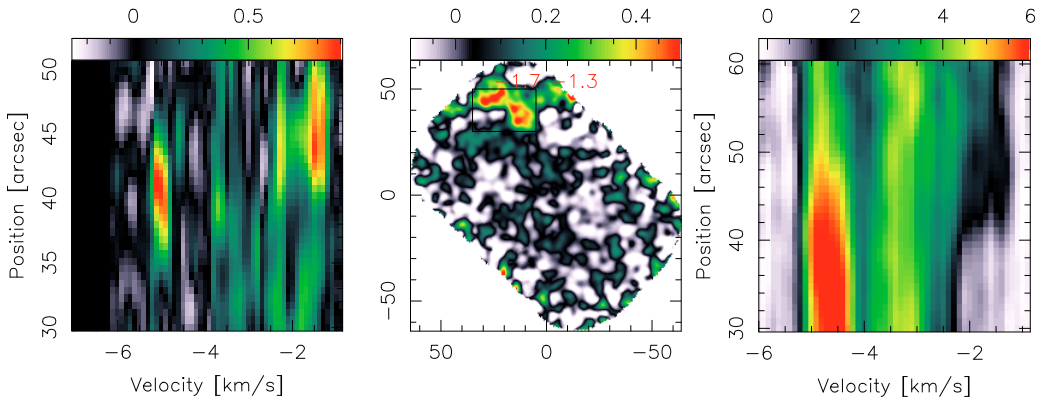

Fig. 7. Position-velocity diagrams across the pair of structures [#3, #8]. *Left*: cut across the PdBI-only map. *Center*: rotated PdBI channel-map [−1.7, −1.3] km s^{-1}, showing the direction and distance (horizontal size of the box) over which the CO emission is averaged for the cut. The cut runs from the southern to northern edge of the box. *Right*: same across the PdBI+30m data cube.

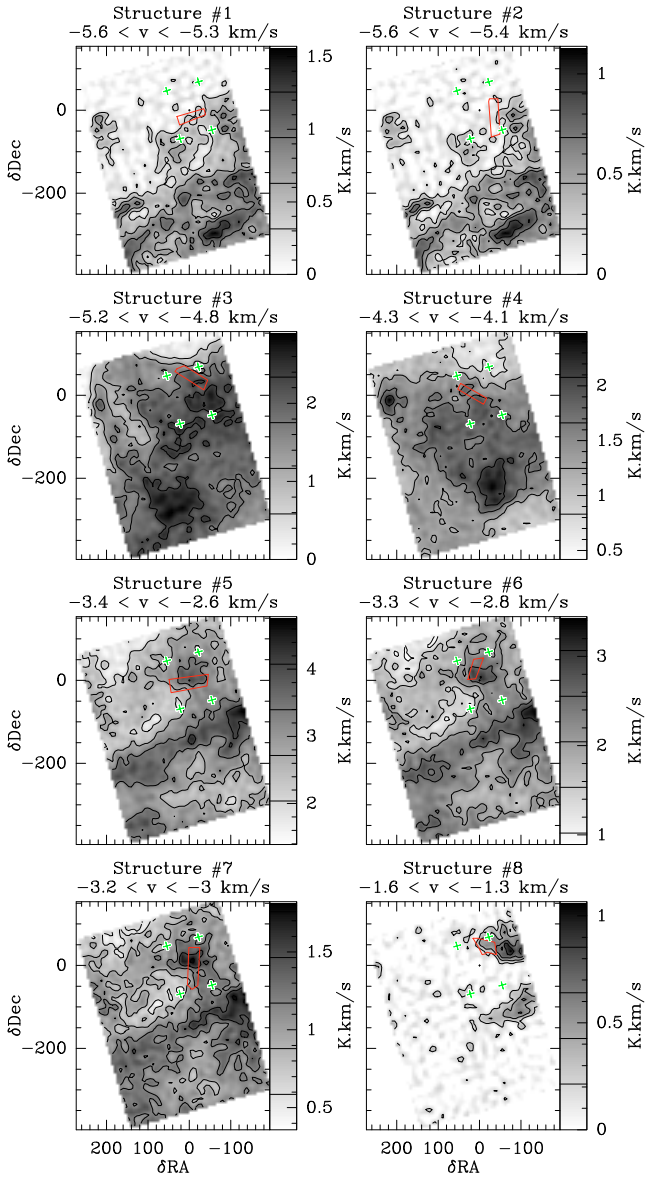

Fig. 8. Integrated maps of the same velocity range as that defined in Fig. 4 of the ^{12}CO (J = 1–0) emission observed at the IRAM-30m. Green crosses delimit the mosaic position and the red polygon as defined in Fig. 4 shows the position of the elongated structures detected at PdBI.

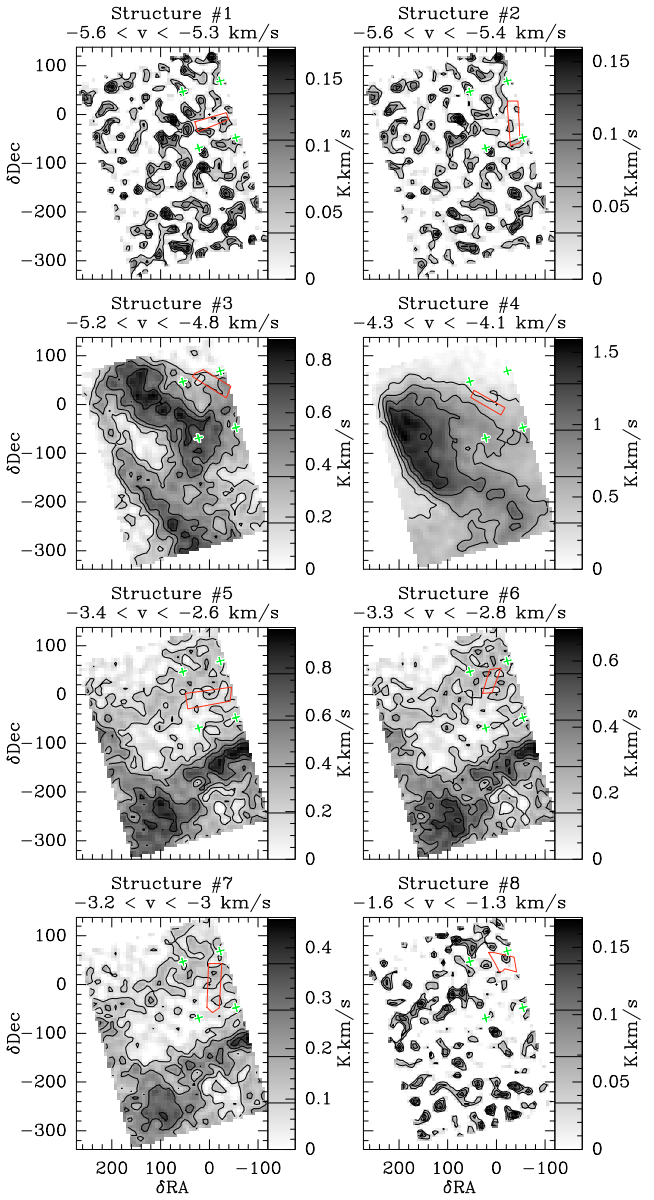

Fig. 9. Same as Fig. 8 except that the single dish map is that of ^{13}CO (J = 1–0).

This statistical argument is reinforced by the presence of pairs. The SEEDS are structures that have sharp edges with only small or null overlaps. If their interface were 2-dimensional (i.e. if the SEEDS were volumes), the small overlap would occur only for an edge-on viewing, an unlikely case. Their interface is therefore 1-dimensional rather than 2-dimensional and the SEEDS are layers of CO emission. This ensures that under any viewing angle the two extended velocity components are detected with only a narrow or null spatial overlap in projection. The SEEDS could still be be 3-dimensional pure velocity-structures, where large velocity-shears produce sharp edges in channel maps of finite spectral resolution (see Sect. 3.1). However, with the same statistical argument as above, concerning density structures, we rule out the possibility that the SEEDS be 3-dimensional velocity structures. These must be CO layers.

In summary, the sharpness of the edges of the SEE(D)S, associated with the fact that we detect 8 cases in the mosaic and three close-pairs that do not overlap in space, implies that the SEE(D)S are thin layers of CO emission rather than volumes.

4. Gas density of the PdBI-structures

4.1. Estimates from CO line emission

Because of the elongated shape of most of the structures and the fact that they are edges of more extended emission, we have not tried to decompose the observed emission using clump finding algorithms such as GAUSSCLUMP (Stutzki & Guesten 1990). We estimate below the gas density in these structures in two independent ways and compare the results to those inferred from the dust continuum emission.

First, we compute upper limits of the H_2 densities (Table 2) by adopting the CO-to-H_2 conversion factor $X = 1.56 \pm 0.05 \times 10^{20}$ cm^{-2} (K km s^{-1})$^{-1}$ (Hunter et al. 1997) so that $n_{H_2} = 5 \times 10^4$ cm^{-3} $W(CO)/l_{mpc}$, for a *los* depth equal to the projected thickness $l_\perp$. Since we are observing edges of layers (see Sect. 3.2), the inferred densities are overestimated by the unknown factor $l_\parallel/l_\perp$. The upper limits of the H_2 densities derived from the galactic CO to H_2 conversion factor (Table 2) vary by a factor 10 only.

Alternatively, one may use a LVG analysis to estimate the gas properties in these structures. Two assumptions are made: (1) the CO emission is not beam-diluted and (2) the excitation is assumed to be the same as measured in the same field with the IRAM-30m so that we adopt the line ratio $R(2-1/1-0) = 0.7 \pm 0.1$ (Falgarone et al. 1998; Hily-Blant et al. 2008). This value may be representative of the excitation of translucent molecular gas because the same line ratio is found in different observations sampling a similar kind of molecular gas (Pety et al. 2008). Under these conditions, the CO column densities per unit velocity are very well determined for all line temperatures. They are given in Table 4 for the brightest, weakest, and most common CO peak temperature observed. The inferred CO column densities differ by only a factor 10 to 16 between the brightest and weakest structure.

Table 4 also gives the range of gas kinetic temperatures and associated range of densities, thermal pressures P_{th}/k and CO abundances of possible solutions. The range of temperatures is bounded towards high values by the thermal width of the CO lines ($T_k < 250$ K for the broadest line, <35 K for the narrowest). Solutions colder than 10 K are unlikely because the gas is poorly shielded from the ambient ISRF. The CO optical depth is therefore smaller than a few, in agreement with the results of Paper II. A similar conclusion has been derived by Heithausen (2006) after he failed to detect the ^{13}CO and C^{18}O($J = 1-0$) line with the PdBI in a nearby small-area molecular structure (SAMS) field.

Each set of H_2 density and kinetic temperature in the LVG solutions, corresponds to a product $X(CO)l_\parallel$ where $X(CO)$ is the CO abundance relative to H_2. The range of CO abundances inferred from the LVG computations are given in Table 2 for $l_\parallel = l_\perp$. They may be overestimated by the unknown ratio $l_\parallel/l_\perp$.

Table 4 shows the range of possible H_2 densities derived from the LVG analysis for gas temperatures between 10 K and 200 K at most. The comparison of these values with the upper limits inferred from the CO-to-H_2 conversion factor (Table 2) provides narrower H_2 density ranges, $n_{H_2} = 800$ to 10^3 cm^{-3}, and 300 to 2×10^3 cm^{-3}, for the weakest and most common structures respectively. In spite of all the uncertainties, the two methods infer consistent H_2 densities that do not exceed 3×10^3 cm^{-3}. Moreover, whether the gas is cold or warm, its thermal pressure is about the same, within a factor of a few, and is in harmony with that inferred from carbon line observations in the local ISM that has an average of $P_{th}/k \sim 3 \times 10^3$ K cm^{-3} with fluctuations up to $\sim 10^5$ K cm^{-3} (Jenkins & Tripp 2007).

4.2. Estimates from the dust continuum emission

In addition to ^{12}CO lines, we have detected continuum emission. This emission is close to the noise level, except for the large bright spot associated to the ^{12}CO peak of emission. A comparison of the continuum emission with the CO contour levels (Fig. 2) suggests that the elongated feature of continuum emission in the north-western corner of the mosaic is also real.

On the basis of the coincidence of the peaks of the ^{12}CO and continuum emission in the mosaic, we ascribe the continuum emission to thermal dust emission. The average continuum brightness over the ^{12}CO peak (Fig. 2) is 2 ± 1 mJy/beam, hence $I_{cont} = 1 \pm 0.5 \times 10^{-20}$ erg cm^{-2} s^{-1} sr^{-1} Hz^{-1}. The dust opacity, $\tau_d = I_{cont}/B_\nu(T_d)$, depends on the dust temperature. We adopt a dust emissivity $\tau_d = 8.7 \times 10^{-26}(\lambda/250\ \mu m)^{-2} N_H$, deduced from COBE data for dust heated by the ambient interstellar radiation field (ISRF) (Lagache et al. 1999). For $T_d = 10$ K and $\nu = 115$ GHz, we find $\tau_d = 3.2 \times 10^{-7}$ and $N_H = 4.0 \times 10^{20}$ cm^{-2} across the peak. For $T_d = 17$ K, the most plausible value in translucent gas of the Solar Neighborhood, this value would be lower by a factor 2 and for $T_d = 8$ K it would be larger by 40%, providing the range $N_H = 2.0 \times 10^{20}$ to 5.6×10^{20} cm^{-2} for high and low dust temperatures, respectively. This estimate of N_H may be compared to that inferred from ^{12}CO in the previous section. If we allow for a column density of atomic hydrogen comparable to that of H_2, as found in the Polaris Flare by Heithausen & Thaddeus (1990), the total H column density inferred from CO for the peak of structure #5 ranges between $N_H = 3N(H_2) = 2 \times 10^{19}$ to 2.4×10^{20} cm^{-2} for the warm and cold solutions respectively (assuming a size of 9 mpc). The two ranges of values would overlap for a depth a few times larger than the observed projected size, allowing for warm and moderate density solutions where the dust temperature is lower than that of the gas. Given the many uncertainties in the different steps (the questionable validity of the CO line analysis, the knowledge of dust emissivity and temperature), the consistency between these two independent estimates is encouraging and we are confident that we have detected the dust thermal emission of the brightest small-scale structure and that its H_2 density is not higher than a few 10^3 cm^{-3}.

Aside from the peak, the rest of the structures have column densities a few times smaller and their dust continuum emission

Table 3. Spatial and kinematic characteristics of the three pairs of parallel PdBI-only structures.

Pair	v_1 km s^{-1}	v_2 km s^{-1}	$\delta v_{\rm LSR}$ km s^{-1}	$\delta l_\perp$ [a] mpc	$\delta v/\delta l_\perp$ km s^{-1} pc^{-1}	a [b] s^{-1}	τ [c] yr	l [d] mpc
#3, #8	–5.0	–1.5	3.5	4.5	777	1.3×10^{-11}	2.5×10^{3}	45
#1, #5	–5.4	–3.0	2.4	9.0	267	4.5×10^{-12}	4×10^{3}	45
#6, #7	–3.0	–3.1	0.1	16	6	10^{-13}	3×10^{5}	40

[a] Averaged separation between the PdBI CO peaks; [b] $a=\frac{1}{2}\delta v/\delta l_\perp$; [c] $\tau=a^{-1}$; [d] length over which the structures are parallel within $\pm10^\circ$.

Table 4. Results of LVG radiative transfer calculations for representative observed values (see Table 2).

	$T_{\rm peak}$ K	N(CO)/Δv [a] cm^{-2}/km s^{-1}	Δv km s^{-1}	N(CO) cm^{-2}	T_k range K	$n_{\rm H_2}$ range [b] cm^{-3}	$P_{\rm th}/k$ range [b] K cm^{-3}	X(CO) range [b] $\times10^{-5}$
brightest	4	$3–4\times10^{15}$	0.4	$1.2–1.6\times10^{15}$	10–200	3×10^{3}–250	$3–5\times10^{4}$	2–20
most common	1.2	1.5×10^{15}	0.2	3×10^{14}	10–140	8×10^{3}–300	$8–4\times10^{4}$	0.16–4
weakest	0.6	1.0×10^{15}	0.1	1.0×10^{14}	7–35	1×10^{4}–800	$7–3\times10^{4}$	0.11–1.4

[a] Assuming $R(2-1/1-0)=0.7\pm0.1$; [b] the LHS (resp. RHS) values correspond to the lowest (resp. highest) gas temperature.

is expected to lie closer to the noise level. In addition, the surface filling factor of the ^{12}CO structures being large in the central area of the mosaic, the PdBI visibility of the continuum emission of individual structures is expected to be highly reduced compared to that of the line which takes advantage of velocity-space. This may be the reason that the continuum emission and the ^{12}CO emission do not coincide elsewhere: the continuum emission is more heavily filtered out by the interferometer than the ^{12}CO emission.

5. What are the SEE(D)S?

5.1. Manifestations of the small-scale intermittency of turbulence

The two largest velocity-shears given in Table 3 are more than two orders of magnitude larger (within the uncertainties due to projections) than the average value of 1 km s^{-1} pc^{-1} estimated on the parsec scale in molecular clouds (Goldsmith & Arquilla 1985). The velocity field in these two SEEDS therefore significantly departs from predictions based on scaling laws obtained from ^{12}CO(1–0) in molecular clouds, such as that shown in Fig. 10. In spite of a significant scatter of the data points, a power law $\delta v_l \propto l^{1/2}$ characterizes the increase of the velocity fluctuations with the size-scale l, at least above ~1 pc. Below that scale-length, the scatter increases and a slope 1/3 would not be inconsistent with the data. According to the former scaling, the velocity-shear should increase as $l^{-1/2}$, therefore by no more than $140^{1/2}=12$ between 1 pc and 7 mpc. If the other scaling is adopted, this factor becomes $140^{2/3}=26$. Now, the observed shears increase by more than two orders of magnitude between these two scales. This is conspicuous in Fig. 10 where the 8 PdBI-structures of Table 2 are plotted either individually or as pairs (i.e. as they would be characterized if the spatial resolution were poorer and individual structures were not isolated in space, providing for instance a linewidth $\Delta v_{1/2}=3.5$ km s^{-1} and a size $l_\perp\sim7$ mpc for the pair [#3, #8]).

This result has to be put in the broader perspective described in Sect. 1. The statistical analysis of the velocity field of this high latitude cloud (Paper III, HF09) shows that the *pdf* of the ^{12}CO line-centroid velocity increments increasingly departs from Gaussian as the lags over which the increments are measured decrease. The locus of the positions that populate the *pdf* non-Gaussian wings forms elongated and thin (~0.03 pc) structures that have a remarkable coherence, up to more than a parsec. HF09 propose, on this statistical basis, but also because of their thermal and chemical properties given in Sect. 1, that these structures trace the intermittency of turbulent dissipation in the field. The pair of structures [#3, #8] belongs to that locus of positions (see their Fig. 3). The extremely large velocity-shears measured in that small field are not just exceptional values: they have to be understood as a manifestation of the small-scale intermittency of interstellar turbulence, as studied on statistical grounds in a much larger field.

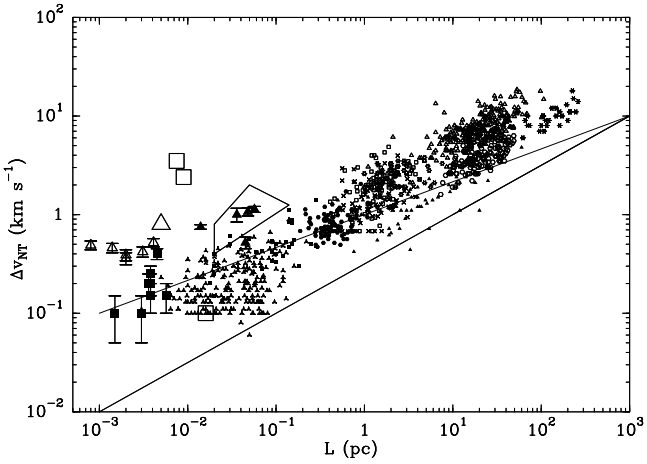

Fig. 10. Size-linewidth relation for a large sample of ^{12}CO(1–0) structures (see Appendix B) to which are added: the SAMS data (single-dish data from Heithausen 2002, 2006 (solid triangles); PdBI data within SAMS2 Heithausen 2004 (open triangles)), a polygon that provides the range of values for the 12 structures of Sakamoto & Sunada (2003) and the eight structures of Table 2 (solid squares). The 3 empty squares without error bars show where the three pairs of PdBI-structures would be if not resolved spatially (i.e. the velocity increment between the two structures would appear as a linewidth for the pair). Same with the large triangle for the pair of structures in SAMS2. The straight lines show the slopes 1/3 and 1/2 for comparison.

5.2. The emergence of CO-rich gas

The PdBI-structures mark sharp edges in the ^{12}CO emission. As discussed in Sect. 3.3 and illustrated in Fig. 7, the CO emission of space-velocity structures extending over arcminutes (the SEE(D)S) drops below the detection level over 4.3″ (the resolution). Therefore, several questions arise: what is the nature of the undetected gas that provides the continuity of the flow? Is it undetected because its density is too low to excite the $J = 1-0$ transition of ^{12}CO? Or is it dense enough but with too low a CO abundance? For simplicity, in the following discussion, "CO-rich" qualifies the gas with $X(\mathrm{CO}) > 10^{-6}$, the CO abundance of the weakest detected structure (Table 4), and "CO-poor" the gas with a lower CO abundance.

Acording to LVG calculations, the 3σ detection limit of our observations allows us to detect CO column densities as low as $N(\mathrm{CO}) \sim$ a few 10^{14} cm^{-2} in gas as diluted as $n_{\mathrm{H}} \sim 50$ cm^{-3}, at any temperature, and for a velocity dispersion of 0.2 km s^{-1}, characteristic of the structures found. This detection limit is very low. Therefore, if the undetected gas on the other side of the edge is CO-rich (with a total hydrogen column density comparable to that of the detected part), it has to be at a density lower than $n_{\mathrm{H}} \sim 50$ cm^{-3}, not to excite the ^{12}CO($J = 1-0$) transition at a detectable level. We rule out this possibility because this density is that of the CNM and it is unlikely that gas at that density be CO-rich (see also the models of Pety et al. 2008).

The alternative is that the undetected gas is CO-poor and that it is not its low density but its low CO abundance that makes it escape detection in ^{12}CO($J = 1-0$). Given the sharpness of the edges of the SEE(D)S, between 3 and 11 mpc (Table 2), the process responsible for this transition has to be able to generate a significant CO enrichment over that small scale.

In the above, we rule out the possibility that the sharp edges (i.e. the PdBI-structures) mark photodissociation fronts, because the orientations of such fronts would not be randomly distributed, as is observed. Moreover, there is no source of UV photons in that high-latitude cloud and the radiation field there is the ambient galactic ISRF. Photodissociation fronts would not have different orientations depending on gas velocities varying by only a few km s^{-1}. The sharp edges are not either folds in layers of CO emission because those who belong to SEES (single structures) lack the second part of the layer, and those who belong to SEEDS have the two parts at different velocities.

We thus infer that the SEE(D)S are the outcome of a dynamical process, that involves large velocity-shears, and takes place in a gas undetected in ^{12}CO(1−0) emission, because it is CO-poor, not because it is too diluted. This gas may be the CNM and the dynamical process has to be able to enrich the CNM in CO molecules within a few 10^3 yr and over a few milliparsec.

6. Comparison with other data sets

Our results broaden the perspective regarding the existence of small-scale CO structures in molecular clouds. Heithausen (2002, 2004, 2006) has found small-area molecular structures (SAMS) that are truly isolated CO features in the high latitude sky. PdBI observations of the SAMS (Heithausen 2004) reveal bright sub-structures that are all brighter and broader than our PdBI-structures. Unfortunately, the emission has been decomposed into clumps, a questionable procedure because short-spacings have not been combined to the PdBI data and the CLEAN procedure tends to create structures on the beam scale. The large H_2 densities inferred are therefore likely overestimated. An interesting feature can be seen in the channel maps, though. Two elongated thin patterns cross the field, reminiscent for their thickness and length of what is found in the present study. A velocity shear of 180 km s^{-1} pc^{-1} is estimated between these two elongated structures for a velocity separation of 0.9 km s^{-1} and a *pos* spatial separation of 10″ on average (or 5 mpc at the assumed distance of 100 pc). This velocity-shear is thus commensurable with the two largest values found in the Polaris field.

Ingalls et al. (2007) have detected milliparsec clumps in a high latitude cloud. They are located in the line-wings of the CO single-dish spectrum and they model them as tiny (1−5 mpc) clumps of density of a few 10^3 cm^{-3}. A more detailed comparison with the present results is not possible because they do not analyze individual structures.

Sakamoto & Sunada (2003) have discovered a number of CO small-scale structures in the low-obscuration regions of long strip maps beyond the edge of the Taurus molecular cloud. Their main characteristics are their large line-width and their sudden appearance, and disappearance, within 0.03 to 0.1 pc. The authors interpret these features as the signature of structure formation induced by the thermal instability of the warm neutral medium (WNM) in the turbulent cloud envelope. These CO small-scale structures thus carry the kinematic signatures of the embedding WNM, hence their large velocity dispersion, both interclump and intraclump. The inferred line ratio, $R(2-1)/(1-0) = 0.4$, is low, consistent with a low excitation temperature and H_2 densities lower than $\sim 10^2$ cm^{-3}. The authors propose that their small-scale CO structures pinpoint molecule-forming regions, driven by the thermal instability in the turbulent diffuse ISM.

Our data therefore share many properties with these different samples. Figure 10 allows a comparison of the projected size and linewidth of the above milliparsec-scale structures with those of ^{12}CO(1−0) structures identified in data cubes from non-star-forming regions of all sizes, up to several 100 pc (see the relevant references in Appendix B). Although some of them (a few individual PdBI-structures of our sample) further extend the general scaling law down to 2 mpc, most of them significantly depart from this law by a large factor. As already mentioned in Sect. 5.1, the departure is the largest for the pairs of PdBI-structures, as they would appear if they were not resolved spatially i.e. as anomalously broad structures with respect to their size. The increased scatter of velocity-widths of the structures below 0.1 pc down to 1 mpc may be seen as another manifestation of the intermittency of turbulence in translucent molecular gas.

7. Comparison with experiments, numerical simulations and chemical models

The present data set discloses small-scale structures of intense velocity-shears that carry the statistical properties of intermittency and, in conjunction with that of HF09, reveals a connexion between parsec-scale and milliparsec scale velocity-shears. The dynamic range of coupled scales in the Polaris Flare is therefore on the order of $\sim 10^3$. Moreover, velocity differences, up to 3.5 km s^{-1}, close to the rms velocity dispersion of the CNM turbulence measured on 10-pc scales (or more) (Miville-Deschênes et al. 2003; Haud & Kalberla 2007), are found in the PdBI field over ∼10 mpc, without any detected density enhancement nor shock signature. We argue that the SEE(D)S are the CO-rich parts of straining sheets in a gas undetected in ^{12}CO(1−0), likely the CNM, and that the fast CO enrichment is driven by enhanced turbulent dissipation in the intense velocity-shears. We show below that these findings may be understood in the light of recent

numerical simulations of incompressible and compressible turbulence, and the TDR chemical model of Godard et al. (2009).

The fact that the most dissipative structures appear to be layers of intense strain-rate is consistent with recent results of numerical simulations of incompressible turbulence at high Reynolds number (Moisy & Jiménez 2004) and laboratory experiments (Ganapathisubramani et al. 2008). These regions are not randomly distributed and form inertial-range clusters (Moisy & Jiménez 2004) or develop at the boundaries regions of high level of vorticity (i.e. vortex tubes) (Ganapathisubramani et al. 2008). Coupling between small-scale statistics of the velocity field and the properties of the large-scale flows is also clearly probed in the high-*Re* numerical simulations of Mininni et al. (2006): correlations are observed between large-scale shear and small-scale intermittency.

In compressible turbulence, the fact that the most dissipative structures are shear-layers is not expected. Yet, in their hydrodynamical simulations of mildly compressible turbulence, Porter et al. (2002) show that the compressible component of the velocity field is weaker than its solenoidal counterpart by a factor ∼3, independent of the nature of the driving process (compressible or solenoidal) and Vestuto et al. (2003) find that the energy fraction in the solenoidal modes is dominant and increases with the magnetic field intensity in compressible magneto-hydrodynamical (MHD) turbulence. These numerical experiments are still far from approaching the ISM conditions but they suggest that turbulent dissipation may occur primarily in solenoidal modes, i.e. without direct gas compression, and that the properties of the small scales are coupled to the large-scales.

In the TDR models of Godard et al. (2009), the chemical enrichment of the CNM is driven by high gas temperatures and enhanced ion-neutral drift, without density enhancement. The temperature increase is due to viscous dissipation in the layers of largest velocity-shears at the boundaries of coherent vortices[4]. The large ion-neutral drift occurs in the layers of largest rotational velocity in which ions and magnetic fields decouple from neutrals. These two dissipative processes trigger endothermic chemical reactions, blocked at the low temperature of the CNM. Enrichments consistent with observations are obtained for turbulent rates-of-strain $a = 10^{-11}$ s^{-1} induced by large scale turbulence and for moderately dense gas ($n_{\rm H} < 200$ cm^{-3}) characteristic of the CNM. There is no direct determination of the rates-of-strain generated by turbulence in the CNM. We note however that the largest observed velocity-shear (Table 3) corresponds, if the projected quantities provide reasonable estimates, to a comparable rate-of-strain. The range of observed CO column densities from $N({\rm CO}) = 10^{14}$ to 1.6×10^{15} cm^{-2} can be reproduced by intense velocity-shears occurring in gas of density 100 to 200 cm^{-3}. In this framework, the energy source tapped to enrich the medium in molecules is the supersonic turbulence of the CNM.

The association between the large observed velocity-shears and local enhanced dissipation rate is therefore supported not only by the earlier works presented in the Introduction but also by a quantitative agreement between the TDR chemical models and the present observational results. We cannot rule out however a contribution of low-velocity C-shocks to the turbulent dissipation. If they propagate in the CNM, they are not visible in the CO lines. Such shocks are not yet reliably modelled (Hily-Blant et al., in preparation).

[4] The "sinews of turbulence" put forward by Moffatt et al. (1994) that link large-scale strain and small-scale vorticity.

8. Conclusions and perspectives

IRAM-PdBI observations of a mosaic of 13 fields in the turbulent environment of a low-mass dense core have disclosed small and weak ^{12}CO(1−0) structures in translucent molecular gas. They are straight and elongated structures but they are not filaments because, once merged with short-spacings data, the PdBI-structures appear as the sharp edges of larger-scale structures. Their thickness is as small as ≈3 mpc (600 AU), and their length, up to 70 mpc, is only limited by the size of the mosaic. Their CO column density is a well determined quantity for the excitation conditions found at larger scale and is in the range $N({\rm CO}) = 10^{14}$ to 10^{15} cm^{-2}. Their H_2 density, estimated in several ways, including the continuum emission of the brightest structure, does not exceed a few 10^3 cm^{-3}. Their well-distributed orientations can be followed in the larger-scale environment of the field. Six of them form three pairs of quasi-parallel structures, physically related. The velocity-shears estimated for the three pairs include the largest ever measured in non-star-forming clouds (up to 780 km s^{-1} pc^{-1}).

The PdBI-structures are therefore not isolated and are the edges of so-called SEE(D)S for sharp-edged extended (double) structures. We show that the SEE(D)S are thin layers of CO-rich gas and that their sharp edges pinpoint a small-scale dynamical process, at the origin of the CO contrast detected by the PdBI. We propose that the SEE(D)S are the outcomes of the chemical enrichment driven by intense dissipation occurring in large velocity-shears and that they are CO-rich layers swept along by the straining field of CNM turbulence.

The present work is the first detection of mpc-scale intense velocity-shears belonging to a parsec-scale shear. The large departure from average of the kinematic properties of these structures, confirms that they are a manifestation of the small-scale intermittency of turbulence in this high latitude field, a property already established on statistical grounds (HF09). The values of the velocity-shears (or rate-of-strain) provide a quantitative constraint on the dissipation rate that can be compared to chemical models. The link between the turbulent dissipation in the diffuse gas and the dense core observed in the vicinity of the PdBI mosaic (Fig. 1) still remains to be established.

Last, we would like to stress that sub-structure still exists in these mpc-scale structures of the diffuse ISM and that the next generation of interferometers (e.g. ALMA) should be able to observe gas at the dissipation scale of turbulence (that is still unknown) or at least observe the effects on the ISM (temperature, excitation, molecular abundances) of the huge release of energy expected to occur there.

Acknowledgements. We thank the IRAM staff at Plateau de Bure and Grenoble for their support during the observations. E.F. is most grateful to Michael Dumke, Emmanuel Dartois, Anne Dutrey and Stéphane Guilloteau for their help during the early stages of the data reduction. E.F. also acknowledges the stimulant discussions over the years with E. Ostriker, P. Hennebelle, A. Lazarian, B. G. Elmegreen, M. M. Mac-Low, E. Vasquez-Semadeni and many others that cannot be listed here. We thank J. Scalo, our (formerly anonymous) referee, for his dedicated efforts at making us write our observational paper accessible to numericists.

Appendix A: Noise level in the mosaic

Mosaic noise is inhomogeneous due to primary beam correction. This is shown in Fig. A.1. The 13-field mosaic produces a large area with uniform noise level. Only at the edge of the mosaic does it increase sharply due to the primary beam correction (the contour shown are at a 2−4 sigma level, 1 sigma being measured at the map center on a channel devoided of signal).

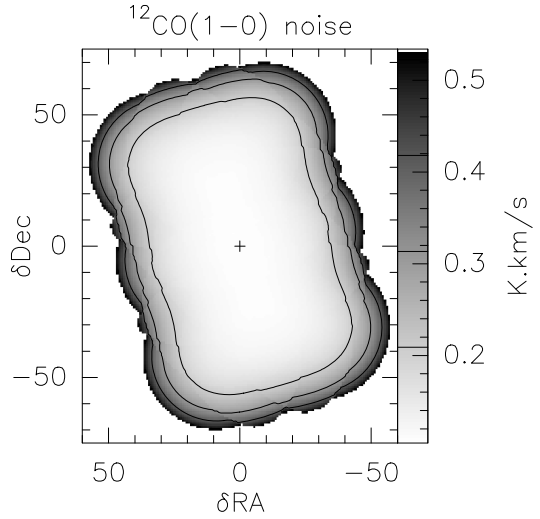

Fig. A.1. Map of the noise level in K km s^{-1} over the 13-field mosaic.

Appendix B: The size-linewidth scaling law

Molecular cloud parameters have long been determined as those of three-dimensional structures isolated in the four-dimensional space of the molecular line data sets $T_L(x, y, v_z)$, the line brightness temperature being a function of position in the *pos* (two coordinates x, y), and one spectral dimension, the projected velocity on the *los* direction v_z. In this 4D space, 3D structures are isolated following different methods (Stutzki & Guesten 1990; Williams et al. 1994; Falgarone & Perault 1987; Loren 1989; Falgarone et al. 1992). The size and linewidth of the large number of clouds displayed in Fig. 10 have been obtained by using published values, corrected in several cases to allow the size and linewidth obey the same definitions in all the samples (see Falgarone 1998). The structures are identified in ^{12}CO(1−0) molecular line surveys of the central parts of the Galaxy (stars, Dame et al. 1986; open triangles Solomon et al. 1987) and of the third quadrant (open hexagons, May et al. 1997), in the Rosette (crosses) and Maddalena (open squares) molecular clouds (Williams et al. 1994), in non-star-forming clouds (solid triangles, Falgarone & Perault 1987; solid squares, Falgarone et al. 1992; tripods, Lemme et al. 1995), in ρ Ophiuchus (solid hexagons, Loren 1989) and in a high latitude cloud (starred triangles, Heithausen et al. 1998).

References

Anselmet, F., Antonia, R. A., & Danaila, L. 2001, Planet. Space Sci., 49, 1177
Arnéodo, A., Benzi, R., Berg, J., et al. 2008, Phys. Rev. Lett., 100, 254504
Chevillard, L., Roux, S. G., Lévêque, E., et al. 2005, Phys. Rev. Lett., 95, 064501
Dame, T. M., Elmegreen, B. G., Cohen, R. S., & Thaddeus, P. 1986, ApJ, 305, 892
de Avillez, M. A., & Breitschwerdt, D. 2007, ApJ, 665, L35
Elmegreen, B. G., & Scalo, J. 2004, ARA&A, 42, 211
Falgarone, E. 1998, in Starbursts: Triggers, Nature, and Evolution, Les Houches School, ed. B. Guiderdoni, & A. Kembhavi, 41
Falgarone, E., & Perault, M. 1987, in Physical Processes in Interstellar Clouds, ed. G. E. Morfill, & M. Scholer, NATO ASIC Proc., 210, 59
Falgarone, E., Puget, J.-L., & Perault, M. 1992, A&A, 257, 715
Falgarone, E., Panis, J.-F., Heithausen, A., et al. 1998, A&A, 331, 669
Falgarone, E., Verstraete, L., Pineau Des Forêts, G., & Hily-Blant, P. 2005, A&A, 433, 997
Falgarone, E., Pineau Des Forêts, G., Hily-Blant, P., & Schilke, P. 2006, A&A, 452, 511
Frisch, U. 1995, Turbulence. The legacy of A.N. Kolmogorov, ed. U. Frisch
Ganapathisubramani, B., Lakshminarasimhan, K., & Clemens, N. T. 2008, Journal of Fluid Mechanics, 598, 141
Godard, B., Falgarone, E., & Pineau Des Forêts, G. 2009, A&A, 495, 847
Goldsmith, P. F., & Arquilla, R. 1985, in Protostars and Planets II, ed. D. C. Black, & M. S. Matthews, 137
Goldsmith, P. F., Heyer, M., Narayanan, G., et al. 2008, ApJ, 680, 428
Gredel, R., Pineau des Forêts, G., & Federman, S. R. 2002, A&A, 389, 993
Gueth, F. 2001, in Proceedings from IRAM Millimeter Interferometry Summer School 2, 207
Gueth, F., Guilloteau, S., & Bachiller, R. 1996, A&A, 307, 891
Haud, U., & Kalberla, P. M. W. 2007, A&A, 466, 555
Heiles, C. 2007, in SINS – Small Ionized and Neutral Structures in the Diffuse Interstellar Medium, ed. M. Haverkorn, & W. M. Goss, ASP Conf. Ser., 365, 3
Heithausen, A. 1999, A&A, 349, L53
Heithausen, A. 2004, ApJ, 606, L13
Heithausen, A. 2006, A&A, 450, 193
Heithausen, A., & Thaddeus, P. 1990, ApJ, 353, L49
Heithausen, A., Bensch, F., Stutzki, J., Falgarone, E., & Panis, J. F. 1998, A&A, 331, L65
Heithausen, A., Bertoldi, F., & Bensch, F. 2002, A&A, 383, 591
Hily-Blant, P., & Falgarone, E. 2007, A&A, 469, 173
Hily-Blant, P., & Falgarone, E. 2009, A&A, 500, L29
Hily-Blant, P., Falgarone, E., & Pety, J. 2008, A&A, 481, 367
Hunter, S. D., Bertsch, D. L., Catelli, J. R., et al. 1997, ApJ, 481, 205
Ingalls, J. G., Bania, T. M., Lane, A. P., Rumitz, M., & Stark, A. A. 2000, ApJ, 535, 211
Ingalls, J. G., Reach, W. T., Bania, T. M., & Carpenter, J. M. 2007, in SINS – Small Ionized and Neutral Structures in the Diffuse Interstellar Medium, ed. M. Haverkorn, & W. M. Goss, ASP Conf. Ser., 365, 201
Jenkins, E. B., & Tripp, T. M. 2007, in SINS – Small Ionized and Neutral Structures in the Diffuse Interstellar Medium, ed. M. Haverkorn, & W. M. Goss, ASP Conf. Ser., 365, 51
Joulain, K., Falgarone, E., Des Forets, G. P., & Flower, D. 1998, A&A, 340, 241
Joung, M. K. R., & Mac Low, M.-M. 2006, ApJ, 653, 1266
Lacour, S., Ziskin, V., Hébrard, G., et al. 2005, ApJ, 627, 251
Lagache, G., Abergel, A., Boulanger, F., Désert, F. X., & Puget, J.-L. 1999, A&A, 344, 322
Lemme, C., Walmsley, C. M., Wilson, T. L., & Muders, D. 1995, A&A, 302, 509
Lis, D. C., Pety, J., Phillips, T. G., & Falgarone, E. 1996, ApJ, 463, 623
Liszt, H. S., & Lucas, R. 1998, A&A, 339, 561
Loren, R. B. 1989, ApJ, 338, 902
Mac Low, M.-M., & Klessen, R. S. 2004, Rev. Mod. Phys., 76, 125
Mac Low, M.-M., Klessen, R. S., Burkert, A., & Smith, M. D. 1998, Phys. Rev. Lett., 80, 2754
May, J., Alvarez, H., & Bronfman, L. 1997, A&A, 327, 325
Mininni, P. D., Alexakis, A., & Pouquet, A. 2006, Phys. Rev. E, 74, 016303
Miville-Deschênes, M.-A., Joncas, G., Falgarone, E., & Boulanger, F. 2003, A&A, 411, 109
Moffatt, H. K., Kida, S., & Ohkitani, K. 1994, Journal of Fluid Mechanics, 259, 241
Moisy, F., & Jiménez, J. 2004, Journal of Fluid Mechanics, 513, 111
Mordant, N., Delour, J., Léveque, E., Arnéodo, A., & Pinton, J.-F. 2002, Phys. Rev. Lett., 89, 254502
Pety, J. 2005, in SF2A-2005: Semaine de l'Astrophysique Française, ed. F. Casoli, T. Contini, J. M. Hameury, & L. Pagani, 721
Pety, J., & Falgarone, E. 2003, A&A, 412, 417
Pety, J., Lucas, R., & Liszt, H. S. 2008, A&A, 489, 217
Porter, D., Pouquet, A., & Woodward, P. 2002, Phys. Rev. E, 66, 026301
Sakamoto, S., & Sunada, K. 2003, ApJ, 594, 340
Scalo, J., & Elmegreen, B. G. 2004, ARA&A, 42, 275
Snow, T. P., & McCall, B. J. 2006, ARA&A, 44, 367
Solomon, P. M., Rivolo, A. R., Barrett, J., & Yahil, A. 1987, ApJ, 319, 730
Stutzki, J., & Guesten, R. 1990, ApJ, 356, 513
Vestuto, J. G., Ostriker, E. C., & Stone, J. M. 2003, ApJ, 590, 858
Williams, J. P., de Geus, E. J., & Blitz, L. 1994, ApJ, 428, 693

A&A 518, A45 (2010)
DOI: 10.1051/0004-6361/201014510
© ESO 2010

Astronomy & Astrophysics

The CO luminosity and CO-H_2 conversion factor of diffuse ISM: does CO emission trace dense molecular gas?⋆

H. S. Liszt[1], J. Pety[2,3], and R. Lucas[4]

[1] National Radio Astronomy Observatory, 520 Edgemont Road, VA 22903-2475 Charlottesville, USA
e-mail: hliszt@nrao.edu
[2] Institut de Radioastronomie Millimétrique, 300 rue de la Piscine, 38406 Saint Martin d'Hères, France
[3] Obs. de Paris, 61 av. de l'Observatoire, 75014 Paris, France
[4] Al-MA, Avda. Apoquindo 3846 Piso 19, Edificio Alsacia, Las Condes, Santiago, Chile

Received 26 March 2010 / Accepted 8 May 2010

ABSTRACT

Aims. We wish to separate and quantify the CO luminosity and CO-H_2 conversion factor applicable to diffuse but partially-molecular ISM when H_2 and CO are present but C^+ is the dominant form of gas-phase carbon.
Methods. We discuss galactic lines of sight observed in HI, HCO^+ and CO where CO emission is present but the intervening clouds are diffuse (locally $A_V \lesssim 1$ mag) with relatively small CO column densities $N_{CO} \lesssim 2 \times 10^{16}$ cm^{-2}. We separate the atomic and molecular fractions statistically using E_{B-V} as a gauge of the total gas column density and compare N_{H_2} to the observed CO brightness.
Results. Although there are H_2-bearing regions where CO emission is too faint to be detected, the mean ratio of integrated CO brightness to N_{H_2} for diffuse ISM does not differ from the usual value of 1 K km s^{-1} of integrated CO brightness per 2×10^{20} H_2 cm^{-2}. Moreover, the luminosity of diffuse CO viewed perpendicular to the galactic plane is 2/3 that seen at the Solar galactic radius in surveys of CO emission near the galactic plane.
Conclusions. Commonality of the CO-H_2 conversion factors in diffuse and dark clouds can be understood from considerations of radiative transfer and CO chemistry. There is unavoidable confusion between CO emission from diffuse and dark gas and misattribution of CO emission from diffuse to dark or giant molecular clouds. The character of the ISM is different from what has been believed if CO and H_2 that have been attributed to molecular clouds on the verge of star formation are actually in more tenuous, gravitationally-unbound diffuse gas.

Key words. ISM: molecules – ISM: clouds

1. Introduction

It is a truism that sky maps of CO emission are understood as uniquely tracing the Galaxy's molecular clouds, dense, cold strongly-shielded regions where the hydrogen is predominantly molecular and the dominant form of gas phase carbon is CO. Moreover, CO emission plays an especially important role in ISM studies as the tracer of cold molecular hydrogen through the use of the so-called CO-H_2 conversion factor which directly scales the integrated ^{12}CO $J = 1$–0 brightness W_{CO} to H_2 column density N_{H_2}. This deceptively simple conversion is critically important to determining molecular and total gas column densities and so to understanding the most basic properties of star formation (Leroy et al. 2008; Bigiel et al. 2008; Bothwell et al. 2009), the origins of galactic dust emission (Draine et al. 2007), and other such fundamentals.

Yet, it is increasingly recognized that CO emission is present along lines of sight lacking high extinction or large molecular column densities (Liszt & Lucas 1998). It is also the case that some very opaque lines of sight showing CO emission are comprised entirely of diffuse material and H_2-bearing diffuse clouds (McCall et al. 2002): a discussion of such a line of sight from our own work is described in Appendix A here. Even in canonical dark clouds like Taurus, detailed high-resolution mapping of the CO emission (Goldsmith et al. 2008) reveals that much of it originates in relatively weakly-shielded gas where ^{13}CO is strongly enhanced through isotopic fractionation, implying that the dominant form of gas phase carbon must be C^+ (Watson et al. 1976).

Conversely, it is also the case that molecular gas is detected in the local ISM even when CO emission is not. Lines of sight with $N_{CO} \gtrsim 10^{12}$ cm^{-2}, $N_{H_2} \gtrsim 10^{19}$ cm^{-2} have long been detectable in surveys of uv absorption (Sonnentrucker et al. 2007; Burgh et al. 2007; Sheffer et al. 2007, 2008), with expected integrated CO brightnesses as low as $W_{CO} = 0.001$ K km s^{-1} (Liszt 2007b). And, as discussed here, mm-wave HCO^+ and CO absorption from clouds with $N_{H_2} \gtrsim 10^{20}$ cm^{-2} are also more common than CO emission along the same lines of sight (see Lucas & Liszt 1996; Liszt & Lucas 2000, and Appendix A).

Thus we are led to ask two questions that are of particular importance to the use of CO emission as a molecular gas tracer. First, where and how does the observed local CO luminosity really originate? Second, how completely is the molecular material represented by CO emission? The approach we take to address these issues is based on radiofrequency surveys of HI, HCO^+ and CO absorption and emission along lines of sight through the Galaxy toward extragalactic background sources. By combining 1) measurements of extinction (constraining the total gas column density); 2) measurements of HI absorption (to determine the gas column of atomic hydrogen); 3) the strength of HCO^+ absorption (tracing H_2 directly) and 4) the integrated CO $J = 1$–0 brightness W_{CO}, we relate W_{CO} to N_{H_2} along sightlines where we

⋆ Appendix E is only available in electronic form at http://www.aanda.org

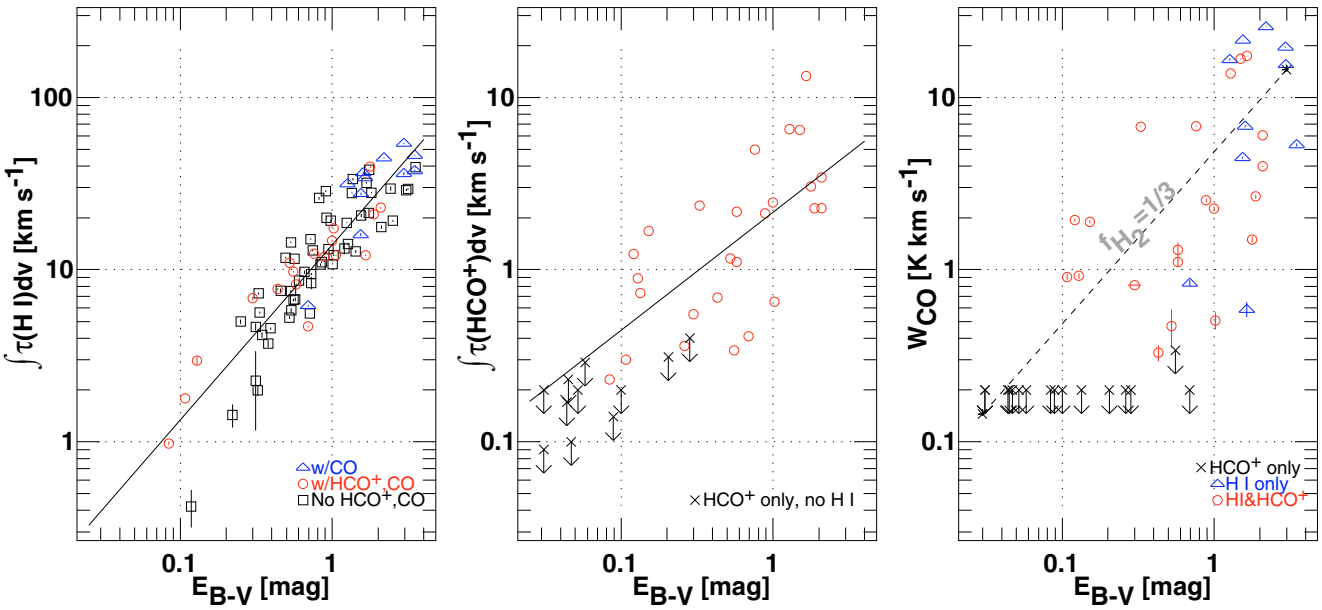

Fig. 1. Atomic and molecular absorption and emission vs. total reddening. *Left*: Integrated VLA HI optical depth from Dickey et al. (1983) and this work. *Middle*: integrated PdBI HCO^+ optical depth from Lucas & Liszt (1996) and this work. *Right*: integrated ARO12m CO J = 1–0 brightness at 1′ resolution. In each case the horizontal axis is the total line of sight reddening E_{B-V} (Schlegel et al. 1998). For explanation of the symbols used in the plots, see Sect. 3.

have previously shown that the intervening gas is diffuse, neither dark nor dense, and the CO column densities are relatively small. The results are somewhat surprising: although there is much variability, the mean CO brightness per H_2-molecule W_{CO}/N_{H_2}, i.e. the CO-H_2 conversion factor, does not differ between diffuse and fully molecular clouds. Although this was phenomenologically inferred long ago, the physical basis for it is now better understood in terms of the radiative transfer and chemistry of H_2- and CO-bearing diffuse and dark gas.

The plan of the present work is as follows. Section 2 describes the observational material that is used here, some of which is new. Section 3 derives the CO-H_2 conversion factor in diffuse gas. Section 4 discusses the fraction of the local galactic CO luminosity (viewed perpendicular to the galactic plane) that can be attributed to diffuse gas. Section 5 discusses the physical processes at play to set the ratio of CO brightness to H_2 column density and explains why the same value may apply to dark and diffuse gas. Section 6 discusses which molecular emission diagnostics might actually be used to distinguish between the CO contributions from diffuse and dark gas. Sections 7 and 8 present a brief summary and discuss how our concept of the ISM might change when a substantial portion of the observed CO emission is ascribed to diffuse rather than dense molecular gas.

2. Observational material

The data used in this work are given in Tables E.1 and E.2 of Appendix E (available online).

2.1. E_{B-V}

Values of the total reddening E_{B-V} along the line of sight are from the work of Schlegel et al. (1998) at a spatial resolution of 6′. The claimed rms error of these measurements is a percentage (16%) of the value. To convert to column density we use the equivalence $N_H = N(H\,I) + 2N_{H_2} = 5.8 \times 10^{21} H\ cm^{-2} E_{B-V}$ established by Bohlin et al. (1978) and Rachford et al. (2009). Typically $A_V = E_{B-V}/3.1$ (Spitzer 1978).

2.2. HI *absorption*

This is mostly taken from the VLA results of Dickey et al. (1983) but a line profile for B2251+158 (3C 454.3) was made available on the website of John Dickey and we took new HI absorption profiles toward J0008+686, J0102+584,B0528+134, B0736+017, J2007+404, J2023+318 and B2145+067 at the VLA in 2005 May and July.

2.3. HCO^+ *absorption*

We used results from the PdBI's HCO^+ survey of Lucas & Liszt (1996) along with the slightly more recent results of Liszt & Lucas (2000) and a few additional profiles that were taken at the PdBI in 2001–2004.

The rotational excitation of HCO^+ above the cosmic microwave background is very weak in diffuse gas (Liszt & Lucas 1996) so that $N_{HCO^+} = 1.12 \times 10^{12}\ cm^{-2} \left(\int \tau(HCO^+)\, dv/1\ km\,s^{-1}\right)$ for an assumed HCO^+ permanent dipole moment of 3.889 Debye. This dipole moment is slightly smaller than the value used in most of our previous work (4.07 D), increasing the inferred HCO^+ column densities by 10%.

2.4. $J = 1–0$ CO *emission*

All the results quoted here are from the ARO12m antenna at 1′ resolution, placed on a main-beam scale by dividing the native T_r^* values by 0.85. Most of these profiles were used on the T_r^* scale in our earlier work (Liszt & Lucas 1996, 1998, 2000) but profiles toward sources with HI absorption and lacking HCO^+ absorption data (noted in Fig. 1) and toward sources with J-names in Tables C.1 and C.2 are new. The velocity resolution was typically 0.1 km s^{-1} and all spectra were taken in frequency-switching mode and deconvolved (folded) using the EKHL algorithm (Liszt 1997a). Where upper limits on CO emission are shown, they are plotted symbolically at very conservative values taken over much wider ranges than are occupied by

HCO^+ emission. The contributions of such sightline to ensemble averages of W_{CO} was taken as zero in each case.

3. The mean N_{H_2}/W_{CO} ratio of diffuse gas

3.1. Considering whole lines of sight

Because the target background sources are extragalactic, the lines of sight considered here traverse the entire galactic gas layer, crossing the entire possible gamut of gas phases. However, they either have low extinction (at $|b| \gtrsim 15$–$20°$) or, more often, can be decomposed into components whose individual molecular column densities are relatively small according to our previous studies of absorption and emission in these directions (see Appendix A for an example). For instance, the highest CO column densities observed for individual components are $N_{CO} \lesssim 2 \times 10^{16}$ cm^{-2} (Liszt & Lucas 1998), representing about 7% of the free carbon column density expected for diffuse ISM at $A_V = 1$ mag (Sofia et al. 2004). ^{13}CO is increasingly strongly fractionated in diffuse clouds having higher N_{CO} (Liszt & Lucas 1998; Liszt 2007a), requiring that carbon must be predominantly in the form of C^+.

3.2. Separating the atomic and molecular gas fractions

In order to derive the N_{H_2}/W_{CO} conversion factor, we need to estimate N_{H_2} independent of the CO emission tracer. To do this, we could use previous estimates of the mean fraction of H_2 in the diffuse ISM, which range from ≳25% (Savage et al. 1977) in uv absorption to 40–45% using a chemically-based approach founded on the observed constancy of $X_{CH} = N_{CH}/N_{H_2}$ (Liszt & Lucas 2002; Sheffer et al. 2008; Weselak et al. 2010). However, as this is the core of our argument, we take two other and more detailed approaches to separating the atomic and molecular column densities along the actual ensemble of lines of sight we have studied. Both methods depend on knowing the total column density N_H from the measured reddening and both are detailed in the following subsections.

3.3. Estimating the atomic gas fraction via HI absorption

In Fig. 1 at left we show the integrated HI absorption plotted against reddening. This diagram is comprised of the entire sample of Dickey et al. (1983) along with a handful of other sightlines observed in HI by us at the VLA and in HCO^+ at the PdBI (see Sect. 2). Symbols differentiate 1) those portions of the sample for which HCO^+ and CO were observed (all sightlines observed in HCO^+ were also observed in CO emission and most in CO absorption); 2) a few for which we only have HI absorption and CO emission data; and 3) those which lack any molecular data. Strictly speaking, only those lines of sight for which we have molecular absorption line data can be proven to be composed wholly of diffuse gas but the sample appears to be very homogeneous in terms of its absorbing properties and many of the lines of sight lacking molecular absorption data show CO emission well beyond the galactic extent of the dense gas layer.

The surprisingly tight, nearly linear correlation between the integrated HI optical depth and reddening (correlation coefficient 0.90, power-law slope 1.02) establishes the applicability of the comparison of reddening values (which are measured on a rather coarse 6′ spatial scale) with HI absorption measurements against the extragalactic continuum sources, sampling sub-arcsecond beams. This excellent correlation between fan and pencil-beam quantities testifies to the high degree to which HI absorbing gas is mixed in the interstellar gas. The sample mean reddening in Fig. 1 at left is $\langle E_{B-V} \rangle = 1.14$ mag and the sample mean integrated HI opacity is $\left\langle \int \tau(\mathrm{HI})\, dv \right\rangle = 16.50\,\mathrm{km\,s^{-1}}$ so that $\left\langle \int \tau(\mathrm{HI})\, dv \right\rangle / \langle E_{B-V} \rangle = 1.45$ km s^{-1}/mag for the sample as a whole.

Estimating the HI column density from the HI absorption must be done with care because the atomic gas is divided between warm and cold phases having widely differing optical depth. Separation of the warm and cold, absorbing and non-absorbing phases was recently considered in great detail by Heiles & Troland (2003) in a new HI emission-absorption survey along many lines of sight. From their tabulated results, it was possible to form the ratio of N_{HI} to $\int \tau(\mathrm{HI})\, dv$ (a small portion of which actually arises in warmer gas) as shown in Fig. B.1 of the appendices and briefly discussed in Sect. B1 there. The sample mean ratio over all lines of sight in the Heiles & Troland (2003) survey is $N_{HI} / \int \tau(\mathrm{HI})\, dv = 2.6 \pm 0.2 \times 10^{20}$ cm^{-2}/km s^{-1} where the error estimate (which is a range, not a standard deviation) reflects the extent to which the ratio can be affected by sample selection criteria based on reddening, galactic latitude, etc. This mean value shows very little variation when computed on subsamples selected on different criteria.

It is then possible to derive the atomic gas fraction, if we assume that our absorption sample has similar properties. Writing

$$f_{HI} \approx \left(\frac{N_{HI}}{\int \tau(\mathrm{HI})\, dv}\right) \times \left(\frac{\int \tau(\mathrm{HI})\, dv}{5.8 \times 10^{21}\, E_{B-V}}\right), \quad (1)$$

taking the first term from our analysis of the results of Heiles & Troland (2003) and the second from the mean for the data shown in Fig. 1. The result is that $f_{HI} = 0.65$, so that $f_{H_2} = 2\, N(H_2)/N(H) = 0.35$.

This estimate of the molecular gas fraction for our sample of sightlines falls in the middle of the range of current general estimates for diffuse gas as noted in the beginning of this Section, i.e. $f_{H_2} \gtrsim 0.25$ from *Copernicus* corrected for sampling biases (Bohlin et al. 1978) and $f_{H_2} \approx 0.40$–0.45 from a sample of lines of sight observed toward bright stars in optical absorption lines observed in CH (Liszt & Lucas 2002), given that $X_{CH} = N_{CH}/N_{H_2}$ is nearly constant at 4.5×10^{-8} (Sheffer et al. 2008; Weselak et al. 2010).

3.4. Checking the molecular gas fraction via molecular chemistry

Shown in the middle panel is the integrated HCO^+ absorption. As noted in Sect. 2.3 the integrated optical depth is directly translatable into HCO^+ column density given the near-absence of rotational excitation in the relatively low density diffuse gas: $N_{HCO^+} = 1.12 \times 10^{12}$ cm^{-2} $\left(\int \tau(\mathrm{HCO^+})\, dv / 1\,\mathrm{km\,s^{-1}}\right)$. The relative abundance of HCO^+ is known to be nearly constant at $X_{HCO^+} \simeq 2$–3×10^{-9} from its fixed ratio with respect to OH in individual clouds (Liszt & Lucas 1996, 2000) and the near-constancy of $X_{OH} \approx 10^{-7}$ (Weselak et al. 2010).

Figure 1 shows that HCO^+ becomes readily detectable at $E_{B-V} \gtrsim 0.1$ mag, which is just where H_2 itself becomes abundant in the diffuse ISM (Savage et al. 1977). When detected, N_{HCO^+} shows a correlation with E_{B-V} (correlation coefficient 0.66 and power law slope 0.7 for the points with detected HCO^+) but the larger scatter in the middle panel, compared to that at left, suggests that the molecular portion of the gas is less well mixed than the absorbing HI.

If X_{HCO^+} is assumed, a value for f_{H_2} could be derived from the data in the middle panel of Fig. 1. Conversely, if $f_{H_2} = 0.35$ is assumed and sample means are used, then $\langle N_{HCO^+}\rangle / (5.8 \times 10^{21}\ \mathrm{cm^{-2}}\ \langle E_{B-V}\rangle) = 5.46 \times 10^{-10}$ and $X_{HCO^+} = N_{HCO^+}/N_{H_2} = 3.1 \times 10^{-9}$, consistent with the previously established value (Liszt & Lucas 1996, 2000). Therefore the decomposition of the ensemble of lines of sight appears to yield consistent results between several independent measures of both the atomic and molecular components.

3.5. The ensemble-averaged CO luminosity and N_{H_2}/W_{CO} conversion factor

Shown at the right in Fig. 1 is the integrated ^{12}CO $J = 1$–0 intensity W_{CO} plotted against E_{B-V}. CO emission is not reliably detected except at $E_{B-V} > 0.3$ mag (i.e. $A_V \gtrsim 1$ mag). In discussing this data, it is important to note that values of N_{CO} have been measured in the diffuse gas (Liszt & Lucas 1998) and they are quite small compared to the column of free gas phase carbon expected at $A_V = 1$ mag (i.e. 3×10^{17} cm^{-2}, see Sofia et al. 2004). Moreover, the lines of sight having the largest values of W_{CO} are composed of several emission components (see Appendix A for an example). The CO emission along these lines of sight orginates in diffuse gas where C^+ is the dominant form of carbon.

If it is accepted that $f_{H_2} = 0.35$, the bulk CO-H_2 conversion factor may be inferred immediately from the data shown in Fig. 1. The sample means are $\langle W_{CO}\rangle = 4.42$ K km s^{-1} and $\langle E_{B-V}\rangle = 0.888$ mag or ($\langle N_{H_2}\rangle = 9.01 \times 10^{20} H_2$ cm^{-2}), implying $W_{CO} = 1$ K km s^{-1} per 2.04×10^{20} H_2 cm^{-2}. Rather strikingly, there is apparently no difference in the *mean* CO luminosity per H_2 in diffuse and fully molecular gas. For insight into the scatter present in the ensemble of sightlines, the right-hand panel of Fig. 1 shows a line corresponding to the ensemble mean conversion factor and $f_{H_2} = 1/3$. The range in f_{H_2} determined for the diffuse gas, roughly 0.25–0.45 or 0.35 ± 0.1, implies a 30% margin of error for the method as a whole.

An alternative approach to this determination based on molecular chemistry, comparing W_{CO} with N_{HCO^+} as a surrogate for N_{H_2} and giving similar results, is discussed in Appendix C.

4. The proportion of CO emission arising from diffuse gas

The similarity of the CO-H_2 conversion factors in diffuse and fully molecular gas must have led to confusion whereby CO emission arising in diffuse gas has been attributed to "molecular clouds", i.e. the truism noted in the Introduction. To quantify this phenomenon we derive the mean luminosity of diffuse molecular gas viewed perpendicular to the galactic plane $W_{CO}(b) \sin|b|$ for a plane-parallel stratified gas layer and we compare that to the equivalent luminosity perpendicular to the galactic plane inferred from surveys of CO emission near the galactic equator.

Shown in Fig. 2 is the distribution of W_{CO} with $1/\sin|b|$. For reference a line is shown corresponding to the canonical CO-H_2 conversion factor and the combination $f_{H_2} \times \sigma_z = 30$ pc, in the simplistic case that the galactic gas layer can be described by a single Gaussian vertical component with dispersion σ_z. For convenience the diffuse gas is usually described by several components having a range of vertical scale heights (Cox 2005) but the neutral gas components of the nearby ISM are not well-described by simple plane-parallel layers (see also Heiles & Troland 2003) owing to local geometry (the local bubble)

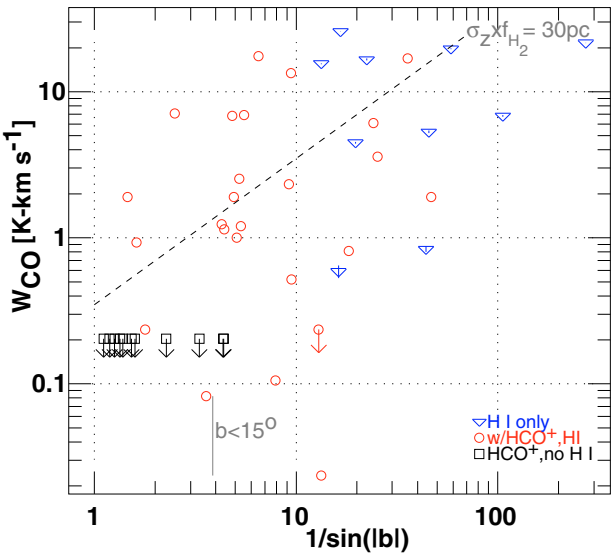

Fig. 2. Integrated CO brightness plotted against $1/\sin(|b|)$. For comparison, a line is shown for the case of a plane-parallel Gaussian layer with vertical dispersion σ_z, when $\sigma_z f_{H_2} = 30$ pc and $N_{H_2}/W_{CO} = 2 \times 10^{20}$ H_2 cm^{-2}/(K km s^{-1}).

combined with the scatter induced by the comparatively long mean free paths between kinematic components.

We quote the ensemble average brightness $\langle W_{CO}\rangle = 4.64$ K km s^{-1} and number of equivalent half-thicknesses $\langle 1/\sin|b|\rangle = 19.75$, implying a mean integrated brightness 0.235 K km s^{-1} per galactic half width[1]. Looking down on the Milky Way vertically from afar the integrated CO brightness of diffuse gas would be twice this, $W_{CO_\perp} = 0.47$ K km s^{-1}.

Galactic surveys of CO emission, on the other hand, calculate a mean CO brightness per kpc of 5 K km s^{-1}/kpc at $z = 0$ pc in the galactic disk at a galactocentric distance $R_\odot = 8$ kpc. Note that this value is scaled from the result of Burton & Gordon (1978) which assumed $R_\odot = 10$ kpc. If the molecular gas layer sampled in these surveys is described by a Gaussian vertical distribution having a dispersion $\sigma_z = 60$ pc (Cox 2005) and z-integral $\sqrt{2\pi\sigma_z^2} = 0.150$ kpc, the galactic survey result translates into an integrated CO brightness $W_{CO_\perp} = 5$ K km s^{-1}/kpc $\times$ 0.150 kpc = 0.75 K km s^{-1} when viewed vertically across the galactic disk as described in Appendix D. This is only 50% higher than that of the diffuse CO alone.

The question then is whether the CO emission and H_2 attributable to diffuse gas exist in addition to that sampled in the CO surveys near the galactic plane, or whether the galactic CO surveys incorporate a significant proportion of diffuse CO emission. If the former – if, for instance the diffuse CO like the diffuse ISM has a larger scale height and is a distinguishable component of the local CO emission – the local H_2 surface density could be higher than previously believed.

The total density of gas near the Sun is usually quoted as 1.2 H-nuclei cm^{-3} from Spitzer (1978) and this is often decomposed into "molecular" and "diffuse" components with roughly 50% attributed to each (for instance see Cox 2005). The CO emissivity measured in galactic plane surveys (5 K km s^{-1}/kpc) conveniently converts to a local mean H_2 density of about 0.33 H_2 cm^{-3}, about half of Spitzer's total. However, recall that the quoted total mean density is based on the statistics of reddening toward A-stars within a few hundred pc of the Sun

[1] The actual ensemble averaged value of $\langle W_{CO} \sin|b|\rangle$ is substantially larger 0.42 ± 0.66 K km s^{-1}.

(Münch 1952) which were very unlikely to have sampled dark cloud lines of sight. GAIA photometry should settle this matter, but the issue of the total mean density of the ISM locally and relative proportions of atomic and molecular material are not as clearly defined as is generally assumed.

5. Rationale for a common CO-H_2 conversion

The very first discussions of the applicability of a common N_{H_2}/W_{CO} conversion factor (Liszt 1982; Young & Scoville 1982) noted that diffuse and dense gas at 60–100 K, or dark dense gas at 12 K, all had similar ratios W_{CO}/N_{H_2}. For instance $W_{CO} \approx 1.5$ K km s^{-1}, $N_{H_2} = 5 \times 10^{20}$ km s^{-1} toward ζ Oph (a typical diffuse line of sight) and $W_{CO} = 450$ K km s^{-1}, $N_{H_2} = 2 \times 10^{23}H_2$ cm^{-2} toward Ori A. By comparison, a dark cloud like L204, near ζ Oph, with $A_V = 5$ mag has $N_{H_2} \approx 5 \times 10^{21}$ cm^{-2}, $N_{CO} \approx 8 \times 10^{17}$ cm^{-2} and an integrated brightness $W_{CO} \approx 15$ K km s^{-1} (Tachihara et al. 2000) or $N_{H_2}/W_{CO} \approx 3 \times 10^{20}H_2$ cm^{-2} (K km s)$^{-1}$. Comparing the two gas phases sampled in CO near ζ Oph it is apparent that the higher CO column density in the dark cloud is more than compensated by the diminished brightness per CO molecule. The result is a nearly constant ratio of W_{CO} to N_{H_2} across phases while the brightness per CO molecule W_{CO}/N_{CO} varies widely.

The physical basis for this behavior has become more apparent recently with closer study of CO in diffuse gas (Pety et al. 2008; Liszt et al. 2009). To begin the discussion we rewrite the CO-H_2 conversion factor χ_{CO} as

$$\frac{1}{\chi_{CO}} = \left(\frac{W_{CO}}{N_{CO}}\right) \times \left(\frac{N_{CO}}{N_{H_2}}\right) = \left(\frac{W_{CO}}{N_{CO}}\right) X_{CO}, \quad (2)$$

separating the coupled and competing effects of cloud structure or radiative transfer (W_{CO}/N_{CO}) and CO chemistry ($N_{CO}/N_{H_2} = X_{CO}$). Simply put, the specific brightness W_{CO}/N_{CO} can be shown to be higher in warmer, subthermally-excited diffuse gas by about the same amount (a factor 30–50) that X_{CO} is lower: $\langle X_{CO} \rangle = 3 \times 10^{-6}$ for the diffuse gas (Burgh et al. 2007) compared to $\approx 10^{-4}$ in dark gas where the carbon is very nearly all in CO.

As noted by Goldreich & Kwan (1974) in the original exposition of the LVG model for radiative transfer, W_{CO}/N_{CO} will be much greater when the excitation of CO is weak – when the kinetic temperature is much greater than the $J = 1$–0 excitation temperature. Moreover when CO is excited somewhat above the cosmic microwave background but well below the kinetic temperature, the brightness of the CO $J = 1$–0 line will be linearly proportional to N_{CO} even when the line is quite optically thick (again, see Goldreich & Kwan 1974). As Michel Guelin pointedly reminded us, this occurs because weak excitation means that there is also little collisional de-excitation so that the gas merely scatters emitted photons until they eventually escape. As Goldreich & Kwan (1974) showed, this proportionality between brightness and column density persists until the opacity is so very large that the transition approaches thermalization through radiative trapping.

The discussion of the previous paragraph also applies to other molecules, but because CO has such a small dipole moment the proportionality between CO brightness and column density is only weakly dependent on ambient physical conditions: a nearly universal ratio $N_{CO}/W_{CO} = 10^{15}$ CO cm^{-2}/(K km s^{-1}) can be calculated for diffuse gas using recent excitation cross-sections (Liszt 2007b). This is in excellent agreement with measured values of N_{CO} and CO $J = 1$–0 excitation temperatures in the diffuse gas seen toward stars in uv absorption (Sonnentrucker et al. 2007; Burgh et al. 2007; Sheffer et al. 2008) or at mm-wavelengths in absorption against distant quasars (Liszt & Lucas 1998). For the observed value $\langle X_{CO} \rangle = 3 \times 10^{-6}$ (Burgh et al. 2007) the N_{H_2}/W_{CO} conversion ratio in diffuse clouds is $N_{H_2}/W_{CO} = 10^{15}/3 \times 10^{-6} = 3.3 \times 10^{20}$ H$_2$ cm^{-2}/(K km s^{-1}).

Finally, note that even if the ratio W_{CO}/N_{CO} is not constant between gas phases, it is still the case that $W_{CO} \propto N_{CO}$ separately in either the dense or diffuse gas. For the diffuse gas the proportionality is based in the microphysics of CO radiative transfer a la Goldreich & Kwan (1974). For the dark cloud case, note that there is a fixed ratio of N_{CO}/N_{H_2} when the gas-phase carbon is in CO and the hydrogen is in H_2 so that a W_{CO}–N_{H_2} conversion is fully equivalent to a W_{CO}–N_{CO} conversion.

6. Discriminating between emission from diffuse and dense gas

There are ways in which mm-wave molecular emission differs between dense and diffuse gas, even if not in ^{12}CO. Emission from molecules like CS, HCN and HCO$^+$ having higher dipole moments is generally thought to single out denser gas than does CO, especially in extreme environments (Wu et al. 2005). Note, however, that surveys of the Milky Way galactic plane find widely-distributed emission in HCO$^+$, CS, HCN, etc. with intensity ratios of 1–2% relative to W_{CO} from essentially all features detected in CO (Liszt 1995; Helfer & Blitz 1997).

Relatively little is known of the emission from mm-wave species in diffuse gas beyond that from CO. Most common is emission from HCO$^+$ because it is chemically ubiquitous and somewhat more easily excited owing to its positive charge and high dipole moment. Although HCO$^+$ emission is weak in the example shown here in Appendix A it appears at levels $\gtrsim$1% of W_{CO} in portions of the diffuse cloud around ζ Oph or in the Polaris flare (Liszt & Lucas 1994; Liszt 1997; Falgarone et al. 2006). Therefore HCO$^+$ emission is probably not a good discriminator but CS and HCN appear with high abundance only when $N_{HCO^+} \gtrsim 10^{12}$ cm^{-2} or $N_{H_2} > 5 \times 10^{20}$ cm^{-2} and should be much more weakly excited in low density gas. In any case, searching for emission that is 100 times weaker than W_{CO} may not be an effective use of observing time and only in very dense, warmer gas like that found in massive, OB star-forming regions like Ori A are the higher dipole moment molecules substantially brighter than 1–2% relative to W_{CO}.

A more effective method of discriminating between CO emission from diffuse and dark or dense gas is afforded by ^{13}CO. Although the abundance of ^{13}CO is enhanced by fractionation (see the example in Appendix A) lowering the observed ^{12}CO/^{13}CO brightness temperature ratios (Liszt & Lucas 1998; Liszt 2007b; Goldsmith et al. 2008), those ratios are still noticeably higher in diffuse gas. Typically they are $\gtrsim$10–15 instead of $\lesssim$3–5 as seen in dark clouds or in surveys of the inner-Galaxy gas in the galactic plane (Burton & Gordon 1978). Recall that the mean ^{12}CO/^{13}CO brightness ratio nearly doubles across the galactic disk (Liszt et al. 1981), which was another, earlier indication that molecular gas near the Solar Circle has a high proportion of diffuse material.

To summarize, we suggest that the most efficient way to ascertain the origin of CO emission is to compare ^{12}CO and ^{13}CO brightnesses because emission from ^{13}CO is much stronger than emission from HCO$^+$, CS, HCN etc., and because there is actually less ambiguity in the brightness ratios relative to W_{CO}.

7. Summary

In Sects. 2 and 3 we described and considered a sample of lines of sight studied in HI and molecular absorption and known to be comprised of diffuse gas. Their molecular component shows features whose CO, HCO^+ and other molecular column densities are small compared to those of dark clouds (in the case of CO, at least 30 times smaller). There is often quite substantial fractionation of ^{13}CO (indicating that the dominant form of carbon is C^+) and the rotational excitation of CO is sub-thermal with implied cloud temperatures typical of those determined directly for diffuse H_2 in optical/uv surveys, i.e. 30 K or more.

Using an externally-determined value for the ratio of total HI column density to integrated HI absorption and the standard equivalence between reddening and N_H we derived the molecular gas fraction for this sample to be $f_{H_2} = 0.35$, in the middle of the range of other estimates for the diffuse ISM as a whole based on optical (mainly CH) and uv (HI and H_2) absorption studies.

We showed that this estimate for f_{H_2} implies the same value $X_{HCO^+} = 3 \times 10^{-9}$ that was previously determined from comparisons of OH and HCO^+ column densities in individual clouds. We then compared measured CO brightnesses with the inferred molecular gas column densities to derive the ensemble mean N_{H_2}/W_{CO} conversion factor. Surprisingly, We found this mean to be just equal to the locally-accepted value $2.0 \times 10^{20} H_2/(\mathrm{K\,km\,s^{-1}})$ for "molecular" gas believed to reside in dense dark fully-molecular clouds near the galactic equator.

Such exact agreement is probably something of an accident of sampling, but the fact that diffuse and dark gas would have very similar N_{H_2}/W_{CO} conversion factors, which had been inferred empirically long ago, now has a firmer physical basis. In Sect. 5 we explained it as the result of the brightening of CO $J = 1$–0 emission per CO molecule that was theoretically predicted for warmer more diffuse gas by Goldreich & Kwan (1974), which compensates for the lower relative abundance X_{CO} there. The mean CO abundance observed in optical absorption in diffuse clouds $\langle X_{CO} \rangle = 3 \times 10^{-6}$, combined with the observed and expected brightness per CO molecule, $W_{CO}/N_{CO} = 1\ \mathrm{K\,km\,s^{-1}}/10^{15}\mathrm{CO\ cm^{-2}}$, can be be combined to form an CO-H_2 conversion factor of $N_{H_2}/W_{CO} = 10^{15}/3{\times}10^{-6} = 3.3 \times 10^{20}\,\mathrm{H_2\,cm^{-2}/(K\,km\,s^{-1})}$.

In Sect. 4 we derived the expected brightness of diffuse gas viewed perpendicular to the galactic plane from afar, $0.47\,\mathrm{K\,km\,s^{-1}}$, and compared that to the value expected from surveys of CO emission in the galactic plane, combined with a narrow (60 pc dispersion) Gaussian vertical distribution; that is $0.75\,\mathrm{K\,km\,s^{-1}}$. This suggests that there has been confusion in the general attribution of CO emission to "molecular clouds" when in fact much of it arises in the diffuse ISM. This view is consistent with the motivations discussed in the Introduction, whereby CO emission is increasingly being found along lines of sight lacking high extinction and whereby CO emission seen along dark lines of sight is found (through molecular absorption studies and in other ways) to originate in components having the relatively small molecular number and column densities typical of diffuse gas. An example of such a line of sight is given in Appendix A here.

We briefly discussed in Sect. 4 the decomposition of the total mean density of neutral gas in the nearby ISM, 1.2 H $\mathrm{cm^{-3}}$ (Spitzer 1978), into its atomic and molecular constituents. We noted that although the balance is generally believed to be roughly 50–50 (Cox 2005), some emission might shift to the diffuse side of the balance sheet if CO emission is reinterpreted. Moreover, we pointed out that the molecular contribution to the true local mean density from large-scale galactic CO surveys in the galactic plane should be questioned more generally because it is unclear to what extent Spitzer's estimate, based on the earlier optical work of Münch, incorporates the contribution of optically-opaque gas.

Although the ability to discriminate between the separate contributions to W_{CO} from diffuse and darker, denser gas is limited when only ^{12}CO is considered, it should be possible to infer the nature of the host gas using other emission diagnostics (see Sect. 6). The most efficient of these is probably the brightness of ^{13}CO, which, although enhanced by fractionation, is still substantially weaker, relative to W_{CO}, in diffuse gas. Searching for emission from species having higher dipole moments such as CS $J = 2$–1 and HCN (and probably not HCO^+ because it is chemically so ubiquitous and more easily excited) are alternatives that might require somewhat longer integration times.

8. Discussion: Interpreting a sky occupied by CO emission from diffuse gas

The usual interpretation of CO sky maps, galactic surveys, etc, is that CO emission mostly traces dark and or "giant" molecular clouds (GMC) composed of dense cold gas occupying a very small fraction of the interstellar volume at high thermal pressure within an ISM that may confine them via its ram or turbulent pressure if they are not gravitationally bound. The balance between GMC and diffuse atomic material may be controlled by quasi-equilibrium between local dynamics and the overlying weight of the gas layer but the molecular material inferred from CO emission is generally believed to be that which is most nearly on the verge of forming stars, for instance through the Schmidt-Kenicutt power-law relation between star formation rate and gas surface density[2] (Leroy et al. 2008; Bigiel et al. 2008).

By contrast, CO emission from diffuse molecular gas originates within a warmer, lower-pressure medium that occupies a much larger fraction of the volume and contributes more substantially to mid-IR dust or PAH emission but only has the requisite density and chemistry to produce CO molecules and CO emission (since $W_{CO} \propto N_{CO}$) over a very limited portion of that volume. In this case a map of CO emission is a map of CO abundance and CO chemistry first, and only secondarily a map of the mass even if the mean CO-H_2 conversion ratio is (as we have shown) "standard". Moreover, although CO emission traces the molecular column density N_{H_2} quite decently where W_{CO} is at detectable levels, it arises in regions that are not gravitationally bound or about to form stars. The CO sky is mostly an image of the CO chemistry.

Acknowledgements. The National Radio Astronomy Observatory is operated by Associated Universites, Inc. under a cooperative agreement with the US National Science Foundation. The Kitt Peak 12-m millimetre wave telescope is operated by the Arizona Radio Observatory (ARO), Steward Observatory, University of Arizona. IRAM is operated by CNRS (France), the MPG (Germany) and the IGN (Spain). This work has been partially funded by the grant ANR-09-BLAN-0231-01 from the French *Agence Nationale de la Recherche* as part of the SCHISM project. We thank Bob Garwood for providing the H I profiles of Dickey et al. (1983) in digital form.

Appendix A: NRAO150: an example of a dark line of sight comprised of diffuse gas

The estimated total extinction along this comparatively low-latitude line of sight at $l = 150.4°$, $b = -1.6°$ (see Table E.2)

[2] It is also recognized that more precise tracers of the high-density star-forming material may be needed in extreme environments such as ULIRG (Wu et al. 2005).

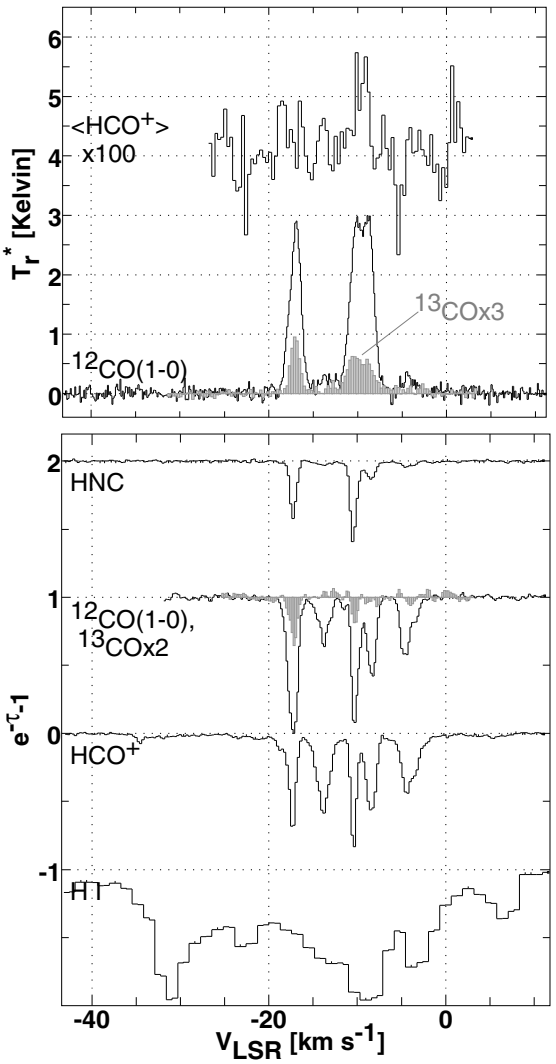

Fig. A.1. Line profiles toward and near B0355+508 = NRAO150. *Bottom*: absorption line profiles of H I, HCO^+, ^{12}CO, ^{13}CO (multiplied by 2) and HNC; HI absorption and emission are present over a much broader velocity range than shown here. *Top*: Emission from ^{12}CO, ^{13}CO (scaled upward by a factor 3) and HCO^+ (scaled upward by a factor 100). The HCO^+ profile is an average over a 3.5′ region around the continuum (to avoid absorption). See Appendix A.

is E_{B-V} = 1.5 mag or $A_V \approx$ 5 mag but it would be quite opaque even if only the atomic gas were present. A lower limit on N_{HI} from the integrated 21 cm emission of the nearest profile in the Leiden-Dwingeloo Survey (Hartmann & Burton 1997) in the optically thin limit is $N_{HI} \gtrsim 7.4 \times 10^{21}$ cm^{-2}, implying $E_{B-V} \gtrsim 1.27$ mag. The H I column density derived by taking the ratio of N_{HI} to HI absorption as discussed in Sect. 3 here is, understandably, slightly larger, $N_{HI} = 1.1 \times 10^{22}$ cm^{-2}.

We show in Fig. A.1 various absorption and emission profiles along and around the line of sight to NRAO150 aka B0355+508. We have published various analyses of this line of sight in the references noted below, and most recently we synthesized the CO emission in a 90″ region around NRAO150 at 6″ resolution (Pety et al. 2008). HI absorption and emission extend well outside the narrow kinematic interval shown here. The weak HCO^+ absorption at −35 km s^{-1} is real, as is the broad wing extending up to −25 km s^{-1}.

CO emission is fairly strong in this direction, W_{CO} = 17 K km s^{-1}, nominally implying $2N_{H_2} \approx 7 \times 10^{21}$, comparable to N_{HI}, but molecular absorption spectra of HCO^+ and CO

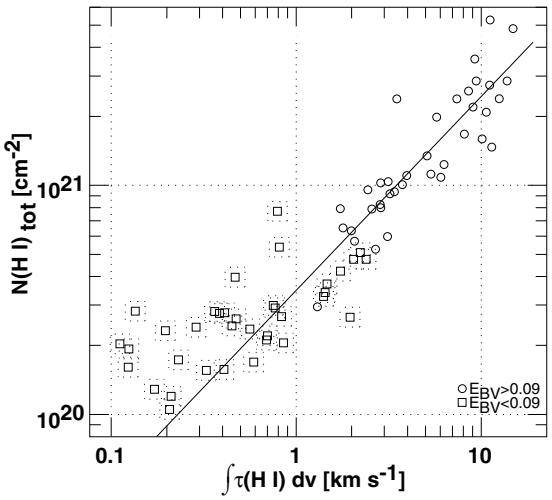

Fig. B.1. Total hydrogen column density vs. integrated HI optical depth for the sources studied by Heiles & Troland (2003). Lines of sight with $E_{B-V} < 0.09$ mag were not included in the regression fit, to point out the upturn at low $\int \tau(\mathrm{HI})\, dv$. See Appendix B.

are much richer than the CO emission. The HCO^+ absorption spectrum (Lucas & Liszt 1996; Liszt & Lucas 2000) shows five prominent components each having $N_{HCO^+} \approx 1.3 \times 10^{12}$ cm^{-2} (Lucas & Liszt 1996) or $2N_{H_2} \approx 9 \times 10^{20}$ cm^{-2} implying E_{B-V} = 0.15 mag per component associated with H_2 if $X_{HCO^+} = 3 \times 10^{-9}$ as discussed in Sect. 3. The H_2, HCO^+ and OH column densities of these components are each nearly equal to what is seen locally along the line of sight to ζ Oph at A_V = 1 mag (Morton 1975; Van Dishoeck & Black 1986; Liszt 1997).

Further evidence of the diffuse nature of the gas is given by the fractionation of ^{13}CO in CO; $N_{^{12}CO}/N_{^{13}CO}$ = 15 ± 2, 25 ± 4 and 32 ± 13 in the components at −17, −11 and −4 km s^{-1}, respectively and $N_{^{13}CO}/N_{C^{18}O} > 36$, >54 and >25 at the 2$\sigma$ level in these components (Liszt & Lucas 1998).

In emission, the $^{12}CO/^{13}CO$ brightness ratios are 12 and 30 for the two strong kinematic components, reflecting both the fractionation and the fact that $W_{CO} \propto N_{CO}$ in the diffuse gas regime as discussed in the text here.

HCO^+ emission is weak in Fig. A.1. The profile shown (from Lucas & Liszt 1996) is an average of positions around the continuum source to avoid contamination from absorption. The low levels of HCO^+ emission seen toward our sample of background continuum sources can be understood as arising from relatively low density gas ($n_{H_2} \lesssim 100$ cm^{-3}) when the electron fraction is as high as expected for diffuse gas, i.e. 2×10^{-4} (Lucas & Liszt 1994, 1996).

Appendix B: The ratio of total to absorbing HI

Shown in Fig. B.1 is a plot of the data from the tables of Heiles & Troland (2003) that were used in Sect. 3 to convert the $\int \tau(\mathrm{HI})\, dv$ measurements in Fig. 1 to a total quantity of HI. The plot shows a regression line (power-law slope 0.84) fit to data points with $E_{B-V} > 0.09$ mag (the range occupied by the HCO^+ *detections* in Fig. 1) to point out a slight upturn at low $\int \tau(\mathrm{HI})\, dv$. The sample means are largely unaffected by setting various sample selection criteria.

Appendix C: A chemistry-based determination of N_{H_2}/W_{CO}

It is also possible to determine W_{CO}/N_{H_2} without the H I measure or formally estimating f_{H_2}, although we preferred not to

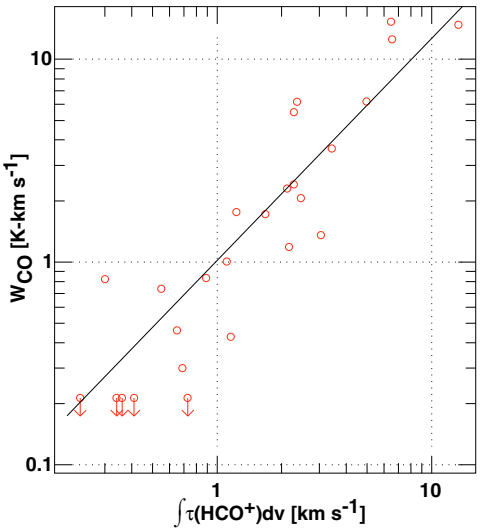

Fig. C.1. Integrated CO $J = 1$–0 brightness plotted against the integrated HCO^+ $J = 1$–0 optical depth. $N_{HCO^+} = 1.12 \times 10^{12}$ cm^{-2} $\left(\int \tau(HCO^+)\, dv/1 \text{ km s}^{-1}\right)$. See Appendix D.

do this in the main discussion. In Fig. C.1 we show the variation of W_{CO} with $\int \tau(HCO^+)\, dv$. CO appears reliably at detectable levels $W_{CO} \gtrsim 0.3$ K km s^{-1}, $N_{CO} \gtrsim 3 \times 10^{14}$ cm^{-2} when $N_{HCO^+} \gtrsim 3 \times 10^{11}$ cm^{-2} or $N_{H_2} \gtrsim N_{HCO^+}/3 \times 10^{-9} = 10^{20}$ cm^{-2}. If $X_{HCO^+} = 3 \times 10^{-9}$ the ensemble mean values $\langle W_{CO} \rangle = 3.45$ K km s^{-1}, $\left\langle \int \tau(HCO^+)\, dv \right\rangle = 2.38$ km s^{-1} imply $W_{CO} = 1$ K km s^{-1} per 2.6×10^{20} H_2 cm^{-2}, just 30% above that derived in Sect. 3.5.

The near linearity of the N_{CO}–N_{HCO^+} relationship in Fig. C.1 results from bulk averaging over whole lines of sight: given the same general mix of conditions, an ensemble of richer and poorer or shorter and longer sightlines will show proportionalities between almost any two quantities in this way. As shown in Fig. A.1 there is no such proportionality on a per-component basis. In detail, and with much scatter, the overall chemical variation is approximately $N_{CO} \propto (N_{H_2})^2$ (Liszt 2007b; Sheffer et al. 2008).

Appendix D: Calculating the CO brightness from galactic survey results

The statistics of observing the clumpy galactic molecular cloud distribution are Poisson (Gordon & Burton 1976; Burton & Gordon 1978) so the integrated CO brightness $W_{CO}(r)$ accumulated when traversing a path of length r in the galactic plane is

$$W_{CO}(r) = W_{CO_0}(1 - \exp(-r/\lambda)) \quad \text{(D.1)}$$

where W_{CO_0} is the characteristic brightness of a clump (GMC) and λ is the geometric mean free path between clumps. Although it is possible to derive W_{CO_0} and λ separately, galactic survey results are given in terms of a hybrid quantity A_{CO} whose units are K km s^{-1} per kpc corresponding to evaluating $W_{CO}(r)$ when $r \ll \lambda$, i.e. $W_{CO}(r) = (W_{CO_0}/\lambda)\, r = A_{CO}\, r$. The coefficient A_{CO} is closely related to the mean density: just convert W_{CO} to N_{H_2}. For H I the integrated brightness per unit distance is directly converted into a mean density n(H I), if it is assumed that the gas is optically thin.

The brightness of the CO cloud ensemble viewed vertically through the galactic disk is then just $A_{CO}\, \Delta z$, where Δz is the equivalent thickness of the disk. For a Gaussian vertical distribution with dispersion σ_z, $\Delta z = (2\pi)^{1/2} \sigma_z$.

References

Bigiel, F., Leroy, A., Walter, F., et al. 2008, AJ., 136, 2846
Bohlin, R. C., Savage, B. D., & Drake, J. F. 1978, ApJ, 224, 132
Bothwell, M. S., Kennicutt, R. C., & Lee, J. C. 2009, MNRAS, 400, 154
Burgh, E. B., France, K., & McCandliss, S. R. 2007, ApJ, 658, 446
Burton, W. B., & Gordon, M. A. 1978, A&A, 63, 7
Cox, D. P. 2005, ARA&A, 43, 337
Dickey, J. M., Kulkarni, S. R., Heiles, C. E., & Van Gorkom, J. H. 1983, ApJSS, 53, 591
Draine, B. T., Dale, D. A., Bendo, G., et al. 2007, ApJ, 663, 866
Falgarone, E., Pineau Des Forêts, G., Hily-Blant, P., & Schilke, P. 2006, A&A, 452, 511
Garwood, R. W., & Dickey, J. M. 1989, ApJ, 338, 841
Goldreich, P., & Kwan, J. 1974, ApJ, 189, 441
Goldsmith, P. F., Heyer, M., Narayanan, G., et al. 2008, ApJ, 680, 428
Gordon, M. A., & Burton, W. B. 1976, ApJ, 208, 346
Hartmann, D., & Burton, W. B. 1997, Atlas of galactic neutral hydrogen (Cambridge; New York: Cambridge University Press)
Heiles, C., & Troland, T. H. 2003, ApJ, 586, 1067
Helfer, T. T., & Blitz, L. 1997, ApJ, 478, 233
Leroy, A. K., Walter, F., Brinks, E., et al. 2008, AJ, 136, 2782
Liszt, H. 1997a, A&ASS, 124, 183
Liszt, H. S. 1982, ApJ, 262, 198
Liszt, H. S. 1995, ApJ, 442, 163
Liszt, H. S. 1997, A&A, 322, 962
Liszt, H. S. 2007a, A&A, 476, 291
Liszt, H. S. 2007b, A&A, 461, 205
Liszt, H., & Lucas, R. 2002, A&A, 391, 693
Liszt, H. S., & Lucas, R. 1994, ApJ, 431, L131
Liszt, H. S., & Lucas, R. 1996, A&A, 314, 917
Liszt, H. S., & Lucas, R. 1998, A&A, 339, 561
Liszt, H. S., & Lucas, R. 2000, A&A, 355, 333
Liszt, H. S., Burton, W. B., & Bania, T. M. 1981, ApJ, 246, 74
Liszt, H. S., Pety, J., & Tachihara, K. 2009, A&A, 499, 503
Lucas, R., & Liszt, H. S. 1994, A&A, 282, L5
Lucas, R., & Liszt, H. S. 1996, A&A, 307, 237
McCall, B. J., Hinkle, K. H., Geballe, T. R., et al. 2002, ApJ, 567, 391
Morton, D. C. 1975, ApJ, 197, 85
Münch, I. G. 1952, ApJ, 116, 575
Pety, J., Lucas, R., & Liszt, H. S. 2008, A&A, 489, 217
Rachford, B. L., Snow, T. P., Destree, J. D., et al. 2009, ApJSS, 180, 125
Savage, B. D., Drake, J. F., Budich, W., & Bohlin, R. C. 1977, ApJ, 216, 291
Schlegel, D. J., Finkbeiner, D. P., & Davis, M. 1998, ApJ, 500, 525
Sheffer, Y., Rogers, M., Federman, S. R., et al. 2008, ApJ, 687, 1075
Sheffer, Y., Rogers, M., Federman, S. R., Lambert, D. L., & Gredel, R. 2007, ApJ, 667, 1002
Sofia, U. J., Lauroesch, J. T., Meyer, D. M., & Cartledge, S. I. B. 2004, ApJ, 605, 272
Sonnentrucker, P., Welty, D. E., Thorburn, J. A., & York, D. G. 2007, ApJSS, 168, 58
Spitzer, L. 1978, Physical processes in the interstellar medium (New York: Wiley-Interscience)
Tachihara, K., Abe, R., Onishi, T., Mizuno, A., & Fukui, Y. 2000, Publ. Astron. Soc. Jpn., 52, 1147
Van Dishoeck, E. F., & Black, J. H. 1986, ApJSS, 62, 109
Watson, W. D., Anicich, V. G., & Huntress, W. T., J. 1976, ApJ, 205, L165
Weselak, T., Galazutdinov, G. A., Beletsky, Y., & Krełowski, J. 2010, Mon. Not. R. Astron. Soc., 402, 1991
Wu, J., Evans, II, N. J., Gao, Y., et al. 2005, ApJ, 635, L173
Young, J. S., & Scoville, N. 1982, ApJ, 258, 467

Pages 9 to 10 are available in the electronic edition of the journal at http://www.aanda.org

Appendix E: Data

The data shown in Fig. 1 are tabulated in Tables E.1 and E.2. The sources of these data are discussed in Sect. 2.

Table E.1. Data used in this work.

Source	l	b	E_{B-V}[a]	$\int \tau(\mathrm{HI})\, dv$[b]	$\int \tau(\mathrm{HCO^+})\, dv$[c]	W_{CO}[d]
	°	°	mag	km s^{-1}	km s^{-1}	K km s^{-1}
B1748-253	3.745	0.635	7.86	45.37(0.40)		
B2005+403	6.816	4.302	0.69	4.67(0.05)	0.41(0.02)	<0.20
B1730-130	12.032	10.812	0.53	10.91(0.17)	1.16(0.02)	0.47(0.12)
B1908-210	16.857	−13.219	0.28		<0.30	<0.20
B1819-131	17.910	0.372	7.99	63.71(1.00)		
B1817-098	20.711	2.293	1.55	20.62(0.49)		
B1819-096	21.047	1.957	3.08	29.01(0.40)		
B1829-106	21.347	−0.629	11.56	66.05(0.53)		
B1741-038	21.591	13.128	0.58	8.20(0.11)	1.11(0.10)	1.11(0.07)
B1849+005	33.498	0.194	16.93	117.62(0.87)		
B1749+096	34.920	17.644	0.09		<0.14	<0.20
B1909+049	39.694	−2.244	2.51	19.23(0.22)		
B1910+052	40.100	−2.336	2.10	17.68(0.41)		
B1843+098	41.112	5.772	0.57	6.71(0.16)		
B1915+062	41.605	−2.928	1.43	12.78(0.27)		
B1909+161	49.658	2.907	1.54	15.98(0.33)		4.47(0.06)
B1905+190	52.496	5.591	0.66	9.69(0.23)		
B1923+210	55.557	2.264	1.87	21.01(0.28)	2.28(0.12)	2.66(0.07)
B1950+253	62.366	−0.956	3.15	29.38(0.33)		
B1901+319	63.029	11.757	0.12	0.42(0.10)		
B1641+399	63.455	40.948	0.04		<0.09	<0.20
B2145+067	63.656	−34.072	0.08	0.98(0.02)	0.23(0.07)	<0.20
B2007+249	64.048	−4.334	1.27	14.12(0.21)		16.62(0.25)
J2023+319	71.397	−3.093	1.06	12.11(0.08)	1.55(0.04)	
B2015+33A	72.226	−0.978	3.48	46.23(0.34)		
B2015+33B	72.226	−0.981	3.48	37.55(0.43)		5.31(0.11)
B2023+336	73.129	−2.368	2.08	22.90(0.26)	3.43(0.02)	6.04(0.04)
B2048+313	74.585	−8.045	0.22	1.43(0.22)		
B2013+370	74.866	1.224	1.78	39.67(0.60)	3.12(0.02)	1.49(0.06)
B1954+513	85.298	11.757	0.15		1.68(0.06)	1.89(0.04)
B1823+568	85.739	26.080	0.06		<0.20	<0.20
B2251+158	86.111	−38.184	0.11	1.78(0.01)	0.30(0.01)	0.91(0.04)
B2037+511	88.808	6.040	1.02	17.32(0.13)	0.65(0.17)	0.51(0.06)
B2022+542	90.093	9.665	0.35	4.17(0.16)		
B2055+508	90.378	3.533	2.95	36.22(0.83)		19.65(0.12)
B2106+494	90.528	1.305	2.97	54.15(0.52)		15.53(0.09)
B2030+547	91.129	8.988	0.38	3.73(0.20)		
B2200+420	92.590	−10.441	0.33	3.74(0.04)	2.36(0.03)	6.78(0.05)
B2154+483	95.584	−4.860	0.53	7.51(0.13)		
B2111+620	100.287	9.429	0.84	10.72(0.18)		
B2146+608	102.570	5.713	0.85	11.04(0.11)		
B2201+62S	104.940	5.833	0.73	9.44(0.14)		
B1928+738	105.625	23.541	0.13		0.73(0.03)	<0.20
B2341+535	112.952	−7.745	0.33	5.62(0.09)		
B2255+702	113.596	9.707	0.52	5.27(0.10)		
B2357+554	115.718	−6.503	0.31	4.65(0.23)		
B2357+55B	115.719	−6.498	0.31	2.27(1.10)		
B2348+644	116.513	2.555	1.26	31.56(0.17)		
B0012+610	118.548	−1.264	1.65	34.20(0.15)		0.59(0.06)
B0016+731	120.644	10.728	0.32	1.99(0.14)		
B0041+660	122.253	3.449	2.18	44.63(0.32)		25.80(0.11)
B0052+681	123.351	5.503	1.00	10.79(0.06)		

Notes. [a] Reddening from Schlegel et al. (1998) rms error is 16%; [b] $\int \tau(\mathrm{HI})\, dv$ from Garwood & Dickey (1989) and (for J-sources) this work see Sect. 2; [c] $\int \tau(\mathrm{HCO^+})\, dv$ from Lucas & Liszt (1996), Liszt & Lucas (2000) and this work see Sect. 2; [d] W_{CO} from Lucas & Liszt (1996), Liszt & Lucas (1998) and this work see Sect. 2.

Table E.2. Data used in this work (continued).

Source	l	b	E_{B-V}[a]	$\int \tau(\mathrm{HI})\,dv$[b]	$\int \tau(\mathrm{HCO^+})\,dv$[c]	W_{CO}[d]
	°	°	mag	km s^{-1}	km s^{-1}	K km s^{-1}
B0056+666	123.782	3.992	1.20	13.30(1.05)		
J0102+584	124.426	−4.436	0.56	9.75(0.10)	0.34(0.01)	<0.34
B0107+562	125.637	−6.231	0.39	4.56(0.07)		
B0125+628	127.109	0.538	1.60	36.54(0.59)		6.81(0.09)
B0212+735	128.927	11.964	0.76	12.36(0.13)	4.98(0.20)	6.81(0.06)
B0205+614	132.064	0.210	1.55	27.59(0.45)		21.54(0.06)
B0224+671	132.122	6.234	1.00	14.73(0.24)	2.46(0.07)	2.27(0.06)
B0241+623	135.636	2.431	0.73	8.38(0.71)		
B0323+55A	143.890	−1.057	1.75	37.96(0.30)		
B0300+471	144.986	−9.863	0.25	4.99(0.14)		
B0954+658	145.746	43.132	0.12		1.23(0.29)	1.94(0.04)
B0332+534	145.952	−1.6810	1.68	31.89(0.35)		
B0334+506	147.809	−3.895	1.24	18.77(0.14)		
B0430+587	148.581	7.536	0.54	5.80(0.19)		
B0355+508	150.377	−1.604	1.50	42.79(1.10)	6.48(0.03)	16.82(0.12)
3C84	150.577	−13.261	0.05		<0.10	<0.20
B0442+506	155.877	3.460	0.94	13.14(0.21)		
B0435+487	156.417	1.317	1.35	27.84(0.22)		
B0235+164	156.772	−39.108	0.03		<0.20	<0.20
B0404+429	156.780	−6.586	0.49	11.73(0.13)		
B0420+417	159.705	−5.382	0.74	12.93(0.12)		
B0458+477	159.712	3.653	0.72	15.07(0.14)		
B0406+386	159.845	−9.484	1.02	12.12(0.12)		
B0429+416	160.965	−4.342	0.56	11.55(0.04)		
B0415+379	161.686	−8.788	1.66	12.14(0.14)	13.34(0.65)	17.45(0.11)
B0442+39A	164.109	−3.656	0.56	6.69(0.12)		
B0509+406	166.502	0.916	0.53	14.45(0.16)		
B0552+398	171.647	7.285	0.44	7.71(0.12)	0.69(0.08)	0.33(0.04)
B0923+392	183.709	46.165	0.10		<0.09	<0.20
B0601+204	189.566	−0.640	1.37	33.58(0.56)		
B0528+134	191.368	−11.012	0.89	11.88(0.20)	2.14(0.02)	2.53(0.06)
B0629+160	196.582	3.204	0.46	7.54(0.25)		
B0622+147	196.983	1.103	0.82	26.07(0.46)		
B0629+104	201.531	0.508	1.81	27.96(0.25)		
B0630+082	203.544	−0.272	0.91	28.65(0.33)		
B0624-058	215.439	−8.067	0.71	5.55(0.02)		
J0008+686	215.752	−13.253	1.28		7.16(0.75)	13.79(0.05)
B0605-085	215.752	−13.523	0.58		2.17(0.25)	1.31(0.13)
B0736+017	216.990	11.380	0.13	2.96(0.17)	0.89(0.10)	0.92(0.04)
B0607-157	222.611	−16.183	0.26		0.36(0.09)	<0.20
B0727-115	227.768	3.140	0.30	6.81(0.14)	0.55(0.02)	0.81(0.04)
B0733-174	233.585	1.444	0.92	20.00(0.13)		
B0709-206	233.670	−5.021	0.98	19.22(0.28)		
B0704-231	235.337	−7.218	0.33	7.28(0.10)		
B1055+018	251.513	52.775	0.20		<0.24	<0.20
3C273	289.954	64.360	0.03		<0.08	<0.20
3C279	305.107	57.062	0.05		<0.07	<0.20
B1334-127	320.026	48.374	0.04		<0.17	<0.20
B1714-397	347.748	−1.142	3.53	39.45(0.20)		
B1705-353	350.339	2.768	1.74	21.39(1.30)		
B1714-336	352.735	2.393	2.42	29.58(0.88)		
B1711-285	356.516	5.884	0.60	8.64(0.27)		

Notes. [a] Reddening from Schlegel et al. (1998) rms error is 16%; [b] $\int \tau(\mathrm{HI})\,dv$ from Garwood & Dickey (1989) and (for J-sources) this work see Sect. 2; [c] $\int \tau(\mathrm{HCO^+})\,dv$ from Lucas & Liszt (1996), Liszt & Lucas (2000) and this work see Sect. 2; [d] W_{CO} from Lucas & Liszt (1996), Liszt & Lucas (1998) and this work see Sect. 2.

A&A 541, A58 (2012)
DOI: 10.1051/0004-6361/201218771
© ESO 2012

Astronomy & Astrophysics

Imaging diffuse clouds: bright and dark gas mapped in CO⋆,⋆⋆

H. S. Liszt[1] and J. Pety[2,3]

[1] National Radio Astronomy Observatory, 520 Edgemont Road, Charlottesville, VA 22903-2475, USA
e-mail: hliszt@nrao.edu
[2] Institut de Radioastronomie Millimétrique, 300 rue de la Piscine, 38406 Saint Martin d'Hères, France
[3] Obs. de Paris, 61 Av. de l'Observatoire, 75014 Paris, France

Received 3 January 2012 / Accepted 14 March 2012

ABSTRACT

Aims. We wish to relate the degree scale structure of galactic diffuse clouds to sub-arcsecond atomic and molecular absorption spectra obtained against extragalactic continuum background sources.
Methods. We used the ARO 12 m telescope to map $J = 1-0$ CO emission at 1′ resolution over 30′ fields around the positions of 11 background sources occulted by 20 molecular absorption line components, of which 11 had CO emission counterparts. We compared maps of CO emission to sub-arcsec atomic and molecular absorption spectra and to the large-scale distribution of interstellar reddening.
Results. 1) The same clouds, identified by their velocity, were seen in absorption and emission and atomic and molecular phases, not necessarily in the same direction. Sub-arcsecond absorption spectra are a preview of what is seen in CO emission away from the continuum. 2) The CO emission structure was amorphous in 9 cases, quasi-periodic or wave-like around B0528+134 and tangled and filamentary around BL Lac. 3) Strong emission, typically 4−5 K at $E_{B-V} \leq 0.15$ mag and up to 10−12 K at $E_{B-V} \lesssim 0.3$ mag was found, much brighter than toward the background targets. Typical covering factors of individual features at the 1 K km s^{-1} level were 20%. 4) CO-H_2 conversion factors as much as 4−5 times below the mean value $N(H_2)/W_{CO} = 2 \times 10^{20}$ H_2 cm^{-2} (K km s^{-1})$^{-1}$ are required to explain the luminosity of CO emission at/above the level of 1 K km s^{-1}. Small conversion factors and sharp variability of the conversion factor on arcminute scales are due primarily to CO chemistry and need not represent unresolved variations in reddening or total column density.
Conclusions. Like *Fermi* and *Planck* we see some gas that is dark in CO and other gas in which CO is overluminous per H_2. A standard CO-H_2 conversion factor applies overall owing to balance between the luminosities per H_2 and surface covering factors of bright and dark CO, but with wide variations between sightlines and across the faces of individual clouds.

Key words. ISM: clouds – ISM: molecules

1. Introduction

With somewhat imprecise boundaries, interstellar clouds are generally classed as diffuse, $A_V \lesssim 1$ mag, or dark, $A_V \gtrsim 4-6$ mag, with an intermediate translucent regime (Snow & McCall 2006). In diffuse clouds the dominant form of carbon is C^+ and hydrogen is mostly atomic, although with a very significant overall admixture of H_2, 25% or more as a global average (Savage et al. 1977; Liszt et al. 2010). In dark or molecular clouds the carbon is overwhelmingly in CO with an admixture of C I and the hydrogen resides almost entirely in H_2. The population of diffuse clouds is sometimes called H I clouds in radio astronomical terms.

The shadows of dark clouds are seen outlined against brighter background fields and the clouds themselves are often imaged in the mm-wave emission of CO and many other species: the ^{12}CO(1−0) sky (Dame et al. 2001) is usually (and in part incorrectly, see below) understood as a map of fully-molecular clouds. The shadows of H I or diffuse clouds are their absorption-line spectra and for the most part, individual diffuse clouds are known only as kinematic features in optical and/or radio absorption spectra. No means exist to image individual diffuse clouds at optical wavelengths and attempts to map individual H I clouds at radio wavelengths are generally frustrated by the blending and overlapping of contributions from multiple clouds and gas phases. This lack of identity has greatly complicated our ability to define diffuse clouds physically because absorption lines do not generally permit a direct determination of the cloud size or internal density.

When diffuse clouds discovered in absorption-line spectra have a sufficiently high complement of molecules they may be imaged at radio wavelengths in species such as OH and CH and, most usefully, CO. Despite a low fractional abundance of CO relative to H_2, $\langle X(CO)\rangle = 3 \times 10^{-6}$ (Burgh et al. 2007), mapping is facilitated by an enhanced brightness of the $J = 1-0$ line in diffuse gas: the temperature is somewhat elevated ($T_K \gtrsim 25$ K), the density is comparatively small at typical ambient thermal pressure (Jenkins & Tripp 2011) and the rotation ladder is subthermally excited. In accord with theory (Goldreich & Kwan 1974), it is found observationally that there is a simple, linear proportionality between the integrated intensity W_{CO} of the CO $J = 1-0$ lines and the CO column density, even when the gas is optically thick: $N(CO) \approx 10^{15}$ cm^{-2} W_{CO}/K km s^{-1} for $W_{CO} \approx 0.2-6$ K km s^{-1} (Liszt & Lucas 1998; Liszt 2007). Per molecule, the ratio W_{CO}/N(CO) is 30−50 times higher in diffuse gas, compared to conditions in dense shielded fully-molecular gas where

⋆ Based on observations obtained with the ARO Kitt Peak 12 m telescope.
⋆⋆ Appendices are available in electronic form at http://www.aanda.org

the rotation ladder is thermalized (Liszt et al. 2010). Of course this is of substantial assistance in the present work. Conversely, the high brightness (5−12 K) of many of lines we detected should *not* be taken as discrediting their origin in diffuse gas.

Earlier we showed that, in the mean, CO-H_2 conversion factors are similar in diffuse and dense fully molecular gas (Liszt et al. 2010), because the small abundance of CO relative to H_2 in diffuse gas is compensated by a much higher brightness per CO molecule. But the proportionality between W_{CO} and N(CO) in diffuse gas, where CO represents such a small fraction of the available gas phase carbon, means that the CO map of a diffuse cloud is really an image of the CO chemistry. Moreover the CO abundance exhibits extreme sensitivities to local conditions that are manifested as order of magnitude scatter in $N(CO)/N(H_2)$ in optical absorption line studies (Sonnentrucker et al. 2007; Burgh et al. 2007; Sheffer et al. 2007, 2008), even beyond the often-rapid variation of $N(H_2)$ with E_{B-V} (Savage et al. 1977) ($E_{B-V} \approx A_V/3.1$). The net result is that the CO emission map of a diffuse cloud can only indirectly be interpreted as tracing the underlying mass distribution, or even that of the H_2. Nonetheless, it should (we hope) provide some impression of the nature of the host gas, especially in the absence of any other means of ascertaining this.

In this paper we present maps of CO J = 1−0 emission at arcminute resolution over 11 sky fields, typically 30′ × 30′ around the positions of compact extragalactic mm-wave continuum sources that we have long used as targets for absorption line studies of the chemistry of diffuse clouds. As is the case for nearly all background sources seen at galactic latitudes $|b| < 15-18°$, and for some sources at higher latitudes, the current targets were known to show absorption from HCO^+ and from one or more other commonly-detected species (OH, CO, C_2H, C_3H_2); most but not all directions also were known to show CO emission in at least some of the kinematic features present in absorption.

This work is organized as follows. The observational material discussed here is summarized in Sect. 2. In Sects. 3−5 we discuss the new maps with sources grouped in order of kinematic complexity. Section 6 is an intermediate summary of the lessons drawn from close scrutiny of the maps. Section 7 briefly discusses the influences of galactic and internal cloud kinematics and Sect. 8 presents a comparison of CO intensity and reddening within a few of the simpler individual fields. Appendix A shows a few position-velocity diagrams that, while of interest, could be considered redundant with those shown in the main text in Figs. 13 and 14. Figures B.1 and B.2 in Appendix B show the target lines of sight in the context of large-scale galactic kinematics sampled in H I emission.

2. Observational material

2.1. CO J = 1–0 emission

On-the-fly maps of CO J = 1−0 emission were made at the ARO 12 m telescope in 2008 December, 2009 January and 2009 December in generally poor weather using filter banks with 100 kHz or 0.260 km s^{-1} channel spacing and spectral resolution. System temperatures were typically 450−750 K. The data were subsequently put onto 20″ pixel grids using the AIPS tasks OTFUV and SDGRD; the final spatial resolution is 1′. Most maps are approximately 30′ × 30′ on the sky and were completed in 4−5 h total observing time. The new CO emission data are presented in terms of the T_R^* scale in use at the 12 m antenna and all velocities are referred to the kinematic Local Standard of Rest. The typical rms channel-channel noise in these maps at 1′ and 0.26 km s^{-1} resolution is 0.4−0.5 K; their sensitivity is rather moderate and the detectability limit is of order 1 K km s^{-1} for a single line component.

More sensitive CO J = 1−0 line profiles at higher spectral resolution (25 kHz) had been previously observed toward the continuum sources as part of our survey efforts, for instance see Liszt & Lucas (1998). It is these profiles that are displayed in the figures shown here representing emission in the specific direction of the background target and used to calculate line profile integrals as quoted in Table 1.

Many interstellar clouds lie at distances of about 150 pc from the Sun, just outside the Local Bubble. At this distance the 1′ resolution of our CO mapping corresponds to 0.041 pc.

2.2. H I absorption and emission and N(H I)

The λ 21 cm H I absorption spectra shown here are largely from the work of Dickey et al. (1983) augmented by a few spectra taken at the VLA in 2005 May. The spectral resolution of this data is 0.4−1.0 km s^{-1}.

Figures B.1 and B.2 of the Appendix B show latitude-velocity diagrams of H I emission drawn from the Leiden-Dwingeloo Survey of Hartmann & Burton (1997).

The H I column densities quoted in Table 1 were derived in one of two ways. Where an H I absorption profile exists we applied the formula given in footnote 3 to Table 1, which is an empirical relation derived by Liszt et al. (2010) using the Arecibo H I emission-absorption survey data of Heiles & Troland (2003). The effective H I spin temperature implied by use of this formula is 143 K. In other cases (see footnote 4 to Table 1) we apply the optically-thin limit to the data of Hartmann & Burton (1997).

2.3. Molecular absorption

Also shown here are spectra of λ18 cm OH absorption from Liszt & Lucas (1996), λ6 cm H_2CO from Liszt et al. (2006), J = 1−0 mm-wave absorption spectra of CO (Liszt & Lucas 1998), HCO^+ (Lucas & Liszt 1996), HCN and HNC (Liszt & Lucas 2001), CS J = 2−1 (Lucas & Liszt 2002) and the 87.32 GHz N = 1−0, J = 3/2−1/2, F = 2−1 transition of C_2H (Lucas & Liszt 2000).

2.4. Reddening

Maps of reddening were constructed from the results of Schlegel et al. (1998). This dataset has 6′ spatial resolution on a 2.5′ pixel grid. The stated single-pixel error is a percentage, 16%, of the pixel value. On average, 1 mag of reddening corresponds to a neutral gas column $N(H) = 5.8 \times 10^{21}$ cm^{-2} (Savage et al. 1977).

2.5. Target fields

The positions and other observational properties are summarized in Table 1 where the sources are grouped according to their order of presentation in Sects. 3−5. The groups appear in order of increasing reddening and gas column density and decreasing distance from the galactic plane. The line profile integrals W_{CO} quoted in Table 1 result from the more sensitive earlier observations noted in Sect. 2.1. The mean values quoted for W_{CO} along individual sightlines are averages over the new map data taken for this work.

Table 1. Continuum target, line of sight and map field properties[1] .

Target	RA (J2000)	Dec (J2000)	l	b	Map size	E_{B-V}[2] mag	N (H I)[3] 10^{20} cm^{-2}	$N(H_2)$[4] 10^{20} cm^{-2}	f_{H_2}[7]	W_{CO} K km s^{-1}	$\langle W_{CO}\rangle$ K km s^{-1}
B0736+017	07:39:18.03	01:37:04.6	216.99	11.38	15′	0.13	7.7	3.3	0.46	0.8	0.4
B0954+658	09:58:47.24	65:33:54.7	145.75	43.13	30′	0.12	5.3[5]	4.8	0.64	1.6	0.6
B1730-130	17:33:02.66	–13:04:49.5	12.03	10.81	30′	0.53	28.3	4.3	0.23	0.4	0.4
B1928+738	19:27:48.58	73:58:01.6	105.63	23.54	20′	0.13	7.2[5]	2.7	0.43	<0.2	0.0
B1954+513	19:55:42.69	51.31:48.5	85.30	11.76	30′	0.15	12.7[5]	5.0	0.44	1.6	0.3
B2251+158	22:53:57.71	16:08:53.4	86.11	–38.18	30′	0.10	4.6	1.2	0.34	0.8	0.2
B0528+134	05:30:46.41	13:31:55.1	191.37	–11.01	30′	0.89	30.9	7.9	0.34	2.2	2.6
B2200+420	22:02:43.24	42:16:39.9	92.59	–10.44	30′	0.33	9.7	8.8	0.66	5.8	3.7
B0212+735	02:17:30.81	73:49:32.6	128.93	11.96	30′	0.76	32.1	18.6	0.54	5.8	1.56
B0224+671	02:28:50.03	67:21:31.3	132.12	6.23	30′	1.00	38.3	9.2	0.32	1.9	4.0
B0355+508	03:59:29.73	50:57:50.1	150.38	–1.60	30′x 50′	(1.50)[6]	111.3	24.2	0.30	14.3	4.2
Mean						0.41	17.7	6.58	0.43	2.09	1.38

Notes. [(1)] Sources are placed in three groups according to their discussion in Sects. 3–5; [(2)] from Schlegel et al. (1998); [(3)] $N(\mathrm{H\ I}) = 2.6 \times 10^{20}\ \mathrm{cm}^{-2} \int \tau(\mathrm{H\ I})dv$ (see Sect. 2) except where noted; [(4)] $N(H_2) = N(HCO^+)/3 \times 10^{-9}$ see Sect. 2.7; [(5)] from Hartmann & Burton (1997), $N(\mathrm{H\ I}) = 1.823 \times 10^{18}\ \mathrm{cm}^{-2} \int T_B(\mathrm{H\ I})dv$; [(6)] at such a low galactic latitude E_{B-V} is not reliably determined; [(7)] $f_{H_2} = 2N(H_2)/(N(\mathrm{H\ I}) + 2N(H_2))$.

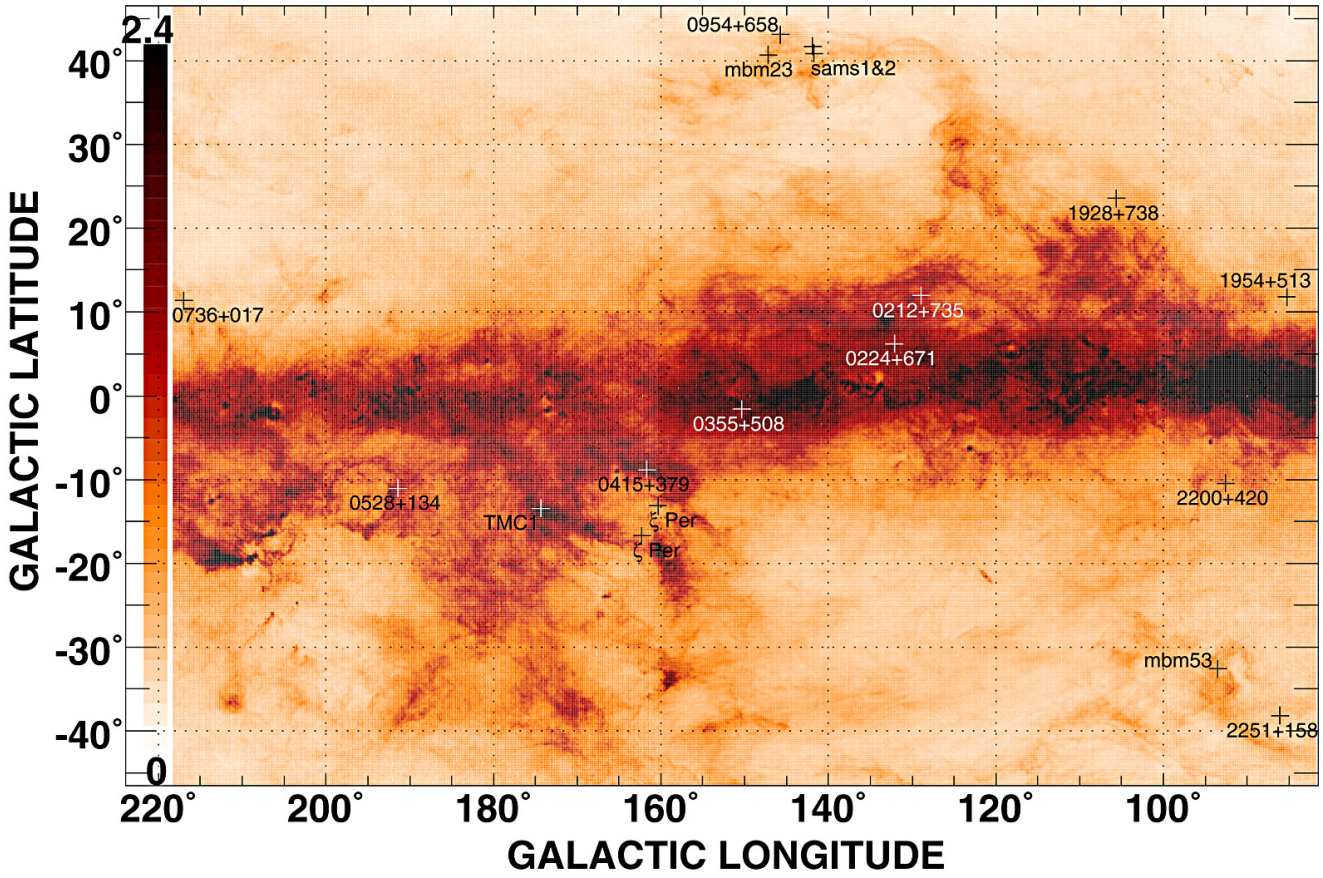

Fig. 1. Outer-galaxy finding chart for the sources studied here except B1730-130 at $l = 12°$, see Table 1. The colored background is reddening at 6′ resolution (Schlegel et al. 1998) truncated at a maximum of 2.4 mag as shown on the bar scale at left. Positions of continuum sources are indicated (see Table 1) along with a few other objects: the high-latitude molecular clouds MBM23 and MBM 53 (Magnani et al. 1985); TMC-1; SAMS 1 and 2 (Heithausen 2004); and two Perseus stars commonly used for optical absorption line studies.

Table 2 gives some pixel statistics about noise levels and spatial covering factors as discussed in Sect. 8.

2.6. Presentation of observations

A finding chart including all sources except B1730-130 is shown in Fig. 1 where the locations of the background targets are shown on a large-scale map of reddening, along with locations of a few other landmark objects as noted in the figure caption.

Maps and spectra of the target fields and background sources are shown in Figs. 2–12. Within each of three groups, sources appear in order of increasing right ascension. Members of the first group, shown in Figs. 2–7 and discussed in Sect. 3, are the simplest kinematically. Figures 8 and 9 show the fields around

Table 2. Noise levels and spatial covering factors.

Target	V km s^{-1}	$\sigma_{\rm profile}$ K	$\sigma_{\rm map}$ K km s^{-1}	$f_{>1}{}^a$	$f_{>2}{}^b$
B0736	5.1,7.2	0.43	0.48	0.18	0.07
B0954	2.6,5.2	0.25	0.33	0.20	0.12
B1730	4.0,6.1	0.36	0.52	0.20	0.03
B1928	–4.2, –0.8	0.46	0.52	0.03	0.00
B1954	–1.0, 2.4	0.33	0.35	0.20	0.13
B2251	–10.8, –7.9	0.28	0.32	0.06	0.02
B0528	0.6.3.7	0.23	0.36	0.07	0.05
	8.9,11.7		0.33	0.69	0.46
B2200	–3.8, 2.8	0.39	0.63	0.61	0.50
B0212	–14.1, –7.9	0.30	0.80	0.26	0.11
	–1.4, 1.0		0.36	0.03	0.01
	1.3, 4.9		0.66	0.34	0.19
B0224	–17.1, –11.9	0.43	0.76	0.14	0.03
	–11.6, –9.2		0.60	0.33	0.20
	–9.2, –5.1		0.56	0.39	0.20
	–4.9, –2.0		0.47	0.47	0.33
	–2.0, –0.2		0.39	0.05	0.28
	–0.2 ... 2.0		0.42	0.09	0.03
B0355	–19.2, –15.9	0.35	0.63	0.18	0.07
	–15.8, –11.7		0.92	0.43	0.28
	–11.1, –9.8		0.59	0.34	0.18
	–9.6, –7.3		0.62	0.34	0.10
	–6.0, –1.4		0.79	0.17	0.04

Notes. $^{(a)}$ Fraction of mapped area with $W_{\rm CO} \geq 1$ K km s^{-1}; $^{(b)}$ fraction of mapped area with $W_{\rm CO} \geq 2$ K km s^{-1}.

the background sources B0528+134 and B2200+420 (BL Lac) that are also kinematically simple but are heavily patterned and rather bright in CO emission; these are discussed in Sect. 4. Figures 10–12 (Sect. 5) show the results over three target fields with rather amorphous structure whose kinematics are too complex to fit into the framework in which the data for the other sources are presented in earlier figures. Two of these sources (B0212+735 and B0224+671) are relatively near each other on the sky and sample similar galactic structure while the third target B0355+508 (NRAO150) is the only source within 2° of the galactic equator (see Table 1).

The format of Figs. 2–11 is: at upper left a 90′ map of E_{B-V} from the dataset of Schlegel et al. (1998), with an inset showing the field of view mapped in CO, typically 30′ on a side; at lower left a map of $W_{\rm CO}$; at lower right various atomic (H I) and molecular absorption spectra showing the kinematic structure toward the background source; at upper right, CO emission spectra of various sorts as depicted in the figure captions. The absorption spectra shown at lower right in these figures are somewhat inhomogeneous because not all sources have the same full complement of profiles. In general, H I is at the bottom wherever possible and above that are spectra of the most common molecules observed in absorption; HCO^+, observed toward all targets, OH, C_2H and/or CO. The uppermost spectrum wherever possible is a species like H_2CO or HNC (Liszt et al. 2006; Liszt & Lucas 2001) that is detected less commonly and is indicative of greater chemical complexity.

Also shown for all sources are CO emission spectra at various locations in the field mapped, as indicated in the spectra. More complex aspects of the presentation are discussed in the individual figure captions.

2.7. Molecular gas properties in the current sample

The sightlines studied here were selected on the basis of their known HCO^+ absorption spectra, creating the possibility that the sample is biased to large molecular fractions and/or strong CO emission. However, it was earlier noticed in a flux-limited survey (Lucas & Liszt 1996) not based on prior knowledge of CO emission that very nearly all sightlines at galactic latitudes within about 15° of the galactic equator show HCO^+ absorption. Our present tally, slightly extending the earlier result, is that HCO^+ absorption occurs toward 19 of 19 sources at $|b| \lesssim 12°$, toward 22 of 25 sources at $|b| \lesssim 18°$ and toward 4 out of 12 sources at $|b| \gtrsim 23°$ including three shown here. Thus it is a near certainty that HCO^+ absorption would be detected over the entirety of the sky fields mapped here below about 15°–18°, no matter what is the covering factor of detectable CO emission. This is discussed in Sect. 8 immediately following the more descriptive portions of the text.

If we discuss the mean properties of the ten sightlines in Table 1 having reliably determined E_{B-V} (all except B0355+508 that lies too near the galactic plane) in the same terms that we used earlier to derive the mean CO-H_2 conversion factor in diffuse gas, (Liszt et al. 2010), we derive an ensemble average

$$\frac{N({\rm H_2})}{W_{\rm CO}} = \frac{5.8\times10^{21}\ {\rm cm^{-2}}\langle E_{B-V}\rangle - \langle N({\rm H\ I})\rangle}{\langle 2W_{\rm CO}\rangle}$$
$$= 1.52\times10^{20}\ {\rm cm^{-2}\ (K\ km\ s^{-1})^{-1}},$$

i.e., 25% smaller than the previous result found a larger sample. In the same terms, the mean atomic gas fraction is $\langle N({\rm H\ I})\rangle/\langle N({\rm H})\rangle = 0.74$, as opposed to 0.65 found earlier.

Estimates of $N(H_2)$ based on assuming the ensemble-average mean value (Liszt et al. 2010) $N(HCO^+)/N(H_2) = 3\times10^{-9}$ along each line of sight are also given in Table 1. They indicate higher molecular fractions and somewhat higher total column densities N(H) than are found using scaled E_{B-V} for N(H) and using the decomposition discussed just above based on subtracting N(H I) from N(H) determined as the scaled E_{B-V}. Specifically the chemistry-based ensemble average is $\langle f_{\rm H_2}\rangle = \langle 2N({\rm H_2})\rangle/\langle (N({\rm H\ I})+2N({\rm H_2})\rangle = 0.43$.

3. Six simple fields at moderate-high latitude

3.1. B0736+0117 ($b \sim 11°$)

The 15′ sky field around B0736+016 shown in Fig. 2 is the smallest and kinematically simplest field studied; the map was made on the spur of the moment in a relatively brief open period between two other larger maps. The reddening is modest over the area of the CO map shown in Fig. 2, $E_{B-V} \lesssim 0.165$ mag but the molecular fraction implied by the entries in Table 1 is of order 30–50%. Toward the source the integrated CO is fairly weak, <0.8 K km s^{-1} but a very slightly blue-shifted 4.5 K line is found within just a few arcminutes.

3.2. B0954+658 ($b \sim 43°$)

This source (Fig. 3) is seen at the upper tip of the Polaris Flare near the location of the M 81 group and the so-called small area molecular structures mapped by Heithausen (2004) (see the finding chart in Fig. 1). As toward B0736+017, a fairly strong CO line, 5 K, is seen within a few arcminutes of the background target where the CO brightness is more modest, 2 K.

The reddening is very moderate but a high molecular fraction, above 50%, is suggested by comparing the value of $N(H_2)$

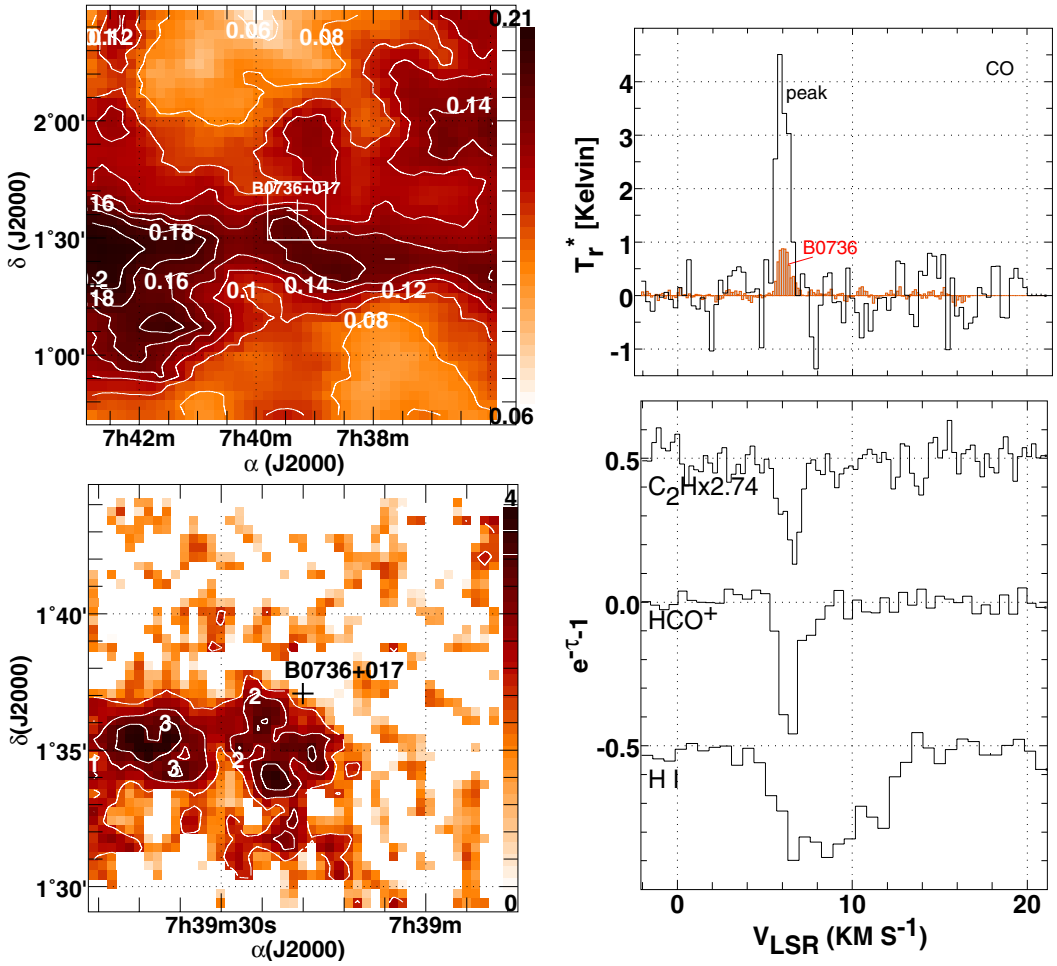

Fig. 2. The sky field around the position of B0736+017. *Upper left*: reddening at 6′ resolution (Schlegel et al. 1998). The inscribed white rectangle shows the smaller region mapped in CO emission. *Lower left*: integrated CO emission W_{CO} in units of K km s^{-1}; contour levels are in 1, 2, ... K km s^{-1}. *Lower right*: absorption line profiles, scaled as noted. *Upper right*: CO emission, toward B0736+017 and at the peak of the nearby CO distribution.

in Table 1 with N(H I) or E_{B-V}. Consistent with this high molecular fraction and the relative simplicity of a higher-latitude line of sight, this field is the only one studied in which there is a strong proportionality between E_{B-V} and W_{CO}, as discussed in Sect. 8. The complement of supporting material is disappointingly slender.

3.3. B1730-130 ($b \sim 11°$)

The reddening is relatively large over this field (Fig. 4) and the HCO$^+$ absorption is strong, implying a molecular fraction of order one-third, but CO emission is very weak toward the background continuum source ($W_{CO} = 0.4$ K km s^{-1}) and absent over most of the field mapped. Much stronger but still rather weak emission (1.5 K) is seen 15′ to the northwest as indicated in Fig. 4. All of the absorption profiles shown in Fig. 4 have a redward wing that is separately visible in the two spatially-averaged CO profiles shown at upper right.

3.4. B1928+738 ($b \sim 23.5°$)

CO emission is absent over the entire 20′ field shown in Fig. 5 despite the presence of fairly strong HCO$^+$ absorption and a suggested molecular fraction approaching 40%. The reddening is modest, approximately 0.15 mag around the target, but the implied CO-H$_2$ conversion factor is very large; from the entries in Table 1 we have $N(H_2)/W_{CO} > 2.5 \times 10^{21}$ cm^{-2} at the 2σ level.

3.5. B1954+513 ($b \sim 12°$)

The reddening in the field around this source is modest, 0.18 mag (see Figs. 6 and 17), and CO emission toward the background continuum source is unimpressive (2 K) but the HCO$^+$ absorption is strong and the molecular fraction is of order 40%. Two kinematic components are found in the field with 4.5 K peak brightness, only one of which is seen toward B1954 in either emission or absorption.

3.6. B2251+158 = 3C 454.3 ($b \sim -38°$)

As shown in Fig. 1, this very strong continuum source is seen about 3° removed from an elongated complex of high-latitude clouds that includes the objects MBM53-55 (Magnani et al. 1985) and new clouds discovered by Yamamoto et al. (2003). B2251+158 lies within the region surveyed by Yamamoto et al. (2003) in CO but the emission detected here (see Fig. 7) escaped their notice, presumably because of their 4′ map sampling of the 2.7′ beam. The reddening is moderate, $E_{B-V} \lesssim 0.11$ mag (see Fig. 7) and CO emission toward the continuum source is quite weak (0.8 K). However, much stronger emission (5 K) is seen

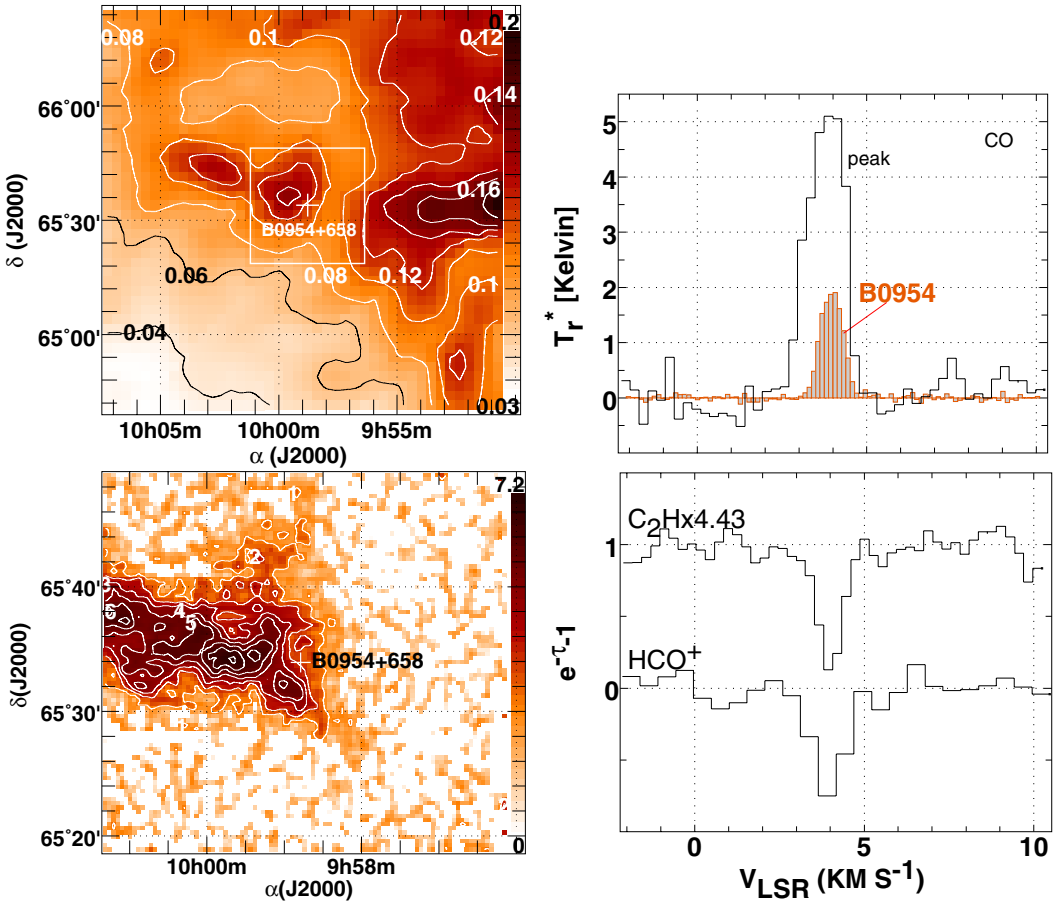

Fig. 3. The sky field around the position of B0954+658, as in Fig. 2.

only 5′ away, as with B0736, B0954 and B1954. There is no obvious large-scale correlation of the CO emission with reddening, as evidenced by the weakness of the CO at the position of highest reddening in the larger field shown at upper left in Fig. 7 (i.e. the spectrum labeled "NW" at upper right there). The relationship between W_{CO} and E_{B-V} is shown in Figs. 16, 17.

The blue wing of the peak emission and the line seen at the northwest reddening peak both fall to the blue of the CO emission or absorption seen toward B2251. Nonetheless they overlap a weaker blue wing of the HCO^+ absorption that has no counterpart in CO emission, and they fill in a portion of the H I absorption spectrum.

4. Two unusual fields at moderate latitude

4.1. B0528+134 ($b \sim -11°$)

Mm-wave absorption toward B0528+134 (Fig. 8) was first discussed by Hogerheijde et al. (1995). This object is viewed against the outer edge of the dark cloud B30 in the λ Orionis ring of molecular clouds (Maddalena & Morris 1987) that is centered on the H II region S264 and its central ionizing star Lambda Ori (Fig. 1). There is a very substantial foreground reddening E_{B-V} = 0.86 mag and much more heavily extincted regions in the field to the South.

Although CO emission toward B0528+134 is fairly weak, 2.3 K, emission over the surrounding field is characterized by a pronounced quasi-periodic pattern with some very strong (10−12 K) and narrow CO emission lines: emission is undetectable over much of the intervening troughs. A similar wavelike pattern may have been observed across the surface of the Orion molecular cloud by Berné et al. (2010).

A weak blue-shifted component of HCO^+ absorption that is absent in CO toward B0528 has a very bright CO emission counterpart to the Southeast as shown in Fig. 8. Despite an 8 km s^{-1} velocity difference, the blueshifted emision line gives the strong visual impression of being physically associated with the main kinematic component at 10 km s^{-1}, see the map at lower left in Fig. 8. The kinematic span of the CO emission seen at top right in Fig. 8 neatly coincides with the extent of the H I absorption toward B0528+134.

4.2. B2200+420 = BL Lac ($b \sim -10.5°$)

This target (see Fig. 9) was the first source seen in mm-wave absorption from diffuse gas (Marscher et al. 1991), in CO actually, and was also the first seen in HCO^+ absorption in our work (Lucas & Liszt 1993). CO emission toward the source is fairly strong, 4 K or 6 K km s^{-1} and the line is quite opaque. The molecular column density indicated by the strong HCO^+ absorption is about as large as N(H) inferred from E_{B-V} = 0.32 mag, given the E_{B-V} − N(H) relationship N(H) = 5.8 × 10^{21} cm^{-2} E_{B-V} of Savage et al. (1977).

The CO emission in this field originates from an unusual filamentary morphology (Fig. 9 at lower left) at the edge of an arched pattern in the reddening map. The integrated intensity takes on very large values within the field, up to 20 K km s^{-1} but the profile is compound and relatively broad. Toward the continuum source only the blue side of the core of H I absorption is

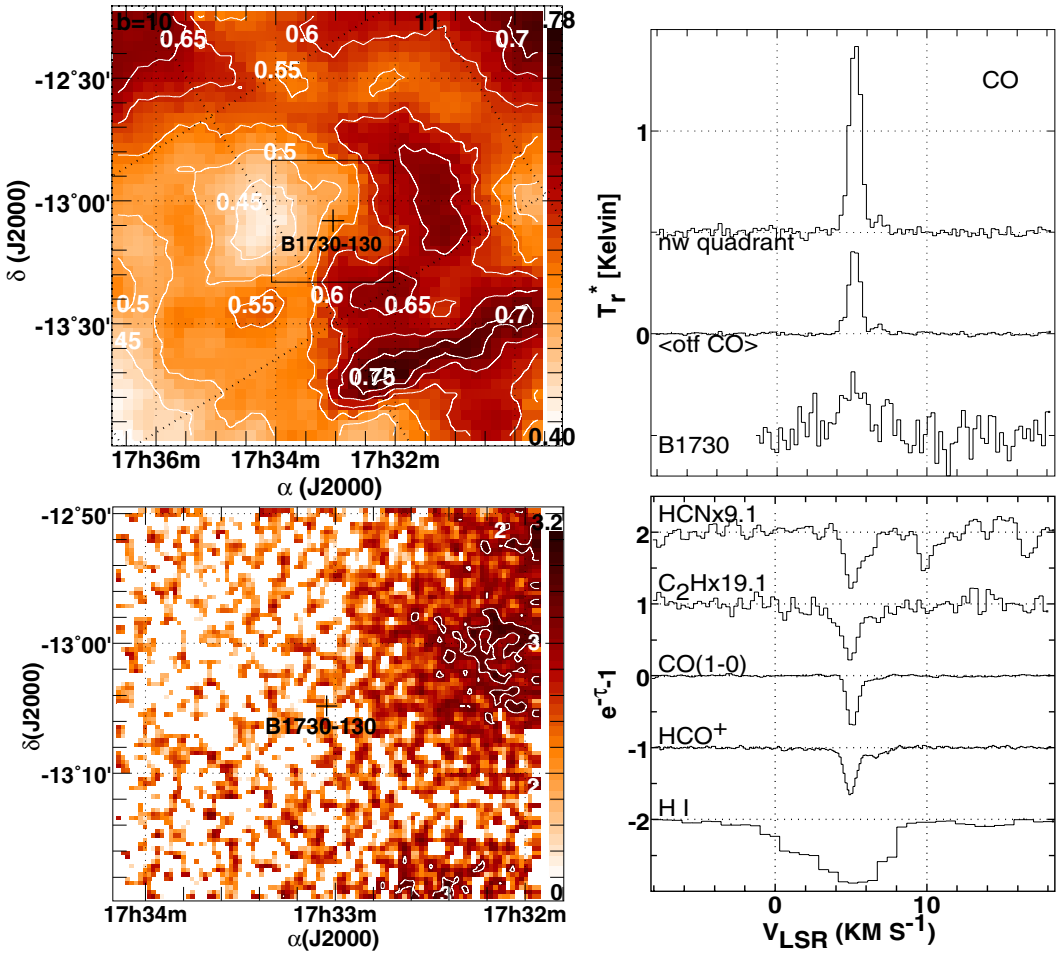

Fig. 4. The sky field around the position of B1730-130, as in Fig. 2. The emission profile labeled "nw quadrant" is an average over that portion of the map. The emission profile labeled ⟨otf CO⟩ is the mean over the entire region mapped in CO.

seen strongly in molecular absorption or CO emission but a redshifted CO emission component overlaying the red side of the H I line core is present to the Northeast as indicated in Fig. 9.

5. Three complex fields at low-moderate latitude

5.1. B0212+735 ($b \sim 12°$)

B0212+735 (Fig. 10) sits in a mild trough with $E_{B-V} \approx 0.76$ mag in a region of substantial reddening at moderate galactic latitude $b = 12°$. It has three molecular absorption components whose balance is entirely opposite to that of H I. Whereas most of the atomic absorption toward B0212+725 occurs in a deep and broad feature at $v \lesssim 10$ km s^{-1}, most of the molecules are concentrated in a narrower-lined feature at $v \approx 4$ km s^{-1}. An obvious molecular absorption feature at 0-velocity is, very unusually, not apparent in H I. It seems possible that the low velocity resolution of the H I profile (1 km s^{-1}) is responsible. The only other published example of this phenomenon is toward B0727-115 (Lequeux et al. 1993).

The CO emission line kinematics have been color coded at lower left in Fig. 10 to display the observed behavior in one panel. The gray-scale background represents the integrated intensity of the gas at 1.5–5 km s^{-1}; higher resolution mapping with the IRAM 30 m telescope to be discussed in a forthcoming paper indicates that the feature is compound but this is not apparent in the present dataset. The blue contours represent the CO profile integral at -16 km s$^{-1} \leq v \leq -9.5$ km s^{-1}; consistent with the prominence of this gas in H I, it is almost as widely distributed over the field as the stronger emission at 1.5–5 km s^{-1} (Table 2: 26% vs. 34%) even if it is barely seen toward the continuum. The profile labeled "A" at upper right is an example. The green contours represent the profile integral at -2 km s$^{-1} \leq v \leq 1$ km s^{-1} and an example is shown at upper right as profile "B". Emission from this gas occurs only at the eastern edge of the map area.

5.2. B0224+671 ($b \sim 6°$)

This line of sight toward B0224+671 (Fig. 11) samples the two lower-velocity features seen toward B0212+735 but at substantially lower galactic latitude $b = 6.2°$, see Table 1. The extinction is large in this field as are the H I and inferred H_2 column densities. CO emission is weak on a per-component basis toward the continuum target but fairly total large values of W_{CO} are attained overall.

The integrated CO emission is compact but rather formless because it is the sum of many kinematic components. Paradoxically, the strongest molecular features seen toward and near B0224+671 are not widely distributed over the map area as shown in the middle panel at right in Fig. 11 comparing the profile toward B0224+671 with the unweighted average of all profiles denoted "⟨otf⟩": the strongest emission peak, at the red edge of the CO emission profile toward B0224+671

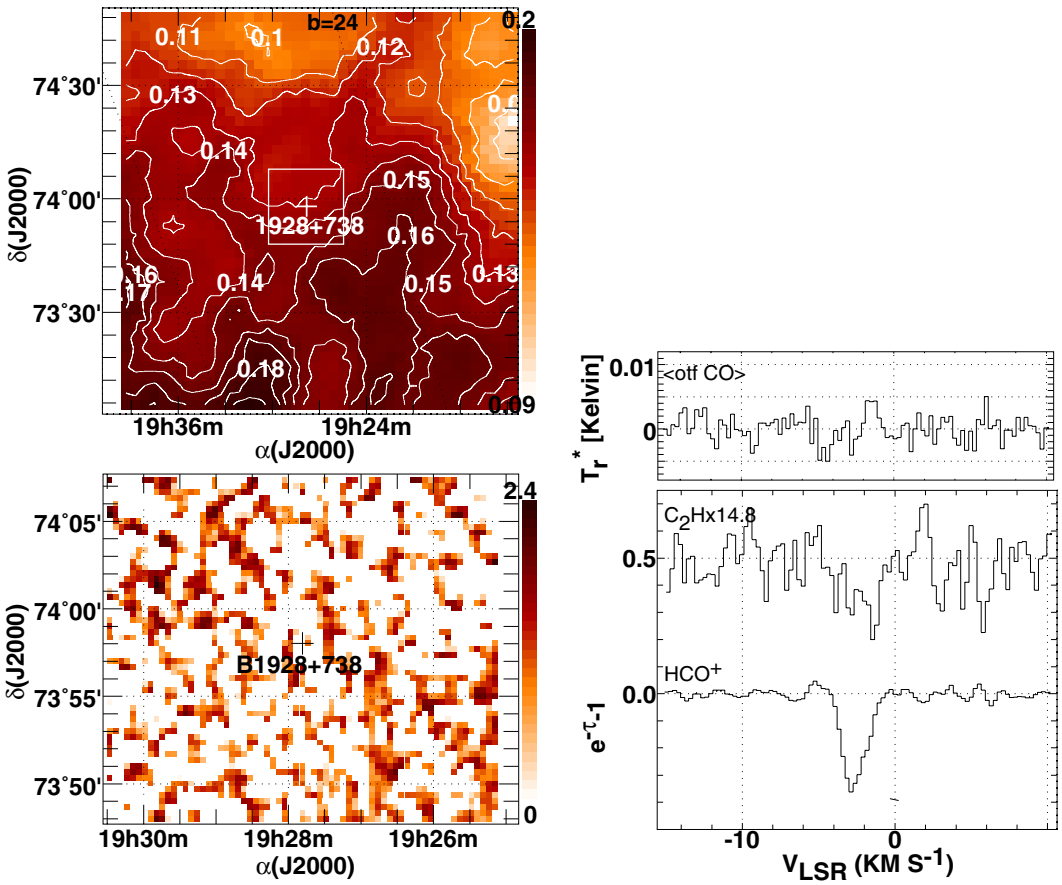

Fig. 5. The sky field around B1928+738. The emission profile at *upper right* labeled ⟨otf CO⟩ is the mean over the 20′ × 20′ region mapped in CO.

is strongly underrepresented in the mean profile. Examples of profiles seen over the map area are shown at upper right in Fig. 11; they were chosen at local peaks in more finely-divided (in velocity) maps of integrated intensity, with velocity increasing from a to g. Especially at $v < 0$ km s^{-1} the lines shown are much stronger than seen toward the continuum. Among them, the various CO emission components cover the range of strong H I absorption toward the continuum source, -15 km s^{-1} $\leq v \leq 2$ km s^{-1}. B0224 and B0212 have similar absorption spectra in that both have stronger atomic absorption at $v < -10$ km s^{-1} where the molecular absorption is weaker. They thus sample the same large-scale gas kinematics although they are separated by about 15 pc, assuming they lie on a sphere of 150 pc radius.

5.3. B0355+508 = NRAO150 ($b \sim -1.6°$)

This is the only low-latitude source studied here. The more strongly blue-shifted gas seen in this direction is likely to be relatively distant. The actual velocity field is probably affected by galactic streaming motions but a typical velocity gradient due to galactic rotation in this direction is 8 km s^{-1} kpc^{-1}.

Figure 12 does not display a map of the reddening for this source because the reddening maps are not believed to be accurate at such low galactic latitudes. Taken as a whole the line of sight is very heavily extincted, with large columns of both H I and H_2 (Table 1). However, the high inferred H_2 column density is the sum of components whose individual values indicate that they have $A_V \approx 1$ mag.

The absorption profiles toward B0355+508 at lower right in Fig. 12 show five obvious HCO^+ and CO components having roughly equal $N(HCO^+) \approx 1.2 \times 10^{12}$ cm^{-2} and somewhat more variable N(CO) (Liszt & Lucas 1998). Only two have substantial abundances of less-common species such as HCN. Less obvious is the fact that the HCO^+ absorption profile has a weak broad blue wing extending to -35 km s^{-1} so that the entire core of the H I absorption line is seen in molecular gas (see Liszt & Lucas 2000).

Shown at the top in Fig. 12 are CO integrated intensity maps made over velocity intervals corresponding to the obvious HCO^+ and CO absorption line features; a map integrated over all velocities is shown in the top right-most panel. The CO emission distribution is heavily structured and very complex. Profiles at positions of local peaks in narrower CO integrated intensity maps are shown at lower left, along with profiles at the integrated emission peak (see Fig. 12 at top right) and toward the background source. At the eastern edge of the map at position "a" there is a blue-shifted CO emission line that (unusually) falls outside the range of the strong molecular absorption toward B0355+508 but is well inside the H I absorption profile. A very bright (>10 K) line is found at $v = -4.5$ km s^{-1} at the northern edge of the map at position f, corresponding to a prominent molecular absorption feature that has only a very weak emission counterpart toward the continuum.

The middle right panel displays the profile toward the continuum background source and the profile averaged over the mapped field of view. The kinematics of this region are shown in more detail in Fig. 15 and discussed in Sect. 7.2. The displacement of the two strong CO emission lines about the centroid of the mean profile results from a coherent kinematic patttern, perhaps a shell or bubble in the underlying gas distribution. Recall,

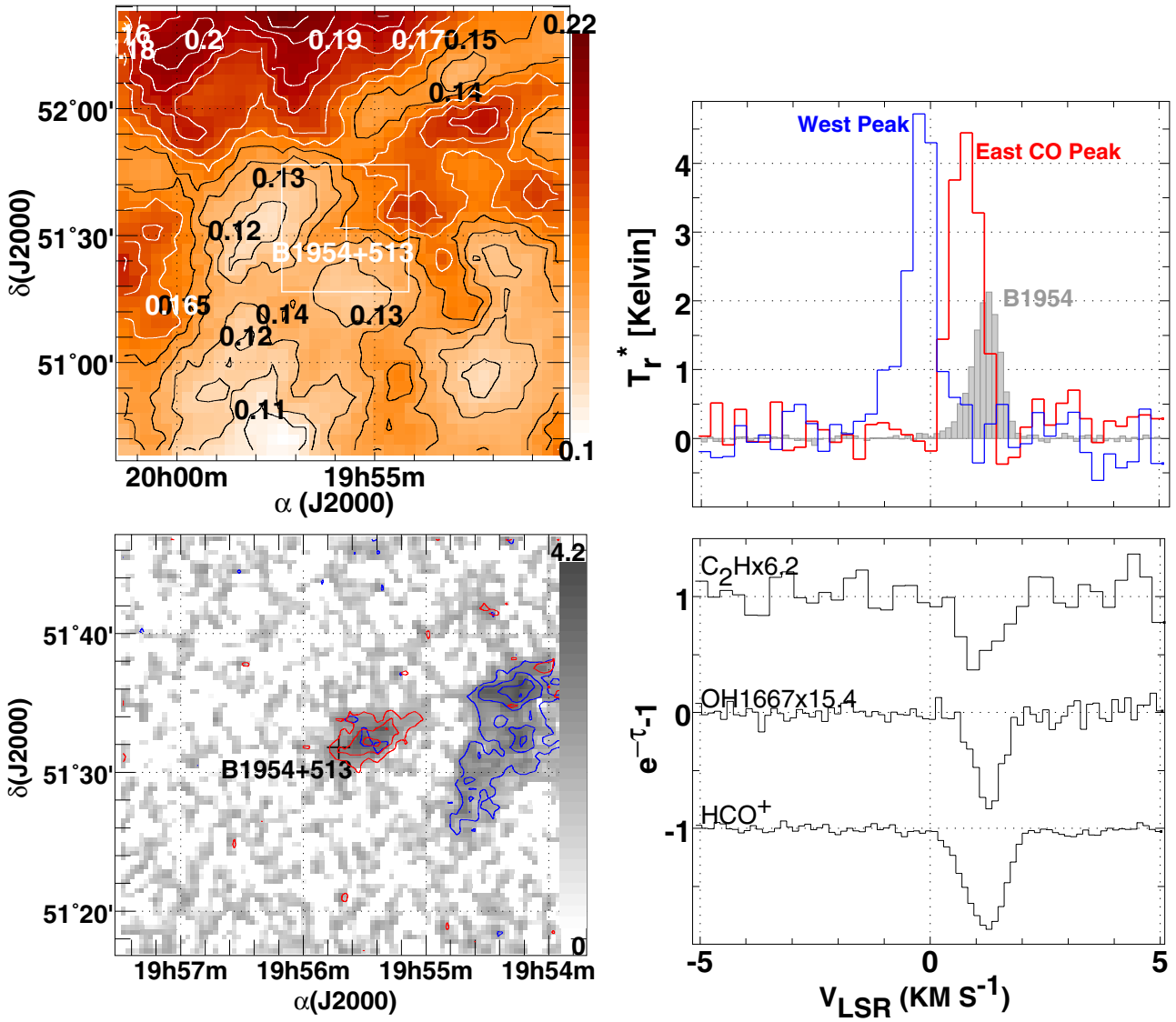

Fig. 6. The sky field around the position of B1954+513, as in Fig. 2. In the map at *lower left* the grayscale represents the total integrated emission at $-1 \le v \le 2$ km s^{-1} and the red and blue contours show the individual distributions of red and blue-shifted components, respectively. Profiles at the peak of the red and blue-shifted emission components are shown at *upper right* along with the profile toward the continuum source (shaded).

however that absorption at the mean field velocity is not absent toward the continuum source.

The complexity of the emission distribution makes the division into ranges based on HCO^+ absorption quite arbitrary. Moreover, the emission and absorption profiles show rather different structure even toward the continuum target. A very detailed discussion of CO emission within a 90″ field centered on NRAO150 was given by Pety et al. (2008). Remarkably, the peak emission brightness seen just 6″ from the background continuum source is almost 13 K. As the spatial resolution increases, the CO emission profile toward B0355 more nearly resembles the absorption and the blended emission at $v \approx -10$ km s^{-1} resolves into two distinct components.

Conversely, in the present dataset, the emission components seen toward B0355+508 lose their identity as the resolution degrades below a 4′ hpbw. Both the peak profile and the mean are broad, largely unstructured and centrally peaked about velocities lying between the two strong CO emission components seen toward the background.

6. Statistical lessons

Faute de mieux, the first surveys for suitable absorption-line targets were conducted in CO emission (Bania et al. 1991; Liszt & Wilson 1993; Liszt 1994) but the discovery of yet more common HCO^+ absorption (Lucas & Liszt 1996) caused a reversal in the search strategy for diffuse molecular gas. Thus, all targets studied here were pre-selected to have absorption from HCO^+ but only some were known to have CO emission. However any division between targets with and without CO emission is misleading because the same sightline may have and lack CO emission on a per-component basis.

Stronger CO emission is always found somewhere else in the map when CO is present toward the continuum but comparably strong CO emission was found, somewhere on the sky, from absorption components lacking CO emission counterparts toward the continuum background. This is true with only one exception, B1928. The implication is that CO emission is somewhat more ubiquitous than is presently believed to be the case because

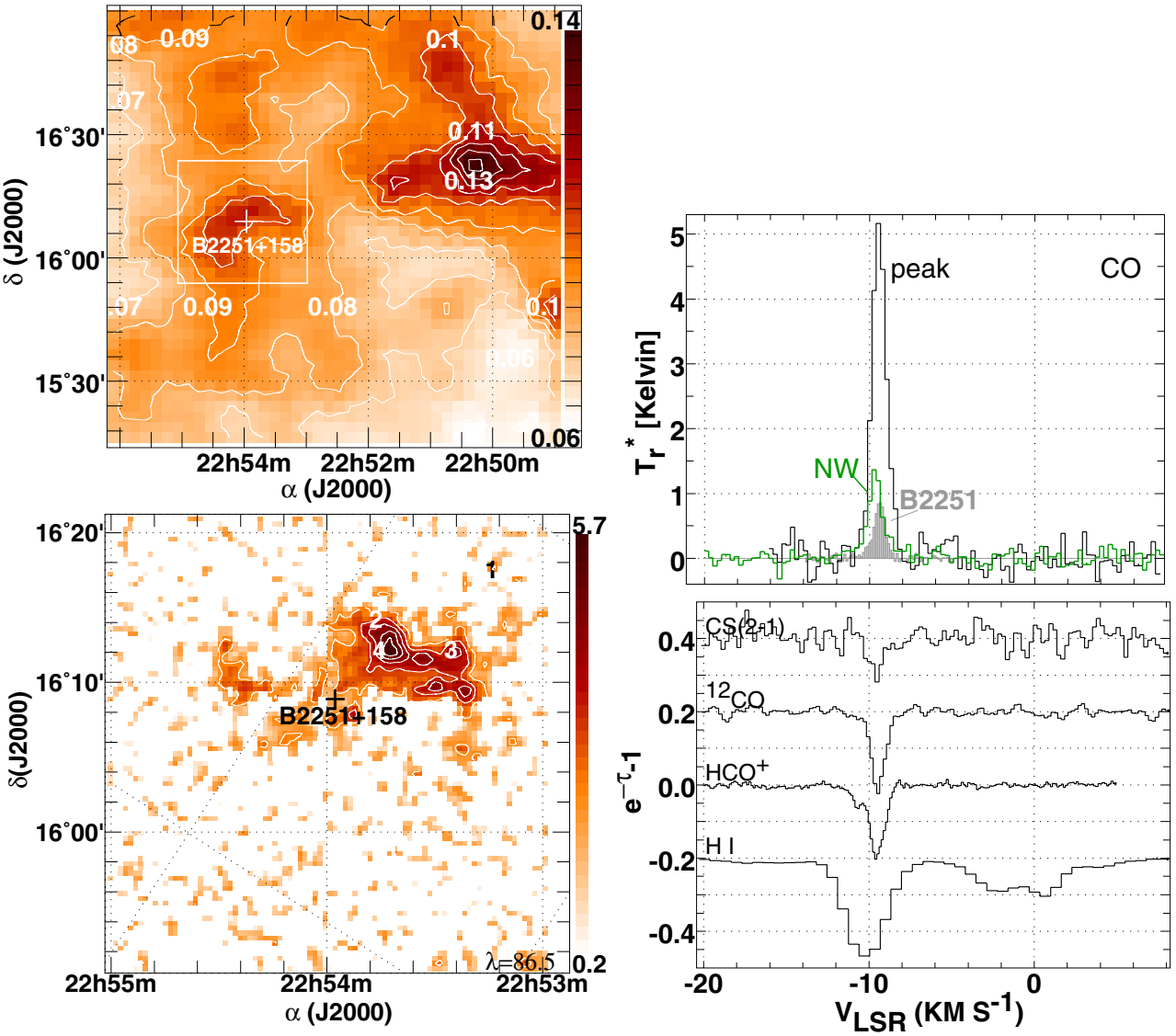

Fig. 7. The sky field around the position of B2251+158 (C454.3), as in Fig. 2. The map of reddening at *upper left* is offset to show a separate peak to the Northwest near 22^H50^M and a profile at the position of this peak is shown at *upper right*, shaded green and labeled "NW", along with profiles toward 3C 454.3 (shaded) and at the peak of the small clump that is seen immediately adjacent to the continuum source.

nearly all HCO^+ absorption components will be found in nearby emission after a small search. In terms of numbers, in this work we observed 20 absorption line components (and a few distinct line wings) with 13 carbon monoxide emission counterparts toward the continuum targets, and we found 23 CO emission components within 15′ of the background continuum source during the mapping.

The following gives some conclusions that are drawn from the preceding presentation; they should generally be understood as applying on a component-by-component basis.

From the standpoint of CO emission.

1) In every case where CO emission was detected toward the background source, much stronger emission was also detected within approximately 15′ and often much less.
2) Near B0355+508, B0528+134 and B2200+430 the nearby stronger emission was very strong indeed, with peak line temperatures of 10−12 K and/or line profile integrals as large as 20 K km s^{-1}.
3) 1) and 2) are also generally true for kinematic components that were present in absorption toward the continuum source but *not* detected in emission there (7 of 20 components).
4) In one case only (B1928+738), representing 1 of 11 fields and 1 of 20 kinematic absorption line components, the entire field mapped was devoid of emission when emission was not detected toward the continuum source (from a kinematic absorption line component). The field mapped around B1928 was only 20′ × 20′ as against 30′ × 30′ or more for all of the other fields.
5) In 2 fields we found an emission feature without a counterpart in molecular absorption toward the background continuum object (B1954 and B0355 at −20 km s^{-1}).

From the standpoint of absorption.

1) The same kinematic components are seen in both absorption and emission with angular separations of up to 15′.
2) The absorption spectra toward a background source are a preview of what will be seen in emission in a larger field about the background source.

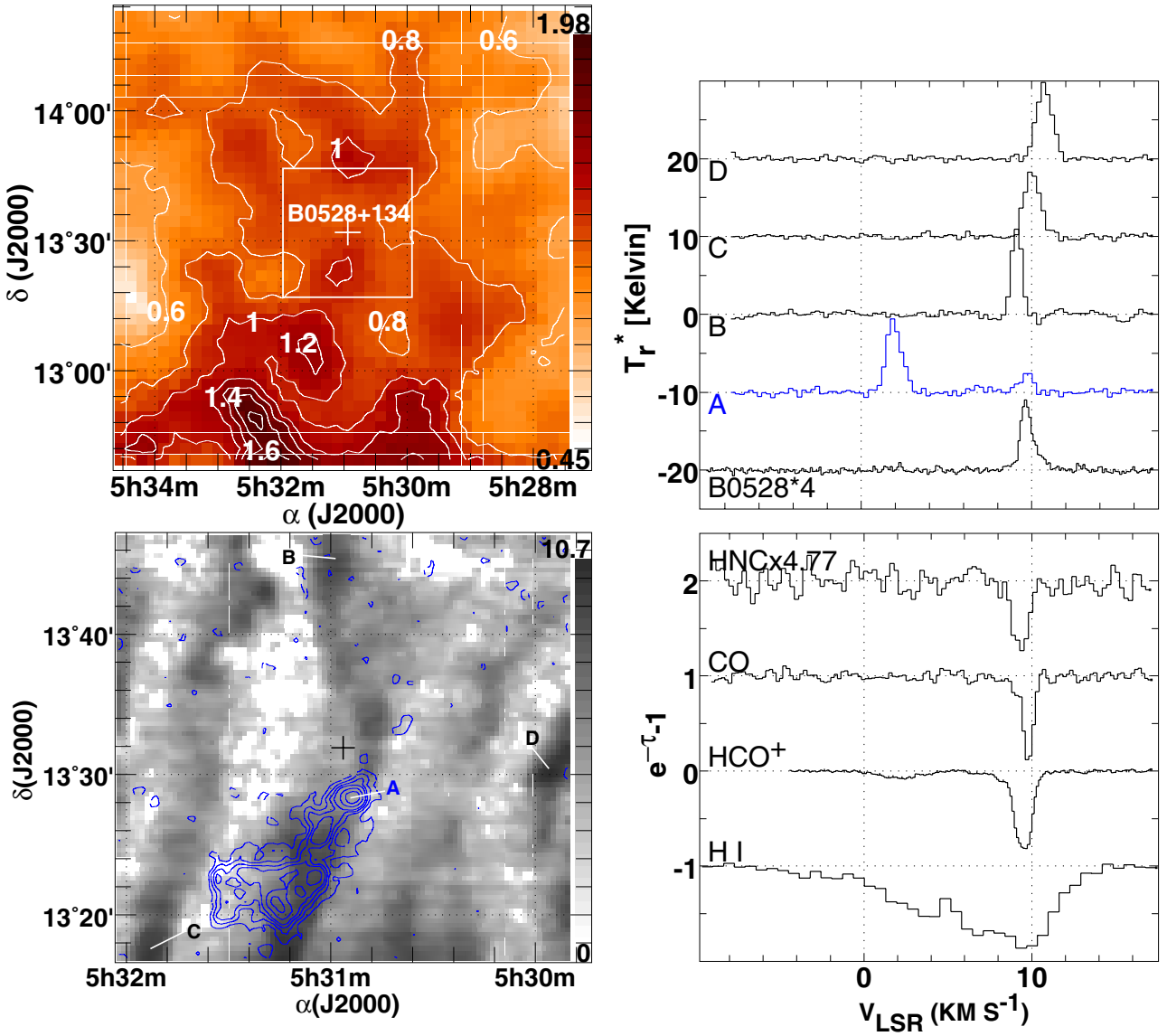

Fig. 8. The sky field around the position of B0528+134, as in Fig. 2. The map of CO emission at lower left superposes the integrated intensity at 0–4 km s^{-1} as blue contours against a background grayscale representing emission at v = 8–12 km s^{-1}. Very strong CO lines are seen in the foreground gas as shown in *the upper right panel*: positions at which they originate are indicated at *lower left*.

3) Molecular absorption components seen toward the continuum source were found in CO emission somewhere in the field except in the smaller region mapped around B1928+738.

From the standpoint of the atomic-molecular transition.

1) The same kinematic components are seen in both atomic and molecular tracers at angular separations between 0′ and 15′.
2) The components seen in molecular absorption are present in H I absorption, although somewhat indistinctly in some cases. For instance, the 0-velocity molecular absorption line in B0212+735 appears only as a blue wing of the 4 km s^{-1} H I absorption component.
3) Portions of H I absorption profiles adjacent to molecular features but lacking a molecular counterpart are seen in CO emission elsewhere in the field in two cases on (B2200+420 and B0528+134).
4) We saw no molecular features in absorption or emission outside the span of the H I absorption (see Appendix B).

7. Kinematics

Molecular gas is generally well-mixed with other components of the ISM (Dame & Thaddeus 1994; Gir et al. 1994) and does not require exceptional kinematics. This is apparent in our work from the coincidence of molecular and atomic absorption features, even if they do not have precisely the same patterns of line depth. The kinematics are affected by galactic structure and local external influences such as shocks, but this only becomes apparent on broad angular scales. The targets B0212+735 and B0224+671 (Figs. 10, 11) are relatively close to each other and both are most strongly absorbed in H I around −15 km s^{-1}. The background target B2251+158 (Fig. 7 and Sect. 3.6) is seen in the outskirts of the MBM53-55 cloud complex, which is part of a large shell that has been extensively mapped in molecular and atomic gas (Gir et al. 1994; Yamamoto et al. 2003).

In individual line profiles and over small scales, the kinematics are often dominated by the internal structure of individual clouds. The internal motions of diffuse molecular gas are

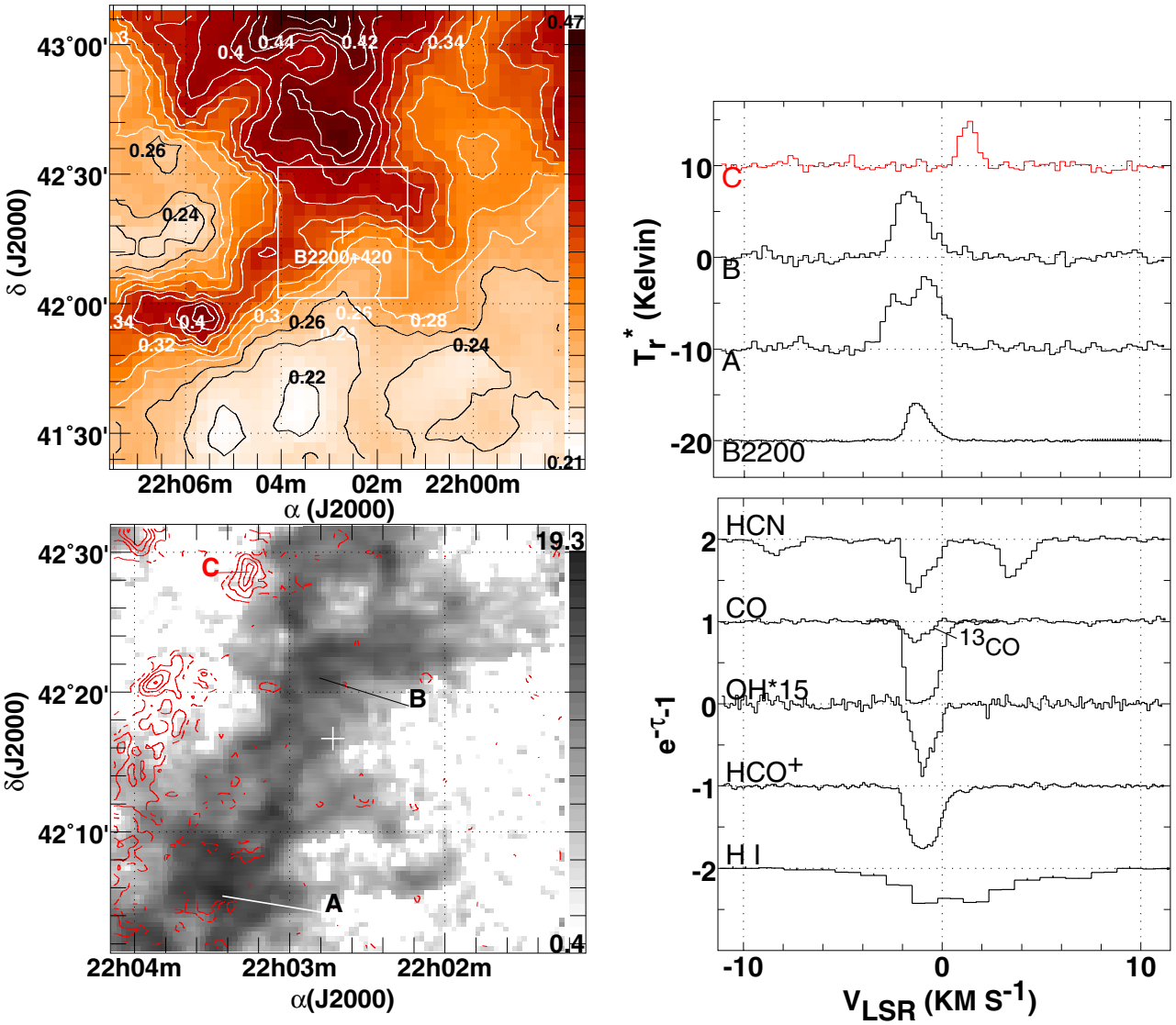

Fig. 9. The sky field around the position of B2200+420 (BL Lac), as in Fig. 2. The map of CO emission at *lower left* superposes the integrated intensity in the range $v = 0-2$ km s^{-1} as red contours against a background grayscale representing emission at $v \leq 0$ km s^{-1}. Molecular absorption and most emission is sequestered in the blue wing of the core of the HI absorption profile but a red-shifted emission component is present to the Northeast as illustrated by the spectrum at position "C" indicated at *lower left*.

now understood to reflect turbulent gas flows (Pety & Falgarone 2003; Hily-Blant & Falgarone 2009) that are characterized by unsteady projected velocity fields with strong shears and abrupt reversals of the velocity gradient. Sakamoto & Sunada (2003) show the transition between diffuse and dense molecular gas at the edge of TMC1 and Liszt et al. (2009) discuss gas flows in the diffuse cloud occulting ζ Oph.

In this section we discuss the kinematics of just two of the fields mapped here. Further examples of CO kinematics in individual sky fields are given in Figs. A.1−A.3 of Appendix A and the galactic context for all fields is given in Figs. B.1 and B.2 of Appendix B, showing large-scale latitude-velocity cuts in HI from the Leiden-Dwingeloo H I survey of Hartmann & Burton (1997) with the locations of the continuum background sources marked in each case.

Figure 13 shows the kinematics in the relatively simple sky field around B1954+513 (Sect. 3.5 and Fig. 6) with the spatially-displaced blue and red-shifted CO emission components that were illustrated in Fig. 6. The red-shifted component seen toward the continuum has a partially-resolved velocity gradient that carries it just to the midpoint of the associated HCO$^+$ absorption profile at the continuum position. It is certain that the blue-shifted CO emission to the West would have an associated HCO$^+$ absorption at its position but the structure of the redward gas cannot be traced away from the continuum and, regrettably we do not have an H I absorption profile that might show both the red and blue-shifted gas in atomic absorption as toward BL Lac (Fig. 9 and Sect. 4.2).

Figure 14 shows the more complicated field at low latitude around B0355+508 (Sect. 5.3, Fig. 12) and illustrates how the partition of a line profile into components, no matter how seemingly obvious, can also be arbitrary and capricious. None of the well-defined absorption features has an obvious CO emission counterpart except perhaps in the immediate vicinity of the continuum target. This is not an artifact of taking a cut in declination, which is actually richer than that in right ascension (see Fig. 12).

Nonetheless, mapping the CO emission does help to clarify interpretation of the absorption profiles. For instance, consider gas near −9 km s^{-1} around the location of B0355 in Fig. 14. In

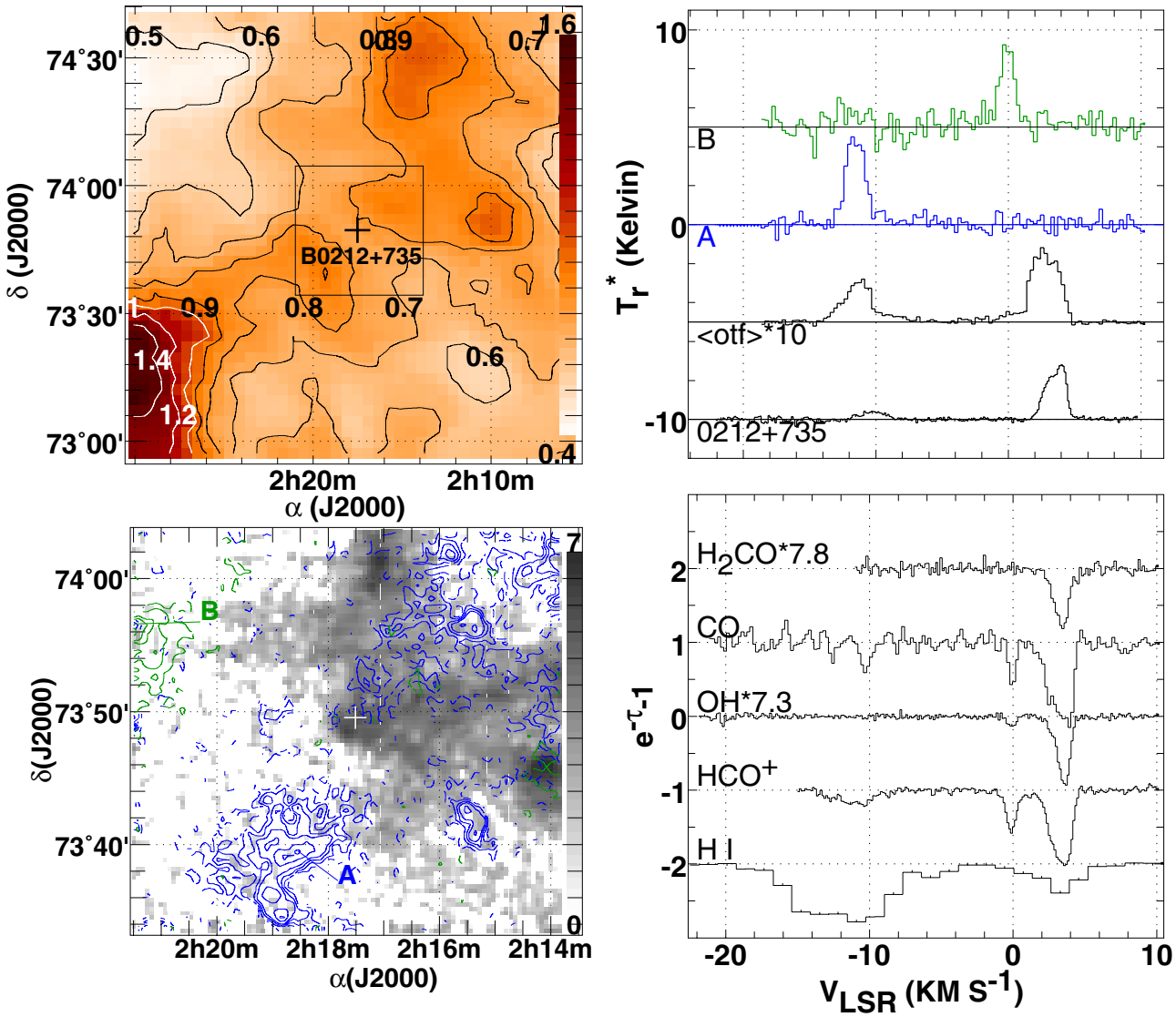

Fig. 10. The sky field around the position of B0212+735, as in Fig. 2. Contours in the CO emission map at *lower left* are color coded in blue for emission at $-15 \le v \le -9.5$ km s^{-1} and in green for emission at $-2 \le v \le 1$ km s^{-1}. The gray scale background represents the integrated emission of the strongest emission component seen toward the continuum source, at $v = 1.5{-}5$ km s^{-1}. ^{12}CO spectra at two locations labeled A and B are shown at *upper right* along with a strongly-scaled mean profile taken over the full map area.

absorption there are two distinct kinematic components at −11 and −8 km s^{-1} that would usually be interpreted as unrelated because, aside from their separation in velocity, they have different patterns of chemical abundances (Fig. 12). However, Fig. 14 shows that the CO emission line has an appreciable velocity gradient across the position of the continuum source, spanning the two absorption lines, making it likely that the two absorption components are part of the same body[1]. Moreover, the CO mapping suggests that the components at −17 and −10 km s^{-1} may also be part of the same structure (and separated by a velocity gradient), which was actually suggested by several coincidences in our earlier high-resolution CO mapping (Pety et al. 2008). The lines at −11 and −17 km s^{-1} are very bright (13 K) at high resolution and have considerable chemical complexity. There are also some seemingly correlated spatial intensity variations. The evidence for an association is entirely indirect but has a clear precedent in the kinematics around B0528+134 (Sect. 4.1 and Fig. 8) where a similar velocity separation occurs between two emission components that are seen superposed in an unusual wave-like spatial configuration.

[1] Pety et al. (2008) show that the overlapping CO emission line is resolved into two kinematic components at 6″ resolution toward the continuum source.

8. The brightness of diffuse cloud CO

8.1. W_{CO} relative to E_{B-V} and f_{H_2}

The large-scale finding chart in Fig. 1 is a map of the total intervening gas column density, except where discrete sources of infrared emission (often H II regions) "leak" into the map (usefully indicating when the background target may have been observed through disturbed foreground gas). Large-scale surveys of CO emission at 8′ resolution show a good correlation with reddening (Dame et al. 2001), contributing to the common interpretation of CO sky maps as displaying the global distribution of dense, fully-molecular gas.

In diffuse gas appreciable scatter in the $W_{CO} - E_{B-V}$ relationship is expected because the reddening is a sum over

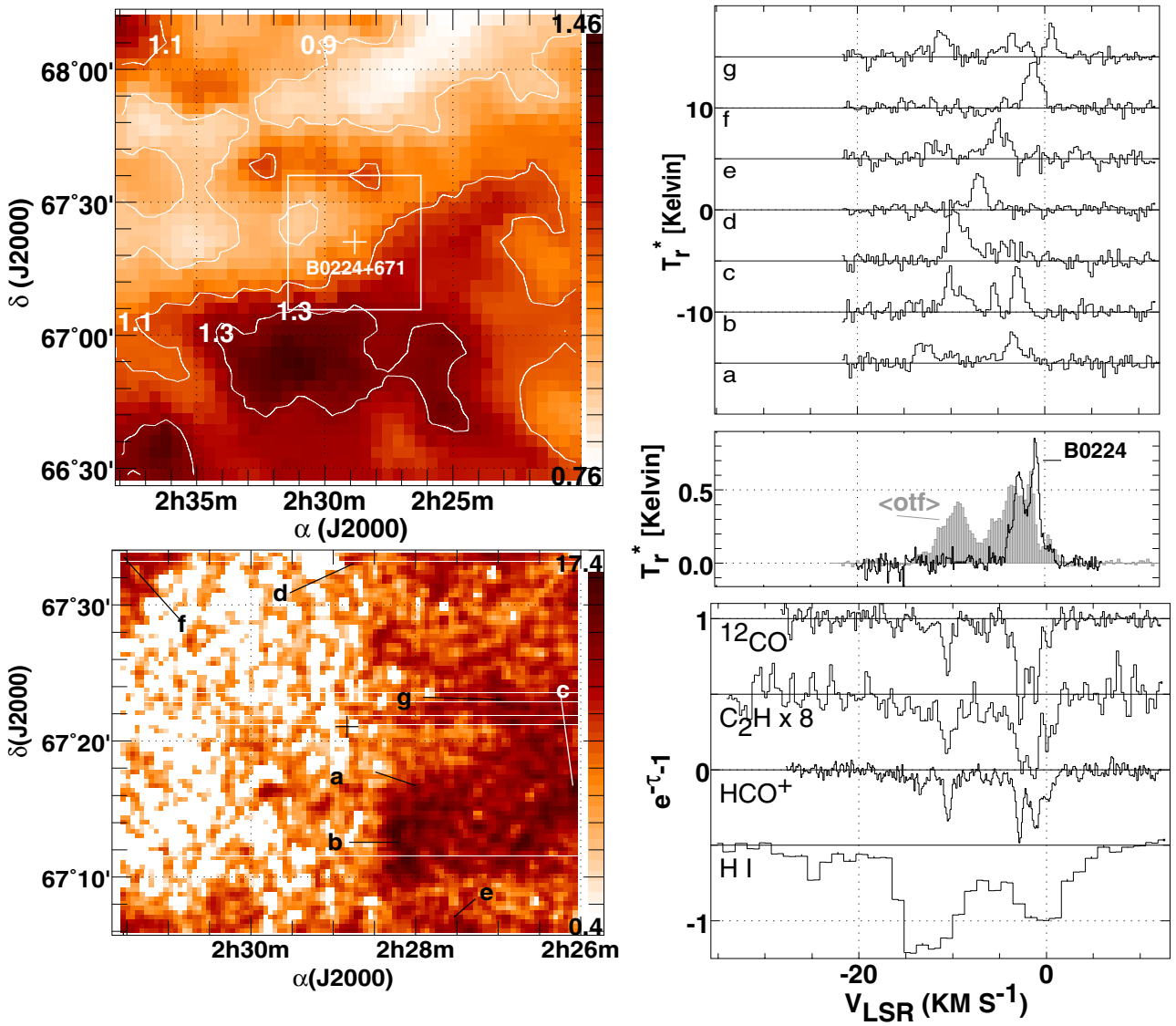

Fig. 11. The sky field around the position of B0224+671, much as in Fig. 2. The map at *lower left* has been integrated over the very wide interval $-15.5 \leq v \leq +2$ km s^{-1}. Shown in *the middle panel* at right are the CO emission spectrum toward B0224+671 and as averaged over the region of the entire CO emission map. At *top right* are example profiles from the positions labeled at *lower left*, chosen from maps of integrated intensity over narrow intervals increasing in velocity from **a**)–**g**).

atomic and molecular components that both make important contributions to N(H), combined with the fact that both $N(H_2)$ and N(CO)/$N(H_2)$ exhibit order-of-magnitude or larger scatter with respect to E_{B-V} even when all quantities are measured along the same microscopic sightlines toward nearby bright stars (Burgh et al. 2007; Rachford et al. 2009). The disparity in angular resolution between the reddening data and our 1′ CO maps presents another sort of complication that is considered in Sect. 8.2 but does not by itself dominate the scatter. Recall also the discussion in Liszt et al. (2010) where a good correlation was shown between E_{B-V} at 6′ resolution compared with the integrated H I optical depth measured in absorption at 21 cm toward a larger set of the same kind of point-like radio-continuum background target considered here.

Small-scale maps of reddening are shown in the various Figs. 2–12 detailing the individual fields. They may visually suggest correlations between E_{B-V} and W_{CO}, and there is a threshold $E_{B-V} \gtrsim 0.09$ mag for detecting CO emission, consistent with the well-known and quite abrupt increase of $N(H_2)/N$(H) at comparable reddening (Savage et al. 1977). However, reddening is not a reliable predictor of CO emission in our sky fields. For instance, in the field around B2251+158 in Fig. 7, CO emission is much weaker at the peak of the reddening map where $E_{B-V} = 0.14$ mag (the profile indicated as "NW" at upper right in Fig. 7) than nearer the continuum source at smaller $E_{B-V} = 0.10$ mag. Around B2200+420 (Fig. 9) the shape of the CO distribution appears to parallel that of the reddening but in detail CO only traces the edge rather than the peak ridge of the E_{B-V} distribution.

In Fig. 15 we show the relationship between W_{CO} and E_{B-V} in the four simple cases discussed in Sect. 3, where the extinction is small and a single narrow CO spectral component is present at each pixel[2]. The rms noise levels in these four datasets (Table 2) are 0.48, 0.33, 0.32 and 0.35 K km s^{-1} reading clockwise from upper left so that datapoints with $W_{CO} \gtrsim 1$ K km s^{-1}

[2] Green diamonds in Figs. 15 and 16 show E_{B-V} and W_{CO} toward the continuum target as given in Table 1.

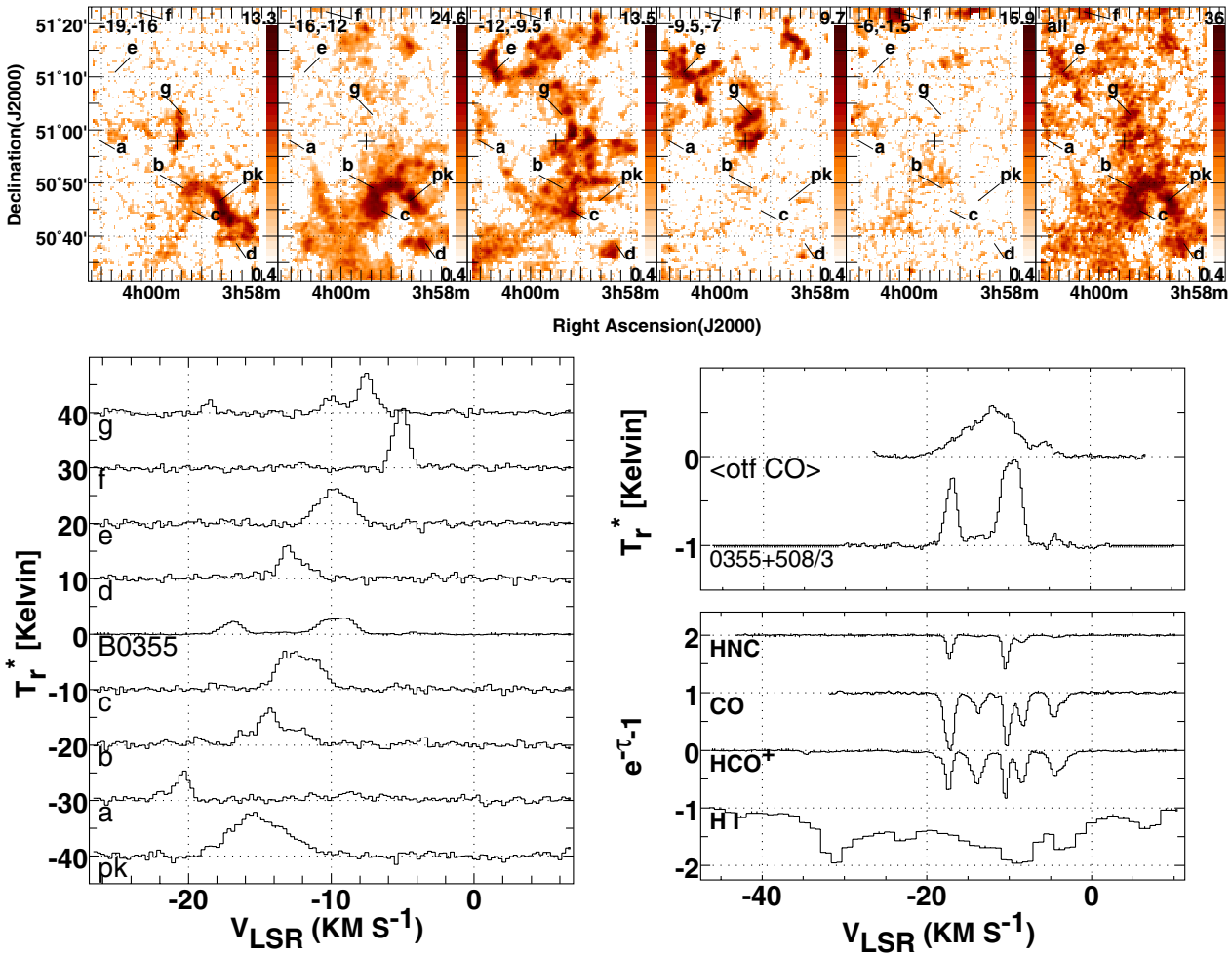

Fig. 12. The sky field around the position of B0355+508. At *top* are maps of integrated CO intensity made over the velocity intervals indicated in each panel, corresponding to the five strong components of the HCO^+ absorption profile seen at *lower right*. CO emission profiles at various locations indicated in the map panels are shown at *lower left*. CO emission profiles toward B0355+508 and averaged over the map area are shown above the absorption line profiles.

(the usual last contour on CO sky maps) are detected at or above the 90% confidence level. To put these brightness and sensitivity levels in context, note that there is a straightforward relationship between W_{CO}, f_{H_2}, and E_{B-V} once the CO-H_2 and $E_{B-V}/N(H)$ conversion factors are fixed; for the *standard* $W_{CO}/N(H_2) = 2 \times 10^{20}$ cm^{-2} H$_2$ (km s^{-1})$^{-1}$ and $N(H)/E_{B-V} = 5.8 \times 10^{21}$ cm^{-2} mag^{-1} one has $W_{CO} = 14.5\ f_{H_2}\ E_{B-V}$ K km s^{-1}. At $E_{B-V} = 0.1$ mag, emission only slightly exceeding 1 K km s^{-1} implies a molecular fraction $f_{H_2} > 1$ and therefore is too bright to be accomodated by a CO-H_2 conversion factor as large as the standard 2×10^{20} cm^{-2} H$_2$ (km s^{-1})$^{-1}$.

Shown in each panel of Fig. 15 are lines representing the CO emission expected if various fractions f_{H_2} of the total neutral gas column are in H_2 with a typical galactic $W_{CO}/N(H_2)$ conversion factor $X_{CO} = 2 \times 10^{20}$ H$_2$ cm^{-2} (K km s^{-1})$^{-1}$. Much of the CO in Fig. 15 occurs above the line corresponding to $f_{H_2} = 1$ and is therefore too bright to be accomodated by the usual CO-H_2 conversion factor; indeed, almost every CO line with $W_{CO} \gtrsim 1$ K km s^{-1} may be described as overly-bright in this way if $f_{H_2} = 0.5$, hence the great majority of all the statistically significant emission represented in Fig. 15 and in the maps shown earlier for these sources. For the brightest pixels $N(H_2)/W_{CO} < 5 \times 10^{19}$ H$_2$ cm^{-2} (K km s^{-1})$^{-1}$.

The same W_{CO}-E_{B-V} diagrams are shown for sources with higher E_{B-V} in Fig. 16. Much of the gas around B2200+420 falls above the line for $f_{H_2} = 1$, and attains such high brightness that its H_2/W_{CO} ratio is 3−4 times below the standard conversion factor. However, this case becomes increasingly harder to make toward the other sources having higher E_{B-V} as in the bottom panels of Fig. 16.

8.2. Sub-structure in reddening would not eliminate large W_{CO}/E_{B-V} ratios

CO emission is heavily structured on arcminute scales, well below the 6′ angular resolution of the reddening maps, and the high values and large scatter in W_{CO}/E_{B-V} in Fig. 15 cannot be accomodated with a fixed ratio of $W_{CO}/N(H_2)$ or $W_{CO}/N(H)$ except by positing strong unresolved variations, essentially clumping, in E_{B-V}. It is important to understand the extent to which this might represent unresolved structure in the total column density, for instance with regard to cleaning maps of the cosmic microwave background (Planck Collaboration 2011). Given the extreme sensitivities of the CO abundance and brightness to $N(H_2)$ in diffuse clouds and the fact that even f_{H_2} may vary in diffuse material, it is entirely possible that the large contrasts seen in W_{CO} do not have strong consequences for the distribution of $N(H)$, E_{B-V}, or even $N(H_2)$.

Shown in Fig. 17 are cumulative distribution functions of the integrated CO emission W_{CO} in the fields around B0954+658

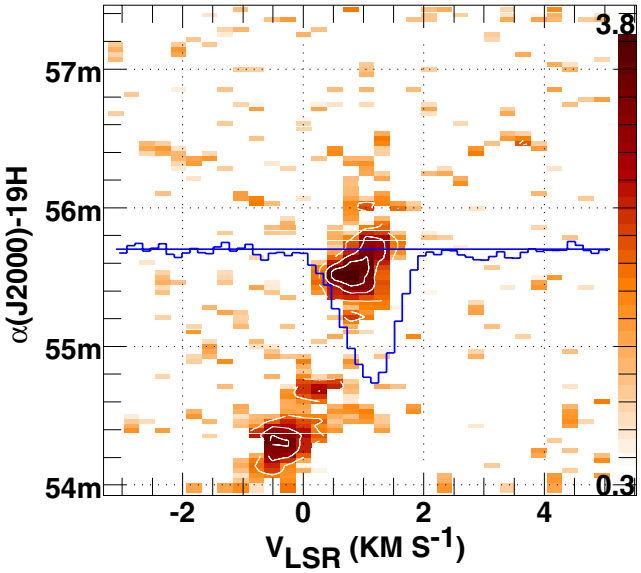

Fig. 13. A right ascension-velocity diagram of CO emission through the position of B1954+513. The HCO^+ (not CO) absorption spectrum toward B1954 is shown with its 0-level at the location of the continuum source; the peak absorption is 90%. Contours are shown at levels 1−3, ... K.

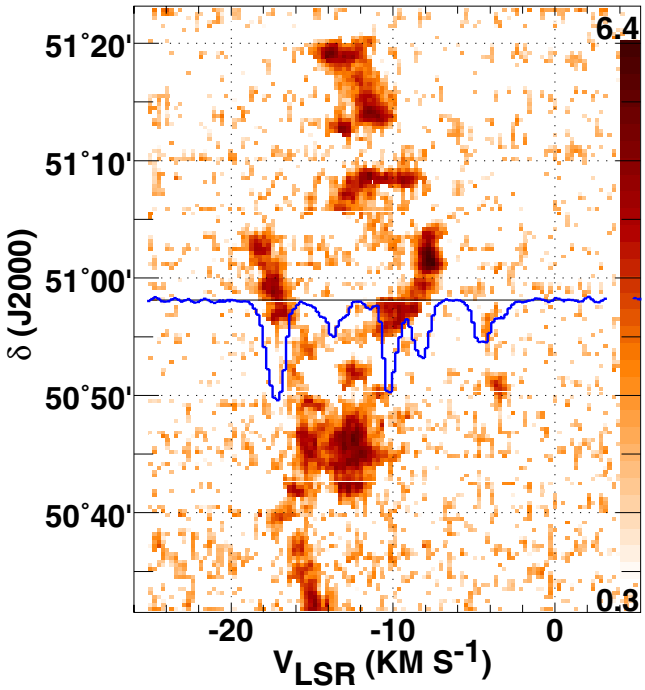

Fig. 14. A declination-velocity diagram of CO emission at the right ascension of B0355+508. The CO absorption spectrum toward B0355+508 is shown with its baseline level at the declination of the background source. The strongest CO absorption line is quite opaque, see Fig. 12.

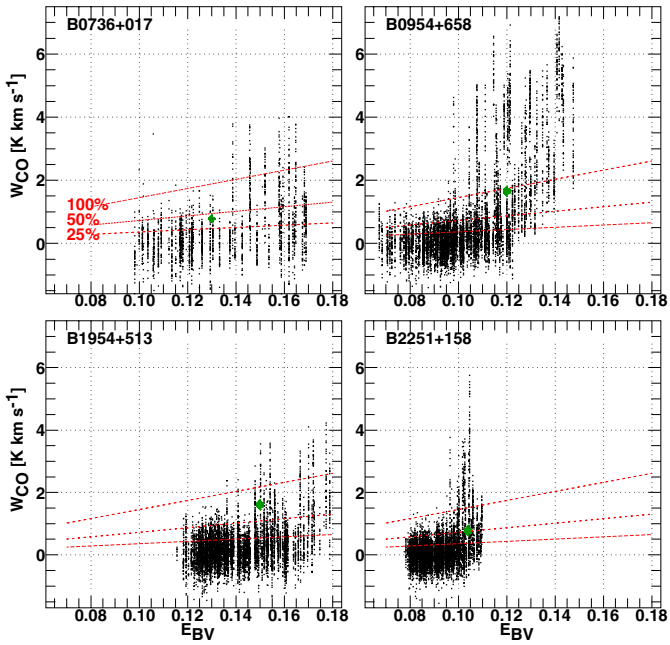

Fig. 15. Distribution of E_{B-V} and W_{CO} for four fields mapped here in CO. Each 20″ pixel in the CO maps is plotted as a separate point. The (red) dashed lines in each panel show the CO emission expected if 25%, 50% and 100% of the gas is in molecular form with a typical value of the W_{CO}-$N(H_2)$ conversion factor, $N(H_2)/W_{CO} = 2 \times 10^{20}$ H_2 cm^{-2} $(K\,km\,s^{-1})^{-1}$. In each panel a (green) filled diamond is shown at the value given in Table 1 toward the background source.

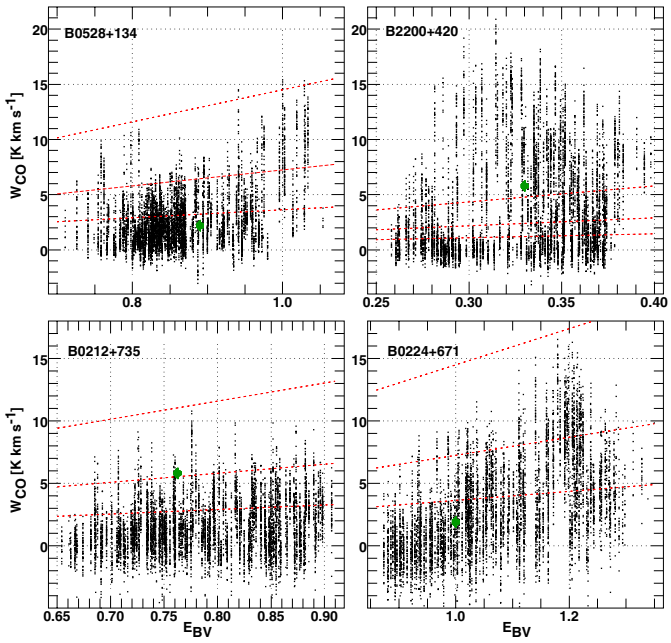

Fig. 16. As in Fig. 15 for four fields with larger reddening.

and BL Lac, using the original ARO data and versions of the data smoothed to lower angular resolution 3′ (similar to NANTEN) and 5′ (similar to *Planck*). The brightness distribution of the CO around B0954+658 is compact in Fig. 3 but still sufficiently extended that 4.5 K km s^{-1} integrated intensities are present at 5′ resolution; this is well above the line for $f_{H_2} = 1$ in Fig. 15.

The distribution of strongly emitting CO around BL Lac is sufficiently broad in angle that 20−30% of the pixels are occupied by CO with $W_{CO} \geq 5$ K km s^{-1} whether the angular resolution is 1′ or 5′; the very strongest CO lines have $W_{CO} \gtrsim 15$ K km s^{-1} at 1−5′ resolution in the BL Lac field. This is consistent with our recent observations of CO emission in the field around ζ Oph (Liszt et al. 2009) where the same peak brightnesses were found in ARO and NANTEN data at 3′ resolution.

Because high CO brightness, and, therefore, impossibly high ratios W_{CO}/E_{B-V} (requiring $f_{H_2} > 1$ for the mean

Table 3. Components with weak CO emission toward the continuum target.

Target	V km s^{-1}	$\tau(1-0)$	T_R^* K	dN(CO)/dV 10^{15} cm^{-2} (km s^{-1})$^{-1}$	$T_{exc}(1-0)$ K	$p(H_2)$ 10^3 cm^{-3} K	$n(H_2)^a$ cm^{-3}	$\int\tau(HCO^+)$dv/total
B0212	–10.3	0.49	0.40	0.65	3.4–3.6	1.9–2.5	75–100	0.122
	–0.05	0.95	<0.14^b	1.11	<3.1–3.2	<0.9–1.1	<35–45	0.102
B0224	–10.6	0.43	<0.10	0.48	<3.0–3.1	<0.8–1.0	<30–40	0.161
B0355	–13.9	0.45	0.31	0.52	3.8–4.0	3.0–3.5	120–140	0.224
	–4.0	0.86	0.37	1.10	3.6–3.8	2.1–2.5	85–100	0.204
B0528	2.8	<0.11	<0.16					0.080
B1730	5.1	1.15	0.24	1.42	3.5–3.7	1.8–2.2	70–90	1.000
B1928	–3	<0.11	<0.11					1.000

Notes. Using CO parameters originally derived by Liszt & Lucas (1998) and $\tau(HCO^+)$ from Lucas & Liszt (1996); $^{(a)}$ at T_K = 25 K ; $^{(b)}$ upper limits in this column are 2σ.

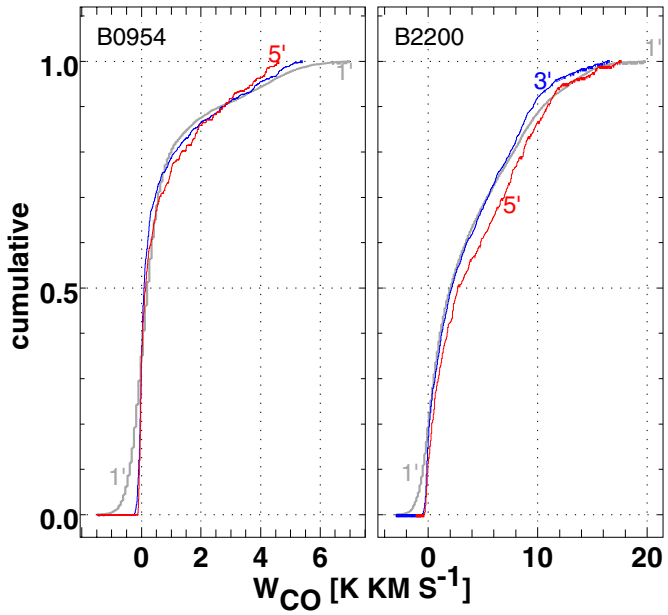

Fig. 17. Cumulative distribution functions for W_{CO} at spatial resolutions of 1′ (gray, thicker), 3′ (blue) and 5′ (red) for B0954 (left) and B2200.

$W_{CO}/N(H_2)$ ratio) persist to low angular resolution, W_{CO} cannot maintain a constant proportionality to $N(H_2)$ over the body of these clouds. The observed variations in W_{CO} are too large to be accomodated by the total amount of material that is present along the line of sight and unresolved structure in reddening cannot account for the high values of W_{CO}/E_{B-V} or the range of variation in that ratio.

8.3. Covering factors and bright and dark CO

In Sect. 2.7 we noted the statistical certainty with which HCO^+ absorption is found in spectra taken within about 15°–18° of the galactic plane. A corollary to this is that molecular gas is certain to be omnipresent over the sky fields mapped in CO at such latitudes, no matter how much of sky we actually found to be occupied by CO emission.

Table 2 shows pixel statistics for the CO emission maps made in the course of this work; shown are profile channel-channel rms noise values and map pixel-pixel rms noise in W_{CO} for each mappable kinematic component. In each case the covering factor was determined by forming a histogram of the W_{CO} values and subtracting a gaussian fit to the component corresponding to the noise, and is apparent in that it extends to unphysical negative values of W_{CO}. This is not a large correction; if the noise in W_{CO} is random at a level σ_{map} the covering factor at/above any given W_{CO} in the absence of signal is $dA(W_{CO})/A = 0.5(1\text{-erf}(W_{CO}/\sqrt{(2)}\sigma_{map}))$. The expected covering factor due to noise at even 2σ significance is already below 3%.

Table 2 shows that typical covering factors are 20–40%, with a few null values and only two sky fields (B0528 and B2200) where the majority of the map area is covered. Very approximately, the covering factors are small to about the same extent that the $W_{CO}/N(H_2)$ conversion factors of the detected CO emission are higher than indicated by the standard CO-H_2 conversion. In the end, some form of spatial averaging over brighter and dimmer CO must be responsible for the global mean CO-H_2 conversion factor whether in fully molecular or diffuse molecular gas. The idea that all gas parcels would show identically the same $W_{CO}/N(H_2)$ is highly unlikely.

8.4. Pressure and density in CO-emitting gas

Partial pressures of molecular hydrogen $p(H_2)/k = n(H_2)T_K$ were derived by Liszt & Lucas (1998) for all of the CO-bearing clouds discussed here, in the directions of the background targets. They generally fall in the range $1-5 \times 10^3$ cm^{-3} K, typical of thermal pressures in the diffuse ISM sampled by neutral atomic carbon (Jenkins & Tripp 2011), which should share the same volume. The CO derivation depends on recognizing that, when the gas is warm and excitation is strongly sub-thermal, the excitation temperature of the $J = 1-0$ transition depends only on $p(H_2)$ and the optical depth of the transition $\tau(1-0)$. In the limit of zero optical depth the excitation temperature of the $J = 1-0$ transition $T_{exc}(1-0)$ is only proportional to $p(H_2)$, not to either the temperature or density independently, making CO a useful barometer. This first became apparent in the work of Smith et al. (1978) and is illustrated in Fig. 11 of Liszt & Lucas (1998): it has persisted over several generations of improved collision cross sections. Moreover, the excitation contribution from atomic hydrogen should be small in CO-bearing gas where the molecular fraction must be appreciable even if H_2 does not dominate the overall atomic-molecular balance (Liszt 2007).

For $\tau(1-0) \lesssim 3$ and $p(H_2)/k \lesssim 2 \times 10^4$ cm^{-3} K the behavior seen in Fig. 11 of Liszt & Lucas (1998) may be straightforwardly parameterized to an accuracy of a few percent as

$$T_{exc}(1-0) - T_{cmb} = 0.303\ \mathrm{K}\left[\frac{p\,(H_2)}{10^3\ \mathrm{cm^{-3}\ K}}\right]^{1.02} e^{\tau(1-0)^{0.6}/2.6}. \quad (1)$$

As examples of the application of this notion, we note:

- For a typical line with $\tau(1-0) = 1.5$ and a Rayleigh-Jeans brightness above the CMB of 1.5 K, $T_{\rm exc}(1-0) = 5.04$ K and $p(H_2)/k = 5 \times 10^3$ cm^{-3} K or $n(H_2) = 200$ cm^{-3} at $T_K = 25$ K.
- For the strongest absorption line component toward B0355 (-17.8 km s^{-1}), $\tau(1-0) = 3.1$ and $T_{\rm exc}(1-0) \approx 6$ K, so that $p(H_2)/k \approx 5 \times 10^3$ cm^{-3} K once more.
- The ≈4.5 K lines observed at the peak positions in several of the simple fields discussed in Sect. 3 require $p(H_2)/k \gtrsim 8.5 \times 10^3$ cm^{-3} K or $\gtrsim 15 \times 10^3$ cm^{-3} K for $\tau(1-0) = 3$ or 1, respectively. Such a heavy over-pressure must be transient.
- The very bright 10–12 K lines seen near B0528+134 and B2200+420 require excitation temperatures of 15 K or more and lie somewhat beyond the range where $W_{\rm CO}$ and N(CO) can be shown to be linearly proportional. They will be discussed separately in a forthcoming publication based on observations of HCO$^+$, HCN, and CS.

8.5. Failing to detect H_2 when CO emission is weak

There are cases where the brightness of the 1–0 line is well below 1 K even when the CO optical depth is appreciable, as summarized in Table 3; unfortunately we do not have a CO absorption profile toward B1928+738 in whose field CO emission was not detected, see Sect. 3.4. The regions of very low $p(H_2)$ toward B0212 and B0224 somehow manage to produce appreciable amounts of CO without exciting it to detectable levels but other lines represented in Table 3 do not arise in regions of especially low pressure.

In Sect. 2.7 we showed that, on the whole, molecular gas is not underrepresented by CO emission in the collection of sightlines comprising this work and earlier we showed that the same is true of the larger sample of absorption-cloud sightlines from which the current sample was drawn (Liszt et al. 2010). Moreover, CO emission from all of the components represented in Table 3 is detected (usually quite strongly) elsewhere in the mapped fields except around B1928. However, the fraction of molecular gas that is detectable in CO along individual sightlines varies substantially. To quantify this we derived the H_2 column density from the integrated optical depth measured in HCO$^+$ (Lucas & Liszt 1996), see the right-most column in Table 3. With H_2 calculated in that way, the fraction of molecular gas that is missed by failing to detect CO emission from particular individual components in four directions is 12% toward B0212, 16% toward B0224, 8% toward B0528+134 and 100% toward B1928. Overall the fraction of molecular gas represented by the weakly-emitting CO summarized in Table 3 is 8% toward B0528, 16% toward B0224, 22% toward B0212, 43% toward B0355 and 100% toward B1730 and B1928.

9. Discussion

Even at $E_{B-V} = 0.1-0.3$ mag, the CO emission traced in this work runs the full gamut from undetectable to having brightness comparable to that seen in fully-molecular dark clouds. CO emission may be undetectably weak (≪1 K) when molecular gas is present in absorption (including that of CO itself) but in other directions it may be so bright that the $N(H_2)/W_{\rm CO}$ ratio is 4–5 times smaller than the typical CO-H_2 conversion factor 2×10^{20} cm^{-2} (K km s^{-1})$^{-1}$. Under the conditions encountered in diffuse clouds, CO emission is foremost an indicator of the CO chemistry, secondarily an indicator of the rotational excitation (which reflects the partial thermal pressure of H_2) and only peripherally a measure of the underlying hydrogen column density distribution as discussed in Sect. 8. Indeed, the simulations of CO emission from the interstellar medium by Shetty et al. (2011) agree with observations for the dense gas. However, a detailed comparison with our results on the diffuse material shows that the brightness per CO molecule is correct but there are up to 4 orders of magnitude difference in $N(H_2)/N$(CO). This is linked to the poorly-understood polyatomic chemistry in the diffuse gas (see Shetty et al. 2011, their Sect. 4.3).

The over-arching issues most relevant to diffuse cloud CO emission are three-fold: 1) how it may be identified for what it is, originating in relatively tenuous gas that is unassociated with star formation; 2) whether it makes a substantial contribution when CO emission is used as a surrogate for $N(H_2)$ in circumstances where emission contributions from diffuse and dense heavily-shielded gas may be blended; 3) how it is related to the so-called "dark" gas discovered by and *Fermi* (Abdo et al. 2010) and *Planck* (Planck Collaboration 2011) that is most prominent at moderate extinction where the transition from atomic to molecular gas occurs and is claimed to host 50–120% of the previously-known CO emitting gas in the solar neighbourhood.

As for the identification of diffuse gas, the $W_{\rm CO}/W_{^{13}\rm CO}$ ratio is the most acessible and direct probe. When diffuse cloud CO is excited to detectable levels it is generally in the regime where $W_{\rm CO} \propto N$(CO) and $W_{^{13}\rm CO} \propto N(^{13}$CO) so that the brightness ratio $W_{\rm CO}/W_{^{13}\rm CO}$ will be much larger than the values 3–5 that are seen when emission arises from optically thick lines from denser gas where the rotation ladder is close to being thermalized. Fractionation progressively lowers the $N(^{12}\rm CO)/N(^{13}\rm CO)$ column density ratio in diffuse gas at larger N(CO) (Liszt & Lucas 1998; Sheffer et al. 2007) but not below about 15. Intensity ratios $W_{\rm CO}/W_{^{13}\rm CO}$ of 8–10 or higher are a strong indicator that there is a major contribution from diffuse material.

Regarding the contribution of diffuse gas we recently assessed it in the case where an outside observer looked down on the Milky Way disk in the vicinity of the Sun (Liszt et al. 2010). We compared the mean emission for the ensemble of lines of sight from which the current background targets were drawn with the vertically-integrated emission expected for the galactic disk component at the Solar Circle drawn from galactic plane surveys. The ensemble mean in our dataset, expressed as an equivalent to looking vertically through the galactic layer, was $2\ \langle W_{\rm CO}\ \sin(|b|)\rangle = 0.47$ K km s^{-1}. The galactic disk contribution was inferred from galactic plane surveys that find A(CO) = 5 K km s^{-1} (kpc)$^{-1}$ and an equivalent disk thickness of 150 pc, implying an integrated intensity through the disk of 5 K km s^{-1} (kpc)$^{-1}$ × 0.15 kpc = 0.75 K km s^{-1}.

Even if viewed as entirely distinct (because it originates at galactic latitudes well above those typically sampled in galactic plane surveys) the diffuse gas contribution to the total seen looking down on the Milky Way from outside would be 0.47/(0.47+0.75) = 38%, a surprisingly high fraction given the supposed absence of molecular gas and CO emission at higher galactic latitudes. The alternative, that the diffuse gas is already incorporated in galactic plane surveys, makes the majority of the gas (0.47/0.75) in the galactic plane diffuse. This is an even more radical proposition, but is consistent with finding that the preponderance of the molecular gas seen toward the heavily-extincted line of sight toward B0355+508 at $b = -1.6°$ is actually diffuse.

In fact, the extent of the diffuse and/or high-latitude contribution to the local CO emission remains to be determined by wide-field CO surveys whose detection limit is substantially better than 1 K km s^{-1} and perhaps no worse than even 0.25 K km s^{-1}.

Assessing the contribution of diffuse gas at lower latitudes awaits a wider examination of the character of the gas seen in the galactic disk, but the contribution of diffuse molecular gas in the inner galactic disk is apparent in recent HERSCHEL/PRISMAS observations of sub-mm absorption spectra toward star-forming regions (Gerin et al. 2010; Sonnentrucker et al. 2010).

10. Summary and conclusions

We compared maps of CO emission with reddening maps on a typical field of view of about $30' \times 30'$ at an angular resolution of $1'$ toward 11 diffuse lines of sight for which we already had sub-arcsec molecular and/or atomic absorption profiles. This allowed us to draw three kinds of conclusions.

10.1. Conclusions about the position-position-velocity structure of the emission

- Although most of the CO emission structure was amorphous or merely blob-like when mapped, the emission around B0528+138 was found to be highly regular and quasi-periodic while that around B2200+420 (BL Lac) was seen to be filamentary and tangled.
- Toward B0355+508 and B0528+134, CO mapping suggests that pairs of absorption lines separated by 6−8 km s^{-1} are physically related, not merely accidental superpositions.
- CO mapping shows that partition of an absorption profile into kinematic components, no matter how seemingly obvious, may actually be arbitrary and capricious: the decomposition may have no apparent validity in emission at positions only slightly removed from the continuum background.

10.2. Conclusions linking the absorption to the emission kinematics

- The same clouds were seen in absorption and emission, and in atomic and molecular phases, although not necessarily in the same location. We failed to find CO emission corresponding to just one out of 20 molecular absorption features, in one relatively small spatial field, i.e. $20' \times 20'$ vs. $30' \times 30'$ or more. Conversely, while mapping away from the continuum background we saw only 2 CO emission features lacking molecular absorption counterparts.
- CO emission was sometimes found in the field at velocities corresponding to features seen only in H I absorption toward the continuum. We saw no molecular features outside the span of the H I absorption.

10.3. Conclusions regarding the CO luminosity of diffuse gas

- We found relatively bright CO emission at modest reddening in the fields we mapped, with peak brightnesses of 4−5 K at $E_{B-V} \lesssim 0.15$ mag and up to 10−12 K at $E_{B-V} \simeq 0.3$ mag (i.e. $A_V \simeq 1$ mag). This was true even for features that were seen only in absorption toward the continuum source in the field center.
- The CO emission lines represent small column densities $N(\mathrm{CO}) \leq 10^{16}$ cm^{-2}, less than 10% of the amount of free gas phase carbon expected along a line of sight with $E_{B-V} = 0.15$ mag or $A_V = 0.5$ mag. The dominant form of gas phase carbon is still C^+.
- When CO emission was detected at levels of 1.5 K km s^{-1} and higher, it was generally over-luminous in the sense of having a small ratio $N(H_2)/W_{CO}$, i.e. a value of the CO-H_2 conversion factor below 2×10^{20} H_2 (K km s^{-1})$^{-1}$. $W_{CO}/N(H_2)$ ratios as small as $N(H_2)/W_{CO} \lesssim 5 \times 10^{19}$ cm^{-2} H_2 (km s^{-1})$^{-1}$ are mandated by the observed reddening in cases where the line of sight was relatively free of extraneous material.
- On average, the $W_{CO}/N(H_2)$ ratio in diffuse gas is locally the same as in dense fully molecular clouds despite the presence of strong variations between individual diffuse gas parcels or sightlines. The global $W_{CO}/N(H_2)$ ratio in diffuse gas is the result of averaging over limited regions where CO emission is readily detectable and overly bright (in the sense of having $W_{CO}/N(H_2)$ much higher than the mean), and with other regions having a significant molecular component (as seen in absorption) but where CO emission is comparatively weak or simply undetectable.
- Small $W_{CO}/N(H_2)$ ratios and sharp variations in the W_{CO}/E_{B-V} ratio are not artifacts of the disparity in resolution between the $1'$ CO emission beam and the $6'$ resolution of the reddening maps, because high CO brightnesses and small W_{CO}/E_{B-V} ratios persist when the resolution of the CO maps is degraded to that of the reddening maps.
- Sharp variations in the CO emission brightness on arcminute scales do not necessarily represent unresolved structure in the reddening maps or in the column density of H or H_2. Detectable CO emission generally arises in the regime where $W_{CO} \propto N(\mathrm{CO})$, and variations in the line brightness represent primarily the CO chemistry with its extreme sensitivity to E_{B-V} and $N(H_2)$. Secondarily the line brightness is influenced by CO rotational excitation since some features are not seen in emission toward continuum sources where there is CO absorption with appreciable optical depth.
- Only marginally does the CO brightness represent the underlying mass or H_2 column density distribution of diffuse molecular gas.

Acknowledgements. The National Radio Astronomy Observatory is operated by Associated Universites, Inc. under a cooperative agreement with the US National Science Foundation. The Kitt Peak 12-m millimetre wave telescope is operated by the Arizona Radio Observatory (ARO), Steward Observatory, University of Arizona. IRAM is operated by CNRS (France), the MPG (Germany) and the IGN (Spain). This work has been partially funded by the grant ANR-09-BLAN-0231-01 from the French *Agence Nationale de la Recherche* as part of the SCHISM project (http://schism.ens.fr/). We thank Edith Falgarone for comments that inspired Sects. 8.4 and 8.5 of this work and we thank the editor, Malcolm Walmsley, for a variety of interesting and stimulating comments and corrections.

References

Abdo, A. A., Ackermann, M., Ajello, M., et al. (Fermi/LAT Collaboration) 2010, ApJ, 710, 133
Bania, T. M., Marscher, A. P., & Barvainis, R. 1991, AJ, 101, 2147
Berné, O., Marcelino, N., & Cernicharo, J. 2010, Nature, 466, 947
Burgh, E. B., France, K., & McCandliss, S. R. 2007, ApJ, 658, 446
Dame, T. M., & Thaddeus, P. 1994, ApJ, 436, L173
Dame, T. M., Hartmann, D., & Thaddeus, P. 2001, ApJ, 547, 792
Dickey, J. M., Kulkarni, S. R., Heiles, C. E., & Van Gorkom, J. H. 1983, ApJS, 53, 591
Gerin, M., de Luca, M., Goicoechea, J. R., Herbst, E., Falgarone, E., et al. 2010, A&A, 521, L16
Gir, B.-Y., Blitz, L., & Magnani, L. 1994, ApJ, 434, 162
Goldreich, P., & Kwan, J. 1974, ApJ, 189, 441
Hartmann, D., & Burton, W. B. 1997, Atlas of galactic neutral hydrogen (Cambridge; New York: Cambridge University Press)
Heiles, C., & Troland, T. H. 2003, ApJ, 586, 1067
Heithausen, A. 2004, ApJ, 606, L13
Hily-Blant, P., & Falgarone, E. 2009, A&A, 500, L29
Hogerheijde, M. R., De Geus, E. J., & Spaans, F. 1995, ApJ, 441, L93

Jenkins, E. B., & Tripp, T. M. 2011, ApJ, 734, 65
Lequeux, J., Allen, R. J., & Guilloteau, S. 1993, A&A, 280, L23
Liszt, H. S. 1994, ApJ, 429, 638
Liszt, H. S. 2007, A&A, 476, 291
Liszt, H. S., & Lucas, R. 1996, A&A, 314, 917
Liszt, H. S., & Lucas, R. 1998, A&A, 339, 561
Liszt, H. S., & Lucas, R. 2000, A&A, 355, 333
Liszt, H., & Lucas, R. 2001, A&A, 370, 576
Liszt, H. S., & Wilson, R. W. 1993, ApJ, 403, 663
Liszt, H., Lucas, R., & Pety, J. 2006, A&A, 448, 253
Liszt, H. S., Pety, J., & Tachihara, K. 2009, A&A, 499, 503
Liszt, H. S., Pety, J., & Lucas, R. 2010, A&A, 518, A45
Lucas, R., & Liszt, H. S. 1993, A&A, 276, L33
Lucas, R., & Liszt, H. S. 1996, A&A, 307, 237
Lucas, R., & Liszt, H. S. 2000, A&A, 358, 1069
Lucas, R., & Liszt, H. S. 2002, A&A, 384, 1054
Maddalena, R. J., & Morris, M. 1987, ApJ, 323, 179
Magnani, L., Blitz, L., & Mundy, L. 1985, ApJ, 295, 402
Marscher, A. P., Bania, T. M., & Wang, Z. 1991, ApJ, 371, L77
Pety, J., & Falgarone, E. 2003, A&A, 412, 417
Pety, J., Lucas, R., & Liszt, H. S. 2008, A&A, 489, 217
Planck Collaboration 2011, A&A, 536, A19
Rachford, B. L., Snow, T. P., Destree, J. D., et al. 2009, ApJS, 180, 125
Sakamoto, S., & Sunada, K. 2003, ApJ, 594, 340
Savage, B. D., Drake, J. F., Budich, W., & Bohlin, R. C. 1977, ApJ, 216, 291
Schlegel, D. J., Finkbeiner, D. P., & Davis, M. 1998, ApJ, 500, 525
Sheffer, Y., Rogers, M., Federman, S. R., Lambert, D. L., & Gredel, R. 2007, ApJ, 667, 1002
Sheffer, Y., Rogers, M., Federman, S. R., et al. 2008, ApJ, 687, 1075
Shetty, R., Glover, S. C., Dullemond, C. P., & Klessen, R. S. 2011, MNRAS, 412, 1686
Smith, A. M., Stecher, T. P., & Krishna Swamy, K. S. 1978, ApJ, 220, 138
Snow, T. P., & McCall, B. J. 2006, ARA&A, 44, 367
Sonnentrucker, P., Welty, D. E., Thorburn, J. A., & York, D. G. 2007, ApJS, 168, 58
Sonnentrucker, P., Neufeld, D. A., Phillips, T. G., Gerin, M., Lis, D. C., et al. 2010, A&A, 521, L12
Yamamoto, H., Onishi, T., Mizuno, A., & Fukui, Y. 2003, ApJ, 592, 217

Pages 21 to 23 are available in the electronic edition of the journal at http://www.aanda.org

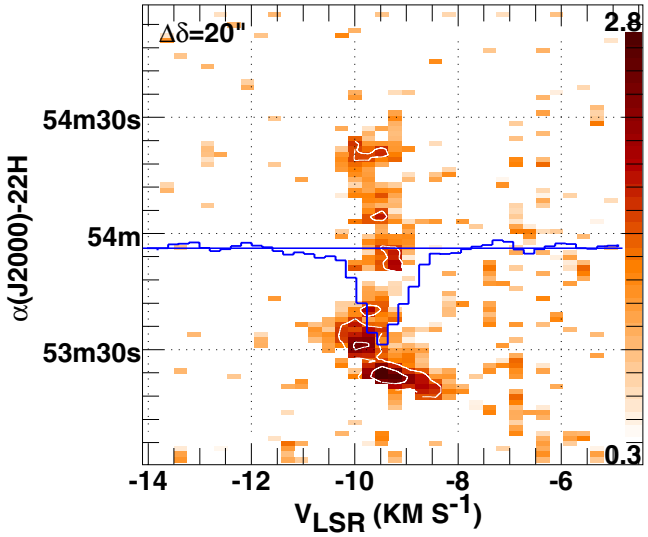

Fig. A.1. A right ascension-velocity diagram of CO emission 20″ North of B2251+158. The CO absorption spectrum toward B2251 is shown with its 0-level at the location of the continuum source; the peak absorption is 22%, see Fig. 7. Contours are shown at levels 1−3, ... K.

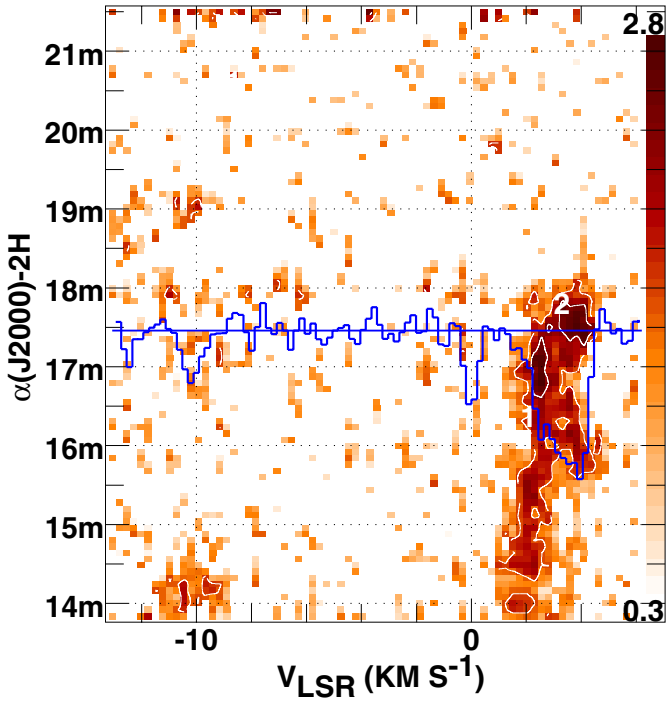

Fig. A.2. A right ascension-velocity diagram of CO emission across the field of B0212+735. The CO absorption spectrum toward B0212 is shown with its 0-level at the location of the continuum source; the strongest absorption line is quite opaque, see Fig. 10. Contours are shown at levels 1−3, ... K.

Appendix A: CO line kinematics around three additional objects

Shown in Figs. A.1−A.3 are position-velocity diagrams in right ascension across the positions of B2251+158, b0212+735 and B0224+671. As in Figs. 13 and 14 in the main text, the HCO^+ absorption spectrum toward the continuum background target is superposed in the figures with its baseline positioned where the diagram most nearly crosses the location of the continuum. These diagrams are intended to show how the features

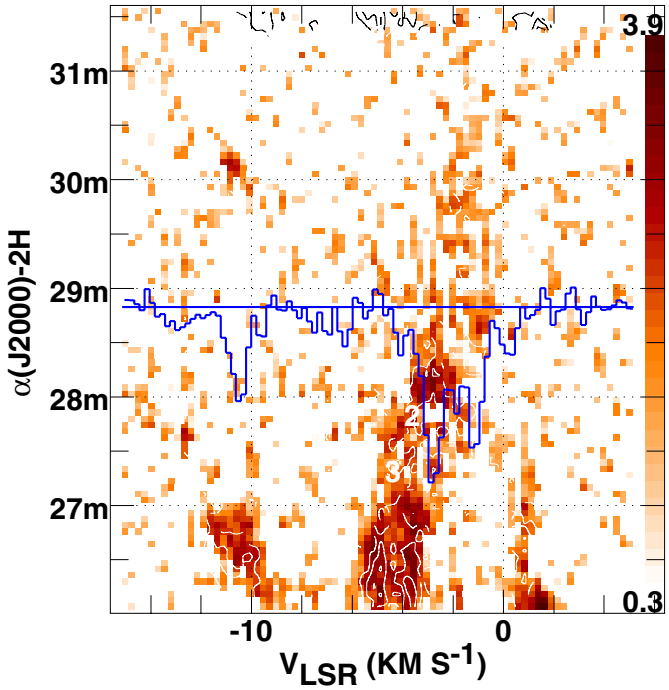

Fig. A.3. A right ascension-velocity diagram of CO emission across the field of B0224+671 at the declination of the continuum source. The CO absorption spectrum toward B0224+671 is shown with its 0-level at the location of the continuum source; the peak optical depth is 1.2, see Fig. 11. Contours are shown at levels 1−3, ... K.

that occur in the absorption line profiles are somewhat haphazard samples of the larger scale gas distribution traced in CO emission but toward B0212+735 the diagram also indicates how the CO emission underrepresents the molecular gas distribution.

Appendix B: The galaxy viewed in atomic gas around the background targets

To provide context for the kinematics seen in the present work, Figs. B.1 and B.2 show large-galactic-scale H I latitude-velocity diagrams for each of the sources studied here, using results of the LDSS survey of Hartmann & Burton (1997). The spatial resolution of these data is 35′ and the data are on a 30′ grid. The diagrams were constructed at the galactic longitude nearest the background target (see Table 1). The latitudes of the sources are marked. Even if it was not apparent from the overlap of the H I and molecular absorption in the figures in the text, these maps make it clear that the molecular gas studied here is part of "normal" galactic structure, mixed into the general ISM.

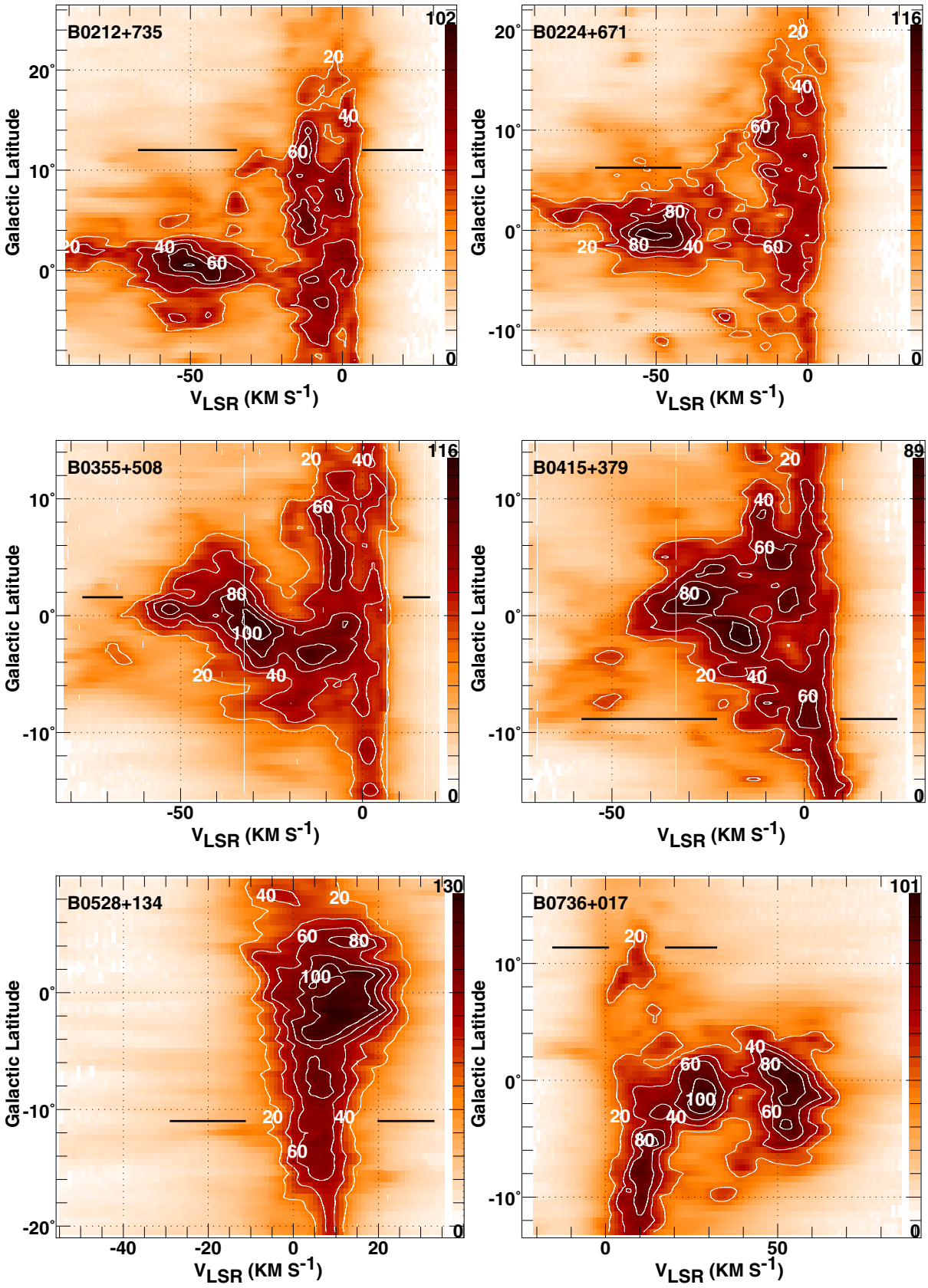

Fig. B.1. Latitude-velocity diagrams of H I brightness around six background targets used for mm-wave molecular absorption studies, using H I data from the LDSS survey (Hartmann & Burton 1997). The spatial resolution is 35′ and the diagrams were constructed at the nearest longitude on the 0.5° grid of the survey datacube. The latitudes of the sources are marked. The line of sight toward B0415+379 (3C 111) is not discussed in this work.

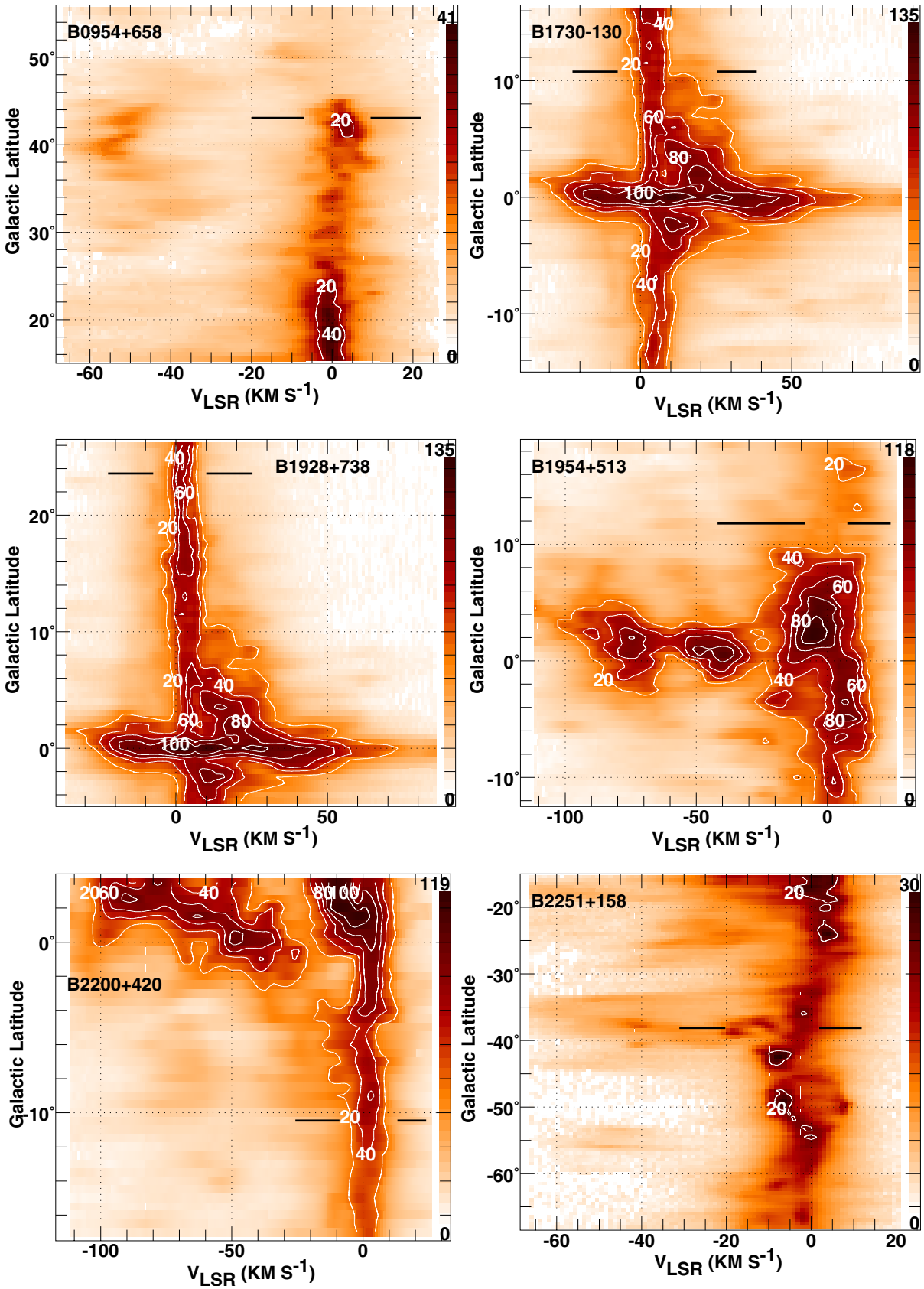

Fig. B.2. Latitude-velocity diagrams of H I brightness around six background targets used for mm-wave molecular absorption studies, using H I data from the LDSS survey (Hartmann & Burton 1997), as in Fig. B.1.

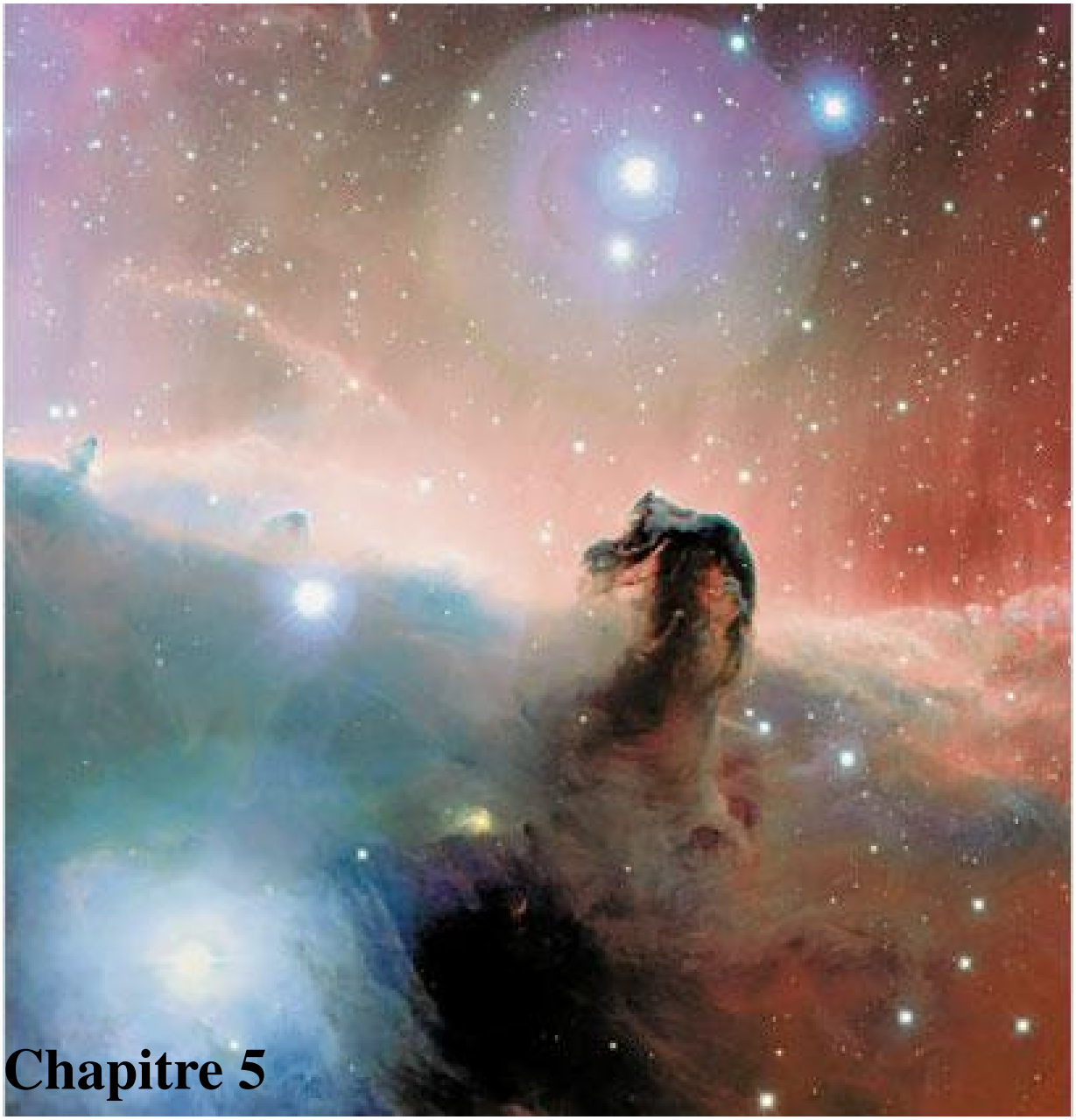

Chapitre 5

Copyright: CFHT/Coelum

La Tête de Cheval : une référence observationnelle pour les modèles chimiques

5.1 Les modèles photochimiques et la Tête de Cheval

Les modèles des régions de photo-dissociations (PDRs) sont utilisés pour comprendre l'évolution de la matière éclairée par le rayonnement UV, à la fois dans notre galaxie et dans les galaxies extérieures. Au vu de la complexité inhérente à la constitution de réseaux et de modèles chimiques fiables, il y a un vrai besoin d'observations bien contraintes qui puissent servir de

référence primaire. Une référence observationnelle idéale donnerait aux chimistes un ensemble d'abondances (avec les incertitudes associées) en fonction de la distance (ou de l'extinction visuelle) à l'étoile excitatrice. Cet objectif est difficile à atteindre pour plusieurs raisons : 1) la géométrie de la source n'est jamais aussi simple que souhaitée, lorsqu'elle est connue ; 2) les spectres produits par les instruments doivent être inversés à l'aide de méthodes complexes de transfert de rayonnement pour obtenir des abondances ; 3) les spectres sont souvent mesurés à des résolutions angulaires très différentes, impliquant de la dilution et/ou du mélange de différentes composantes du gaz dans le lobe du télescope.

Dans ce contexte, la PDR présente dans la crinière de la Tête de Cheval est un cas particulièrement intéressant parce que 1) la transition du gaz diffus, chaud et ionisé au gaz dense, froid et noir est brusque ; 2) la géométrie de la PDR est simple (pratiquement unidimensionnelle, vue de profil). Le profil de densité à travers la PDR est bien contraint et nous faisons des efforts pour contraindre à son tour le profil thermique. La combinaison d'une faible distance à la Terre (à 400 pc, $1''$ correspond à 0.002 pc), d'un faible éclairement UV ($\chi = 60$) et d'une grande densité ($n_{\rm H} = 10^5\,{\rm cm}^{-3}$), implique que tous les processus physiques et chimiques importants peuvent être testés dans un champ de vue de moins de $50''$ avec des échelles spatiales allant de 1 à $10''$.

5.2 Une physique bien contrainte et une chimie riche

Dans les 10 dernières années, j'ai mis en œuvre avec M. Gerin (Obs. de Paris/LERMA) et J. Goicoechea (Centro de Astrobiología, CSIC) un programme ambitieux et cohérent d'observations de cette PDR. Nous avons utilisé les mêmes instruments et les mêmes méthodes d'observation, de réduction et d'analyse des données. Pour chaque espèce chimique, nous avons essayé 1) d'observer au moins deux transitions à une résolution angulaire similaire (de 5 à $15''$) pour contraindre proprement les conditions d'excitations, et 2) d'observer les isotopologues[1] associés pour inférer des densités de colonne et des abondances précises. L'obtention de cartes de l'émission étendue s'est aussi révélée essentielle pour comprendre les distributions spatiales des émissions des diverses espèces.

Cet effort a conduit à la publication de 8 articles dans *A&A* avec les résultats suivants :

1. La PDR a un gradient de densité très pentu, augmentant jusqu'à $n_{\rm H} = 10^5\,{\rm cm}^{-3}$ en moins de $10''$, à une pression approximativement constante de $P = 4\,10^6\,{\rm K\,cm}^{-3}$ [A28].
2. Les abondances des petits hydrocarbures sont plus grandes que les prédictions émanant de modèles de chimie en phase uniquement gazeuse. Cela suggère qu'un chemin chimique supplémentaire pour la formation de ces petites chaînes hydrocarbonnées doit être considéré dans les PDRs. Nous avons proposé que le surplus de petits hydrocarbures pourrait provenir de la photo-érosion des PAHs [A29, A32].
3. La déplétion du soufre en phase gazeuse, nécessaire pour expliquer les abondances de CS et de HCS^+, est inférieure de plusieurs ordres de grandeur à celle invoquée dans toutes les études précédentes, quelle que soit la source [A25].
4. Un cœur dense et froid ($T \sim 20\,{\rm K}$, $n > 2\,10^5\,{\rm cm}^{-3}$) existe juste derrière la PDR. Dans ce cœur dense, le fractionnement du deutérium est efficace, ce qui donne $[DCO^+]/[HCO^+] >$

[1] Des isotopologues sont des molécules qui diffèrent uniquement dans leur composition isotopique, par exemple CS et $C^{34}S$.

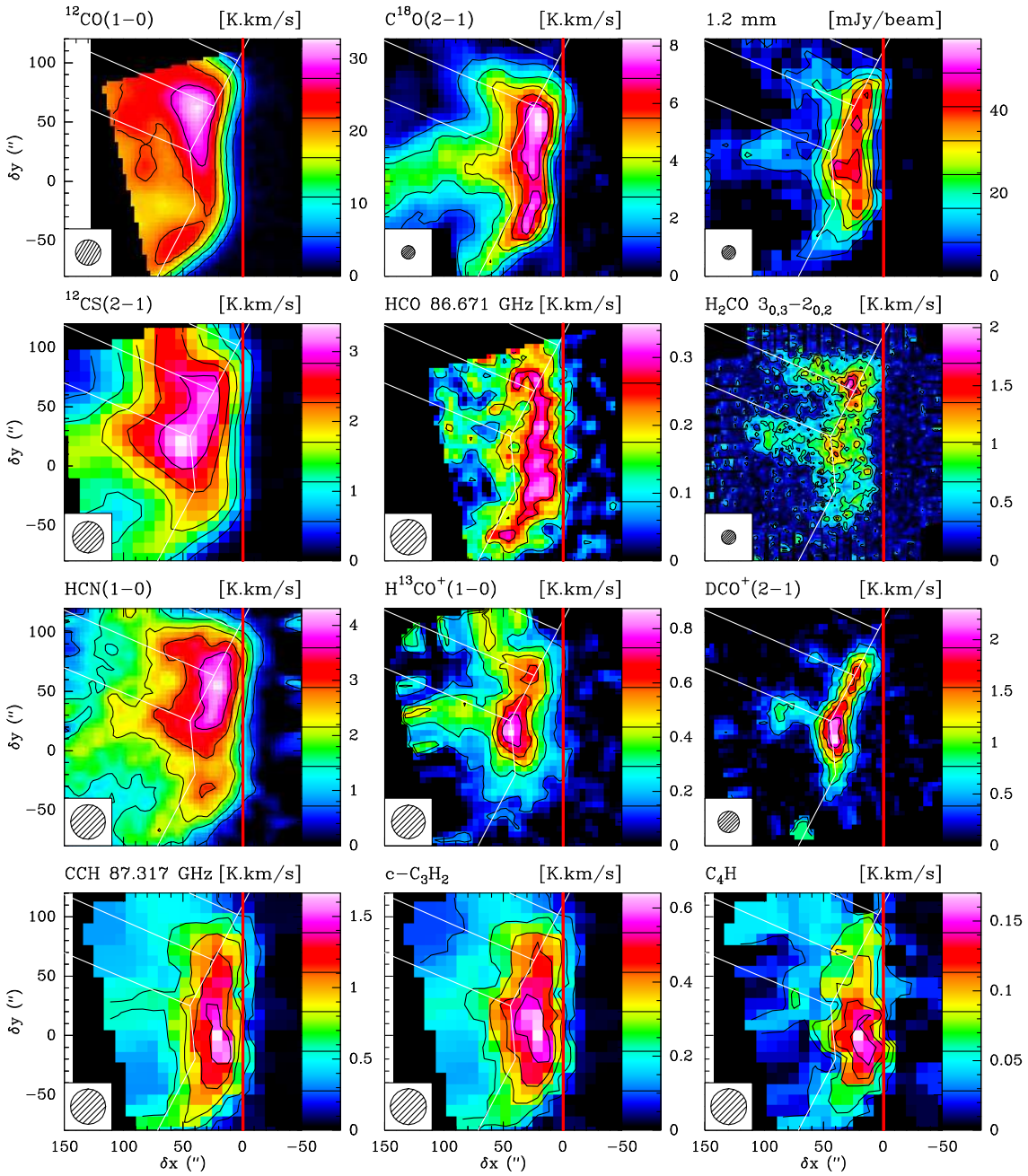

FIG. 5.1 – Région de photo-dissociation (PDR) de la Tête de Cheval révélée par l'émission de divers traceurs moléculaires à des résolutions angulaires allant de $11''$ à $32''$. Le champ de vue couvre $200'' \times 200''$. Les cartes ont été tournées de $14°$ dans le sens inverse des aiguilles d'une montre autour du centre de l'image pour amener la direction de l'étoile excitatrice à l'horizontal car cela simplifie la comparaison de la stratification des divers traceurs. La barre verticale indique le bord de la PDR. Le squelette blanc, défini sur la carte d'émission de DCO^+, est reproduit sur toutes les images pour fournir une référence spatiale. Le lobe angulaire des observations est dessiné à l'échelle dans le coin en bas, à gauche. L'émission des raies a été intégrée entre 10.1 and 11.1 $\mathrm{km\,s^{-1}}$. La valeur des niveaux de contours est indiquée sur les tables de couleur, à droite de chaque image.

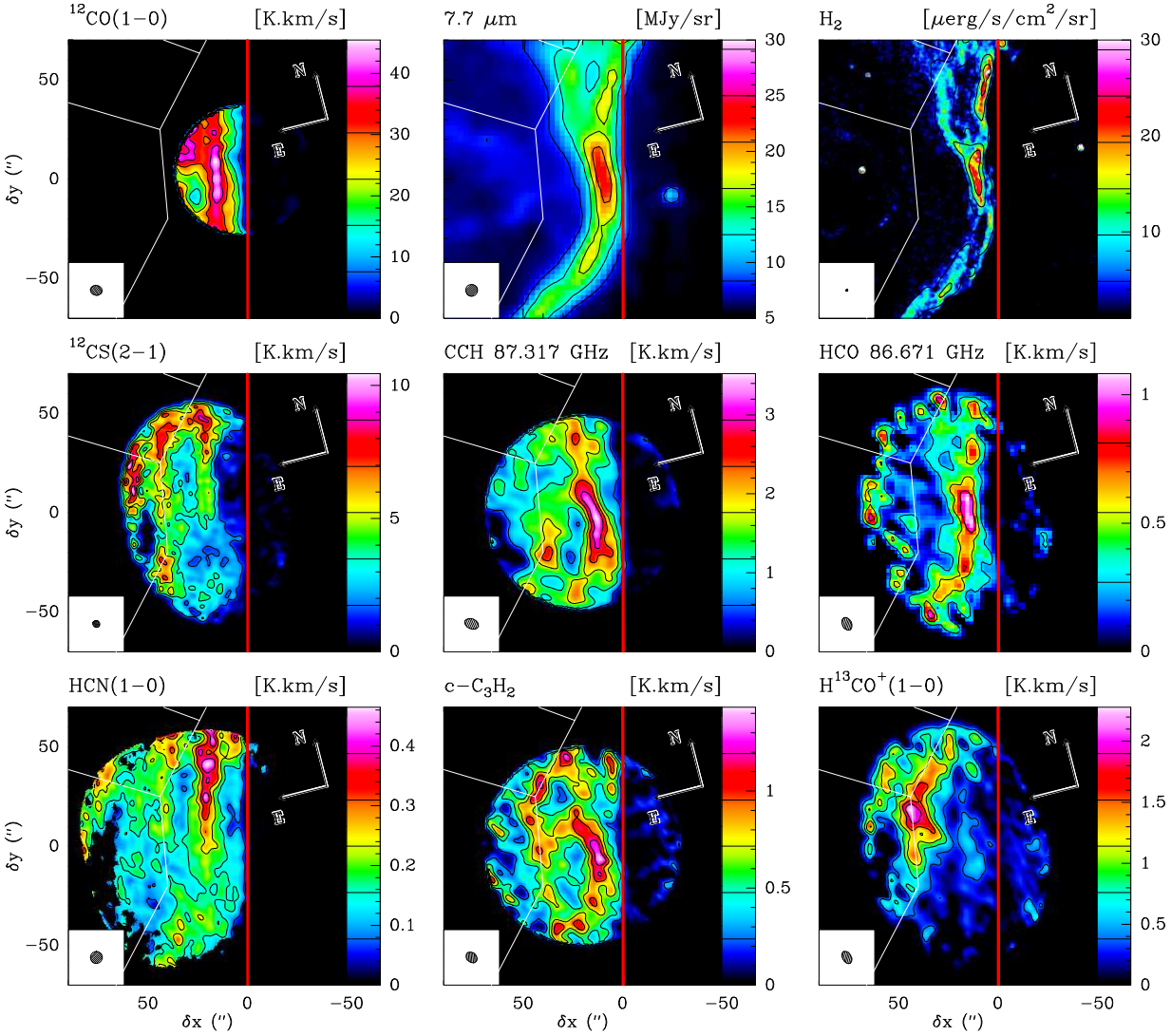

FIG. 5.2 – Même description que la Figure 5.1, mais il s'agit cette fois de zooms en grande partie obtenus à l'aide de l'interféromètre du Plateau de Bure. Le champ de vue couvre $140'' \times 140''$ et les résolutions angulaires sont comprises entre $1''$ et $6''$.

0.02 [A21].

5. Alors que DCO^+ est un bon traceur du cœur moléculaire dense et froid, totalement protégé du rayonnement UV, le radical HCO apparaît comme un excellent traceur des zones denses affectées par le rayonnement [A13]. Ce radical est détecté avec une abondance 100 fois supérieure aux prédictions des modèles. Nous avons proposé une alternative pour rendre compte de cette surabondance. La réaction $\mathrm{O} + \mathrm{CH_2} \rightarrow \mathrm{HCO} + \mathrm{H}$ pourrait reproduire l'abondance mesurée à condition que la constante de vitesse de cette réaction ne s'effondre pas à basse température. HCO pourrait également être synthétisé sur les manteaux des grains et libéré en phase gazeuse par des processus non-thermiques. La confirmation d'une de ces deux hypothèses nécessite des données de laboratoire qui permettraient une évaluation quantitative.
6. La photo-désorption des glaces par le rayonnement UV est nécessaire pour expliquer la grande quantité de H_2CO mesurée la PDR de la Tête de Cheval [A2].
7. Nous avons exploité les mesures des ions moléculaires pour étudier la variation de l'abondance électronique depuis les zones les plus éclairées jusqu'aux zones les plus sombres [A12]. Nous avons étudié en détail l'influence des principales sources d'électron (le taux d'ionisation par les rayons cosmiques et l'abondance des métaux) ainsi que l'influence de la présence de PAH. Cette étude a renforcé notre intérêt pour la chimie du soufre, puisque l'abondance du soufre et son état de charge sont des paramètres déterminants pour le degré d'ionisation dans les zones translucentes (A_v de quelques magnitudes).

Presque tous ces résultats étaient inattendus à l'origine du projet, ce qui illustre l'importance d'avoir de bonnes sources astrophysiques de référence pour contraindre les modèles chimiques.

5.3 Perspectives : des relevés de raies sensibles et non-biaisés

Cet effort a été amplement reconnu. Nous avons encore de nombreuses données à exploiter afin de compléter l'inventaire des molécules simples et de commencer l'étude de molécules plus complexes : 1) des cartes de SO et de H_2S obtenues à l'IRAM-30m pour compléter les données publiées sur CS et HCS^+ ; 2) des cartes des raies de rotation-inversion de NH_3 obtenues avec Effelsberg et le VLA pour contraindre la température du gaz ; et 3) des cartes de CN, HCN et HNC obtenues avec l'IRAM-30m et l'interféromètre du Plateau de Bure[2] pour commencer l'étude de la chimie de l'azote. Nous allons obtenir des cartes de C^+ et de CO de niveau J élevé dans le cadre du temps ouvert 1 avec Herschel/HIFI (c'est une partie d'un programme sur 2 PDRs dont le PI est C. Joblin). En août 2011 et février 2012, nous avons surtout obtenu au 30m le premier relevé de raies non-biaisé à 3 et 1 mm avec les nouveaux spectromètres à transformée de Fourier (cf. section 7). La figure 5.3 montre le relevé à 3 mm. Avec V. Guzman, étudiante chilienne en thèse avec nous sur la chimie en phase solide depuis mars 2010, et P. Gratier, post-doc à l'IRAM depuis janvier 2011, nous avons réalisé grâce à ce relevé la deuxième détection de CF^+, la première détection en millimétrique de CH_3NC, et la première détection d'un nouvel ion réactif. Dans le cadre du projet ANR SCHISM, nous prévoyons de mettre les données publiées à disposition de la communauté pour augmenter l'impact de nos travaux.

[2]Ces données ont fait l'objet du stage de master 2 de J. Montillaud en 2008.

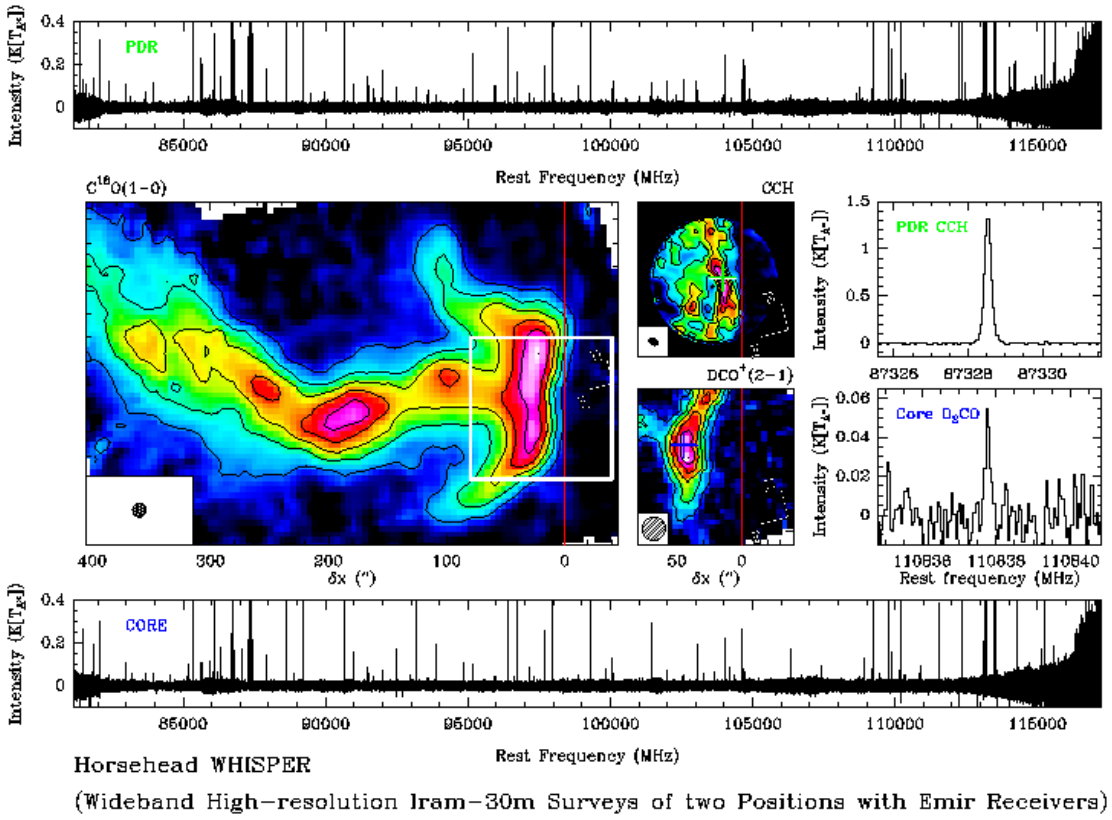

FIG. 5.3 – Les spectres en haut et en bas montrent les relevés de raie dans la bande à 3 mm à une résolution spectrale de 49 kHz pour deux positions dans la nébuleuse de la Tête de Cheval, spectres obtenus en $\sim$ 60 heures à l'IRAM-30m à l'aide des récepteurs EMIR et des nouveaux spectromètres à transformée de Fourier. Chaque spectre a environ 740 000 canaux, c.-à-d. autant d'informations que dans une image de 860×860 pixels ! Le bruit médian est ~ 8 mK $[T_{\rm A}^*]$. Les positions des relevés de raies correspondent aux deux environnements typiques à l'intérieur du carré blanc sur l'image de l'intensité intégrée de $C^{18}O$ (grande image à gauche obtenue avec le multi-pixel IRAM/HERA) : 1) la région de photo-dissociation (PDR) indiquée par une croix verte sur la carte d'émission intégrée de CCH (image zoomée au centre haut obtenue avec l'IRAM/PdBI), et 2) le cœur dense indiqué par une croix bleue sur la carte d'émission intégrée de DCO^+ (image zoomée au centre bas obtenue avec l'IRAM/PdBI). Les spectres au centre à droite montrent comment des raies fortes ou faibles sont résolues.

A&A 435, 885–899 (2005)
DOI: 10.1051/0004-6361:20041170
© ESO 2005

Astronomy & Astrophysics

Are PAHs precursors of small hydrocarbons in photo-dissociation regions? The Horsehead case

J. Pety[1,2], D. Teyssier[3,4], D. Fossé[1], M. Gerin[1], E. Roueff[5], A. Abergel[6], E. Habart[7], and J. Cernicharo[3]

[1] LERMA, UMR 8112, CNRS, Observatoire de Paris and Ecole Normale Supérieure, 24 rue Lhomond, 75231 Paris Cedex 05, France
e-mail: [fosse;gerin]@lra.ens.fr
[2] IRAM, 300 rue de la Piscine, 38406 Grenoble Cedex, France
e-mail: pety@iram.fr
[3] Instituto de Estructura de la Materia, CSIC, Serrano 121, 28006 Madrid, Spain
e-mail: [cerni;teyssier]@damir.iem.csic.es
[4] Space Research Organization Netherlands, PO Box 800, 9700 AV Groningen, The Netherlands
[5] LUTH UMR 8102, CNRS and Observatoire de Paris, Place J. Janssen 92195 Meudon Cedex, France
e-mail: evelyne.roueff@obspm.fr
[6] IAS, Université Paris-Sud, Bât. 121, 91405 Orsay Cedex, France
e-mail: abergel@ias.u-psud.fr
[7] Osservatorio Astrofisico di Arcetri, L.go E. Fermi 5, 50125 Firenze, Italy
e-mail: habart@arcetri.astro.it

Received 27 April 2004 / Accepted 11 January 2005

Abstract. We present maps at high spatial and spectral resolution in emission lines of CCH, c-C_3H_2, C_4H, ^{12}CO and $C^{18}O$ of the edge of the Horsehead nebula obtained with the IRAM Plateau de Bure Interferometer (PdBI). The edge of the Horsehead nebula is a one-dimensional Photo-Dissociation Region (PDR) viewed almost edge-on. All hydrocarbons are detected at high signal-to-noise ratio in the PDR where intense emission is seen both in the H_2 ro-vibrational lines and in the PAH mid-infrared bands. $C^{18}O$ peaks farther away from the cloud edge. Our observations demonstrate that CCH, c-C_3H_2 and C_4H are present in UV-irradiated molecular gas, with abundances nearly as high as in dense, well-shielded molecular cores.
PDR models i) need a large density gradient at the PDR edge to correctly reproduce the offset between the hydrocarbons and H_2 peaks; and ii) fail to reproduce the hydrocarbon abundances. We propose that a new formation path of carbon chains, in addition to gas phase chemistry, should be considered in PDRs: because of intense UV-irradiation, large aromatic molecules and small carbon grains may fragment and feed the interstellar medium with small carbon clusters and molecules in significant amounts.

Key words. ISM: clouds – ISM: molecules – ISM: individual object: Horsehead nebula – radio lines: ISM

1. Introduction

Due to the ISO mission, the knowledge of interstellar dust has significantly progressed in the recent years. With its instruments sensitive in the mid-infrared, ISO revealed the spatial distribution and line profile of the Aromatic Infrared Bands (AIBs at 3.3, 6.2, 7.7, 8.6 and 11.3 μm features), which have shed light on the emission mechanism and their possible carriers (Boulanger et al. 2000; Rapacioli et al. 2005). However, no definite identification of individual species has been possible yet because the bands are not specific for individual molecules. The most likely carriers are large polycyclic aromatic hydrocarbons (PAHs) with about 50 carbon atoms (Allain et al. 1996b; Le Page et al. 2003). The ubiquity of the aromatic band emission in the interstellar medium has triggered a wealth of theoretical and laboratory work in the past two decades, which has led to a revision of astrophysical models. PAHs are now suspected to play a major role in both interstellar medium physics and chemistry. With their small size, they are the most efficient particles for the photo-electric effect (Bakes & Tielens 1994; Weingartner & Draine 2001; Habart et al. 2001). Their presence also affects the ionization balance (Flower & Pineau des Forêts 2003; Wolfire et al. 2003), and possibly the formation of H_2 (Habart et al. 2004). The role of PAHs in the neutralization of atomic ions in the diffuse interstellar medium has been recently reconsidered by Liszt (2003), following previous work by Lepp et al. (1988). As emphasized soon after their discovery (Omont 1986; Lepp & Dalgarno 1988), PAHs

Article published by EDP Sciences and available at http://www.edpsciences.org/aa or http://dx.doi.org/10.1051/0004-6361:20041170

also play a role in gas chemistry: some laboratory experiments and theoretical calculations suggest that PAHs may fragment into small carbon clusters and molecules under photon impact (C_2, C_3, C_2H_2, etc.) (Joblin 2003; Le Page et al. 2003; Allain et al. 1996b,a; Leger et al. 1989; Scott et al. 1997). In addition, investigation of the lifetimes of interstellar PAHs implies that photo-dissociation may be the main limiting process for their life in the interstellar medium (Verstraete et al. 2001).

It is therefore appropriate to wonder whether PAHs could fragment continuously and feed the interstellar medium with small hydrocarbons and carbon clusters. This hypothesis is attractive for the following reasons:

i) Cyclopropenylidene (c-C_3H_2) is widely distributed in the interstellar medium (Matthews & Irvine 1985; Matthews et al. 1986; Cox et al. 1988; Lucas & Liszt 2000).
ii) Recent works have shown that the diffuse interstellar medium is more chemically active than previously thought with molecules as large as C_3 (Goicoechea et al. 2004; Oka et al. 2003; Ádámkovics et al. 2003; Roueff et al. 2002; Maier et al. 2001) and c-C_3H_2 (Lucas & Liszt 2000) widely distributed. The abundances of C_3 and c-C_3H_2 are tightly connected to those of smaller molecules, C_2 and CCH respectively, with abundance ratios of $[C_2]/[C_3] \sim 10-40$ (Oka et al. 2003) and $[CCH]/[c\text{-}C_3H_2] \sim 27.7 \pm 8$ (Lucas & Liszt 2000).
iii) Thorburn et al. (2003) have found a correlation between the abundance of C_2 and the strength of some (weak) Diffuse Interstellar Bands (DIBs).

As PAHs are present in the diffuse interstellar medium, could they contribute to form both the small carbon clusters (C_2, C_3) and larger hydrocarbon molecules which could be the DIB carriers?

Unfortunately, studies of the PAH emission bands in the diffuse interstellar clouds where the carbon clusters have been detected is extremely difficult because of the low column densities, and also because the bright background stars used for visible spectroscopy prohibit the use of sensitive IR cameras which would be saturated. Photo-Dissociation regions (PDRs) are the first interstellar sources in which AIBs have been found and for which the PAH hypothesis has been proposed (Sellgren 1984; Leger & Puget 1984). It is therefore interesting to investigate the carbon chemistry in these sources. Fossé et al. (2000) and Teyssier et al. (2004) have discussed medium spatial resolution (30″) observations of various hydrocarbons in nearby PDRs. They show that CCH, c-C_3H_2 and C_4H are ubiquitous in these regions, with abundances almost as high as in dark, well shielded clouds, despite the strong UV radiation. Fuente et al. (2003) also report high abundances of c-C_3H_2 in NGC 7023 and the Orion Bar. Heavier molecules may be present in PDRs as Teyssier et al. (2004) report a tentative detection of C_6H in the Horsehead nebula. PDRs and diffuse clouds therefore seem to share the same carbon chemistry, but because of their larger H_2 column density and gas density, PDRs offer more opportunities to detect rare species.

Teyssier et al. (2004) and Fuente et al. (2003) propose that the presence of carbon chains is in favor of a causal link between small hydrocarbons and PAHs, but they lack the spatial resolution to draw firm conclusions. In the present work, we present high spatial resolution observations of one source studied by Teyssier et al. (2004), the Horsehead nebula, obtained with the Plateau de Bure interferometer. We describe the observations in Sect. 2. We show the interferometer maps in Sect. 3. Section 4 presents a comparison with chemical models.

2. Observations and data reduction

2.1. The Horsehead nebula

The Horsehead nebula, also called Barnard 33, appears as a dark patch of ∼5′ extent against the bright HII region IC 434. Emission from the gas and dust associated with this globule has been detected from mid-IR to millimeter wavelengths (Abergel et al. 2002, 2003; Teyssier et al. 2004; Pound et al. 2003). From the analysis of the ISOCAM images, Abergel et al. (2003) conclude that the Horsehead nebula is a PDR viewed edge-on and illuminated by the O9.5V star σOri at a projected distance of 0.5° (3.5 pc for a distance of 400 pc, Anthony-Twarog 1982). The far-UV intensity of the incident radiation field is $G_0 = 60$ relative to the average interstellar radiation field in Draine units (Draine 1978). The gas density, derived from the excitation of molecular lines and from the penetration depth of the UV-radiation, is a few $10^4\,\mathrm{cm}^{-3}$ (Abergel et al. 2003). From a combined analysis of maps of both CO and atomic carbon, Lis & Guesten (2005) obtain similar figures for the gas density. Habart et al. (2004, 2005) have modeled the emission of H_2 (from narrow band images of the H_2 ro-vibrational line), PAHs and CO, and conclude that i) the gas density follows a steep gradient at the cloud edge, rising to $n_H = 10^5\,\mathrm{cm}^{-3}$ in less than 10″ (i.e. 0.02 pc); and ii) this density gradient model is essentially a constant pressure model (with $P = 4 \times 10^6\,\mathrm{K\,km\,s}^{-1}$).

The edge of the Horsehead nebula is particularly well delineated by the mid-IR emission due to PAHs, with a bright 7.7 μm-peak (hereafter named the "IR peak") reaching 25 MJy/sr at $\alpha_{2000} = 05^h40^m53.70^s, \delta_{2000} = -02°28'04''$. Figure 1 shows the region observed with the IRAM PdBI centered near the "IR peak". Two mosaics (one for hydrocarbon lines and the other for the CO lines) have been observed. Their set-ups are detailed in Table 1.

2.2. Observations

2.2.1. c-C_3H_2 and C_4H

First PdBI observations dedicated to this project were carried out with 6 antennae in the CD configuration (baseline lengths from 24 to 229 m) during March-April 2002. The 580 MHz instantaneous IF-bandwidth allowed us to simultaneously observe c-C_3H_2 and C_4H at 3 mm using 3 different 20 MHz-wide correlator windows. One other window was centered on the $C^{18}O$ ($J = 2-1$) frequency. The full IF bandwidth was also covered by continuum windows both at 3.4 and 1.4 mm. c-C_3H_2 and C_4H were detected but the weather quality precluded use of 1.4 mm data.

We observed a seven-field mosaic in a compact hexagonal pattern with full Nyquist sampling at 1.4 mm and

Article published by EDP Sciences and available at http://www.edpsciences.org/aa or http://dx.doi.org/10.1051/0004-6361:20041170

Table 1. Observation parameters.

	Phase center		Number of fields
Mosaic 1	$\alpha_{2000} = 05^h40^m54.27^s$	$\delta_{2000} = -02°28'00''$	7
Mosaic 2	$\alpha_{2000} = 05^h40^m53.00^s$	$\delta_{2000} = -02°28'00''$	4

Molecule and Line	Frequency	Beam	PA	Noise[a]	Obs. date
	GHz	arcsec	°	K km s^{-1}	
Mosaic 1					
c-C_3H_2 $2_{1,2}-1_{0,1}$	85.339	6.13×4.75	36	3.1×10^{-2}	Mar. 2002 and Apr. 2002
C_4H-1 $N = 9-8$, $J = 19/2-17/2$	85.634	6.11×4.74	36	2.6×10^{-2}	Mar. 2002 and Apr. 2002
C_4H-2 $N = 9-8$, $J = 17/2-15/2$	85.672	6.11×4.74	36	3.4×10^{-2}	Mar. 2002 and Apr. 2002
CCH-1 $N = 1-0$, $J = 3/2-1/2$ $F = 2-1$	87.316	7.24×4.99	54	3.4×10^{-2}	Dec. 2002 and Mar. 2003
CCH-2 $N = 1-0$, $J = 3/2-1/2$ $F = 1-0$	87.328	7.24×4.99	54	2.5×10^{-2}	Dec. 2002 and Mar. 2003
CCH-3 $N = 1-0$, $J = 1/2-1/2$ $F = 1-1$	87.402	7.24×4.99	54	3.4×10^{-2}	Dec. 2002 and Mar. 2003
CCH-4 $N = 1-0$, $J = 1/2-1/2$ $F = 0-1$	87.407	7.24×4.99	54	2.3×10^{-2}	Dec. 2002 and Mar. 2003
$C^{18}O$ $J = 2-1$	219.560	6.54×4.31	65	9.8×10^{-2}	Mar. 2003
Mosaic 2					
^{12}CO $J = 1-0$	115.271	5.95×5.00	65	1.2×10^{-1}	Nov. 1999
^{12}CO $J = 2-1$	230.538	2.97×2.47	66	1.7×10^{-1}	Nov. 1999

[a] The noise values quoted here are the noises at the mosaic center (Mosaic noise is inhomogeneous due to primary beam correction; it steeply increases at the mosaic edges). Those noise values have been computed in 1 km s^{-1} velocity bin.

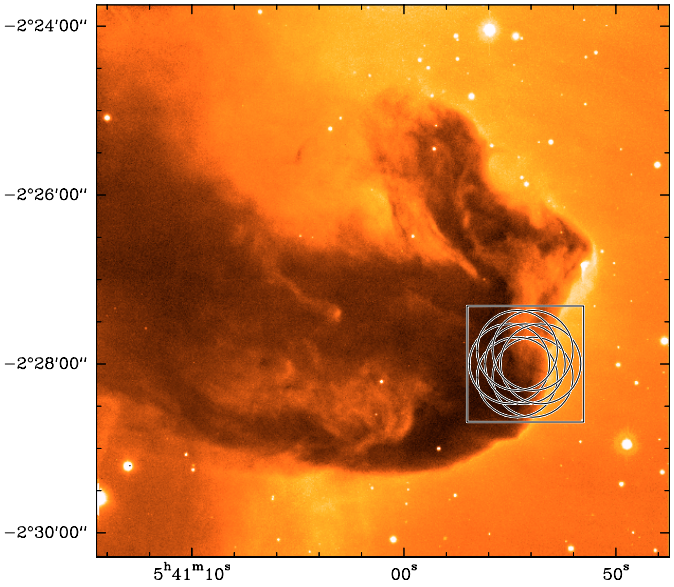

Fig. 1. The field of view covered when mapping small hydrocarbons at 3.4 mm with the Plateau de Bure Interferometer (PdBI) is shown as a square over this ESO–VLT composite image (B, V and R bands) of the Horsehead nebula. Each circle indicates the 3.4 mm primary beam of the PdBI at one of the 7 observed positions. Those positions are largely oversampled at the hydrocarbon wavelength (3.4 mm) to ensure simultaneous Nyquist-sampling at 1.4 mm used to observe $C^{18}O$. A linear combination of the 7 pointed observation is done to obtain the final dirty image.

large oversampling at 3.4 mm. This mosaic, centered on the IR peak, was observed for about 6h of on-source observing time per configuration. The rms phase noises were between 15 and 40° at 3.4 mm, which introduced position errors <0.5″. Typical 3.4 mm resolution was 6″.

2.2.2. CCH and $C^{18}O$

As a follow-up, we carried out observations of CCH at PdBI with 6 antennae in CD configuration during December 2002 and March 2003. We used a similar correlator setup: three 20 MHz-wide windows were centered so as to get the four 3.4 mm hyperfine components of CCH; one 20 MHz-wide window was centered on the $C^{18}O$ ($J = 2-1$) frequency; the remaining windows were used to observe continuum at 3.4 and 1.4 mm.

Exactly the same mosaic (center and field-pattern) and approximately the same on-source observing time per configuration (~6 h) as before were used. The rms phase noises were between 10 and 40° except during 4 h in D configuration where they were between 8 and 20° at 3.4 mm. The data of those 4 h have been used to build the $C^{18}O$ map as the 1 mm phase noises were then low enough (between 20 to 45°). We thus ended up with a 6″ typical resolution both at 3.4 mm and 1.4 mm. Both CCH and $C^{18}O$ were easily mapped while no continuum was detected at a level of 2 mJy/beam in a 6″-beam.

2.2.3. ^{12}CO

As part of another project (A. Abergel, private communication), the ^{12}CO ($J = 1-0$) and ^{12}CO ($J = 2-1$) lines were simultaneously observed during 6h on-source at PdBI in November 1999 (only 5 antennae were then available) in

Article published by EDP Sciences and available at http://www.edpsciences.org/aa or http://dx.doi.org/10.1051/0004-6361:20041170

Table 2. Calibrator fluxes in Jy.

	B0420−014		B0607−157		B0528+134	
	3 mm	1 mm	3 mm	1 mm	3 mm	1 mm
27.11.1999					3.5	1.4
30.03.2002	4.8		2.3			
16.04.2002	4.8		2.5			
22.04.2002	4.8		2.4			
23.12.2002	12.5		2.6			
18.03.2003	12.0	7.8	2.1	0.87		
26.03.2003	12.8		2.1			

configuration C (baseline lengths from 24 to 82 m). The observation consisted of a 4-field mosaic, fully sampled at 1.3 mm. The mosaic center is slightly shifted compared to the two other observations. The weather was excellent with phase noise from 3 to 5° and 6 to 10° at 2.6 mm and 1.3 mm, respectively. Typical resolutions were 5″ at 2.6 mm and 2.5″ at 1.3 mm.

2.2.4. Other data: H_2, ISO-LW2 and 1.2 mm dust continuum

The H_2 $v = 1{-}0$ S(1) map shown here is a small part of Horsehead observations obtained at the NTT using SOFI. The resolution is ∼1″. Extensive explanations of the data reduction and analysis are discussed elsewhere (Habart et al. 2004, 2005). The ISO-LW2 map (published by Abergel et al. 2003) shows aromatic features at 7.7 μm with a resolution of ∼6″. The 1.2 mm dust continuum was obtained at the IRAM-30 m telescope with a resolution of ∼11″ and has already been presented by Teyssier et al. (2004).

2.3. PdBI data processing

All data reduction was done with the GILDAS[1] softwares supported at IRAM. Standard calibration methods using close calibrators were applied to all the PdBI data. The calibrator fluxes used for the absolute flux calibration are summarized in Table 2.

Following Gueth et al. (1996), single-dish, fully sampled maps obtained with the IRAM-30 m telescope (Teyssier et al. 2004; Abergel et al. 2003) were used to produce the short-spacing visibilities filtered out by each mm-interferometer (e.g. spatial frequencies between 0 and 15 m for PdBI). Those pseudo-visibilities were merged with the observed, interferometric ones. Each mosaic field were then imaged and a dirty mosaic was built combining those fields in the following optimal way in terms of signal-to-noise ratio (Gueth 2001):

$$J(\alpha,\delta) = \sum_i \frac{B_i(\alpha,\delta)}{\sigma_i^2} F_i(\alpha,\delta) \Big/ \sum_i \frac{B_i(\alpha,\delta)^2}{\sigma_i^2}.$$

In this equation, $J(\alpha,\delta)$ is the brightness distribution in the dirty mosaic image, B_i are the response functions of the primary antenna beams, F_i are the brightness distributions of the individual dirty maps, and σ_i are the corresponding noise values. As may be seen in this equation, the dirty intensity distribution is corrected for primary beam attenuation. This implies that noise is inhomogeneous. In particular, noise strongly increases near the edges of the field of view. To limit this effect, both the primary beams used in the above formula and the resulting dirty mosaics are truncated. The standard level of truncation is set at 20% of the maximum in GILDAS. In our case, the intensity distribution does not drop to zero at all field edges. Hence, we used a much lower level of truncation of the beam (i.e. 5%) to ensure a better deconvolution of the side lobes of the sources sitting just at the field edges. We then use the standard adaptation to mosaics of the Högbom CLEAN algorithm to deconvolve (Gueth 2001). The sharp edge of the H_2 emission defines a boundary that may be used as a priori knowledge in the deconvolution of the PdBI images: we use this boundary as a numerical support (in the language of signal processing) to exclude the search for CLEAN components outside the PDR front (i.e. in the direction of the exciting star). We finally truncated the noisy clean mosaic edges using the standard truncation level. The C_4H maps are particularly difficult to deconvolve due to their low signal-to-noise ratio, $S/N < 10$ to 15.

[1] See http://www.iram.fr/IRAMFR/GILDAS for more information about the GILDAS softwares.

3. Results

3.1. Maps

The PdBI maps are shown in Figs. 2 and 3 together with the 7 μm ISOCAM image (Abergel et al. 2003), the 1.2 mm dust emission map (Teyssier et al. 2004) and the map of the H_2 2.1 μm line emission (Habart et al. 2004, 2005) for comparison. For all lines, we obtained excellent spatial resolutions, similar to or even better than the ISOCAM pixel size of 6″ (see Table 1). Figure 2 shows the maps in the natural Equatorial coordinate system while Fig. 3 shows the maps in a coordinate system where the x-axis is in the direction of the exciting star and the y-axis defines an empirical PDR edge that corresponds to the sharp boundary of the H_2 emission (i.e. the maps have been rotated by 14° counter-clockwise and horizontally shifted by 20″). The latter presentation enables a much better comparison of the PDR stratification.

The main structure in all hydrocarbon maps is an approximatively N-S filament, following nicely the cloud edge and corresponding closely to the mid-IR filament on the ISO-LW2 image. A weaker and more extended emission is also detected, which has no counterpart in the ISO-LW2 image and can be attributed to the bulk of the cloud. It is interesting to note that the hydrocarbon emission presents a minimum behind the main filament, and a weaker secondary maximum within the extended emission. The hydrocarbon emission is stronger on the edges of the dust 1.2 mm emission and avoids the region of maximum dust emission where the gas is likely denser. This confirms a tendency revealed by chemical surveys of dense cores (study of TMC-1 by Pratap et al. 1997 and L134N by Dickens et al. 2000; Fossé 2003): i.e. carbon chains (CCH, C_4H,...) generally avoid the densest and more depleted cores.

Article published by EDP Sciences and available at http://www.edpsciences.org/aa or http://dx.doi.org/10.1051/0004-6361:20041170

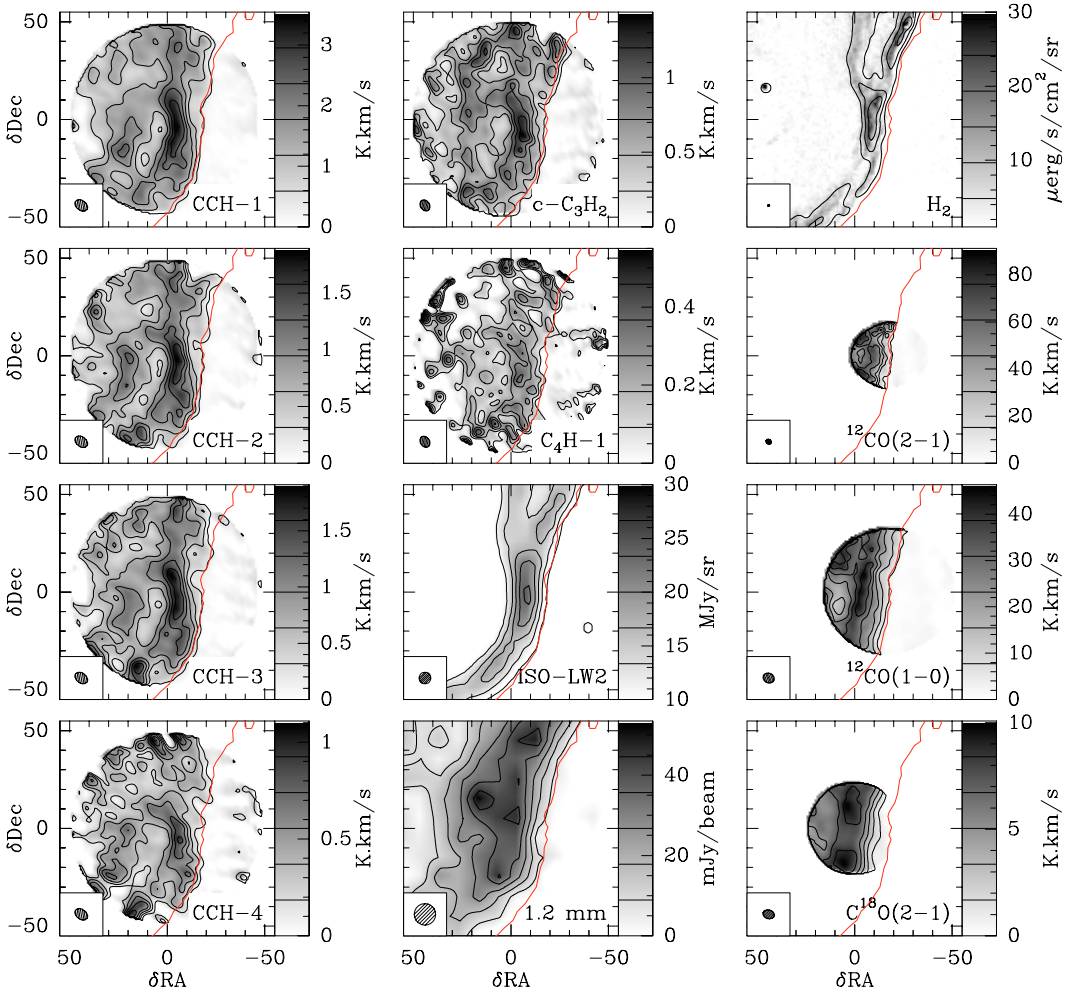

Fig. 2. Integrated emission maps obtained with the Plateau de Bure Interferometer. Maps of i) the H_2 $v = 1{-}0$ S(1) emission (Habart et al. 2004, 2005); ii) the mid-IR emission (Abergel et al. 2003, labeled ISO-LW2); and iii) the 1.2 mm dust continuum (Teyssier et al. 2004, labeled 1.2mm) are also shown for comparison. The center of all maps has been set to the mosaic 1 phase center: RA(2000) = 05h40m54.27s, Dec(2000) = −02°28′00″. The map size is 110″ × 110″, with ticks drawn every 10″. Either the synthesized beam or the single dish beam is plotted in the bottom left corner. The emission of all the lines observed at PdBI is integrated between 10.1 and 11.1 km s^{-1}. Values of contour level are shown on each image wedge (contours of the H_2 image have been computed on an image smoothed to 5″ resolution). The sharp edge of the H_2 emission (*upper right panel*) defines a boundary, which is used as a numerical support (in the language of signal processing) for deconvolution of the other images. This deconvolution support is overplotted in red on each panel.

Even at the high spatial resolution provided by the plateau de Bure Interferometer, the maps of all hydrocarbons remain very similar. Detailed inspection of the maps shows small differences between CCH and c-C_3H_2, but these do not affect the overall similarity. Indeed, the joint histogram describing the correlation of line maps for i) the two most intense CCH lines; ii) c-C_3H_2 and CCH; and iii) C_4H and CCH are displayed in Fig. 4. As expected the two CCH lines are extremely well correlated as illustrated by the elongated shape (approaching a straight line) of the joint histogram. The correlations between c-C_3H_2 and CCH, and between C_4H and CCH are excellent too, although the signal-to-noise ratio is not as good for C_4H. For this plot, we have used all points lying inside the support used for the deconvolution.

The high resolution c-C_3H_2 map appears to show more structure than the CCH maps, particularly in the well-shielded cloud interior (on the left hand side of the main filament). This effect seems real since it does not appear for the satellite CCH line maps, which have similar intensities and signal-to-noise ratio as the c-C_3H_2 map. The C_4H maps are too noisy for a detailed analysis but are nevertheless very well correlated with the CCH map. *The correlations found at low spatial resolution (Teyssier et al. 2004) are not an artifact but persist at high spatial resolution.*

The correspondence of hydrocarbons with CO and $C^{18}O$ is not as good. The $C^{18}O$ ($J = 2{-}1$) map presents two maxima, located on either side of the CCH peak along the N-S direction: the CCH peak is associated with a local minimum of $C^{18}O$ emission. Also, the $C^{18}O$ emission peak is displaced farther inside the cloud (East) compared to CCH and the other hydrocarbons.

To illustrate further the differences in the spatial distribution of CO, $C^{18}O$ and the hydrocarbons, we show two series of cuts across the PDR in Fig. 5. The UV radiation comes from

Article published by EDP Sciences and available at http://www.edpsciences.org/aa or http://dx.doi.org/10.1051/0004-6361:20041170

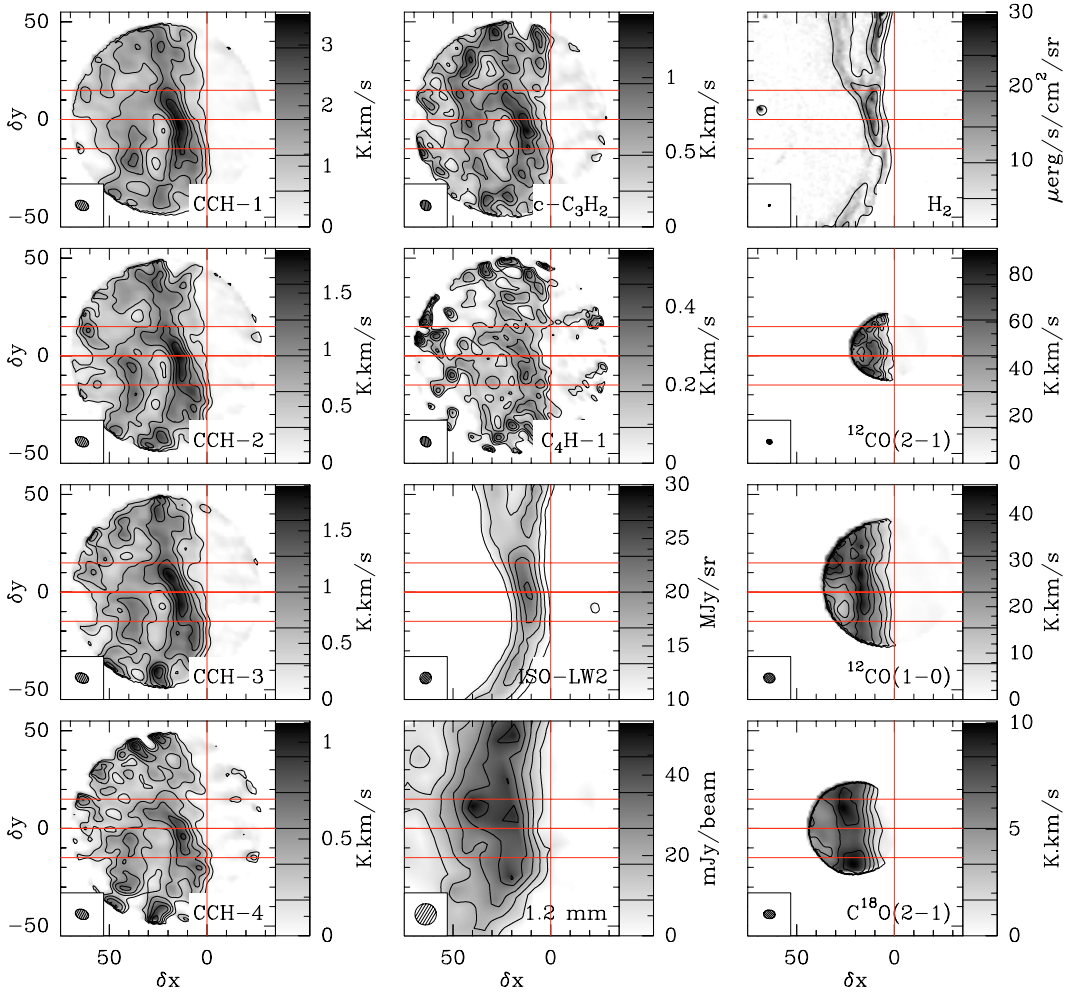

Fig. 3. Same as Fig. 2 except that maps have been rotated by 14° counter-clockwise around the image center to bring the exciting star direction in the horizontal direction as this eases the comparison of the PDR tracer stratifications. Maps have also been horizontally shifted by 20″ to set the horizontal zero at the PDR edge delineated as the vertical red line. Horizontal red lines delimit the two lanes that have been vertically averaged to produce the two series of cuts shown in Fig. 5.

σ Ori far to the right side of Fig. 3. The cuts have been taken along the σ Ori direction (i.e. PA = −104°). The main peak for all hydrocarbons is located near an offset of $\delta x \simeq 12-15''$ at less than 5″ of the H_2 peak. The ISO-LW2 peak is located halfway between hydrocarbons and H_2 peaks. Intense ^{12}CO emission in both the $J = 1-0$ and $J = 2-1$ lines is also detected in the same region, while the C^{18}O ($J = 2-1$) emission arises farther (at least 5″) inside the cloud.

As shown in Fig. 6, the ^{12}CO ($J = 2-1$) emission (convolved at the same angular resolution as the ^{12}CO $J = 1-0$ transition) is very bright (≥50 K at 10.6 km s^{-1}, the line peak velocity) and more intense than ^{12}CO ($J = 1-0$) in the most external layers of the PDRs, directly facing σOri. The line intensity ratio $T_b(1-0)/T_b(2-1)$ rises from ∼0.3 to ∼0.8 from West to East. Combined with the high brightness temperature detected for both lines, the higher brightness temperature of the ^{12}CO(2−1) line is a clear sign of the presence of warm and dense gas. We have estimated the kinetic temperature using an LVG model. We assumed that the emission is resolved and fills the beam. We explored the kinetic temperature dependence upon the density by solving for 5 different proton densities going from 1.6×10^4 cm^{-3} to 10^5 cm^{-3}. Under these hypotheses, the ^{12}CO line intensity ratio and brightness temperature constrain the kinetic temperature to increase from 60 K in the inner PDR (15″ = 0.03 pc from the PDR edge) to more than 100 K in the outer layers for proton densities larger than 4×10^4 cm^{-3}. For lower proton densities, the kinetic temperature still starts from 60 K in the inner PDR but increases much more stiffly. The kinetic temperature derived from single dish observations (Abergel et al. 2003) is lower, in the 30−40 K range and corresponds to the bulk of the cloud, rather than to the warm UV-illuminated edge.

3.2. Abundances

We have computed the CO and hydrocarbon column densities at three representative positions in the maps: the "IR peak" where the PAH and hydrocarbon emission is the largest, the "IR edge" 10″ West which represents the region with the most intense UV-radiation and a "Cloud" position behind the IR filament. Table 3 lists the derived column densities and abundances relative to the total number of protons for these

Article published by EDP Sciences and available at http://www.edpsciences.org/aa or http://dx.doi.org/10.1051/0004-6361:20041170

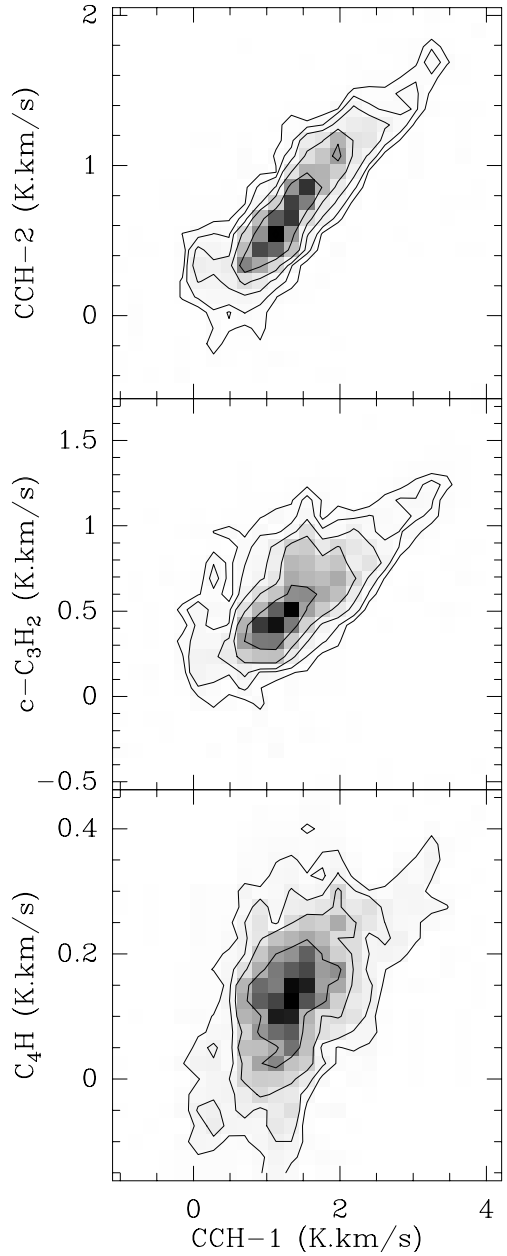

Fig. 4. Joint histogram of the integrated emission of i) the second brightest CCH line (*top*); ii) c-C_3H_2 (*middle*); and iii) one C_4H line (*bottom*) vs. the main CCH line. The value at a given position of this joint histogram is the percentage of pixels of the input images whose intensities lies in the respective vertical and horizontal bins. Only image pixels lying inside the deconvolution support (shown in Fig. 2) have been used in the histogram computation. Contour levels are set to 0.125, 0.25, 0.5, 1, 2, 4 and 8% of points per pixel.

3 positions. We have used a LVG model with different uniform total hydrogen density[2] (from 10^4 cm^{-3} to 10^5 cm^{-3}) and a kinetic temperature of 40 K for the "cloud" position, and between 60 and 100 K for the IR positions. The variance of the column densities therefore reflects both the systematic effect due to the imperfect knowledge of the physical conditions, and the random noise of the data. In most cases, the former contribution is the largest. The H_2 column densities are derived from the dust 1.2 mm emission assuming the same dust properties for all positions but a dust temperature range of 20 to 40 K for the "Cloud" position and 40 to 80 K for the IR positions.

The LVG solution implies a typical ^{12}CO column density of 2×10^{17} cm^{-2}. This is inconsistent with the derived column density of C^{18}O and the local ISM ^{16}O/^{18}O element ratio (560, Wilson & Rood 1994). Figure 7 shows clear indications of self-absorption of the ^{12}CO spectra (asymmetries and dips in the top of the line profiles) while the C^{18}O spectra are Gaussian. The same behaviour is seen in the single dish data discussed by Abergel et al. (2003) (cf. their Fig. 5). This explains why the LVG solution does not succeed in correctly inferring the ^{12}CO column density. Conversely, the C^{18}O abundance relative to H is fairly constant for all positions at [C^{18}O] = 1.0×10^{-7}. Assuming a local ISM ^{16}O/^{18}O element ratio, this corresponds to a CO abundance relative to the total number of hydrogen atoms of [CO] = 5.6×10^{-5}, in rather good agreement with the gas phase abundance of carbon derived from CO in warm molecular clouds, and to the carbon abundance in diffuse clouds (Lacy et al. 1994; Sofia & Meyer 2001). In addition, using IRAM-30 m spectra of ^{13}CO and C^{18}O published by Abergel et al. (2003), we found [^{13}CO]/[C^{18}O] $\sim$ 7. This good agreement with the local ISM isotopic ratio make us confident that we can use our LVG analysis on the PdBI C^{18}O spectra to estimate the CO density. According to Lis & Guesten (2005), atomic carbon is less abundant than CO in the PDR. The peak column density of neutral carbon, observed with a 15″ beam, is $\sim 1.6 \times 10^{17}$ cm^{-2} corresponding to a carbon abundance of [C] = 5×10^{-6}. Even if we take into account the difference in linear resolution, we do not expect an increase of the column density larger than a factor of two based on the comparison of the low resolution single dish data with the interferometer maps of other tracers. Finally, although the H_2 column densities are fairly similar at the "IR peak" and "cloud" positions, the abundances of hydrocarbons are larger by a factor of at least 5.0 at the "IR peak". The abundances seem to be even larger at the "IR edge" than at the cloud position.

4. Discussion

4.1. Comparison with models

We have used a monodimensional PDR code (Le Petit et al. 2002, `http://aristote.obspm.fr/MIS/`) to model the observations of the Horsehead nebula. The slab geometry is locally appropriate as seen in Fig. 3. We did not take into account projection effects as the source is viewed almost edge-on. Indeed, Habart et al. (2005) show that the main effect of the PDR possible small inclination (<6°) is to enlarge the peak profiles and to shift them all compared to the model edge. The model includes a detailed treatment of the photo-dissociation of H_2 and the CO isotopes as well as the statistical equilibrium of their rovibrational (rotational, respectively) states in a steady state approach. The parameters of the model include the element abundances, the cosmic ray ionization rate, the scaling factor of the interstellar ultraviolet radiation field (ISRF) measured in Draine units, the density profile and the grain

[2] "Total hydrogen density" is an abbreviation of the total density of hydrogen in all forms.

Article published by EDP Sciences and available at http://www.edpsciences.org/aa or http://dx.doi.org/10.1051/0004-6361:20041170

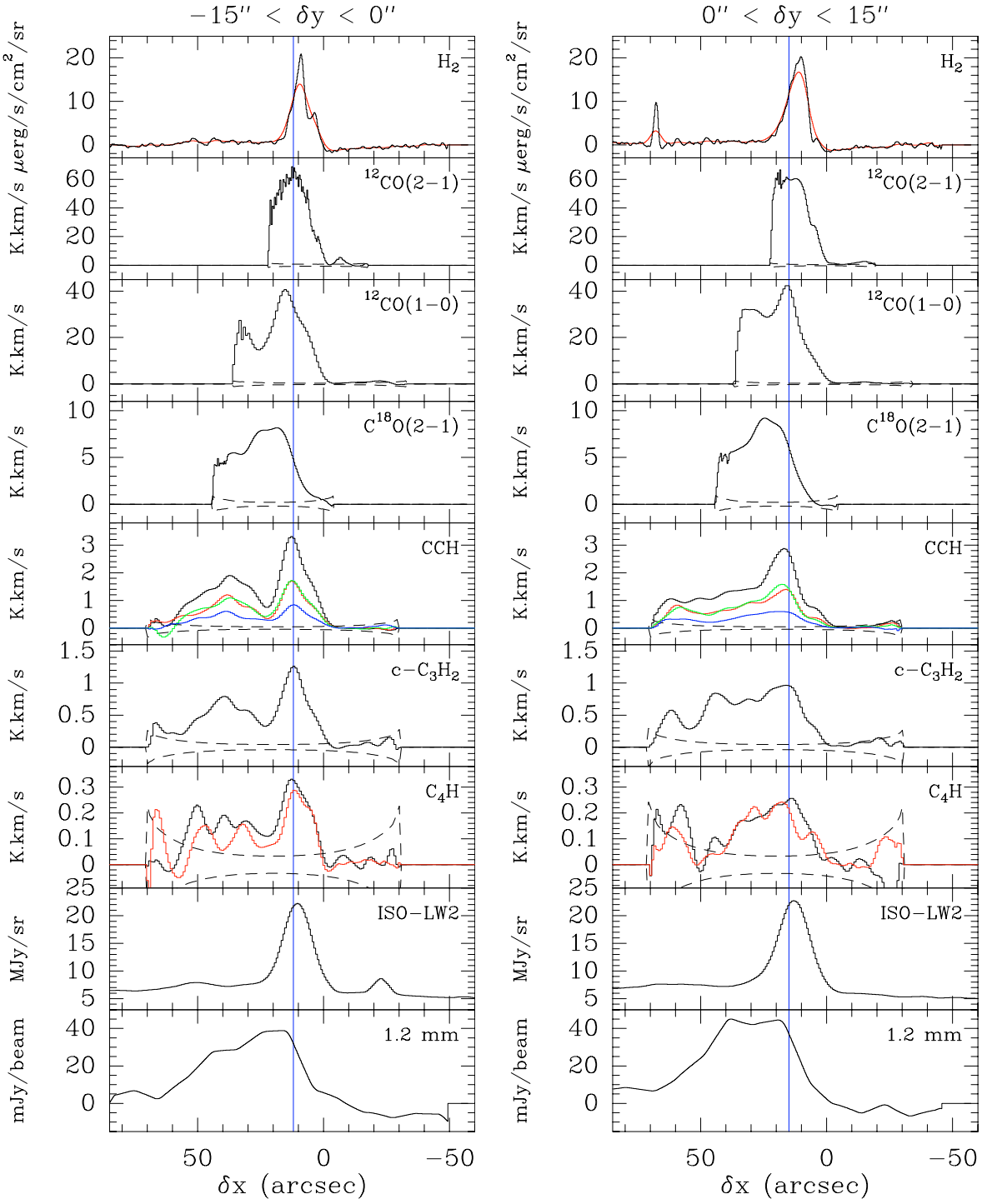

Fig. 5. Emission profiles along the exciting star direction (PA = −104° in the equatorial coordinate system). To improve the signal-to-noise ratio, those emission profiles have been integrated along the perpendicular direction between $-15'' < \delta y < 0''$ (*left column*) and $0'' < \delta y < +15''$ (*right column*). The comparison of those two series of mean cuts gives an idea of the influence of the local conditions (either excitation effects or chemical differentiation). We show from top to bottom, H_2 $v = 1{-}0$ S(1) (full resolution in black, smoothed at a 5″-resolution in red), ^{12}CO $J = 2{-}1$, ^{12}CO $J = 1{-}0$, $C^{18}O$ $J = 2{-}1$, CCH lines (1 black, 2 green, 3 red and 4 blue, respectively following the ratios 1:0.5:0.5:0.25), c-C_3H_2, C_4H lines (1 black, 2 red), ISO-LW2 and the 1.2 mm dust continuum. For the PdBI data, the 3-σ noise level is indicated by the dashed lines. It rises at the cut edges due to the primary beam correction. Note that the fields of view of the ^{12}CO and $C^{18}O$ data are smaller than the field of view of the hydrocarbon data because of the smaller mosaic size and/or the higher frequency. The blue vertical lines are guidelines to localize the hydrocarbon peaks. They have been drawn at $\delta x = +12''$ (*left column*) and $\delta x = +15''$ (*right column*). Note that the bumps at $\delta x = -20''$ in the ISO-LW2 cut (*left column*) and at $\delta x = 70''$ in the H_2 cut (*right column*) are due to field stars.

Article published by EDP Sciences and available at http://www.edpsciences.org/aa or http://dx.doi.org/10.1051/0004-6361:20041170

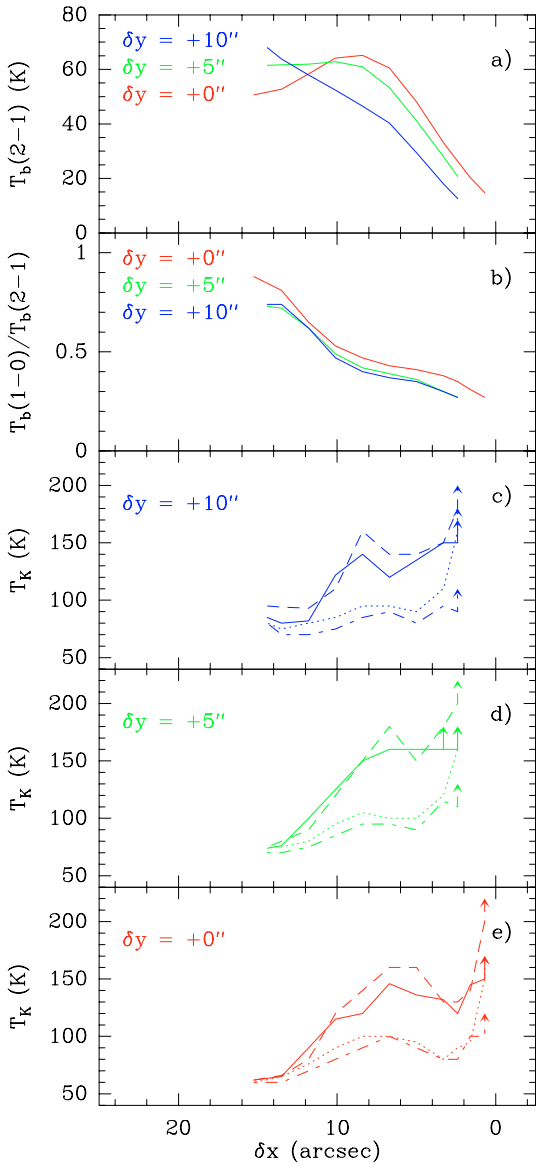

Fig. 6. Spatial variation along the direction of the exciting star of **a)** the ^{12}CO $J = 2-1$ brightness temperature (convolved at the same angular resolution as the $J = 1-0$ transition); **b)** 1−0/2−1 ratio and **c)**, **d)**, **e)** the kinetic temperature. $(\delta x, \delta y)$ offsets refer to the coordinate system defined in Fig. 3. The cuts at $\delta y = +10''$ are drawn in blue, those at $\delta y = +5''$ in green and those $\delta y = +0''$ in red. The data cuts have been taken from the 10.6 km s^{-1} velocity channel corresponding to the ^{12}CO line peak. The kinetic temperature is derived from an LVG model assuming i) unity beam filling factor; and ii) uniform total hydrogen density of $n_H = 1.6 \times 10^4$ cm^{-3} (dashed lines), 2×10^4 cm^{-3} (full lines), 4×10^4 cm^{-3} (dotted lines) and 10^5 cm^{-3} (dotted-dashed lines). Arrows indicate lower limits.

parameters. As the observations involve complex carbon molecules, we have used the so-called "new standard model" chemical rate file of Herbst and collaborators (Lee et al. 1998), available on the web site[3]. In a previous paper (Teyssier et al. 2004), we have found that the other extensive chemical rate file provided by the UMIST group (Le Teuff et al. 2000) gave close

[3] http://www.physics.ohio-state.edu/~eric/research_files/cddata.july03

Table 3. Molecular column densities and abundances at 3 different positions of the PDR named "Cloud", "IR peak" and "IR edge". Equatorial offsets refer to the Mosaic 2 map center given in Table 1. $(\delta x, \delta y)$ offsets refer to the coordinate system defined in Fig. 3. H_2 column densities have been derived from the 1.2 mm dust continuum emission using a dust temperature range of 20 to 40 K for the "Cloud" position and 40 to 80 K for the IR positions. Others column densities used LVG models with a representative set of densities and kinetic temperature. 1-σ uncertainties thus reflect the systematics due to the approximate knowledge of density and kinetic temperature. Abundances are computed with respect to the number of protons, i.e. $[X] = 0.5\,N(X)/N(H_2)$.

	δRA	δDec	δx	δy
Cloud	+6″	−4″	+24.9″	−5.3″
IR peak	−6″	−4″	+12.2″	−2.4″
IR edge	−12″	−4″	+7.4″	−1.0″

Quantity	Unit	Cloud	IR peak	IR edge
$S_{1.2\,mm}$	mJy/Beam	38 ± 2	35 ± 2	12 ± 2
$N(H_2)$	10^{21} cm^{-2}	27 ± 9.5	10.5 ± 4	3.6 ± 1.7
$N(C^{18}O)$	10^{15} cm^{-2}	5.8 ± 0.5	4 ± 0.5	1 ± 0.3
N(CCH)	10^{13} cm^{-2}	5.5 ± 1	30 ± 5	11 ± 3
N(c-C_3H_2)	10^{12} cm^{-2}	2.3 ± 0.7	24 ± 10	9.5 ± 5
$N(C_4H)$	10^{12} cm^{-2}	20 ± 10	40 ± 10	37 ± 10

Quantity	Unit	Cloud	IR peak	IR edge
[$C^{18}O$]	10^{-7}	1.07	1.9	1.4
[CCH]	10^{-8}	0.10	1.4	1.5
[c-C_3H_2]	10^{-10}	0.43	11.4	13.2
[C_4H]	10^{-9}	0.37	1.9	5.2

results for the carbon chain molecules. As $C^{18}O$ observations are reported, we have added to this reaction set the main isotopic molecules involving ^{18}O and introduced the corresponding fractionation reactions (Graedel et al. 1982). We have also introduced the photo-dissociation rates given by van Dishoeck (1988), when available, which have been calculated specifically with the Draine ISRF and which were different from the values reported in the chemical rate file. The resulting chemical network involves about 450 chemical species and 5000 reactions. Only the most stable isomeric forms of hydrocarbons are considered here.

We define a reference model (hereafter named model A) of the Horsehead nebula as a uniform sheet of gas and dust of total hydrogen density $n_H = 10^5$ cm^{-3} exposed to a ISRF of 100 measured in Draine units. The cosmic ray ionization rate has a value of 5×10^{-17} s^{-1} and the elemental abundances are as follows: C/H = 1.38×10^{-4}, O/H = 3.02×10^{-4}, ^{18}O/H = 6×10^{-7}, N/H = 7.95×10^{-5}, S/H = 5.8×10^{-8}, Cl/H = 1.86×10^{-9}, P/H = 9.3×10^{-10}, Fe/H = 1.7×10^{-9}, Mg/H = 10^{-8}, Na/H = 2.3×10^{-9}. The properties of the grains are the same as described in Le Petit et al. (2002), i.e. the size distribution law is taken from Mathis et al. (1977) with an exponent of −3.5 and we describe the attenuation of grains from the

Article published by EDP Sciences and available at http://www.edpsciences.org/aa or http://dx.doi.org/10.1051/0004-6361:20041170

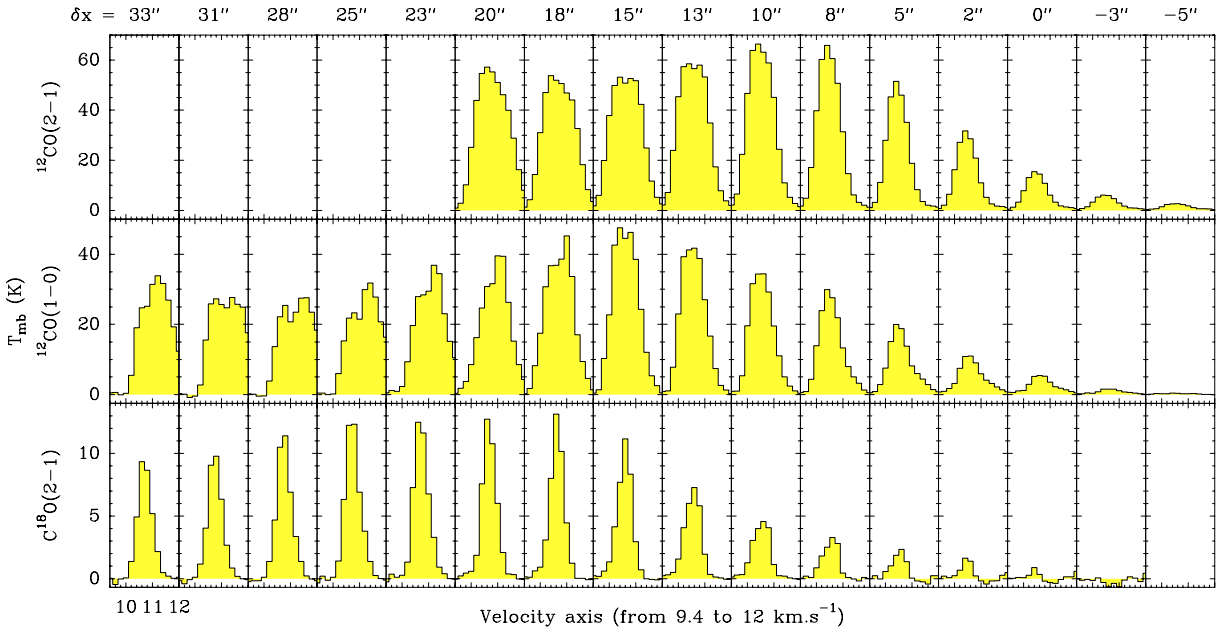

Fig. 7. CO spectra (convolved at the same angular resolution) along the direction of the exciting star at $\delta y = -2.5''$. In the cuts, the label $\delta x = 13''$ indicates the IR peak position (cf. Table 3). Note that ^{12}CO $J = 2-1$ peak intensity decreases at positions $\delta x = 13''$ and $15''$ while ^{12}CO $J = 1-0$ increases even reaching its maximum at $\delta x = 15''$. In addition, both ^{12}CO lines show a small but clear dip (i.e. the center channel intensity is lower than its first neighbours) at $\delta x = 15''$. Finally, while C^{18}O spectra are very close to Gaussian, ^{12}CO spectra show asymmetric profiles. Spectra cuts at other close δy values show the same trends.

far-UV to the visible via the galactic extinction curve given as an analytic function of $1/\lambda$ by including the coefficients derived by Fitzpatrick & Massa (1988). Charge exchange reactions between C^+ and PAHs are not taken into account. The gas to dust mass ratio is 100.

Figure 8 shows i) the abundance of the H_2 rovibrationally excited in the $v = 1$, $J = 3$ level at the origin of the 2.12 μm line (this abundance is hereafter referred to as $[H_2^\star]$); and ii) the C, CO and hydrocarbon abundances for this reference model and 5 variants. We ensure that the $[H_2^\star]$ peak position is set at $\delta x = 10''$ as in the observations. Our reference model correctly reproduces the observed 3 to 5″ offset between the hydrocarbon and H_2 peaks. The C^{18}O also peaks behind the hydrocarbons at $\delta x = 20-25''$. However, the H_2 profile is not correctly modeled here.

In model B, we replaced the Galactic extinction curve by one more representative of molecular gas. We have chosen HD 147889 in Ophiuchus. Its extinction curve has a rather strong far-UV rise ($E_{B-V} = 1.09$, Fitzpatrick & Massa 1988). Its ratio between the total and selective extinctions, R_V, is 4.2 a figure typical of molecular gas (Gordon et al. 2003; Cardelli et al. 1989). The PDR stratification does not qualitatively change compared to model A: It is just compressed. In model C, we added reactions of charge exchange between C^+ and PAHs. This enhances the neutral atomic carbon abundance but does not have a large effect on the hydrocarbons: only CCH peaks closer to the H_2 peak compared to model A. Neither model B nor C improves the modeling of the H_2 profile.

As shown by model D, E and F, the density structure has a major impact on the PDR structure. Figure 9 shows the density profiles associated with each model. When keeping the total hydrogen density uniform but decreasing its value to 2×10^4 cm^{-3} (as in model D), the carbon and hydrocarbon abundance peaks are highly broadened and shifted inward by more than 20″, a prediction clearly violated by the high resolution PdBI data. Models E and F use a density profile provided by Habart et al. (2004, 2005) to fit the 2.12 μm-H_2 emission. Indeed, the $[H_2^\star]$ profile qualitatively changes (it is now a peak rising from zero at the PDR edge) but it also reproduces the H_2 filament width. Those two models, which impose a steep total hydrogen density gradient at the PDR edge, are the only ones that succeed in correctly reproducing the offset between the hydrocarbon and H_2 peaks as well as the form of the H_2 peak. The only difference between models E and F is the gaseous sulfur abundance: sulfur is depleted from the gas phase in model E ($S/H = 5.8 \times 10^{-8}$) while the gaseous sulfur abundance is solar in model F ($S/H = 10^{-5}$).

Figure 10 is a zoom in our two best models (i.e. E and F) of the spatial variations of the abundances of hydrocarbons relative to i) total hydrogen density (top panel); and ii) CCH (bottom panel). The observed abundances are overplotted with their error bars. The dashed vertical line separates the zone where the proton gas density is constant from the zone where the proton gas density rapidly decreases outward. This latter zone is associated with the PDR. The sulfur element abundance has different effects in the two regions. In the region of moderate visual extinction (i.e. the "IR edge" and the "IR peak" where $A_V \lesssim 1$), the charge transfer reaction between C^+ and S leading to S^+ and C reinforces the abundance of neutral carbon and thus enables the formation of carbon chains via the rapid neutral-carbon atom reactions. However this effect is small. Indeed this is in the dark region where the sulfur elemental

Article published by EDP Sciences and available at http://www.edpsciences.org/aa or http://dx.doi.org/10.1051/0004-6361:20041170

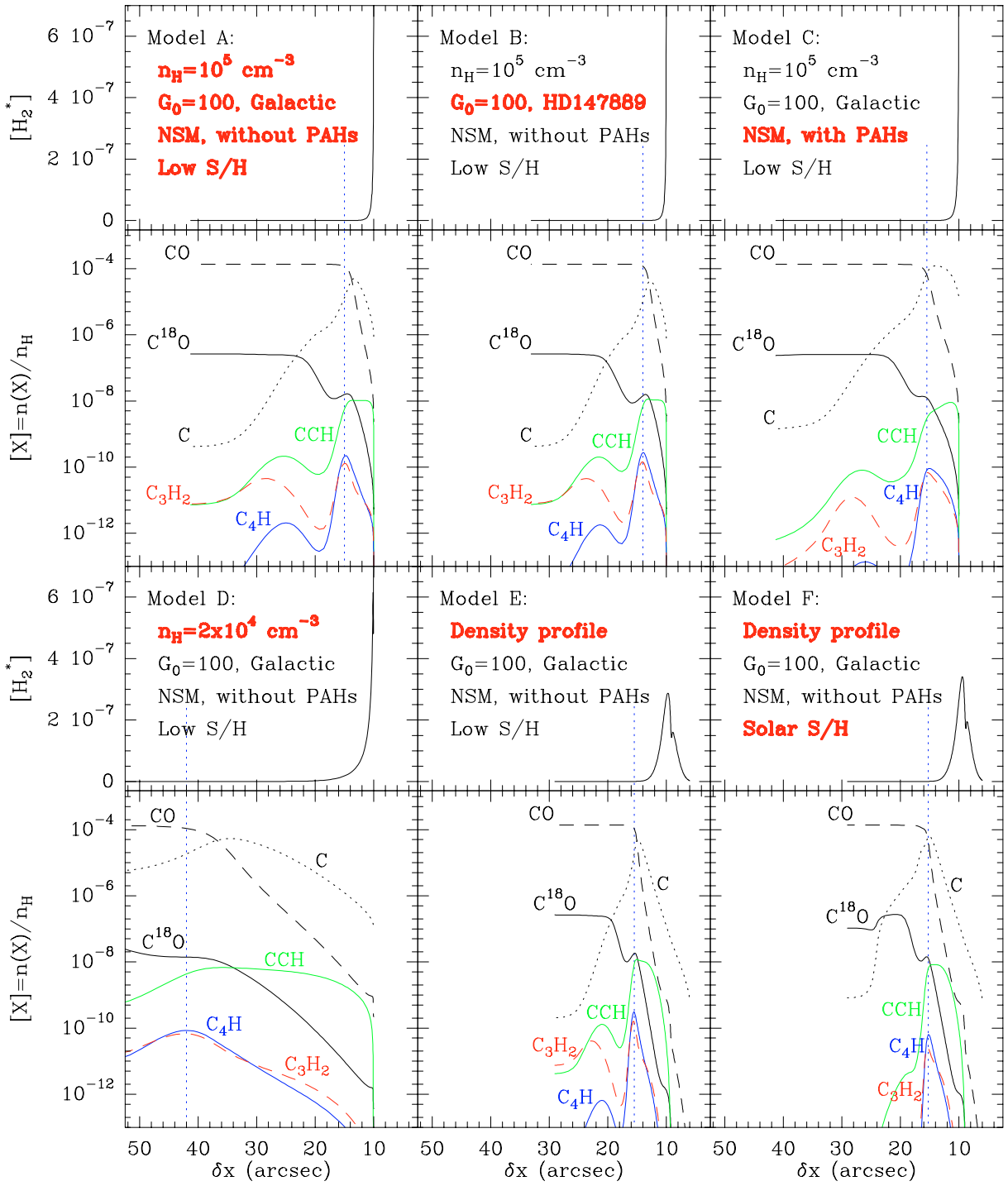

Fig. 8. Predictions of the spatial variation of the abundance relative to H_2, using a unidimensional PDR code. For each model, the abundance of the population of the the upper level of the 2.12 μm H_2 line (i.e. $v = 1$, $J = 3$), written $[H_2^\star]$, is shown on a linear scale (*top*). The C, CO and hydrocarbon abundances are shown on a logarithmic scale (*bottom*). The modeled cloud is illuminated from the right-hand side. The δx-axis origin has been set so that $[H_2^\star]$ peaks at the position of the observed H_2 peak (i.e. $\delta x = 10''$). The vertical dotted blue line indicates the peak of the c-C_3H_2 and C_4H abundances. Each model is described in 4 lines: i) the density structure; ii) the UV-field properties; iii) the chemical network used; and iv) the gaseous sulfur abundance. 6 different models are compared here. Our reference model is labeled A. The total hydrogen density is kept uniform at a value of $n_H = 10^5$ cm^{-3}. The far-UV intensity of the radiation field is $G_0 = 100$ (in Draine units) and the extinction curve is the mean Galactic one. The chemical network rate file is the New Standard Model one with minor modifications described in the text. Charge exchange reactions between C^+ and PAHs are not taken into account. The gaseous sulfur abundance is low compared to solar (i.e. $S/H = 5.8 \times 10^{-8}$). The parameters varied in other models are emphasized in red. Model B uses a different extinction curve. Model C adds reactions of charge exchange between C^+ and PAHs. Model D decreases the uniform total hydrogen density. Models E and F use the density profile derived from the model of the H_2 observations (Habart et al. 2004, 2005). Model F uses a solar gaseous sulfur abundance (i.e. $S/H = 10^{-5}$).

Article published by EDP Sciences and available at http://www.edpsciences.org/aa or http://dx.doi.org/10.1051/0004-6361:20041170

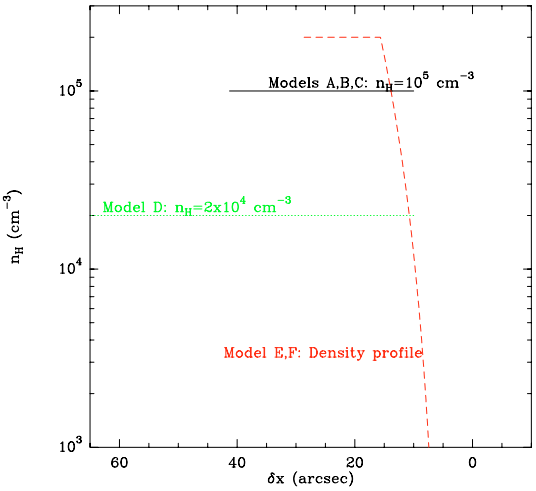

Fig. 9. Spatial variation of the total hydrogen density in models A to F. In model E and F, the density increases as a power law of scaling exponent 4 in the first 10″ and then is kept constant at a value of 2×10^5 cm^{-3}. As in Fig. 8, the x-axis origin has been set so that $[H_2^\star]$ peaks at the position of the observed 2.12 μm, H_2 line peak (i.e. δx = 10″).

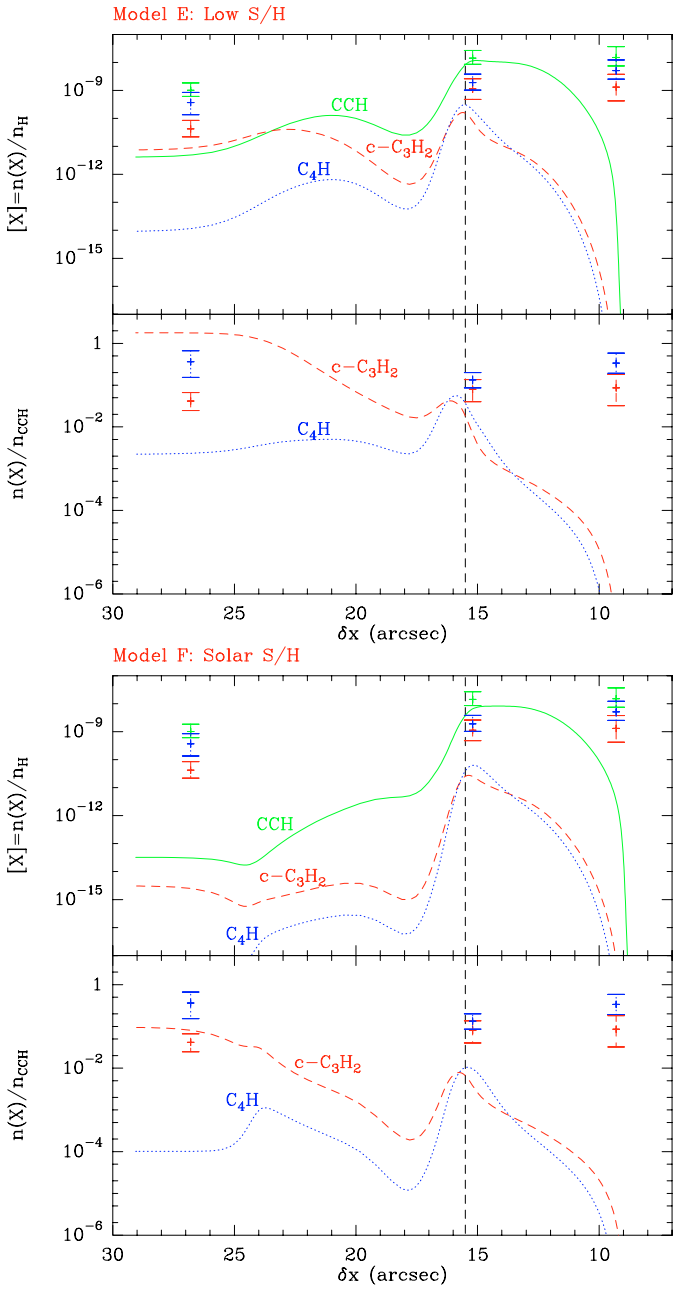

Fig. 10. Comparison between our two best models (curves) and observed (points with error bars) abundances of the small hydrocarbons. CCH is shown as a green solid line, c-C_3H_2 as a dashed red line and C_4H as a blue dotted line. The top and bottom panels respectively show abundances relative to the total hydrogen density and CCH. The dashed vertical line shows the position where the total hydrogen density profile changes from a steep gradient to a constant.

abundance has a large effect. When the sulfur abundance is solar, the small carbon chains C_2, CCH, C_2H_2, C_3H, C_3H_2 and C_4H react with S^+ to give C_2S^+, CCS^+, HC_2S^+, C_3S^+, HC_3S^+ and C_4S^+. In this main destruction path of the small carbon chains, one hydrogen atom is released impairing the reformation of the carbon chains. When S is higly depleted as in Model E, this destruction mechanism is superseded by other pathways involving C^+. Those pathways form carbon chain ions which in turn contribute to the formation of other carbon chains. Overall, model E (i.e. low S/H) performs better in the comparison with observed abundances. The only exception is the n(c-C_3H_2)/n(CCH) ratio at the "cloud" position. We will thus use model E only for comparison with the observations. At the IR peak (median point at δx = 15.5″), the CCH abundance is correctly reproduced while c-C_3H_2 and C_4H abundances are underestimated by at least a factor of 3. Discrepancies are much higher both at the "cloud" (point to the right at δx = 27″) and the "IR edge" (point to the left at δx = 9″) positions. In the UV-illuminated edge, the modeled [CCH] has a quite shallow increase with δx while the modeled [c-C_3H_2] and [C_4H] share the same steep abundance profile. In contrast, the observed ("IR edge") abundances are very similar for the 3 species, reflecting the very good spatial correlation between the different hydrocarbons (see Fig. 4). This discrepancy is independent of our knowledge of the total hydrogen density as it is also seen when comparing abundances relative to CCH.

In summary, *none* of our models is able to correctly reproduce the relative stratification of H_2 and small hydrocarbons. Comparison of model A and C shows that to reproduce the observed offset between hydrocarbon and H_2 peaks, we need a high total hydrogen density (10^5 cm^{-3}). By varying the profile density (model E and F), a shallow total hydrogen density increase at the PDR edge is needed to reproduce the profile of the 2.12 μm H_2 line. However, the shallower the total hydrogen density increase, the larger the modeled offset between H_2 and the hydrocarbons. A good compromise is provided by a total hydrogen density profile increasing as a power law with a scaling exponent 4 on the first 10″ and then constant at a value of 2×10^5 cm^{-3}. Habart et al. (2005) show that this model essentially corresponds to a constant pressure model (with $P = 4 \times 10^6$ K km s^{-1}). Model E with low sulfur elemental abundance performs better than model F with solar abundance. Nonetheless, even model E does not succeed in

Article published by EDP Sciences and available at http://www.edpsciences.org/aa or http://dx.doi.org/10.1051/0004-6361:20041170

reproducing the good hydrocarbon correlation seen in the illuminated part of the PDR: while CCH is correctly predicted to have a smooth abundance increase, modeled c-C_3H_2 and C_4H abundances show a much too steep increase.

4.2. Can the fragmentation of PAHs contribute to the synthesis of small hydrocarbons?

Examining the model predictions in more detail, three hypotheses can be proposed to explain the discrepancies between model calculations and observations:

i) The photo-dissociation rates used in the models may be incorrect. As the main destruction process near the cloud edge is photo-dissociation, the actual values of the photo-dissociation rates are critical for an accurate prediction. However, similar results are obtained with the UMIST95 and NSM rate files. The photo-dissociation rates for c-C_3H_2, C_3H and C_4H are 10^{-9} s^{-1} for both rate files, and differ by a factor of two for CCH (i.e. 0.51×10^{-9} s^{-1} for UMIST95 and 10^{-9} s^{-1} for NSM). The photo-dissociation rates of larger chains are similar. In most cases, except for CCH and acetylene, the numbers given in the rate files are not well documented. For instance, van Dishoeck (1988) discusses the photo-dissociation rate of c-C_3H_2 and concludes that it is accurate within an order of magnitude. More accurate photo-dissociation rates are clearly needed for the carbon chains and cycles. Recent calculations have been performed for C_4H showing that the photo-dissociation threshold is 5.74 eV, but that efficient photo-dissociation requires more energetic photons, typically above 6.5 eV (Graf et al. 2001). However, it is unlikely that the rates are low enough to explain the large discrepancies between the models and the data since these molecules are known to be sensitive to UV-radiation (Jackson et al. 1991; Song et al. 1994).

ii) Another possibility is that the chemical networks are missing important reactions for the synthesis of hydrocarbons. Neutral-neutral reactions are progressively included in the rate files, but still are much less numerous than ion-molecule reactions. It is now known that atomic carbon, diatomic carbon and CCH may react with hydrocarbons (Kaiser et al. 2003; Stahl et al. 2002; Mebel & Kaiser 2002). More work remains to be done. However, preliminary tests using a more extended data base of chemical reactions have not led to significant improvement.

iii) The excellent spatial correlation between the mid-IR emission due to PAHs and the distribution of carbon chains suggests a last hypothesis: the fragmentation of PAHs due to the intense far UV-radiation could seed the interstellar medium with a variety of carbon clusters, chains and rings (Scott et al. 1997; Verstraete et al. 2001; Le Page et al. 2003; Joblin 2003, and references therein). These species would then further react with gas phase species (C, C^+, H, H_2, etc.) and participate in the synthesis of the observed hydrocarbons. Fuente et al. (2003) also favor this explanation to explain the abundance of c-C_3H_2 they observed in other PDRs.

A correct exploration of this third hypothesis needs a good qualitative and quantitative description of both the fragmentation and reformation of PAHs, which is out of the scope of this paper. We here give only a few indications. Omont (1986) pioneered attempts to understand the role of PAHs in interstellar chemistry. Elaborating on this work, Lepp & Dalgarno (1988) suggested that the participation of PAHs in the ion chemistry of *dense clouds* leads to large increases in the abundances of small hydrocarbons. Indeed, when the PAH fractional abundance exceeds $\sim 10^{-7}$, the formation of PAH^- triggers mutual neutralization of the positive atomic and molecular ions and introduces new pathways for the formation of complex molecules. The equilibrium abundances of neutral atomic carbon C, CCH and c-C_3H_2 may thus be enhanced by two orders of magnitude. By comparison, our model C which includes charge exchange between C^+ and PAHs, shows a decrease of C_4H and c-C_3H_2 abundances by at least an order of magnitude in the dark region. Introduction of mutual neutralization between C^+ and PAH^- could be an interesting alternative to our "artificial" lowering of the sulfur abundance. We are currently acquiring CS data at PdBI to constrain the S chemistry independently.

Lepp et al. (1988) suggested that the ion chemistry of *diffuse clouds* has little impact on the CH, OH and HD abundance, but can lead to a large increase in the abundance of other species (H_2, NH_3 and most noticeably CH_4 and C_2H_2) by successive reactions of PAH and PAH^- with carbon and hydrogen atoms. Talbi et al. (1993) suggested that Coulombic explosion of doubly ionized PAH could create c-C_3H_2 through the electronic dissociative recombination of $C_3H_3^+$. Laboratory experiments by Jochims et al. (1994) suggested that PAHs with less than 30–40 carbon atoms will be UV-photodissociated in HI regions while larger ones will be stable. Based on those results, models by Allain et al. (1996b,a) indicate that only PAHs with more than 50 carbon atoms survive the high UV radiation field of the diffuse interstellar medium, whereas smaller PAHs such as coronene or ovalene are destroyed by the loss of acetylenic groups. Destruction timescales are a few years for neutral species and typically five time shorter for the corresponding cations. All those reactions start from neutral or cation PAHs. They will be in competition with charge exchange and mutual neutralization discussed above. Mutual neutralization has a maximal effect in the transition region where the gas is molecular but the electronic abundance is significant. This region corresponds more or less to the region of maximum emission from the PAHs or slightly deeper in the molecular cloud. All other cited reactions are more efficient toward the illuminated edge where PAHs are mainly neutral. Recently, Le Page et al. (2003) discussed the possibility of addition reactions with ionized carbon, starting from the high reaction rate between C^+ and anthracene measured by Canosa et al. (1995). If similar reaction rates persist for heavier PAHs, addition reactions with carbon would be very efficient in counteracting the destruction by far-UV photons.

From the observational point of view, the mid-IR emission due to PAHs is extended in interstellar clouds. On the other hand, a detailed analysis of the mid and far-IR images obtained by IRAS led Boulanger et al. (1990) and Bernard et al. (1993) to conclude that PAHs disappear in the dense cold cloud

Article published by EDP Sciences and available at http://www.edpsciences.org/aa or http://dx.doi.org/10.1051/0004-6361:20041170

interiors, probably because they coagulate and/or condense. Stepnik et al. (2003) describe a convincing case for such a process in a small filament of the Taurus cloud. Rapacioli et al. (2005) have found clear evidence for spatial variations of the aromatic infrared band profiles, likely due to the spatial variation of the nature of their carriers. A sophisticated analysis of ISOCAM-CVF data allowed them to separate the mid-IR spectra of the ionized and neutral PAHs from the spectra of carbonaceous very small grains (possibly PAH aggregates). The very small grains are located at a larger distance from the illuminating stars than the PAHs, lending support to the idea that PAHs are produced from the photo-evaporation of these very small grains. While more examples are needed to understand the origin and fate of interstellar PAHs, it appears nonetheless that these macro molecules are released in the gas phase in the UV-illuminated regions of the interstellar medium, i.e. in the diffuse clouds, in PDRs, etc. In those regions, the destruction of the carbon skeleton is the main process limiting the smallest possible PAH size. It is likely that some carbon-bearing molecules are released in the gas phase in the UV-illuminated regions, either as a secondary product of the evaporation of the dust particles giving rise to PAHs, or as products of the destruction of the PAH carbon skeleton.

5. Summary and conclusions

We have presented maps of the edge of the Horsehead nebula in rotational lines of excited H_2, CO, $C^{18}O$ and simple hydrocarbon molecules, CCH, c-C_3H_2 and C_4H with $6''$ resolution. All the hydrocarbon maps are strikingly similar to each other, and to the mid-IR emission mapped by ISOCAM (Abergel et al. 2003) while we measured a 3 to $5''$ offset between the hydrocarbon and H_2 peaks. State-of-the-art chemical models fail to reproduce both the PDR hydrocarbon stratification and the absolute abundances of 2 of 3 observed hydrocarbons. We have examined three hypotheses to improve the models, and we conclude that the most likely explanation is that we are witnessing the fragmentation of PAHs in the intense far-UV radiation due to σOri.

A detailed modeling of the chemistry including this new mechanism is beyond the scope of this paper. Indeed, such a modeling requires rates for both the growth (by addition of molecules or of carbon and hydrogen atoms) and the fragmentation of PAHs. This last item requires an accurate description of the fragmentation cascade of PAHs, in all their possible equilibrium states (ionized, neutral, partially or totally dehydrogenated, ...). Laboratory experiments such as the ion cyclotronic resonance cell PIRENEA (Joblin 2003) are key instruments to provide such information. In addition, the rate files used by the model need to be updated, especially the photodissociation rates of the simple carbon chains. A critical review of the role of neutral-neutral reactions in interstellar chemistry is also warranted.

Acknowledgements. We are grateful to the IRAM staff at Plateau de Bure, Grenoble and Pico Veleta for competent help with the observations and data reduction. IRAM is supported by the INSU/CNRS (France), MPG (Germany) and IGN (Spain). This work has benefited from many discussions with C. Joblin and C.M. Walmsley. We thank D. Lis for the communication of the (CI) map of the Horsehead nebula in advance of publication. We also thank E. Herbst for providing an updated chemical rate file. M.G. is grateful to the CSO for the hospitality of its office in Hilo where she worked on this paper. We acknowledge funding by the French CNRS/PCMI program. We thank the referee, J. Black, for insightful comments which improved the presentation and the discussion of our results.

References

Ádámkovics, M., Blake, G. A., & McCall, B. J. 2003, ApJ, 595, 235
Abergel, A., Bernard, J. P., Boulanger, F., et al. 2002, A&A, 389, 239
Abergel, A., Teyssier, D., Bernard, J. P., et al. 2003, A&A, 410, 577
Allain, T., Leach, S., & Sedlmayr, E. 1996a, A&A, 305, 602
Allain, T., Leach, S., & Sedlmayr, E. 1996b, A&A, 305, 616
Anthony-Twarog, B. J. 1982, AJ, 87, 1213
Bakes, E. L. O., & Tielens, A. G. G. M. 1994, ApJ, 427, 822
Bernard, J., Boulanger, F., & Puget, J. 1993, A&A, 277, 609
Boulanger, F., Cox, P., & Jones, A. P. 2000, in Infrared Space Astronomy, Today and Tomorrow, 251
Boulanger, F., Falgarone, E., Puget, J., & Helou, G. 1990, ApJ, 364, 136
Canosa, A., Laubé, S., Rebrion, C., et al. 1995, Chem. Phys. Lett., 245
Cardelli, J. A., Clayton, G. C., & Mathis, J. S. 1989, ApJ, 345, 245
Cox, P., Guesten, R., & Henkel, C. 1988, A&A, 206, 108
Dickens, J. E., Irvine, W. M., Snell, R. L., et al. 2000, ApJ, 542, 870
Draine, B. T. 1978, ApJS, 36, 595
Fitzpatrick, E. L., & Massa, D. 1988, ApJ, 328, 734
Flower, D. R., & Pineau des Forêts, G. 2003, MNRAS, 343, 390
Fossé, D., Cesarsky, D., Gerin, M., Lequeux, J., & Tiné, S. 2000, in ISO Beyond the Peaks: The 2nd ISO Workshop on Analytical Spectroscopy, ESA SP-456, 91
Fossé, D. 2003, Ph.D. Thesis, Université Paris VI
Fuente, A., Rodrıguez-Franco, A., Garcıa-Burillo, S., Martın-Pintado, J., & Black, J. H. 2003, A&A, 406, 899
Goicoechea, J. R., Rodríguez-Fernández, N. J., & Cernicharo, J. 2004, ApJ, 600, 214
Gordon, K. D., Clayton, G. C., Misselt, K. A., Landolt, A. U., & Wolff, M. J. 2003, ApJ, 594, 279
Graedel, T. E., Langer, W. D., & Frerking, M. A. 1982, ApJS, 48, 321
Graf, S., Geiss, J., & Leutwyler, S. 2001, J. Chem. Phys., 114, 4542
Gueth, F. 2001, in Proc. IRAM Millimeter Interferometry Summer School, 2, 207
Gueth, F., Guilloteau, S., & Bachiller, R. 1996, A&A, 307, 891
Habart, E., Abergel, A., Walmsley, C. M., & Teyssier, D. 2004, in 4th Cologne-Bonn-Zermatt Symp.: The dense interstellar medium in galaxies
Habart, E., Abergel, A., Walmsley, C. M., Teyssier, D., & Pety, J. 2005, A&A, accepted
Habart, E., Boulanger, F., Verstraete, L., Walmsley, C. M., & Pineau des Forêts, G. 2004, A&A, 414, 531
Habart, E., Verstraete, L., Boulanger, F., et al. 2001, A&A, 373, 702
Jackson, W. M., Anes, D. S., & Continetti, R. E. 1991, J. Chem. Phys., 95, 7327
Joblin, C. 2003, in Semaine de l'Astrophysique Francaise, SF2A-2003
Jochims, H. W., Ruhl, E., Baumgartel, H., Tobita, S., & Leach, S. 1994, ApJ, 420, 307
Kaiser, R. I., Vereecken, L., Peeters, J., et al. 2003, A&A, 406, 385
Lacy, J. H., Knacke, R., Geballe, T. R., & Tokunaga, A. T. 1994, ApJ, 428, L69

Article published by EDP Sciences and available at http://www.edpsciences.org/aa or http://dx.doi.org/10.1051/0004-6361:20041170

Le Page, V., Snow, T. P., & Bierbaum, V. M. 2003, ApJ, 584, 316
Le Petit, F., Roueff, E., & Le Bourlot, J. 2002, A&A, 390, 369
Le Teuff, Y. H., Millar, T. J., & Markwick, A. J. 2000, A&AS, 146, 157
Lee, H.-H., Roueff, E., Pineau des Forets, G., et al. 1998, A&A, 334, 1047
Leger, A., D'Hendecourt, L., Boissel, P., & Desert, F. X. 1989, A&A, 213, 351
Leger, A., & Puget, J. L. 1984, A&A, 137, L5
Lepp, S., & Dalgarno, A. 1988, ApJ, 324, 553
Lepp, S., Dalgarno, A., van Dishoeck, E. F., & Black, J. H. 1988, ApJ, 329, 418
Lis, D., & Guesten, R. 2005, in preparation
Liszt, H. 2003, A&A, 398, 621
Lucas, R., & Liszt, H. S. 2000, A&A, 358, 1069
Maier, J. P., Lakin, N. M., Walker, G. A. H., & Bohlender, D. A. 2001, ApJ, 553, 267
Mathis, J. S., Rumpl, W., & Nordsieck, K. H. 1977, ApJ, 217, 425
Matthews, H. E., Avery, L. W., Madden, S. C., & Irvine, W. M. 1986, ApJ, 307, L69
Matthews, H. E., & Irvine, W. M. 1985, ApJ, 298, L61
Mebel, A. M., & Kaiser, R. I. 2002, Chem. Phys. Lett., 360, 139
Oka, T., Thorburn, J. A., McCall, B. J., et al. 2003, ApJ, 582, 823
Omont, A. 1986, A&A, 164, 159
Pound, M. W., Reipurth, B., & Bally, J. 2003, AJ, 125, 2108
Pratap, P., Dickens, J. E., Snell, R. L., et al. 1997, ApJ, 486, 862
Rapacioli, M., Joblin, C., & Boissel, P. 2005, A&A, 429, 193
Roueff, E., Felenbok, P., Black, J. H., & Gry, C. 2002, A&A, 384, 629
Scott, A., Duley, W. W., & Pinho, G. P. 1997, ApJ, 489, L193
Sellgren, K. 1984, ApJ, 277, 623
Sofia, U. J., & Meyer, D. M. 2001, ApJ, 554, L221
Song, X., Bao, Y., & Urdahl, R. S. 1994, Chem. Phys. Lett., 217, 216
Stahl, F., Schleyer, P. V. R., Schaefer, H. F., & Kaiser, R. I. 2002, Plan. Sp. Sci., 50, 685
Stepnik, B., Abergel, A., Bernard, J.-P., et al. 2003, A&A, 398, 551
Talbi, D., Pauzat, F., & Ellinger, Y. 1993, A&A, 268, 805
Teyssier, D., Fossé, D., Gerin, M., et al. 2004, A&A, 417, 135
Thorburn, J. A., Hobbs, L. M., McCall, B. J., et al. 2003, ApJ, 584, 339
van Dishoeck, E. F. 1988, in Rate Coefficients in Astrochemistry, ASSL, 146, 49
Verstraete, L., Pech, C., Moutou, C., et al. 2001, A&A, 372, 981
Weingartner, J. C., & Draine, B. T. 2001, ApJ, 563, 842
Wilson, T. L., & Rood, R. 1994, ARA&A, 32, 191
Wolfire, M. G., McKee, C. F., Hollenbach, D., & Tielens, A. G. G. M. 2003, ApJ, 587, 278

Article published by EDP Sciences and available at http://www.edpsciences.org/aa or http://dx.doi.org/10.1051/0004-6361:20041170

A&A 456, 565–580 (2006)
DOI: 10.1051/0004-6361:20065260
© ESO 2006

Astronomy & Astrophysics

Low sulfur depletion in the Horsehead PDR⋆,⋆⋆

J. R. Goicoechea[1], J. Pety[1,2], M. Gerin[1], D. Teyssier[3], E. Roueff[4], P. Hily-Blant[2], and S. Baek[1]

[1] LERMA–LRA, UMR 8112 CNRS, Observatoire de Paris and École Normale Supérieure, 24 Rue Lhomond, 75231 Paris Cedex 05, France
e-mail: [javier;gerin]@lra.ens.fr
[2] IRAM, 300 rue de la Piscine, 38406 Grenoble Cedex, France
e-mail: [pety;hilyblan]@iram.fr
[3] European Space Astronomy Centre, Urb. Villafranca del Castillo, PO Box 50727, Madrid 28080, Spain
e-mail: dteyssier@sciops.esa.int
[4] LUTH UMR 8102, CNRS and Observatoire de Paris, Place J. Janssen, 92195 Meudon Cedex, France
e-mail: evelyne.roueff@obspm.fr

Received 23 March 2006 / Accepted 9 June 2006

ABSTRACT

Aims. We present 3.65″ × 3.34″ angular-resolution IRAM *Plateau de Bure Interferometer* (PdBI) observations of the CS J = 2–1 line toward the Horsehead *Photodissociation Region* (PDR), complemented with IRAM-30m single-dish observations of several rotational lines of CS, $C^{34}S$ and HCS^+. We analyse the CS and HCS^+ photochemistry, excitation and radiative transfer to obtain their abundances and the physical conditions prevailing in the cloud edge. Since the CS abundance scales to that of sulfur, we determine the gas phase sulfur abundance in the PDR, an interesting intermediate medium between translucent clouds (where sulfur remains in the gas phase) and dark clouds (where large depletions have been invoked).
Methods. A nonlocal non-LTE radiative transfer code including dust and cosmic background illumination adapted to the Horsehead geometry has been developed to carefuly analyse the CS, $C^{34}S$, HCS^+ and $C^{18}O$ rotational line emission. We use this model to consistently link the line observations with photochemical models to determine the CS/HCS^+/S/S^+ structure of the PDR.
Results. Densities of $n(H_2) \simeq (0.5–1.0) \times 10^5$ cm^{-3} are required to reproduce the CS and $C^{34}S$ J = 2–1 and 3–2 line emission. CS J = 5–4 lines show narrower line widths than the CS low-J lines and require higher density gas components not resolved by the ∼10″ IRAM-30m beam. These values are larger than previous estimates based in CO observations. We found $\chi(CS) = (7 \pm 3) \times 10^{-9}$ and $\chi(HCS^+) = (4 \pm 2) \times 10^{-11}$ as the averaged abundances in the PDR. According to photochemical models, the gas phase sulfur abundance required to reproduce these values is S/H = $(3.5 \pm 1.5) \times 10^{-6}$, only a factor $\lesssim$4 less abundant than the solar sulfur elemental abundance. Since only lower limits to the gas temperature are constrained, even lower sulfur depletion values are possible if the gas is significantly warmer.
Conclusions. The combination of CS, $C^{34}S$ and HCS^+ observations together with the inclusion of the most recent CS collisional and chemical rates in our models implies that sulfur depletion invoked to account for CS and HCS^+ abundances is much smaller than in previous studies.

Key words. astrochemistry – ISM: clouds – ISM: molecules – ISM: individual objects: Horsehead nebula – radio lines: ISM – radiative transfer

1. Introduction

Sulfur is an abundant element (the solar photosphere abundance is S/H = 1.38×10^{-5}; Asplund et al. 2005), which remains undepleted in diffuse interstellar gas (e.g. Howk et al. 2006) and HII regions (e.g. Martín-Hernández et al. 2002; García-Rojas et al. 2006, and references therein) but it is historically assumed to deplete on grains in higher density molecular clouds by factors as large as $\sim 10^3$ (Tieftrunk et al. 1994). This conclusion is simply reached by adding up the observed gas phase abundances of S-bearing molecules in well known dark clouds such as TMC1 (e.g. Irvine et al. 1985; Ohishi & Kaifu 1998). As sulfur is easily ionized (ionization potential ∼10.36 eV), sulfur ions are probably the dominant gas-phase sulfur species in translucent gas. Ruffle et al. (1999) proposed that if dust grains are typically negatively charged, S^+ may freeze-out onto dust grains during cloud collapse more efficiently than neutral species such as oxygen. However, the nature of sulphur on dust grains (either in mantles or cores) is not obvious. Van der Tak et al. (2003) observed large abundances of gas phase OCS, $\sim 10^{-8}$, in star forming regions, and suggested that together with the detection of solid OCS (with an abundance of $\sim 10^{-7}$; Palumbo et al. 1997), it implies that OCS is a major sulfur carrier in dust grains. However, the ∼4.9 μm ice feature attributed to OCS is best reproduced when OCS is mixed with methanol. In fact, the band is blended with a methanol overtone whose contribution has not been studied in detail (Dartois 2005). In any case, the absence of strong IR features due to S-bearing ices in many ISO's mid-IR spectra (e.g. Boogert et al. 2000; Gibb et al. 2004) and

⋆ Based on observations obtained with the IRAM Plateau de Bure interferometer and 30 m telescope. IRAM is supported by INSU/CNRS (France), MPG (Germany), and IGN (Spain).
⋆⋆ Appendix A is only available in electronic form at http://www.edpsciences.org

Article published by EDP Sciences and available at http://www.edpsciences.org/aa or http://dx.doi.org/10.1051/0004-6361:20065260

Table 1. Observation parameters.

	Phase center		Number of fields
Mosaic 1	$\alpha_{2000} = 05^h40^m54.27^s$	$\delta_{2000} = -02°28'00''$	7
Mosaic 2	$\alpha_{2000} = 05^h40^m53.00^s$	$\delta_{2000} = -02°28'00''$	4

Molecule & Line	Frequency (GHz)	Beam (arcsec)	PA (°)	Noise[a] (K km s^{-1})	Obs. date
Mosaic 1					
^{12}CS J = 2–1	97.981	3.65×3.34	48	1.2×10^{-1}	Aug. & Oct. 2004 and Mar. 2005
C^{18}O J = 2–1	219.560	6.54×4.31	65	9.8×10^{-2}	Mar. 2003
Mosaic 2					
^{12}CO J = 1–0	115.271	5.95×5.00	65	1.2×10^{-1}	Nov. 1999
^{12}CO J = 2–1	230.538	2.97×2.47	66	1.7×10^{-1}	Nov. 1999

[a] The noise values quoted here are the noises at the mosaic center (Mosaic noise is inhomogeneous due to primary beam correction; it steeply increases at the mosaic edges). Those noise values have been computed in 1 km s^{-1} velocity bin.

the presence of S II recombination lines in dark clouds such as Rho Ophiuchi (Pankonin & Walmsley 1978) all argue against a large depletion of sulfur from the gas phase. In this case, the abundance of species such as CS may indicate that something important is lacking from chemical models or that an abundant sulfur-bearing carrier has been missed. Therefore, the abundances of sulfur species remain interesting puzzles for interstellar chemistry. In the case of dense clouds, standard chemical models predict that most of the gas phase sulfur is shared between S, SO and CS (Millar & Herbst 1990), while H_2S is also abundant in the Orion Bar PDR (Jansen et al. 1995). In all these cases, a large sulfur depletion, $\sim 10^2$, was required in the models to explain the observed abundances.

PDRs offer an ideal intermediate medium between diffuse and dark cloud gas to investigate the sulfur depletion problem. In this work we have tried to determine the CS abundance in the Horsehead PDR as a tool for estimating the sulfur gas phase abundance. However, CS chemistry is an open issue itself in different environments, from hot cores (e.g. Wakelam et al. 2004) to extragalactic sources (e.g. Martín et al. 2005). Recent laboratory experiments on dissociative recombination of HCS^+ and OCS^+ (Montaigne et al. 2005) imply a substantial modification of previous reaction rate coefficients, dissociative channels and branching ratios used in chemical models. The latest available reaction rates and collisional coefficients have been used in our photochemical and radiative transfer models.

1.1. The Horsehead nebula

The Horsehead nebula, appears as a dark patch of $\sim 5'$ diameter against the bright HII region IC 434. Emission from gas and dust associated with this globule has been detected from IR to millimeter wavelengths (Abergel et al. 2002, 2003; Pound et al. 2003; Teyssier et al. 2004, Habart et al. 2005; Pety et al. 2005a), although the first astronomical plates were taken $\sim$120 yr ago. In particular, the Horsehead western edge is a PDR viewed nearly edge-on and illuminated by the O9.5V star σOri at a projected distance of $\sim$3.5 pc (Anthony-Twarog 1982). The intensity of the incident FUV radiation field is $\chi \simeq 60$ relative to the interstellar radiation field (ISRF) in Draine's units (Draine 1978).

According to the evolutionary view of Reipurth & Bouchet (1984), the Horsehead nebula was a quiescent and dense cloud core embedded in a more diffuse cloud (L1630). The erosive action of the UV radiation from σOri on the ambient gas led to the apparent emergence of the core cloud, as in the earliest stages of Bok globules still attached to their parental cloud. However, the observed morphology together with the velocity gradients of the cloud, require a more involved description including a pre-existing rotating velocity field as well as density inhomogeneities in the initial structures (Pound et al. 2003; Hily-Blant et al. 2005). The erosive effect of the ionizing and dissociating radiation field together with these initial conditions explain the peculiar shaping of the Horsehead nebula. In particular, the densest regions of the initial inhomogeneities are now believed to be the East-West filamentary material connecting it to the parental cloud, and the PDR. In this work we have studied the PDR through CS, C^{34}S and HCS^+ observations.

2. Observations and data reduction

2.1. Observations

2.1.1. Pico Veleta single-dish

The single-dish data presented in this paper have been gathered between February and October 2004 at the IRAM 30-m telescope. The Horsehead nebula PDR was mapped in the CS J = 2–1 and 5–4 lines in order to provide the short-spacings for the interferometric observations presented thereafter. The final map consists of 5 on-the-fly coverages performed along perpendicular scanning directions, and combined with the PLAIT algorithm introduced by Emerson & Gräve (1888), allowing to efficiently reduce the stripes over the map. The noise levels (1σ rms) per regridded pixel and resolution channel of 80 kHz are of the order of 0.15 K at 3 mm, and 0.64 K at 1.3 mm. The latter value was not low enough to provide any useful mapping information at 1.3 mm since the CS J = 5–4 line peak is $\lesssim$1 K.

In complement to these data, dedicated positions were probed over a larger set of species and transitions. The frequency switching mode was used to observe CS J = 2–1, 3–2 and 5–4 lines, as well as C^{34}S J = 2–1, 3–2, and HCS^+ J = 2–1 lines. Table 2 summarizes the corresponding observing parameters. Longer integrations allowed to reach, in a resolution channel of 40 kHz, rms noise levels of 25, 42 and 36 mK at 3, 2, and 1.3 mm respectively. All CS and C^{34}S lines were detected with a S/N ratio better than 10. Figures 4 and 8 show some spectra collected at positions inside and across the PDR.

The data were first calibrated to the T_A^* scale using the so-called chopper wheel method (Penzias & Burrus 1973), and finally converted to main beam temperatures using efficiencies ($B_{\rm eff}/F_{\rm eff}$) of 0.81, 0.74 and 0.50 at 3, 2 and 1.3 mm respectively.

Table 2. Line parameters for the IRAM 30-m CS observations.

Molecule	Transition	Frequency (GHz)	*HPBW* (arcsec)
CS	J = 2–1	97.980968	25
	J = 3–2	146.96905	16
	J = 5–4	244.93561	10
$C^{34}S$	J = 2–1	96.412982	25
	J = 3–2	144.61715	16
HCS^+	J = 2–1	85.347884	29

Table 3. Calibrator fluxes in Jy.

Date	B0420−014		B0607−157	
	3 mm	1 mm	3 mm	1 mm
20.08.2004	3.4	2.9	1.4	0.93
04.10.2004	3.4	2.9	1.6	0.90
27.02.2005	3.5	2.9	1.6	0.90
02.03.2005	3.2	2.3	1.6	0.89
12.03.2005	3.2	2.3	1.6	0.90
13.03.2005	3.2	2.3	1.6	1.00

2.1.2. Plateau de Bure Interferometer

PdBI observations dedicated to this project were carried out with 6 antennae in the BCD configuration (baseline lengths from 24 to 331 m) from August 2004 to March 2005. The 580 MHz instantaneous IF-bandwidth allowed us to simultaneously observe CS, l-C_3H and ^{34}SO at 3 mm using 3 different 20 MHz–wide correlator windows. Another window was centered on the ^{13}CO J = 2–1 line frequency at 1 mm. The full IF bandwidth was also covered by continuum windows both at 3.4 and 1.4 mm. Only CS J = 2–1 and ^{13}CO J = 2–1 (not shown here) were detected.

We observed a seven-field mosaic. The mosaic was Nyquist sampled in declination at 3.4 mm and Nyquist sampled in Right Ascension at 1.3 mm. This ensures correct sampling in the illuminating star direction both at 3 and 1 mm while maximizing the field of view along the edge of the PDR eases the deconvolution. This mosaic, centered on the IR peak (Abergel et al. 2003), was observed for about 30 h of *telescope* time with 6 antennas. This leads to an *on-source* integration time of useful data of 10 h after filtering out data with tracking errors larger than 1″ and with phase noise worse than 40° at 3.4 mm. The rms phase noises were between 15 and 40° at 3.4 mm, which introduced position errors <0.5″. Typical 3.4 mm raw resolution was 2.5″.

2.2. Data processing

All data reduction was done with the `GILDAS`[1] softwares supported at IRAM (Pety 2005b). Standard calibration methods using nearby calibrators were applied to all the PdBI data. The calibrator fluxes used for the absolute flux calibration are summarized in Table 3.

Following Gueth et al. (1996), single-dish, fully sampled maps obtained with the IRAM-30 m telescope (see Sect. 2.1.1) were used to produce the short-spacing visibilities filtered out by each mm-interferometer (e.g. spatial frequencies between 0 and 15 m for PdBI). Those pseudo-visibilities were merged with the observed, interferometric ones. For imaging, we followed the method described by Pety et al. (2005) to produce images in different lines of the same source. This results in inhomogeneous noise. In particular, the noise strongly increases near the edges of the field of view. To limit this effect, the mosaic field-of-view is truncated.

Moreover, the natural synthesized beam (3.58″ × 1.89″ at PA 37°) is very asymmetric due to the low declination of the Horsehead nebula. We chooe to taper the weights of the *uv* visibilities before imaging using a Gaussian of size 400 m × 115 m at PA 80° to obtain an almost circular clean beam (3.65″ × 3.34″ at PA 48°). This considerably eased the deconvolution as 1) the larger beam increases the brightness sensitivity and 2) the secondary sidelobes of the dirty beam are much less patchy. Deconvolved image nevertheless still shows low-level, fake, patchy structures at the scale of the clean beam, mainly along the vertical direction. This is a known artifact of the Högbom CLEAN algorithm when a large spatial dynamic (field-of-view/resolution ∼110/3.5 = 30) is combined with high enough signal-to-noise ratio.

[1] See `http://www.iram.fr/IRAMFR/GILDAS` for more information about the `GILDAS` software.

3. Results

The PdBI integrated emission map of the CS J = 2–1 line, complemented with previous maps of CO J = 1–0, 2–1 and $C^{18}O$ J = 2–1 lines (Pety et al. 2005a), is shown in Fig. 1. Integrated emission profiles for these lines and for the small hydrocarbon c–C_3H_2 2_{12}–1_{01} line emission and 1.2 mm continuum emission (Pety et al. 2005a) are shown in Fig. 2. In Fig. 1 the four panels are shown in a coordinate system adapted to the source: i.e. maps have been rotated by 14° counter-clockwise around the image center to bring the exciting star direction in the horizontal direction as this eases the comparison with edge-on PDR models. Maps have also been horizontally shifted by 20″ to the east in order to set the horizontal zero at the PDR edge (delineated by the vertical line). Therefore, the coordinate system is converted from δRA to δx and from δDec to δy in arcsec (see Fig. 1). In the following, our spatial scale to interpret the PdBI maps will refer to the δx scale.

PdBI observations show that the CS emission is strikingly different from that of other species observed at comparable spatial resolutions. CS does not follow the filamentary pattern along the cloud edge revealed by mid-IR (Abergel et al. 2003), H_2 (Habart et al. 2005) or CCH and c–C_3H_2 emission (Pety et al. 2005a). Instead, the behavior of the CS J = 2–1 line emission is more similar to that of CO and shows a steep rise across the PDR and a plateau in the shielded region. Besides, the CS J = 2–1 line emission peak occurs in the well-shielded regions and does not coincide with the $C^{18}O$ J = 2–1 nor with the 1.2 mm continuum peaks (i.e. the temperature weighted density peaks, see Fig. 2). Therefore, PdBI observations suggests that CS is more abundant in the lower density regions and/or it shows line opacity effects in the denser regions. These results confirm that there are differences in the spatial distribution of small hydrocarbons (Pety et al. 2005a) and other species with similar excitation requirements. PdBI CO, $C^{18}O$ and CS line spectra along the direction of the exciting star (δy = 0″) are shown in Fig. 3. The CS J = 2–1 emission peak and line widths are comparable to those of $C^{18}O$ J = 2–1. Nevertheless, the CS emission distribution profile in the δx direction is less smooth, which can be an artifact of the data reduction and/or related to the CS photochemistry. The CS emission increases like the $C^{18}O$ emission in the PDR edge but in the shielded gas, CS rises when $C^{18}O$ decreases. On the other hand, ^{12}CO peaks closer to the PDR edge and lines have broader line widths (Pety et al. 2005a) indicative of their much larger opacities.

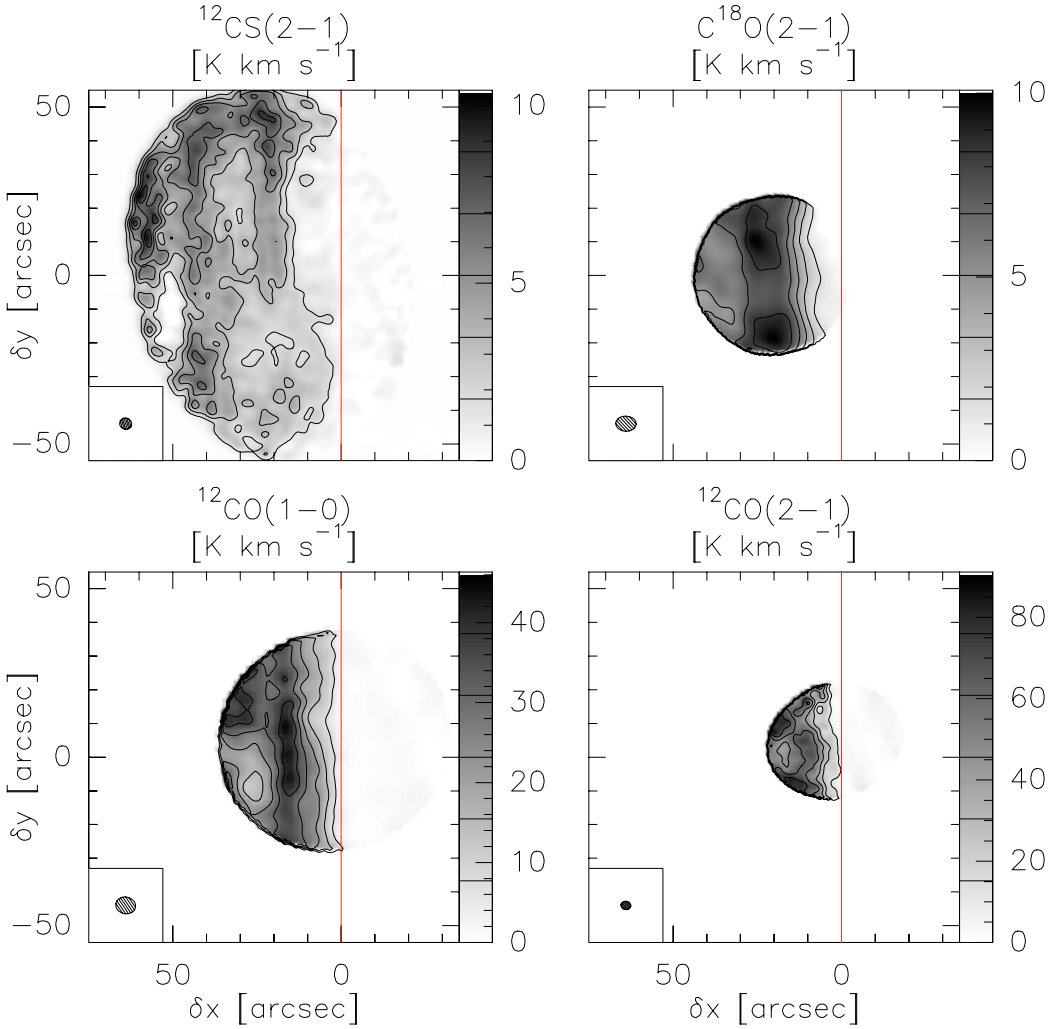

Fig. 1. Integrated emission maps obtained with the Plateau de Bure Interferometer. The center of all maps has been set to the mosaic phase center: RA(2000) = 05h40m54.27s, Dec(2000) = −02°28′00″. The map size is 110″ × 110″, with ticks drawn every 10″. The synthesized beam is plotted in the bottom left corner. The emission of all lines is integrated between 10.1 and 11.1 km s^{-1}. Values of contour level are shown on each image wedge. The four panels are shown in a coordinate system adapted to the source: i.e. maps have been rotated by 14° counter-clockwise around the image center to bring the exciting star direction in the horizontal direction as this eases the comparison of the PDR models. Maps have also been horizontally shifted by 20″ to set the horizontal zero at the PDR edge, delineated by the vertical line.

CS and C^{34}S single-dish observations at larger spatial scales are presented in Fig. 4. CS line ratios are similar in all observed PDR positions. However, there is a trend for CS lines to peak where C^{18}O emission decreases. Again, this is indicative of larger abundances in the lower density regions and/or line opacity effects in the denser regions. The latter hypothesis is playing a role because CS J = 3–2 lines show asymmetrical profiles in the whole region, especially red-wing like self-absorptions. See for example the (−52, −40) position with respect to the IRAM-30 m C^{18}O J = 2–1 map of Hily-Blant et al. (2005; Fig. 4). In addition, CS J = 3–2 and 2–1 lines must be optically thick since their intensity is only a factor ∼5 stronger than the analogous C^{34}S lines, significantly lower than the ^{32}S/^{34}S = 23 solar isotopic ratio (Bogey et al. 1981). In addition, CS $\frac{3-2}{2-1}$ line ratios are ∼0.7 while the optically thin C^{34}S $\frac{3-2}{2-1}$ line ratios are larger ∼0.9. Therefore, the CS J = 3–2 line is likely to be the most opaque CS line. Finally, Fig. 8 shows clear detections of the HCS$^+$ J = 2–1 line. As the expected HCS$^+$ abundance is lower than that of C^{34}S, these lines are weak and should be optically thin. Line intensities are quite similar in all observed PDR positions.

4. Numerical methodology

4.1. Photochemical models

We have used the *Meudon PDR code* (publicly available at `http://aristote.obspm.fr/MIS/`), a photochemical model of a unidimensional stationary PDR (Le Bourlot et al. 1993). The model has been described in detail elsewhere (Le Petit et al. 2006). In few words, the PDR code solves the FUV radiative transfer in an absorbing and diffusing medium of gas and dust. This allows the explicit computation of the FUV radiation field (continuum+lines) and therefore, the explicit integration of consistent C and S photoionization rates together with H_2, CO, ^{13}CO, and C^{18}O photodissociation rates. Penetration of FUV radiation into the cloud strongly depends on dust properties through dust absorption and scattering of FUV photons. Properties of dust grains are those described in Pety et al. (2005). We have taken a single dust albedo coefficient of 0.42 and an scattering asymmetry parameter of 0.6.

Once the FUV field has been determined, the steady-state chemical abundances are computed for a given chemical network. The *Ohio State University (osu)*

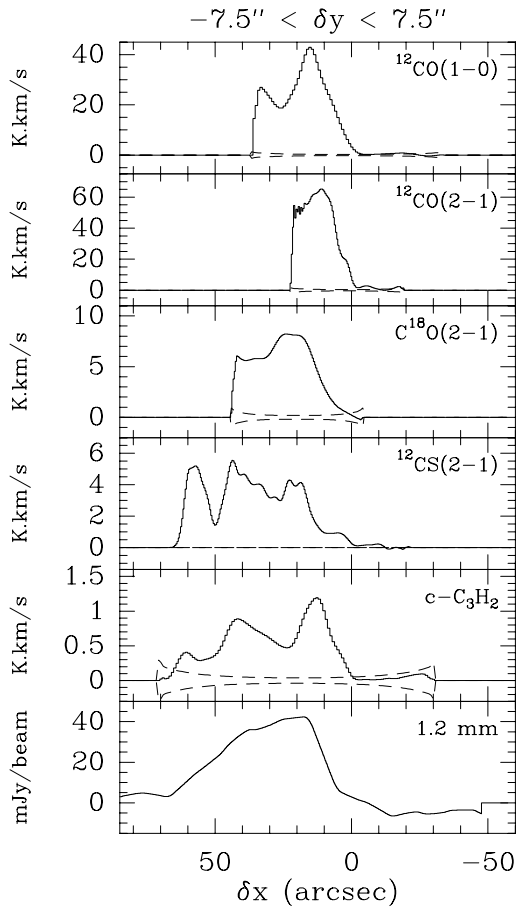

Fig. 2. Emission profiles along the exciting star direction (PA = −104° in the equatorial coordinate system). To improve the signal-to-noise ratio, emission profiles have been integrated along the perpendicular direction between $-7.5'' < \delta y < +7.5''$. We show from top to bottom ^{12}CO J = 2–1, ^{12}CO J = 1–0, C^{18}O J = 2–1, ^{12}CS J = 2–1, c-C_3H_2 2_{12}–1_{01} and 1.2 mm dust continuum emission (Pety et al. 2005a). The 3σ noise level is indicated by the dashed lines. It rises at the cut edges due to the primary beam correction. Note that the fields of view of the ^{12}CO and C^{18}O data are smaller than the field of view of the ^{12}CS data because of the smaller mosaic size and/or the higher frequency.

gas-phase chemical network (osu.2005; September 2005 release; `http://www.physics.ohio-state.edu/~eric/research.html`) has been used as our chemical framework. The most important changes compared to previous versions are the decrease, by a factor of 2, of rate coefficients of photoionization and photodissociation reactions produced by cosmic-ray-induced H_2 secondary photons, the inclusion of fluorine (F) and its chemistry (see Neufeld et al. 2005) and the update of several reaction rates. In addition, several changes have been carried out by us on the chemical network. In particular, we have introduced different ^{18}O bearing species into the chemical network by assuming similar reaction rates to those involving the major isotopologues. Fractionation reactions have been added following Graedel et al. (1982) and specific photodissociation cross-sections for C^{18}O are explicitly introduced to compute the corresponding photodissociation rate. When available, we have also used the photodissociation rates given by van Dishoeck (1988), which are explicitly calculated for the Draine interstellar radiation field (ISRF). Finally, we have further upgraded the sulfur network by adding the most recent reaction rates, dissociation channels and branching ratios

Table 4. IRAM-30 m line observation parameters from Gaussian fits.

Molecule/ Transition	Offset (″)	Δv_{FWHM} (km s^{-1})	$\int T_A^* \, dv$ (K km s^{-1})
CS J = 2–1	−52, −40	0.75 ± 0.01	2.60 ± 0.01
	−64, +30	0.89 ± 0.01	3.63 ± 0.01
	−35, −25	0.78 ± 0.01	3.68 ± 0.01
	−20, −15	0.77 ± 0.01	3.55 ± 0.01
CS J = 3–2	−52, −40	0.72 ± 0.01	1.82 ± 0.02
	−64, +30	0.93 ± 0.01	2.58 ± 0.02
	−35, −25	0.76 ± 0.01	2.73 ± 0.02
	−20, −15	0.80 ± 0.01	2.40 ± 0.02
CS J = 5–4	−52, −40	0.43 ± 0.02	0.35 ± 0.01
	−64, +30	0.76 ± 0.02	0.62 ± 0.02
	−35, −25	0.58 ± 0.02	0.52 ± 0.01
	−20, −15	0.60 ± 0.03	0.40 ± 0.02
C^{34}S J = 2–1	−52, −40	0.47 ± 0.02	0.26 ± 0.01
	−64, +30	0.67 ± 0.04	0.38 ± 0.02
	−35, −25	0.59 ± 0.02	0.40 ± 0.01
	−20, −15	0.58 ± 0.03	0.45 ± 0.02
C^{34}S J = 3–2	−52, −40	0.48 ± 0.04	0.20 ± 0.01
	−64, +30	0.74 ± 0.05	0.28 ± 0.02
HCS$^+$ J = 2–1	−52, −40	0.8 ± 0.3	0.07 ± 0.03
	−35, −25	0.6 ± 0.3	0.05 ± 0.03
	−20, −15	0.9 ± 0.4	0.10 ± 0.03

of HCS$^+$ and OCS$^+$ dissociative recombination (Montaigne et al. 2005) and by including the CS photoionization (ionization potential ∼11 eV). These processes have direct impact on CS chemistry. The resulting network involves ∼450 species and ∼5000 reactions. Finally, the model computes the thermal structure of the PDR by solving the balance between the most important processes heating and cooling the gas (see Le Bourlot et al. 1993). Our *standard conditions* for the model of the Horsehead PDR include a power-law density profile (Eq. (2)) and a FUV radiation field enhanced by a factor $\chi = 60$ with respect to the Draine ISRF (see Table 6). Different sulfur gas phase abundances, S/H, have been investigated. To be consistent with PdBI CO observations, thermal balance was solved until the gas temperature reached a minimum value of 30 K, then a constant temperature was assumed.

4.2. Radiative transfer models

We have used a simple nonlocal non-LTE radiative transfer code to model our millimeter line observations. The code handles spherical and plane-parallel geometries and accounts for line trapping, collisional excitation, and radiative excitation by absorption of microwave cosmic background and dust continuum photons. Arbitrary density, temperature or abundance profiles, and complex velocity gradients can be included. A more detailed description is given in the Appendix. The choice of a nonlocal treatment is needed to analyze optically thick lines of abundant, high-dipole moment molecules, such as CS, in regions where the gas density is below the critical densities of the associated transitions. Table 5 shows the critical densities of observed C^{18}O, HCS$^+$ and CS lines. Under these conditions, radiative transfer and opacity effects may dominate the line profile formation. Our radiative transfer analysis has been used to infer abundances and physical conditions directly from observations but also to predict line spectra from the photochemical model results. The

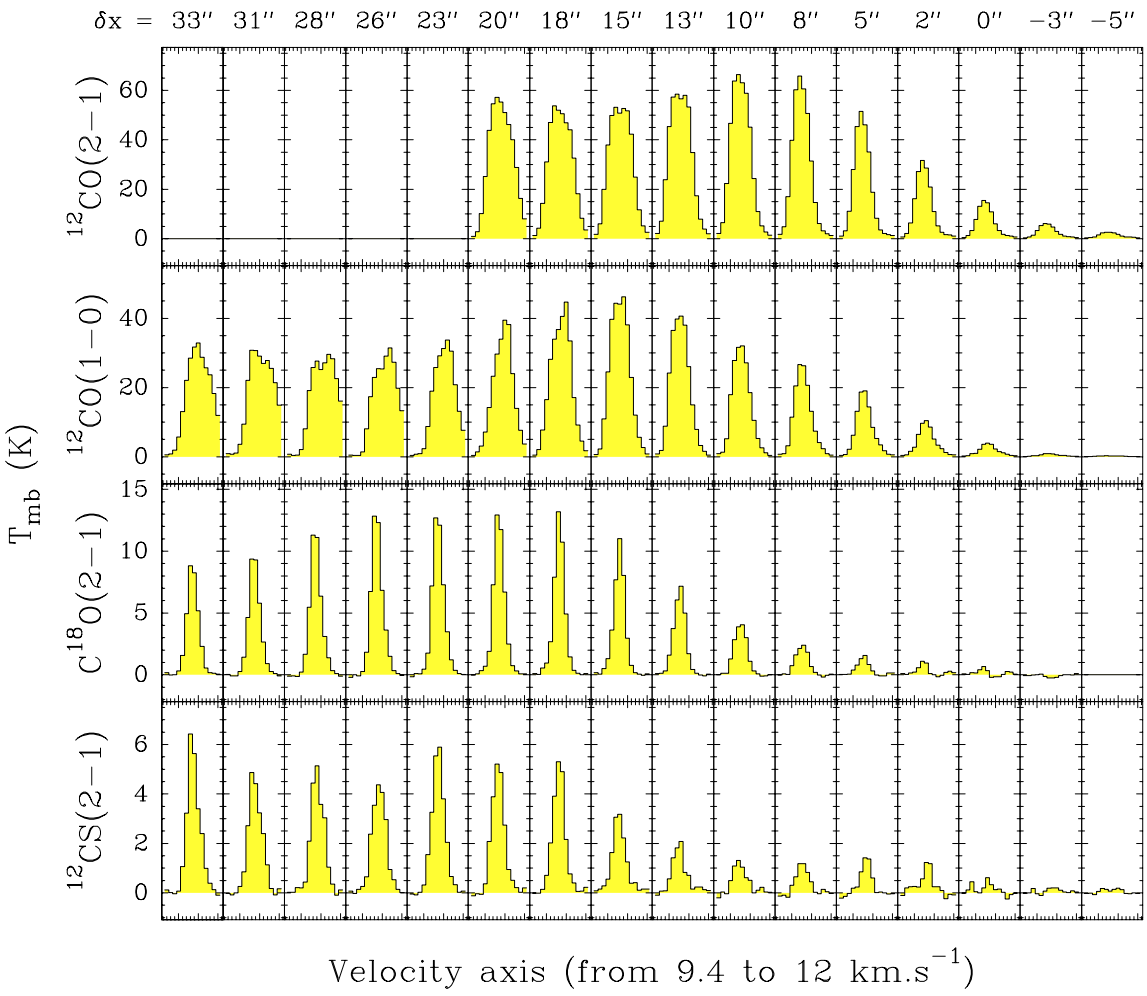

Fig. 3. Spectra along the direction of the exciting star at $\delta y = 0''$. ^{12}CO J = 1–0, C^{18}O J = 2–1 and ^{12}CS J = 2–1 spectra cubes were smoothed by a 15″-*FWHM* 1D-Gaussian along the y direction perpendicular to the illuminating star direction. Due to their small field of view (in particular in the y direction), the ^{12}CO J = 2–1 data were just smoothed by a 5″-*FWHM* circular Gaussian.

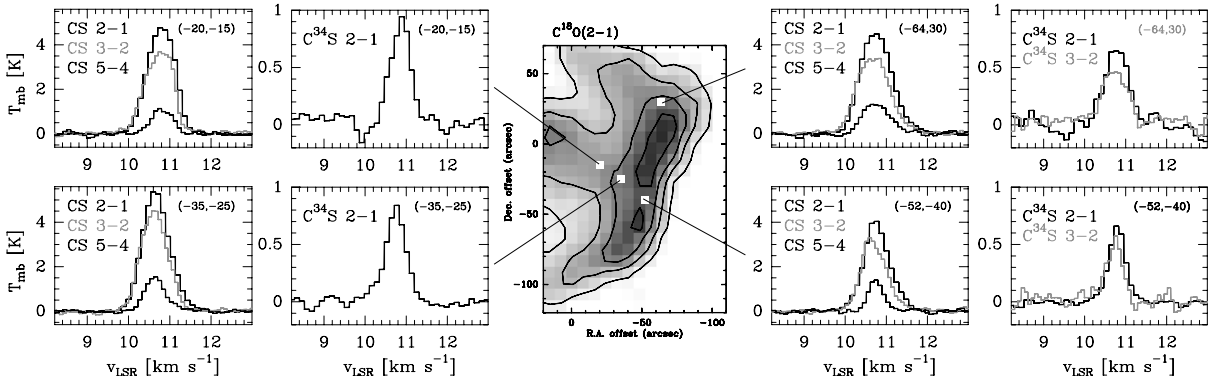

Fig. 4. IRAM-30 m CS J = 2–1, 3–2 and 5–4, and C^{34}S J = 2–1 and 3–2 single-dish observations (histograms) at different positions of the Horsehead PDR single-dish C^{18}O J = 2–1 emission centered at $\alpha_{2000} = 05^{h}40^{m}58^{s}$, $\delta_{2000} = -02°27'20''$ (from Hily-Blant et al. 2005).

following temperature dependent collisional rate coefficients[2] have been adopted:

– for CS: we have used the latest CS + He collisional rates from Lique et al. (2006), kindly provided by F. Lique prior to publication, scaled by the reduced mass factor $(\mu_{CS-H_2}/\mu_{CS-He})^{1/2}$. Most of the models were repeated with the older collisional rates of Turner et al. (1992).
– for C^{34}S: same as CS but using C^{34}S spectroscopy to compute collisional excitation rates through detailed balance.
– for C^{18}O: CO + H_2 de-excitation rates from Flower (2001) but using C^{18}O spectroscopy to compute collisional excitation rates through detailed balance.

[2] Some of them retrieved from BASECOL, a data base for collisional excitation data at `http://www.amdpo.obspm.fr/basecol`. We considered H_2, He and H as the collisional partners in all CS, C^{34}S, HCS$^+$ and C^{18}O excitation models. See Appendix.

Table 5. Einstein coefficients, transition upper level energies and critical densities for the range of temperatures considered in this work.

Molecule	Transition	A_{ij} (s^{-1})	E_i (K)	n_{cr} (cm^{-3})
$C^{18}O$	J = 2–1	6.01×10^{-7}	15.8	$\sim 8 \times 10^3$
HCS^+	J = 2–1	1.11×10^{-5}	6.1	$\sim 5 \times 10^4$
$C^{34}S$	J = 2–1	1.60×10^{-5}	6.9	$\sim 4 \times 10^5$
	J = 3–2	5.79×10^{-5}	13.9	$\sim 1 \times 10^6$
CS	J = 2–1	1.68×10^{-5}	7.1	$\sim 4 \times 10^5$
	J = 3–2	6.07×10^{-5}	14.1	$\sim 1 \times 10^6$
	J = 5–4	2.98×10^{-4}	35.3	$\sim 5 \times 10^6$

– for HCS^+: HCS^+ + He collisional rates from Monteiro (1984), scaled by the reduced mass factor $(\mu_{HCS^+-H_2}/\mu_{HCS^+-He})^{1/2}$, have been used.

5. Modeling and interpretation

5.1. CS, $C^{34}S$ and HCS^+ single-dish emission

In order to get a first order approximation of the CS excitation and column density, we have assumed that level populations are only determined by a Boltzmann distribution at a single rotational temperature. If one accepts that lines are optically thin, this approach corresponds to the widely used rotational-diagram. However, observed CS/$C^{34}S$ intensity ratios, and CS line profiles (see Fig. 4) clearly show that the low-J CS lines are optically thick towards the Horsehead. Therefore, we have included optical depth effects and built a rotational-diagram corrected for opacity through:

$$\ln \frac{N_i^{\rm thin}}{g_i} + \ln C_\tau = \ln N - \ln Q - \frac{E_i}{T_{\rm rot}} \quad (1)$$

where $N_i^{\rm thin}$ are the upper level populations determined from observations in the optically thin limit (underestimated if lines are optically thick), E_i is the upper i-level energy in K, Q is the partition function at $T_{\rm rot}$ and C_τ is the line opacity correction factor $\frac{\tau_{ij}}{1-e^{-\tau_{ij}}} > 1$ (Goldsmith & Langer 1999). We have performed this analysis at different cloud positions. Resulting diagrams are shown in Fig. 5 as a function of different CS J = 2–1 line opacities (τ_{2-1} = 0, 1 and 5). In the optically thin limit CS column densities are N(CS) $\sim 5 \times 10^{13}$ cm^{-2} and they have to be considered as lower limits. Low excitation temperatures ($T_{\rm rot} \sim$ 6–9 K) are also inferred from the rotational-diagrams. These values, much lower than expected gas temperatures in a PDR, are suggestive of radiative excitation effects in CS lines and level populations far from thermalization. Therefore, we only use the rotational-diagrams as input for the first iteration of a more complex analysis.

In order to obtain a more detailed overview of the CS excitation, we have made several statistical equilibrium calculations (see Appendix) around the expected physical conditions in the Horsehead. In particular, we have run a grid of single-component models for T_k = 10, 20, 30, 50 and 70 K, $n(H_2)$ = 10^4, 5×10^4, 10^5 and 5×10^5 cm^{-3}, and χ(CS) from 10^{-10} to 10^{-7}. As a reference value, the cloud total extinction is assumed to be constant and equal to A_V = 20 mag in all models, i.e. the spatial length is changed accordingly. Figure 6 specifically shows selected results for T_k = 30 K, which gives appropriate absolute intensities for the CS lines. In particular, integrated line intensity ratios of observed lines as a function of CS abundance for different densities are shown. Averaged ratios from

Table 6. Horsehead standard conditions and gas phase abundances.

Parameter	Value
Radiation field χ	60 (Draine units)
Cosmic ray ionization rate ζ	$5 \times 10^{-17} s^{-1}$
Density profile $n_H = n(H) + 2n(H_2)$	50 to 2×10^5 cm^{-3}
Line of sight spatial depth $l_{\rm depth}$	0.05–0.1 pc
Line of sight inclination angle φ	0° to 5°
He/H = n(He)/n_H	1.00×10^{-1}
O/H	3.02×10^{-4}
C/H	1.38×10^{-4}
N/H	7.95×10^{-5}
^{18}O/H	6.04×10^{-7}
Cl/H	1.00×10^{-7}
Si/H	1.73×10^{-8}
Mg/H	1.00×10^{-8}
F/H	6.68×10^{-9}
Na/H	2.30×10^{-9}
Fe/H	1.70×10^{-9}
P/H	9.33×10^{-10}

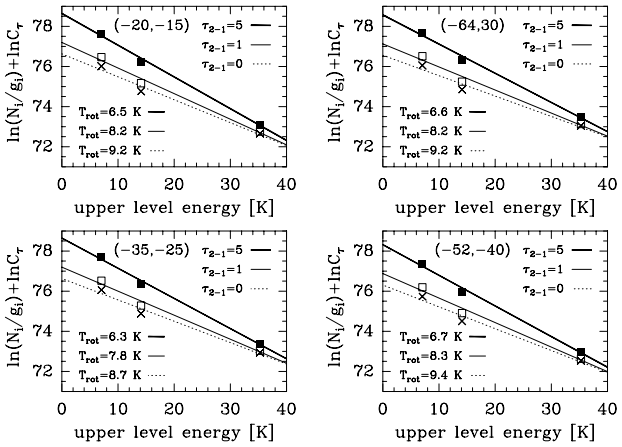

Fig. 5. CS rotational-diagrams corrected for line opacity effects at each observed position of Fig. 4. Rotational-diagrams for different considered CS J = 2–1 line opacities (τ_{2-1}) are shown in each box. Rotation temperatures for each opacity correction are also indicated.

CS single-dish observations are $\frac{3-2}{2-1} \sim 0.7$, $\frac{5-4}{2-1} \sim 0.2$ and $\frac{5-4}{3-2} \sim 0.3$. Therefore, densities $\geq 5 \times 10^4$ cm^{-3} are needed to populate the CS intermediate-J levels. On the other hand, for high densities ($\geq 5 \times 10^5$ cm^{-3}), collisions start to efficiently populate these levels and the predicted line ratios involving the CS J = 5–4 line become much larger than observed. Thus, mean densities are in the range $n(H_2) \simeq (0.5–1.0) \times 10^5$ cm^{-3}, i.e. lower than CS critical densities (Table 5). Excitation temperatures are predicted to be subthermal, $T_{\rm ex} < T_k$, especially for the highest frequency lines. Due to line-trapping, the maximum $T_{\rm ex}$ is reached at the center of the cloud, while it graduately drops at both surfaces where line photons are optically thin and line trapping is not efficient. The only exception is the CS J = 1–0 transition which shows an increase of the excitation temperature, $T_{\rm ex}^{1-0}$, at both surfaces. This rising in $T_{\rm ex}^{1-0}$ is due to the significant collisional excitation coupling from the J = 0 to J = 2 level, and to the large radiative de-excitation rates from J = 2 to J = 1 level. At both surfaces, where optically thin CS J = 2–1 line photons can easily escape from the cloud ($T_{\rm ex}^{2-1}$ decreases), the above excitation conditions favor the population of the J = 1 level with respect to the J = 0 level. Therefore, $T_{\rm ex}^{1-0}$ can reach large suprathermal values. A typical example is shown in Fig. A.2. Thus, within this

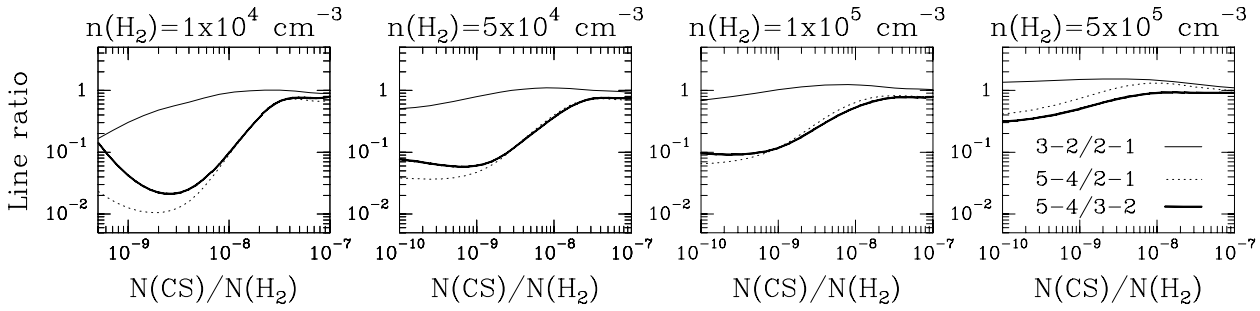

Fig. 6. Grid of CS single-component models assuming T_k = 30 K and a fixed extinction of 20 mag. Panels show different line ratios as a function of $\chi(CS)$. Each panel correspond to a single density, from $n(H_2) = 10^4$ to 5×10^5 cm^{-3}. Mean observed ratios are $\frac{3-2}{2-1} \simeq 0.7$, $\frac{5-4}{2-1} \simeq 0.2$ and $\frac{5-4}{3-2} \simeq 0.3$.

range of parameters and even if physical conditions are homogeneous, excitation gradients must be taken into account.

For these temperatures and densities, $T_k \simeq$ 20–30 K and $n(H_2) \simeq (0.5–1.0) \times 10^5$ cm^{-3}, the CS $\frac{5-4}{2-1}$ and $\frac{5-4}{3-2}$ line ratios are better fitted in the interval $\chi(CS) \simeq (0.2–1.0) \times 10^{-8}$. Nevertheless, the $\frac{3-2}{2-1}$ line ratio is systematically predicted to be larger than observed in these single-component models. Therefore, a more complex density structure and/or additional opacity effects in low-J CS lines may be affecting the observed profiles. The latter hypothesis is clearly favored by the fact that the C^{34}S $\frac{3-2}{2-1}$ line intensity ratio is larger (~0.9) than the CS $\frac{3-2}{2-1}$ ratio (~0.7) and thus closer to the single-component model predictions. Since the C^{34}S emission is optically thin, radiative transfer effects are less important and C^{34}S column densities can be accurately determined.

C^{34}S single-component radiative transfer models for selected positions within the region have been run (Fig. 7). Since C^{34}S emission can arise from different gas components of higher density, not resolved by the large single-dish beam, we have modeled each position in spherical geometry. This allows to explore different components of different beam filling factors. The maximum extinction in the models varies from A_V = 20 to 12 mag depending on the cloud position. These values are consistent with those obtained from single-dish 1.2 mm dust continuum emission observations (Teyssier et al. 2004; Pety et al. 2005a). Following our previous general excitation calculations we have considered gas temperatures in the range 20–25 K. For these conditions, densities between $n(H_2) = 7 \times 10^4$ and 1.2×10^5 cm^{-3} satisfactorily reproduce the observed C^{34}S absolute intensities. Best fits are obtained for turbulence velocities (see Appendix for the definition of v_{turb}) between 0.3 and 0.4 km s^{-1} (Table 7). Although C^{34}S is slightly enhanced where C^{18}O decreases, we have averaged the 4 positions to find the mean C^{34}S abundance in the region covered with single-dish observations and found $\chi(C^{34}S) = (3 \pm 1) \times 10^{-10}$. Since nucleosynthesis models favor a constant galactic ^{32}S/^{34}S ratio and many observations reproduce the solar ratio within their error bars (Wannier et al. 1980; Frerking et al. 1980), especially in local diffuse clouds (Lucas & Liszt 1998), we adopt ^{32}S/^{34}S = 23 here as the isotopic ratio in the Horsehead. Therefore, the derived $\chi(C^{34}S)$ abundance translates to $\chi(CS) = (7 \pm 3) \times 10^{-9}$. The same physical conditions at each position have been used to model the HCS$^+$ J = 2–1 lines (see Fig. 8). Lines are reproduced for an averaged abundance of $\chi(HCS^+) = (4 \pm 2) \times 10^{-11}$, therefore, a CS/HCS$^+$ $\simeq$ 175 abundance ratio is derived.

Using the CS abundance inferred from the C^{34}S analysis, we have now tried to fit the CS lines at each position. Since a single-component model does not reproduce the observed line ratios and absolute intensities, we have explored other possibilities. In principle, CS low-J lines are optically thick and may not trace the high density gas revealed by C^{34}S, especially if the

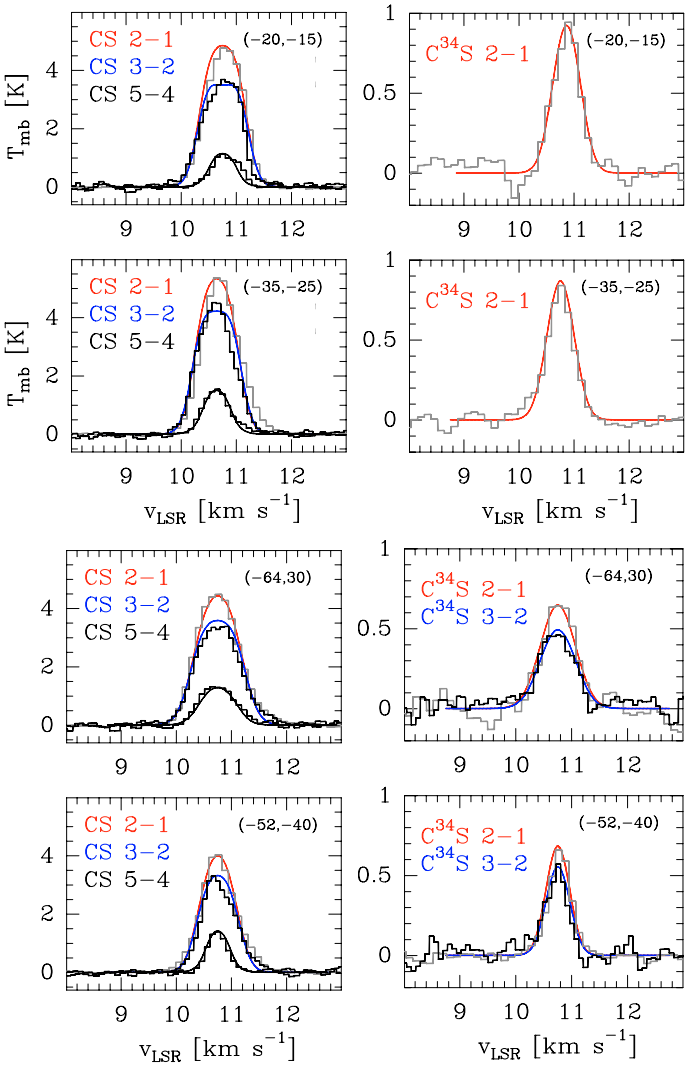

Fig. 7. Radiative transfer models for CS and C^{34}S discussed in the text (curves) that best fits the IRAM-30 m observations (histograms). Offsets in arcsec refer to the (0,0) position of the C^{18}O(2–1) map (see Fig. 4). Predicted line profiles have been convolved with the telescope angular resolution at each frequency. Intensity scale is in main beam temperature.

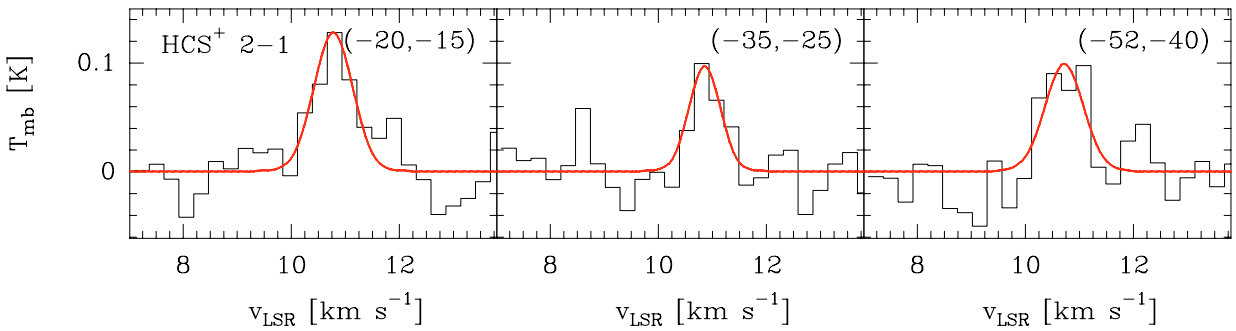

Fig. 8. IRAM-30 m HCS^+(2–1) single-dish observations (histograms) at different positions of the Horsehead. Offsets in arcsec refer to the (0,0) position of the $C^{18}O$(2–1) map (see Fig. 4). Radiative transfer models for HCS^+ at selected positions are also shown (curves). Predicted line profiles have been convolved with the telescope angular resolution at each frequency. Intensity scale is in main beam temperature.

Table 7. Single-component radiative transfer model parameters.

Parameter	Value
T_k	20–25 K
$n(H_2)$	(7–12) × 10^4 cm^{-3}
v_{turb}	0.3–0.5 km s^{-1}
$\chi(C^{34}S)$	(3 ± 1) × 10^{-10}
$\chi(HCS^+)$	(4 ± 2) × 10^{-11}

Table 8. Two-component radiative transfer model parameters.

Parameter	Value
T_k	20–25 K
$n(H_2)$	(3–7) × 10^4 cm^{-3}
dense component	(2–6) × 10^5 cm^{-3}
(filling factor)	0.3
v_{turb}	0.3–0.4 km s^{-1}
dense component	0.2–0.3 km s^{-1}
χ(CS)	(7 ± 3) × 10^{-9}
S/H	(3.5 ± 1.5) × 10^{-6}

medium is inhomogeneous and dense clumps and a more diffuse interclump medium coexist. The same argumentation has been used to interpret HCN and $H^{13}CN$ observations in the Orion Bar PDR (Lis & Schilke 2003). In addition, it is well known that low-J CS lines may not be a good column density tracer if their emission is scattered by a low density halo (González-Alfonso & Cernicharo 1993). This process can be a common effect in optically thick lines of high-dipole moment molecules such as CS or HCO^+ (Cernicharo & Guélin 1987). In this scenario, the CS J = 3–2 and 2–1 lines from the dense medium will be attenuated and scattered over larger areas than the true spatial extend of the dense clumps. This possibility has been analyzed in more detail in the next section. Fortunately, observations of the CS J = 5–4 line allow to directly trace the dense clumps more safely (Table 8). In particular, we found that these lines can only be reproduced with denser gas components, $n(H_2) = (4 \pm 2) \times 10^5$ cm^{-3}, not resolved by the ∼10″ beam of the IRAM-30 m telescope at ∼250 GHz. Note that the CS J = 5–4 line widths are fitted if the turbulent velocity in the denser gas is ∼0.2 km s^{-1}, a factor 2 lower than the one required by the $C^{34}S$ J = 3–2 and 2–1 lines (Fig. 7). Thus, a different spatial origin for this line emission is favored.

At this stage we have a general knowledge of the CS and HCS^+ excitation and abundance in the region. In the following sections we concentrate in the photochemistry of these species. Only higher angular observations provide the appropriate linear scale to resolve the most important physical gradients in the PDR edge. Hence, interferometric observations should allow a better comparison with chemical predictions.

5.2. The PDR edge

PdBI $C^{12}O$ J = 2–1, 1–0, $C^{18}O$ J = 2–1, and CS J = 2–1 observations along the direction of the exciting star (at $\delta y = 0''$) are shown in Fig. 3. Here we take these spectra as representative of the PDR edge and try to constrain its physical conditions through a combined analysis of photochemical and radiative transfer models. Both models use a unidimensional plane-parallel description of the geometry. Although some physical processes require more complex geometries, the main physical and chemical gradients across the illuminated direction can be consistently described in this way. Plane-parallel geometry was judged to be the best approach for this edge-on PDR since H_2 and PAH emissions are only observed at the illuminated edge and not deeper inside the cloud (Habart et al. 2005).

In this analysis, we have used the PdBI CS J = 2–1 and $C^{18}O$ J = 2–1 lines. As low-J ^{12}CO optical depths are very high, they do not trace the bulk of material. The intensity peak of these lines only provide a good estimation of the CO excitation temperatures (i.e. a lower limit to the gas temperature). Since the asymptotic brightness temperature of CO J = 1–0 lines is ∼30 K, we take this value as the minimum of T_k in the PDR. We note that lower temperatures do not reproduce the observed line intensities. For the rest of the (warmer) positions closer to the PDR edge, the gas temperature was determined by solving the thermal balance. The predicted gas temperature in the density peak is ∼50 K while it rises to ∼200–250 K in the H_2 emitting regions where the density is $n_H \simeq 10^3$–10^4 cm^{-3}. More exact temperature values require observations of higher-J CO lines at comparable spatial resolution. We are currently analysing ^{13}CO J = 3–2 data from the SMA interferometer.

Regarding the density structure, both the observed H_2 and PAH mid-IR emission, together with their spatial segregation, are much better reproduced with a steep density gradient than with an uniform density (Habart et al. 2005). The same density gradient is needed to correctly reproduce the observed offset between the small hydrocarbons (Pety et al. 2005a) and H_2 emission (where the density is not at its peak). Therefore, in order to reproduce PdBI observations of CS and $C^{18}O$, a steep power-law density gradient at the illuminated regions and a step-density in the more shielded region have been assumed.

The following methodology was carried out: a full PDR model with Horsehead *standard conditions* (see Sect. 4.1)

was run with a particular choice of the density gradient described in Eq. (2). Afterwards, the PDR output was used as input for the nonlocal radiative transfer calculation in a fashion described in Appendix A.2. In this way, physical parameters can be tuned more accurately by iteration of different radiative transfer models. Once better parameters have been found, a new PDR computation is performed with this choice of physical parameters. Hence, the most appropriate physical and chemical description of the PDR edge was found through the *PDR model→transfer model→check with observations→transfer model→PDR model* iterative process. Therefore, synthetic CS and $C^{18}O$ abundance profiles are consistently computed as a function of the edge distance δx (in arcsec) and directly compared with observations.

Different PDR spatial depths were investigated. Depending on the adopted density profile, the spatial depth $l_{\rm depth}$ is determined by the line of sight visual extinction. However, the $A_{\rm V}$ value depends on the method used to measure it. If optically thin 1.2 mm dust emission is used (Teyssier et al. 2004; Pety et al. 2005a; Habart et al. 2005), the resulting column densities depend on the usually unknown grain properties and on the assumed temperature. Taking into account our poor knowledge of the cloud thermal structure, a factor ∼2 of uncertainty in $A_{\rm V}$ can be assumed. In addition, the angular resolution of millimeter continuum observations is at least a factor ∼2 worse than PdBI molecular line observations. Due to the steep decrease of the density towards the edge, and due to the ∼11″ beam of 1.2 mm continuum observations, the observed emission peak will appear deeper inside the cloud, shifted a few arcsec from the real density peak (which is closer to the edge). Therefore, together with the PDR edge location, the exact peak density position can also be uncertain by a few arcsec. Finally, beam dilution has to be also taken into account when comparing single-dish versus interferometric observations. Here we have chosen $l_{\rm depth} = 0.05$–0.1 pc, which implies extinction peaks around $A_{\rm V} \simeq$ 15–30 mag. These values are expected in compact globules (Reipurth & Bouchet 1984). Since CS and $C^{18}O$ excitation and line transfer are quite different, the following combined analysis provides an accurate description of the edge density structure. The empirical density profile in the models, $n_{\rm H} = n({\rm H}) + 2n({\rm H_2})$, as a function of δx is:

$$n_{\rm H}(\delta x) = \begin{cases} n_{\rm H}(0) + [n_{\rm H}(\delta x_1) - n_{\rm H}(0)] \left(\frac{\delta x}{\delta x_1}\right)^{\beta}; \delta x_1 \geq \delta x \geq 0 \\ n_{\rm H}(\delta x_1); \delta x_2 \geq \delta x > \delta x_1 \\ n_{\rm H}(\delta x_2); \delta x > \delta x_2 \end{cases} \quad (2)$$

where δx is the distance away from the PDR edge, $n_{\rm H}(0)$ is the ambient density at the edge, and $n_{\rm H}(\delta x_1)$ and $n_{\rm H}(\delta x_2)$ are constant densities in the $\delta x_2 \geq \delta x > \delta x_1$ and $\delta x > \delta x_2$ regions respectively. Selected photochemical models are shown in Fig. 9. The normalized population of the H_2 $v = 1$, $J = 3$ level is shown in the *upper* panel and is used to place the δx-axis origin of the models and thus to accurately check with observations. Although some uncertainty in the location of the PDR edge exists, we place the peak of this curve at the maximum of observed H_2 1–0 S(1) 2.12 μm excited line ($\delta x \sim 10''$; Habart et al. 2005). Best models are found for a peak density around $n_{\rm H}(\delta x_1) = 2 \times 10^5$ cm^{-3}. This density is reached in a length of ∼2.5″–5″ (or 5–10×10^{-3} pc) and stays constant in a length of $\delta x_2 - \delta x_1 \lesssim 20''$ (or 0.04 pc). In order to fit the smooth decrease of $C^{18}O$ emission and also of the 1.2 mm continuum emission, the density has to decrease again by at least a factor ∼2. We have simply modeled this as a step-function for $\delta x > \delta x_2$ and decrease the density to $n_{\rm H}(\delta x_2) = 10^5$ cm^{-3}. We have chosen $\delta x_1 = 12''$ and $\delta x_2 = 30''$. Our models confirm that high density gas and a large gradient slope, $\beta \sim 3$–4, are needed to reproduce the PdBI and H_2 observations (Habart et al. 2005), although we found a slightly smaller gradient scale length.

As proposed by Habart et al. (2005) the PDR edge can be slightly inclined with respect to the line of sight by a small angle φ. In plane-parallel geometry, the maximum inclination can be estimated assuming that the observed spatial extend of the H_2 emission, $d_{\rm H_2}$, is mainly due to the projection of $l_{\rm depth}$ in the plane of the sky, thus $\sin\varphi \simeq d_{\rm H_2}/l_{\rm depth}$. Since $d_{\rm H_2} \sim$ 0.01 pc, an inclination angle $\varphi \sim 5°$, has been considered in the radiative transfer models (see Appendix A.2). As expected, even such a small inclination shifts the emission peak significantly and should therefore be taken into account. Figure 10 shows the PdBI $C^{18}O$ line observations and the combined PDR+transfer modeling including such geometrical effects. The agreement is excellent, probably favored by the well-established CO photochemistry (Fig. 9) and because $C^{18}O$ $J = 2$–1 lines do not show complex radiative transfer effects ($\tau_{2-1} \sim 0.8$).

To analyse the spatial distribution of the CS abundance predicted by photochemical models at the PDR edge we have also tried to fit the PdBI CS $J = 2$–1 lines. Figure 9 shows the effects of different sulfur abundances; S/H = 2×10^{-5} and S/H = 2×10^{-6}. Figure 11 (no inclination) and Fig. 12 (inclination considered) show the resulting synthetic CS map, using S/H = 2×10^{-6} and a minimum gas temperature of 30 K, over PdBI observations at two constant δy cuts ($\delta y = 30''$ and $0''$). Contrary to $C^{18}O$, the CS emission detected with the PdBI at a fixed δx near the edge shows an emission gradient in the δy direction, e.g. line peaks are brighter as δy increases. As a consequence model predictions fit better the $\delta y = 30''$ cut than the $\delta y = 0''$ one. Besides, larger gas phase sulfur abundances are obtained if the bulk of the gas in the PDR edge is warmer, i.e. minimum gas temperatures of ∼100 K (Fig. 9, right panel). This may be an indication of larger temperatures at the cloud edge and lower sulfur depletions. Note that an accurate estimation of the CS abundance at high resolution from a single PdBI line is not straightforward. Such determination requires aperture synthesis observations of additional CS lines to have a minimum idea of the CS excitation in different positions.

In addition, since $C^{34}S$ observations at the same high-angular resolution were not available, we could not estimate additional opacity effects in previous PdBI CS models ($\tau_{2-1} \gtrsim 2$). In the following we have tried to estimate the worse possible scenario affecting the CS lines in the line-of-sight, i.e. the presence of a surrounding low density halo. Of course, the greatest effect can appear in the shielded regions where the gas column density is largest. Therefore we modelled a typical position where CS is well spatially resolved with the following parameters: $l_{\rm depth} =$ 0.1 pc, $T_k = 30$ K, $n({\rm H_2}) = 10^5$ cm^{-3}, $v_{\rm turb} = 0.35$ km s^{-1} and $\chi({\rm CS}) = 7 \times 10^{-9}$, (the averaged CS abundance obtained from the detailed CS and $C^{34}S$ excitation analysis of previous section). We consider in addition that a low density halo of diffuse gas with the same χ(CS) surrounds the region. We take $T_k =$ 10 K, $v_{\rm turb} = 0.7$ km s^{-1} and densities in the interval $n({\rm H_2}) =$ $(5$–$10) \times 10^3$ cm^{-3}. The same modeling was carried out for $C^{34}S$. Figure 13 shows model results. As expected, a low density halo efficiently self-absorbs CS line photons in the most opaque lines, i.e. the low-J CS lines. As a result, the observed CS line intensities are attenuated and abundances can be easily underestimated. However, this effect can be different at different positions, since the line opacity also changes. Apart from uncertainties in sulfur chemistry or instrumental effects in interferometric observations, diffuse gas can also contribute to explain differences between models and observations in Figs. 11 and 12. Since, optically

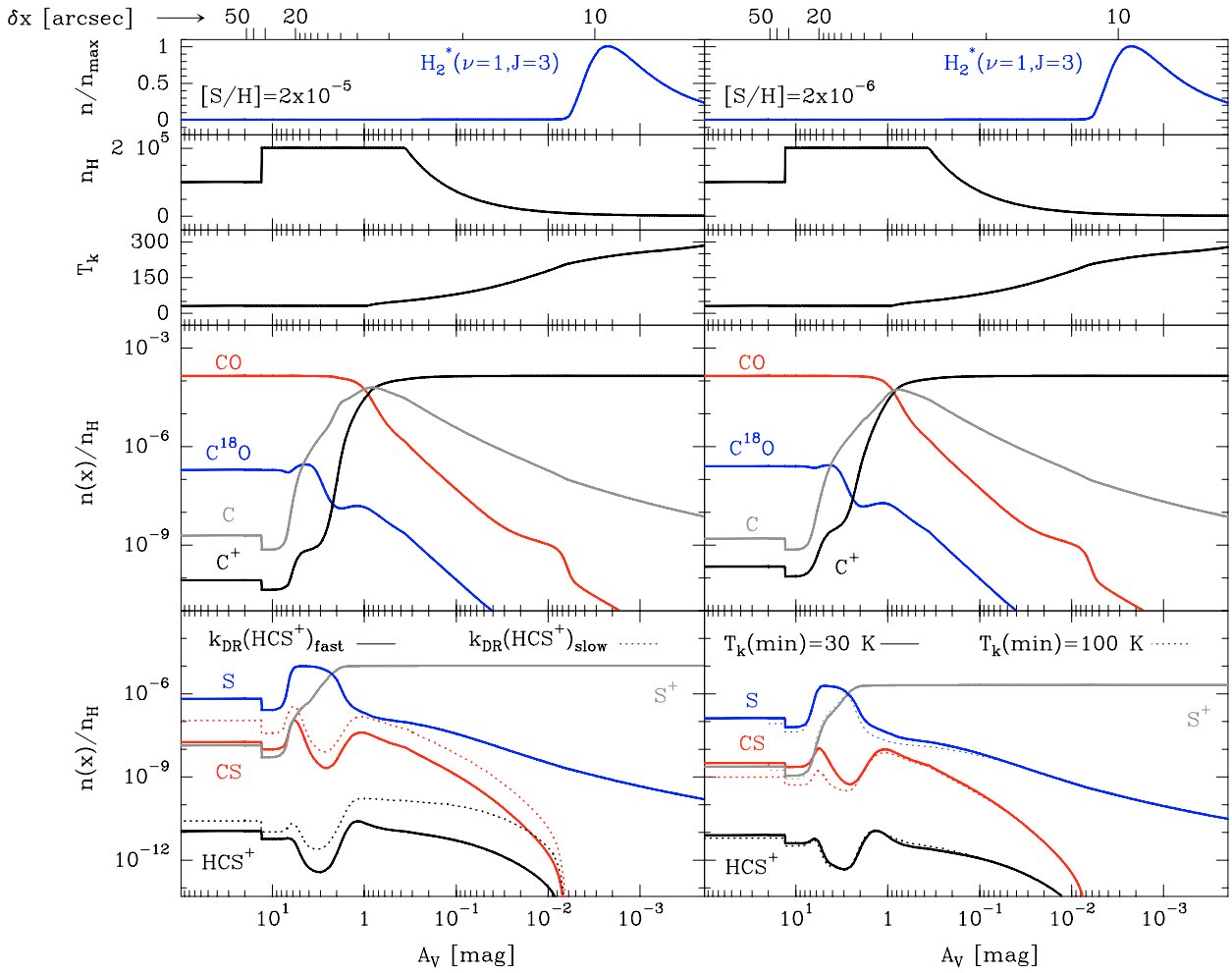

Fig. 9. Photochemical models using a unidimensional PDR code for two different sulfur gas phase abundances, (S/H = 2×10^{-5}; *left*) and the minimum value found for the Horsehead (S/H = 2×10^{-6}; *right*). The predicted normalized population of the H_2 $v = 1$, $J = 3$ level is shown in the *upper* panel and is used to place the δx-axis origin for the models. The peak of this curve is placed at the maximum of the observed H_2 1–0 $S(1)$ 2.12 μm line emission ($\delta x \sim 10''$; Habart et al. 2005). Next panel shows the density profile ($n_H = n(H) + 2n(H_2)$ in cm^{-3}) used in the PDR calculations that better fits the CS and $C^{18}O$ IRAM-PdBI observations. Next panel shows the gas temperature (in K) consistently computed in thermal balance until reaches a minimum value of 30 K. *Lower* panels show the spatial variation of $C^{18}O$/CO/C/C^+ and CS/HCS^+/S/S^+ abundances (relative to n_H) across the PDR. The far-UV radiation field is $\chi = 60$ times the Draine field. Chemical rates are those of the *Ohio State University (osu)* gas-phase chemical network (September 2005 release) plus several modifications (see text). *Bottom left* panel shows the effect of using the older rate and branching ratios for the HCS^+ dissociative recombination on the CS and HCS^+ abundances (dashed curves). *Bottom right* panel shows the effect of using a minimum gas temperature of 100 K in the chemistry. Lower CS abundances and thus larger S/H values are possible as the temperature increases (dashed curves).

thick lines are affected by this effect (Fig. 13), only the observation of ^{13}CS or $C^{34}S$ isotopologues can help to provide more accurate abundance determinations. In the following, the CS chemistry is analyzed in more detail.

5.3. CS chemistry and S-abundance

Predicted $C^{18}O$/CO/C/C^+ and CS/HCS^+/S/S^+ structures for a unidimensional PDR with Horsehead *standard conditions* are shown in Fig. 9 (see Sect. 4.1). Variation of the sulfur elemental abundance almost does not affect the CO or $C^{18}O$ abundance profiles, but it slightly modifies the predicted C/C^+ abundance profiles because charge transfer reactions between C^+ and S, and between C and S^+ are clearly altered by the sulfur depletion. The following results are of course determined by our present knowledge and uncertainties on S-chemistry, and on reaction rates at different temperatures. According to the latest *ion storage ring* experiments (Montaigne et al. 2005), only 19% of the HCS^+ dissociative recombination results in CS + H while the fracture of the C-S bond dominates the dissociation (81%). Since these experiments can not separate the contribution of the CH + S or SH + C channels in the latter process, we have adopted the same branching ratio (0.405) for both channels. The reaction rate coefficient is $k_{DR}(HCS^+)_{fast} = 9.7 \times 10^{-7}(T/300)^{-0.57}$ cm^3 s^{-1}. We have also included the latest OCS^+ dissociative recombination rates from Montaigne et al. (2005). The CS + O production channel now occurs at a rate 3 times slower than in previous chemical networks. All these modifications clearly influence the amount of CS formed from a given sulfur abundance, and thus the sulfur depletion estimations. Figure 9 (left panel) also shows the effect of adopting the older HCS^+ and OCS^+ dissociative recombination rates and branching ratios. In particular, $k_{DR}(HCS^+)_{slow} = 5.8 \times 10^{-8}(T/300)^{-0.75}$ cm^3 s^{-1}. However, since $HCS^+ + e^- \rightarrow CS + H$ was the only channel considered and the $OCS^+ + e^- \rightarrow CS + O$ process was faster, smaller sulfur abundances were required to obtain the same CS abundances.

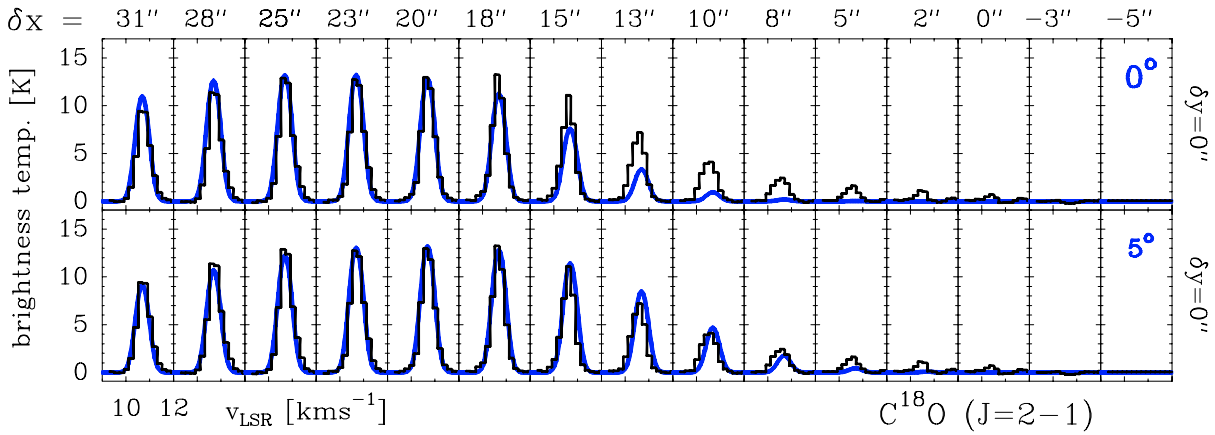

Fig. 10. IRAM-PdBI $C^{18}O$ J = 2–1 spectra along the direction of the exciting star at $\delta y = 0''$ (histograms). Radiative transfer models using the output of PDR models for $C^{18}O$ (blue curve) for a density gradient and physical conditions discussed in the text. *Lower panel* shows inclination effects assuming that the PDR is inclined relative to the line of sight by a $\varphi = 5°$ angle. Modeled line profiles have been convolved with an appropriate Gaussian beam corresponding to each synthesized beam. Intensity scale is in brightness temperature and abscissa in LSR velocity.

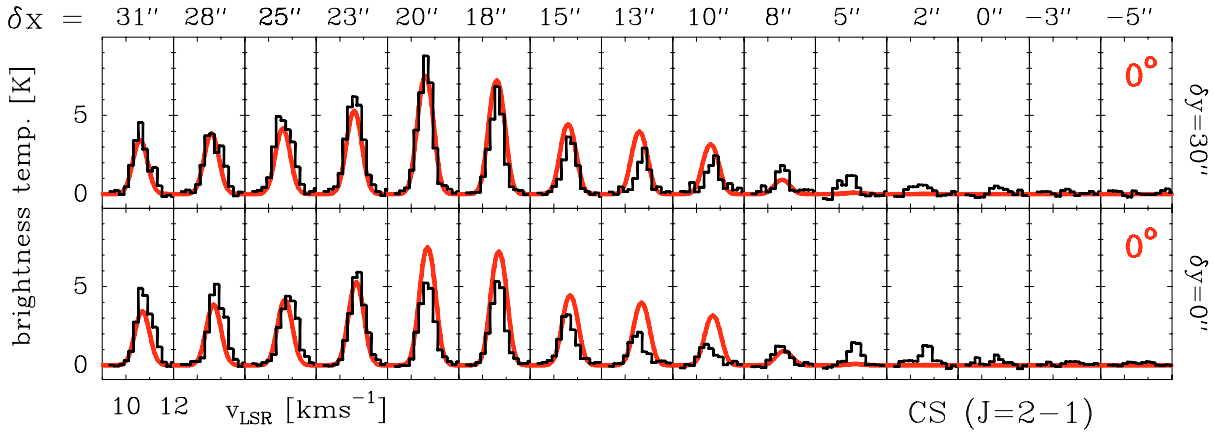

Fig. 11. IRAM-PdBI CS J = 2–1 spectra along the direction of the exciting star at $\delta y = 30''$ (*upper panel*) and $\delta y = 0''$ (*lower panel*). Radiative transfer models using the output of PDR models for CS (red curve) for a density gradient and physical conditions discussed in the text (assuming that the PDR is not inclined relative to the line of sight). Modeled line profiles have been convolved with an appropriate Gaussian beam corresponding to each synthesized beam. Intensity scale is in brightness temperature and abscissa in LSR velocity.

In the most external layers of the cloud, still dominated by the FUV radiation field, CS is predominantly formed by HCS^+ dissociative recombination and principally destroyed by photodissociation and charge transfer with H^+. Once the gas is shielded, OCS^+ dissociative recombination and reaction of C with SO also contributes to CS formation, while its destruction is now governed by ion-molecule reactions, mainly with HCO^+ but also with H_3O^+. These last two reactions with abundant molecular ions return HCS^+ again. The peak abundance of HCS^+ occur at $A_V \lesssim 2$ mag, where it is formed by reaction of CS^+ with H_2 and destroyed by dissociative recombination. For this reason, an order of magnitude change in $k_{DR}(HCS^+)$ clearly modifies its peak abundance in the outer PDR layers. In the more shielded regions, HCS^+ destruction is dominated by dissociative recombination and reaction with atomic oxygen to form HCO^+ and OCS^+. Since the predicted CS abundance scales with S/H, and CS formation is dominated by HCS^+ dissociative recombination, we have used our $CS/C^{34}S/HCS^+$ observations and modeling to estimate S/H.

Figure 14 shows results of a grid of photochemical models for different sulfur elemental abundances from S/H = 10^{-8} to 2×10^{-5}, using the latest HCS^+ and OCS^+ dissociative recombination rates. CS and HCS^+ abundances with respect to H_2 are shown as a function of S/H at two different PDR positions ($A_v \sim 10$ and ~ 2 mag respectively; see Fig. 9). Densities at these positions are the same, $n(H_2) = 10^5$ cm^{-3}, but we have taken different PDR positions in order to plot the HCS^+ maximum abundance and to get the CS/HCS^+ ratio closer to observations. Inside the cloud, the predicted maximum HCS^+ abundances are a factor $\sim$3 lower than observed. Horizontal shaded regions mark the CS and HCS^+ abundances derived from observations and radiative transfer modeling. For clarity, HCS^+ abundances have been multiplied by a factor of 1000. Finally, the vertical shaded region shows the estimated sulfur elemental abundance in the Horsehead derived from the overlap region between observed and predicted abundances. We derive S/H $\sim (3.5 \pm 1.5) \times 10^{-6}$ as the mean value for the PDR. Note that CS is used for the upper limit and HCS^+ for the lower limit. However, according to the inferred HCS^+ abundance, larger sulfur abundances are still possible.

6. Discussion

Our multi-transition single-dish and aperture synthesis observations and modeling of CS and related species allow us to

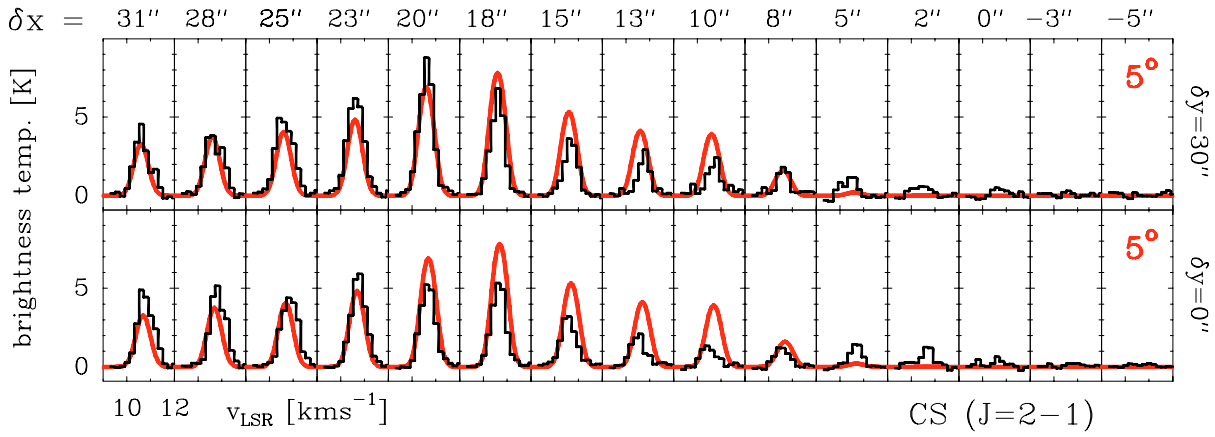

Fig. 12. IRAM-PdBI CS J = 2–1 spectra along the direction of the exciting star at δy = 30″ (*upper panel*) and δy = 0″ (*lower panel*). Radiative transfer models using the output of PDR models for CS (red curve) for a density gradient and physical conditions discussed in the text (assuming that the PDR is inclined relative to the line of sight by a $\varphi = 5°$ angle). Modeled line profiles have been convolved with an appropriate Gaussian beam corresponding to each synthesized beam. Intensity scale is in brightness temperature and abscissa in LSR velocity.

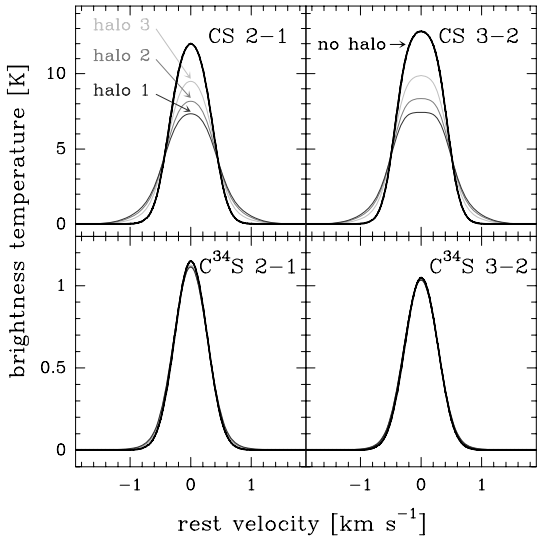

Fig. 13. CS and $C^{34}S$ synthetic line profiles for a cloud with a depth of 0.1 pc, T_k = 30 K, $n(H_2) = 10^5$ cm^{-3} and $\chi(CS) = 7 \times 10^{-9}$ (thick curves). Thin curves show the resulting spectra if the same cloud is surrounded by different diffuse halos (3: $n(H_2) = 5 \times 10^3$ cm^{-3}, 2: $n(H_2) = 8 \times 10^3$ cm^{-3} and 1: $n(H_2) = 1 \times 10^4$ cm^{-3}). The CS abundance in the cloud is determined more precisely from CS high-J and $C^{34}S$ low-J observations, otherwise it is underestimated. Note that the intensity levels are comparable to those observed in the Horsehead.

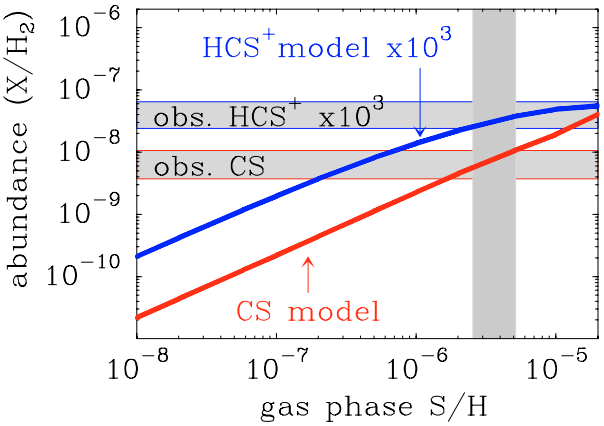

Fig. 14. Photochemical model predictions for the physical and FUV illuminating conditions prevailing in the Horsehead PDR showing the CS and HCS^+ abundance as a function of the sulfur gas phase abundance. Horizontal shaded regions show the CS and HCS^+ abundances derived from the single-dish observations and radiative transfer modeling. Note that for clarity HCS^+ abundances have been multiplied by a factor of 1000. The shaded vertical region shows the estimated sulfur abundance in the Horsehead nebula derived from the constrained fits of CS and HCS^+ abundances.

constrain the sulfur gas phase chemistry in the Horsehead PDR and it also gives some insights on the dense gas properties.

6.1. Densities

The densities found in this work, $n(H_2) \simeq 10^5$ cm^{-3}, are larger to those inferred from previous studies based on single-dish CO observations (Abergel et al. 2003; Teyssier et al. 2004). This may be the indication of an inhomogeneous medium characterized by a interclump medium (well traced by CO) and a denser clump medium (better traced by high dipole molecules). Both high densities and inhomogeneous medium are common in other PDRs such as the Orion Bar (Lis & Schilke 2003). In particular, we have shown that unresolved gas components up to $n(H_2) \simeq$ (2–6) $\times 10^5$ cm^{-3} are required to explain the CS J = 5–4 line emission in the Horsehead. However, Abergel et al. (2003) did not find inhomogeneities in analysing ISOCAM images of the Horsehead. Nevertheless, they noted that clumpiness at scales smaller than the upper limit of the FUV penetration depth (~0.01 pc) could not be excluded. Our best models of the CS J = 5–4 line emission require an unresolved component with a radius of $\sim 5 \times 10^{-3}$ pc. This component can of course be further fragmented itself. Nevertheless, it is difficult to distinguish between clumpiness at scales below ~0.01 pc and the presence of a lower density envelope surrounding the cloud. Since CO J = 1–0 and 2–1 line opacities easily reach large values, their observed profiles are formed in the very outer layers of the cloud and thus they can arise from the most diffuse gas ($n(H_2) \sim 5 \times 10^3$ cm^{-3}). Interferometric observations of intermediate-J lines of high dipole species such as CS or HCO^+ will help to clarify the scenario.

The high angular resolution provided by PdBI CS and $C^{18}O$ observations reveals that the Horsehead PDR edge is

characterized by steep density gradient rising from ambient densities to $n(H_2) \sim 10^5$ cm^{-3} in a length of ∼0.01 pc and kept roughly constant up to ∼0.05 pc, where the density decreases again at least a by factor 2. The exact density values still depend on the assumed cloud depth and temperatures. In any case, the inferred *shell* of dense molecular gas has high thermal pressures ∼(5–10) × 10^6 K cm^{-3} and this can be the signature of the processes driving the slow expansion of the PDR. Therefore, the most shielded clumps undergo effective line cooling and the regions of lower density should be compressed due to their lower internal pressure. Recent hydrodynamical simulations of the expansion of ionization and dissociation fronts around massive stars also predict that a high density molecular *shell* (10–100 times the ambient density) will be swept up behind the ionization front (Hosokawa & Inutsuka 2005a,b). The density, pressure and temperature profiles and values predicted by these simulations at ∼0.5 Myr (the Horsehead formation timescale derived from its velocity gradients by Pound et al. 2003 and Hily-Blant et al. 2005) qualitatively reproduce the values inferred from our molecular line observations and modeling. Hence, a shock front driven by the expansion of the ionized gas is probably compressing the cloud edge to the high densities observationally inferred in this work. Specific hydrodynamical simulations for the particular source physical conditions and comparison with observations will be appreciated. As noted by Hosokawa & Inutsuka (2005), the dynamical expansion of a HII region, PDR and molecular *shell* in a cloud with a density gradient has not been studied well. We suggest the Horsehead PDR as a good target.

6.2. Temperatures

Molecular excitation, radiative transfer and chemical models are used to derive realistic abundances. The gas temperature impacts many aspects of these computations (e.g. chemical reaction rates and collisional excitation), and thus, the density and abundance uncertainties also reflects our incomplete knowledge of the thermal structure. The problem is not straightforward, since a steep temperature gradient is also expected in PDRs, and also because the most appropriate tracers of the warm gas lie at higher frequencies. The Horsehead PDR may not be an extreme case, since its FUV radiation field is not very high and photoelectric heating alone will not heat the gas to high temperatures as long as the gas is FUV-shielded. Nevertheless, our thermal balance calculations quickly lead to $T_k \simeq 10$ K. According to observations, this temperature is too low, especially in the first $\delta x \sim 30''$ representing the PDR edge. In this work we have (observationally) adopted $T_k = 30$ K as the minimum gas temperature in our PDR calculations. In forthcoming works we will concentrate on the thermal structure of the PDR. Here we only note that either the cooling is not so effective and/or extra heating mechanisms need to be considered. The cosmic ray ionization rate was also increased by a factor ∼5 but it only modifies the gas temperature by $\Delta T_k \sim 4$ K.

Under these circumstances we have to conclude that the gas, or at least a fraction of it, is likely to be warmer than predicted. We note that this problem is not new. Again, high-J ^{13}CO and NH_3 observations have previously probed the existence of warm gas (∼150 K) in regions where standard heating mechanisms fail to predict those values (Graf et al. 1990; Batrla & Wilson 2003). More recently, Falgarone et al. (2005) reported ISO observations of H_2 in the lowest five pure rotational lines $S(4)$ to $S(0)$ (8 μm to 28 μm) toward diffuse ISM gas. The observed $S(1)/S(0)$ and $S(2)/S(0)$ line ratios are too large to be compatible with the PDR models. These authors suggested that MHD shocks (Flower & Pineau des Forets 1998) or magnetized vortices, which are natural dissipative structures of the intermittent dissipation of turbulence (Joulain et al. 1998), locally heat the gas at temperatures up to ≈1000 K. These structures add two heating sources: *i)* viscous heating through large velocity shear localized in tiny regions and *ii)* ion-neutral drift heating due to the presence of magnetic fields (ambipolar diffusion). As shown by Falgarone et al. (2006), these dissipative structures are also able to trigger a hot chemistry, that is not accessible to models that do not take into account the gas dynamics. These results suggest that additional mechanical heating processes are at work. We propose that the shock waves driven by the expansion of the HII region and PDR compress the molecular gas in the cloud edge and provide it with an additional heating source.

6.3. CS and HCS^+ chemistry

According to the last (but not least) molecular data affecting CS chemistry and excitation, the mean CS abundance in the Horsehead PDR, $\chi(CS) = (7 \pm 3) \times 10^{-9}$, implies a gas sulfur abundance of S/H ∼ $(3.5 \pm 1.5) \times 10^{-6}$, only a factor ≲4 smaller than the solar value (Asplund et al. 2005). Even lower sulfur depletion values are possible if the gas is significantly warmer than 30 K. Thus, the gas phase sulfur abundance is very close to the undepleted value observed in the diffuse ISM and not to the depleted value invoked in dense molecular clouds (e.g. Millar & Herbst 1990). However, the observed $CS/HCS^+ \simeq 175$ abundance ratio can only be reproduced by photochemical models by considering the HCS^+ peak abundance, otherwise, larger ratios (∼10^3) are predicted. Therefore, either the observed HCS^+ only traces the surface of the cloud where its abundance peaks, or chemical models underestimate the HCS^+ production rate. In any case, the predicted CS/HCS^+ abundance ratio scales with the gas phase sulfur abundance. The largest ratios are expected at the lowest sulfur depletions. However, the observed $CS/HCS^+ \sim 10$ ratio in the diffuse ISM (Lucas & Listz 2002) is even lower than in the Horsehead. Thus, we have to conclude that present chemical models still fail to reproduce the observed CS/HCS^+ abundance ratio, at least in the stationary regime. Time-dependent photochemical computations may also help to understand the dynamical expansion of the dissociation front and the evolving molecular abundances. Besides, Gerin et al. (1997) noted that larger HCS^+ abundances are expected if the gas is in a high ionization phase. We have computed that if the cosmic ray ionization rate is increased by a factor of ∼5, the predicted HCS^+ abundance inside the cloud ($A_V = 10$ mag) interestingly matches our inferred value and the CS/HCS^+ abundance ratio gets much closer to the observed ratio without the need of taking the HCS^+ abundance peak.

For the physical and FUV illuminating conditions prevailing in the Horsehead PDR, most of the gas phase sulfur is locked in S^+ for $A_V \lesssim 2$ mag and $\chi(HCS^+)$ reaches its maximum value. Besides, the derived gas phase sulfur abundance is large enough to keep $\chi(e^-) > 10^{-7}$ for $A_V \lesssim 3.5$ mag. HCS^+ and S II recombination lines trace the skin of molecular clouds where S^+ is still the dominant form of sulfur. In the scenario proposed by Ruffle et al. (1999), these S^+ layers will be responsible of the sulfur depletion due to more efficient sticking collisions on negatively charged dust grains than in the case of neutral atoms such as oxygen. Even in these regions, still dominated by photodissociation, CS and HCS^+ abundances are quickly enhanced compared to other sulfur molecules. In fact, we predict that CS is the most abundant S-bearing molecule in the external layers where S^+ is

still more abundant than neutral sulfur. These results are consistent with our PdBI detection of CS close to the PDR edge and show that CS is a PDR tracer. These findings are consistent with observations of S-bearing species in the diffuse ISM where CS is more abundant than SO_2, H_2S and SO (Lucas & Listz 2002).

Between $A_V \sim 2$ and ~8 mag the S^+ abundance smoothly decreases. Since S^+ is a good source of electrons, the electronic fractionation also decreases accordingly. HCS^+, and thus CS, present an abundance minimum in these layers. Neutral atomic sulfur is now the most abundant S-bearing species. Therefore, observations of the [S I]25 μm fine structure line will basically trace these intermediate layers of gas where S-bearing molecules have not reached their abundance peak. However, the exctitation energy of the [S I]25 μm line (the upper level energy is ~570 K) is too high compared to the thermal energy available in the regions where the neutral sulfur abundance peaks ($T_k \simeq 30$ K) and no detectable emission is expected. In fact, no Spitzer/IRS line detection has been reported in the Horsehead (L. Verstraete, private com.). However, since most of the neutral atomic sulfur will remain in the ground-state, the presence of a background IR source (e.g. in face-on PDRs) may allow, with enough spectral resolution and continuum sensitivity, the detection of the [S I]25 μm line in absorption.

On the other hand, sulfur in diffuse ionized gas outside the molecular cloud is in the form of sulfur ions. Mid-IR [S III] fine structure lines have been detected around the Horsehead with IRS/Spitzer (L. Verstraete, private com.). In the shielded gas, sulfur is mostly locked in S-bearing molecules together with a smaller fraction in atomic form. Our models predict that species such as SO will be particularly abundant. Jansen et al. (1995) also noted that the low gas phase sulfur abundance needed to explain the CS abundance in the Orion Bar PDR was incompatible with the observed high $H_2S/CS \sim 0.5$ abundance ratio. Therefore, a complete understanding of the sulfur chemistry will only be achieved when all the major sulfur molecules can be explained. In a forthcoming paper we analyse the photochemistry, excitation and radiative transfer of several S-bearing molecules detected by us in the Horsehead PDR.

7. Summary and conclusion

We have presented interferometric maps of the Horsehead PDR in the CS $J = 2$–1 line at a $3.65'' \times 3.34''$ resolution together with single-dish observations of several rotational lines of CS, $C^{34}S$ and HCS^+. We have studied the CS photochemistry, excitation and radiative transfer using the latest HCS^+ and OCS^+ dissociative recombination rates (Montaigne et al. 2005) and CS collisional cross-sections (Lique et al. 2006). The main conclusions of this work are as follows:

1. CS and $C^{34}S$ rotational line emission reveals mean densities around $n(H_2) = (0.5\text{–}1.0) \times 10^5$ cm^{-3}. The CS $J = 5$–4 lines show narrower line widths than the low-J CS lines and require higher density gas components, $\sim(2\text{–}6) \times 10^5$ cm^{-3}, not resolved by a ~10″ beam. These values are larger than previous estimates based on CO observations. It is likely that clumpiness at scales below ~0.01 pc and/or a low density envelope play a role in the CS line profile formation.
2. Nonlocal, non-LTE radiative transfer models of optically thick CS lines and optically thin $C^{34}S$ lines provide an accurate determination of the CS abundance, $\chi(CS) = (7 \pm 3) \times 10^{-9}$. We show that radiative transfer and opacity effects play a role in the resulting CS line profiles but not in $C^{34}S$ lines. Assuming the same physical conditions for the HCS^+ molecular ion, we find $\chi(HCS^+) = (4 \pm 2) \times 10^{-11}$.
3. According to photochemical models, the gas phase sulfur abundance required to reproduce these CS and HCS^+ abundances is $S/H = (3.5 \pm 1.5) \times 10^{-6}$, only a factor ~4 less abundant than the solar elemental abundance. Larger sulfur abundances are possible if the gas is significantly warmer. Thus, the sulfur abundance in the PDR is very close to the undepleted value observed in the diffuse ISM. The predicted CS/HCS^+ abundance ratio is close to the observed value of ~175, especially if predicted HCS^+ peak abundances are considered. If not, the HCS^+ production is underestimated unless the gas is in a higher ionization phase, e.g. if the cosmic ray ionization rate is increased by ~5.
4. High angular resolution PdBI maps reveal that the CS emission does not follow the same morphology shown by the small hydrocarbons emission in the PDR edge. In combination with previous PdBI $C^{18}O$ observations we have modeled the PDR edge and confirmed that a steep density gradient is needed to reproduce CS and $C^{18}O$ observations. The resulting density profile qualitatively agrees to that predicted in numerical simulations of a shock front compressing the PDR edge to high densities, $n(H_2) \simeq 10^5$ cm^{-3}, and high thermal pressures, $\simeq(5\text{–}10) \times 10^6$ K cm^{-3}.
5. Conventional PDR heating and cooling mechanisms fail to reproduce the temperature of the warm gas observed in the region by at least a factor ~2. Additional mechanical heating mechanisms associated with the gas dynamics may be needed to account for the warm gas. The thermal structure of the PDR edge is still not fully constrained from observations. This fact adds uncertainty to the abundances predicted by photochemical models.

We have shown that many physical and chemical variations in the PDR edge occur at small angular scales. In addition, the molecular inventory as a function of the distance from the illuminating source can only be obtained from millimeter interferometric observations. High angular resolution observations contain detailed information about density, temperature, abundance and structure of the cloud, but only detailed radiative transfer and photochemical models for each given source are able to extract the information. A minimum description of the source geometry is usually needed. Future observations with ALMA will allow us to characterize in much more details many energetic surfaces such as PDRs.

Acknowledgements. We are grateful to the IRAM staff at Plateau de Bure, Grenoble and Pico Veleta for the remote observing capabilities and competent help with the observations and data reduction. We also thank BASECOL, for the quality of data and information provided, and F. Lique for sending us the CS collisional rates prior to publication. JRG thanks J. Cernicharo, F. Daniel and I. Jiménez-Serra for fruitful discussions. We finally thank John Black, our referee, for useful and encouraging comments. JRG was supported by the french *Direction de la Recherche* and by a *Marie Curie Intra-European Individual Fellowship* within the 6th European Community Framework Programme, contract MEIF-CT-2005-515340.

References

Abergel, A., Bernard, J. P., Boulanger, F., et al. 2002, A&A, 389, 239
Abergel, A., Teyssier, D., Bernard, J. P., et al. 2003, A&A, 410, 577
Anthony-Twarog, B. J. 1982, A&J, 87, 1213
Asplund, M., Grevesse, N., & Sauval, A. J. 2005, in Cosmic Abundances as Records of Stellar Evolution and Nucleosynthesis, ed. F. N. Bash, & T. G. Barnes, ASP Conf. Ser., 336, 25
Batrla, W., & Wilson, T. L. 2003, A&A, 408, 231
Bernes, C. 1979, A&A, 73, 67
Bogey, M., Demuynck, C., & Destombes, J. L. 1981, Chem. Phys. Lett., 81, 256

Boogert, A. C. A., Tielens, A. G. G. M., Ceccarelli, C., et al. 2000, A&A, 360, 683
Cernicharo, J., & Guelin, M. 1987, A&A, 176, 299
Dartois, E. 2005, Space Sci. Rev., 119, 293
Draine, B. T. 1978, ApJS, 36, 595
Draine, B. T., & Lee, H. M. 1984, ApJ, 285, 89
Emerson, D. T., & Graeve, R. 1988, A&A, 190, 353
Falgarone, E., Verstraete, L., Pineau Des Forets, G., & Hily-Blant, P. 2005, A&A, 433, 997
Falgarone, E., Pineau Des Forets, G., Hily-Blant, P., & Schilke, P. 2006, A&A, 452, 511
Flower, D. R., & Pineau des Forets, G. 1998, MNRAS, 297, 1182
Flower, D. R. 2001, JPhB, 34, 2731
Frerking, M. A., Wilson, R. W., Linke, R. A., & Wannier, P. G. 1980, ApJ, 240, 65
García-Rojas, J., Esteban, C., Peimbert, M., et al. 2006, MNRAS, 368, 253
Gerin, M., Falgarone, E., Joulain, K., et al. 1997, A&A, 318, 579
Gibb, E. L., Whittet, D. C. B., Boogert, A. C. A., & Tielens, A. G. G. M. 2004, ApJS, 151, 35
Goicoechea, J. R. 2003, Ph.D. Thesis, Universidad Autonoma de Madrid, September 2003
Goldsmith, P. F., & Langer, W. D. 1999, ApJ, 517, 209
González-Alfonso, E., & Cernicharo, J. 1993, A&A, 279, 506
Graedel, T. E., Langer, W. D., & Frerking, M. A. 1982, ApJS, 48, 321
Graf, U. U., Genzel, R., Harris, A. I., et al. 1990, ApJ, 358, L49
Gueth, F., Guilloteau, S., & Bachiller, R. 1996, A&A, 307, 891
Habart, E., Abergel, A., Walmsley, C. M., Teyssier, D., & Pety, J. 2005, A&A, 437, 177
Hily-Blant, P., Teyssier, D., Philipp, S., & Gusten, R. 2005, A&A, 440, 909
Hosokawa, T., & Inutsuka, S. 2005a, ApJ, 623, 917
Hosokawa, T., & Inutsuka, S. 2005b [arXiv:astro-ph/0511165]
Howk, J. C., Sembach, K. R., & Savage, B. D. 2006, ApJ, 637, 333
Irvine, W. M., Schloerb, F. P., Hjalmarson, A., & Herbst, E. 1985, Protostars and planets II (A86-12626 03-90), Tucson, AZ, University of Arizona Press, 579
Jansen, D. J., Spaans, M., Hogerheijde, M. R., & van Dishoeck, E. F. 1995, A&A, 303, 541
Joulain, K., Falgarone, E., Pineau des Forets, G., & Flower, D. 1998, A&A, 340, 241
Le Bourlot, J., Pineau Des Forets, G., Roueff, E., & Flower, D. R. 1993, A&A, 267, 233
Le Petit, F., Nehmé, C., Le Bourlot, J., & Roueff, E. 2005, ApJS, preprint, doi:10.10861/503252
Lique, F., Spielfiedel, A., & Cernicharo, J. 2006, A&A, 451, 1125
Lis, D. C., & Schilke, P. 2003, ApJ, 597, L145
Lucas, R., & Liszt, H. 1998, A&A, 337, 246
Lucas, R., & Liszt, H. 2002, A&A, 384, 1054
Martín-Hernández, N. L., Peeters, E., Morisset, C., et al. 2002, A&A, 381, 606
Martín, S., Martín-Pintado, J., Mauersberger, R., Henkel, C., & García-Burillo, S. 2005, ApJ, 620, 210
Millar, T. J., & Herbst, E. 1990, A&A, 231, 466
Montaigne, H., Geppert, W. D., Semaniak, J., et al. 2005, ApJ, 631, 653
Monteiro, T. 1984, MNRAS, 210, 1
Neufeld, D. A., Wolfire, M. G., & Schilke, P. 2005, ApJ, 628, 60
Ohishi, M., & Kaifu, N. 1998, Chemistry and Physics of Molecules and Grains in Space, Faraday Discussions No. 109, The Faraday Division of the Royal Society of Chemistry, London, 205
Ossenkopf, V., & Henning, Th. 1994, A&A, 291, 943
Palumbo, M. E., Geballe, T. R., & Tielens, A. G. G. M. 1997, ApJ, 479, 839
Pankonin, V., & Walmsley, C. M. 1978, A&A, 64, 333
Penzias, A. A., & Burrus, C. A. 1973, ARA&A, 11, 51
Pety, J., Teyssier, D., Fossé, D., et al. 2005a, A&A, 435, 885
Pety, J. 2005b, in SF2A-2005: Semaine de l'Astrophysique Francaise, 721
Pound, M. W., Reipurth, B., & Bally, J. 2003, A&J, 125, 2108
Reipurth, B., & Bouchet, P. 1984, A&A, 137, 1
Ruffle, D. P., Hartquist, T. W., Caselli, P., & Williams, D. A. 1999, MNRAS, 306, 691
Tieftrunk, A., Pineau des Forets, G., Schilke, P., & Walmsley, C. M. 1994, A&A, 289, 579
Teyssier, D., Fossé, D., Gerin, M., et al. 2004, A&A, 417, 135
Turner, B. E., Chan, K. W., Green, S., & Lubowich, D. A. 1992, ApJ, 399, 114
van der Tak, F. F. S., Boonman, A. M. S., Braakman, R., & van Dishoeck, E. F. 2003, A&A, 412, 133
van Dishoeck, E. F. 1988, Rate Coefficients in Astrochemistry, ed. T. J. Millar, & D. A. Williams (Dordrecht, Boston: Publisher, Kluwer Academic Publishers), 49
van Zadelhoff, G.-J., Dullemond, C. P., van der Tak, F. F. S., et al. 2002, A&A, 395, 373
Wakelam, V., Caselli, P., Ceccarelli, C., Herbst, E., & Castets, A. 2004, A&A, 422, 159
Wannier, P. G. 1980, ARA&A, 18, 399
Zhou, S., Jaffe, D. T., Howe, J. E., et al. 1993, ApJ, 419, 190

Online Material

Appendix A: Nonlocal, non-LTE radiative transfer

Radiative transfer in a medium dominated by gas phase molecules and dust grains requires the solution of the radiative transport (RT) equation for the radiation field together with the equations governing the relative level populations of the considered species. In the case of rotational line emission (far-IR to mm domain), scattering from dust grains can be usually neglected from the RT equation and steady state statistical equilibrium can be assumed for molecular populations. However, physical conditions in ISM clouds are such that molecular excitation is usually far from LTE. Therefore, a minimum treatment of the nonlocal coupling between line+continuum radiation and level populations is required. In this appendix we describe in more detail the simple model developed for this work.

A.1. Monte Carlo methodology for gas and dust radiative transfer in plane-parallel geometry

The Monte Carlo methodology or its modifications is a simple and widely adopted approach when one has to deal with moderately thick lines and flexibility to explore different geometries is required (see van Zadelhoff et al. 2002, and references therein). In this work, the *classical* description of the Monte Carlo approach for non-LTE line transfer (Bernes 1979) has been extended to include the dust emission/absorption and their effect on the source function. The code was originally developed in *fortran90* for spherical symmetry (Goicoechea 2003) and has been enlarged to semi-infinite plane-parallel geometry (from face- to edge-on). Thus, numerical discretization is transformed from spherical shells to slabs. The model includes illumination from the cosmic background at both surfaces.

The variation of the radiation field intensity along any photon path s is related to the emission and absorption properties of the medium (scattering neglected) through

$$\frac{\mathrm{d}I_\nu}{\mathrm{d}s} = j_\nu - \alpha_\nu I_\nu \tag{A.1}$$

where α_ν [cm^{-1}] and j_ν [erg s^{-1} cm^{-3} Hz^{-1} sr^{-1}] are the total (gas+dust) absorption and emissivity coefficients at a given frequency ν. The normal path to any plane-parallel slab is thus $\mathrm{d}z = \mu\ \mathrm{d}s$, with $\mu = \cos\theta$ and where θ is the angle between z and s (see Fig. A.1). Equation (A.1) is thus written as

$$\mu \frac{\mathrm{d}I_\nu}{\mathrm{d}\tau} = S_\nu - I_\nu \tag{A.2}$$

where the differential optical depth is given by gas and dust contributions, $\mathrm{d}\tau = \alpha_\nu\ \mathrm{d}z$, and $S_\nu = j_\nu/\alpha_\nu$ is referred to as the source function. Continuum emissivity from dust is assumed to be thermal and given by

$$j_\nu^{\mathrm{dust}} = \alpha_\nu^{\mathrm{dust}} B_\nu(T_\mathrm{d}) \tag{A.3}$$

where B_ν is the Planck function at a given dust temperature, T_d, and $\alpha_\nu^{\mathrm{dust}}$ is computed from any of the dust mass absorption cross-sections available in the literature (e.g. Draine & Lee 1984; Ossenkopf & Henning 1994). For practical purposes, the dust absorption coefficient is assumed to be constant in all the passband around each line frequency. Hence, the number of dust continuum photons emitted per second in a given cell of material is $(4\pi/hc)\ j_\nu^{\mathrm{dust}}\ V_m\ \Delta v$ where V_m is the cell volume and Δv the considered passband in velocity units. Although the inclusion of dust almost does not affect molecular excitation in our work, it is included for consistency and for making predictions of higher frequency lines where it has larger effects.

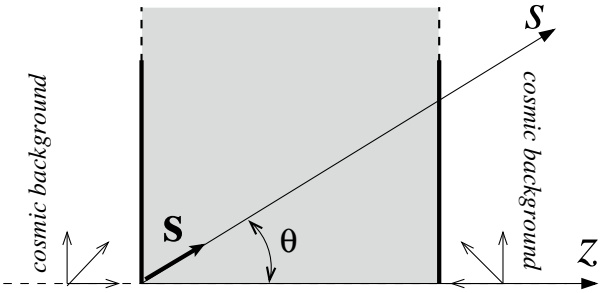

Fig. A.1. Plane-parallel geometry for a cloud isotropically illuminated by the cosmic microwave background at both surfaces.

Molecular lines occur at discrete frequencies, ν_{ij}, where i and j refer to upper and lower energy levels with n_i and n_j [cm^{-3}] populations respectively. Gas emission and absorption coefficients, as a function of velocity, are defined as

$$j_\nu^{\mathrm{gas}} = \frac{hc}{4\pi} n_i A_{ij}\, \phi \quad ; \quad \alpha_\nu^{\mathrm{gas}} = \frac{hc}{4\pi} (n_j B_{ji} - n_i B_{ij})\, \phi \tag{A.4}$$

where B_{ji}, B_{ij}, and A_{ij} are the transition probabilities, or Einstein coefficients, for absorption, and for induced and spontaneous emission respectively. We have assumed the same line Doppler profile (in velocity units) for emission and absorption

$$\phi = \frac{1}{b\sqrt{\pi}} \exp\left(-\frac{\boldsymbol{v} + \boldsymbol{v}_\mathrm{f} \cdot \boldsymbol{s}}{b}\right)^2 \tag{A.5}$$

and thus considered Gaussian Doppler microturbulent and thermal broadening characterized by the broadening parameter $b^2 = v_{\mathrm{turb}}^2 + v_{\mathrm{th}}^2$. Note that any arbitrary velocity field $\boldsymbol{v}_\mathrm{f}$ can be included. Here we take the possibility of having a velocity field normal to the slabs, i.e. $\boldsymbol{v}_\mathrm{f} = v_\mathrm{f}(z)$.

Generally speaking, the relative level populations of a considered molecule m are determined by collisions with other molecules, and/or by radiative effects caused by the cosmic background and/or by the dust continuum emission. The particular physical conditions, type of molecule and spectral domain will determine the dominant processes through the steady state statistical equilibrium equations

$$n_i \sum_{j\neq i} [R_{ij} + C_{ij}] = \sum_{j\neq i} n_j [R_{ji} + C_{ji}] \quad ; \quad n_{\mathrm{tot}} = \sum_{J=1}^{\text{rot levels}} n_J \tag{A.6}$$

where C_{ij} and R_{ij} [s^{-1}] are the collisional and radiative transition rates between i and j levels. For the collisional rates of species m (CS, C^{34}S, C^{18}O and HCS$^+$) we have considered

$$C_{ij} = \gamma_{ij}^m(\mathrm{H_2})\ n(\mathrm{H_2}) + \gamma_{ij}^m(\mathrm{He})\ n(\mathrm{He}) + \gamma_{ij}^m(\mathrm{H})\ n(\mathrm{H}) \tag{A.7}$$

where γ_{ij}^m [cm^3 s^{-1}] are the temperature dependent collisional de-excitation rate coefficients of m with collisional partners H_2 or He. If unknown, excitation rate coefficients are computed through detailed balance. For consistency with the PDR modeling we have estimated the collisional rates with H atoms (simply by scaling from the He rates), since H may be the dominant partner in the diffuse regions. Radiative rates are

$$R_{ij} = A_{ij} + B_{ij}\bar{J}_{ij} \quad ; \quad R_{ji} = B_{ji}\bar{J}_{ji} \tag{A.8}$$

where $\bar{J}_{ij}$ is the intensity of the radiation field integrated over solid angles and over the line profile. External illumination by cosmic background, dust continuum emission and line photons

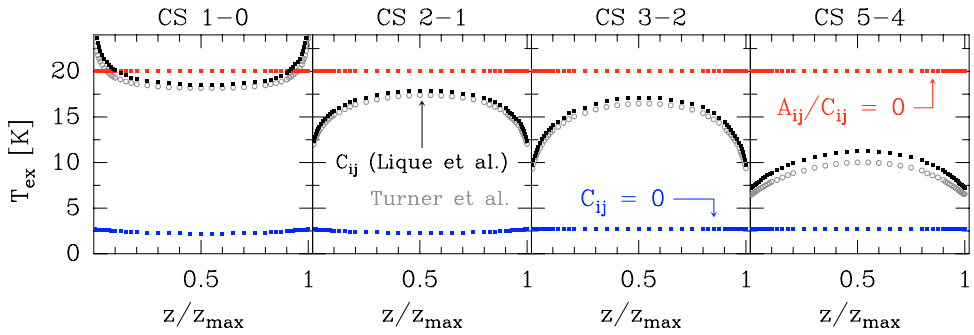

Fig. A.2. Thermalization tests for a plane-parallel cloud illuminated by the cosmic background at both surfaces (z/z_{max} = 0,1).

from different spatial regions contribute to $\bar{J}_{ij}$. Hence, the solution of molecular excitation implicitly depends on the non-local radiation field, which obviously depends on level populations in many cloud points. $\bar{J}_{ij}$ is explicitly computed in the Monte Carlo approach, and thus, the RT-excitation problem is solved iteratively until desired convergence in some physical parameter (generally the level populations) is achieved. LTE level populations at a constant fictitious T_{ex} were used for the first iteration. In the case of CS modeling, T_{rot} from the observational rotational-diagrams (Fig. 5) was used.

The RT problem is then simulated by the emission of a determined number of model photons (both sides external illumination, continuum and line photons) in a similar way to that originally described by Bernes (1979). Model photons represent a large quantity of *real* photons randomly distributed over the line profile A.5 and emitted at random cloud positions and directions. Each model photon is followed through the different slabs until it escapes the cloud or until the number of represented real photons become insignificant. Note that the angle θ between the photon direction and the normal to the slabs remains constant in all the photon path. In spherical geometry the θ angle between the photon direction and the radial direction changes in each photon step and thus has to be computed repeatedly. In addition, model photons sent in the cos $\theta \simeq 0$ direction in semi-infinite plane-parallel geometry will almost never escape the cloud. Thus, a minimum number of represented real photons is defined otherwise the photon is not followed anymore. In this way, the Monte Carlo simulation explicitly computes the induced emissions caused by the different types of model photons in all the slabs. At the end of the simulation, an averaged value for the $B_{ij}\bar{J}_{ij}$ that independently accounts for external illumination, continuum emission and line emission is stored for every slab ($\sum S_{ij,m}$ in Bernes formalism). Populations are then obtained in each slab by solving:

$$n_i \sum_{j\neq i} \left[A_{ij} + \sum S_{ij,m} + C_{ij}\right] = \sum_{j\neq i} n_j \left[\frac{g_i}{g_j} \sum S_{ij,m} + C_{ji}\right]. \quad \text{(A.9)}$$

A reference field for all types of model photons was included to reduce the inherent random fluctuations (i.e. the variance) of any Monte Carlo simulation (see Bernes 1979, for details). When a prescribed convergence in level the populations is reached, the total (gas+dust) source function is completely determined and the emergent intensity can be easily computed by integrating Eq. (A.2).

For spherical geometry, the code was successfully benchmarked against two test problems, the *Bernes' CO cloud* (Bernes 1979) and the *HCO$^+$ collapsing cloud, problem 2a* of the 1999 Leiden benchmark (van Zadelhoff et al. 2002). In the case of plane-parallel geometry, several thermalization tests for the

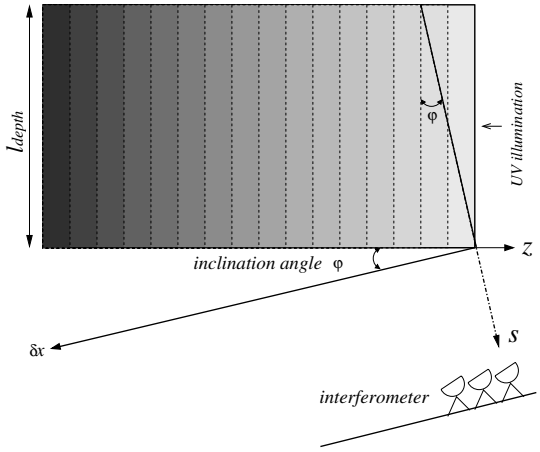

Fig. A.3. Adopted geometry for a plane-parallel PDR inclined by an small angle φ relative to the line of sight s. In this sketch, z denotes the normal direction to the slabs and also the UV illumination direction.

CS excitation (without dust emission) were successfully performed. Excitation temperatures as a function of the normal coordinate to slabs z are shown for CS J = 1–0, 2–1, 3–2 and 5–4 transitions in Fig. A.2. Model parameters are T_k = 20 K, $n(H_2) = 10^5$ cm^{-3} and χ(CS) = 7×10^{-9}. Different excitation conditions are considered. Upper model: A_{ij}/C_{ij} = 0 and T_{ex} is correctly thermalized to T_{kin} (LTE). Middle model: collisional rates from Lique et al. (filled squares; 2006) and Turner et al. (empty circles; 1992) and resulting non-LTE excitation (see Sect. 5.1). As noted by Lique et al., their new collisional rates produce larger excitation temperatures, especially as J increases. For the Horsehead physical conditions this implies that the estimated densities and/or abundances with Turner et al. collisional rates are ∼10% larger. Lower model: collisional excitation neglected and T_{ex} is radiatively thermalized to the cosmic background temperature at T_{bg} = 2.7 K.

A.2. A model for an edge-on cloud with inclination

In order to benchmark the spatial distribution of the PDR code abundance predictions with our interferometric line observations, we now can use the simple model described above to compute the synthetic spectrum of a required molecule. To do that, the PDR code output was used as an input for the RT calculation. In particular, the density profile (both $n(H_2)$ and n(H)), temperature profile (both T_k and T_d) and species abundance are carefully interpolated from the PDR spatial grid output. In practice, the slab discretization for the RT calculation has to be precise enough to sample the abundance, density and temperature varia-

tions at the edge of the PDR (where most of the changes occur). In most RT computations, ∼50 slabs were judged to give satisfactory sampling of the PDR variations. For an edge-on configuration, after a Monte Carlo simulation, RT Eq. (A.2) was integrated in a grid of different lines of sight (similar to impact parameters in spherical geometry) as depicted in Fig. A.3. Lines of sight can be inclined by an angle φ respect to the slabs normal ($\mathrm{d}s = \mathrm{d}z/\sin\ \varphi$). Therefore, the maximum integration path is $l_{\rm depth}/\cos\ \varphi$ where $l_{\rm depth}$ is the assumed cloud spatial depth. To produce a synthetic map, results are then convolved in a grid of cloud points with an angular resolution characterized by a Gaussian with hpbw equal to that of the synthesized interferometric beam.

A&A 464, L41–L44 (2007)
DOI: 10.1051/0004-6361:20067009
© ESO 2007

Astronomy & Astrophysics

Letter to the Editor

Deuterium fractionation in the Horsehead edge⋆

J. Pety[1,2], J. R. Goicoechea[2], P. Hily-Blant[1], M. Gerin[2], and D. Teyssier[3]

[1] IRAM, 300 rue de la Piscine, 38406 Grenoble Cedex, France
e-mail: [pety;hilyblan]@iram.fr
[2] LERMA, UMR 8112, CNRS, Observatoire de Paris and École Normale Supérieure, 24 rue Lhomond, 75231 Paris Cedex 05, France
e-mail: [javier;gerin]@lra.ens.fr
[3] European Space Astronomy Centre, Urb. Villafranca del Castillo, PO Box 50727, Madrid 28080, Spain
e-mail: dteyssier@sciops.esa.int

Received 22 December 2006 / Accepted 22 January 2007

ABSTRACT

Context. Deuterium fractionation is known to enhance the [DCO^+]/[HCO^+] abundance ratio over the D/H $\sim 10^{-5}$ elemental ratio in the cold and dense gas typically found in pre-stellar cores.
Aims. We report the first detection and mapping of very bright DCO^+ $J = 3-2$ and $J = 2-1$ lines (3 and 4 K respectively) towards the Horsehead photodissociation region (PDR) observed with the IRAM-30 m telescope. The DCO^+ emission peaks close to the illuminated warm edge of the nebula (<50″ or ∼0.1 pc away).
Methods. Detailed nonlocal, non-LTE excitation and radiative transfer analyses have been used to determine the prevailing physical conditions and to estimate the DCO^+ and $H^{13}CO^+$ abundances from their line intensities.
Results. A large [DCO^+]/[HCO^+] abundance ratio (≥0.02) is inferred at the DCO^+ emission peak, a condensation shielded from the illuminating far-UV radiation field where the gas must be cold (10–20 K) and dense ($\geq 2 \times 10^5$ cm^{-3}). DCO^+ is not detected in the warmer photodissociation front, implying a lower [DCO^+]/[HCO^+] ratio ($<10^{-3}$).
Conclusions. According to our gas phase chemical predictions, such a high deuterium fractionation of HCO^+ can only be explained if the gas temperature is below 20 K, in good agreement with DCO^+ excitation calculations.

Key words. ISM: clouds – ISM: molecules – ISM: individual objects: Horsehead nebula – radio lines: ISM

Molecules are enriched in deuterium over the elemental D/H abundance ($1-2 \times 10^{-5}$, Linsky et al. 2006) in many different astrophysical environments. These include cold, dense cores (Guelin et al. 1982), mid-planes of circumstellar disks (van Dishoeck et al. 2003; Guilloteau et al. 2006), hot molecular cores (Hatchell et al. 1998), and even PDRs (Leurini et al. 2006). Multiply deuterated species were first detected several years ago, e.g. D_2CO in warm gas (Turner 1990) and NHD_2 in cold gas (Roueff et al. 2000). Solomon & Woolf (1973) and Watson (1974) first proposed that deuterium fractionation is mostly caused by gas-phase ion-molecule reactions. Smith et al. (1982) and Roberts & Millar (2000a) confirmed that the deuteration of H_3^+ at low temperatures (<25 K) and of CH_3^+ at higher temperatures (up to ∼70 K) are important precursor reactions in the subsequent deuteration of other species. Roberts & Millar (2000b), Walmsley et al. (2004) and Flower et al. (2006) succeeded in reproducing the amount of several multiply deuterated molecules in cold gas by adding to pure gas-phase chemistry the accretion (freeze-out) of gas-phase molecules onto the surfaces of dust grains. Finally the observed deuterium fractionation in hot cores is thought to result from the liberation of deuterated molecules, trapped in ice mantles in the prestellar phase.

Although it has been studied thoroughly for 30 years, deuterium chemistry is not yet fully understood. With many chemical and physical processes competing for efficient fractionation, models are easier to compare with observations for sources with well described physical conditions. In this letter, we report the detection of very bright DCO^+ lines in the Horsehead edge. In particular, the mane of the Horsehead nebula is a PDR viewed nearly edge-on (inclination <5°) illuminated by the O9.5V star σOri (Abergel et al. 2003; Philipp et al. 2006). Habart et al. (2005) showed that the PDR has a very steep gradient, rising to $n_{\rm H} \sim 2 \times 10^5$ cm^{-3} in less than 10″ or 0.02 pc, at a roughly constant thermal pressure of $\sim 4 \times 10^6$ K cm^{-3}. The newly detected DCO^+ lines arise from a condensation adjacent to the PDR, first detected by Hily-Blant et al. (2005). According to its submillimeter continuum emission, this core (B33-SMM1) is 0.13×0.31 pc long and has an average H_2 density of $\sim 10^4$ cm^{-3} and a peak density of $\sim 6 \times 10^5$ cm^{-3} (Ward-Thompson et al. 2006).

1. Observations and data reduction

The DCO^+ $J = 3-2$ line was observed during 2 h of excellent winter weather (∼0.7 mm of water vapor) using the first polarization (i.e. nine of the eighteen available pixels) of the IRAM-30 m/HERA single sideband multi-beam receiver. We used the frequency-switched, on-the-fly observing mode. We observed along and perpendicular to the direction of the exciting star in zigzags (i.e. ± the lambda and beta scanning direction). The multi-beam system was rotated by 9.6° with respect to the

⋆ Based on observations obtained with the IRAM Plateau de Bure interferometer and 30 m telescope. IRAM is supported by INSU/CNRS (France), MPG (Germany), and IGN (Spain).

Article published by EDP Sciences and available at http://www.aanda.org or http://dx.doi.org/10.1051/0004-6361:20067009

Table 1. Observation parameters. The projection center of all the data is $\alpha_{2000} = 05^h40^m54.27^s$, $\delta_{2000} = -02°28'00''$.

Molecule	Transition	Frequency GHz	Instrument	# Pix.[a]	$F_{\rm eff}$[a]	$B_{\rm eff}$[a]	Resol. arcsec	Resol. km s^{-1}	Int. Time[a,b] hours	Noise[c] K	Obs. date[a]
$H^{13}CO^+$	$J = 3-2$	260.255339	30 m/HERA	9	0.90	0.46	13.5″	0.20	5.9/11.3	0.06	Mar. 2006
$H^{13}CO^+$	$J = 1-0$	86.754288	30 m+PdBI	2	0.95	0.78	6.7″	0.20	2.6/4.5	0.10	Sep. 2006
DCO^+	$J = 3-2$	216.112582	30 m/HERA	9	0.90	0.52	11.4″	0.11	1.5/2.0	0.10	Mar. 2006
DCO^+	$J = 2-1$	144.077289	30 m/CD150	2	0.93	0.69	18.0″	0.08	5.9/8.7	0.18	Sep. 2006
$C^{18}O$	$J = 2-1$	219.560319	30 m/HERA	9	0.91	0.55	11.2″	0.11	–	0.26	May 2003
Continuum at 1.2 mm			30 m/MAMBO	117	–	–	11.7″	–	–	–	–

[a] Those columns apply to the 30 m data but not to the PdBI data for the $H^{13}CO^+$ $J = 1-0$ line. [b] Two values are given for the integration time: the on-source time and the telescope time. [c] Noise values estimated at the position of the DCO^+ peak.

scanning direction. This ensured Nyquist sampling between the rows except at the edges of the map. The DCO^+ $J = 2-1$ was observed during 11.3 h using the C150 and D150 single-side band receivers of the IRAM-30 m under ~8.5 mm of water vapor. We used the frequency-switched, on-the-fly observing mode over a 160″ × 170″ portion of the sky. Scanned lines and rows were separated by 8″ ensuring Nyquist sampling. A detailed description of the $C^{18}O$ $J = 2-1$ and 1.2 mm continuum observations and data reductions can be found in Hily-Blant et al. (2005). We estimate the absolute position accuracy to be 3″.

We also use a small part of the $H^{13}CO^+$ ($J = 1-0$ and $J = 3-2$) data, which were obtained with the IRAM PdBI and 30 m telescopes. The whole data set will be comprehensively described in a forthcoming paper studying the fractional ionization across the Horsehead edge (Hily-Blant et al. 2007, in prep.). In short, the $H^{13}CO^+$ $J = 3-2$ line was observed under averaged winter weather (~3.5 mm of water vapor) in rasters along the direction of the exciting star using the first polarization of the unrotated HERA. Each pointing of the rasters was observed in frequency-switched mode. This resulted in a 140″ × 75″ map, Nyquist sampled along the direction of the exciting star but slightly undersampled in the orthogonal direction (i.e. rows separated by 6″ instead of 4.75″). The noise increases quickly at the map edges which were seen only by a fraction of the HERA pixels. We finally used a frequency-switched, on-the-fly map of the $H^{13}CO^+$ $J = 1-0$ line, obtained at the IRAM-30 m using the A100 and B100 3 mm receivers (~7 mm of water vapor) to produce the short-spacings needed to complement a 7-field mosaic acquired with the 6 PdBI antennae in the CD configuration (baseline lengths from 24 to 176 m).

The data processing was done with the GILDAS[1] softwares (Pety 2005). The IRAM-30 m data were first calibrated to the $T_{\rm A}^*$ scale using the chopper wheel method (Penzias & Burrus 1973), and finally converted to main beam temperatures ($T_{\rm mb}$) using the forward and main beam efficiencies ($F_{\rm eff}$ and $B_{\rm eff}$) displayed in Table 1. The resulting amplitude accuracy is ~10%. Frequency-switched spectra were folded using the standard shift-and-add method, after baseline subtraction. The resulting spectra were finally gridded through convolution by a Gaussian.

2. Results and discussion

Figure 1 presents the DCO^+ $J = 2-1$ and $J = 3-2$ and the $C^{18}O$ $J = 2-1$ integrated intensity maps, together with 1.2 mm continuum emission. All maps are presented in a coordinate system adapted to the source geometry, as described in the figure caption. The DCO^+ emission is concentrated in a narrow, arc-like structure, delineating the left edge of the dust continuum emission. A second maximum is found at the extreme left of the map, associated with a smaller dust continuum peak. Figure 2 shows the $H^{13}CO^+$ and DCO^+ spectra in a cut along the direction of the exciting star at $\delta y = 15''$ (horizontal dashed line of Fig. 1). This cut intersects the DCO^+ emission peak which is close to the illuminated edge of the nebula (<50″ or ~0.1 pc). To our knowledge, this is the brightest DCO^+ emission (4 K) detected in an interstellar cloud close to a bright H_2/PAH emitting region (Habart et al. 2005; Pety et al. 2005). The 15″ spatial shift between the DCO^+ and $C^{18}O$/continuum emission peaks likely results from the steep thermal gradient. The region where the DCO^+ emission is produced, is probably cooler than the region where the $C^{18}O$ lines and 1.2 mm continuum emission peak, i.e. cooler than 30 K, the minimum temperature needed to explain the intensity of the $C^{18}O$ $J = 2-1$ lines in the cloud edge (Goicoechea et al. 2006).

In order to constrain the $[DCO^+]/[HCO^+]$ abundance[2] ratio from the observed line emission, we assumed that both species

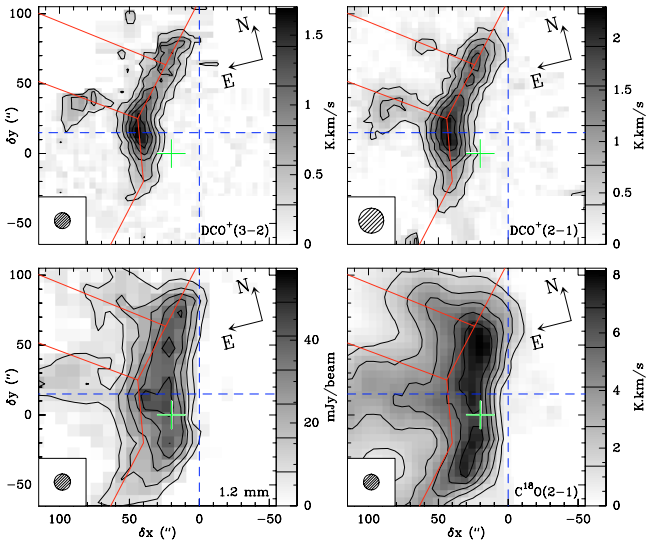

Fig. 1. IRAM-30 m integrated intensity maps. Maps have been rotated by 14° counter-clockwise around the projection center, shown as the green cross at $(\delta x, \delta y) = (20'', 0'')$, to bring the exciting star direction in the horizontal direction and the horizontal zero has been set at the PDR edge, delineated by the dashed blue vertical line. The spatial resolution is plotted in the bottom left corner. Values of contour levels are shown on each image lookup table. The emission of all lines is integrated between 10.1 and 11.1 km s^{-1}.

[1] See http://www.iram.fr/IRAMFR/GILDAS for more information about the GILDAS softwares.

[2] $[DCO^+] = n(DCO^+)/n(H_2)$.

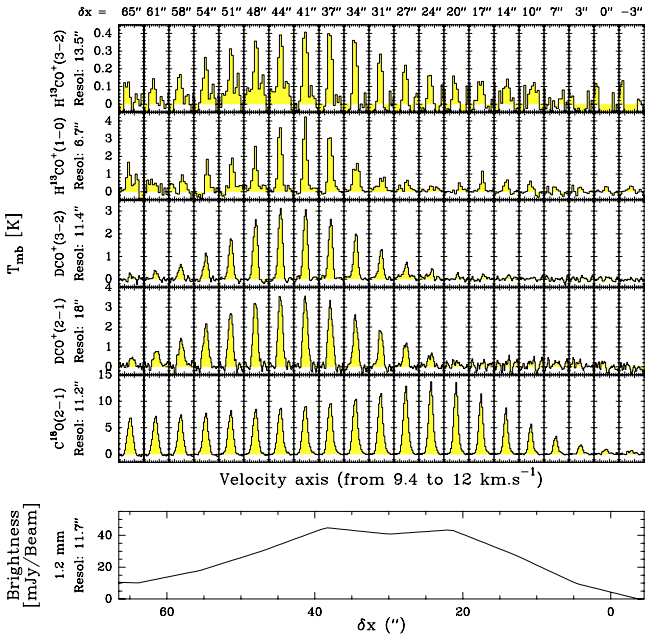

Fig. 2. Cut along the direction of the exciting star at $\delta y = 15''$.

coexist within the same gas (implying the same physical conditions). This assumption is mainly justified by the spatial coincidence of the $H^{13}CO^+$ and DCO^+ emission *peaks* (i.e. where $T_{\rm mb}\{DCO^+(2-1)\}/T_{\rm mb}\left\{H^{13}CO^+(1-0)\right\} \simeq 1$). Besides, we used the $H^{13}CO^+$ lines to determine the line-of-sight HCO^+ column density. Indeed, the direct determination of the HCO^+ column density from its rotational line emission is hampered by the large HCO^+ line opacities and their propensity to suffer from self-absorption and line scattering effects (Cernicharo & Guelin 1987). In addition, large critical densities for HCO^+ (and its isotopologues) are expected even for the lowest-J transitions due to its high dipole moment: ∼4 D (Table 2). Hence, thermalization will only occur at very high densities. For lower densities, $n < n_{\rm crit}$, subthermal excitation dominates as J increases. Therefore, in order to accurately determine the mean physical conditions and the $[DCO^+]/[H^{13}CO^+]$ ratio at the DCO^+ peak, we have used a nonlocal, non-LTE radiative transfer code including line trapping, collisional excitation and radiative excitation by cosmic background photons (Goicoechea 2003; Goicoechea et al. 2006). Collisional rates of $H^{13}CO^+$ and DCO^+ with H_2 and He have been derived from the HCO^+–H_2 rates of Flower (1999).

Assuming a maximum extinction depth of $A_V \simeq 50$ along the line-of-sight where DCO^+ peaks (Ward-Thompson et al. 2006), the observed DCO^+ $J = 2-1$ and $J = 3-2$ line intensities are well reproduced (with line opacities ∼1.5) only if the gas is cold (10−20 K) and dense ($n(H_2) \geq 2 \times 10^5\,{\rm cm}^{-3}$). This high density is consistent with the one required to reproduce the CS $J = 5-4$ excitation (Goicoechea et al. 2006) and with the value derived from dust submm continuum emission (Ward-Thompson et al. 2006). The weakness of the $H^{13}CO^+$ $J = 3-2$ line compared to the DCO^+ $J = 3-2$ line is caused in part by its larger Einstein coefficient (a factor ∼1.7 larger) and its higher energy level (see Table 2). This implies that the $H^{13}CO^+$ $J = 3-2$ line is *more* subthermally excited than the analogous DCO^+ line for the derived densities and temperatures. Note that we have not included collisions with electrons in this excitation analysis. In fact, the expected ionization fraction in such a cold and dense

Table 2. Einstein coefficients, upper level energies and critical densities for the range of temperatures considered in this work.

Molecule	Transition	A_{ij} (s^{-1})	$E_{\rm up}$ (K)	$n_{\rm crit}$ (cm^{-3})
$H^{13}CO^+$	$J = 1-0$	3.9×10^{-5}	4.2	$\sim 2 \times 10^5$
$H^{13}CO^+$	$J = 3-2$	1.3×10^{-3}	25.0	$\sim 3 \times 10^6$
DCO^+	$J = 2-1$	2.1×10^{-4}	10.4	$\sim 6 \times 10^5$
DCO^+	$J = 3-2$	7.7×10^{-4}	20.7	$\sim 2 \times 10^6$

condensation is usually low, $<10^{-7}$ (Caselli et al. 1999). The derived DCO^+ and $H^{13}CO^+$ column densities toward the DCO^+ peak are $\simeq (0.5-1) \times 10^{13}\,{\rm cm}^{-2}$ (i.e., $[DCO^+] \simeq [H^{13}CO^+] \simeq (1-2) \times 10^{-10}$). Assuming a $^{12}C/^{13}C = 60$ isotopic ratio (Milam et al. 2005), we finally find a $[DCO^+]/[HCO^+] \geq 0.02$ abundance ratio.

In order to understand the observed deuterium fractionation in the dense gas close to the Horsehead PDR, we have modeled the steady state deuterium gas phase chemistry in a cloud with a proton density $n_{\rm H} = n({\rm H}) + 2n(H_2) = 4 \times 10^5\,{\rm cm}^{-3}$ illuminated by a far-UV field 60 times the mean interstellar radiation field. We used the `Meudon PDR code`[3], a photochemical model of a unidimensional PDR (see Le Bourlot et al. 1993; Le Petit et al. 2006, for a detailed description) and its associated chemical reaction network. As this network only includes singly deuterated species, we added the D_2 and HD_2^+ species and associated reactions from Flower et al. (2006). Nevertheless, these additional reactions do not affect much the predicted DCO^+ abundances. Only H_2, HD and D_2 form on grain surfaces because the used chemical network allows only H and D atoms to accrete onto dust grains. We chose the following gas phase abundances: D/H = 1.6×10^{-5}, He/H = 0.1, O/H = 3×10^{-4}, C/H = 1.4×10^{-4}, N/H = 8×10^{-5}, N/H = 8×10^{-5}, S/H = 3.5×10^{-6} (Goicoechea et al. 2006), Si/H = 1.7×10^{-8}, Na/H = 2.3×10^{-9} and Fe/H = 1.7×10^{-9}.

We first investigated the role of gas thermodynamics in the HCO^+ deuterium fractionation. To do this, we stopped to solve the thermal balance when the far-UV absorption was large enough so that the temperature reaches a minimum value that we kept constant in the most shielded regions of the PDR. Figure 3 shows the predicted temperature profiles as well as the $[H_2D^+]/[H_3^+]$ and $[DCO^+]/[HCO^+]$ abundance ratios as a function of the cloud depth for a minimum value of $T_{\rm k} = 15$, 20, 30 and 60 K. The predicted $[DCO^+]/[HCO^+]$ ratio scales with the $[H_2D^+]/[H_3^+]$ ratio, as expected when DCO^+ gets fractionated by the reaction of CO with H_2D^+ and mainly destroyed by dissociative recombination with electrons (see e.g. Guelin et al. 1982). The displayed models also imply that low gas temperatures (≤20 K) are needed to reproduce the observed $[DCO^+]/[HCO^+]$ ratio at $\delta x = 40-45''$ ($A_V \sim 10-20$ depending on the assumed density profile). This is easily understood because the exchange reaction between H_3^+ and HD is most efficient at low temperatures (Gerlich et al. 2002). Therefore, the observed $[DCO^+]/[HCO^+] \geq 0.02$ abundance ratio can be reproduced using gas phase chemistry only if the gas cools down from the photodissociation front to ≤20 K, in good agreement with the DCO^+ excitation calculations. Note, however, that CO freeze-out is believed to further enhance the $[DCO^+]/[HCO^+]$ ratio over the values predicted by pure gas phase fractionation by increasing the abundance of H_3^+ and H_2D^+ (Brown & Millar 1989;

[3] Publicly available at `http://aristote.obspm.fr/MIS/`

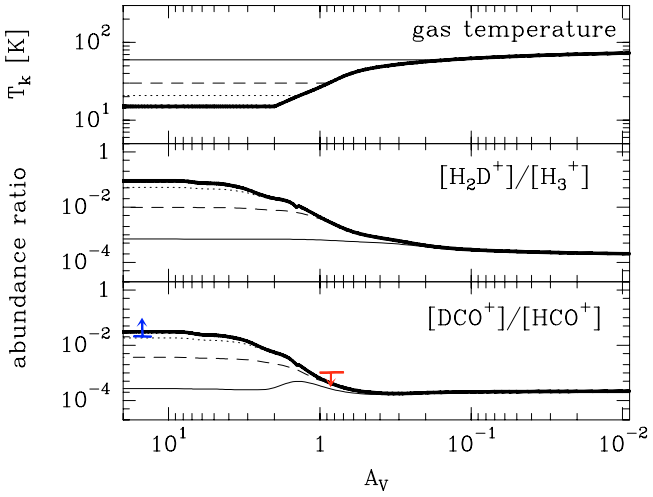

Fig. 3. Chemical models for different minimum gas temperatures: 15, 20, 30 and 60 K. The density is $n_H = 4 \times 10^5$ cm^{-3} and the illuminating radiation field is $\chi = 60$. Temperature profiles and predicted $[H_2D^+]/[H_3^+]$ and $[DCO^+]/[HCO^+]$ abundance ratios are shown as a function of A_V. The $[DCO^+]/[HCO^+]$ ratios inferred from observations in the cold condensation at $\delta x \sim 40-45''$ and in the warm PDR gas at $\delta x \sim 10-15''$ are shown respectively with the blue and red arrows.

Caselli et al. 1999). The $C^{18}O$ $J = 2-1$ emission shown in Fig. 2 substantially decreases at the DCO^+ peak. This behavior is reminiscent of CO depletion but it could also come from a combination of lower excitation and of opacity effects. Future observations of molecular tracers of gas depletion are needed to constrain the dominant scenario.

The DCO^+ lines stay undetected in the warm gas where HCO^+ (not shown here) and $H^{13}CO^+$ still emit. Indeed, DCO^+ can not be abundant in the photodissociation front, where the large photoelectric heating rate implies warm temperatures ($T_k > 50$ K), because the reaction of H_2D^+ with H_2 dominates and implies a low H_2D^+ abundance ($[H_2D^+]/[H_3^+] \simeq 2 \times 10^{-4}$). From the upper limit of the DCO^+ emission at $\delta x = 10-15''$ ($A_V \sim 1$), we estimate a low abundance ratio $[DCO^+]/[HCO^+] < 10^{-3}$ in the far-UV photodominated gas, in agreement with the model predictions.

The small distance to the Horsehead nebula (~400 pc), its low FUV illumination and its high gas density imply that many physical and chemical processes, with typical gradient lengthscales ranging between 1″ and 10″, can be probed in a small field-of-view (less than 50″). The Horsehead edge thus offers the opportunity to study in great detail the transition from the warmest gas, dominated by photodissociation processes and photoelectric heating, to the coldest and shielded gas where strong deuterium fractionation is taking place. Therefore, the Horsehead edge is the kind of source needed to serve as a reference for PDR models (Pety et al. 2006) and offers a realistic template to analyze more complex galactic or extragalactic sources.

Acknowledgements. We thank M. Guelin for useful comments and the IRAM PdBI and 30 m staff for their support during the observations. J.R.G. was supported by an *individual Marie Curie fellowship*, contract MEIF-CT-2005-515340.

References

Abergel, A., Teyssier, D., Bernard, J. P., et al. 2003, A&A, 410, 577
Brown, P. D., & Millar, T. J. 1989, MNRAS, 237, 661
Caselli, P., Walmsley, C. M., Tafalla, M., Dore, L., & Myers, P. C. 1999, ApJ, 523, L165
Cernicharo, J., & Guelin, M. 1987, A&A, 176, 299
Flower, D. R. 1999, MNRAS, 305, 651
Flower, D. R., Pineau Des Forêts, G., & Walmsley, C. M. 2006, A&A, 449, 621
Gerlich, D., Herbst, E., & Roueff, E. 2002, Planet. Space Sci., 50, 1275
Goicoechea, J. R. 2003, Ph.D. Thesis, Universidad Autonoma de Madrid
Goicoechea, J. R., Pety, J., Gerin, M., et al. 2006, A&A, 456, 565
Guelin, M., Langer, W. D., & Wilson, R. W. 1982, A&A, 107, 107
Guilloteau, S., Piétu, V., Dutrey, A., & Guélin, M. 2006, A&A, 448, L5
Habart, E., Abergel, A., Walmsley, C. M., Teyssier, D., & Pety, J. 2005, A&A, 437, 177
Hatchell, J., Millar, T. J., & Rodgers, S. D. 1998, A&A, 332, 695
Hily-Blant, P., Teyssier, D., Philipp, S., & Güsten, R. 2005, A&A, 440, 909
Le Bourlot, J., Pineau Des Forets, G., Roueff, E., & Flower, D. R. 1993, A&A, 267, 233
Le Petit, F., Nehmé, C., Le Bourlot, J., & Roueff, E. 2006, ApJS, 164, 506
Leurini, S., Rolffs, R., Thorwirth, S., et al. 2006, A&A, 454, L47
Linsky, J. L., Draine, B. T., Moos, H. W., et al. 2006, ApJ, 647, 1106
Milam, S. N., Savage, C., Brewster, M. A., Ziurys, L. M., & Wyckoff, S. 2005, ApJ, 634, 1126
Penzias, A. A., & Burrus, C. A. 1973, ARA&A, 11, 51
Pety, J. 2005, in SF2A-2005: Semaine de l'Astrophysique Française, ed. F. Casoli, T. Contini, J. M. Hameury, & L. Pagani, 721
Pety, J., Goicoechea, J. R., Gerin, M., et al. 2006, in SF2A-2006: Semaine de l'Astrophysique Française [arXiv:astro-ph/0612588]
Pety, J., Teyssier, D., Fossé, D., et al. 2005, A&A, 435, 885
Philipp, S. D., Lis, D. C., Güsten, R., et al. 2006, A&A, 454, 213
Roberts, H., & Millar, T. J. 2000a, A&A, 364, 780
Roberts, H., & Millar, T. J. 2000b, A&A, 361, 388
Roueff, E., Tiné, S., Coudert, L. H., et al. 2000, A&A, 354, L63
Smith, D., Adams, N. G., & Alge, E. 1982, ApJ, 263, 123
Solomon, P. M., & Woolf, N. J. 1973, ApJ, 180, L89
Turner, B. E. 1990, ApJ, 362, L29
van Dishoeck, E. F., Thi, W.-F., & van Zadelhoff, G.-J. 2003, A&A, 400, L1
Walmsley, C. M., Flower, D. R., & Pineau des Forêts, G. 2004, A&A, 418, 1035
Ward-Thompson, D., Nutter, D., Bontemps, S., Whitworth, A., & Attwood, R. 2006, MNRAS, 369, 1201
Watson, W. D. 1974, ApJ, 188, 35

A&A 498, 771–783 (2009)
DOI: 10.1051/0004-6361/200811496
© ESO 2009

Astronomy & Astrophysics

The ionization fraction gradient across the Horsehead edge: an archetype for molecular clouds⋆

J. R. Goicoechea[1], J. Pety[2,3], M. Gerin[3], P. Hily-Blant[4], and J. Le Bourlot[5]

[1] Laboratorio de Astrofísica Molecular. Centro de Astrobiología. CSIC-INTA. Carretera de Ajalvir, Km 4. Torrejón de Ardoz, 28850 Madrid, Spain
e-mail: goicoechea@damir.iem.csic.es
[2] IRAM, 300 rue de la Piscine, 38406 Grenoble Cedex, France
e-mail: pety@iram.fr
[3] LERMA - LRA, UMR 8112, CNRS, Observatoire de Paris and École Normale Supérieure, 24 rue Lhomond, 75231 Paris, France
e-mail: maryvonne.gerin@lra.ens.fr
[4] Laboratoire d'Astrophysique, Observatoire de Grenoble, BP 53, 38041 Grenoble Cedex 09, France
e-mail: pierre.hilyblant@obs.ujf-grenoble.fr
[5] LUTH, UMR 8102 CNRS, Université Paris 7 and Observatoire de Paris, Place J. Janssen, 92195 Meudon, France
e-mail: Jacques.Lebourlot@obspm.fr

Received 10 December 2008 / Accepted 11 February 2009

ABSTRACT

Context. The ionization fraction (i.e., the electron abundance) plays a key role in the chemistry and dynamics of molecular clouds.
Aims. We study the $H^{13}CO^+$, DCO^+ and HOC^+ line emission towards the Horsehead, from the shielded core to the UV irradiated cloud edge, i.e., the photodissociation region (PDR), as a template to investigate the ionization fraction gradient in molecular clouds.
Methods. We analyze an IRAM *Plateau de Bure Interferometer* map of the $H^{13}CO^+$ $J = 1$–0 line at a $6.8'' \times 4.7''$ resolution, complemented with IRAM-30 m $H^{13}CO^+$ and DCO^+ higher-J line maps and new HOC^+ and CO^+ observations. We compare self-consistently the observed spatial distribution and line intensities with detailed depth-dependent predictions of a PDR model coupled with a non-local radiative transfer calculation. The chemical network includes deuterated species, ^{13}C fractionation reactions and HCO^+/HOC^+ isomerization reactions. The role of neutral and charged PAHs in the cloud chemistry and ionization balance is investigated.
Results. The detection of the HOC^+ reactive ion towards the Horsehead PDR proves the high ionization fraction of the outer UV irradiated regions, where we derive a low $[HCO^+]/[HOC^+] \simeq 75$–$200$ abundance ratio. In the absence of PAHs, we reproduce the observations with gas-phase metal abundances, [Fe+Mg+...], lower than 4×10^{-9} (with respect to H), and a cosmic-ray ionization rate of $\zeta = (5 \pm 3) \times 10^{-17}$ s^{-1}. The inclusion of PAHs modifies the ionization fraction gradient and increases the required metal abundance.
Conclusions. The ionization fraction in the Horsehead edge follows a steep gradient, with a scale length of ∼0.05 pc (or ∼25″), from $[e^-] \simeq 10^{-4}$ (or $n_e \sim$ 1–5 cm^{-3}) in the PDR to a few times $\sim 10^{-9}$ in the core. PAH^- anions play a role in the charge balance of the cold and neutral gas if substantial amounts of free PAHs are present ($[PAH] > 10^{-8}$).

Key words. astrochemistry – ISM: clouds – radiative transfer – radio lines: ISM – ISM: molecules – ISM: abundances

1. Introduction

The electron abundance ($[e^-] = n_e/n_H$) plays a fundamental role in the chemistry and dynamics of interstellar gas. The degree of ionization determines the preponderance of ion-neutral reactions, i.e., the main formation route for most chemical species in molecular clouds (Herbst & Klemperer 1973; Oppenheimer & Dalgarno 1974). In addition, the ionization fraction constrains the coupling of matter and magnetic fields, which drives the dissipation of turbulence and the transfer of angular momentum, thus having crucial implications in protostellar collapse and accretion disks (e.g., Balbus & Hawley 1991).

High-angular resolution observations of interstellar clouds reveal steep density, temperature and turbulence gradients as well as sharp chemical variations. Accordingly, the electron abundance should vary within a cloud depending on the relative ionizing sources and prevailing chemistry.

Rotational line emission of molecular ions such as DCO^+ and HCO^+ have been traditionally used to estimate the ionization fraction in molecular clouds because (i) they are abundant and easily observable; (ii) dissociative recombination is their main destruction route, and thus their abundances are roughly inversely proportional to the electron abundance (e.g., Guélin et al. 1982; Wootten et al. 1982; de Boisanger et al. 1996; Williams et al. 1998; Caselli et al. 1998; Maret & Bergin 2007; Hezareh et al. 2008). On the other hand, the presence of reactive ions (species such as HOC^+ or CO^+ that react rapidly with H_2) is predicted to be a sensitive indicator of high ionization fraction regions, e.g., the UV irradiated cloud surfaces (e.g., Smith et al. 2002; Fuente et al. 2003).

In order to constrain the ionization fraction gradient from models, the cloud chemistry and physics cannot be simplified much because the charge balance depends on parameters such

⋆ Based on observations obtained with the IRAM Plateau de Bure interferometer and 30 m telescope. IRAM is supported by INSU/CNRS (France), MPG (Germany), and IGN (Spain).

Table 1. Observation parameters of the PdBI maps shown in Fig. 1.

Molecule	Transition	Frequency GHz	Instrument	Config.	Beam arcsec	PA °	Vel. Resol. km s^{-1}	Int. Time[a] hours	T_{sys} K	Noise[b,†] K	Obs. date
$H^{13}CO^+$	1–0	86.754288	PdBI	C & D	6.8×4.7	13	0.2	6.5	150	0.10	2006-07
HCO	$1_{0,1}$ 3/2, 2–$0_{0,0}$ 1/2, 1	86.670760	PdBI	C & D	6.7×4.4	16	0.2	6.5	150	0.09	2006-07

[a] We observed a 7-field mosaic centered on the IR peak at $\alpha_{2000} = 05^h40^m54.27^s$, $\delta_{2000} = -02°28'00''$ (Abergel et al. 2003) with the following offsets: (−5.5″, −22.0″), (5.5″, −22.0″), (11.0″, 0.0″), (0.0″, 0.0″), (−11.0″, 0.0″), (−5.5″, 22.0″) and (5.5″, 22.0″). The total field-of-view is 80.1″ × 102.1″ and the half power primary beam is 58.1″. The mosaic was Nyquist sampled in declination at 3.4 mm and largely oversampled in right ascension. This maximizes the field of view along the PDR edge while the oversampling in the perpendicular direction eases the deconvolution. On-source time was computed as if the source was always observed with 6 antennae; [b] the noise values refer to the mosaic phase center (mosaic noise is inhomogeneous due to primary beam correction; it steeply increases at the mosaic edges).

Table 2. Observation parameters of the IRAM-30 m observations.

Molecule	Transition	Frequency GHz	Instrument	F_{eff}	B_{eff}	Resol. arcsec	Resol. km s^{-1}	Int. Time hours	Noise[†] K	Observing Mode	Obs. date
HCO^+	J = 1–0	89.188523	30 m/A100	0.95	0.78	27.6″	0.20	4.7	0.02	ON-OFF	2008
HOC^+	J = 1–0	89.487414	30 m/A100	0.95	0.78	27.5″	0.20	4.7	0.02	ON-OFF	2008
CO^+	2, 5/2–1, 3/2	236.062578	30 m/A230	0.91	0.52	10.4″	0.20	4.7	0.05	ON-OFF	2008
$H^{13}CO^+$	J = 1–0	86.754288	30 m/AB100	0.95	0.78	28.4″	0.20	2.6	0.10	OTF map	2006-07
$H^{13}CO^+$	J = 3–2	260.255339	30 m/HERA	0.90	0.46	13.5″	0.20	5.9	0.06	OTF map	2006
DCO^+	J = 2–1	144.077289	30 m/CD150	0.93	0.69	18.0″	0.08	5.9	0.18	OTF map	2006
DCO^+	J = 3–2	216.112582	30 m/HERA	0.90	0.52	11.4″	0.11	1.5	0.10	OTF map	2006

[†] The noise (in T_{mb} scale) refers to the channel spacing obtained by averaging adjacent channels to the velocity resolution given in the tables.

as the penetration of UV radiation, the cosmic-ray ionization rate (ζ) and the abundance of key species (e.g., metals and PAH).

Compared to other works, in this paper we determine the ionization fraction gradient by direct comparison of $H^{13}CO^+$ and DCO^+ high-angular resolution maps and HOC^+ pointed observations, with detailed depth-dependent chemical and radiative transfer models covering a broad range of cloud physical conditions. Indeed, the observed field-of-view contains the famous Horsehead PDR (the UV illuminated edge of the cloud) and a dense and cold core discovered by us from its intense DCO^+ line emission (Pety et al. 2007). Due to its simple geometry and moderate distance ($d \simeq 400$ pc), the Horsehead PDR and associated core are good templates to study the steep gradients expected in molecular clouds (e.g., Pety et al. 2005, 2007; Goicoechea et al. 2006; Gerin et al. 2009).

The paper is organized as follows. The observations are presented in Sect. 2 and the models used to interpret them are described in Sect. 3. The chemistry of $H^{13}CO^+$, DCO^+ and HOC^+ (our observational probes of the ionization fraction) is analyzed in Sect. 4. In Sect. 5 we investigate the role of metals, PAHs and ζ on the electron abundance determination. The main results and constrains are presented in Sect. 6 and discussed in Sect. 7.

2. Observations

2.1. Observations and data reduction

Tables 1 and 2 summarize the observation parameters of the data obtained with the PdBI and the IRAM–30 m telescope that we shall study in this work. The $H^{13}CO^+$ J = 1–0 line emission map was first presented in Gerin et al. (2009). Frequency-switched, on-the-fly maps (OTF) obtained at the IRAM-30 m were used to produce the short-spacings needed to complement a 7-field mosaic acquired with the 6 PdBI antennae in the CD configuration (baseline lengths from 24 to 176 m). Correlator backends were used (VESPA for IRAM-30 m observations). The high angular resolution PdBI $H^{13}CO^+$ J = 1–0 map complements our previous $H^{13}CO^+$ J = 3–2 and DCO^+ J = 2–1 and 3–2 maps taken with the IRAM-30 m telescope and first presented in Pety et al. (2007).

In this work we present new IRAM–30 m deeper integrations in the HOC^+, $H^{13}CO^+$ and HCO^+ J = 1–0 lines, and an upper limit for the CO^+ emission towards the PDR (defined here as the HCO emission peak; Gerin et al. 2009). The position switching observing mode was used. The on-off cycle duration was 1 mn and the off-position offsets were $(\Delta\alpha, \Delta\delta) = (-100'', 0'')$, i.e., the H II region ionized by σOri and free of molecular gas emission. Position accuracy is estimated to be ∼3″ for the 30 m data and better than 0.5″ for the PdBI data. The data processing was done with the GILDAS[1] softwares (e.g., Pety 2005b). The IRAM-30 m data were first calibrated to the T_A^* scale using the chopper wheel method (Penzias & Burrus 1973), and finally converted to main beam temperatures T_{mb} using the forward and main beam efficiencies F_{eff} and B_{eff} displayed in Table 2 (e.g., Greve et al. 1998). The amplitude accuracy for heterodyne observations with the IRAM–30 m telescope is ∼10%. PdBI data and short-spacing data were merged before imaging and deconvolution of the mosaic, using standard techniques of GILDAS and used in our previous works (see e.g., Pety et al. 2005).

2.2. DCO^+ and $H^{13}CO^+$ spatial distribution, HOC^+ detection

Figure 1 shows $H^{13}CO^+$ J = 1–0, HCO $1_{0,1}$-$0_{0,0}$ (PdBI) and DCO^+ J = 2–1, 3–2 integrated line intensity maps (IRAM-30 m; Pety et al. 2007), as well as the aromatic infrared band emission (AIB, observed with ISOCAM, Abergel et al. 2003) that traces the UV illuminated edge of the cloud, i.e., the PDR. The DCO^+ emission is concentrated in a narrow, arclike structure of dense and cold gas behind the PDR (Pety et al. 2007). Hence, it shows a very different spatial distribution than the emission of "PDR tracers" such as C_2H, C_4H, c-C_3H_2 (Pety et al. 2005), HCO radicals (Gerin et al. 2009), vibrationally excited H_2 (Habart et al. 2005) or the AIB emission (Compiègne et al. 2008). The $H^{13}CO^+$ J = 1–0 emission follows the DCO^+

[1] See http://www.iram.fr/IRAMFR/GILDAS

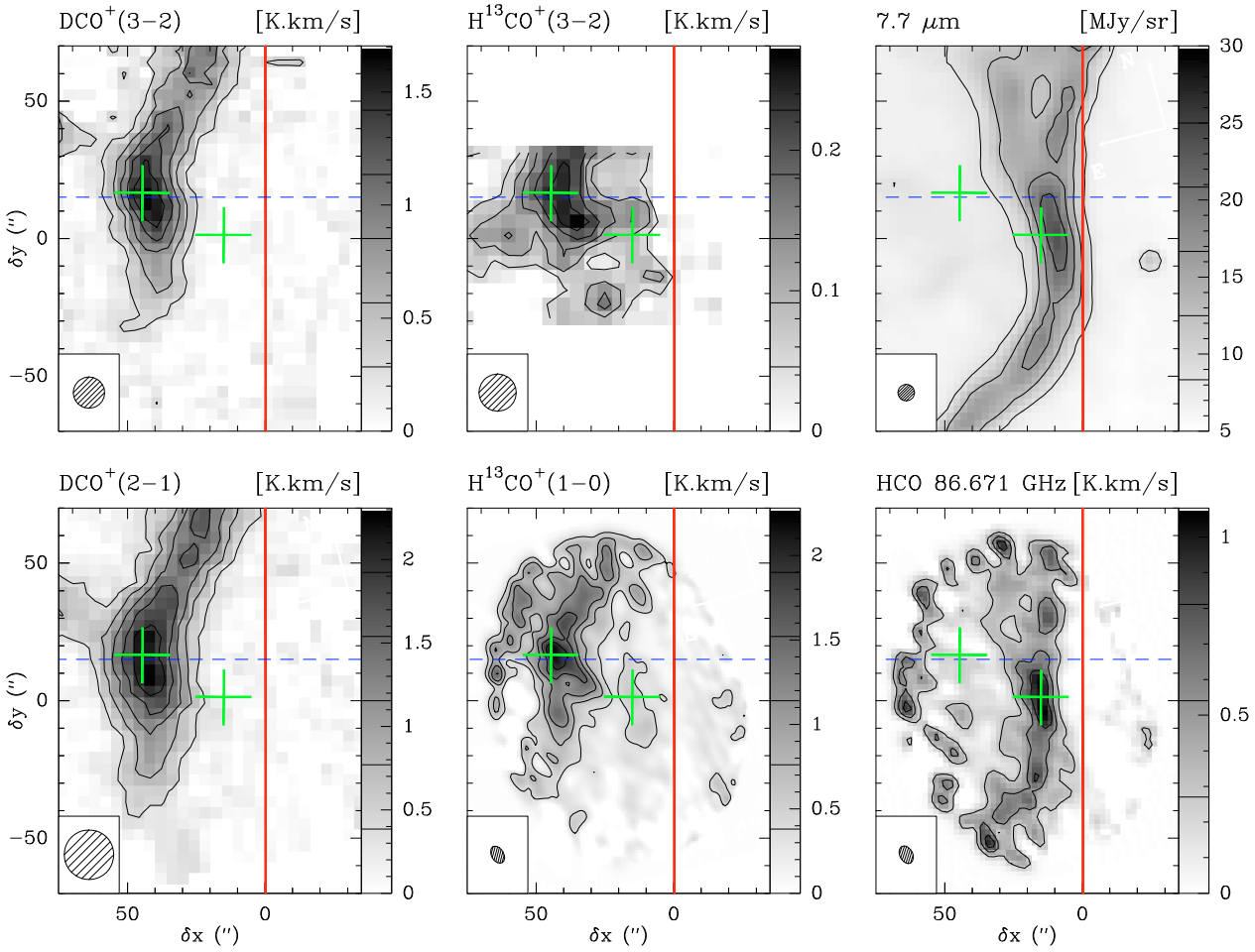

Fig. 1. DCO^+ J = 3–2 and 2–1 (IRAM-30 m; from Pety et al. 2007), $H^{13}CO^+$ J = 1–0 (PdBI) and 3–2 (IRAM-30 m) line integrated intensity maps, aromatic infrared band emission (ISOCAM, from Abergel et al. 2003) and HCO (PdBI, from Gerin et al. 2009). Maps have been rotated by 14° counter–clockwise around the projection center, located at $(\delta x, \delta y) = (20'', 0'')$, to bring the illuminated star direction in the horizontal direction. The horizontal zero has been set at the cloud edge ($\delta x = 0''$). The $H^{13}CO^+$, DCO^+ and HCO emission is integrated between 10.1 and 11.1 km s^{-1}. Integrated intensities are expressed in the T_{mb} scale. Contour levels are displayed on the grey scale lookup tables. The red vertical line shows the PDR edge and the green crosses shows two representative positions: the *"shielded core"* (the DCO^+ emission peak at $\delta x \sim 45''$; Pety et al. 2007) and the *"PDR"* (the HCO emission peak at $\delta x \sim 15''$; Gerin et al. 2009). The dashed blue line shows the horizontal cut analyzed in this work.

distribution and it mostly delineates the dense core that coincides with the DCO^+ emission peak. Nevertheless, while DCO^+ is not detected in the illuminated edge, $H^{13}CO^+$ does show a faint emission in the PDR. Therefore, the small field-of-view shown in Fig. 1 contains two different environments: a warm PDR and a cold core shielded from the external UV radiation field. In the following sections we analyze these emission maps to determine the ionization fraction gradient in the region.

Figure 2 shows long integration spectra of the HOC^+, $H^{13}CO^+$ and HCO^+ J = 1–0 lines towards the PDR. This is the first detection of the HOC^+ reactive ion towards the Horsehead, and adds to previous detections in interstellar environments with high electron abundances (Woods et al. 1983; Ziurys & Apponi 1995; Fuente et al. 2003; Rizzo et al. 2003; Savage & Ziurys 2004; Liszt et al. 2004). $H^{12}CO^+$ lines are optically thick, as shown by the low $H^{12}CO^+/H^{13}CO^+$ J = 1–0 line intensity ratio (~7), much lower than the expected $^{12}C/^{13}C \simeq$ 60 abundance ratio (Langer & Penzias 1990; Savage et al. 2002) and references therein). The high opacity of $H^{12}CO^+$ lines even towards the PDR justifies the use of $H^{13}CO^+$ lines as tracers of the HCO^+ abundance.

Table 3. Main spectroscopic parameters of the studied lines.

Species	Transition J_{upp}–J_{low}	Frequency (GHz)	A_{ij} (s^{-1})	E_{upp} (K)
HCO^+	1–0	89.188523	4.2×10^{-5}	4.3
HOC^+	1–0	89.487414	2.2×10^{-5}	4.3
$H^{13}CO^+$	1–0	86.754288	3.9×10^{-5}	4.2
CO^+	2(5/2)–1(3/2)	236.062578	4.7×10^{-4}	17.2
$H^{13}CO^+$	3–2	260.255339	1.3×10^{-3}	25.0
DCO^+	2–1	144.077289	2.1×10^{-4}	10.4
DCO^+	3–2	216.112582	7.7×10^{-4}	20.7

3. Analysis: models

In this work we couple the depth-dependent abundances predicted by a PDR model (for the varying physical conditions prevailing in the Horsehead edge) with detailed excitation and radiative transfer calculations adapted to the cloud geometry. This technique allows us to analyze different chemical models by direct comparison with observed line intensities. This methodology was introduced to study our interferometric CS and $C^{18}O$

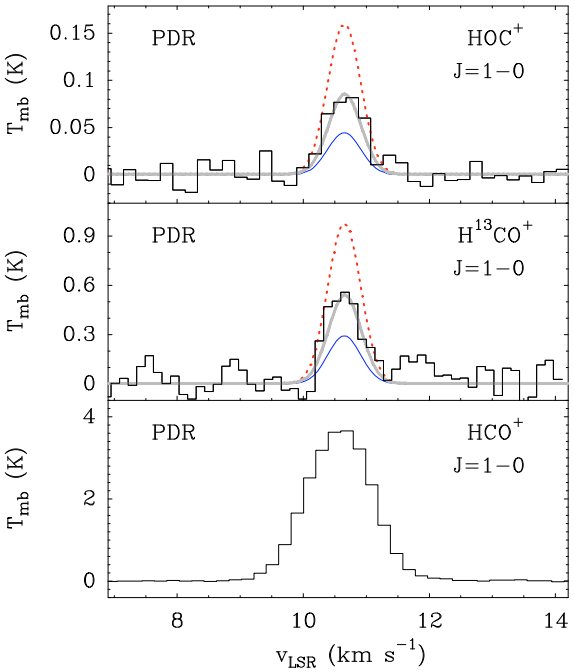

Fig. 2. HOC^+ and $H^{13}CO^+$ J = 1–0 lines towards the Horsehead PDR (*upper and middle panels*) observed with the IRAM-30 m telescope. Solid lines are radiative transfer models with T_k = 60 K, $n(H_2)$ = 5×10^4 cm^{-3}, n(H) = 500 cm^{-3} and [e$^-$] = 5×10^{-5}. Three different abundances are shown, thick-grey line: [HOC^+] = 4.0×10^{-12} and [$H^{13}CO^+$]= 1.5×10^{-11}; red dashed line: abundances ×2; blue thin line: abundances ÷2. For completeness, the HCO^+ J = 1–0 line towards the PDR is also shown (*lower panel*). This transition is very opaque, as shown by the low $H^{12}CO^+/H^{13}CO^+$ J = 1–0 line intensity ratio (∼7). The resulting line profile is thus broadened and it suffers from scattering by low-density foreground gas that we do not model here.

maps of the Horsehead edge (Goicoechea et al. 2006). It enables us to observationally benchmark the abundance gradients predicted by chemical models, even if it does not produce perfect fits to line profiles in all cloud positions. In this paper, we analyze a horizontal cut of the $H^{13}CO^+$ and DCO^+ line emission along the direction of the illuminating star ($\delta y = 15''$). Figure 1 shows that this cut (blue dashed line) goes across the DCO^+ emission peak ($\delta x \sim 45''$), which we identify as the "shielded core", and across the HCO emission peak, the "PDR" ($\delta x \sim 15''$).

3.1. Geometry and density gradient

The Horsehead edge has an almost edge-on geometry with a line-of-sight depth of $l_{depth} \simeq 0.1$ pc (e.g., Habart et al. 2005) and a spatial scale in the plane of the sky of ≃0.002 pc arcsec^{-1}. We determine the density profile from observations by fitting the 1.2 mm dust continuum emission (IRAM-30 m/MAMBO) along the $\delta y = 15''$ direction (Hily-Blant et al. 2005). In this fit, we adopt a dust opacity per unit (gas+dust) mass column density of $\kappa_{1.2} = 0.003$ cm^2 g^{-1} at 1.2 mm (computed for "MRN grains": Mathis et al. 1977, see below), our best knowledge of the dust grains temperature (from ∼15 K in the core to ∼30 K in the PDR; e.g., Ward-Thompson et al. 2006) and a power-law density profile $n_H(r) = n(H)+2n(H_2) \propto r^{-p}$, where r is the distance from the shielded core towards the illuminated edge of the cloud. Best fits are obtained for a steep density gradient in the cloud edge ($p \simeq 3$) and a flatter one towards the core ($p \simeq 0.5$). The turnover point occurs at a core radius of $r \simeq 0.04$ pc (or $\delta x \simeq 23''$ in the maps). The resulting density gradient used in the photochemical and radiative transfer models is shown in Fig. 4. In the next sections we constrain the ionization fraction gradient in the cloud by comparing synthetic and observed $H^{13}CO^+$ and DCO^+ spectra along the same cut.

3.2. Photochemical models

We have updated the *Meudon PDR code* to model our observations of the Horsehead. The code has been described in detail elsewhere (e.g., Le Bourlot et al. 1993; Le Petit et al. 2006; Goicoechea & Le Bourlot 2007) and benchmarked against other PDR codes by Röllig et al. (2007). In this section we summarize the most relevant upgrades and model features for this work.

3.2.1. UV radiative transfer and dust properties

The code solves the UV radiative transfer problem taking into account dust scattering and gas absorption. Anisotropic scattering of UV photons by dust grains is included by explicity calculating the wavelength-dependent grain albedo and g-asymmetry parameters (Goicoechea & Le Bourlot 2007). This enables the specific computation of the UV radiation field (continuum+lines) and thus, the direct integration of consistent photoionization and photodissociation rates. We use two types of dust populations: (i) a mixture of graphite+silicate grains; and (ii) PAHs (see next paragraph). More precisely, we adopt a power-law size distribution ($n(a) \propto a^{-3.5}$) with minimum and maximum radius of ∼5 and ∼250 nm respectively (for graphite+silicate grains). Wavelength-dependent optical properties (Q efficiencies and g factors) are interpolated from Laor & Draine (1993) tabulations. With a standard gas-to-dust mass ratio (∼100), this grain mixture ("MRN grains") reproduces the main characteristics of the standard interstellar extinction curve with $N_H/A_V = 1.9 \times 10^{21}$ cm^{-2} and $R_V = 3.1$.

In order to complete our description of the dust populations, in this work we have also added smaller aromatic grains. Observationally, the AIB emission towards the Horsehead (produced by free PAHs according to the most accepted theory; Léger & Puget 1984; Allamandola et al. 1985) clearly separates the H II region and PDR (where the emission is bright) from the regions shielded from UV radiation, where no AIB emission is detected (Abergel et al. 2003; Habart et al. 2005; Compiègne et al. 2007; 2008). However, the size distribution and PAH abundance in dense regions shielded from UV radiation are uncertain. It may vary from "negligible", if PAHs coagulate into larger PAH aggregates (Boulanger et al. 1990; Rapacioli et al. 2006) to "high" abundances (though they will not be detected in the mid–IR due to the lack of UV photons to excite them). We used the following PAH properties: a size distribution with ∼0.4 and ∼1.2 nm radii limits (Desert et al. 1990) and optical parameters from Li & Draine (2001). This size distribution is compatible with PAHs having a mean radius of ∼0.6 nm and $N_C \sim 100$ carbon atoms assuming $N_C \simeq 500\ a^3$ (Bakes & Tielens 1994). The extinction curve and the efficiency of the photoelectric heating mechanism depend on the mass fraction put into PAHs (Bakes & Tielens 1994). Depending on the PAH abundance, they contribute to the total dust mass by ∼1% for [PAH] = 10^{-7} and ∼10% for [PAH] = 10^{-6}.

Table 4. Key chemical reaction rates[†] adopted in this work.

Reaction	Rate [cm^3 s^{-1}]
$HCO^+ + e^- \rightarrow CO + H$	$2.4 \times 10^{-7}(300\,K/T)^{0.69}$ [a]
$HCO^+ + PAH^- \rightarrow PAH + CO + H$	$1.4 \times 10^{-8}(300\,K/T)^{0.50}$ [b]
$M^+ + e^- \rightarrow M + h\nu$	$3.7 \times 10^{-12}(300\,K/T)^{0.65}$
$M^+ + PAH^- \rightarrow M + PAH$	$1.0 \times 10^{-8}(300\,K/T)^{0.50}$ [b]
$C^+ + H_2O \rightarrow HCO^+ + H$	$8.9 \times 10^{-10}(300\,K/T)^{0.50}$
$C^+ + H_2O \rightarrow HOC^+ + H$	$1.8 \times 10^{-9}(300\,K/T)^{0.50}$
$CO^+ + H_2 \rightarrow HCO^+ + H$	7.5×10^{-10}
$CO^+ + H_2 \rightarrow HOC^+ + H$	7.5×10^{-10}
$HOC^+ + H_2 \rightarrow HCO^+ + H_2$	3.8×10^{-10} [c]

[†] Rates are from the *UDFA* and *OSU* databases unless indicated; [a] cited in the text as $\alpha(HCO^+)$, it also applies to DCO^+ and $H^{13}CO^+$; [b] rate is from (Flower & Pineau des Forêts 2003); [c] rate is from (Smith et al. 2002).

3.2.2. Chemical network and elemental abundances

Once the UV field is determined at each cloud position, steady-state chemical abundances are computed for a given network of chemical reactions. The model also computes the temperature profile by solving the thermal balance between the most important gas heating and cooling mechanisms (Le Petit et al. 2006). Our chemical network contains ~160 species and ~2000 reactions. It includes deuteration, ^{13}C fractionation (Graedel et al. 1982) and HCO^+/HOC^+ isomerization reactions. When available, we used the photodissociation rates given by van Dishoeck (1988), which are explicitly calculated for Draine's interstellar radiation field (ISRF). The most critical reaction rates for our determination of the ionization fraction are listed in Table 4. Most reactions were checked against *OSU* (Herbst and co-workers) and *UDFA* (Woodall et al. 2006) networks. Also, we benchmarked our network with more extended ones by comparing the predicted abundances of simple species such as CO and DCO^+.

Following Flower & Pineau des Forêts (2003), we have also included interactions (~60 reactions) of gas phase species with very small aromatic grains (neutral PAH and singly charged $PAH^{\pm}$). In particular, we take into account PAH-gas processes such as neutralization reactions of atomic and molecular cations on PAH^-, PAH electron attachment and photodetachment of PAH^- and PAH by UV photons. Such processes can play a significant role in the ionization balance of dense molecular clouds (e.g., Lepp & Dalgarno 1988; Bakes & Tielens 1998; Flower et al. 2007, Wakelam & Herbst 2008; Wolfire et al. 2008). We have not included larger grains in the network in order to isolate the role of PAHs in the gas-phase chemistry. We thus assume that recombinations of ions with grains are much less frequent than recombinations with electrons and PAH^-. This is partially justified by the fact that, according to their size and mass, the fractional abundance of "MRN grains" is low: $n_g/n_H \approx 10^{-10}$ and their *effective* cross section per H nucleus is $(n_g/n_H)\pi a^2 \approx 10^{-21}$ cm^{-2} (the product of the grain abundance and the mean grain cross section). Grain growth towards the denser parts the cloud will result in even lower grain abundances and smaller *effective* cross sections if the gas-to-dust mass ratio has to be preserved: e.g., $(n_g/n_H) \approx 10^{-13}$ and $(n_g/n_H)\pi a^2 \approx 10^{-22}$ cm^{-2} if the grain radii a increase by ~10. Therefore, the resulting lower abundance of charged grains and their smaller *effective* cross section for ion-grain recombinations will not alter our estimations of the ionization fraction much.

Table 5. Standard conditions and gas-phase elemental abundances. Molecular, atomic and electron abundances, noted [x], refer to H.

Parameter	Value
Radiation field χ	60 (Draine units)
Density $n_H(r) = n(H) + 2n(H_2)$	$\propto r^{-3}$, up to $\sim 2 \times 10^5$ cm^{-3}
Line of sight depth l_{depth}	0.1 pc
$[He] = n(He)/n_H$	1.00×10^{-1}
[O]	3.02×10^{-4}
$[^{12}C]$	1.38×10^{-4}
[N]	7.95×10^{-5}
[D]	1.60×10^{-5}
[S]	3.50×10^{-6}
$[^{13}C]=[^{12}C]/60$	2.30×10^{-6}
[PAH]	variable: 0–10^{-7}
[metals] ≡ [M] ≡ [Fe + Mg + ...]	variable: 10^{-11}–10^{-5}
Cosmic-ray ionization rate ζ	variable: 10^{-18}–10^{-15} s^{-1}

The adopted elemental abundances are shown in Table 5. Low ionization potential heavy *metals* ($\lesssim$8 eV; Fe^+, Mg^+ or Na^+) are all represented by a single element, "M^+". In our model, such metals slowly recombine with electrons (through radiative recombinations), can be photoionized and can exchange charge with ions and neutrals (including PAHs). However, they are assumed to be chemically inert and thus do not form *metallic* molecules (e.g., Oppenheimer & Dalgarno 1974).

Once the physical and geometrical parameters of the cloud are constrained, the only free parameters in the model are the cosmic-ray ionization rate and the metal and PAH abundances.

3.3. From abundances to spectra: mm radiative transfer

We use the PDR model predictions (molecular abundance, $n(H_2)$, $n(H)$, gas temperature and ionization fraction gradients) as input for a nonlocal radiative transfer calculation able to compute DCO^+ and $H^{13}CO^+$ line intensities as a function of cloud position. Our radiative transfer code handles edge-on plane-parallel geometry, and accounts for line trapping, collisional excitation[2], and radiative excitation by absorption of continuum photons. After the level populations are determined in each modeled slab, emergent line intensities along each line of sight are computed and convolved with the telescope angular resolution at each frequency. A more detailed description is given in Goicoechea et al. (2006; Appendix). Since typical densities in the Horsehead (~10^4–10^5 cm^{-3}) are below the critical densities of the observed high-dipole moment molecular ions (a few ~10^5–10^6 cm^{-3} for the studied transitions) our approach allows us to properly take into account non-LTE excitation effects (e.g., subthermal excitation), as well as opacity and line profile formation.

4. Chemistry of the ionization fraction probes

4.1. $H^{13}CO^+$ and DCO^+ chemistry in the UV shielded core

The detection of very bright DCO^+ emission towards the shielded core (Pety et al. 2007) implies cold gas temperatures ($T_k \simeq$ 10–20 K) and thus efficient HCO^+ deuterium fractionation (i.e., $[DCO^+]/[HCO^+] \gg D/H$). From our observations we

[2] PDR-like environments require us to consider inelastic collisions with H_2, H, He and e^-. $H^{13}CO^+$, DCO^+ and HOC^+ collisional rates with H_2, H and He have been scaled from those of Flower (1999), while collisional rates with e^- were kindly provided by Faure and Tennyson (see e.g., Faure & Tennyson 2001).

infer $[DCO^+] \simeq 8.0 \times 10^{-11}$, $[H^{13}CO^+] \simeq 6.5 \times 10^{-11}$ and thus a $[DCO^+]/[HCO^+] \simeq 0.02$ abundance ratio towards the core peak. Such gas-phase DCO^+ enhancement is achieved via the reaction:

$$H_3^+ + HD \rightleftarrows H_2D^+ + H_2 + \Delta E \quad (1)$$

which is endothermic by ~232 K in the right-to-left direction (Gerlich et al. 2002), followed by

$$CO + H_2D^+ \rightarrow DCO^+ + H_2 \quad (2)$$

which dominates the DCO^+ formation in the cold and dense gas. The absence of significant DCO^+ line emission in the PDR is consistent with the higher temperatures (>60 K) expected in the illuminated edge of the cloud.

The detection of intense $H^{13}CO^+$ emission towards the shielded core and its vicinity (see Fig. 1) implies low ionization fractions. In terms of excitation and opacity effects, $H^{13}CO^+$ is a much more reliable tracer of HCO^+ column density than $H^{12}CO^+$ itself (as the latter suffers from very large opacities and line photon scattering by low-density halos; e.g., Cernicharo & Guélin 1987). In terms of its chemistry, two main processes dominate the formation of $H^{13}CO^+$ in the low temperature shielded gas:

$$^{13}CO + H_3^+ \rightarrow H^{13}CO^+ + H_2 \quad (3)$$

and isotopic fractionation through

$$^{13}CO + H^{12}CO^+ \rightleftarrows H^{13}CO^+ + {}^{12}CO + \Delta E \quad (4)$$

which is endothermic by only ~9 K in the right-to-left direction (Langer et al. 1984) and competes with dissociative recombination in the destruction of $H^{13}CO^+$ where the abundance of electrons is low. For the physical conditions prevailing in the shielded core, we predict $[H^{12}CO^+]/[H^{13}CO^+]$ abundance ratios down to ~0.7 times lower than the elemental $[^{12}C]/[^{13}C]$ isotopic ratio. Since both $H^{13}CO^+$ and DCO^+ are mainly destroyed by fast dissociative recombination with electrons:

$$H^{13}CO^+ + e^- \rightarrow {}^{13}CO + H \quad (5)$$

$$DCO^+ + e^- \rightarrow CO + D \quad (6)$$

their abundances inversely scale with that of electrons. In this work we have used a *"standard"* HCO^+ dissociative recombination rate (i.e., $\alpha(HCO^+) = 2.4 \times 10^{-7}(300/T)^{0.69}$ cm^3 s^{-1}) recommended in most astrochemical databases. We note, however, that there is a certain discrepancy among different theoretical calculations and measurements of this key chemical rate (see discussion by Florescu-Mitchell & Mitchell 2006, and references therein). In Sect. 7 we discuss the influence of adopting a smaller, *"non standard"* $\alpha'(HCO^+)$ rate on our results.

4.2. HOC^+ and $H^{13}CO^+$ chemistry in the PDR

In order to extract the $[HOC^+]$ and $[H^{13}CO^+]$ abundances towards the Horsehead PDR, we have modeled the observed lines (Fig. 2) using our best knowledge of the prevailing physical conditions: T_k = 60–120 K, $n(H_2) = 5 \times 10^4$ cm^{-3}, $n(H) = 500$ cm^{-3}, $[e^-] = 5 \times 10^{-5}$ and a 0.1 pc line-of-sight depth (or $N_H \simeq 3.1 \times 10^{22}$ cm^{-2}) all accurate within a factor ~2. From the observed lines we derive the following column densities: $N(HOC^+) = (1.2–2.5) \times 10^{11}$ cm^{-2} and $N(H^{13}CO^+) = (4.7–7.8) \times 10^{11}$ cm^{-2}, which translates into $[HOC^+]=(0.4–0.8) \times 10^{-11}$ and $[H^{13}CO^+] = (1.5–2.5) \times 10^{-11}$. This computation assumes that the HOC^+ and $H^{13}CO^+$ emission fills the IRAM-30 m beam. However, HOC^+ has not been mapped and its emission could well arise from the same ~12″–width filament where the emission of small hydrocarbons and HCO radical is concentrated (Pety et al. 2005; Gerin et al. 2009). In this case, $[HOC^+]$ increases by a factor ~3. Therefore, we conclude that the $[HOC^+]/[H^{13}CO^+]$ abundance ratio towards the PDR lies in the range ≃0.3–0.8. These values are orders of magnitude higher than the value expected in the UV shielded gas.

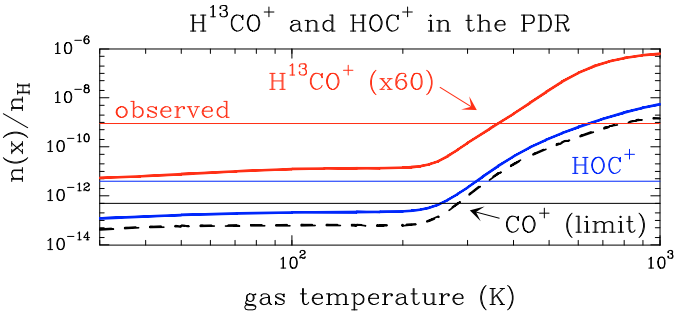

Fig. 3. Predicted $H^{13}CO^+$, HOC^+ and CO^+ peak abundances in the PDR ($A_V \simeq 0.5$–1.5) as a function of gas temperature. $H^{13}CO^+$ and HOC^+ abundances (and CO^+ abundance upper limit) derived from observations towards the PDR position are shown with horizontal thin lines.

Our chemical models (see next section) reproduce the $[HOC^+]/[H^{13}CO^+]$ abundance ratio towards the PDR but the absolute abundances derived from observations are larger than those predicted by the model. The discrepancies between observed and modeled abundances for HOC^+ and $H^{13}CO^+$ likely have a common origin. In particular, the formation of HOC^+ in UV irradiated gas is driven by reactions involving C^+ and species such as H_2O and CO^+ (from $C^+ + OH$ reaction) that efficiently form at high temperatures, that is:

$$C^+ + H_2O \rightarrow HCO^+/HOC^+ + H \quad (7)$$

$$CO^+ + H_2 \rightarrow HCO^+/HOC^+ + H \quad (8)$$

where reaction 7 predominantly produces HOC^+ whereas reaction 8 has similar branching ratios for the HCO^+ and HOC^+ formation (e.g., Scott et al. 1997; Savage & Ziurys 2004). The HOC^+ destruction is governed by the isomerization reaction:

$$HOC^+ + H_2 \rightarrow HCO^+ + H_2. \quad (9)$$

Laboratory experiments show that the reaction rate is lower than previously thought (Smith et al. 2002), allowing interstellar HOC^+ to exist at detectable amounts.

The intensity peak of the CO J = 2–1 optically thick lines observed with the PdBI ($T_{mb} \simeq 60$ K $\approx T_{ex}$; Pety et al. 2005), together with the observed CO J = 4–3/2–1 line ratio (Philipp et al. 2006), provide a lower limit to the gas temperature in the PDR ($T_k \simeq$ 60–120 K). Temperatures in this range are predicted by the PDR model but are not enough to overcome the activation energy barriers of the neutral-neutral reactions leading to the formation of abundant H_2O, OH and CO^+ (e.g., Neufeld et al. 1995; Cernicharo et al. 2006). Therefore, our models predict HOC^+ and $H^{13}CO^+$ abundances lower than observed because their precursor molecules have low abundances, and reactions 7 and 8 are not efficient enough.

We have computed that gas temperatures around ~350 K are needed to reproduce the observed HOC^+ and $H^{13}CO^+$ abundances in the PDR through the previous scheme (see Fig. 3). Our models of the Horsehead (low UV radiation field) include photoelectric heating from PAHs and grains but do not predict such a warm gas component even if the PAH abundance is significantly

increased. However, we do not model the PDR gas dynamics and thus processes such as shock waves, driven by the expansion of the H II region that compress the cloud edge, may provide additional gas heating sources to trigger this *warm chemistry*. This reasoning is partially consistent with the non detection of CO^+ lines, at least at the sensitivity level of our long integration observation (rms $\sim$ 50 mK in a 0.20 km s^{-1} velocity width channel or $[CO^+] \leq 5 \times 10^{-13}$).

If the gas in the PDR has not gone through such a *warm phase*, reaction 8 has to be ruled out as the main chemical pathway for HOC^+ formation and an alternative formation scenario is required. In this case, we propose that the enhanced HOC^+ abundance in the PDR can still be related to the high abundance of C^+ (and thus high ionization fraction), but also to grain photodesorption of water-ice mantles formed in earlier evolutionary stages of the cloud.

In this picture, the low χ/n ratio in the Horsehead ($\sim 10^{-3}$) will allow water-ices to be photodesorbed close to the illuminated edge of the cloud (see predictions by Hollenbach et al. 2009), increasing the water vapor abundance well above the pure gas phase predictions. Reaction 7 will then dominate the HOC^+ formation in the PDR. Taking into account that isomerization, dissociative recombination and photodissociation contribute to HOC^+ destruction, we estimate that the required water vapor abundance needed to explain the inferred HOC^+ abundance in the PDR is $[H_2O] \simeq 1800 \times [HOC^+] \simeq (0.7\text{–}2.2) \times 10^{-8}$. *Herschel Space Observatory* observations will enable the detection of C^+ and H_2O lines in a large sample of PDRs, confirming whether or not water vapor is abundant at the *edges* of molecular clouds (e.g., Cernicharo et al. 2006).

5. Determination of the ionization fraction

Figure 4 presents depth–dependent predictions of several photochemical models across the Horsehead edge. Each model shows the main physical parameters (density and temperature), the ionization fraction gradient, the DCO^+, $H^{13}CO^+$ and HOC^+ abundances (our observational probes of the ionization fraction) and the abundances of key chemical species for the charge balance in the cloud: CO/C/C^+, M/M^+, PAH^-/PAH/PAH^+.

Four sets of models are displayed. *Top/bottom* models use a *low* ($\zeta = 3 \times 10^{-17}$ s^{-1}) and *high* ($\zeta = 3 \times 10^{-16}$ s^{-1}) cosmic-ray ionization rate respectively. *Left/right* models exclude and include the effects of PAHs. In the latter case, we include PAHs in the UV radiative transfer (as a source of absorption and scattering of UV photons), in the photoelectric heating and in the chemical network. We start the chemistry computation by including neutral PAHs alone with an initial abundance of $[PAH] = 10^{-7}$. In each set of models (each panel), the only parameter that varies is the abundance of metals: *high* metallicity with $[M] = 10^{-6}$ (dashed curves) and *low* metallicity with $[M] = 10^{-9}$ (solid curves). The low metallicity case implies a large metal depletion from the gas phase.

In terms of the chemical species observed in this work, a salient feature of all models is the constancy of the $DCO^+/H^{13}CO^+$ abundance ratio once the gas is shielded from UV radiation ($A_V \gtrsim 6$). This feature agrees with the almost identical spatial distribution of DCO^+ and $H^{13}CO^+$ emission observed beyond the PDR (see Fig. 1). This similarity was already noticed in the lower resolution DCO^+ and $H^{13}CO^+$ pioneering maps of several molecular clouds (e.g., Guélin et al. 1982). Also, the predicted $[HOC^+]/[H^{13}CO^+]$ abundance ratio towards the PDR is in good agreement with the value inferred from observations. In this UV irradiated region where the C^+ and electron abundances are very high, the HCO^+ destruction rate becomes comparable to the isomerization rate (reaction 9). This implies that the $[HOC^+]/[H^{13}CO^+]$ abundance ratio in the cloud achieves the highest value in the PDR.

5.1. The role of ionized carbon and metals

According to the ionization fraction gradient all models show two differentiated environments separated by a transition region: the "PDR" ($A_V \simeq$ 0–2) and the "shielded core" ($A_V \gtrsim 6$). The electron density at every cloud position is given by the difference of cations and anions densities;

$$n_e = \sum_i n_i(\text{cations}^+) - \sum_j n_j(\text{anions}^-). \quad (10)$$

In the PDR, carbon, the most abundant heavy element with a ionization potential below 13.6 eV, provides most of the charge: $n(e^-) \simeq n(C^+)$. Therefore, the ionization fraction in the PDR is high, $[e^-] \sim 10^{-4}$, and independent of elemental abundances other than carbon.

As A_V increases inwards the cloud, the C^+ abundance decreases by several orders of magnitude and so does the abundance of electrons. In the shielded core ($A_V \gtrsim 6$), low ionization heavy metal ions (e.g., Fe^+, Mg^+ or Na^+) determine much of the ionization fraction (Oppenheimer & Dalgarno 1974; Guélin et al. 1982). In the absence of PAHs, abundant molecular ions m^+ transfer charge rapidly to heavy metal atoms M through $m^+ + M \rightarrow m + M^+$ reactions. Metal ions recombine orders of magnitude slower than molecular ions (Table 4), and thus a large fraction of them is kept ionized (higher [M] implies higher electron abundances). Therefore, the ionization fraction in the core is highly dependent on the adopted metallicity, and varies from a few $\times 10^{-9}$ for $[M] = 10^{-9}$, to a few $\times 10^{-7}$ for $[M] = 10^{-6}$.

5.2. The role of PAHs

Depending on their abundances, the presence of PAHs can alter the chemistry and the ionization balance in dense clouds (e.g., Lepp & Dalgarno 1988). For our adopted abundance of $[PAH] = 10^{-7}$ the right and left panels in Fig. 4 shows that the presence of PAHs most modifies the ionization fraction at $A_V \gtrsim 2$. Hence, if not all PAHs accrete onto bigger grains or coagulate towards cloud interiors, PAH^- can be abundant through the cloud because the radiative electron attachment rate

$$PAH + e^- \rightarrow PAH^- + h\nu \quad (11)$$

is high ($\geq 10^{-7}$ cm^3 s^{-1}), although probably dependent on the PAH size (Omont 1986; Allamandola et al. 1989; Flower et al. 2007; Wakelam & Herbst 2008). In the shielded core PAH^- is destroyed by recombination with atomic (M^+,...) and molecular cations (HCO^+, H_3O^+,...) which are orders of magnitude less abundant than the available cations in the PDR (C^+, S^+,...). Negative PAH ions thus reach high abundances ($[PAH^-] \simeq 2 \times 10^{-8}$). For our choice of PAH parameters, this means that PAH^- can be the most abundant negatively charged species, more than electrons for $A_V \geq 5$. In addition, recombination of atomic ions on PAH^- is by far more efficient than the slow radiative recombination on electrons. This is a very important point since heavy metal ions and molecular ions are now neutralized at similar rates. As a result, both the abundance of metal cations and the ionization fraction decreases when PAHs are included, while molecular ions such as $H^{13}CO^+$ and DCO^+ increase their abundances (see Fig. 4 *right panels*).

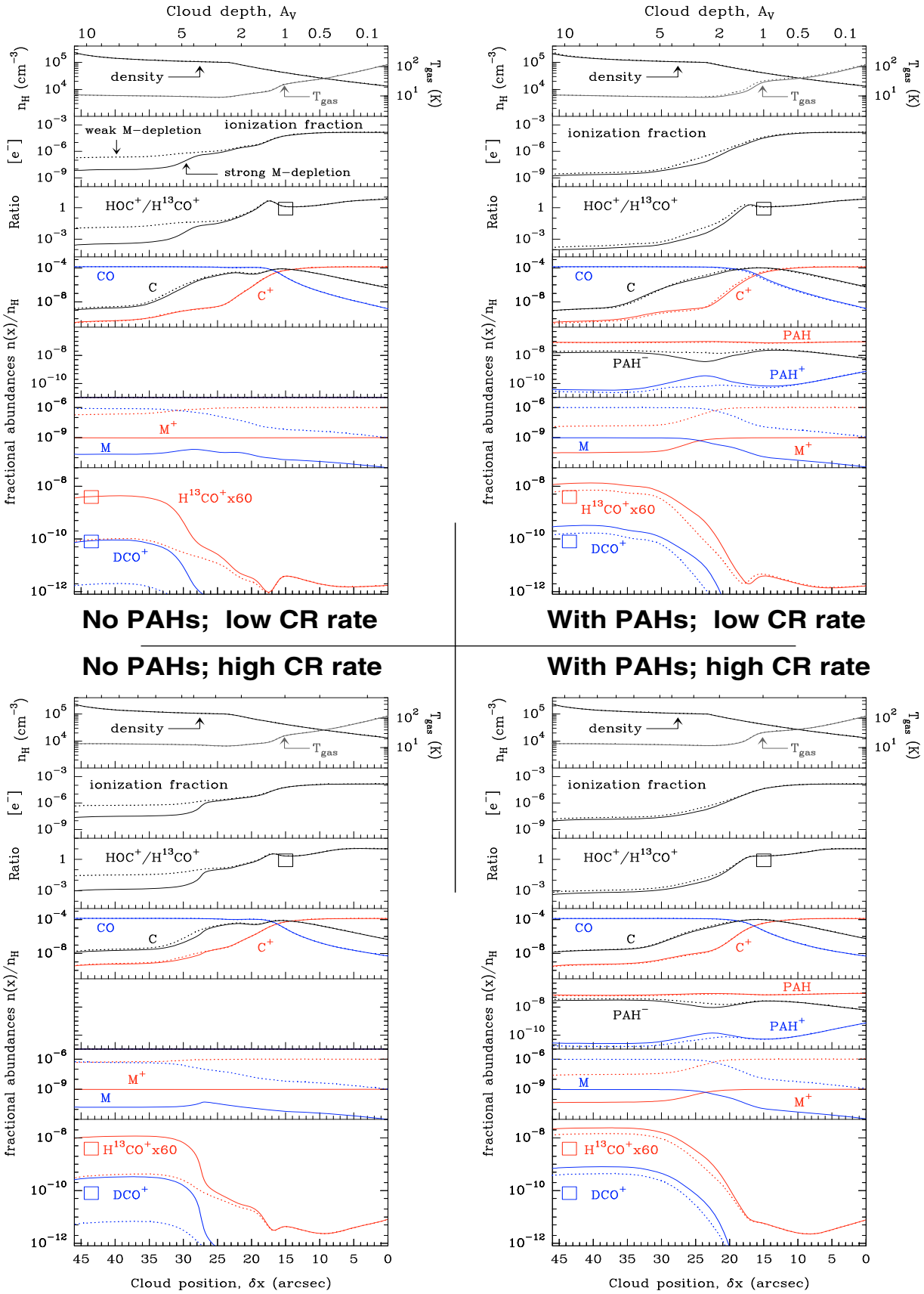

Fig. 4. Grid of chemical models for 2 different metal abundances, *low-metallicity* with [M] = 10^{-9} (*strong metal depletion case*, solid curves) and *high-metallicity* with [M] = 10^{-6} (*weak metal depletion case*, dashed curves). "Low CR rate" refers to models with $\zeta = 3 \times 10^{-17}$ s^{-1} while models with "high CR rate" refer to $\zeta = 3 \times 10^{-16}$ s^{-1}. Models "with PAH" include PAH-gas interactions in the chemical network (with [PAH] = 10^{-7}) while models with "no PAH" are pure gas-phase models. The black empty square represents the [HOC^+]/[$H^{13}CO^+$] abundance ratio inferred towards the PDR from observations. The blue and red empty squares represent the DCO^+ and $H^{13}CO^+$ abundances derived towards the core.

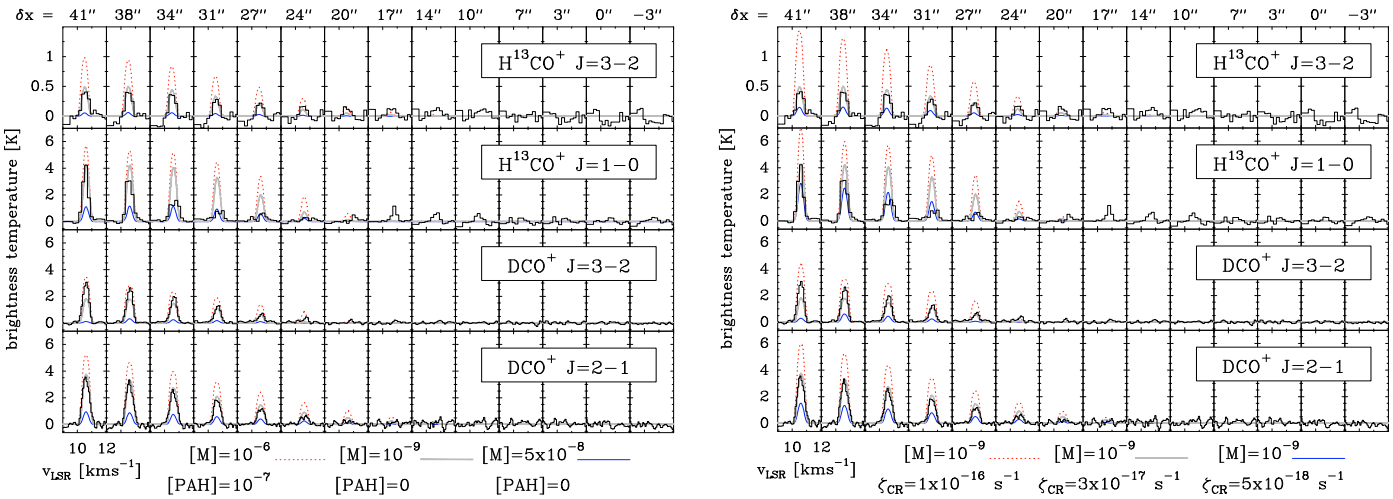

Fig. 5. *Left*: $H^{13}CO^+$ and DCO^+ spectra along the direction of the exciting star at $\delta y = 15''$ (histograms). Radiative transfer models using the output of PDR models for a fixed cosmic-ray ionization rate ($\zeta = 3 \times 10^{-17}$ s^{-1}) and varying metallicities. *Thin blue curves* for [M] = 5×10^{-8} and no PAHs; *thick grey curves* for [M] = 10^{-9} and no PAHs; *dashed red curves* for [M] = 10^{-6} and [PAH] = 10^{-7}. Modeled line profiles have been convolved with the appropriate Gaussian beam at each observed frequency (the angular resolution for each line are quoted in Tables 1 and 2). *Right*: same as left but for a fixed metal abundance ([M] = 10^{-9}), no PAHs and varying cosmic-ray ionization rate ζ. *Thin blue curves* for a model with $\zeta = 5 \times 10^{-18}$ s^{-1}; *thick grey curves* for $\zeta = 3 \times 10^{-17}$ s^{-1}; *dashed red curves* for $\zeta = 10^{-16}$ s^{-1}.

At the illuminated edge of the cloud, PAH^- is predominantly destroyed by UV photons through electron detachment,

$$PAH^- + h\nu \rightarrow PAH + e^- \quad (12)$$

and through recombination with atomic cations which are very abundant in the PDR (e.g., Bakes & Tielens 1998; Wolfire et al. 2008). As a consequence, the abundance of ions such as S^+ in the PDR decreases with respect to models without PAHs. This effect is important to determine the elemental abundances and depletion factors. Despite the higher PAH^- destruction rates in the PDR, the high electron density and relatively low UV field in the Horsehead allows PAH^- to form efficiently through electron attachment (reaction 11). Hence the resulting PAH^- abundance is also high in the PDR. On the other hand, the predicted abundance of positively charged PAH^+ in our models is ∼500 times smaller than the abundance of PAH^- (due to fast electronic recombination) and therefore PAH^+ do not seem to play a major role in the ionization balance inside the cloud (see also Lepp & Dalgarno 1988; Wakelam & Herbst 2008).

5.3. The role of the cosmic-ray ionization rate

Cosmic rays affect the ionization state and the physics of molecular clouds, being the dominant source of heating and ionization in the gas shielded from interstellar radiation fields. Indeed, *secondary* UV photons are created in cloud interiors by H_2 electron cascades following H_2 excitation by collisions with cosmic rays (Prasad & Tarafdar 1983). Therefore, cosmic rays maintain a certain ionization degree in the shielded gas and play a fundamental role in the ion-neutral chemistry by setting the abundance of key ions (Herbst & Klemperer 1973).

Most studies based on the interpretation of observed molecular ions set a range of a few 10^{-17} to a few 10^{-16} s^{-1} for the cosmic-ray ionization rate (Le Petit et al. 2004; van der Tak 2006; Dalgarno 2006 and references therein). However, it is still debated whether or not ζ depends on environmental conditions (e.g., galactic center vs. disk clouds) or if it varies from source to source (e.g., from dense molecular cores to more translucent clouds). In many ways, PDRs offer an interesting intermediate medium to analyze the transition between translucent and dark clouds.

In terms of our observations, the DCO^+ and $H^{13}CO^+$ abundances directly scale with ζ in the UV shielded gas. Indeed, these ions are direct products of the H_3^+ destruction (through reactions 2 and 3), and the H_3^+ formation is proportional to $\simeq \zeta\, n_H$. However, ζ and the metal abundance cannot be constrained independently from the inferred DCO^+ and $H^{13}CO^+$ abundances since both parameters control the ionization fraction, and thus the destruction of these ions through reactions 5 and 6.

6. Results: observational constraints

In this section we compare the synthetic and observed $H^{13}CO^+$ and DCO^+ spectra as a function of cloud position. We then explore the range of metallicities and cosmic-ray ionization rates compatible with the $H^{13}CO^+$ and DCO^+ inferred abundances (see Table 6). The influence of PAHs is also investigated. We finally compare the $[HOC^+]/[H^{13}CO^+]$ ratio obtained towards the Horsehead with the values derived in other PDRs.

6.1. Constraints to the metals abundance

Figure 5 *left* shows the spectra along the direction of the exciting star (histograms) and radiative transfer models using the output of several PDR models for a fixed ionization rate ($\zeta = 3 \times 10^{-17}$ s^{-1}) and varying metallicities. In particular, the model with [M] = 10^{-9} (and no PAHs) displays a notable agreement with both the DCO^+ and $H^{13}CO^+$ spatial distribution and with the inferred peak abundances towards the core (Table 6). In addition, Fig. 6 *left* shows the predicted ionization fraction and $[H^{13}CO^+]$ and $[DCO^+]$ abundances at the core peak ($A_V > 10$) as a function of [M] (blue-solid curves). These models (no PAHs, fixed ζ) show that the upper limit metallicity compatible with observations is [M] $\leq 4 \times 10^{-9}$, which implies an ionization fraction of $[e^-] = (7 \pm 1) \times 10^{-9}$ at the core peak. Higher metal abundances increase the ionization fraction (see Fig. 6 *left*), which translates into weaker lines than observed (Fig. 5 *left*: thin-blue curves). Therefore, the gas-phase metal abundance is depleted by ∼4

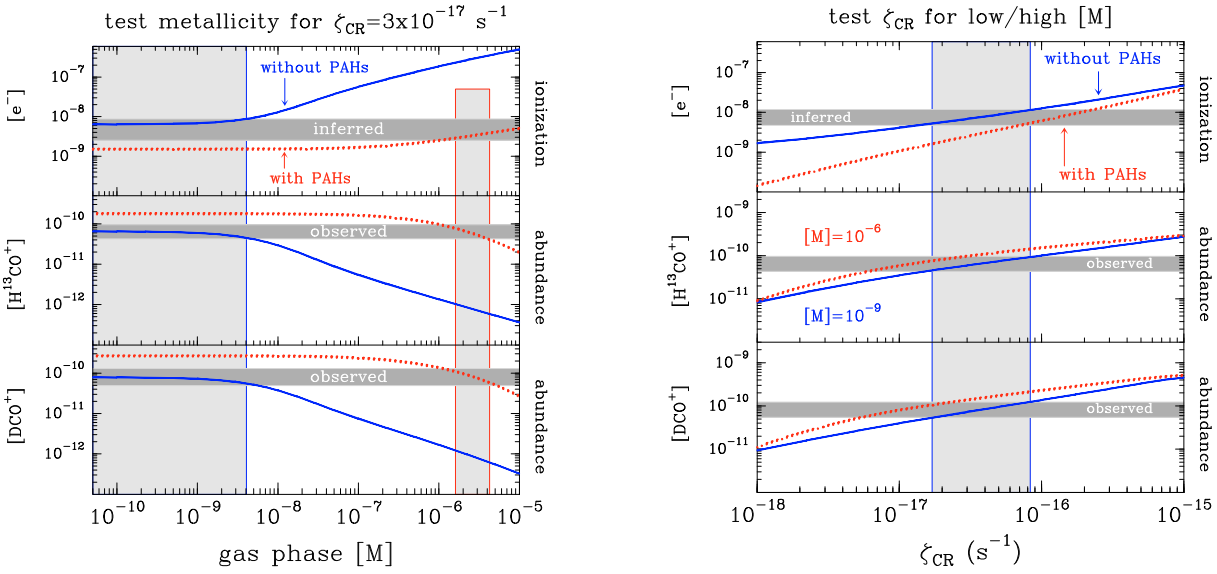

Fig. 6. *Left*: model predictions for the shielded core (the "DCO$^+$ peak" at $A_V > 10$). The ionization rate due to cosmic rays is fixed to $\zeta = 3 \times 10^{-17}$ s^{-1}. The different panels show (*upper*): the ionization fraction, (*middle*): the H^{13}CO$^+$ abundance and (*lower*): the DCO$^+$ abundance as a function of gas phase metallicity. Blue-solid curves for models without PAHs, and red-dotted curves for models with neutral and charged PAHs ([PAH] = 10^{-7}). Horizontal shaded regions show the H^{13}CO$^+$ and DCO$^+$ abundances derived from observations towards the core, while vertical shaded regions show the parameter space compatible with observations. *Right*: same as previous figure but for a fixed low metallicity of [M] = 10^{-9} (no PAH; blue-solid curves) and a fixed high metallicity of [M] = 10^{-6} ([PAH] = 10^{-7}; red-dotted curves). The different panels show (*upper*): the ionization fraction, (*middle*): the H^{13}CO$^+$ abundance and (*lower*): the DCO$^+$ abundance as a function of the ionization rate due to cosmic rays.

Table 6. Inferred abundances [x]=N(x)/N_H where N_H=N(H)+2N(H$_2$).

Species	Shielded core $A_V \geq 6$ $\delta x \simeq 45''$	PDR A_V = 0–2 $\delta x \simeq 15''$
N_H (cm^{-2})	5.8×10^{22}	3.1×10^{22}
[H^{13}CO$^+$]	6.5×10^{-11}	1.5×10^{-11}
[H^{12}CO$^+$]	3.9×10^{-9}	9.0×10^{-10}
[DCO$^+$]	8.0×10^{-11}	(–)
[HOC$^+$]	(–)	0.4×10^{-11} †
[CO$^+$]	(–)	$\leq 5.0 \times 10^{-13}$
[e$^-$]	$(1–8) \times 10^{-9}$	10^{-6}–10^{-4}

† Assuming extended emission. It would be 1.2×10^{-11} if HOC$^+$ arises from a 12″–width filament as HCO (Gerin et al. 2009).

orders of magnitude with respect to the Sun ([M] $\simeq 8.5 \times 10^{-5}$, Anders & Grevesse 1989). This range of depletion is similar to that obtained in other prestellar cores such as Barnard 68 (Maret & Bergin 2007). We shall refer it as the *strong metal depletion* case.

The inclusion of PAH interactions implies lower ionization fractions and enhanced molecular ion abundances (see Fig. 6 *left*) which result in overestimated H^{13}CO$^+$ and DCO$^+$ line intensities towards the core. Therefore, the abundance of metals (e.g., indirectly the ionization fraction) has to be increased to match the observed intensities. In particular, Fig. 5 *left* shows that a model with [PAHs] = 10^{-7} and [M] = 10^{-6} (red-dashed curves) displays only a factor <2 brighter lines than models with 3 orders of magnitude lower metallicities and no PAHs (thick-grey curves). As shown in Fig. 6 *left*, the inclusion of PAHs makes the range of metal abundances compatible with observations much higher now, [M] = $(3 \pm 1) \times 10^{-6}$. The required abundance of metals is at least a factor ~500 larger than the former case without PAHs. Thus, we refer to it as the *weak metal depletion* case. Note that this metallicity is still below the gas-phase abundance of Fe+Mg+... elements in the diffuse interstellar gas (e.g., Wolfire et al. 1995; Howk et al. 2006) and is consistent with the incorporation of metals into dust grains in higher density regions (e.g., Wolfire et al. 1995). On the other hand, the ionization fraction required to reproduce the H^{13}CO$^+$ and DCO$^+$ abundances does not change much, [e$^-$] = $(4 \pm 1) \times 10^{-9}$ at the core peak (red-dashed curves Fig. 6 *left*). Therefore, it is not easy to distinguish between the *strong metal depletion* (no PAHs) and *weak metal depletion* (with PAHs) cases in terms of the ionization fraction. The observation of forbidden lines from metals such as [Fe II] towards the UV illuminated edges of molecular clouds may help to remove this apparent degeneracy. In one of the few positive cases, the S140 PDR, the detection of a weak [Fe II]26.0 μm fine-structure line emission suggests that iron is depleted, but with an abundance of $\sim 5 \times 10^{-8}$ relative to H (Timmermann et al. 1996). Nevertheless, without mapping and comparing with other PDR tracers, it is not obvious to disentangle whether [Fe II] lines arise from the PDR gas or from the adjacent (HII) ionization front (e.g., Marconi et al. 1998; Kaufman et al. 2006).

6.2. Constraints to the cosmic-ray ionization rate

Figure 5 *right* shows again the observed spectra along the direction of the exciting star (histograms) and radiative transfer models using the output of PDR models that vary the cosmic ray rate, without PAHs and a fixed metal abundance of [M] = 10^{-9}. The adopted metal abundance is, within an order of magnitude, the usual value estimated in prestellar cores (e.g., Caselli et al. 1999; Maret & Bergin 2007) and is compatible with our *strong metal depletion case*. Therefore, Fig. 5 *right* shows the effects of different ionization rates directly on the DCO$^+$ and H^{13}CO$^+$ line intensities. For the adopted physical conditions and chemical network, our observations constrain ζ within a factor ~2. In

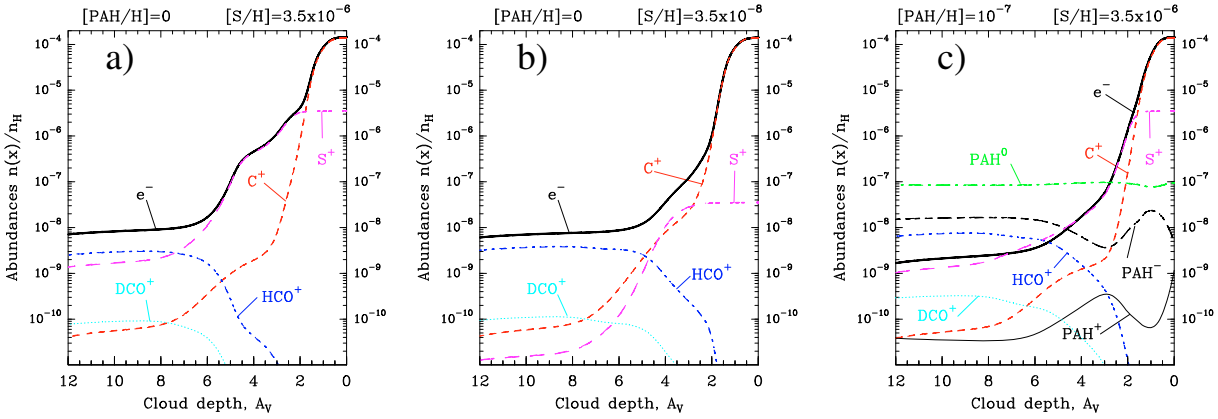

Fig. 7. Derived abundance profiles for the most significant ions studied in this work for different PAH and sulfur elemental abundances. An enhanced UV radiation field 60 times the mean ISRF illuminates the cloud from the right. The metal abundance ([M] = 10^{-9}) and the cosmic-ray rate ($\zeta = 3 \times 10^{-17}$ s^{-1}) are fixed in all models. **a)** Model with [PAH]=0 and [S] = 3.5×10^{-6} (low sulfur depletion). **b)** Model with [PAH] = 0 and [S] =3.5×10^{-8} (high sulfur depletion). **c)** Model with [PAH] = 10^{-7} and [S] = 3.5×10^{-6}.

particular, Fig. 6 *right* shows the predicted [e$^-$], [H^{13}CO$^+$] and [DCO$^+$] abundances at the core peak ($A_V > 10$) as a function of ζ, and suggests that in the absence of PAHs, the cosmic ray ionization rate range compatible with the observations of the Horsehead edge is $\zeta = (5 \pm 3) \times 10^{-17}$ s^{-1} (solid-blue curves). If PAHs are included in the chemistry, the metal abundance has to be increased accordingly to reproduce the observations. For our [PAH] = 10^{-7} model case, the required metal abundance needs to be above [M] $\simeq 10^{-6}$ to obtain ionization rates above $\zeta \simeq 10^{-17}$ s^{-1} (Fig. 6 *right*; red-dotted curves).

Note that given the fact that the H^{13}CO$^+$ formation in the PDR is not dominated by the ^{13}CO + H$_3^+$ reaction, the H^{13}CO$^+$ abundance in the UV illuminated gas does not scale with ζ. Therefore, we cannot further investigate if ζ varies significantly in the transition from diffuse regions to the shielded core (e.g., McCall et al. 2003; Padoan & Scalo 2005).

6.3. High ionization fraction in the PDR

The bright [C II]158 μm (Zhou et al. 1993) and [C I]492 GHz (Philipp et al. 2006) fine structure line emission towards the Horsehead PDR, together with subtle chemical effects such as the large [l-C$_3$H$_2$]/[c-C$_3$H$_2$] linear-to-cyclic abundance ratio (Teyssier et al. 2005) all show observationally that the ionization fraction is higher in the UV illuminated edge than towards the cloud interior. Nevertheless, all those studies lacked the angular resolution to properly measure the ionization fraction gradient.

The abundances of reactive ions such as HOC$^+$ are also predicted to be enhanced in the UV illuminated gas, where we have shown that the ionization fraction is high, up to [e$^-$] $\sim 10^{-4}$, and that the HOC$^+$ formation is linked to the availability of C$^+$. On the other hand, the H^{13}CO$^+$ abundance increases as the electron abundance decreases towards the shielded core. Therefore, we predict that the [HOC$^+$]/[H^{13}CO$^+$] abundance ratio scales with the ionization fraction gradient, reaching the highest values in the PDR (Fig. 4). In particular, we derive a high [HOC$^+$]/[H^{13}CO$^+$] = 0.3–0.8 ratio (or a low [HCO$^+$]/[HOC$^+$] $\simeq$ 75–200 ratio) towards the PDR, similar to that observed in other PDRs such as NGC 7023 (Fuente et al. 2003).

7. Discussion

7.1. The ionization fraction gradient

Star forming clouds display different environments depending on the dominant physical and chemical processes. These environments are, to a first approximation, similar to those studied here: (i) a low density *cloud edge* directly exposed to a UV radiation field from nearby stars; (ii) a *transition* region or *ridge* where the H$_2$ density increases as the gas temperature decreases due to the attenuation of the external radiation field. UV photons can still play a significant role depending on their penetration depths (e.g., cloud clumpiness, grain properties, etc.); and (iii) the denser *shielded cores* that may be externally triggered to form a new generation of stars depending on their stability against gravitational collapse (e.g., Goicoechea et al. 2008).

Assuming that the observed field-of-view in the Horsehead nebula is representative of the above 3 environments, our maps and chemical models reveal that the ionization fraction follows a steep gradient in molecular clouds: from [e$^-$] $\simeq 10^{-4}$ at the *edge* of the cloud (the "C$^+$ dominated" region) to a few times $\sim 10^{-9}$ in the *shielded cores*. The prevailing chemistry and the abundance of atomic ions such as C$^+$ and S$^+$ determine the "slope" of the ionization fraction gradient in the *transition* regions. In particular, sulfur (with a ionization potential of ~10.36 eV) is a good source of charge behind the "C$^+$ dominated" region. Advection and time-dependent effects may also modify the ionization fraction gradient with time. However, Morata & Herbst (2008) have shown models for (uniform) physical conditions similar to those in the Horsehead where [HCO$^+$] (and [e$^-$] presumably) does not change with time appreciably.

Figure 7 shows the predicted ionization fraction gradient, with a scale length of ~0.05 pc (or ~25″), and the main charge carriers for 3 representative models with fixed *standard* metal abundance (our *strong metal depletion case*) and *standard* cosmic-ray rate. Panel 7*a* shows a model without PAHs and high gas-phase sulfur abundance ([S] = 3.5×10^{-6}; Goicoechea et al. 2006). The ionization fraction gradient in the *core* / *transition* / *edge* zones, is mainly determined by the [HCO$^+$+S$^+$+M$^+$+...] / [S$^+$] / [C$^+$] abundances respectively. Sulfur ions control the charge balance in the *transition* layers, and due to their high abundance and slow radiative recombination rate with electrons, the ionization fraction is high, a few times 10^{-7}, and the gradient is smooth. This model qualitatively agrees with the observed more extended emission and narrower

line-widths of sulfur recombination lines compared to carbon recombination lines in dark clouds, as well as with the relatively low (<10) carbon-to-sulfur recombination lines intensity ratio (e.g., Pankonin & Walmsley 1978; Falgarone et al. 1978). All these signatures argue in favor of extended regions with significant amounts of gas-phase S^+.

Panel 7*b* shows the same model but sulfur abundances smaller by two orders of magnitude (strong gas-phase sulfur depletion). The ionization fraction in the cloud *core* ($A_V > 6$) and *edge* ($A_V < 2$) are nearly the same as in the previous high sulfur abundance model. However, the lack of abundant S^+ in the *transition* layers decreases the electron abundance considerably, and makes the ionization fraction gradient much steeper. Observational constraints to the atomic and ionic S abundances from far-IR fine structure lines or recombination lines, and a careful treatment of the sulfur chemistry (i.e., which are the most abundant S-bearing species as a function of cloud depth?) are thus required to quantify the S^+ abundance at large A_V and its impact on the charge balance.

Panel 7*c* shows a model with high sulfur abundance but including PAHs (with [PAH] = 10^{-7}). As presented in Sect. 5.2, negatively charged PAH^- efficiently form by radiative electron attachment and their abundance remains high through the cloud. Given the much higher recombination rates of atomic ions on PAH^- than on electrons, the abundance of atomic ions such as S^+ in the *transition zone*, or M^+ in the *shielded cores*, quickly decreases. Hence, lower ionization fractions (and a much weaker dependence on the assumed metal elemental abundance) are predicted by the model with PAHs. These results agrees with theoretical predictions for UV shielded gas (Lepp & Dalgarno 1988; Flower et al. 2007; Wakelam & Herbst 2008).

In summary, a high abundance of PAHs *throughout* the molecular cloud (not only in the PDR) plays a role in the ionization balance and in the abundance of molecular ions, which affects the determination of elemental abundances (e.g., S) from fractional molecular abundances (e.g., HCS^+/CS, SO^+/SO, etc.).

7.2. The PAH abundance in UV shielded gas

The PAH abundance in the dense and UV shielded gas is far from being well constrained. Different approaches to analyze ISO and Spitzer mid-IR observations towards several PDRs all argue in favor of an evolution of dust grain sizes: from the illuminated cloud edge where the emission of PAH bands dominates, to the shielded interiors where the continuum emission from bigger grains dominates (Rapacioli et al. 2005; Berné et al. 2007; Compiègne et al. 2008). It is not trivial to disentangle whether this is a physical effect (i.e., free PAHs are not present in the shielded regions) or an excitation effect (i.e., lack of UV photons). Even if the PAH abundance drastically decreases towards cloud interiors, a chemically significant fraction of them may survive. Unfortunately, while the effects of grain growth in the UV extinction curve have been modelled by us (Goicoechea & Le Bourlot 2007), including PAH coagulation/accretion in the chemistry is beyond the scope of this work. All we can say at this point is that a better description of the cloud chemistry may be a decreasing PAH abundance gradient or an increasing PAH size distribution towards the cloud interior. In any case, we have shown that the presence of free PAHs in molecular clouds modifies the prevailing chemistry. As a result, the predicted high abundance of PAH^- can dominate the recombination of metal ions and reduce the ionization fraction.

The presence of abundant free PAHs, or large molecules to which electron attach (Lepp & Dalgarno 1988), can thus be crucial in determining the coupling of the gas with magnetic fields in molecular clouds, but also in collapsing cores or in the "dead" zones of protoplanetary disks (magnetically inactive regions where accretion cannot occur if the ionization fraction is very low). According to our models, the PAH abundance threshold required to affect the metal and electron abundance determination in the UV shielded gas is [PAH] > 10^{-8}. *Herschel* observations might allow the identification of specific PAH carriers through their far-IR skeletal modes (Joblin et al. 2002; Mulas et al. 2006), thus providing clues to their composition and abundance variations in different environments.

7.3. "Non standard" HCO^+ dissociative recombination rate

We conclude by discussing the sensitivity of our determination of the ionization fraction from $H^{13}CO^+$ and DCO^+ abundances. In particular, we have checked the effects of adopting a smaller, *"non standard"* HCO^+ dissociative recombination rate, $\alpha'(HCO^+) = 0.7 \times 10^{-7}(300/T)^{0.50}$ cm^3 s^{-1} (Sheehan 2000, Florescu-Mitchell & Mitchell 2006). For models without PAHs, the predicted $H^{13}CO^+$ and DCO^+ abundances increase by a factor of ~3 with respect to models using the *"standard"* $\alpha(HCO^+)$ rate (Table 4), but the metallicity required to fit the observed lines has to be increased to [M] $\simeq 5 \times 10^{-8}$ and the predicted ionization fraction increases to [e^-] $\simeq 5 \times 10^{-8}$ in the core. This value should be regarded as the upper limit of our determination. On the other hand, the influence of $\alpha'(HCO^+)$ in models with PAHs is less important. It also requires high metallicities to fit the observed intensities (*weak metal depletion* case), but the predicted [e^-] in the shielded core remains low (below ~10^{-8}).

8. Summary and conclusions

We have presented the first detection of HOC^+ reactive ion towards the Horsehead PDR. Combined with our previous IRAM-PdBI $H^{13}CO^+$ J = 1–0 (Gerin et al. 2009) and IRAM-30 m $H^{13}CO^+$ and DCO^+ higher-J lines maps (Pety et al. 2007) we performed a detailed analysis of their chemistry, excitation and radiative transfer to constrain the ionization fraction as a function of cloud position. The observed field contains 3 different environments: (i) the UV illuminated *cloud edge*; (ii) a *transition* region or *ridge*; and (iii) a dense and cold shielded *core*. We have presented a study of the ionization fraction gradient in the above environments, which can be considered as templates for most molecular clouds. Our main conclusions are the following:

1. The ionization fraction follows a steep gradient, with a scale length of ~0.05 pc (~25″), from [e^-] $\simeq 10^{-4}$ ($n_e \sim$ 1–5 cm^{-3}) at the cloud *edge* (the "C^+ dominated" regions) to a few times ~10^{-9} in the *shielded core* (with ongoing deuterium fractionation). Sulfur, metal and PAH ions play a key role in the charge balance at different cloud depths.
2. The detection of HOC^+ towards the PDR, and the high [HOC^+]/[$H^{13}CO^+$] $\simeq$ 0.3–0.8 abundance ratio inferred, proves the high ionization fraction in the UV irradiated gas. However, the $H^{13}CO^+$ and HOC^+ abundances derived from observations are larger than the PDR model predictions. We propose that either the gas is/was warmer than predicted or that significant water ice-mantle photodesorption is taking place and HOC^+ is mainly formed by the $C^+ + H_2O$ reaction.
3. The ionization fraction in the shielded core depends on the metal abundance and on the cosmic-ray ionization rate. Assuming a *standard* rate of $\zeta = 3 \times 10^{-17}$ s^{-1} and pure gas-phase chemistry (no PAHs), the metal abundance has to be

lower than 4×10^{-9} (strong metal depletion). Conversely, assuming a *standard* metal abundance of [M] = 10^{-9}, our observations can only be reproduced with $\zeta = (5\pm3)\times10^{-17}$ s^{-1}.

4. The inclusion of PAHs modifies the ionization fraction gradient and decreases the metal depletion required to reproduce the observations if [PAH] $> 10^{-8}$ (i.e., if not all PAHs coagulate/accrete onto bigger grains). In such a case, PAH^- acquire large abundances also in the shielded gas. Recombination of atomic ions on PAH^- is much more efficient than on electrons and thus metal ions and molecular ions are neutralized at similar rates. For [PAH] = 10^{-7}, the metal abundance consistent with observations increases to [M] = $(3\pm1)\times10^{-6}$ (still below the heavy metals abundance in the diffuse ISM).

Acknowledgements. We thank the IRAM staff for their support during observations and D. Talbi and B. Godard for useful advice regarding the HCO^+ dissociative recombination rate. Inelastic collisional rates of HCO^+ with electrons were kindly provided by A. Faure and J. Tennyson. We also thank M. Walmsely for several interesting comments. We acknowledge the use of *OSU* (http://www.physics.ohio-state.edu/~eric/research.html) and *UDFA* (http://www.udfa.net/) chemical reaction databases. We finally acknowledge financial support from CNRS/INSU research programme PCMI. JRG is supported by a *Ramón y Cajal* research contract from the Spanish MICINN and co-financed by the European Social Fund.

References

Abergel, A., Teyssier, D., Bernard, J. P., et al. 2003, A&A, 410, 577
Allamandola, L. J., Tielens, A. G. G. M., & Barker, J. R. 1985, ApJ, 290, L25
Allamandola, L. J., Tielens, A. G. G. M., & Barker, J. R. 1989, ApJS, 71, 733
Anders, E., & Grevesse, N. 1989, Geochim. Cosmochim. Acta, 53, 197
Bakes, E. L. O., & Tielens, A. G. G. M. 1994, ApJ, 427, 822
Bakes, E. L. O., & Tielens, A. G. G. M. 1998, ApJ, 499, 258
Balbus, S. A., & Hawley, J. F. 1991, ApJ, 376, 214
Berné, O., Joblin, C., Deville, Y., et al. 2007, A&A, 469, 575
Boulanger, F., Falgarone, E., Puget, J. L., & Helou, G. 1990, ApJ, 364, 136
Caselli, P., Walmsley, C. M., Terzieva, R., & Herbst, E. 1998, ApJ, 499, 234
Caselli, P., Walmsley, C. M., Tafalla, M., Dore, L., & Myers, P. C. 1999, ApJ, 523, L165
Cernicharo, J., & Guélin, M. 1987, A&A, 176, 299
Cernicharo, J., Goicoechea, J. R., Pardo, J. R., & Asensio-Ramos, A. 2006, ApJ, 642, 940
Compiègne, M., Abergel, A., Verstraete, L., et al. 2007, A&A, 471, 205
Compiègne, M., Abergel, A., Verstraete, L., & Habart, E. 2008, A&A, 491, 797
Dalgarno, A. 2006, Proceedings of the National Academy of Science, 103, 33, 12269
de Boisanger, C., Helmich, F. P., & van Dishoeck, E. F. 1996, A&A, 310, 315
Desert, F.-X., Boulanger, F., & Puget, J. L. 1990, A&A, 237, 215.
Falgarone, E., Cesarsky, D. A., Encrenaz, P. J., & Lucas, R. 1978, A&A, 65, L13
Faure, A., & Tennyson, J. 2001, MNRAS, 325, 443
Florescu-Mitchell, A. I., & Mitchell, J. B. A. 2006, Phys. Rep., 430, 277
Flower, D. R. 1999, MNRAS, 305, 651
Flower, D. R., & Pineau des Forêts, G. 2003, MNRAS, 343, 390
Flower, D. R., Pineau des Forêts, G., & Walmsley, C. M. 2007, A&A, 474, 923
Fuente, A., Rodríguez-Franco, A., García-Burillo, S., Martín-Pintado, J., & Black, J. H. 2003, A&A, 406, 899
Fuente, A., García-Burillo, S., Usero, A., et al. 2008, A&A, 492, 675
Gerin, M., Goicoechea, J. R., Pety, J., & Hily-Blant, P. 2009, A&A, in press
Gerlich, D., Herbst, E., & Roueff, E. 2002, Planetary and Space Science, 50, 12, 1275
Goicoechea, J. R., & Le Bourlot, J. 2007, A&A, 467, 1
Goicoechea, J. R., Pety, J., Gerin, M., et al. 2006, A&A, 456, 565
Goicoechea, J. R., Berné, O., Gerin, M., Joblin, C., & Teyssier, D. 2008, ApJ, 680, 466
Graedel, T. E., Langer, W. D., & Frerking, M. A. 1982, ApJS, 48, 321
Greve, A., Kramer, C., & Wild, W. 1998, A&AS, 133, 271
Guélin, M., Langer, W. D., & Wilson, R. W. 1982, A&A, 1982, 107, 107
Habart, E., Abergel, A., Walmsley, C. M., Teyssier, D., & Pety, J. 2005, A&A, 437, 177
Herbst, E., & Klemperer, W. 1973, ApJ, 185, 505
Hezareh, T., Houde, M., McCoey, C., Vastel, C., & Peng, R. 2008, ApJ, 684, 1221
Hily-Blant, P., Teyssier, D., Philipp, S., & Güsten, R. 2005, A&A, 440, 909
Hollenbach, D., Kaufman, M. J., Bergin, E. A., & Melnick, G. J. 2009, ApJ, 690, 1497
Howk, J. C., Sembach, K. R., & Savage, B. D. 2006, ApJ, 637, 333
Joblin, C., Toublanc, D., Boissel, P., & Tielens, A. G. G. M. 2002, Mol. Phys., 100, 3595
Kaufman, M. J., Wolfire, M. G., & Hollenbach, D. J. 2006, ApJ, 644, 28
Langer, W. D., & Penzias, A. A. 1990, ApJ, 357, 477
Langer, W. D., Graedel, T. E., Frerking, M. A., & Armentrout, P. B. 1984, A&A, 277, 581
Laor, A., & Draine, B. T. 1993, 402, 441
Le Bourlot, J., Pineau Des Forets, G., Roueff, E., & Flower, D. R. 1993, A&A, 267, 233
Leger, A., & Puget, J. L. 1984, A&A, 137, L5
Le Petit, F., Roueff, E., & Herbst, E. 2004, A&A, 417, 993
Le Petit, F., Nehmé, C., Le Bourlot, J., & Roueff, E. 2006, ApJS, 64, 506
Lepp, S., & Dalgarno, A. 1988, ApJ, 324, 553
Li, A., & Draine, B. T. 2001, ApJ, 554, 778
Liszt, H., Lucas, R., & Black, J. H. 2004, A&A, 428, 117L
Marconi, A., Testi, L., Natta, A. & Walmsley, C. M. 1998, A&A, 330, 696
Maret, S., & Bergin, E. A. 2007, ApJ, 664, 956
Mathis, J. S., Rumpl, W., & Nordsieck, K. H. 1977, ApJ, 217, 425
McCall, B. J., Huneycutt, A. J., Saykally, R. J., et al. 2003, Nature, 422, 500
Morata, O., & Herbst, E. 2008, MNRAS, 390, 1549
Mulas, G., Malloci, G., Joblin, C., & Toublanc, D. 2006, A&A, 460, 93
Neufeld, D. A., Lepp, S., & Melnick, G. J. 1995, ApJS, 100, 132
Omont, A., 1986, A&A, 164, 159
Oppenheimer, M., & Dalgarno, A. 1974, ApJ, 192, 29
Padoan, P., & Scalo, J. 2005, ApJ, 624, L97
Pankonin, V., & Walmsley, C. M. 1978, A&A, 67, 12
Penzias, A. A., & Burrus, C. A. 1973, ARA&A, 11, 51
Pety, J., Teyssier, D., Fossé, D., et al. 2005, A&A, 435, 885
Pety, J. 2005, Semaine de l'Astrophysique Française, meeting held in Strasbourg, France, ed. F. Casoli, T. Contini, J. M. Hameury, & L. Pagani (EDP Sciences), SF2A-2005, 721
Pety, J., Goicoechea, J. R., Hily-Blant, P., Gerin, M., & Teyssier, D. 2007, A&A, 464, L41
Philipp, S. D., Lis, D. C., Güsten, R., Kasemann, C., Klein, T., & Phillips, T. G. 2006, A&A, 454, 213
Prasad, S. S., & Tarafdar, S. P. 1983, ApJ, 267, 603
Rapacioli, M., Joblin, C., & Boissel, P. 2005, A&A, 429, 193
Rapacioli, M., Calvo, F., Joblin, C., et al. 2006, A&A, 460, 519
Rizzo, J. R., Fuente, A., Rodríguez-Franco, A., & García-Burillo, S. 2003, ApJ, 597, L153
Röllig, M., Abel, N. P., Bell, T., et al. 2007, A&A, 467, 187
Savage, C., & Ziurys, L. M. 2004, ApJ, 616, 966
Savage, C., Apponi, A. J., Ziurys, L. M., & Wyckoff, S. 2000, ApJ, 578, 211
Scott, G. B. I., Fairley, D. A., Freeman, C. G., et al. 1997, J. Chem. Phys., 106, 3982
Sheehan, C. H. 2000, Ph.D. Thesis, the University of Western Ontario, London, Canada
Smith, M. A., Schlemmer, S., von Richthofen, J., & Gerlich, D. 2002, ApJ, 578, L87
Teyssier, D., Fossé, D., Gerin, M., et al. 2004, A&A, 417, 135
Teyssier, D., Hily-Blant, P., Gerin, M., et al. 2005, in Proceedings of the dusty and molecular universe: a prelude to Herschel and ALMA, ed. A. Wilson, ESA SP-577 (Noordwijk, Netherlands: ESA Publications Division), 423
Timmermann, R., Bertoldi, F., Wright, C. M., et al. 1996, A&A, 315, L281
van der Tak, Floris, F. S. 2006, Royal Soc. London Trans. Ser. A, 364, 1848, 3101
van Dishoeck, E. F. 1988, Rate Coefficients in Astrochemistry, ed. T. J. Millar, & D. A. Williams (Dordrecht, Boston: Kluwer Academic Publishers), 49
Wakelam, V., & Herbst, E. 2008, ApJ, 680, 371
Ward-Thompson, D., Nutter, D., Bontemps, S., Whitworth, A., & Attwood, R. 2006, MNRAS, 369, 1201
Williams, J. P., Bergin, E. A., Caselli, P., Myers, P. C., & Plume, R. 1998, ApJ, 503, 689
Wolfire, M. G., Hollenbach, D., McKee, C. F., Tielens, A. G. G. M., & Bakes, E. L. O. 1995, ApJ, 443, 152
Wolfire, M. G., Tielens, A. G. G. M., Hollenbach, D., & Kaufman, M. J. 2008, ApJ, 680, 384
Woodall, J., Agúndez, M., Markwick-Kemper, A. J., & Millar, T. J. 2006, A&A, 466, 1197
Woods, R. C., Gudeman, C. S., Dickman, R. L., et al. 1983, ApJ, 270, 583
Wootten, A., Loren, R. B., & Snell, R. L. 1982, ApJ, 255, 160
Zhou, S., Jaffe, D. T., Howe, J. E., et al. 1993, ApJ, 419, 190
Ziurys, L. M., & Apponi, A. J. 1995, J, 455, 73

A&A 494, 977–985 (2009)
DOI: 10.1051/0004-6361:200810933
© ESO 2009

Astronomy & Astrophysics

HCO mapping of the Horsehead: tracing the illuminated dense molecular cloud surfaces⋆,⋆⋆

M. Gerin[1], J. R. Goicoechea[1,⋆⋆⋆], J. Pety[2,1], and P. Hily-Blant[3]

[1] LERMA–LRA, UMR 8112, CNRS, Observatoire de Paris and École Normale Supérieure, 24 Rue Lhomond, 75231 Paris, France
e-mail: maryvonne.gerin@lra.ens.fr; jrgoicoechea@fis.ucm.es
[2] IRAM, 300 rue de la Piscine, 38406 Grenoble cedex, France
e-mail: pety@iram.fr
[3] Laboratoire d'Astrophysique, Observatoire de Grenoble, BP 53, 38041 Grenoble Cedex 09, France
e-mail: pierre.hilyblant@obs.ujf-grenoble.fr

Received 8 September 2008 / Accepted 14 November 2008

ABSTRACT

Context. Far-UV photons (FUV) strongly affect the physical and chemical state of molecular gas in the vicinity of young massive stars.
Aims. Finding molecular tracers of the presence of FUV radiation fields in the millimeter wavelength domain is desirable because IR diagnostics (for instance PAHs) are not easily accessible along high extinction line-of-sights. Furthermore, gas phase diagnostics provide information on the velocity fields.
Methods. We have obtained maps of the HCO and $H^{13}CO^+$ ground state lines towards the Horsehead edge at 5″ angular resolution with a combination of Plateau de Bure Interferometer (PdBI) and the IRAM-30 m telescope observations. These maps have been complemented with IRAM-30 m observations of several excited transitions at two different positions.
Results. Bright formyl radical emission delineates the illuminated edge of the nebula, with a faint emission remaining towards the shielded molecular core. Viewed from the illuminated star, the HCO emission almost coincides with the PAH and CCH emission. HCO reaches a similar abundance to HCO^+ in the photon dissociation region (PDR), $\simeq 1$–2×10^{-9} with respect to H_2. To our knowledge, this is the highest HCO abundance ever measured. Pure gas-phase chemistry models fail to reproduce the observed HCO abundance by ∼2 orders of magnitude, except if reactions of atomic oxygen with carbon radicals abundant in the PDR (i.e., CH_2) play a significant role in the HCO formation. Alternatively, HCO could be produced in the PDR by non-thermal processes such as photo-processing of ice mantles and subsequent photo-desorption of either HCO or H_2CO, and further gas phase photodissociation.
Conclusions. The measured $HCO/H^{13}CO^+$ abundance ratio is large towards the PDR (≃50), and much lower toward the gas shielded from FUV radiation (≲1). We propose that high HCO abundances ($\gtrsim10^{-10}$) together with large $HCO/H^{13}CO^+$ abundance ratios (≳1) are sensitive diagnostics of the presence of active photochemistry induced by FUV radiation.

Key words. astrochemistry – ISM: clouds – ISM: molecules – ISM: individual objects: Horsehead nebula – radiative transfer – radio lines: ISM

1. Introduction

Photodissociation region (PDR) models are used to understand the evolution of far-UV (FUV; $h\nu < 13.6$ eV) illuminated matter both in our Galaxy and in external galaxies. These sophisticated models have been benchmarked Röllig et al. (2007) and are continuously upgraded (e.g., Goicoechea & Le Bourlot 2007; González-García et al. 2008). Given the large number of physical and chemical processes included in such models, it is necessary to build reference data sets that can be used to test the predictive accuracy of models. Our team has contributed to this goal by providing a series of high resolution interferometric observations of the Horsehead nebula (see Pety et al. 2007b, for a summary). Indeed, this source is particularly well suited because of its favorable orientation and geometry, and its moderate distance (∼400 pc; Habart et al. 2005). We have previously studied the carbon (Teyssier et al. 2004; Pety et al. 2005) and sulfur chemistry (Goicoechea et al. 2006) of the nebula, and detected the presence of a cold dense core, with active deuterium fractionation (Pety et al. 2007a).

The formyl radical, HCO, is known to be present in the interstellar medium since the late 1970's Snyder et al. (1976). Snyder et al. (1985) give a detailed description of the HCO structure and discuss the energy diagram for the lowest energy levels. HCO is a bent triatomic asymmetric top with an unpaired electron. *a*-type and *b*-type transitions are allowed, with a stronger dipole moment (1.36 Debye) for the *a*-type transitions Landsberg et al. (1977), which are therefore more easily detectable. The strongest HCO ground state transitions lie at 86.670, 86.708, 86.777 and 86.805 GHz, very close to the ground state transition of $H^{13}CO^+$ and to the first rotationally excited SiO line. Therefore HCO can be observed simultaneously with SiO and $H^{13}CO^+$. HCO ground state lines have been detected in the Orion Bar as well as in the dense PDRs NGC 2023, NGC 7023 and S 140 Schilke et al. (2001). From limited mapping, they have shown that HCO is

⋆ Based on observations obtained with the IRAM Plateau de Bure interferometer and 30 m telescope. IRAM is supported by INSU/CNRS (France), MPG (Germany), and IGN (Spain).
⋆⋆ 30m maps of the ground state lines are only available in electronic form at the CDS via anonymous ftp to cdsarc.u-strasbg.fr (130.79.128.5) or via http://cdsweb.u-strasbg.fr/cgi-bin/qcat?J/A+A/494/977
⋆⋆⋆ *Current address*: Centro de Astrobiología. Consejo Superior de Investigaciones Científicas, Madrid, Spain.

Table 1. Observation parameters for the maps shown in Figs. 1 and 5. The projection center of all the maps is $\alpha_{2000} = 05^h40^m54.27^s$, $\delta_{2000} = -02°28'00''$.

Molecule	Transition	Frequency GHz	Instrument	Config.	Beam arcsec	PA °	Vel. Resol. km s^{-1}	Int. Time[a] h	T_{sys} K	Noise[b] K	Obs. date
$H^{13}CO^+$	1–0	86.754288	PdBI	C & D	6.76×4.65	13	0.2	6.5	150	0.10	2006–2007
HCO	$1_{0,1}$ 3/2, 2–$0_{0,0}$ 1/2, 1	86.670760	PdBI	C & D	6.69×4.39	16	0.2	6.5	150	0.09	2006–2007
CCH	1, 3/2 (2)–0, 1/2 (1)	87.316925	PdBI	C & D	7.24×4.99	54	0.2	6.9	130	0.07	2002–2003

[a] On-source time computed as if the source were always observed with 6 antennae. [b] The noise values quoted here are the values at the mosaic phase center (Mosaic noise is inhomogeneous due to primary beam correction; it steeply increases at the mosaic edges).

Molecule	Transition	Frequency GHz	Instrument	# Pix.	F_{eff}	B_{eff}	Resol. arcsec	Resol. km s^{-1}	Int. Time[a] h	T_{sys} K	Noise mK	Obs. date
$H^{13}CO^+$	J = 1–0	86.754288	30 m/AB100	2	0.95	0.78	28.4	0.2	2.6/5.0	133	69	2006–2007
HCO	$1_{0,1}$ 3/2, 2–$0_{0,0}$ 1/2, 1	86.670760	30 m/AB100	2	0.95	0.78	29.9	0.2	2.6/5.0	133	63	2006–2007
HCO	$1_{0,1}$ 3/2, 1–$0_{0,0}$ 1/2, 0	86.708360	30 m/AB100	2	0.95	0.78	29.9	0.2	2.6/5.0	133	63	2006–2007
HCO	$1_{0,1}$ 1/2, 1–$0_{0,0}$ 1/2, 1	86.777460	30 m/AB100	2	0.95	0.78	29.9	0.2	2.6/5.0	133	66	2006–2007
HCO	$1_{0,1}$ 1/2, 0–$0_{0,0}$ 1/2, 1	86.805780	30 m/AB100	2	0.95	0.78	29.9	0.2	2.6/5.0	133	66	2006–2007

[a] Two values are given for the integration time: the on-source time and the telescope time.

Table 2. Observation parameters for the HCO deep integrations shown in Fig. 1. Associated transitions can be found in Table 3. The RA and Dec offsets are computed with reference to $\alpha_{2000} = 05^h40^m54.27^s$, $\delta_{2000} = -02°28'00''$. The positions are also given in the coordinate system used to display the maps in Figs. 1 and 5. In this coordinate system, maps are rotated by 14° counter-clockwise around the projection center, located at $(\delta x, \delta y) = (20'', 0'')$, to bring the illuminated star direction in the horizontal direction and the horizontal zero has been set at the PDR edge.

Position name	(δRA, δDec) arcsec	(δx, δy) arcsec
"DCO^+ peak"	$(20'', 22'')$	$(44.7'', 16.5'')$
"HCO peak"	$(-5, 0'')$	$(15.1'', 1.2'')$

Position	Frequency GHz	Line area[a] K km s^{-1}	Instrument	F_{eff}	B_{eff}	Resol. arcsec	Resol. km s^{-1}	Int. Time[b] h	T_{sys} K	Noise mK	Obs. date
"DCO^+ peak"	86.670760	0.23 ± 0.009	30 m/B100	0.95	0.78	28.4	0.27	0.75/1.5	134	11	2008
	86.708360	0.12 ± 0.009	30 m/B100	0.95	0.78	28.4	0.27	0.75/1.5	134	11	2008
"HCO peak"	86.670760	0.52 ± 0.008	30 m/B100	0.95	0.78	28.4	0.27	0.75/1.5	127	10	2008
	86.708360	0.31 ± 0.007	30 m/B100	0.95	0.78	28.4	0.27	0.75/1.5	127	10	2008
	173.3773770	0.47 ± 0.023	30 m/C150	0.93	0.65	14.2	0.067	2.0/4.0	667	66	2008
	173.4060816	0.26 ± 0.018	30 m/C150	0.93	0.65	14.2	0.067	2.0/4.0	667	66	2008
	173.4430648	0.23 ± 0.020	30 m/C150	0.93	0.65	14.2	0.067	2.0/4.0	667	66	2008
	260.0603290	0.16 ± 0.019	30 m/C270	0.88	0.46	9.5	0.18	3.0/6.0	740	59	2008
	260.0821920	0.14 ± 0.020	30 m/C270	0.88	0.46	9.5	0.18	3.0/6.0	740	59	2008
	260.1335860	0.12 ± 0.017	30 m/C270	0.88	0.46	9.5	0.18	3.0/6.0	740	59	2008
	260.1557690	0.06 ± 0.016	30 m/C270	0.88	0.46	9.5	0.18	3.0/6.0	740	59	2008

[a] Values obtained from Gaussian fits performed on the spectra using the main beam temperature scale. [b] Two values are given for the integration time: the on-source time and the telescope time.

sharply peaked in the Orion Bar PDR, confirming earlier suggestions that HCO is a tracer of the cloud illuminated interfaces de Jong et al. (1980). García-Burillo et al. (2002) have mapped HCO and $H^{13}CO^+$ in the nearby galaxy M 82. HCO, CO and the ionized gas present a nested ring morphology, with the HCO peaks being located further out compared to CO and the ring of H II regions. The chemistry of HCO is not well understood. Schilke et al. (2001) concluded that it is extremely difficult to understand the observed HCO abundance in PDRs with gas phase chemistry alone. As a possible way out, they tested the production of HCO by the photodissociation of formaldehyde. In this model, H_2CO is produced in grain mantles, and released by non-thermal photo-desorption in the gas phase in the PDR. However, even with this favorable hypothesis, the model cannot reproduce the abundance and spatial distribution of HCO because the photo-production is most efficient at an optical depth of a few magnitudes where the photodissociation becomes less effective.

In this paper, we present maps of the formyl radical ground state lines at high angular resolution towards the Horsehead nebula, and the detection of higher energy level transitions towards two particular lines of sights, one in the PDR region and the other in the associated dense core. These observations enable us to accurately study the HCO spatial distribution and abundance. We present the observations and data reduction in Sect. 2, while the results and HCO abundance are given in Sect. 3, and the discussion of HCO chemistry and PDR modeling is given in Sect. 4.

2. Observations and data reduction

Tables 1 and 2 summarize the observation parameters for the data obtained with the IRAM PdBI and 30 m telescopes. The HCO ground state lines were observed simultaneously with $H^{13}CO^+$ and SiO. Frequency-switched, on-the-fly maps of the $H^{13}CO^+$ J = 1–0 and HCO ground state lines (see Fig. 5), obtained at the IRAM-30 m using the A100 and B100 3 mm receivers (~7 mm of water vapor) were used to produce the short-spacings needed to complement a 7-field mosaic acquired with the 6 PdBI antennae in the CD configuration (baseline lengths from 24 to 176 m). The whole PdBI data set will be comprehensively described in a forthcoming paper studying the

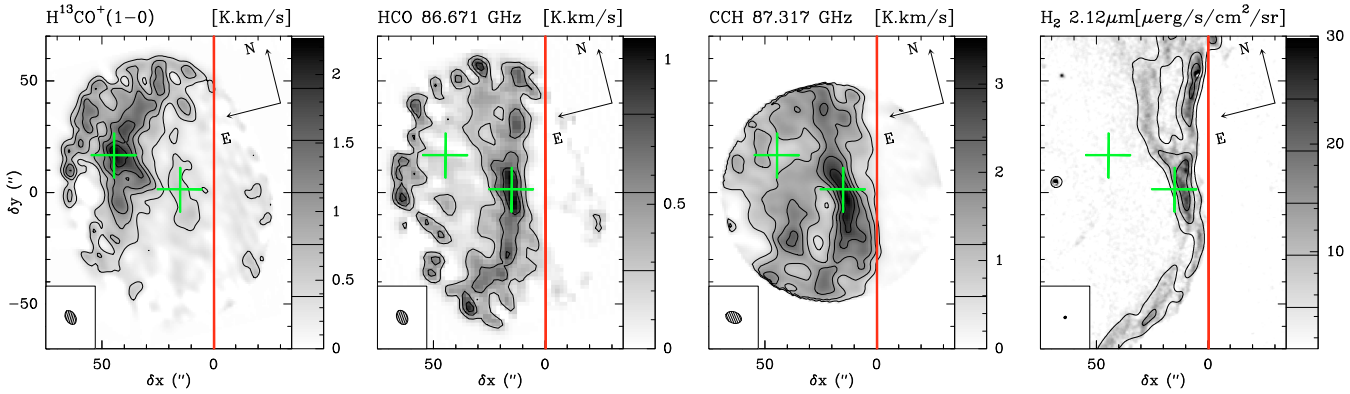

Fig. 1. High angular resolution maps of the integrated intensity of $H^{13}CO^+$, HCO, CCH and vibrationally excited H_2 emission. $H^{13}CO^+$ and HCO have been observed simultaneously, both with the IRAM-30 m and IRAM-PdBI. Maps have been rotated by 14° counter-clockwise around the projection center, located at $(\delta x, \delta y) = (20'', 0'')$, to bring the illuminated star direction in the horizontal direction and the horizontal zero has been set at the PDR edge. The emission of all lines is integrated between 10.1 and 11.1 km s^{-1}. Displayed integrated intensities are expressed in the main beam temperature scale. Contour levels are displayed on the grey scale lookup tables. The red vertical line shows the PDR edge and the green crosses show the positions (DCO^+ and HCO peaks) where deep integrations have been performed at IRAM-30 m (see Fig. 2). The H_2 map is taken from Habart et al. (2005).

fractional ionization across the Horsehead edge (Goicoechea et al. 2009). The CCH data shown in Fig. 1 have been extensively described in Pety et al. (2005). The high resolution HCO $1_{0,1}-0_{0,0}$ data are complemented by observations of the $2_{0,2}-1_{0,1}$ and $3_{0,3}-2_{0,2}$ multiplets with the IRAM 30 m telescope centered on the PDR and the dense core. To obtain those deep integration spectra, we used the position switching observing mode. The on-off cycle duration was 1 min and the off-position offsets were $(\delta\mathrm{RA}, \delta\mathrm{Dec}) = (-100'', 0'')$, i.e. the H II region ionized by σOri and free of molecular emission. Position accuracy is estimated to be about 3″ for the 30 m data and less than 0.5″ for the PdBI data.

The data processing was done with the GILDAS[1] softwares (Pety 2005b). The IRAM-30 m data were first calibrated to the T_A^* scale using the chopper wheel method (Penzias & Burrus 1973), and finally converted to main beam temperatures (T_{mb}) using the forward and main beam efficiencies (F_{eff} & B_{eff}) displayed in Table 2. The resulting amplitude accuracy is ∼10%. Frequency-switched spectra were folded using the standard shift-and-add method, after baseline subtraction. The resulting spectra were finally gridded through convolution by a Gaussian. Position-switched spectra were co-added before baseline subtraction. Interferometric data and short-spacing data were merged before imaging and deconvolution of the mosaic, using standard techniques of GILDAS (see e.g. Pety et al. 2005, for details).

3. Results and discussion

3.1. Spatial distribution

Figure 1 shows a map of the integrated intensity of the strongest HCO line at 86.671 GHz, of the $H^{13}CO^+$ $J = 1$–0 line and of the strongest CCH line at 87.317 GHz. Figure 2 displays high signal-to-noise ratio spectra of several hyperfine components of three HCO rotational transitions towards the HCO and the DCO^+ emission peaks.

Most of the formyl radical emission is concentrated in a narrow structure, delineating the edge of the Horsehead nebula. Low level emission is however detected throughout the nebula, including towards the dense core identified by its strong DCO^+ and $H^{13}CO^+$ emission Pety et al. (2007a). The HCO emission is resolved by our PdBI observations. From 2-dimensional Gaussian fits of the image, we estimate that the emission width is $\sim 13 \pm 4''$ in the plane of the sky. The $H^{13}CO^+$ emission shows a different pattern: most of the signal is associated with the dense core behind the photodissociation front, and faint $H^{13}CO^+$ emission detected in the illuminated edge. The CCH emission pattern is less extreme than HCO, but shows a similar enhancement in the PDR.

In summary, the morphology of the HCO emission is reminiscent of the emission of the PDR tracers, either the PAH emission (Abergel et al. 2002) or the emission of small hydrocarbons, which is strongly enhanced towards the PDR (Teyssier et al. 2004; Pety et al. 2005). In contrast, the HCO emission becomes very faint where the gas is dense and shielded from FUV radiation. These regions are associated with bright DCO^+ and $H^{13}CO^+$ emission (Pety et al. 2007a). Our maps therefore confirm that HCO is a PDR species.

3.2. Column densities and abundances

3.2.1. Radiative transfer models of HCO and $H^{13}CO^+$

Einstein coefficients and upper level energies of the studied HCO and $H^{13}CO^+$ lines are given in Table 3. As no collisional cross-sections with H_2 nor He have been calculated for HCO so far, we have computed the HCO column densities assuming a single excitation temperature T_{ex} for all transitions. Nevertheless our calculation takes into account thermal, turbulent and opacity broadening as well as the cosmic microwave background and line opacity Goicoechea et al. (2006). For $H^{13}CO^+$, detailed non-local and non-LTE excitation and radiative transfer calculations have been performed using the same approach as in our previous PdBI CS and $C^{18}O$ line analysis (see Appendix in Goicoechea et al. 2006). $H^{13}CO^+$-H_2 collisional rate coefficients were adapted from those of Flower (1999) for HCO^+, and specific $H^{13}CO^+$-electron rates where kindly provided by Faure & Tennyson (in prep.).

[1] See http://www.iram.fr/IRAMFR/GILDAS for more information about the GILDAS softwares.

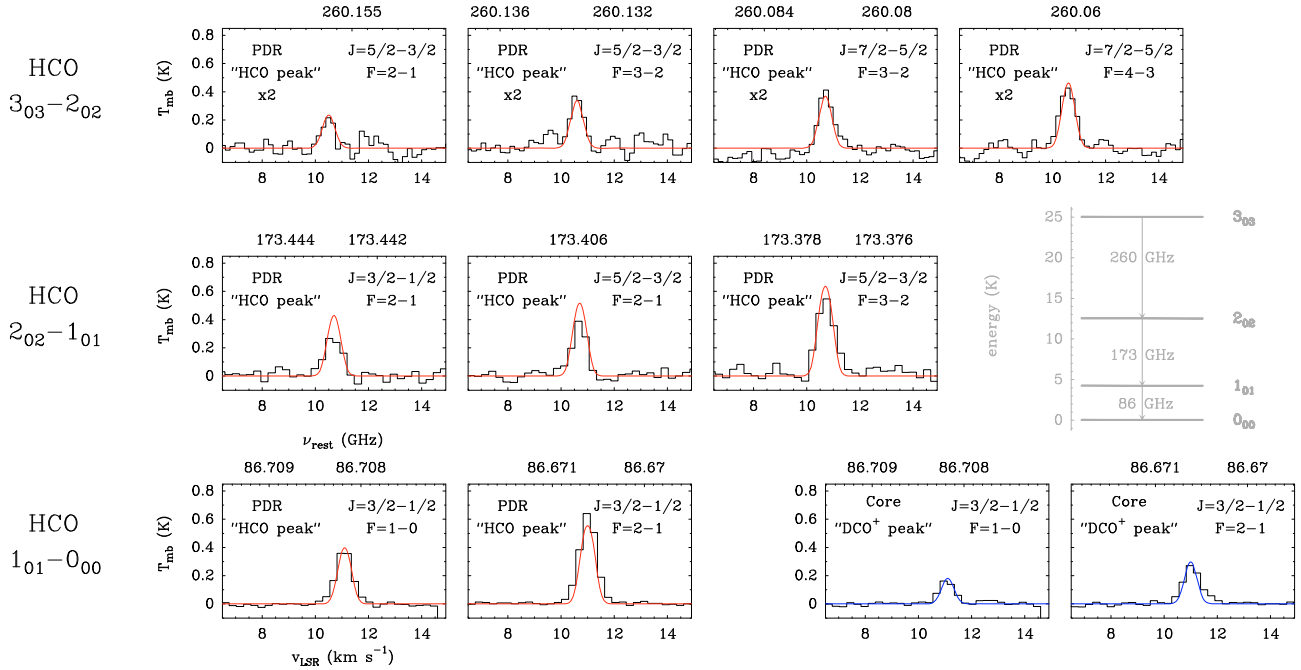

Fig. 2. IRAM-30 m observations (histograms) of several HCO hyperfine components of the 1_{01}–0_{00}, 2_{02}–1_{01} and 3_{03}–2_{02} rotational transitions towards the PDR ("HCO peak") and towards the dense core ("DCO$^+$ peak") Pety et al. (2007a). Solid lines are single-T_{ex} radiative transfer models of the PDR-filament (red curves) and line-of-sight cloud surface (blue curves). A sketch of the HCO rotational energy levels is also shown (*right corner*).

Table 3. Einstein coefficients and upper level energies.

Molecule	Transition $J, F-J', F'$	Frequency GHz	A_{ij} (s^{-1})	E_{up} (K)
HCO	$1_{01}-0_{00}$			
	3/2, 2−1/2, 1	86.670760	4.69×10^{-6}	4.2
	3/2, 1−1/2, 0	86.708360	4.60×10^{-6}	4.2
	1/2, 1, 1/2, 0	86.777460	4.61×10^{-6}	4.2
	1/2, 0−1/2, 1	86.805780	4.71×10^{-6}	4.2
	$2_{02}-1_{01}$			
	5/2, 3−3/2, 2	173.3773770	4.51×10^{-5}	12.5
	5/2, 2−3/2, 1	173.4060816	4.43×10^{-5}	12.5
	3/2, 2−1/2, 1	173.4430648	3.39×10^{-5}	12.5
	$3_{03}-2_{02}$			
	7/2, 4−5/2, 3	260.0603290	1.63×10^{-4}	25.0
	7/2, 3−5/2, 2	260.0821920	1.61×10^{-4}	25.0
	5/2, 3−3/2, 2	260.1335860	1.45×10^{-4}	25.0
	5/2, 2−3/2, 1	260.1557690	1.37×10^{-4}	25.0
$H^{13}CO^+$	J = 1–0	86.754288	3.2×10^{-5}	4.2
	J = 3–2	260.2553390	1.3×10^{-3}	25.0

The line frequencies and intensities were extracted from the JPL Pickett et al. (1998) and CDMS (Müller et al. 2001, 2005) molecular spectroscopy data bases for HCO and $H^{13}CO^+$ respectively.

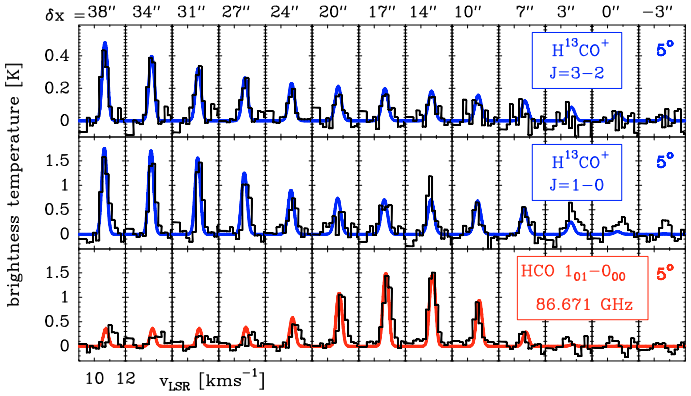

Fig. 3. Observations along a horizontal cut through "the HCO peak" (histograms). The $H^{13}CO^+$ J = 1–0 and HCO 1_{01}–0_{00} lines were mapped with the PdBI at an angular resolution of 6.8″, whereas the $H^{13}CO^+$ J = 3–2 line was mapped with HERA-30 m (and smoothed to a spatial resolution of 13.5″). Radiative transfer models of an edge-on cloud with a line of sight extinction of A_V = 20, inclined 5° relative to the line of sight for HCO (red curve), and $H^{13}CO^+$ (blue curves) are shown. The single-T_{ex} HCO model assumes a 12″ width filament with a column density of 3.2×10^{13} cm^{-2}, while N(HCO) is 4.6×10^{12} cm^{-2} behind the filament. The $H^{13}CO^+$ model assumes a constant density of $n(H_2) = 5\times10^4$ cm^{-3} with T_k = 60 K and $N(H^{13}CO^+) = 5.8\times10^{11}$ cm^{-2} for $\delta x < 35''$; and T_k = 10 K and $N(H^{13}CO^+) = 7.6\times10^{11}$ cm^{-2} for $\delta x > 35''$. Modeled line profiles have been convolved with an appropriate Gaussian beam corresponding to each PdBI synthesized beam or 30 m main beam resolution.

3.2.2. Structure of the PDR in HCO and $H^{13}CO^+$

For more insight into the spatial variation of the HCO and $H^{13}CO^+$ column densities and abundances, we have analyzed a cut through the PDR, centered on the "HCO peak" at $\delta y = 0''$ (see Fig. 3). The cut clearly shows that HCO is brighter than $H^{13}CO^+$ in the PDR and vice-versa in the dense core. Taking into account the different level degeneracies of both transitions (a factor of 2.4) and the fact that the associated Einstein coefficients A_{ij} differ by a factor ∼8 (due to the different permanent dipole moments, see Table 3), $N(H^{13}CO^+)$ must be significantly lower than N(HCO) towards the PDR.

We modeled the PDR as an edge-on cloud inclined by ∼5° relative to the line-of-sight. We have chosen a cloud depth

of ~0.1 pc, which implies an extinction of $A_V \simeq 20$ mag for the considered densities towards the "HCO peak". These parameters are the best geometrical description of the Horsehead PDR-edge (e.g., Habart et al. 2005) and also reproduce the observed 1.2 mm continuum emission intensity. The details of this modeling will be presented in Goicoechea et al. (2009). In the following, we describe in detail the determination of the column densities and abundances for two particular positions, namely the "HCO peak" and the "DCO^+ peak" (offsets relative to the map center can be found in Table 2).

3.2.3. HCO column densities

We used the three detected rotational transitions of HCO (each with several hyperfine components, see Fig. 2) to estimate the HCO column densities in the direction of the "HCO" peak. We have taken into account the varying beam dilution factors of the HCO emission at the "HCO peak" by modeling the HCO emission as a Gaussian filament of ~12″ width in the δx direction, and infinite in the δy direction. The filling factors at 260, 173 and 87 GHz are thus ~0.8, 0.6 and 0.4, respectively.

A satisfactory fit of the IRAM–30 m data towards the "HCO peak" is obtained for $T_{ex} \simeq 5$ K and a turbulent velocity dispersion of $\sigma = 0.225\,km\,s^{-1}$ ($FWHM = 2.355 \times \sigma$). Line profiles are reproduced for $N(HCO) = 3.2 \times 10^{13}$ cm^{-2} (see red solid curves in Fig. 2). The most intense HCO lines at 86.67 and 173.38 GHz become marginally optically thick at this column density ($\tau \gtrsim 1$). Therefore, opacity corrections need to be taken into account. We checked that the low value of T_{ex} (subthermal excitation as $T_k \simeq 60$ K) is consistent with detailed excitation calculations carried out for $H^{13}CO^+$ in the PDR which are described below.

Because the HCO signals are weaker towards the "DCO^+peak", we only detected 2 hyperfine components of the 1_{01}–0_{00} transition. Assuming extended emission and the same excitation temperature as for the "HCO peak", 5 K, we fit the observed lines with a column density of 4.6×10^{12} cm^{-2} (blue solid lines in Fig. 2). Both HCO lines are optically thin at this position. This simple analysis shows that the HCO column density is ~7 times larger at the "HCO peak" in the PDR, than towards the dense cold core.

3.2.4. $H^{13}CO^+$ column densities

Both the $H^{13}CO^+$ J = 3–2 and 1–0 line profiles at the "HCO peak" are fitted with $n(H_2) \simeq 5 \times 10^4\,cm^{-3}$, $T_k \simeq 60$ K and $e^-/H \simeq 5 \times 10^{-5}$ (as predicted by the PDR models below). The required column density is $N(H^{13}CO^+) = 5.8 \times 10^{11}$ cm^{-2}. For those conditions, the excitation temperature, T_{ex}, of the J = 3–2 transition varies from ≃4 to 6 K, which supports the single-T_{ex} models of HCO. Both $H^{13}CO^+$ lines are optically thin towards the "HCO peak".

The $H^{13}CO^+$ line emission towards the "DCO^+ peak" has been studied by Pety et al. (2007a). Both $H^{13}CO^+$ lines are moderately optically thick towards the core, and the $H^{13}CO^+$ column density is $N(H^{13}CO^+) \simeq 5.0 \times 10^{12}$ cm^{-2}, which represents an enhancement of nearly one order of magnitude relative to the PDR. According to our 1.2 mm continuum map, the extinction towards the core is $A_V \gtrsim 30$ mag compared to 20 mag in the PDR. The $H^{13}CO^+$ column density enhancement therefore corresponds to a true abundance enhancement.

Table 4. Inferred column densities and abundances with respect to molecular hydrogen, e.g. $\chi(X) = N(X)/N(H_2)$.

Molecule	Method	HCO peak	DCO^+ peak
$N(H_2)$ [cm^{-2}]	1.2 mm cont.	1.9×10^{22}	2.9×10^{22}
$N(HCO)$ [cm^{-2}]	$T_{ex} = 5$ K	3.2×10^{13}	4.6×10^{12}
$N(H^{13}CO^+)$ [cm^{-2}]	Full excitation	5.8×10^{11}	5.0×10^{12} *
$N(HCO^+)$ [cm^{-2}]	$^{12}C/^{13}C = 60$	3.5×10^{13}	3.0×10^{14}
$\chi(HCO)$		1.7×10^{-9}	1.6×10^{-10} †
$\chi(H^{13}CO^+)$		3.1×10^{-11}	1.7×10^{-10}
$\chi(HCO^+)$		1.8×10^{-9}	1.0×10^{-8}

* Pety et al. (2007a).
† 1.7×10^{-9} if HCO arises only from the cloud surface ($A_V \simeq 3$).

3.2.5. Comparison of HCO and $H^{13}CO^+$ abundances

Table 4 summarizes the inferred HCO and $H^{13}CO^+$ column densities and abundances towards the 2 selected positions: the "HCO peak" in the PDR and the "DCO^+ peak" in the FUV-shielded core. Both species exhibit strong variations of their column densities and abundances relative to H_2 between the PDR and the shielded region. In the PDR, we found that both the HCO abundance relative to H_2 ($\chi(HCO) \simeq 1$–2×10^{-9}) and the HCO/$H^{13}CO^+$ column density ratio (≈50) are high. These figures are higher than all previously published measurements (at lower angular resolution). Besides, the formyl radical and HCO^+ reach similar abundances in the PDR.

The situation is reversed towards the "DCO^+ peak", i.e. the observed HCO/$H^{13}CO^+$ column density ratio is lower (≈1) than towards the "HCO peak". Nevertheless, while the bulk of the observed $H^{13}CO^+$ emission arises from cold and shielded gas, the origin of HCO emission is less clear. HCO could either (i) coexist with $H^{13}CO^+$ or (ii) arise predominantly from the line-of-sight cloud surface. In the former case, our observations show that the HCO abundance drops by one order of magnitude between the PDR and the dense core environment. However, it is possible that the abundance variation is even more pronounced, if the detected HCO emission arises from the line of sight cloud surface. We have estimated the depth of the cloud layer, assuming that HCO keeps the "PDR abundance" in this foreground layer: a cloud surface layer of $A_V \simeq 3$ (illuminated by the mean FUV radiation field around the region) also reproduces the observed HCO lines towards the cold and dense core (blue solid lines in Fig. 2).

In this case, both the HCO abundance and the HCO/$H^{13}CO^+$ abundance ratio in the dense core itself will be even lower than listed in Table 4. We have tried to discriminate between the scenarios by comparing the HCO 1_{01}–0_{00} (J = 3/2–1/2, F = 2–1) and $H^{13}CO^+$ J = 1–0 line profiles towards this position. Both lines have been observed simultaneously with the IRAM-30 m telescope. Because of their very similar frequencies (~86.7 GHz), the beam profile and angular resolution is effectively the same. In this situation, any difference in the measured linewidths reflects real differences in the gas kinematics and turbulence of the regions where the line profiles are formed. Gaussian fits of the HCO and $H^{13}CO^+$ lines towards "the DCO^+ peak" provides line widths of $\Delta v(HCO) = 0.81 \pm 0.06\,km\,s^{-1}$ and $\Delta v(H^{13}CO^+) = 0.60 \pm 0.01\,km\,s^{-1}$. Therefore, even if the $H^{13}CO^+$ J = 1–0 lines are slightly broadened by opacity and do not represent the true line of sight velocity dispersion, HCO lines are broader at the 3σ level of confidence. This remarkable difference supports the scenario (ii) where the $H^{13}CO^+$ line

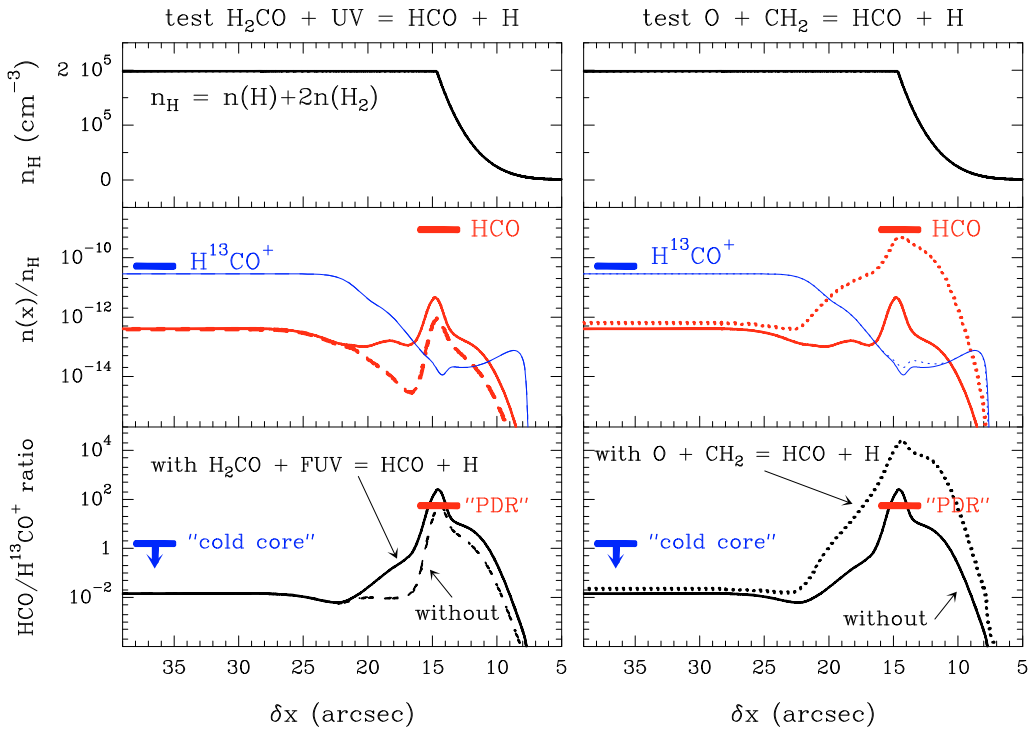

Fig. 4. Photochemical models of a unidimensional PDR. *Upper panels* show the density gradient (n_H = n(H) + 2n(H$_2$) in cm^{-3}) used in the calculation. *Middle panels* show the predicted HCO and H^{13}CO$^+$ abundances (relative to n_H). The H^{13}CO$^+$ abundance inferred from observations in the cold core ("the DCO$^+$ peak", see the offsets in Table 2) is shown with blue lines. The HCO abundance inferred from observations in the PDR ("the HCO peak", see the offsets in Table 2) is shown with red lines. *Lower panels* show the HCO/H^{13}CO$^+$ abundance ratio predicted by the models whereas the HCO/H^{13}CO$^+$ column density ratio inferred from observations is shown as blue arrows and red lines (for the cold core and PDR respectively). Each panel compares two different models: *left-side models* show a *standard chemistry* (dashed curves) versus the same network upgraded with the addition of the H$_2$CO + photon → HCO + H photodissociation (solid curves). *Right-side models* show the previous upgraded *standard* model (solid curves) versus a chemistry that adds the O + CH$_2$ → HCO + H reaction with a rate of 5.01×10^{-11} cm^3 s^{-1} (dotted curves). The inclusion of the O + CH$_2$ reaction has almost no effect on H^{13}CO$^+$ for the physical conditions prevailing in the Horsehead, but triggers an increases of the HCO abundance in the PDR by two orders of magnitude.

emission towards the "the DCO$^+$ peak" arises from the quiescent, cold and dense core, whereas HCO, in the same line of sight, arises predominantly from the warmer and more turbulent outer cloud layers. We note that the presence of a foreground layer of more diffuse material ($A_V \sim 2$ mag) was already introduced by Goicoechea et al. (2006) to fit the CS J = 2–1 scattered line emission. The analysis of CO J = 4–3 and CI $^3P_1$–$^3P_0$ maps led Philipp et al. (2006) to propose the presence of a diffuse envelope, with $A_V \sim 2$ mag, and which contributes to about half the mass of the dense filament traced by C^{18}O and the dust continuum emission. The hypothesis of a surface layer of HCO is therefore consistent with previous modeling of molecular emission of the Horsehead.

We conclude 1) that HCO and HCO$^+$ have similar abundances in the PDR; and 2) that the HCO abundance drops by at least one order of magnitude between the dense and warm PDR region and the cold and shielded DCO$^+$ core.

4. HCO chemistry

4.1. Gas-phase formation: PDR models

In order to understand the HCO and H^{13}CO$^+$ abundances and HCO/H^{13}CO$^+$ column density ratio inferred from observations, we have modeled the steady state gas phase chemistry at the Horsehead edge. The density distribution in the PDR is well represented by a density gradient $n_H(\delta x) \propto \delta x^4$, where δx is the distance from the edge towards the cloud interior and n_H = n(H) + 2n(H$_2$) (see the top panels of Fig. 4). The density reaches a constant n_H value of 2×10^5 cm^{-3} in an equivalent length of ~10″ Habart et al. (2005); Goicoechea et al. (2006). The cloud edge is illuminated by a FUV field 60 times the mean interstellar radiation field (G_0 = 60 in Draine units). We used the `Meudon PDR code`[2], a photochemical model of a unidimensional PDR (see Le Bourlot et al. 1993; Le Petit et al. 2006; Goicoechea & Le Bourlot 2007, for a detailed description). Our standard chemical network is based on a modified version of the *Ohio State University (osu)* gas-phase network, updated for photochemical studies (see Goicoechea et al. 2006). It also includes ^{13}C fractionation reactions Graedel et al. (1982) and specific computation of the ^{13}CO photodissociation rate as a function of depth. The ionization rate due to cosmic rays in the models is $\zeta = 5 \times 10^{-17}$ s^{-1}. Following our previous work, we chose the following elemental gas phase abundances: He/H = 0.1, O/H = 3×10^{-4}, C/H = 1.4×10^{-4}, N/H = 8×10^{-5}, S/H = 3.5×10^{-6}, ^{13}C/H = 2.3×10^{-6}, Si/H = 1.7×10^{-8} and Fe/H = 1.0×10^{-9}.

In Fig. 4, we investigate the main gas-phase formation routes for HCO in a series of models "testing" different pathways leading to the formation of HCO. HCO and H^{13}CO$^+$ predictions are shown in Fig. 4 (middle panels). In all models the HCO abundance peaks near the cloud surface at $A_V \simeq 1.5$ ($\delta x \simeq 14''$) where the ionization fraction is high (e$^-$/H ~ 5×10^{-5}). Due to the low abundance of *metals* in the model (as represented by the low abundance of Fe), the ionization fraction in the shielded

[2] Publicly available at `http://aristote.obspm.fr/MIS/`

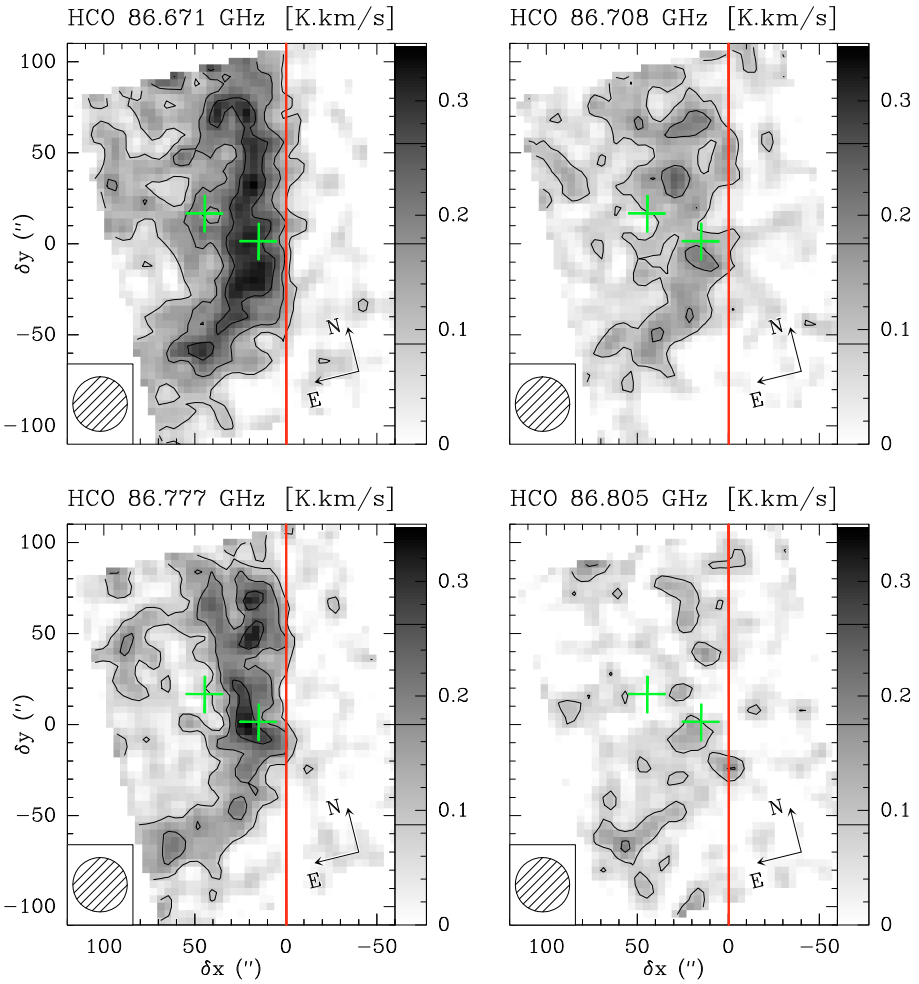

Fig. 5. Medium angular resolution maps of the integrated intensity of the 4 hyperfine components of the fundamental transition of HCO. These lines have been observed simultaneously at IRAM-30 m. Maps have been rotated by 14° counter-clockwise around the projection center, located at $(\delta x, \delta y) = (20'', 0'')$, to bring the illuminated star direction in the horizontal direction and the horizontal zero has been set at the PDR edge. The emission of all lines is integrated between 9.6 and 11.4 km s^{-1}. Displayed integrated intensities are expressed in the main beam temperature scale. Contour levels are displayed on the grey scale lookup tables. The red vertical line shows the PDR edge and the green crosses show the positions (DCO^+ and HCO peaks) where deep integrations have been performed at IRAM-30 m (see Fig. 2).

regions is low ($e^-/H \lesssim 10^{-8}$), and therefore the $H^{13}CO^+$ predictions matches the observed values (Goicoechea et al. 2009). Besides, a low metalicity reduces the efficiency of charge exchange reactions of HCO^+ with metals, e.g.,

$$Fe + HCO^+ \rightarrow HCO + Fe^+ \quad (1)$$

which are the main gas-phase formation route of HCO in the FUV-shielded gas in our models. Hence, the HCO abundance remains low inside the core. Nevertheless, even though such models do reproduce the observed HCO distribution, which clearly peaks at the PDR position, the predicted absolute HCO abundances can vary by orders of magnitude depending of the dominant formation route.

In our *standard* model (left-side models: dashed curves), the formation of HCO in the PDR is dominated by the dissociative recombination of H_2CO^+, while its destruction is dominated by photodissociation. Even if the predicted HCO/$H^{13}CO^+$ abundance ratio satisfactorily reproduces the value inferred from observations, the predicted HCO abundance peak is ~3 orders of magnitude lower than observed. In order to increase the gas-phase formation of the HCO in the PDR we have added a new channel in the photodissociation of formaldehyde, the production HCO, in addition to the normal channel producing CO:

$$H_2CO + photon \rightarrow HCO + H. \quad (2)$$

This channel is generally not included in standard chemical networks but very likely exists Troe (2007); Yin et al. (2007). We included this process with an unattenuated photodissociation rate of $\kappa_{diss}(H_2CO) = 10^{-9}$ s^{-1} and a depth dependence given by $\exp(-1.74\,A_V)$. This is the same rate as the one given by van Dishoeck (1988) for the photodissociation of H_2CO producing CO, which is explicitly calculated for the Draine (1978) radiation field. Model results are shown in Fig. 4 (left-side models: solid curves). The inclusion of Reaction 2, which becomes the dominant HCO formation route, increases the HCO abundance in the PDR by a factor of ~5. But the HCO production rate is still too low to reproduce the abundance determined from observations.

Another plausible possibility to increase the HCO abundance in the PDR by pure gas-phase processes is to include additional reactions of atomic oxygen with carbon radicals that reach high abundances only in the PDR. Among the investigated reactions, the most critical one,

$$O + CH_2 \rightarrow HCO + H \quad (3)$$

is known to proceed with a relatively fast rate at high temperatures (5.01×10^{-11} cm^3 s^{-1} at T_k = 1200–1800 K; Tsuboi & Hashimoto 1981). This is the rate recommended by NIST Mallard et al. (1994) and UMIST2006 Woodall et al. (2007) and that we adopt for our lower temperature domain (~10–200 K). Model predictions are shown in Fig. 4 (right-side models: dotted curves). While the predicted HCO abundance in the shielded gas remains almost the same, the HCO abundance is dramatically increased in the PDR (by a factor of ~125) and the O + CH_2 reaction becomes the HCO dominant production reaction. Therefore, such a pure gas-phase model adding reactions 2 and 3 not only reproduces the $H^{13}CO^+$ abundance in the shielded core,

but also reproduces the observed HCO absolute abundances in the PDR. In this picture, the enhanced HCO abundance that we observe in the Horsehead PDR edge would be fully determined by the gas-phase chemical path:

$$C^+ \xrightarrow[H_2]{} CH_2^+ \xrightarrow[H_2]{} CH_3^+ \xrightarrow{e^-} CH_2 \xrightarrow{O} HCO. \quad (4)$$

The validity of the rate of Reaction 3 used in our PDR model remains, of course, to be confirmed theoretically or experimentally at the typical ISM temperatures (10 to 200 K).

4.2. Other routes for HCO formation: Grain photodesorption

If Reaction 3 is not included in the chemical network, the predicted HCO abundance is ∼2 orders of magnitude below the observed value towards the PDR. As a consequence, the presence of HCO in the gas-phase should be linked to grain mantle formation routes, and subsequent desorption processes (not taken into account in our modeling). In particular, Schilke et al. (2001) proposed that HCO could result from H_2CO photodissociation, if large quantities of formaldehyde are formed on grain mantles and then released in the gas phase. Even with this assumption, their model could not reproduce the observed HCO abundance in highly illuminated PDRs such as the Orion Bar. The weaker FUV-radiation field in the Horsehead, but high density, prevent dust grains from acquiring high temperatures over large spatial scales. In fact, both gas and grains cool down below ∼30 K in ≃10″–20″ (or $A_V \simeq 1$–2) as the FUV-radiation field is attenuated. Therefore, thermal desorption of dust ice-mantles (presumably formed before σ-Orionis ignited and started to illuminate the nebula) should play a negligible role. Hence a non-thermal desorption mechanism should be considered to produce the high abundance of HCO observed in the gas phase. This mechanism could either produce HCO directly or a precursor molecule such as formaldehyde.

Since high HCO abundances are only observed in the PDR, FUV induced ice-mantle photo-desorption (with rates that roughly scale with the FUV-radiation field strength) seems the best candidate (e.g., Willacy & Williams 1993; Bergin et al. 1995). Laboratory experiments have shown that HCO radicals are produced in irradiated, methanol containing, ice mantles Bernstein et al. (1995); Moore et al. (2001); Bennett & Kaiser (2007). The formyl radical could be formed through the hydrogenation of CO in the solid phase. It is an important intermediate radical in the synthesis of more complex organic molecules such as methyl formate or glycolaldehyde Bennett & Kaiser (2007). However, the efficiency of the production of radicals in FUV irradiated ices remains uncertain, and very likely depends on the ice-mantle composition. The formation of species like formaldehyde and methanol in CO-ice exposed to H-atom bombardment has been reported by different groups Hiraoka et al. (1994); Watanabe et al. (2002); Linnartz et al. (2007), further confirming the importance of HCO as an intermediate product in the synthesis of organic molecules in ices. Indeed, hydrogenation reactions of CO-ice, which form HCO, H_2CO, CH_3O and CH_3OH in grain mantles (e.g., Tielens & Whittet 1997; Charnley et al. 1997), are one important path which warrants further studies.

To compare with our observations, we further need to understand how the radicals are released in the gas phase, either directly during the photo-processing, or following FUV induced photo-desorption. Recent laboratory measurements have started to shed light on the efficiency of photo-desorption, which depends on the ice composition and molecule to be desorbed. For species such as CO, the rate of photo-desorbed molecules per FUV photon is much higher than previously thought (e.g., Öberg et al. 2007). Similar experiments are required to constrain the formation rate of the various species that can form in interstellar ices and to determine their photo-desorption rates.

We can use the measured gas phase abundance of HCO to constrain the efficiency of photo-desorption. We assume that the PDR is at steady state, and that the main HCO formation mechanism is non thermal photo-desorption from grain mantles (with a F_{HCO} rate), while the main destruction mechanism is gas-phase photodissociation (with a D_{HCO} rate), therefore:

$$D_{HCO} = G_0\, \kappa_{diss}(HCO)\, \chi(HCO)\, n(H_2) \quad [cm^{-3}\, s^{-1}] \quad (5)$$

$$F_{HCO} = G_0\, \kappa_{pd}(HCO)\, \chi(HCO_{ice})\, \frac{n(H_2O_{ice})}{n(H_2)}\, n(H_2)\ [cm^{-3}\, s^{-1}] \quad (6)$$

where χ(HCO) is the gas phase abundance of HCO relative to H_2, $\chi(HCO_{ice})$ is the solid phase abundance relative to water ice, and $n(H_2O_{ice})/n(H_2)$ is the fraction of water in the solid phase relative to the total gas density. κ_{diss}(HCO) and κ_{pd}(HCO) are the HCO photodissociation and photo-desorption rates respectively.

By equaling the formation and destruction rates, we get:

$$\kappa_{pd}(HCO) = \kappa_{diss}(HCO)\, \frac{\chi(HCO)}{\chi(HCO_{ice})}\, \frac{n(H_2)}{n(H_2O_{ice})} \quad [s^{-1}] \quad (7)$$

or

$$\frac{\kappa_{pd}(HCO)}{s^{-1}} \approx 10^{-12}\, \frac{\kappa_{diss}(HCO)}{10^{-9}}\, \frac{\chi(HCO)/10^{-9}}{\chi(HCO_{ice})/10^{-2}}\, \frac{10^{-4} n(H_2)}{n(H_2O_{ice})} \quad (8)$$

where we have used typical figures for the HCO abundance in the gas phase (∼10^{-9}, see above) and solid phase (∼10^{-2} see e.g. Bennet & Kaiser 2007) and for the amount of oxygen present as water ice in grain mantles.

Assuming standard ISM grains with a radius of 0.1 μm the required photodesorption efficiency (or yield) Y_{pd}(HCO):

$$Y_{pd}(HCO) \simeq \frac{\kappa_{pd}(HCO)}{G_0\, \exp(-2A_V)\, \pi a^2} \quad [molecules\, photon^{-1}] \quad (9)$$

(see e.g., d'Hendecourt et al. 1985; Bergin et al. 1995) converts to $Y_{pd}(HCO) \approx 10^{-4}$ molecules per photon (for the FUV radiation field in the Horsehead and $A_V \simeq 1.5$, where HCO peaks). Therefore, the production of HCO in the gas phase from photo-desorption of formyl radicals could be a valid alternative to gas phase production, if the photo-desorption efficiency is high and HCO abundant in the ice mantles. This mechanism also requires further laboratory and theoretical studies.

Because the formyl radical is closely related to formaldehyde and methanol and the three species are likely to coexist in the ice mantles, a combined analysis of the H_2CO, CH_3OH and HCO line emissions towards the Horsehead nebula (PDR and cores) is needed to provide more information on the relative efficiencies of gas-phase and solid-phase routes in the formation of complex organic molecules in environments dominated by FUV-radiation. This will be the subject of a future paper.

5. Summary and conclusions

We have presented interferometric and single-dish data showing the spatial distribution of the formyl radical rotational lines in the Horsehead PDR and associated dense core. The HCO emission delineates the illuminated edge of the nebula and coincides with the PAH and hydrocarbon emission. HCO and HCO^+ reach similar abundances (≃1–2 × 10^{-9}) in these PDR regions

where the chemistry is dominated by the presence of FUV photons. For the physical conditions prevailing in the Horsehead edge, pure gas-phase chemistry is able to reproduce the observed HCO abundances (high in the PDR, low in the shielded core) if the $O + CH_2 \rightarrow HCO + H$ reaction is included in the models. This reaction connects the high abundance of HCO, through its formation from carbon radicals, with the availability of C^+ in the PDR.

The different linewidths of HCO and $H^{13}CO^+$ in the line of sight towards the "DCO^+ peak" suggest that the $H^{13}CO^+$ line emission arises from the quiescent, cold and dense gas completely shielded from the FUV radiation, whereas HCO predominantly arises from the outer surface of the cloud (its illuminated *skin*). As a result we propose the HCO/$H^{13}CO^+$ abundance ratio, and the HCO abundance itself (if $\gtrsim 10^{-10}$), as sensitive diagnostics of the presence of FUV radiation fields. In particular, regions where the HCO/$H^{13}CO^+$ abundance ratio (or intensity ratio if lines are optically thin) is greater than $\simeq 1$ should reflect ongoing FUV-photochemistry.

Given the rich HCO spectrum and the possibility of mapping its bright millimeter line emission with interferometers, we propose HCO-H_2 as a very interesting molecular system for calculations of the ab initio inelastic collision rates.

Acknowledgements. We thank the IRAM PdBI and 30 m staff for their support during the observations. We thank A. Faure and J. Tennyson for sending us the $H^{13}CO^+$-e^- collisional rates prior to publication, B. Godard for useful discussions on the chemistry of carbon ions in the diffuse ISM, and A. Bergeat and A. Canosa for interesting discussions on radical-atom chemical reactions. J.R.G. is supported by a *Ramón y Cajal* research contract from the Spanish MICINN and co-financed by the European Social Fund. This research has benefitted from the financial support of the CNRS/INSU research programme, PCMI. We acknowledge the use of the JPL (Pickett et al. 1998) and Cologne (Müller et al. 2001, 2005) spectroscopic data bases, as well as the UMIST chemical reaction data base Woodall et al. (2007).

References

Abergel, A., Bernard, J. P., Boulanger, F., et al. 2002, A&A, 389, 239
Bennett, C. J., & Kaiser, R. I. 2007, ApJ, 661, 899
Bergin, E. A., Langer, W. D., & Goldsmith, P. F. 1995, ApJ, 441, 222
Bernstein, M. P., Sandford, S. A., Allamandola, L. J., Chang, S., & Scharberg, M. A. 1995, ApJ, 454, 327
Charnley, S. B., Tielens, A. G. G. M., & Rodgers, S. D. 1997, ApJ, 482, L203
d'Hendecourt, L. B., Allamandola, L. J., & Greenberg, J. M. 1985, A&A, 152 130
Draine, B. T. 1978, ApJS, 36, 595
de Jong, T., Boland, W., & Dalgarno, A. 1980, A&A, 91, 68
Flower, D. R. 1999, MNRAS, 305, 651
García-Burillo, S., Martín-Pintado, J., Fuente, A., Usero, A., & Neri, R. 2002, ApJ, 575, L55
Goicoechea, J. R., & Le Bourlot, J. 2007, A&A, 467, 1
Goicoechea, J. R., Pety, J., Gerin, M., et al. 2006, A&A, 456, 565
Goicoechea, J. R., Pety, J., Gerin, M., et al. 2009, A&A, in press
González-García, M., Le Bourlot, J., Le Petit, F., & Roueff, E. 2008, A&A, 485, 127
Graedel, T. E., Langer, W. D., & Frerking, M. A. 1982, ApJS, 48, 321
Habart, E., Abergel, A., Walmsley, C. M., Teyssier, D., & Pety, J. 2005, A&A, 437, 177
Hiraoka, K., Ohashi, N., Kihara, N., et al. 1994, Chem. Phys. Lett., 229, 408
Landsberg, B. M., Merer, A. J., & Oka, T. 1977, J. Mol. Spec., 67, 459
Le Bourlot, J., Pineau Des Forets, G., Roueff, E., & Flower, D. R. 1993, A&A, 267, 233
Le Petit, F., Nehmé, C, Le Bourlot, J., & Roueff, E. 2006, ApJS, 64, 506
Linnartz, H., Acharyya, K., Awad, Z., et al. 2007, Molecules in Space and Laboratory, ed. J. L. Lemaire, & F. Combes
Mallard, et al. 1994, NIST Chemical Kinetics Database, NIST, Gaithersburg, MD
Moore, M. H., Hudson, R. L., & Gerakines, P. A. 2001, Spec. Acta part A, 57, 843
Müller, H. S. P., Thorwirth, S., Roth, D. A., & Winnewisser, W. 2001, A&A, 370, L49
Müller, H. S. P., Schlöder, F., Stutzki, J., & Winnewisser, W. 2005, J. Mol. Struct., 742, 215
Öberg, K. I., Fuchs, G. W., Awad, Z., et al. 2007, ApJ, 662, L23
Penzias, A. A., & Burrus, C. A. 1973, ARA&A, 11, 51
Pety, J., Teyssier, D., Fossé, D., et al. 2005, A&A, 435, 885
Pety, J. SF2A-2005: Semaine de l'Astrophysique Française, meeting held in Strasbourg, France, ed. F. Casoli, T. Contini, J. M. Hameury, & L. Pagani (EDP Sciences, Conf. Ser.), 721
Pety, J., Goicoechea, J. R., Hily-Blant, P., Gerin, M., & Teyssier, D. 2007a, A&A, 464, L41
Pety, J., Goicoechea, J. R., Gerin, M., et al. 2007b, Proceedings of the Molecules in Space and Laboratory conference, ed. J. L. Lemaire, & F. Combes
Philipp, S. D., Lis, D. C., Güsten, R., et al. 2006, A&A, 454, 213
Pickett, H. M., Poynter, R. L., Cohen, E. A., et al. 1998, J. Quant. Spectrosc. Rad. Transfer, 60, 883
Röllig, M., et al. 2007, A&A, 467, 187
Schilke, P., Pineau des Forets, G., Walmsley, C. M., & Martín-Pintado, J. 2001, A&A, 372, 291
Snyder, L. E., Hollis, J. M., & Ulich, B. L. 1976, ApJ, 208, L91
Snyder, L. E., Schenewerk, M. S., & Hollis, J. M. 1985, ApJ, 298, 360
Teyssier, D., Fossé, D., Gerin, M., et al. 2004, A&A, 417, 135
Tielens, A. G. G. M., & Whittet, D. C. B. 1997, in Molecules in astrophysics: probe and processes, ed. E. F. van Dishoeck (Dordrecht: Kluwer), 45
Troe, J. 2007, J. Phys. Chem., 111, 3868
Tsuboi, T., & Hashimoto, K. 1981, J. Combust. Flame, 42
van Dishoeck, E. F. 1988, Rate Coefficients in Astrochemistry, ed. T. J. Millar, & D. A. Williams (Dordrecht, Boston: Kluwer Academic Publishers), 49
Watanabe, N., & Kouchi, A. 2002, ApJ, 571, L173
Willacy, K., & Williams, D. A. 1993, MNRAS, 260, 635
Woodall, J., Agúndez, M., Markwick-Kemper, A. J., & Millar, T. J. 2007, A&A, 466, 1197
Yin, H. M., Rowling, S. T., Büll, A., & Kable, S. H. 2007, J. Chem. Phys., 064302

A&A 534, A49 (2011)
DOI: 10.1051/0004-6361/201117257
© ESO 2011

Astronomy & Astrophysics

H_2CO in the Horsehead PDR: photo-desorption of dust grain ice mantles

V. Guzmán[1,2], J. Pety[2,1], J. R. Goicoechea[3], M. Gerin[1], and E. Roueff[4]

[1] LERMA – LRA, UMR 8112, Observatoire de Paris and École Normale Supérieure, 24 rue Lhomond, 75231 Paris, France
e-mail: [viviana.guzman;maryvonne.gerin]@lra.ens.fr
[2] IRAM, 300 rue de la Piscine, 38406 Grenoble Cedex, France
e-mail: pety@iram.fr
[3] Departamento de Astrofísica, Centro de Astrobiología, CSIC-INTA, Carretera de Ajalvir, Km 4, Torrejón de Ardoz, 28850 Madrid, Spain
e-mail: jr.goicoechea@cab.inta-csic.es
[4] LUTH UMR 8102, CNRS and Observatoire de Paris, Place J. Janssen, 92195 Meudon Cedex, France
e-mail: evelyne.roueff@obspm.fr

Received 13 May 2011 / Accepted 22 August 2011

ABSTRACT

Aims. For the first time we investigate the role of the grain surface chemistry in the Horsehead photo-dissociation region (PDR).
Methods. We performed deep observations of several H_2CO rotational lines toward the PDR and its associated dense-core in the Horsehead nebula, where the dust is cold ($T_{dust} \simeq 20-30$ K). We complemented these observations with a map of the p-H_2CO $3_{03}-2_{02}$ line at 218.2 GHz (with 12″ angular resolution). We determine the H_2CO abundances using a detailed radiative transfer analysis and compare these results with PDR models that include either pure gas-phase chemistry or both gas-phase and grain surface chemistry.
Results. The H_2CO abundances ($\simeq 2–3 \times 10^{-10}$) with respect to H-nuclei are similar in the PDR and dense-core. In the dense-core the pure gas-phase chemistry model reproduces the observed H_2CO abundance. Thus, surface processes do not contribute significantly to the gas-phase H_2CO abundance in the core. In contrast, the formation of H_2CO on the surface of dust grains and subsequent photo-desorption into the gas-phase are needed in the PDR to explain the observed gas-phase H_2CO abundance, because the gas-phase chemistry alone does not produce enough H_2CO. The assignments of different formation routes are strengthen by the different measured ortho-to-para ratio of H_2CO: the dense-core displays the equilibrium value (~3) while the PDR displays an out-of-equilibrium value (~2).
Conclusions. Photo-desorption of H_2CO ices is an efficient mechanism to release a significant amount of gas-phase H_2CO into the Horsehead PDR.

Key words. astrochemistry – ISM: clouds – ISM: molecules – ISM: individual objects: Horsehead nebula – radiative transfer – radio lines: ISM

1. Introduction

Photo-dissociation region (PDR) models are used to understand the evolution of the far-UV illuminated matter both in our Galaxy and in external galaxies. The spectacular instrumental improvements, which happen in radioastronomy with the advent of Herschel, ALMA and NOEMA, call for matching progresses in PDR modeling. In particular, the physics and chemistry of the dust grains and of the gas-phase are intricately intertwined. It is well known that the formation of ice grain mantles leads to the removal of chemical reservoirs like CO, O, and other abundant species from the gas phase, enabling new chemical routes to be opened and others to be closed. Despite their low temperature, the mantles are chemically active. Hydrogenation/deuteration reactions are known to be efficient, because hydrogen (or deuterium atoms) can migrate on the surfaces, but reactions with O, N, and C must also be considered. Complex molecules may therefore be formed before they are released into the gas phase. Moreover, the release of the products into the gas phase happens either through thermal processes (evaporation) or non-thermal ones (cosmic ray or far-UV photon-induced desorption). Recent photo-desorption experiments on water and CO ices show that this mechanism is much more efficient than previously thought (Öberg et al. 2009b,a; Muñoz Caro et al. 2010). These results led various groups to include photo-desorption into PDR models (see the results on H_2O and O_2 by Hollenbach et al. 2009; Walsh et al. 2010; Hassel et al. 2010). The availability of well-defined observations is essential here to distinguish between chemical assumptions about the significant grain surface processes, i.e., adsorption, desorption, and diffusion. It is now confirmed that some interstellar species are mostly formed in the gas-phase (CO for instance), others on grains (CH_3OH, Garrod et al. 2007), while the chemical routes for other complex species such as formaldehyde, are still debated because it is likely that solid and gas-phase processes are both needed.

Formaldehyde (H_2CO) was the first organic molecule discovered in the interstellar medium (Snyder et al. 1969). It is a relatively simple organic molecule that can be formed in the gas-phase and on the surface of dust grains. In the warm gas, H_2CO can trigger the formation of more complex organic molecules (Charnley et al. 1992). It is one of the most popular molecules used for studying the physical conditions of the gas in astrophysical sources. Indeed, it is a good probe of the temperature and density of the gas (Mangum & Wootten 1993). Owing to its

Table 1. Observation parameters for the maps shown in Fig. 1.

Molecule	Transition	Frequency GHz	Instrument	Beam arcsec	PA °	Vel. resol. km s^{-1}	Int. time hours	T_{sys} K (T_A^*)	Noise K (T_{mb})	Obs. date
	Continuum at 1.2 mm		30m/MAMBO	11.7 × 11.7	0	–	–	–	–	–
DCO^+	3–2	216.112582	30m/HERA	11.4 × 11.4	0	0.11	1.5/2.0[a]	230	0.10	2006 Mar.
p-H_2CO	3_{03}–2_{02}	218.222190	30m/HERA	11.9 × 11.9	0	0.05	2.1/3.4[a]	280	0.32	2008 Jan.
HCO	$1_{0,1}$ 3/2, 2–$0_{0,0}$ 1/2, 1	86.670760	PdBI/C&D	6.69 × 4.39	16	0.20	6.5[b]	150	0.09[c]	2006–2007

Notes. The projection center of all maps is $\alpha_{2000} = 05^h40^m54.27^s$, $\delta_{2000} = -02°28'00''$. [(a)] Two values are given for the integration time: the on-source time and the telescope time. [(b)] On-source time computed as if the source were always observed with six antennae. [(c)] The noise values quoted here are the noises at the mosaic phase center (mosaic noise is inhomogeneous because of the primary beam correction; it steeply increases at the mosaic edges).

Table 2. Observation parameters of the deep integrations of the o-H_2CO and p-H_2CO lines toward the PDR and the dense-core.

Position	Molecule	Transition	ν [GHz]	Line area K km s^{-1}	Instrument	F_{eff}	B_{eff}	Int. time hours	T_{peak} K (T_{mb})	rms K	S/N
	o-H_2CO	2_{12}–1_{11}	140.839	1.75 ± 0.02	30-m/C150	0.93	0.70	1.9	1.87	0.061	31
	p-H_2CO	2_{02}–1_{01}	145.603	1.32 ± 0.02	30-m/D150	0.93	0.69	1.9	1.61	0.047	34
	o-H_2CO	2_{11}–1_{10}	150.498	1.41 ± 0.02	30-m/C150	0.93	0.68	1.4	1.52	0.053	29
PDR	o-H_2CO	3_{13}–2_{12}	211.211	1.24 ± 0.03	30-m/B230	0.91	0.57	1.1	1.46	0.096	15
	p-H_2CO	3_{03}–2_{02}	218.222	0.77 ± 0.01	30-m/B230	0.91	0.55	3.9	1.11	0.052	21
	p-H_2CO	3_{22}–2_{21}	218.476	0.17 ± 0.01	30-m/B230	0.91	0.55	2.0	0.27	0.055	5
	o-H_2CO	3_{12}–2_{11}	225.698	0.84 ± 0.02	30-m/A230	0.91	0.54	6.5	1.12	0.079	14
	o-H_2CO	2_{12}–1_{11}	140.839	2.56 ± 0.01	30-m/C150	0.93	0.70	3.7	3.46	0.036	96
	p-H_2CO	2_{02}–1_{01}	145.603	1.75 ± 0.02	30-m/D150	0.93	0.69	1.9	2.62	0.044	60
	o-H_2CO	2_{11}–1_{10}	150.498	1.89 ± 0.01	30-m/C150	0.93	0.68	1.5	2.52	0.052	49
	o-H_2CO	3_{13}–2_{12}	211.211	1.93 ± 0.02	30-m/B230	0.91	0.57	2.0	3.02	0.065	47
	p-H_2CO	3_{03}–2_{02}	218.222	1.03 ± 0.01	30-m/B230	0.91	0.55	3.0	1.83	0.057	32
	p-H_2CO	3_{22}–2_{21}	218.476	0.04 ± 0.01	30-m/B230	0.91	0.55	4.5	0.06	0.037	2
Dense-core	o-H_2CO	3_{12}–2_{11}	225.698	1.27 ± 0.02	30-m/A230	0.91	0.54	8.4	1.96	0.073	27
	o-$H_2^{13}CO$	2_{12}–1_{11}	137.450	0.09 ± 0.02	30-m/D150	0.95	0.70	2.0	0.11	0.063	2
	p-$H_2^{13}CO$	2_{02}–1_{01}	141.984	0.10 ± 0.01	30-m/D150	0.95	0.70	1.5	0.11	0.060	2
	HDCO	2_{11}–1_{10}	134.285	0.13 ± 0.01	30-m/C150	0.94	0.71	2.0	0.32	0.042	8
	HDCO	3_{12}–2_{11}	201.341	0.05 ± 0.01	30-m/A230	0.91	0.59	3.5	0.13	0.032	4
	p-D_2CO	2_{12}–1_{11}	110.838	0.04 ± 0.01	30-m/A100	0.95	0.75	4.9	0.08	0.031	3
	o-D_2CO	4_{04}–3_{03}	231.410	0.04 ± 0.01	30-m/A230	0.91	0.53	4.5	0.09	0.068	1

large dipole moment (2.3 Debye), its rotational lines are easy to detect from ground-based observations. It is present in a variety of environments, such as Galactic HII regions (e.g., Downes et al. 1980), proto-stellar cores (e.g., Young et al. 2004; Maret et al. 2004), young stellar objects (e.g., Araya et al. 2007), PDRs (e.g., Leurini et al. 2010), starburst galaxies (e.g., Mangum et al. 2008) and comets (e.g., Snyder et al. 1989; Milam et al. 2006).

The Horsehead PDR is particularly well-suited to investigate grain surface chemistry in a UV irradiated environment. It is viewed nearly edge-on (Habart et al. 2005) at a distance of 400 pc (implying that 10″ correspond to 0.02 pc). Thus, it is possible to study the interaction of far-UV radiation with dense interstellar clouds and the transition from warm to cold gas in a PDR with a simple geometry, very close to the prototypical kind of source needed to serve as a reference to chemical models. Its relatively low UV illumination (χ = 60 in Draine units, Draine 1978) and high density ($n_H \sim 10^4$–10^5 cm^{-3}) implies low dust grain temperatures, from $T_{dust} \sim 30$ K in the PDR to $T_{dust} \sim 20$ K deeper inside the cloud (Goicoechea et al. 2009a). The release of the grain mantle products into the gas phase is consequently dominated by photo-desorption, while regions with warmer dust (the Orion bar or the star-forming cores) provide mixed information on the thermal and non-thermal processes (e.g., Bisschop et al. 2007).

In this paper we present deep observations of several formaldehyde lines toward two particular positions in the Horsehead nebula: the PDR, corresponding to the peak of the HCO emission (Gerin et al. 2009), where the gas is warm ($T_{kin} \sim$ 60 K); and the dense-core, a cold ($T_{kin} \leq 20$ K) condensation located less than 40″ away from the PDR edge, where HCO^+ is highly deuterated (Pety et al. 2007). We present the observations and data reduction in Sect. 2, while the results and abundances are given in Sect. 3. In Sect. 4 we present the H_2CO chemistry and PDR modeling. A discussion is given in Sect. 5 and we conclude in Sect. 6.

2. Observations and data reduction

Tables 1 and 2 summarize the observation parameters for the data obtained with the IRAM-30 m and PdBI telescopes. Figure 1 displays the p-H_2CO, HCO, DCO^+ and 1.2 mm continuum maps. The p-H_2CO line was mapped during 3.3 h of good winter weather (∼1 mm of water vapor) using the first polarization (i.e. nine of the eighteen available pixels) of the IRAM-30m/HERA single-sideband multi-beam receiver. We used the frequency-switched, on-the-fly observing mode. We observed along and perpendicular to the direction of the exciting star in zigzags (i.e. ± the lambda and beta scanning direction). The multi-beam system was rotated by 9.6° with respect to the scanning direction. This ensured Nyquist sampling between the rows except at the edges of the map. The fully sampled part of the map covered a 150″ × 150″ portion of the sky. A detailed description

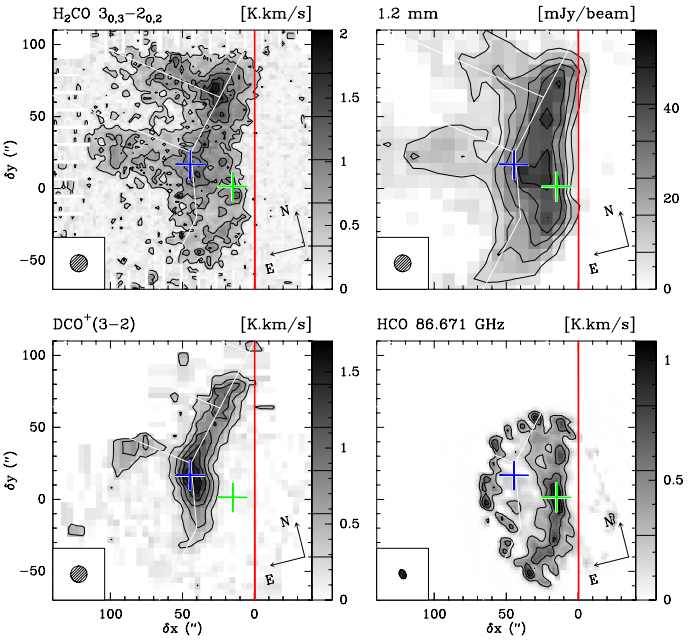

Fig. 1. Integrated intensity maps of the Horsehead edge. The intensities are expressed in the main-beam temperature scale. Maps were rotated by 14° counter-clockwise around the projection center, located at $(\delta x, \delta y) = (20'', 0'')$, to bring the exciting star direction in the horizontal direction and the horizontal zero was set at the PDR edge, delineated by the red vertical line. The crosses show the positions of the PDR (green) and the dense-core (blue), where deep integrations were performed at IRAM-30m (see Fig. 3). The spatial resolution is plotted in the bottom left corner. Values of contour levels are shown on each image lookup table. The emission of all lines is integrated between 10.1 and 11.1 km s^{-1}.

of the HCO, DCO^+ and 1.2 mm continuum observations and data reductions can be found in Gerin et al. (2009), Pety et al. (2007), and Hily-Blant et al. (2005).

We performed deep integrations of o-H_2CO and p-H_2CO low-energy rotational lines (see Figs. 2 and 3) centered on the PDR and the dense-core. To obtain these deep integration spectra, we used the position-switching observing mode. The on-off cycle duration was 1 min and the off-position offsets were (δ RA, δ Dec) = (−100″, 0″), i.e. the H II region ionized by σOri and free of molecular emission. From our knowledge of the IRAM-30 m telescope we estimate the absolute position accuracy to be 3″.

The data processing was made with the GILDAS[1] softwares (Pety 2005). The IRAM-30m data were first calibrated to the T_A^* scale using the chopper-wheel method (Penzias & Burrus 1973), and finally converted to main-beam temperatures (T_{mb}) using the forward and main-beam efficiencies (F_{eff} and B_{eff}) displayed in Table 2. The resulting amplitude accuracy is ∼ 10%. Frequency-switched spectra were folded using the standard shift-and-add method before baseline subtraction. The resulting spectra were finally gridded through convolution with a Gaussian to obtain the maps.

3. Results

3.1. H_2CO spatial distribution

The 218.2 GHz p-H_2CO integrated line-intensity map is shown in Fig. 1 together with the 86.7 GHz HCO, 216.1 GHz DCO^+ integrated line-intensity maps and the 1.2 mm continuum-emission map. Formaldehyde emission is extended throughout the Horsehead with a relatively constant intensity. The H_2CO spatial distribution ressembles the 1.2 mm continuum emission: it follows the top of the famous Horsehead nebula from its front to its mane. It also delineates the throat of the Horsehead. The peak of the H_2CO emission spatially coincides with the peak of the DCO^+ emission, which arises from a cold dense-core. However, H_2CO emission is also clearly present along the PDR, which is traced by the HCO emission. The PDR and dense-core, namely the peaks of the HCO and DCO^+ emission are shown with green and blue crosses respectively. Gaussian fits of the H_2CO lines at the HCO peak result in broader line widths than at the DCO^+ peak. That the lines are broader in the PDR confirms that H_2CO lines toward the DCO^+ peak arise from the dense-core rather than from the illuminated surface of the cloud. There is a peak in the H_2CO emission toward the north-west region of the nebula, near the edge of the PDR, where two protostars have been identified (B33-1 and B33-28, Bowler et al. 2009). These protostars heat the dust around them, so it is likely that H_2CO has been evaporated from the grain ice mantles.

[1] See http://www.iram.fr/IRAMFR/GILDAS for more information about the GILDAS softwares.

Table 3. Spectroscopic parameters of the observed lines obtained from the CDMS data base (Müller et al. 2001).

Molecule	Transition	ν [GHz]	E_u [K]	A_{ul} [s^{-1}]	g_u
o-H_2CO	$2_{12}-1_{11}$	140.839	21.92	5.3×10^{-5}	15
p-H_2CO	$2_{02}-1_{01}$	145.603	10.48	7.8×10^{-5}	5
o-H_2CO	$2_{11}-1_{10}$	150.498	22.62	6.5×10^{-5}	15
o-H_2CO	$3_{13}-2_{12}$	211.211	32.06	2.3×10^{-4}	21
p-H_2CO	$3_{03}-2_{02}$	218.222	20.96	2.8×10^{-4}	7
p-H_2CO	$3_{22}-2_{21}$	218.476	68.09	1.6×10^{-4}	7
o-H_2CO	$3_{12}-2_{11}$	225.698	33.45	2.8×10^{-4}	21
o-$H_2^{13}CO$	$2_{12}-1_{11}$	137.450	10.51	4.9×10^{-5}	15
p-$H_2^{13}CO$	$2_{02}-1_{01}$	141.984	2.37	7.2×10^{-5}	5
HDCO	$2_{11}-1_{10}$	134.285	17.63	4.6×10^{-5}	5
HDCO	$3_{12}-2_{11}$	201.341	27.29	2.0×10^{-4}	7
o-D_2CO	$2_{12}-1_{11}$	110.838	13.37	2.6×10^{-5}	5
p-D_2CO	$4_{04}-3_{03}$	231.410	27.88	3.5×10^{-4}	18

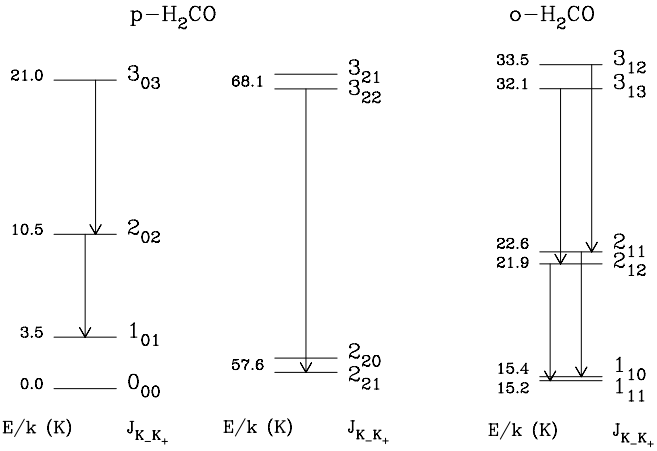

Fig. 2. Lower energy rotational levels of para- (*left*) and ortho-H_2CO (*right*). The energy above para ground-state is shown at the left of each level. The arrows indicate the transitions detected in the Horsehead.

3.2. H_2CO column density

We computed the column densities of H_2CO at the PDR and the dense-core positions. For this we first used the $H_2^{13}CO$ lines to

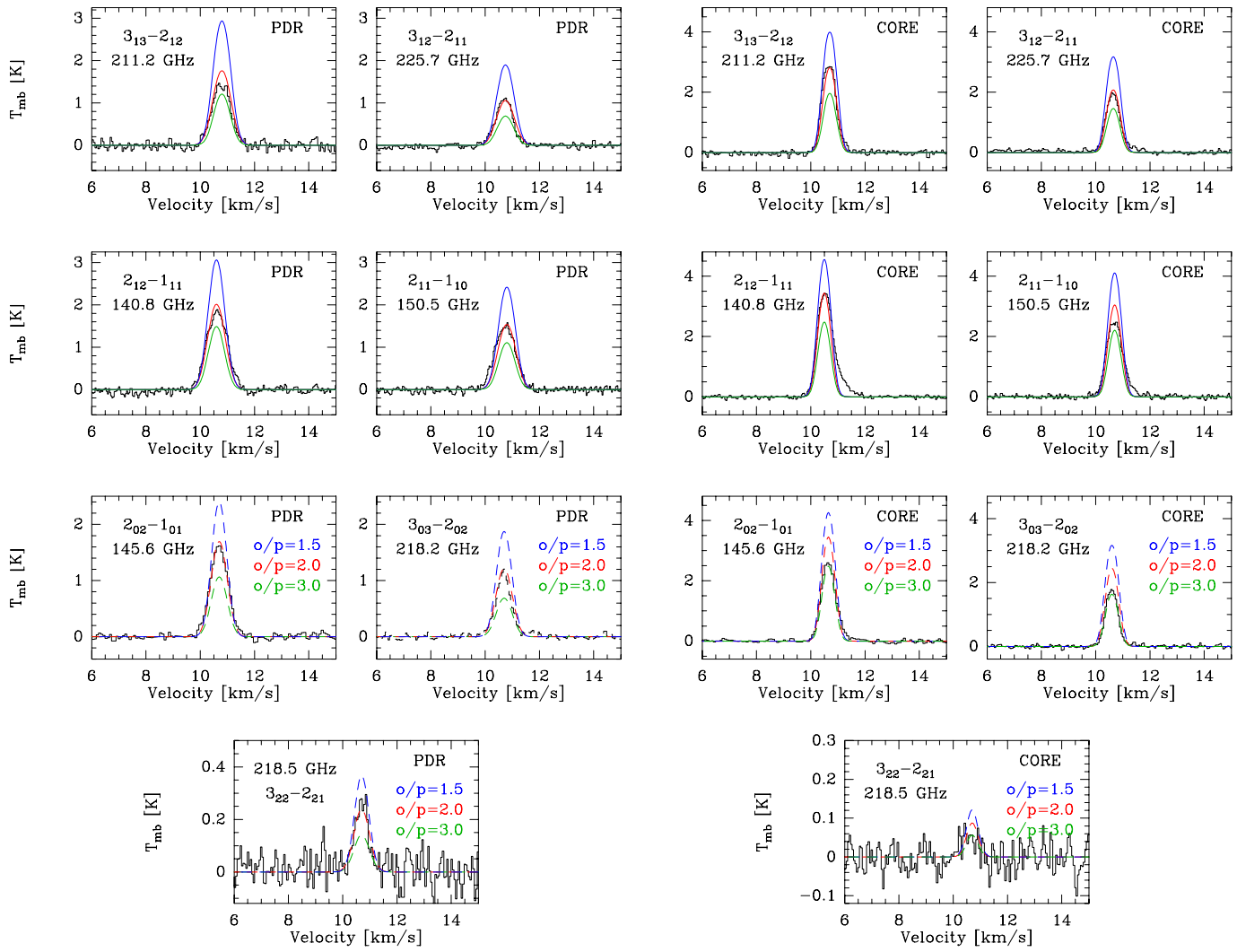

Fig. 3. Radiative transfer modeling of H_2CO lines for two positions toward the Horsehead. *Two left columns*: the PDR position (T_{kin} = 60 K, $n(H_2) = 6 \times 10^4$ cm^{-3}, N(o-H_2CO) = 7.2×10^{12} cm^{-2}) and *two right columns*: the dense-core position (T_{kin} = 20 K, $n(H_2) = 10^5$ cm^{-3}, N(o-H_2CO) = 9.6×10^{12} cm^{-2}). The *two top rows* display the ortho lines, for which we varied the column density around the best match (red curve) by a factor of 1.5 (blue curve) and 1/1.5 (green curve). The *two bottom rows* display the para lines, for which we kept the column density of the best match for o-H_2CO (red curves) constant and varied the ortho-to-para ratio of H_2CO: o/p = 1.5 (dashed blue), o/p = 2 (dashed red) and o/p = 3 (dashed green).

estimate the optical depth of the H_2CO lines. Then, we made a first estimate of the column densities and excitation temperatures using rotational diagrams. Finally, we used these first estimates as an input for a detailed nonlocal non-LTE excitation and radiative transfer analysis to compute the H_2CO abundances. The spectroscopic parameters for the detected transitions (shown in Fig. 2) are given in Table 3. We assumed that the emission is extended and fills the 30 m beam, as shown by the map of the $3_{03}-2_{02}$ transition (see Fig. 1).

3.2.1. Opacity of the H_2CO lines

We detected two transitions of the formaldehyde isotopologue $H_2^{13}CO$ in the dense-core position (see upper panels in Fig. 4). By comparing the flux between H_2CO and $H_2^{13}CO$ for the same transition it is possible to estimate the opacity of the H_2CO line, assuming that the $H_2^{13}CO$ line is optically thin, as follows:

$$\frac{F_{H_2CO}}{F_{H_2^{13}CO}} = \frac{[^{12}C]}{[^{13}C]}\beta \qquad (1)$$

where β is the escape probability function, which in the case of a homogeneous slab of gas (de Jong et al. 1980) is equal to

$$\beta = \frac{1 - \exp(-3\tau)}{3\tau}. \qquad (2)$$

The isotopic abundance ratio $^{12}C/^{13}C \simeq 60$ (Langer & Penzias 1990; Savage et al. 2002) is almost twice the line intensity ratio between formaldehyde and its isotopologue, and therefore the H_2CO lines have moderate opacities. From the observations we estimate $\tau_{2_{12}-2_{11}} \sim 1.6$ and $\tau_{2_{02}-1_{01}} \sim 1.9$ for H_2CO in the dense-core.

3.2.2. Rotational diagram analysis

First-order estimates of the beam-averaged column densities and the rotational temperatures can be found by means of the widely used rotational diagram analysis (Goldsmith & Langer 1999). To do this, we assume that the gas is under LTE, and therefore all excitation temperatures are the same, and the energy levels

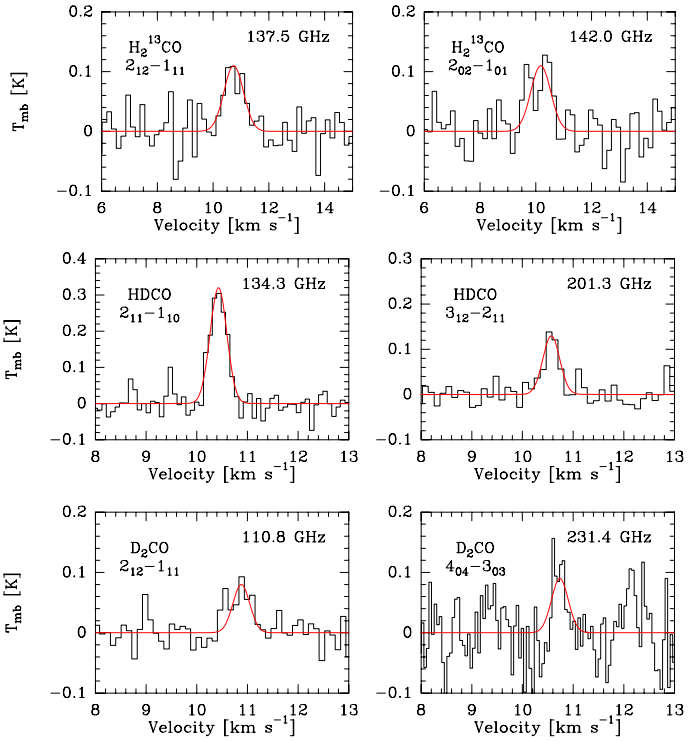

Fig. 4. $H_2^{13}CO$ and deuterated H_2CO lines detected toward the dense-core. Gaussian fits are shown with red lines. For HDCO and D_2CO the line width was fixed to the width of the HDCO ($2_{11}-1_{10}$) line, because it has the best signal-to-noise ratio.

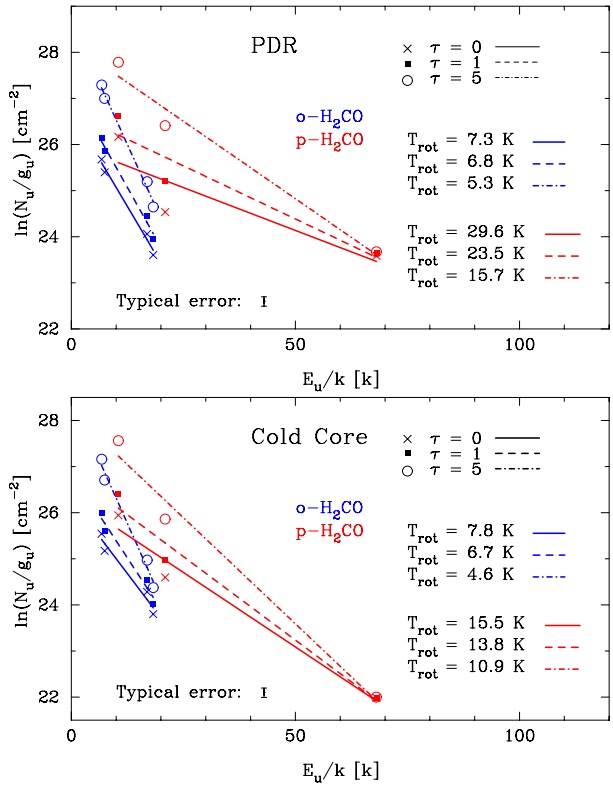

Fig. 5. H_2CO rotational diagrams corrected for line-opacity effects at the PDR and dense-core position. Rotational temperatures are shown for each considered opacity.

are populated following Boltzmann's law. We built rotational diagrams corrected for line-opacity effects through

$$\ln \frac{N_u^{thin}}{g_u} + \ln C_\tau = \ln \frac{N}{Z} - \frac{E_u}{kT_{rot}}, \quad (3)$$

where N is the total column density of the molecule, g_u is the level degeneracy, E_u/k is the energy of the upper level in K, Z is the partition function at the rotational temperature T_{rot}, $C_\tau = \frac{\tau}{1-e^{-\tau}} \leq 1$ is a line-opacity correction factor, where τ is the opacity of the line, and N_u^{thin} is the column density of the upper level for an optically thin line when the source fills the beam. This last parameter is given by

$$N_u^{thin} = \frac{8\pi k \nu^2 W}{hc^3 A_{ul}}, \quad (4)$$

where k is the Boltzmann constant, ν is the line frequency, W is the integrated line intensity, h is the Planck constant, c is the speed of light and A_{ul} is the Einstein coefficient for spontaneous emission.

Ortho- and para forms of H_2CO are treated as different species because radiative transitions between them are forbidden. Resulting rotational diagrams are shown in Fig. 5 for three different o-H_2CO ($2_{12}-1_{11}$) and p-H_2CO ($2_{02}-1_{01}$) line-opacities (τ = 0, 1 and 5). We find column densities of $N \sim 10^{12}-10^{13}$ cm^{-2}, depending on the opacity. We infer very different rotational temperatures for o-H_2CO ($T_{rot} \sim 4-8$ K) and p-H_2CO ($T_{rot} \sim 10-30$ K), which are also lower than the well-known conditions in the PDR ($T_{kin} \sim 60$ K) and in the dense-core ($T_{kin} \sim 20$ K). This suggests that the gas is far from thermalization, and therefore we used these column densities and rotational temperatures as an input for a more complex analysis to derive the H_2CO column densities.

Table 4. H_2CO critical densities (cm^{-3}) for three different colliding partners computed for T_{kin} = 60 K.

$J_{K_aK_c}$	p-H_2	o-H_2	He
2_{02}	7.2×10^5	3.6×10^5	1.3×10^6
3_{03}	1.6×10^6	9.9×10^5	4.2×10^6
3_{22}	5.8×10^5	4.7×10^5	2.5×10^6
2_{12}	3.7×10^5	2.5×10^5	8.1×10^5
2_{11}	4.3×10^5	2.2×10^5	8.7×10^5
3_{13}	9.7×10^5	7.0×10^5	2.3×10^6
3_{12}	1.3×10^6	7.9×10^5	3.2×10^6

3.2.3. Radiative transfer models

The critical density of a given collisional partner corresponds to the density at which the sum of spontaneous radiative de-excitation rates is equal to the sum of collisional de-excitation rates (γ) of a given level

$$n_{cr}(J_{K_aK_c}, T_{kin}) = \frac{\sum_{J'_{K'_aK'_c}} A(J_{K_aK_c} \rightarrow J'_{K'_aK'_c})}{\sum_{J'_{K'_aK'_c}} \gamma(J_{K_aK_c} \rightarrow J'_{K'_aK'_c}, T_{kin})}. \quad (5)$$

Formaldehyde lines have high critical densities ($\sim10^6$ cm^{-3}, see Table 4) compared to the H_2 density in the Horsehead ($\sim10^4-10^5$ cm^{-3}). Because we expect subthermal emission ($T_{ex} \ll T_{kin}$) for transitions with high critical densities compared to the H_2 density, we used a nonlocal non-LTE radiative transfer code adapted to the Horsehead geometry to model the observed H_2CO line intensities (Goicoechea et al. 2006). We used a nonlocal code to take into account the radiative coupling between different cloud positions that might affect the population of the energy levels. The code is able to predict the line

Table 5. Column densities and abundances.

	Molecule	PDR	Dense-core
Column densities [cm^{-2}]	N_H	3.8×10^{22}	6.4×10^{22}
	N(o-H_2CO)	7.2×10^{12}	9.6×10^{12}
	N(p-H_2CO)	3.6×10^{12}	3.2×10^{12}
	N(HCO)[a]	3.2×10^{13}	$<4.6 \times 10^{12}$
	N(HDCO)[b]	–	1.6×10^{12}
	N(o-D_2CO)[b]	–	5.1×10^{11}
	N(p-D_2CO)[b]	–	5.1×10^{11}
Abundances $[X] = \frac{N(X)}{(N(H)+2\,N(H_2))}$	[o-H_2CO]	1.9×10^{-10}	1.5×10^{-10}
	[p-H_2CO]	9.5×10^{-11}	5.0×10^{-11}
	[HCO]	8.4×10^{-10}	$<7.2 \times 10^{-11}$
	[HDCO]	–	2.5×10^{-11}
	[D_2CO]	–	1.6×10^{-11}

Notes. [a] Gerin et al. (2009). [b] For T_{ex} = 6 K (LTE).

profiles. It takes into account line trapping, collisional excitation and radiative excitation by absorption of cosmic microwave background and dust continuum photons. We included 40 rotational levels for o-H_2CO and 41 rotational levels for p-H_2CO, where the maximum energy level lies at ~285 K for both species. We considered o-H_2, p-H_2 and He as collision partners with the following collisional excitation rates:

- collisional rates of o-H_2CO and p-H_2CO with He are taken from Green (1991);
- collisional rates of o-H_2CO with o-H_2 and p-H_2 from Troscompt et al. (2009) for the first 10 energy levels, i.e. $E_u \leq 50$ K. We complemented these data with He collision rates of Green (1991) scaled to H_2. Following the new H_2CO-H_2 collisional rate calculations, we scaled the H_2CO-He rates by a factor 2.5 instead of the usual ~1.4 mass factor (A. Faure, priv. comm.);
- collisional rates of p-H_2CO with o-H_2 and p-H_2 from Troscompt et al. (to be submitted).

Results are presented in Fig. 3 for three different column densities. Best matches (see Table 5) are for column densities of N(o-H_2CO) = 7.2×10^{12} cm^{-2} and N(p-H_2CO) = 3.6×10^{12} cm^{-2} in the PDR position, and N(o-H_2CO) = 9.6×10^{12} cm^{-2} and N(p-H_2CO) = 3.2×10^{12} cm^{-2} in the dense-core position. In the excitation- and radiative transfer models we adopt an H_2 ortho-to-para ratio of 3 (high-temperature limit), although it is likely that the ortho-to-para ratio is lower in the Horsehead (e.g., Habart et al. 2011). Indeed, the H_2CO column densities are not sensitive to the change of the H_2 ortho-to-para ratio for the physical conditions of the Horsehead (see Appendix A).

3.3. H_2CO ortho-to-para ratio

The ratio between the column densities of o-H_2CO and p-H_2CO provides information about the formation of the molecule, because the characteristic conversion time from one symmetry state to the other is longer than the H_2CO lifetime (Tudorie et al. 2006). When the molecule forms in the gas-phase, a ratio of 3 is expected, which corresponds to the statistical weight ratio between the ground states of the ortho- and para species. A ratio lower than 3 is expected when the molecule is formed on the surface of cold ($T_{dust} \lesssim 20$ K) dust grains (Kahane et al. 1984; Dickens & Irvine 1999). From the derived column densities we infer H_2CO ortho-to-para ratios of ~2 in the PDR and of ~3 in the dense-core. This suggests that in the dense-core H_2CO is mainly formed in the gas-phase, whereas in the PDR H_2CO is formed on the surface of dust grains. Dickens & Irvine (1999) measured H_2CO ortho-to-para ratios between 1.5 and 2 toward star-forming cores with outflows, and ratios near 3 toward three quiescent cores. Jørgensen et al. (2005) also found an ortho-to-para ratio of 1.6 in the envelopes around low-mass protostars.

3.4. HDCO and D_2CO column densities

We detected HDCO and D_2CO in the dense-core (see two bottom rows in Fig. 4), and we estimated their abundances assuming LTE. For T_{ex} = 6 K we obtain N(HDCO) = 1.6×10^{12} cm^{-2}, $N(D_2CO) = 5.1 \times 10^{11}$ cm^{-2} and a D_2CO ortho-to-para ratio of 1, which translates into relative abundances or fractionation levels [HDCO]/[H_2CO] = 0.11 and [D_2CO]/[H_2CO] = 0.04 for the inferred formaldehyde column densities in the dense-core.

Deuterium fractionation can occur in the gas-phase by means of ion-molecule reactions, where D is transferred from HD to other species. High abundances of deuterated molecules compared to the elemental D/H abundance (~1.5×10^{-5}, Linsky et al. 2006) have been observed in different astrophysical environments, from cold dense cores and hot molecular cores even to PDRs. Pety et al. (2007) found high deuteration ([DCO^+]/[HCO^+] > 0.02) in the Horsehead dense-core. A pure gas-phase chemical model was able to reproduce the observed fractionation level of HCO^+ for $T_{kin} \leq 20$ K. Parise et al. (2009) found high fractionation levels for DCN and HDCO toward the Orion Bar PDR ([XD]/[XH] ~ 0.01). They found that these ratios are consistent with pure gas-phase chemistry models where the gas is warm (>50 K), so the deuterium chemistry is driven mainly by CH_2D^+, as opposed to colder regions ($\lesssim$20 K) like the Horsehead dense-core, where H_2D^+ is the main actor. Owing to the low temperature in the core it is likely that a non-negligible fraction of CO is frozen on the dust grains, enhancing the deuterium fractionation.

Another way to form deuterated molecules in cold environments is trough D addition or H-D substitution reactions on the surface of dust grains (Hidaka et al. 2009). In the Horsehead core though, desorption from the grain mantles is not efficient in releasing products into the gas-phase (see Sect. 4). It is then more likely that the gas-phase HDCO and D_2CO molecules detected here are formed in the gas-phase. Nevertheless, there can still be a considerable amount of deuterated H_2CO trapped in the ices around dust grains.

4. H_2CO chemistry

We used a one-dimensional, steady-state photochemical model (Le Bourlot et al. 1993; Le Petit et al. 2006) to study the H_2CO chemistry in the Horsehead. The physical conditions have already been constrained by our previous observational studies and we keep the same assumptions for the density profile (displayed in the upper panel of Fig. 6), radiation field (χ = 60 in Draine units), elemental gas-phase abundances (see Table 6 in Goicoechea et al. 2009b) and cosmic ray ionization rate ($\zeta = 5 \times 10^{-17}$ s^{-1}).

Unlike other organic molecules like methanol, which can only be efficiently formed on the surface of grains (Tielens & Whittet 1997; Woon 2002; Cuppen et al. 2009), formaldehyde can be formed in both the gas-phase and on the surface of grains. Next, we investigate these two different scenarios.

4.1. Pure gas-phase chemistry models

We used the *Ohio State University (osu)* pure gas-phase chemical network upgraded to photochemical studies. We included the

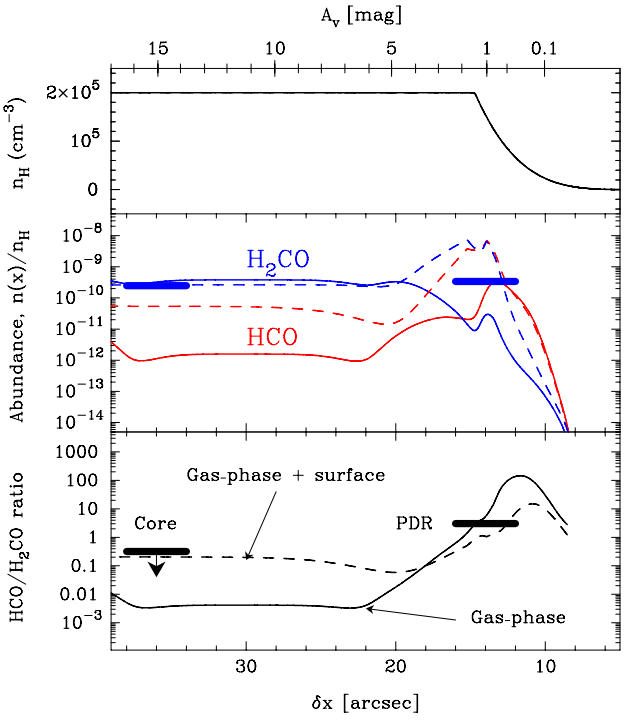

Fig. 6. Photochemical model of the Horsehead PDR. *Upper panel*: PDR density profile ($n_H = n(H) + 2n(H_2)$ in cm^{-3}). *Middle panel*: predicted abundance (relative to n_H) of H_2CO (blue) and HCO (red). *Lower panel*: predicted HCO/H_2CO abundance ratio. In the two bottom panels, models shown as solid lines include pure gas-phase chemistry and models shown as dashed lines include gas-phase as well as grain surface chemistry. The horizontal bars show the measured H_2CO abundances and abundance ratios.

photo-dissociation of HCO and of H_2CO (leading to CO and H_2) with rates of $1.1\times10^{-9}\exp(-0.8A_V)$ and $10^{-9}\exp(-1.74A_V)$ s^{-1}, respectively (van Dishoeck 1988). We also included the H_2CO photo-dissociation channel that leads to HCO and H (see e.g., Yin et al. 2007; Troe 2007) with the same rate of the one that leads to CO and H_2, and the atomic oxygen reaction with the methylene radical (CH_2) to explain the high abundance of HCO in the PDR (Gerin et al. 2009).

The predicted HCO and H_2CO abundance profiles and the HCO/H_2CO abundance ratio are shown as solid lines in Fig. 6 (middle and lower panel, respectively). The formation of H_2CO in the PDR and dense-core is dominated by reactions between oxygen atoms and the methyl radical (CH_3). The destruction of H_2CO in the PDR is dominated by photo-dissociation, while it is dominated by reactions with ions in the dense-core. The pure-gas phase model satisfactorily reproduces the observed H_2CO abundance in the dense-core ($\delta x \sim 35''$) but it predicts an abundance in the PDR ($\delta x \sim 15''$) that is at least one order of magnitude lower than the observed value.

4.2. Grain chemistry models

We considered the surface chemistry reactions introduced by Stantcheva et al. (2002), which include the following sequence of hydrogen addition reactions on CO to form formaldehyde and methanol

$$\mathrm{CO} \underset{\mathrm{H}}{\rightarrow} \mathrm{HCO} \underset{\mathrm{H}}{\rightarrow} \mathrm{H_2CO} \underset{\mathrm{H}}{\rightarrow} \mathrm{H_3CO} \underset{\mathrm{H}}{\rightarrow} \mathrm{CH_3OH}.$$

We also introduce water formation via hydrogenation reactions of O, OH until H_2O.

Adsorption, desorption and diffusive reactions were introduced in the Meudon PDR code in the rate equations approach. The corresponding implementation will be described in a specific paper (Le Bourlot et al., to be submitted) and we simply mention the main processes included in the present study. We distinguish between mantle molecules, which may accumulate in several layers (e.g., H_2O, H_2CO, CH_3OH), and light species (e.g., H, H_2), which stay on the external layer. Photo-desorption can be an efficient mechanism to release molecules to the gas phase in regions exposed to strong radiation fields, as shown recently in laboratory studies (Öberg et al. 2009b,a; Muñoz Caro et al. 2010). Thermal desorption is also introduced. It critically depends on the desorption barrier values, which are somewhat uncertain. Diffusive reactions occur on grain surfaces and the diffusion barriers are assumed to be 1/3 of the desorption energy values. Photodesorption efficiencies have been measured in the laboratory for CO, CO_2, H_2O and CH_3OH. These experiments have shown that all common ices have photodesorption yields of a few 10^{-3} molecules per incident UV photon (Öberg et al. 2007, 2009a,b,c). Therefore, we also take a photo-desorption efficiency of 10^{-3} for those species that have not been studied in the laboratory. We assume in addition that for formaldehyde the two branching ratios toward H_2CO and HCO+H channels are identical, i.e. 5×10^{-4}. Given the high density in the dense-core, the grains are assumed to be strongly coupled to the gas in the inner region, so that their temperatures become equal to 20 K in the dark region, whereas the illuminated dust grains reach temperature values of about 30 K.

The predicted HCO and H_2CO abundances are shown as dashed lines in Fig. 6. This model reproduces the observed H_2CO abundance in the dense-core and predicts a similar abundance as the pure gas-phase model. This way, formation on grain surfaces does not contribute significantly to the observed gas-phase H_2CO abundance in the dense-core. This is because of the low photo-desorption rates in the core caused by the shielding from the external UV field. On the other hand, the H_2CO abundance can increase by up to three orders of magnitude in the illuminated part of the cloud ($A_V \lesssim 4$) when including the grain surface reactions. The H_2CO abundance now even peaks in the PDR, while it peaked in the dense-core in the pure gas-phase model. The model predicts a H_2CO abundance peak in the PDR that is higher than the observed abundance averaged over the 30 m (~16″). This limited resolution prevents us from resolving the predicted abundance peak. Interferometric observations are needed to prove the existence of this peak in the PDR.

5. Discussion

H_2CO has been detected in a variety of different astrophysical environments, with a wide range of gas temperatures and densities. It has been detected in diffuse clouds with high abundances (~10^{-9}), observed in absorption against bright HII regions (e.g., Liszt & Lucas 1995; Liszt et al. 2006). It is not well understood how H_2CO can be formed and survive in such harsh environments, because gas-phase process cannot compete with the photo-dissociation and dust grain temperatures are too high for molecules to freeze on their surfaces. Roueff et al. (2006) detected absorption lines of H_2CO at 3.6 μm toward the high-mass protostar W33A, and estimated an H_2CO abundance of ~10^{-7} where the gas has a temperature of ~100 K. Recently, Bergman et al. (2011) found H_2CO abundances ~5×10^{-9} in the ρ Ophiuchi A cloud core. Abundances of H_2CO and other more complex molecules toward hot cores and protostars are high. In these regions the gas is dense and hot, so the dust grains also

have high temperatures (>100 K). Therefore, the ice mantles, formed in the cold pre-stellar phase, are completely evaporated. Once these molecules are in the gas-phase, they trigger an active chemistry in the hot gas, forming even more complex molecules (Charnley et al. 1992).

H_2CO has also been observed in other PDRs. Leurini et al. (2010) detected H_2CO in the Orion Bar PDR toward both the clump ($n_H \sim 10^6$ cm^{-3}) and the inter-clump ($n_H \sim 10^4$ cm^{-3}) gas components. They found higher H_2CO abundances ($\sim 10^{-9}$–10^{-7}) than the ones inferred in this work for the Horsehead ($\sim 10^{-10}$). Molecules trapped in the ice mantles can be thermally desorbed when the dust grains are warm enough. The dust temperature at which a significant amount of H_2CO evaporates can be estimated by equating the flux of desorbing molecules from the ices to the flux of adsorbing molecules from the gas (see Eq. (5) in Hollenbach et al. 2009). Taking an H_2CO desorption energy of 2050 K (Garrod & Herbst 2006), we obtain an evaporation temperature of ~41 K. In the Orion Bar the dust grains have temperatures of $T_{dust} > 55$–70 K, so molecules can be desorbed from the icy mantles both thermally and non-thermally. But in the Horsehead PDR dust grains are colder ($T_{dust} \sim 20$–30 K), therefore molecules can only be desorbed non-thermally. Hence, the main desorption mechanism in the PDR is photo-desorption. In this respect, the Horsehead PDR offers a cleaner environment to isolate the role of FUV photo-desorption of ice mantles. In the Horsehead dense-core dust grains are also cold (~20 K), but photo-desorption is not efficient because the dust is shielded from the external UV field. Cosmic rays can desorb molecules from the ice mantles, but this contribution is not significant because the desorption rates are too low compared to the H_2CO formation rates in the gas-phase. Both the measured H_2CO abundance and ortho-to-para ratio agree with the scenario in which H_2CO in the dense-core is formed in the gas phase with no significant contribution from grain surface chemistry.

We have shown that photo-desorption is an efficient mechanism to form gas-phase H_2CO in the Horsehead PDR. But, to understand the importance of grain surface chemistry over gas-phase chemistry in the formation of complex organic molecules, a similar analysis of other molecules, such as CH_3OH and CH_2CO, is needed. In particular, CH_3OH is one of final products in the CO hydrogenation pathway on grain surfaces. It can also form H_2CO when it is photo-dissociated. Therefore, their gas-phase abundance ratios will help us to constrain their dominant formation mechanism and the relative contributions of gas-phase and grain surface chemistry. Similar studies in different environments will also bring additional information about the relative efficiencies of the different desorption mechanisms.

6. Summary and conclusions

We have presented deep observations of H_2CO lines toward the Horsehead PDR and a shielded condensation less than 40″ away from the PDR edge. We complemented these observations with a p-H_2CO emission map. H_2CO emission is extended throughout the Horsehead with a relatively constant intensity and resembles the 1.2 mm dust continuum emission. H_2CO beam-averaged abundances are similar ($\simeq 2$–3×10^{-10}) in the PDR and dense-core positions. We infer an equilibrium H_2CO ortho-to-para ratio of ~3 in the dense-core, while in the PDR we find a non-equilibrium value of ~2.

For the first time we investigated the role of grain surface chemistry in our PDR models of the Horsehead. Pure gas-phase and grain surface chemistry models give similar results of the H_2CO abundance in the dense-core, both consistent with the observations. This way, the observed gas-phase H_2CO in the core is formed mainly trough gas-phase reactions, with no significant contribution from surface process. In contrast, photo-desorption of H_2CO ices from dust grains is needed to explain the observed H_2CO gas-phase abundance in the PDR, because gas-phase chemistry alone does not produce enough H_2CO. These different formation routes are consistent with the inferred H_2CO ortho-to-para ratios. Thus, photo-desorption is an efficient mechanism to produce complex organic molecules in the PDR. Because the chemistries of H_2CO and CH_3OH are closely linked, we will continue this investigation in a next paper by studying the chemistry of CH_3OH in detail.

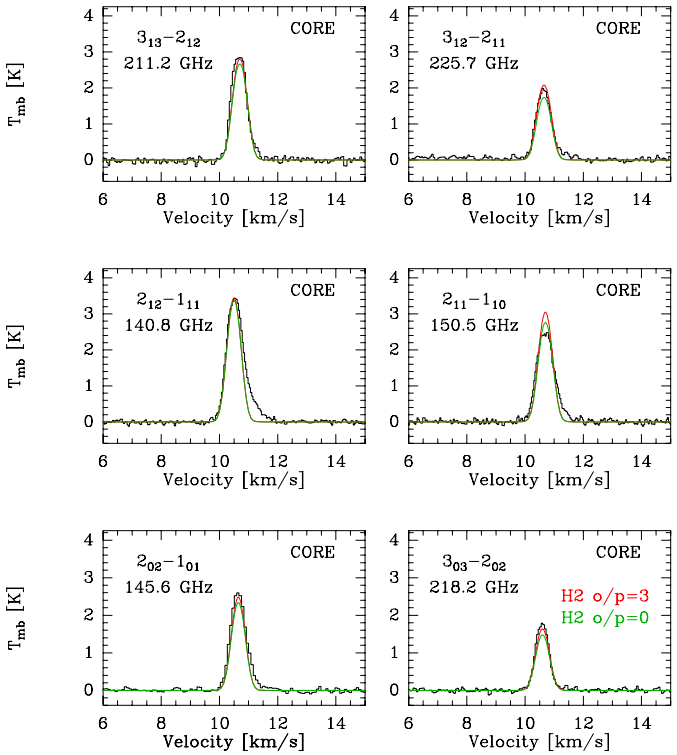

Fig. A.1. Radiative-transfer modeling of H_2CO lines for the core position in the Horsehead. The two top rows display the ortho lines and the bottom row displays the para lines. The best-match models are given in colors ($T_{kin} = 20$ K, $n(H_2) = 10^5$ cm^{-3}, N(o-H_2CO) = 9.6×10^{12} cm^{-2}, N(p-H_2CO) = 3.2×10^{12} cm^{-2}), taking a H_2 ortho-to-para ratio of 3 (red lines) and of 0 (green lines).

Acknowledgements. We thank A. Faure and N. Troscompt for sending us the p-H_2CO – o-H_2 and p-H_2CO – p-H_2 collisional rates prior to publication. We thank the referee for a careful reading of the manuscript and interesting comments. V.G. thanks support from the Chilean Government through the Becas Chile scholarship program. This work was also funded by grant ANR-09-BLAN-0231-01 from the French *Agence Nationale de la Recherche* as part of the SCHISM project. J.R.G. thanks the Spanish MICINN for funding support through grants AYA2009-07304 and CSD2009-00038. J.R.G. is supported by a Ramón y Cajal research contract from the Spanish MICINN and co-financed by the European Social Fund.

Appendix A: H_2 ortho-to-para ratio

We investigated the influence of the H_2 ortho-to-para ratio adopted in the excitation and radiative transfer models. In Fig. A.1 we show the best-match models for the H_2CO lines toward the core position in the Horsehead assuming two different values for the H_2 ortho-to-para ratio. We show models for an H_2

ortho-to-para ratio of 3 in red (high temperature limit), and we show models for the extreme case where the H_2 ortho-to-para ratio is 0 in green (low temperature limit). The difference between the models is less than 10%, which is within the observational uncertainties and therefore not significant.

References

Araya, E., Hofner, P., Goss, W. M., et al. 2007, ApJS, 170, 152
Bergman, P., Parise, B., Liseau, R., & Larsson, B. 2011, A&A, 527, A39
Bisschop, S. E., Jørgensen, J. K., van Dishoeck, E. F., & de Wachter, E. B. M. 2007, A&A, 465, 913
Bowler, B. P., Waller, W. H., Megeath, S. T., Patten, B. M., & Tamura, M. 2009, AJ, 137, 3685
Charnley, S. B., Tielens, A. G. G. M., & Millar, T. J. 1992, ApJ, 399, L71
Cuppen, H. M., van Dishoeck, E. F., Herbst, E., & Tielens, A. G. G. M. 2009, A&A, 508, 275
de Jong, T., Boland, W., & Dalgarno, A. 1980, A&A, 91, 68
Dickens, J. E., & Irvine, W. M. 1999, ApJ, 518, 733
Downes, D., Wilson, T. L., Bieging, J., & Wink, J. 1980, A&AS, 40, 379
Draine, B. T. 1978, ApJS, 36, 595
Garrod, R. T., & Herbst, E. 2006, A&A, 457, 927
Garrod, R. T., Wakelam, V., & Herbst, E. 2007, A&A, 467, 1103
Gerin, M., Goicoechea, J. R., Pety, J., & Hily-Blant, P. 2009, A&A, 494, 977
Goicoechea, J. R., Pety, J., Gerin, M., et al. 2006, A&A, 456, 565
Goicoechea, J. R., Compiègne, M., & Habart, E. 2009a, ApJ, 699, L165
Goicoechea, J. R., Pety, J., Gerin, M., Hily-Blant, P., & Le Bourlot, J. 2009b, A&A, 498, 771
Goldsmith, P. F., & Langer, W. D. 1999, ApJ, 517, 209
Green, S. 1991, ApJS, 76, 979
Habart, E., Abergel, A., Walmsley, C. M., Teyssier, D., & Pety, J. 2005, A&A, 437, 177
Habart, E., Abergel, A., Boulanger, F., et al. 2011, A&A, 527, A122
Hassel, G. E., Herbst, E., & Bergin, E. A. 2010, A&A, 515, A66
Hidaka, H., Watanabe, M., Kouchi, A., & Watanabe, N. 2009, ApJ, 702, 291
Hily-Blant, P., Teyssier, D., Philipp, S., & Güsten, R. 2005, A&A, 440, 909
Hollenbach, D., Kaufman, M. J., Bergin, E. A., & Melnick, G. J. 2009, ApJ, 690, 1497
Jørgensen, J. K., Schöier, F. L., & van Dishoeck, E. F. 2005, A&A, 437, 501
Kahane, C., Lucas, R., Frerking, M. A., Langer, W. D., & Encrenaz, P. 1984, A&A, 137, 211
Langer, W. D., & Penzias, A. A. 1990, ApJ, 357, 477
Le Bourlot, J., Pineau Des Forets, G., Roueff, E., & Flower, D. R. 1993, A&A, 267, 233
Le Petit, F., Nehmé, C., Le Bourlot, J., & Roueff, E. 2006, ApJS, 164, 506
Leurini, S., Parise, B., Schilke, P., Pety, J., & Rolffs, R. 2010, A&A, 511, A82
Linsky, J. L., Draine, B. T., Moos, H. W., et al. 2006, ApJ, 647, 1106
Liszt, H., & Lucas, R. 1995, A&A, 299, 847
Liszt, H. S., Lucas, R., & Pety, J. 2006, A&A, 448, 253
Mangum, J. G., & Wootten, A. 1993, ApJS, 89, 123
Mangum, J. G., Darling, J., Menten, K. M., & Henkel, C. 2008, ApJ, 673, 832
Maret, S., Ceccarelli, C., Caux, E., et al. 2004, A&A, 416, 577
Milam, S. N., Remijan, A. J., Womack, M., et al. 2006, ApJ, 649, 1169
Muñoz Caro, G. M., Jiménez-Escobar, A., Martín-Gago, J. Á., et al. 2010, A&A, 522, A108
Müller, H. S. P., Thorwirth, S., Roth, D. A., & Winnewisser, G. 2001, A&A, 370, L49
Öberg, K. I., Fuchs, G. W., Awad, Z., et al. 2007, ApJ, 662, L23
Öberg, K. I., Garrod, R. T., van Dishoeck, E. F., & Linnartz, H. 2009a, A&A, 504, 891
Öberg, K. I., Linnartz, H., Visser, R., & van Dishoeck, E. F. 2009b, ApJ, 693, 1209
Öberg, K. I., van Dishoeck, E. F., & Linnartz, H. 2009c, A&A, 496, 281
Parise, B., Leurini, S., Schilke, P., et al. 2009, A&A, 508, 737
Penzias, A. A., & Burrus, C. A. 1973, ARA&A, 11, 51
Pety, J. 2005, in SF2A-2005: Semaine de l'Astrophysique Francaise, ed. F. Casoli, T. Contini, J. M. Hameury, & L. Pagani, 721
Pety, J., Goicoechea, J. R., Hily-Blant, P., Gerin, M., & Teyssier, D. 2007, A&A, 464, L41
Roueff, E., Dartois, E., Geballe, T. R., & Gerin, M. 2006, A&A, 447, 963
Savage, C., Apponi, A. J., Ziurys, L. M., & Wyckoff, S. 2002, ApJ, 578, 211
Snyder, L. E., Buhl, D., Zuckerman, B., & Palmer, P. 1969, Phys. Rev. Lett., 22, 679
Snyder, L. E., Palmer, P., & de Pater, I. 1989, AJ, 97, 246
Stantcheva, T., Shematovich, V. I., & Herbst, E. 2002, A&A, 391, 1069
Tielens, A. G. G. M., & Whittet, D. C. B. 1997, in IAU Symp. 178, ed. E. F. van Dishoeck, 45
Troe, J. 2007, J. Phys. Chem. A, 111, 3868
Troscompt, N., Faure, A., Wiesenfeld, L., Ceccarelli, C., & Valiron, P. 2009, A&A, 493, 687
Tudorie, M., Cacciani, P., Cosléou, J., et al. 2006, A&A, 453, 755
van Dishoeck, E. F. 1988, in Rate Coefficients in Astrochemistry, Proceedings of a Conference held in UMIST, Manchester, United Kingdom, September 21–24, 1987. ed. T. J. Millar, & D. A. Williams (Dordrecht, Boston: Kluwer Academic Publishers), 49
Walsh, C., Millar, T. J., & Nomura, H. 2010, ApJ, 722, 1607
Woon, D. E. 2002, ApJ, 569, 541
Yin, H.-M., Rowling, S. J., Büll, A., & Kable, S. H. 2007, J. Chem. Phys., 127, 064302
Young, K. E., Lee, J., Evans, II, N. J., Goldsmith, P. F., & Doty, S. D. 2004, ApJ, 614, 252

Copyright: Rogelio Bernal Andreo (Deep Sky Colors)

Chapitre 6

Le projet SCHISM, financé par l'Agence Nationale de la Recherche

6.1 Résumé

L'astrochimie a connu un fort développement ces 20 dernières années. C'est maintenant un domaine scientifique reconnu, prêt à tirer parti des capacités sans précédent des nouveaux instruments de l'IRAM, puis d'ALMA et d'Herschel pour la spectroscopie et l'imagerie à haute résolution. Les instruments et les modes d'observations seront-ils suffisamment flexibles pour s'adapter à des besoins toujours plus variés ? Les observations s'adosseront-elles à des méthodes d'analyse puissantes et à des modèles exploitant l'évolution des connaissances des processus fondamentaux ? Le projet ANR SCHISM, que je coordonne depuis le 1er septembre 2009 pour une durée de 4 ans, explore plusieurs facettes de ces questions, dont le couplage de la chimie en phase gazeuse à celle à la surface des grains, et le couplage de la chimie avec la turbulence magnéto-hydrodynamique (MHD) (phénomènes de transport, structures dissipatives, chocs). Sa pertinence vient du lien fort entre développements numériques pointus et observations utilisant les instruments les plus performants du domaine : le satellite Herschel et les interféromètres millimétriques (Plateau de Bure et ALMA).

Alors que la chimie en phase gazeuse est de mieux en mieux comprise, la chimie en phase solide est encore balbutiante, malgré le rôle majeur de tels processus pour la formation de H_2 et d'autres espèces (par exemple H_2CO et CH_3OH). De plus, l'activité chimique est intimement couplée à la dynamique du gaz, et par conséquent à son évolution. La chimie affecte les mouvements du gaz via le rayonnement des molécules polaires qui constitue le principal agent de

refroidissement du gaz dans de nombreux milieux : ces molécules contrôlent l'équation d'état du gaz et donc sa dynamique. En retour, la dynamique du gaz affecte la chimie parce que les écoulements sont turbulents, supersoniques et plus ou moins couplés au champ magnétique. Combiner des codes chimiques sophistiqués avec des observations de raies moléculaires est à la fois une étape capitale pour exploiter pleinement la richesse des observations de raies moléculaires et un formidable défi du fait de la non-linéarité 1) de la dynamique des fluides et 2) des réactions chimiques. Le but du projet est, d'une part, de rassembler des théoriciens et des observateurs[1] pour développer et tester les modèles numériques décrivant l'interaction des gaz moléculaires avec le rayonnement (le code PDR de Meudon), et avec une perturbation supersonique (code de choc MHD), et, d'autre part, d'apporter les jeux de données appropriés pour tester les codes et une nouvelle méthode améliorant l'efficacité des observations en interférométrie pour les sources étendues.

[1]Le projet SCHISM comporte trois partenaires : 1) l'IRAM (PI : J. Pety, participants : S. Bardeau, P. Gratier, V. Guzman, E. Reynier, N. Rodriguez-Fernandez), 2) le LERMA/LRA (PI : M. Gerin, participants : S. Cabrit, M. De Luca, E. Falgarone, B. Goddard, A. Gusdorf, P. Lesaffre), 3) le LUTH/ISM (PI : F. Le Petit, participants : J. Le Bourlot, S. Myake, E. Roueff) et des participants extérieurs (J.R. Goicoechea, P. Hily-Blant, H. Liszt, R. Lucas, G. Pineau des Forêts).

Acronyme	**SCHISM**		
Titre du projet en français	Structure et chimie du milieu interstellaire		
Titre du projet en anglais	**Structure and Chemistry of the Inter-Stellar Medium**		
CSD principale	☐ 1 ☐ 2 ☐ 3 ☐ 4 ☐ 5 **X** 6 ☐ 7 ☐ 8 ☐ 9		
CSD secondaire ***(si interdisciplinarité)***	☐ 1 ☐ 2 ☐ 3 ☐ 4 ☐ 5 ☐ 6 ☐ 7 ☐ 8 ☐ 9		
Aide totale demandée	488 450 €	**Durée du projet**	48 mois

SOMMAIRE

1. CONTEXTE ET POSITIONNEMENT DU PROJET / CONTEXT AND POSITIONNING OF THE PROPOSAL 3
2. DESCRIPTION SCIENTIFIQUE ET TECHNIQUE / SCIENTIFIC AND TECHNICAL DESCRIPTION 5
2.1. État de l'art / Background, state of the art 5
2.2. Objectifs et caractère ambitieux/novateur du projet / Rationale highlighting the originality and novelty of the proposal 7
2.2.1 Goal 1: Delivering numerical codes which couple (1) gas phase and grain surface chemistry and/or (2) chemistry and dynamics 7
2.2.2 Goal 2: Delivering two legacy surveys: (1) the first observations of some simple hydrides and (2) the chemical inventory of a template source for numerical models 8
2.2.3 Goal 3: Wide-field, high resolution imaging of the diffuse gas and several interstellar pillars to unveil how the interstellar medium structures itself 8
2.2.4 Goal relations 9
3. PROGRAMME SCIENTIFIQUE ET TECHNIQUE, ORGANISATION DU PROJET / SCIENTIFIC AND TECHNICAL PROGRAMME, PROJECT MANAGEMENT 10
3.1. Programme scientifique et structuration du projet / scientific programme, specific aims of the proposal 10
3.1.1 Tool development (task 1 to 5) 10
3.1.2 Data sets (task 6 to 9) 11
3.2. Coordination du projet / project management 12
3.3. Description des travaux par tâche / detailed description of the work organised by tasks 14
3.3.1 Task 1: Interferometric on-the-fly observing mode (in charge: IRAM, N. Rodriguez-Fernandez) 14
3.3.2 Task 2: Coupling the gas-phase and grain-surface chemistry in the Meudon PDR code (in charge: LUTH-ISM, E. Roueff) 15
3.3.3 Task 3: Including turbulent mixing formalism in the Meudon PDR code (in charge: LUTH-ISM, F. Le Petit, in collaboration with LERMA-LRA) 16
3.3.4 Task 4: Time-dependent MHD shocks and chemistry (in charge: LERMA-LRA, P. Lesaffre, in collaboration with G. Pineau des Forêts) 17

3.3.5 Task 5: Dissipative structures of turbulence and chemistry (in charge: LERMA-LRA, E. Falgarone & B. Godard in collaboration with P.Hily-Blant & G. Pineau des Forêts) 18
3.3.6 Task 6: Imaging experiment 1: Connecting the chemistry of diffuse gas with its dynamics (in charge: IRAM, H. Liszt in collaboration with R. Lucas) 19
3.3.7 Task 7: Legacy survey 1: An extensive study of simple hydrides as part of the Herschel guaranteed time key project PRISMAS (in charge, LRA, M. Gerin, in collaboration with LUTH-ISM) 20
3.3.8 Task 8: Legacy survey 2: Establishing the Horsehead mane PDR as an observational benchmark for chemical models (in charge: IRAM, J. Pety, in collaboration with LERMA-LRA, LUTH-ISM, J. R. Goicoechea and D. Teyssier) 22
3.3.9 Task 9: Imaging experiment 2: Is the Horsehead nebula a typical pillar? (in charge: IRAM, J. Pety, in collaboration with LERMA-LRA and P.Hily-Blant) 24
3.4. Calendrier des tâches, livrables et jalons / planning of tasks, deliverables and milestones 25
4. STRATEGIE DE VALORISATION DES RESULTATS ET MODE DE PROTECTION ET D'EXPLOITATION DES RESULTATS / DATA MANAGEMENT, DATA SHARING, INTELLECTUAL PROPERTY AND RESULTS EXPLOITATION 27
5. ORGANISATION DU PARTENARIAT / CONSORTIUM ORGANISATION AND DESCRIPTION 28
5.1. Description, adéquation et complémentarité des partenaires / relevance and complementarity of the partners within the consortium 28
5.2. Qualification du coordinateur du projet / qualification of the project coordinator 29
5.3. Qualification, rôle et implication des participants / contribution and qualification of each project particpant 29
6. JUSTIFICATION SCIENTIFIQUE DES MOYENS DEMANDES / SCIENTIFIC JUSTIFICATION OF REQUESTED BUDGET 30
6.1. partner 1 : IRAM 30
6.2. partner 2 : LERMA-LRA 31
6.3. partner 3: LUTH-ISM 32
7. ANNEXES 33
7.1. Références bibliographiques / references 33
7.2. Biographies / CV, Resume 35
7.3. Implication des personnes dans d'autres contrats / involvement of project participants to other grants, contracts, etc 40

1. CONTEXTE ET POSITIONNEMENT DU PROJET / CONTEXT AND POSITIONNING OF THE PROPOSAL

The field of observational astrochemistry has developed since the early 70s, following the progresses of radioastronomy detectors and antennae. It is now maturing, outgrowing the Galactic interstellar medium into new environments from high-z galaxies to proto-planetary disks. And it will in the near future take advantage of the unprecedented spatial and spectroscopic capabilities of ALMA, Herschel and other instruments. Will instrumentation and observing modes be flexible enough to adapt to evolving scientific requirements? Will observations be matched on the theoretical side by physical insight into fundamental processes and supported by modelling tools and analysis methods appropriate to the diversity of astrophysical environments ? The SCHISM project addresses several facets of this vast issue, related to the coupling of gas-phase and grain-surface chemistry and to the coupling of chemistry with magneto-hydrodynamical turbulence (shocks, turbulent mixing and transport, dissipative structures). One of its strengths is that it offers a close connexion of state-of-the-art numerical developments with cutting-edge observations with the Herschel satellite and current and future world-leader (sub)-millimeter interferometers (IRAM-PdBI, ALMA).

Molecules are by far the most versatile tracers of diffuse matter in the universe, from high-z galaxies to star forming regions and proto-planetary disks, because their internal and external degrees of freedom bear the full signature of the physical conditions in their environment. Indeed, molecules are affected by many processes: Gas phase chemical reactions with other species, photo-ionisation and photo-dissociation by UV photons, condensation on grains, solid state reactions in cold media and thermal or photo-desorption, etc. Moreover, this chemical activity is tightly coupled to the gas dynamics. Chemistry affects the gas motions because 1) the ionisation state controls the coupling to the magnetic field, and 2) the line radiation from polar molecules is the main cooling agent over a broad range of astrophysical environments, controlling the equation of state and therefore affecting the dynamics. Conversely, the gas dynamics affects the chemistry because the various perturbations lead to steep and time-variable density and velocity gradients, which change the rates of molecule formation and destruction by order of magnitudes. While the fields of astrochemistry and gas dynamics have initially evolved on parallel tracks, it is now recognized that combining existing sophisticated chemical codes with gas dynamics is a vital step to fully benefit from the versatility of molecular line data. It is also a tremendous challenge given the non-linearity of the fluid dynamics and the stiffness of the chemical reactions.

Moreover, gas phase chemistry alone cannot account for the formation of many important molecules. For instance, the most abundant molecule in the Universe, H2, is formed on the surface of dust grains. There is also significant evidence that more complex molecules observed in the interstellar medium, such as CH3OH, are formed on dust grain surface. Indeed, while gas phase reactions in cold clouds mainly produce unsaturated molecules [1], surface processes are dominated by hydrogen-addition reactions, which result in saturated molecules, such as the main ice constituents (H2O, NH3, CH3OH, C4H, …) [2,3,4]. Hence, the main formation path for water, methanol and other species, is thought to be solid phase reaction on grains, followed by thermal and/or non-thermal desorption processes. It is thus essential to include a theoretical description of these processes in the codes. As the simple rate equation method, describing the gas phase reactions, cannot be used for grain surface reactions, the main challenge is to find a theoretical description, which is both accurate and computationally efficient. Up to now, most descriptions are based on stochastic methods which can be extremely computationally intensive [5,6], and therefore of limited usefulness. Approximate methods have therefore been developed but their accuracy is not warranted [7].

Observations of the same astrophysical environments with many different tracers are needed to characterize them. For instance, the determination of density, ionisation rate, electron density and magnetic field require deep spectroscopic observations of key molecules (e.g. H13CO+, HOC+,

DCO+, CN, etc…) [8,9]. The physical parameters are inferred from a detailed comparison of measured molecular abundances with predictions from sophisticated radiative transfer and chemical models. Because many different processes act conjointly to control these parameters, this analysis method must be benchmarked on extensive sets of very well defined observations. Although already sophisticated, state of the art models still fail to reproduce some observed properties of the interstellar medium (ISM). Key features are obviously lacking in today chemical models.

Major new modelling and observational steps forward are thus needed to start solving the numerous issues raised by observations. From the modelling side, the coupling of the chemistry with the gas dynamics on one hand, and the coupling of the gas phase and solid state chemistry on the other, are two missing points, which clearly inhibit our ability to understand the evolution of the interstellar medium from the most diffuse phases to the dense cores and formation of stars and planets. From the observational side, it became increasingly clear in recent years that the understanding of the structure of the interstellar medium requires mapping of large fields-of-view at high angular resolution. Indeed, the interstellar medium has many interfaces (photo-dissociation regions, shocks,…), which are both very thin and elongated. In addition, because of the lack of a well-constrained 3D geometry, the characterization of the properties of the interstellar medium must go through statistical methods, which requires maps with a large number of independent pixels [10]. Both steps (modelling and observations) are cutting-edge challenges.

In this project, we propose to join observational and numerical efforts to make a significant step forward in the understanding of the interstellar structure and chemistry. We propose

1. To add important new modelling capabilities to existing numerical codes in order to couple 1) chemistry and dynamics; and 2) gas phase and grain surface chemistry;
2. To set up legacy surveys to establish observational benchmarks for chemical models, both by focusing on the key family of hydrides and by extensively probing a template source, i.e. the Horsehead mane photo dissociation region (PDR);
3. To set up observing programs which will give a broader perspective to the conclusions derived from the surveys and which will help to understand how the interstellar medium structures itself in diffuse and dense phases (mapping of the diffuse medium and mapping of the unstable interfaces between hot, dilute, ionised gas and cold, dense, neutral gas, e.g. the Pillars of Creation in the Eagle Nebula).

The expected outcome of the SCHISM ANR is a validation of our understanding of the physical and chemical processes ruling the evolution of diffuse and dense matter. The choice of our scientific goal, i.e. to probe the diffuse and dense interstellar matter, has been guided by the possibility to make high sensitivity and high resolution observations of this medium. However, the deep understanding which results from these observations are very valuable for the understanding of other environments where the same processes are involved. In particular, we propose here to benchmark and deliver to the worldwide community observing and modelling tools which are required to understand e.g. the formation of galaxies both in the local and distant universe, the formation of protostars and protoplanetary disks, the building of the chemical complexity in the interstellar medium.

With the advent of new and powerful instruments such as Herschel and ALMA, the time is ripe for major advances in theory, matching the discovery potential of these facilities. The ESA-NASA Herschel satellite, whose launch is foreseen in April 2009, will completely open the domain of far-infrared and submillimeter wavelengths to astronomical observations. A large fraction of the time is already distributed between a collection of ~ 20 (guaranteed and open) key programs, one of which is lead by a member of the SCHISM team. The remaining telescope time will be allocated later in the satellite lifetime. It is foreseen that the teams able to scientifically validate and publish the Herschel key program observations will be the most efficient at getting additional Herschel time. The commissioning and science verification of the ALMA interferometer will start in 2009 in Chile. The early science phase should start in 2011 and the delivery of the instrument should happen in 2013. There will ***not*** be any garanteed time and the competition for observing time will be worldwide. One of the goals of the SCHISM ANR is to prepare, and test, in a timely manner, the theoretical tools

needed 1) to analyse and understand the Herschel observations and 2) to prepare and propose competitive ALMA projects.

References

[1] Herbst, E., J. Phys. Chem., 2005, A 109, 4017.
[2] Hiraoka, K, Miyagoshi, T. Takayama, T, et al., 1998, ApJ, 498, 710.
[3] Hidaka, H., Watanabe, N, Shiraki, T., et al., 2004, ApJ, 614, 1124.
[4] Hidaka, H., Miyauchi, N., Kouchi, A., Watanabe, N., 2008, Chem. Phys. Lett, 456, 36.
[5] Biham, O., Furman, I., Pirronello, V., Vidali, G., 2001, ApJ, 553, 595.
[6] Stantcheva, T., Herbst, E., 2003, MNRAS, 340, 983.
[7] Vasyunin, A. I, Semenov, D. A., 2008, astro-ph 0810.1591.
[8] Maret, S., Bergin, E., 2007, ApJ, 664, 956.
[9] Falgarone, E., Troland, T. H., Crutcher, R. M. et Paubert, G., 2008, A&A, 481, 367
[10] Hily-Blant, P., Falgarone, E., Pety, J., 2008, A&A, 474, 923.

2. DESCRIPTION SCIENTIFIQUE ET TECHNIQUE / SCIENTIFIC AND TECHNICAL DESCRIPTION

2.1. ÉTAT DE L'ART / BACKGROUND, STATE OF THE ART

Interstellar matter is distributed in different states (gas, solid) and different phases (hot and ionized, warm, neutral and diffuse, cold, molecular and dense) [1] in different environments (e.g. dark or illuminated, turbulent or quiet). The matter cycles between different states, phases and environments with direct consequences on the physical evolution of astrophysical objects. Indeed, as the matter evolves chemically it changes both its thermodynamic state (through a change of the heating and cooling agents) and its coupling to the magnetic field (through ionization and neutralization) and the velocity field (through the cycle between gas and solid phase). A clear understanding of the chemistry is all the more important because recent progresses in radioastronomy (more sensitive receivers, multi-beam arrays, larger instantaneous receiver bandwidths, higher angular resolution through mm-interferometry) have enabled the observation of chemical tracers in new and extreme environments like proto-planetary disks [2,3] and high-redshift galaxies [4].

As an example of the importance of chemistry to the evolution of astronomical bodies, consider that star formation is known to occur exclusively in the shielded interiors of molecular cloud cores when gravity wrests control from supporting thermal, magnetic and turbulent pressures and collapse ensues [5]. However, despite much effort in the last 20 years, the initiation of this process is among the least understood steps even though it is key to understand some fundamental aspects of star formation, such as the initial mass function, the star formation efficiency and binary fraction, as well as their dependence on the stellar mass. H_2 being invisible in this cold environment, much of our insight in the structure of starless cloud cores results from observations of the millimeter thermal dust emission. However, such observations yield only a partial picture of the cloud structure since coagulation of dust is a key process at the high densities of inner starless cores and this will change the grain opacity coefficient and effectively "hide" much of the mass of the dust from view. Moreover, dust studies do not provide direct insight into the dynamics of these cores. Likewise, many molecular observations are affected by the freeze-out of species onto ice mantles at the low temperature of cloud cores [6]. A few species (nitrogen-bearing and their deuterated counterparts) are expected to escape this behaviour. They can shed light on the initiation of star formation if their relationship to the bulk of the matter (*i.e.* their chemistry) is well-enough understood. This example illustrates the need to identify molecular tracers of the physical properties, small-scale structure, and evolutionary stages of astrophysical environments. For this purpose, it is essential that the chemistry be well understood and the rate of the most relevant processes accurately known.

However, this pre-requisite is most often not fulfilled. While the basic physical and chemical processes in both dense and diffuse gas are **qualitatively** known, many quantitative aspects still elude our grasp. For instance, although ISM chemistry has been studied in diffuse gas for 70 years, the range of CH^+ column densities measured in the visible since the 1940's is inconsistent with steady-state low-temperature chemistry because the main CH^+ formation route is the endothermic reaction between C^+ and H_2, which is ineffective at diffuse cloud temperatures. Although CH^+ is the most prominent case, marked discrepancies between state of the art steady-state models and observations exist for many other molecules, especially reactive ions (HCO^+, CO^+, SO^+). The existence of such species therefore requires specific heating mechanisms, driven for instance by the dissipation of supersonic turbulence. Conversely, a recent issue is the origin of complex organic molecules in the gas phase [7,8]. Since the discovery of ice mantles around dust grains, it has been proposed that complex organics are formed in the solid phase. Simple freeze-out from the gas phase to ice mantles where hydrogenation reactions are extremely efficient leads to the formation of water, ammonia and methane ices among other species. Various energetic events (e.g. absorption of UV photons or cosmic rays) can also alter the grain mantle composition, trigger chemical reactions in the solid phase, and allow a fraction of the ices to be released into the gas phase for further processing [8,9]. While the pattern is sketched, the **quantitative** details still must be worked out.

There is good evidence that chemistry and dynamics are coupled in all molecular environments: 1) Thermal energy is too low to overcome the activation barriers in the formation of some molecules, implying the need for compression, dissipative heating and/or ion-neutral drifts as additional energy sources enhancing the reaction rates [10,11]; 2) Chemistry determines the gas heating/cooling function [12]; 3) Estimated ages of astrophysical objects (e.g. through outflows in the case of young stellar objects) are often short compared to the time scales needed to reach steady-state, which emphasizes the importance of having time-dependent modelling codes. Last, understanding the coupling of turbulence and chemistry is relevant because the interstellar medium is turbulent [13]. As the mean free path of atoms and molecules is barely smaller than the viscous dissipation length of turbulence, the large scales and their energetic content are directly and naturally coupled to those of microphysics (elastic collisions, chemical reactions) by the turbulent cascade. These characteristics generate specific challenges, which include the need for non-equilibrium chemistry when the chemical and thermal inertia of the medium are large compared to the shortest timescales of the gas dynamics.

The failures of state of the art theoretical understanding appeared either 1) when models were critically benchmarked with sensitive observations of sources with well defined properties (geometry, illumination condition, kinematics [14 to 20], or 2) with extensive and sensitive surveys of the gas properties [21 to 25]. Such comprehensive observation programs are the only ones able to identify the discrepancies with the theory, but also to discover new features which lead to the recognition of the missing physical and chemical processes. For instance, although many generic aspects of the interstellar medium were first noticed in diffuse clouds (for instance, chemistry, ionisation balance and the multi-phase ISM), it is still difficult to say exactly what diffuse clouds are, beyond the common definition that they should have extinctions (A_v) of 1 mag or less. Nevertheless, recent studies of millimeter-wave absorption with interferometers have shown that the molecular content and chemical complexity of such clouds are much greater than had been believed [21 to 24] and that their hierarchical structure and chemical diversity are two consequences of the strong magneto-hydrodynamical (MHD) turbulence pervading the diffuse ISM [25,26].

References

[1] Wolfire, M. G., Hollenbach, D., McKee, C. F., Tielens, A. G. G., Bakes, E. L. O .1995, ApJ, 443, 152.
[2] Dutrey, A., Guilloteau, S., Ho, P., 2007, Protostars and Planets V.
[3] Aikawa, Y., Nomura, H., 2008, Physica scripta, 130, Proceeding of the Nobel symposium 135.
[4] Solomon, P. M & Vanden Bout, P.A, 2005, ARAA, 43, 677.
[5] Bergin, E., Tafalla, M., 2007, ARAA, 45, 339.
[6] Brown, Paul D., Charnley, S. B 1990, MNRAS, 244, .432.
[7] Garrod, R. T. & Herbst, E 2006, A&A, 457, 927.

[8] Garrod, R. T., et al., 2008, ApJ, 682, 283.
[9] Oberg, K. et al., 2007, ApJ, 662, L23.
[10] Joulain, K., Falgarone, E., Pineau Des Forêts, G., Flower, D. 1998A&A, 340, 241
[11] Godard, B, Falgarone, E., et al., 2008, A&A, in press.
[12] Neufeld, D. A., Lepp, S., Melnick, G.J. 1995 ApJS, 100, 132
[13] Scalo & Elmegreen, 2004, ARAA, 42, 275
[14] Abergel, A., et al. 2003, *A&A*, **410,** 577
[15] Compiègne, M. et al. 2007, *A&A*, **471,** 205
[16] Goicoechea, J.R., et al. 2006, *A&A*, **456,** 565
[17] Gerin, M., et al. 2008, *A&A,* in press.
[18] Habart, E., et al. 2005, *A&A*, **437,** 177
[19] Pety, J., et al. 2005, *A&A*, **435,** 885
[20] Pety, J., et al. 2007, *A&A*, **464,** L41
[21] Liszt & Lucas, 1998, A&A, 339, 561.
[22] 1996, A&A, 307, 237.
[23] 2002, A&A, 384. 1054.
[24] 2000, A&A, 355, 333L.
[25] Pety, Liszt & Lucas, 2008, A&A, 489, 219.
[26] Hily-Blant, P., Falgarone, E., Pety, J., 2008, A&A, 481, 367.

2.2. OBJECTIFS ET CARACTÈRE AMBITIEUX/NOVATEUR DU PROJET / RATIONALE HIGHLIGHTING THE ORIGINALITY AND NOVELTY OF THE PROPOSAL

2.2.1 GOAL 1: DELIVERING NUMERICAL CODES WHICH COUPLE (1) GAS PHASE AND GRAIN SURFACE CHEMISTRY AND/OR (2) CHEMISTRY AND DYNAMICS

Many current astrochemical codes extensively solve the gas-phase chemical equations. However, the introduction of the grain surface chemistry in an efficient way is a real challenge. We propose to include the surface chemistry into the Meudon PDR code using the recent and efficient formalism known as moment equations, developed by Prof. Ofer Biham from the Hebraic University of Jerusalem [1] (see task 2).

Due to the complexity of the problem, the codes coupling chemistry and dynamics are often slow. We propose two innovative approaches, which for instance will enable to reach the solution of a given numerical problem in less than one hour on a single workstation. In the first approach, we will add to the Meudon PDR code the steady-state solution of turbulent mixing, modelled as a turbulent diffusion coefficient parametrised by a single correlation length (see task 3). Some preliminary work on advection, which can mathematically be viewed as a simple aspect of diffusion, is underway. In the second approach, we will provide numerical tools to implement an already-published algorithm [2] and model a one-dimensional MHD shock for arbitrary shock parameters and shock age, using the chemical network relevant to observations (see task 4).

A major gain of those new codes is the consistency of the description: 1) The chemistry controls the gas cooling/heating function which in turn changes the thermodynamics and thus the dynamics of the gas; 2) A dynamical code is able to predict the velocities at which the molecules are produced and thus to consistently reproduce the spectroscopic measurements which couple velocities and abundances.

References

[1] Lipshtat & Biham 2003, A&A, 400, 585
[2] Lesaffre et al. 2004, A&A, 427, 157

2.2.2 GOAL 2: DELIVERING TWO LEGACY SURVEYS: (1) THE FIRST OBSERVATIONS OF SOME SIMPLE HYDRIDES AND (2) THE CHEMICAL INVENTORY OF A TEMPLATE SOURCE FOR NUMERICAL MODELS

(1) Task 7: Hydrides play a central role in interstellar chemistry, as significant reservoirs of heavy elements. Hydrides are at the root of the reaction chains theorized to form gas phase molecules -- and hence are the most sensitive tests of these theories. Observations of interstellar hydrides are therefore critical in advancing our understanding of astrochemistry. Unfortunately, the large opacity of Earth's atmosphere at far infrared and submillimeter wavelengths has severely limited the ability of ground-based observatories to probe hydrides containing just a single heavy element atom. Thus the properties of hydrides, with ground state rotational transitions at submillimeter wavelengths, are less well known than those of non-hydrides -- with larger reduced masses -- that radiate in the millimeter region. Our team is heavily engaged in a comprehensive spectroscopic survey of simple hydrides in the interstellar medium which will be carried out with the submillimeter HIFI instrument of the Herschel satellite, as part of the accepted PRISMAS (PRobing InterStellar Molecules with Absorption line Studies, PI: M.Gerin) project. As part of a guaranteed time project, the reduced observations need to be quickly delivered to the community (less than 12 months after data acquisition). Due to the observing strategy (observation in absorption of intervening diffuse gas against strong continuum sources), we will be able to deliver precise column densities of a key family of species not yet measured.

(2) Task 8: Benchmarks of numerical models describing the chemistry of a molecular cloud have been performed to compare their predictions and to ensure that all models agree not only qualitatively but also quantitatively on at least simple, probably unrealistic, cases (see http://www.ph1.uni-koeln.de/pdr-comparison/intro1.htm [1]). A direct outcome of this work was an accurate description of the different assumptions used in these complex codes to describe the physical and chemical processes. However, considering the intrinsic complexity of building reliable chemical networks and models, there is an obvious need for well-defined observations that can serve as basic references. Although a handful of interstellar sources have been used to validate the output from chemical models (e.g. the Orion bar PDR), the data are highly heterogeneous in terms of position, field of view, sensitivity, etc. Photo Dissociation Regions are particularly well suited to serve as references because they make the link between diffuse and dark clouds, thus enabling to probe a large variety of physical and chemical processes. In this context the PDR of the Horsehead mane is a particularly interesting case because 1) the transition from the diffuse, hot and ionised gas to the dense, cold and shielded gas is sharp, 2) the PDR geometry is simple (almost 1D, viewed edge-on) and 3) the source is close to the Sun (~ 400 pc) [2]. We propose to deliver a database as complete as possible of the different chemical tracers of this source.

References

[1] Röllig et al. 2007, A&A, 467, 187.
[2] Pety, J., et al. 2007, Molecules in Space and Laboratory, 13.

2.2.3 GOAL 3: WIDE-FIELD, HIGH RESOLUTION IMAGING OF THE DIFFUSE GAS AND SEVERAL INTERSTELLAR PILLARS TO UNVEIL HOW THE INTERSTELLAR MEDIUM STRUCTURES ITSELF

In parallel to extensive studies of the chemical properties of diffuse clouds through observations of absorption features, we propose to investigate in emission the small scale structure of the gas in the same regions (see task 6). Maps both in ^{12}CO and ^{13}CO will allow us to test the idea that turbulence makes the locally optically thick ^{12}CO macroscopically optically-thin. We will be helped here by the current installation at IRAM of a new generation of receivers, whose design benefited from the research and development done for ALMA and Herschel, and which brings at least a factor 4 increase in time efficiency. We also propose to improve the knowledge about the so-called "pillars" (e.g. Pillars of Creation in the Eagle Nebula), which are the unstable interfaces between hot, ionized regions and dense, cold gas. They are still poorly–understood although these structures bridge the gap between the diffuse and the star-forming gas (see task 9). In particular, we are interested to know whether the Horsehead nebula (see Goal 2) is a particular or a typical case of a pillar.

These observations will benefit from the interferometric on-the-fly observing mode, which will enable the observations of large fields-of-view at high angular resolution with a much better image quality than the standard stop-and-go mosaicing techniques used today in millimeter interferometry. In the framework of the European FP6 "ALMA Enhancement" project, several members of our team are today engaged in developing the missing imaging and deconvolution algorithms needed to reduce the data coming from this observing mode. We propose here to use our observational projects to scientifically validate this effort and to make this observing mode a user-friendly mode at Plateau de Bure Interferometer (see task 1).

2.2.4 GOAL RELATIONS

Those goals are tightly coupled for several reasons: 1) The chemistry and structure (velocity, density, temperature) of the interstellar medium are coupled, implying the need for complex chemical codes to understand the structure of the interstellar medium; 2) Current observations clearly indicate that new physics and chemistry are needed in existing modelling codes; 3) The development of reliable modelling codes needs well-defined observations, which can serve as reference points. Hence, while trying to answer long-standing questions about the chemistry and structure of the interstellar medium, this project will provide the community, in a timely fashion, with important tools for the good use and analysis of the data coming from the two important projects in radio-astronomy of the next decade: Herschel and ALMA.

3. PROGRAMME SCIENTIFIQUE ET TECHNIQUE, ORGANISATION DU PROJET / SCIENTIFIC AND TECHNICAL PROGRAMME, PROJECT MANAGEMENT

3.1. PROGRAMME SCIENTIFIQUE ET STRUCTURATION DU PROJET / SCIENTIFIC PROGRAMME, SPECIFIC AIMS OF THE PROPOSAL

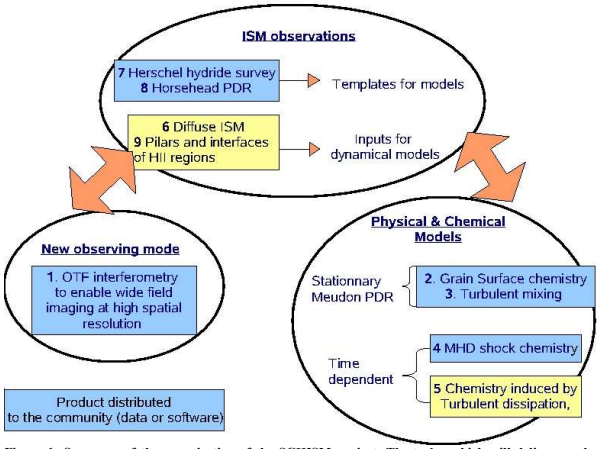

Figure 1: Summary of the organisation of the SCHISM project. The tasks, which will deliver products (data, software, ...) to the astronomical community, are indicated in blue (or grey if printed in B&W) boxes.

3.1.1 TOOL DEVELOPMENT (TASK 1 TO 5)

Our aim is here to produce powerful tools, which will be used to acquire and analyse the data sets described in the next section. We plan to greatly enhance existing code and/or development efforts. For the data acquisition side, the interferometric On-The-Fly (OTF) observing mode is a promising replacement for the standard stop-and-go mosaicing mode to produce wide-field imaging at high angular resolution in millimeter interferometry. On the data analysis side, we will produce tools to predict gas phase molecular abundances in the presence of a grain phase chemistry and/or within a given dynamical context which is conducive to form molecules. By direct comparison with the observations, we should then be able (1) to yield the physical parameters that best fit the observations, (2) to discriminate between the different possible chemical routes and/or dynamical pictures and (3) to predict abundances of species outside the spectral range/resolution of the current observations.

In order to be of use for the interpretation of observational data, these codes need to be fast (i.e., we would like to compute the observational outcome of a given model and set of parameters in less than an hour on a single workstation). However, the minimal chemical networks necessary to describe the cooling function of the gas and hence its dynamics is already quite rich in the case of the interstellar medium (32 species are commonly needed, to be compared with the 7 fundamental variables of a 1D bi-fluid MHD calculation). Furthermore, as more complex molecules are detected, the size of the networks required to obtain reliable estimates for their abundance increases (e.g. the Meudon PDR code routinely deals with 450 species and 4000 chemical reactions). In addition, chemistry on grain surfaces is not well-understood and involves complex modelling. We will hence restrict ourselves to 1D codes in well-defined geometries (slab, sphere or cylinder, for example). For the coupling to grain surface chemistry, we will implement the formalism of moment equations in the present code, allowing to take into account the finite number of adsorbing sites on small grains (Lipshtat & Biham, 2003). For the coupling with the gas dynamics, we aim at simplifying or using some aspects of existing codes in order to be able to incorporate the larger chemical networks needed for the comparison with observations while keeping most of the dynamical information. We will explore and compare the influence on the chemistry of three different dynamical aspects: 1) The turbulent mixing; 2) MHD shocks; and 3) Solenoidal dissipative structures (e.g. vortices) of turbulence. With these new codes, an important axis of research will be the study of the formation of some puzzling species such as CH^+, HCO^+, H_3^+ in diffuse gas and the H_2 formation and excitation in warm PDRs.

3.1.2 DATA SETS (TASK 6 TO 9)

Our aim here is to produce four different consistent datasets, all of them trying to shed a particular light on the chemistry and structure of the interstellar medium. Two of the datasets will be legacy surveys delivered to the community through databases by the end of this project: 1) A submillimter survey of a chemically key family, the hydrides; and 2) A chemical inventory of the Horsehead mane PDR to turn this source into an observational benchmark for chemical models. The two other datasets will be mapping experiments designed to explore the link between chemistry and dynamics: 1) Imaging in emission the environment of diffuse lines of sights whose chemical content has already been extensively constrained by absorption studies; 2) Imaging pillars (molecular edges of photoevaporation fronts of HII regions associated with OB stars) as a connection with our work on the Horsehead nebula. In each category (legacy survey and mapping experiments), one dataset will focus on the diffuse gas while the other will focus on the interface between HII regions and molecular clouds. These four experiments will thus allow us to explore how chemistry and dynamics structure both the diffuse and the dense gases of the interstellar medium.

The PRISMAS survey has been directly designed with a single instrument in mind, e.g. HIFI aboard the Herschel satellite: It will be observed as part of the Herschel guaranteed time key projects. The three other observational tasks are designed as multi-instrument observational campaigns of a few sources with the goal to produce consistent data sets, which can be used to benchmark and/or answer well-defined questions. This implies multi-year observational campaigns (with repeated answers to calls for proposals) because of observing constraints, e.g. needed winter time to get a transparent enough atmosphere at sub-millimeter wavelengths, a 1.5 year cycle for the VLA configurations, the need to wait for the reparation of broken instruments or the installation of new instruments,… The multiplicity of our observational tasks will ensure that we will be able to complete a large fraction of them in this project lifetime, despite possible observational hazards.

3.2. COORDINATION DU PROJET / PROJECT MANAGEMENT

The SCHISM project is built around 3 main groups, which share the same interest and questioning about the structure and chemistry of the interstellar medium. Their domain of expertise is complementary:

1. A group of astronomers and engineers, in charge of the data reduction softwares used for IRAM instruments (both single-dish and interferometer);
2. A group of astronomers at LERMA-LRA, specialists of observations and modelling of the interstellar medium.
3. A group of astronomers at LUTH-ISM, in charge of the development and maintenance of the Meudon PDR code;

Their expertise is internationally recognized as can be judged by their participation to other international grants (i.e. FP6 "ALMA enhancement", FP6 "Molecular Universe", ASTRONET, …). Where expertise was missing in those 3 groups (e.g. radiative transfer in the millimeter and infra-red domain), internationally recognized experts sharing the same scientific interests have been added to the SCHISM team. The SCHISM members already have a strong record of collaboration. We propose that the SCHISM ANR project formalize these collaborations into a single team gathering various expertises (conception and realisation of cutting-edge observations, data analysis and modelling). This expertise will serve to tackle in innovative ways the problem of the structuration of the interstellar medium. We will pursue this goal by developing observation/modelling tools and reference data sets, generic enough to serve well beyond the original aims of this project. Indeed, the deep understanding of more fashionable scientific topics rely on the availability of modelling tools. Conversely, the planned synergy between observations and models in the SCHISM project is expected to be extremely fruitful because the modelling tools cannot be tuned without high angular resolution, high signal-to-noise ratio reference data sets. This team will also have the critical size and expertise to be positioned in favourable terms in the extreme competition for time of the new generation of millimeter radioastronomy instruments, ALMA and Herschel.

The SCHISM project has been structured as a set of 9 tasks, all of which will shed a new light on the structure and chemistry of the interstellar medium. While many of the tasks will benefit from the completion of other tasks, we devised the tasks to be as independent as possible of the others. This maximizes the number of tasks fully completed at the end of the project. We propose to have a fruitful dialog between tasks. As the project will mature, the partially or fully completed task results will be used by the other tasks to improve their results. We propose the following organisation to ensure team collaboration:

- A wiki dedicated to the SCHISM ANR project, will be open. It will be used to store all relevant activities of the project with links towards the sites where the deliverables are posted.
- In the first 3 months after the project acceptance, an all-hands, two-days, face-to-face meeting will be organised to finalize a consortium agreement. After this first meeting, all-hands, two-days, face-to-face meetings will be organised every 9 months, a periodicity which is a compromise between the need to meet and the need to achieve new goals between two meetings. A last such meetings will be organised 3 months before the end of the contract. In total, 6 such all-hands meetings will be organised in the 4 years of the project.
- Informal meetings between members of different partners will be encouraged.
- Monthly teleconferences will be organised. Before-telecon agenda and after-telecon minutes will be posted to the wiki. In those teleconferences, the advancement of all tasks will be discussed with a particular emphasis on difficulties and ways to overcome them.
- Monthly minutes will be compiled in bi-annual reports.

The 3 partner coordinators (J. Pety for IRAM, M. Gerin for LERMA-LRA and F. Le Petit for LUTH-ISM) have permanent positions. They have been chosen because they are experienced managers and they know most of the technical aspects of the tasks for which the partner is responsible. Most of the daily life of the project (budget, post-doc recruitment, …) will be managed by the local coordinators.

J.Pety, the SCHISM coordinator, will in addition be in charge of the global management tasks described above (wiki, consortium agreement, all-hands meetings, monthly telecons, bi-annual reports) in collaboration with all the SCHISM team, in particular M. Gerin and F. Le Petit. Any potential conflict will be discussed and solved by the 3 partner coordinators. The load of the management task is estimated at 1 month/year per partner coordinator and 2 months/year for the project coordinator.

Finally, we propose to spread the requested temporary manpower equally between partners (2 years of post-doc per partner) and between modelling (3 years of post-doc) and observational tasks (3 years of post-doc). We stress that putting code and data sets on line and making them freely available implies a large amount of work. This work goes much beyond the usual algorithmic developments or the standard acquisition of data for direct publication. For both kinds of release, good documentation is needed to enable use by third parties. Code releases require in addition well-designed user interfaces but above all, stability and robustness, which can be achieved only through extensive tests. The release of large data sets, which may come from different instruments, implies several cycles of data reduction to ensure the consistency of the data, for instance a good relative calibration. This is often achieved by the creation of pipeline processing procedures. These request to install software suites dedicated to the calibration of different instruments and a large amount of bookkeeping of the intermediate states of the data. *All these efforts require sufficient manpower and will not be possible without the ANR support.* Note also that the multiplicity of our numerical and observational tasks will ensure 1) that we will have the possibility to compare observations and models in many different ways, thus improving both the model testing and the understanding of the observations and 2) that we will be able to complete a large fraction of them in this project lifetime, despite possible observational hazards. The manpower requested to ANR will work at most on 2 tasks per post-doc. Should one of the observational part be impossible (e.g. a problem with the Herschel satellite), we would use the manpower to expand others tasks.

Involved partners for task 0 (management): IRAM, LERMA-LRA, LUTH-ISM
Manpower: 16 months in total
- **J. Pety**: 8 months;
- M. Gerin: 4 months;
- F. Le Petit: 4 months.

Timescale: From month 1 to month 48.
Deliverables:
- After 3 months: 1st all-hands meeting to set up the consortium agreement;
- After 6 months: Project report #1;
- After 12 months: All-hands meeting and project report #2;
- After 18 months: Project report #3;
- After 21 months: All-hands meeting;
- After 24 months: Project report #4;
- After 30 months: All-hands meeting and project report #5;
- After 36 months: Project report #6;
- After 39 months: All-hands meeting;
- After 42 months: Project report #7;
- After 45 months: Last all-hands meeting;
- After 48 months: Final report.

3.3. DESCRIPTION DES TRAVAUX PAR TÂCHE / DETAILED DESCRIPTION OF THE WORK ORGANISED BY TASKS

3.3.1 TASK 1: INTERFEROMETRIC ON-THE-FLY OBSERVING MODE (IN CHARGE: IRAM, N. RODRIGUEZ-FERNANDEZ)

Most of the mapping observations proposed in this project require at the same time 1) a high angular resolution (at least 5"), which is achievable only by interferometry at millimeter wavelengths, and 2) the mapping of large enough fields of view, e.g. a few square arcminutes. Wide-field imaging in mm interferometry is currently done through the classical stop-and-go mosaicing technique, which limits both the efficiency and the observed field-of-view. The mosaicing technique used in interferometry may be compared to raster mapping for a single-dish. It is well-known that wide-field mapping made a spectacular improvement on single-dishes with the advent of the On-The-Fly (OTF) technique, where the data is acquired continuously as the antenna slews through the sky. In the same spirit, the interferometric OTF observing mode presents several advantages with respect to stop-and-go mosacing: 1) Overhead is reduced due to the absence of acceleration-deceleration during the mosaicing; 2) Larger portions of the sky may be observed under the same weather and instrumental conditions, which makes OTF data more homogeneous than mosacing data; 3) Theoretical considerations show that the OTF mode enables recovery of information at spatial frequencies not accessible in standard mosaicing [1]. Points 1 and 2 imply that larger fields of view can be imaged in OTF mode. Point 3 implies a better final image quality.

The OTF observing mode has never been used before with any millimeter interferometer due to inexistent imaging and deconvolution algorithms. In the framework of the European FP6 "ALMA Enhancement" project, IRAM has been granted two positions (one engineer and one astronomer from 2006 to 2010) to commission the OTF technique for the ALMA interferometer. Up to 2009, it has been foreseen that the OTF technique will be first developed at the IRAM Plateau de Bure interferometer (PdBI). The needed tools will then be implemented in the ALMA environment. However, transforming the PdBI test into a standard observing mode requires a large effort, beyond the initial algorithmic development. We propose to use our observing projects, which need wide-field images at high angular resolution, to serve as the scientific validation of the interferometric on-the-fly observing mode. We will release to the IRAM community all the additional tools (e.g. a user-friendly interface to the data reduction) developed during the validation. The experience from the advent of the On-The-Fly observing mode at the IRAM-30m showed that this additional effort (scientific validation and friendly user interface) is instrumental in getting the new observing mode widely used.

Involved partners: IRAM
Manpower: 20 months in total
- **N. Rodriguez-Fernandez**: 8 months
- E. Reynier: 12 months

Timescale: From month 1 to month 24.
Deliverables:
- After 12 months: Delivery of mapping and deconvolution algorithms usable on interferometric On-The-Fly data in the framework of the European FP6 "ALMA Enhancement" project.
- After 24 months: Delivery of a friendly user interface developed during the scientific validation phase.

References

[1] Ekers, R. & Rots, A., "Short Spacing Synthesis from a Primary Beam Scanned Interferometer » in Image Formation from Coherence Functions in Astronomy, Proceedings of IAU Colloq. 49, held in Groningen, Netherlands, August 10-12, 1978. Edited by C. van Schooeveld, C. D. Reidel Publishing Co. (Astrophysics and Space Science Library. Volume 76), 1979, p.61

3.3.2 TASK 2: COUPLING THE GAS-PHASE AND GRAIN-SURFACE CHEMISTRY IN THE MEUDON PDR CODE (IN CHARGE: LUTH-ISM, E. ROUEFF)

The Meudon PDR code [1,2,2',3,4] computes the stationary structure of a 1D slab of dust and gas illuminated from one or two sides by a given UV radiation field. Most physical and chemical processes are self-consistently solved at each point of the slab. They include: 1) The UV radiative transfer taking into account absorption both by the dust and by the discrete transitions of H and H_2; 2) Detailed treatment of the photoionization and photodissociation of many species, such as C, S H_2, HD, CO; 3) The thermal balance with the photo-electric effect on dust, cosmic ray ionization, exothermic chemical reactions as heating sources and infrared and millimeter emission of the most abundant atoms and molecules as cooling sources; 4) The chemical balance of the gas-phase chemical species; 5) The excitation state of a few important species (H_2, HD, CO, CS; HCO^+, H_2O, …). The code is then able to derive column densities and emissivities/intensities. Recent developments in the code are: 1) An exact UV radiative transfer treatment [3], which is particularly important for diffuse clouds and PDR structures; 2) The implementation of grain size distributions varying with position in the cloud [3]; 3) The development of an exact infra-red/submillimeter radiative transfer for the cooling lines, in particular H_2O in preparation for Herschel observations [4].

In this task, we propose to introduce the physical and chemical mechanisms occurring on grain surfaces in the Meudon PDR code. This will be the result of the conjunction of three different efforts: 1) Our current work with Prof. Ofer Biham from Jerusalem University to include the surface processes using the moment equations approach [10,11,12]; 2) The improvement of the grain heating by our PhD student M. Gonzalez-Garcia; and 3) the recent introduction of the variation with position of the grain size distribution [3]. Our first work will be to investigate the mechanisms leading to the formation of H_2 in PDRs. Indeed, while laboratory experiments have shown that H_2 forms on surfaces in a very narrow grain temperature window between 10-24 K [6], the measured grain temperature in PDR is typically between 20-30 K [7]. In addition, the excitation state of H_2 via its several infra-red transitions detected in PDRs remain unexplained [5]. Among the hypotheses to explain the H_2 observations, there are chemical possibilities like physisorbed/chemisorbed sites, rough structure of grains [8,9], dissociation of PAHs, and physical possibilities such as the mixing of hot gas with cooler gas at the edge of PDRs by mechanical processes (diffusion, turbulence, …). We will here test whether a consistent treatment of the grains physics for the surface reactions (using different kinds of grains: amorphous silicates or carbons), the extinction of the UV field and the thermal balance / grain temperature helps to reproduce the observations.

Once this first test of the moment equation formalism is validated, we will extend its use in the Meudon PDR code to other species for which the chemistry on grain surfaces is thought to be an important formation route, e.g. H_2CO, CH_3OH, … This will be done in particular to interpret the observations foreseen in this project (see e.g. Task 8 about the Horsehead mane PDR).

Involved partners: LUTH-ISM
Manpower: 40 months in total
- **E. Roueff**: 12 months
- J. Le Bourlot: 4 months
- ANR post-doc (during the 1st and 2nd year of the project): 24 months

Timescale: From month 1 to month 24
Deliverables:
- After 12 months: Inclusion of grain surface processes of formaldehyde and methanol in the PDR code using the formalism of the moment equation. First publication.
- After 24 months: Introduction of the first and second moments of the probabilities of presence of adsorbed species, enabling a versatile extension of the moment equation formalism. Application to deuteration processes on dust surfaces. Second publication.

References

[1] Le Bourlot J. Pineau des forêts G., Roueff E., Flower D., 1993, A&A 267, 233
[2] Le Petit F., Roueff E., Le Bourlot J., 2002, A&A 390, 369
[2'] Le Petit F., Nehme C., Le Bourlot J. Roueff E., 2006, ApJS 164, 506
[3] Goicoechea J. R. & Le Bourlot 2007, A&A, 467, 1
[4] Gonzalez-Garcia et al. 2008, A&A, 485, 127
[5] Habart et al. 2004, A&A, 414, 531.
[6] Perets H.B. et al. 2007, ApJ 661, L163.
[7] Habart et al. 2005, A&A 437, 177.
[8] Cuppen et al. 2005, MNRAS, 361, 565.
[9] Cuppen et al. 2006, MNRAS, 376, 1757.
[10] Lipshtat A. & Biham O., 2003, A&A 400, 585
[11] Barzel B., Biham O., 2007, AJ 658, L37
[12] Barzel B., Biham O., 2007, J. Chem. Phys. 127, 4703

3.3.3 TASK 3: INCLUDING TURBULENT MIXING FORMALISM IN THE MEUDON PDR CODE (IN CHARGE: LUTH-ISM, F. LE PETIT, IN COLLABORATION WITH LERMA-LRA)

Lesaffre, Gerin, Hennebelle [1] showed that turbulent mixing could bring together hot and tenuous gas with cold and H_2 rich gas, thus leading to the formation of a wealth of molecules. This work was aimed at modelling the typical situation in diffuse cloud interfaces where the natural turbulence of the interstellar medium could play the role of the mixing agent. The same approach can be used in PDR where strong shear flows or even ablation winds might drive mixing between the cold and shielded interiors and the warm photodissociated gas, which could impact the chemical and thermal contents of the gas. These authors used a version of the Lesaffre et al. code [2] which contained an enhanced thermal and chemical diffusivity in order to approximately describe the turbulent mixing likely to occur in such astrophysical media. The simulations were run until a stationary state was reached in order to lose memory of the rather *ad-hoc* initial conditions. That was hence a rather expensive (CPU wise) way to achieve a stationary state, and we propose a novel approach which will enable us to treat a much more complex chemical network. Finally, since the turbulent diffusion coefficient was parametrised by a single correlation length only, this approximation can be easily implemented in tools producing synthetic observations.

In this task, we plan to include enhanced diffusion in already existing stationary models of PDR, which contain all the needed micro-physics and chemistry. We will start from the Meudon PDR code because it already provides extensive facilities for data interpretation and it is widely tested and used as a public code. In contrast to stationary PDR models, the diffusion problem is a two-point boundary problem. Its solution is specified by two constraints (generally on the heat and particle fluxes) given at both sides of the computational domain. This will require to change the structure of the solver in the PDR code and to replace it either with a shooting/fitting at midpoint method (as a matter of fact, another two-point boundary solver has just recently been implemented in the Meudon code in its radiative transfer component: see [3]) or a relaxation scheme. Preliminary work on advection, a simpler case than diffusion, is underway. The resulting code should be able to find the equilibrium solution for a given diffusion parameter in less than an hour. We will then be able to provide a grid of models for a range of diffusion coefficients, which will serve as a basis for modelling observations. This will be provided to the community through the Meudon PDR VO-database developed at Paris Observatory thanks to external grants from Euro-VO and the Astronet project STARFORMAT.

Involved partners: LUTH-ISM and LERMA-LRA
Manpower: 28 months in total
- **F. Le Petit**: 8 months
- J. Le Bourlot: 4 months
- P. Lesaffre: 4 months
- ANR post-doc (during the 3rd year of the project): 12 months.

Timescale: From month 24 to month 36
Deliverables:

- After 30 months: 1st version of the PDR code with a new solver to include diffusion.
- After 36 months: Grid of models.

References

[1] Lesaffre, Gerin, Hennebelle, 2007, A&A, 469, 949.
[2] Lesaffre et al. 2004a, A&A, 427, 157.
[3] Goicoechea & Le Bourlot 2007, A&A, 467, 1.

3.3.4 TASK 4: TIME-DEPENDENT MHD SHOCKS AND CHEMISTRY (IN CHARGE: LERMA-LRA, P. LESAFFRE, IN COLLABORATION WITH G. PINEAU DES FORETS)

Ion-neutral drift in MHD shocks helps to form molecules [1]. Chièze et al. [2] and Lesaffre et al. [3] produced the first astrophysical codes able to strictly couple the dynamics of the gas to its chemistry. They showed that the time to reach a steady state is generally long compared to the estimated ages of structures: The interpretation of observational data hence requires time-dependent codes. These codes usually solve partial differential equations, which make them very slow even in 1D for the chemical minimal networks relevant for dynamics. However, Lesaffre et al. [4] have designed an algorithm based on steady-state models, which is able to produce a snapshot of a shock at an arbitrary age. This algorithm has never yet effectively been used. We plan to implement it in a numerical tool that will produce a model of shocks, in a few minutes, for arbitrary parameters and age, and using the chemical networks relevant to observations. The algorithm can work with any integrator of stationary shocks. It iterates on the velocity profiles until it finds the correct parameters and point of truncation of the stationary model for the given age entry. The resulting snapshot is then obtained as a juxtaposition of several stationary models.

The simplest comparison with the observations is obtained by comparison of the column densities yielded by integration over the profile. However, the codes coupling dynamics and chemistry can provide a much better comparison with the observations. Indeed, a simple radiative transfer method (e.g. LVG) can produce synthetic spectra with well-defined characteristics like their line widths, which are the simplest dynamical signature of their birth context. Lesaffre, Gerin, Hennebelle [5] used this technique to assess qualitative aspects of the relationship between line widths and column-densities (*e.g.* they showed that turbulent mixing would produce broader CH^+ lines than CH, as is observed). Finally we plan to design optimisation tools to fit the parameters of the shock to a given observation.

Involved partners: LERMA-LRA
Manpower: 12 months in total
- **P. Lesaffre**: 8 months
- S. Cabrit: 4 months
- External contributor: G. Pineau des Forêts

Timescale: From month 12 to month 45
Deliverables:
- After 27 months: Delivery of a quasi-stationary version of the MHD code from Lesaffre et al (2004a).
- After 33 months: LVG radiative transfer post-processing.
- After 45 months: Delivery of a code to determine the linear stability of the above shocks.

References

[1] Flower, Pineau des Forêts, Hartquist, 1985, MNRAS, 216, 775.
[2] Chièze et al. 1998, MNRAS, 295, 672.
[3] Lesaffre et al. 2004a, A&A, 427, 147.
[4] Lesaffre et al. 2004b, A&A, 427, 157.
[5] Lesaffre, Gerin, Hennebelle, 2007, A&A, 469, 949.

3.3.5 TASK 5: DISSIPATIVE STRUCTURES OF TURBULENCE AND CHEMISTRY (IN CHARGE: LERMA-LRA, E. FALGARONE & B. GODARD IN COLLABORATION WITH P.HILY-BLANT & G. PINEAU DES FORÊTS)

Intermittent dissipation of turbulence has been proposed to be the source of energy to enhance the production of molecular species in the diffuse interstellar medium, whose abundances cannot be explained in the framework of standard steady-state chemistry [1,2]). The quantitative modeling of the impact of the dissipation occuring in the solenoidal modes (e.g. vortices) of a turbulent flow on the chemistry observed along a given line-of-sight is done in four steps [3]:

1. The dynamics of a bi-fluid (neutrals + ions) incompressible vortex coupled to the ambient magnetic field is modeled as follows. An exact vortex solution of the Navier-Stokes equation is chosen for the neutral flow. This vortex has a rotational velocity set by the ambient turbulence (as found in numerical simulations) and it is fully described by a unique parameter, the rate of strain due to larger scale turbulence. The evolution of the ions and of the magnetic field immersed in the imposed neutral vortex is then computed up to a steady state solution, which *a posteriori* secures the hypothesis of weak feedback of the ions on the neutral dynamics.
2. The chemical composition of the gas in the vortex is then computed with a 1D time-dependent chemical code. This code follows, in the Lagrangian reference frame, the chemical and thermal evolution of a gas cell trapped in the vortex. This gas cell displays a warm chemistry because it is violently heated both by viscous dissipation and ion-neutral friction over a few hundred years as it spiral into the vortex. A database (1400 runs) of resulting chemical composition is computed as a function of the rate of strain and gas density.
3. At the end of the vortex lifetime, the relaxation phase of the gas cell is then followed in an Eulerian reference frame. During this phase, the gas cools down and continues its chemical evolution. However, it retains a memory of the molecular enrichment of phase (2) during several thousand years.
4. The chemical composition of an observed line-of-sight is finally built by taking into account the relative durations of the active and relaxing phases, the latter being different for each molecular species. The line crosses many identical active and relaxing regions both occupying a tiny fraction of the available volume mainly filled by the diffuse ambient medium. The number and lifetime of active vortices along the line of sight are set in order to reproduce the turbulent energy available in the interstellar cascade.

A systematic comparison of the results to the chemical content of galactic diffuse clouds deduced from observations is then performed. Those observations include absorption line measurements in the millimeter domain against extragalactic continuum sources [4] and water absorption lines in the submillimeter domain against bright star forming regions [5,6]. Godard et al. [3] find that the model reproduces the observed ranges of CH^+, OH, H_2O and HCO^+ column densities, the excitation diagram of the pure rotational levels of H_2 (J=3 to J=5) [7] and several observed correlations between molecules (CH^+ and excited H_2 (J=5), C_2H and CS, C_2H and C_3H_2, CN and HCN) in diffuse gas. Interestingly the range of rates of strain consistent with the observed abundances and column densities includes values derived from observations of the velocity field at small scales in molecular clouds [8,9].

The next step is to improve the description of the dynamics of the medium to take advantage of the kinematical information contained in the line profiles. To do this, we will statistically analyse the output of 3D MHD compressible turbulence numerical simulations (produced with the RAMSES Adaptative Mesh Refinement code) to compute the probability distribution function of the rate of strain in the flow. This distribution will then be coupled to the above database of chemical composition as a function of the rate of strain to provide synthetic molecular line spectra produced by a realistic turbulent line-of-sight. The spectra will then be directly compared with the observations (in particular, the PRISMAS data, see below).

Involved partners: LERMA-LRA
Manpower: 14 months in total

- **E. Falgarone**: 8 months;
- B. Godard: 6 months;
- External contributors: G. Pineau des Forêts & P. Hily-Blant.

Timescale: From month 1 to month 12
Deliverables:
- After 12 months: Implementation of the statistical analysis of the simulations of 3D MHD compressible turbulence to improve the description of the turbulent medium.

References

[1] K. Joulain, E. Falgarone, G. Pineau des Forêts, D. Flower, A&A, 340, 241 (1998).
[2] E. Falgarone, G. Pineau des Forêts, P. Hily-Blant, P. Schilke, A&A, 452, 511 (2006).
[3] B. Godard, E. Falgarone, G. Pineau des Forêts, P. Hily-Blant, A&A, in press (2008).
[4] H.S. Liszt, R. Lucas, A&A, 391, 693 (2002).
[5] D. Neufeld et al., ApJ, 580, 278 (2002).
[6] G. Olofsson et al., submitted to A&A.
[7] C. Gry, F. Boulanger, C. Nehmé, G. Pineau des Forêts, E. Habart, E. Falgarone, A&A, 391, 675 (2002).
[8] E. Falgarone, J. Pety, P. Hily-Blant, submitted to A&A.
[9] Hily-Blant, P. & Falgarone, E. In preparation.

3.3.6 TASK 6: IMAGING EXPERIMENT 1: CONNECTING THE CHEMISTRY OF DIFFUSE GAS WITH ITS DYNAMICS (IN CHARGE: IRAM, H. LISZT IN COLLABORATION WITH R. LUCAS)

By probing intervening gas along lines of sight toward strong extragalactic mm-wave continuum sources, the chemistry of interstellar molecules in local diffuse clouds has been inventoried. This work has led to many surprises, chief among them the occurrence of a strong polyatomic chemistry [1] in regions which sometimes are unable to excite even CO to detectable levels of emission [2]. Quiescent chemical models of diffuse clouds fail to reproduce observed abundances by factors larger than 10 [2,3,4]. No obvious trace of energetic processes (e.g. shocks) seems to have been imprinted on the line profiles. Small secular variations in the absorption line profiles, such as we observed in HCO^+, are typically taken to suggest the presence of denser embedded gas but the weakness of emission (except CO) makes such an explanation difficult in the present cases [5]. To summarize, we have seen an extraordinary chemistry in diffuse gas, but find no clear suggestion in the existing data as to what might be driving it.

The next step is the direct investigation of structure in the gas by imaging the host clouds. A major goal of this work is to understand whether the line kinematics signal the deposition of enough energy to drive the absorption line chemistry. Although CO is sometimes absent in emission even when it has appreciable optical depth in absorption, the typical CO emission strength toward our continuum sources at arcminute spatial resolution is 2-3 K[2]; for HCO^+ it is 0.02-0.03 K [3] and for ^{13}CO 0.1 K [2]. In 2006-2007, we mapped CO J=1-0 emission in a field of 100" x 100" in the direction of the continuum source NRAO150 at 6" resolution with the PdBI+30m [6]. At some positions there are peak CO brightnesses 12-13 K, which are hardly expected for diffuse gas. The bright spots emerge from a continuous distribution but position-velocity diagrams display abrupt velocity structure resembling simulations of compressible turbulence as first shown by Falgarone *et al.* [7].

To pursue this imaging work we have adopted several approaches. We recently analyzed 3' resolution NANTEN CO data over a 7° field around the archetypal diffuse cloud line of sight toward ς Oph [8], again finding bright (10-12 K) lines at $A_v \sim 1$ mag and complex kinematic patterns characteristic of turbulent flow [7]. This work is now in press at A&A. Line profiles at individual pixels within sharp spatial-velocity gradients usually have subsonic linewidths, raising the possibility that higher-resolution imaging to be performed next Spring at the Arizona Radio Observatory (ARO) telescopes will resolve the structure into even sharper velocity gradients in thermally-broadened lines, at which point no further kinematic information can be extracted.

In 2008, we were granted time at the IRAM 30m to image gas in the vicinity (few arcminutes) of background sources at higher galactic latitudes, for which the diffuse cloud distances are better known than toward NRAO150 [2]; these maps will serve as short-spacing input to further synthesis mapping. In most cases we again found very bright CO lines, even when the best available maps of galactic reddening [9] (6' resolution) do not indicate the presence of dark gas. We have a commitment of several weeks observing at the ARO 12m and Sub-Millimeter-Telescope instruments for the 2008/2009 observing season, during which time we will perform higher-resolution imaging of the gas around ς Oph, we will make more and larger images of CO and ^{13}CO from the host bodies occulting our mm-wave continuum background sources and we will begin to survey the chemistry at the bright CO peaks in emission, assisted by the presence at ARO and IRAM of a new generation of ALMA mixers with greatly reduced noise temperatures.

Involved partners: IRAM
Manpower: 16 months in total
- **H. Liszt**: 12 months;
- J. Pety: 4 months;
- External contributor: R. Lucas.

Timescale: From month 1 to month 36
Deliverables:
- After 12 months: Initial publication of CO images of mm-wave absorption-line host clouds;
- After 24 months: Acquisition, data reduction and publication of ^{13}CO emission maps and observation of C^{18}O and HCO$^+$ emission at the peak of the ^{13}CO maps;
- After 36 months: Higher resolution ARO observations of CO and other species in the ς Oph cloud.

References
[1] The chemistry is summarized in a series of five papers ending with 2006 A&A, 448, 253.
[2] Liszt & Lucas, 1998, A&A, 339, 561.
[3] 1996, A&A, 307, 237.
[4] 2002, A&A, 384. 1054.
[5] 2000, A&A, 355, 333L.
[6] Pety, Liszt & Lucas, 2008, A&A, 489, 219
[7] Falgarone *et al*. 1994, ApJ, 438, 728.
[8] Tachihara *et al*. 2000, PASJ, 52, 1147
[9] Schlegel *et al*. 1998, ApJ, 500, 525.

3.3.7 TASK 7: LEGACY SURVEY 1: AN EXTENSIVE STUDY OF SIMPLE HYDRIDES AS PART OF THE HERSCHEL GUARANTEED TIME KEY PROJECT PRISMAS (IN CHARGE, LRA, M. GERIN, IN COLLABORATION WITH LUTH-ISM)

The observation of hydrides with high-resolution spectroscopy has been hindered so far because of the limited sky transparency at submillimeter wavelengths. Indeed, hydrides can be probed by means of optical or ultraviolet absorption line spectroscopy of background stars: The hydrides CH and CH$^+$ were among the first three molecules detected at optical wavelengths in the early 1940's, e.g. [1,2]. However, submillimeter and far-IR observations of rotational transitions have many critical advantages over optical/UV observations of electronic transitions: (1) submillimeter/far-IR absorption line observations can be carried along sightlines of larger visual extinction, allowing the chemistry of translucent and dense clouds to be probed; (2) many hydrides have electronic transitions at UV wavelengths that are inaccessible with current instrumentation and/or subject to confusion with H_2 Lyman and Werner bands; (3) submillimeter/far-IR transitions can be observed both in absorption and emission, providing a more complete sampling of the molecular clouds under investigation; (4) optical/UV observations are limited by spectral resolution -- except for optical observations of the brightest background sources -- and thus fail to fully elucidate the velocity structure of the absorbing molecules, hence the coupling of the gas dynamics with chemistry. The great capabilities of

heterodyne spectroscopy in the submillimeter have been demonstrated by the SWAS and ODIN satellites, and by the detection of the ground state line of ^{13}CH$^+$ at 830 GHz [3].

As discussed above, probing diffuse gas molecules in absorption against bright continuum sources has proven to be an efficient method for studying the first steps of interstellar chemistry and their interrelation with the interstellar medium dynamics and evolution. The HIFI instrument on board the Herschel Space Observatory is ideally suited to study the submillimeter lines of many hydrides. A comprehensive spectroscopic survey of hydrides in the interstellar medium will thus be carried out with HIFI, as part of the PRISMAS (PRobing InterStellar Molecules with Absorption line Studies; PI: M Gerin) guaranteed time project. The target hydrides contain the elements H, D, C, N, O, F and Cl. This investigation will provide a wealth of new information about interstellar hydrides - addressing key puzzles posed by previous observations from the ground since the 1940's, and recently with ISO, SWAS, and ODIN - and leaving an important legacy to astrochemistry and science of the interstellar medium. For instance, combined observations of CH$^+$, CH, OH and the N-hydrides will provide a unique database for investigating warm chemistry in the cold diffuse medium because their formation are known to be governed (at different levels) by reactions with significant activation barriers, which make difficult to reproduce their observed column densities by standard steady-state low-temperature chemistry models. The observations of the N-hydride ($NH^+/NH/NH_2/NH_3$) and O-hydride ($OH^+/OH/H_2O/H_3O^+$) families will provide the needed information to disentangle the roles of gas phase and solid phase processes in initiating the chemistry.

The observations will be performed early in the mission life, and must be rapidly reduced and analysed to provide feedback to the community on the Herschel capabilities. The current planning foresees a launch in April 2009 and the first scientific observations 6 months later. We plan to use both the Herschel pipeline and the GILDAS software, but we foresee that we will develop additional data processing routines to extract the maximum scientific information from the data. The sources have been selected to take advantage of the strong dust emission from massive star forming regions to detect multiple absorption components from foreground clouds of diverse properties that are known to intersect the selected sight-lines, along with emission and absorption intrinsic to the background sources. We thus expect complex spectra combining multiple emission lines from the background source and hydride absorption features from the intervening clouds along the line of sight. Additional complexity in the hydride spectra stems from multiple hyperfine components. Effort will be put on the analysis of these multiple components. While the raw data will be accessible through the ESA archive, we will release the reduced data through a database developed conjointly with the software engineer J.F. Rabasse.

A ground-based preparatory program has been started using the IRAM and Caltech Submillimeter Observatory facilities. These observations will add value to the Herschel data, by expanding the list of sampled species and by providing additional information on the environment of the target sources. The high spatial resolution data acquired with PdBI will be used to probe the small scale structure of the intervening clouds, a key piece of information in the analysis of the low resolution Herschel/HIFI data. It is essential to analyse the IRAM data, and make use of these to computed synthetic Herschel/HIFI data, in order to further optimise the observing modes, once the Herschel/HIFI performances will be checked in flight during the Performance and Verification phase. We therefore have started the analysis and scientific exploitation of the IRAM data in 2008. We will continue this in 2009, and we will move to Herschel data as soon as they are available.

Involved partners: LERMA-LRA and LUTH-ISM
Manpower: 54 months in total
- **M. Gerin**: 12 months;
- E. Falgarone: 4 months;
- M. De Luca: 16 months;
- J. R. Goicoechea: 6 months;
- F. Le Petit: 4 months;

- ANR post-doc (during the 4th year of the project): 12 months.

Timescale: From month 1 to month 48
Deliverables:
- After 12 months: Publication of IRAM related data;
- Probably after 36 months (i.e. 18 months after reception of the first data set from Herschel): Delivery of the PRISMAS database.
- After 48 months: Global analysis with the new chemical models developed in tasks 2 to 5.

References
[1] Swings & Rosenfeld, 1937, ApJ, 86, 483.
[2] Douglas & Herzberg 1941, ApJ, 94, 381.
[3] Falgarone et al., 2005, ApJ, 634, L149.

3.3.8 TASK 8: LEGACY SURVEY 2: ESTABLISHING THE HORSEHEAD MANE PDR AS AN OBSERVATIONAL BENCHMARK FOR CHEMICAL MODELS (IN CHARGE: IRAM, J. PETY, IN COLLABORATION WITH LERMA-LRA, LUTH-ISM, J. R. GOICOECHEA AND D. TEYSSIER)

Models of Photo-Dissociation Regions (PDRs) are used to understand the evolution of the UV illuminated matter both in our Galaxy and in external galaxies. In view of the intrinsic complexity of building reliable chemical networks and models, there is a clear need for well-defined observations which can serve as basic references. An ideal observational benchmark would deliver to chemists a set of abundances (with the associated uncertainties) as a function of the distance (or extinction) to the illuminating star. This goal is difficult to achieve for several reasons: 1) The geometry of the source is never as simple as wished when it is known at all; 2) The spectra produced by the instruments must be inverted to obtain abundances; 3) The spectra are often measured at very different angular resolutions, implying beam dilution and/or mixing of different gas components.

In this context the PDR of the Horsehead mane is a particularly interesting case because the transition from the diffuse, hot and ionised gas to the dense, cold and shielded gas is sharp and the PDR geometry is simple (almost 1D, viewed edge-on [1]). The density profile across the PDR is well constrained and we are making several efforts to constrain the thermal profile. The combination of small distance to Earth (at 400 pc, 1" corresponds to 0.002 pc), low illumination (χ = 60) and high density ($n_H \sim 10^5$ cm^{-3}) implies that all the interesting physical and chemical processes can be probed in a field-of-view of less than 50″ with typical spatial scales ranging between 1 and 10″ [9].

We have already obtained a wealth of observations of the Horsehead mane PDR, using similar instruments and the same methods of observation, data reduction and data analysis. For each chemical species, we have tried 1) to observe at least two transitions at similar angular resolutions (from 5″ to 15″) to properly constrain the excitation conditions and 2) to observe the associated isotopologues to derive accurate column densities and abundances. Obtaining maps of the extended emission has proved to be essential to understand the spatial distributions of the species.

This effort led to 7 refereed papers with the following results: 1) The PDR has a very steep gradient, rising to $n_H = 10^5$ cm^{-3} in less than 10", at a roughly constant pressure of P = 4.10^6 K cm^{-3} [6]; 2) The hydrocarbon abundances are higher than the predictions based on pure gas phase chemical models suggesting that an additional formation path of carbon chains should be considered in PDRs [7]; 3) The gas sulfur depletion invoked to account for CS and HCS$^+$ abundances is orders of magnitude lower than in previous studies of the sulfur chemistry [3]; 4) A dense and cold core (T < 20K, n > 2.10^5 cm^{-3}) has formed just behind the PDR, where the deuterium fractionation is efficient, with [DCO$^+$]/[HCO$^+$]> 0.02 [8]; 5) Significantly neutral PAHs are detected ahead of the Horsehead mane. Their presence in the ionised gas could be the result of the photoevaporation of dense neutral material into the HII region [2]. All those results were unexpected, illustrating the importance of having a good astrophysical reference to constrain chemical models.

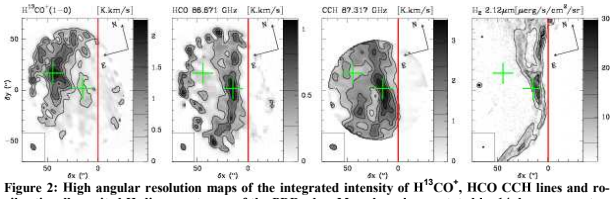

Figure 2: High angular resolution maps of the integrated intensity of H^{13}CO$^+$, HCO CCH lines and ro-vibrationally excited H_2 line as a tracer of the PDR edge. Maps have been rotated by 14 degrees counter-clockwise around the projection center, located at (dx,dy)=(20",0"), to bring the illuminated star direction in the horizontal direction and the horizontal zero has been set at the PDR edge. The emission of all lines is integrated between 10.1 and 11.1 km/s. Displayed integrated intensities are expressed in the main beam temperature scale. Contour levels are displayed on the grey scale lookup tables. The red vertical line shows the PDR edge and the green crosses shows the DCO$^+$ and HCO peaks, which are typical position of respectively the shielded dense core and the UV illuminated PDR. The differences in molecular line maps illustrate the diagnostic potential of molecules and the need for high fidelity, high spatial resolution maps.

In 2007, we have obtained: 1) SO and H_2S maps at IRAM to complement our already published CS and HCS$^+$ data [4]; 2) HCO interferometric maps at IRAM to complement our HCO$^+$ study (Gerin et al. 2008); 3) NH_3 rotation-inversion maps with Effelsberg and VLA, complemented with a N_2H^+ map at IRAM [10]; 4) maps of the 3mm (ground state) and 1mm lines of CN, HCN & HNC with both the IRAM single-dish and interferometer; 5) Upper limits for ND_2H at the Caltech Submillimeter Observatory. In 2008, we have been granted time at IRAM 1) to map H_2CO, CH_3OH and 2) to make a selective survey of more complex organic molecules (ketene, etc…) and deuterated species (HDCO, NH_2D, etc…). In 2009, we plan to ask for an inventory of reactive ions (CO$^+$, SO$^+$, etc…). This extensive observing effort has been widely recognized. However, the limited manpower available so far has limited our capability of distributing consistent data sets to the community, which would significantly increase the impact of our work.

Involved partners: IRAM, LERMA-LRA and LUTH-ISM
Manpower: 32 months in total.
- **J. Pety**: 6 months;
- J. R. Goicoechea: 6 months;
- M. Gerin: 4 months;
- E. Roueff: 4 months;
- ANR post-doc (during the 3rd year of the project): 12 months.
- External contributor: D. Teyssier.

Timescale: From month 1 to month 48
Deliverables:
- After 12 months: At least 1 publication on available data.
- After 24 months: At least 1 publication on available data.
- After 36 months: Set up of a pipeline for consistent recalibration.
- After 48 months: Global analysis with the new dynamical models before the release of the published data.

References
[1] Abergel, A., et al. 2003, *A&A*, **410,** 577
[2] Compiègne, M. et al. 2007, *A&A*, **471,** 205
[3] Goicoechea, J.R., et al. 2006, *A&A*, **456,** 565
[4] Goicoechea, J.R., et al. 2009, in prep.
[5] Gerin, M., et al. 2008, *A&A*, in press.
[6] Habart, E., et al. 2005, *A&A*, **437,** 177

[7] Pety, J., et al. 2005, *A&A*, **435,** 885
[8] Pety, J., et al. 2007a, *A&A*, **464,** L41
[9] Pety, J., et al. 2007b, Molecules in Space and Laboratory, 13.
[10] Teyssier, D., et al. 2004, *A&A*, **417,** 135
[11] Teyssier, D., et al. 2009, in prep.

3.3.9 TASK 9: IMAGING EXPERIMENT 2: IS THE HORSEHEAD NEBULA A TYPICAL PILLAR? (IN CHARGE: IRAM, J. PETY, IN COLLABORATION WITH LERMA-LRA AND P.HILY-BLANT)

Although pillars are parts of the most impressive structures of the interstellar medium (e.g. see the pillars of creation in the Eagle nebula), these structures have been poorly studied at mm-wavelengths. Pillars usually point towards an exciting O/B star with a strong far-UV flux, responsible for the propagation of an ionization front into the pillar. There is a general agreement that they are formed through the photo-evaporation of low density material around the pillar which was protected by the shadow of denser material at its edge. However, other formation scenarios are possible: For instance, the development of a Rayleigh-Taylor instability in the ionization front. Pound et al. (2003) were the first to cast the Horsehead nebula in the category of the pillars. Our study of the Horsehead in many different tracers clearly shows that the creation of this pillar results from the photoevaporation of a pre-existing over-density. Indeed, we showed that the gas goes from a diffuse, warm, far UV illuminated environment to a dense, cold, dark environment in about 40" (or 0.08 pc).

If this mechanism of pillar formation is really universal, pillars should then be good candidates as observational references to models, which combine both chemistry and dynamics. Indeed, their formation is by definition dynamical. Moreover, the transition between the ionised and the molecular gas is much clearer in those kinds of structures than, e.g., in the Orion Bar which has been used as a prototype for PDR for 30 years (Pety *et al*. 2008, EAS Publications Series, Volume 31, pp.35-41). We propose to observe several pillars with different far UV illumination to see how this factor impacts the relationship between chemistry and dynamics. This will provide the first consistent dataset of these interstellar medium structures, allowing us to perform a comparative study of pillars. We will first propose a survey of theses structures at the IRAM-30m single-dish telescope, in ^{12}CO, ^{13}CO and C^{18}O, to get a global view of their geometry and kinematics. We will then study the chemistry and thus the thermodynamic of the most interesting ones, by using the best tracers of the different gas phases (as defined by our Horsehead study). This second part will benefit greatly from the use of the interferometric on-the-fly observing modes because many pillar regions are located between two and four times farther away than the Horsehead nebula. Finally, the analysis of the data requires the kind of numerical models developed in this project because timescales in these structures are such that radiative processes, chemistry, and dynamics are coupled.

Involved partners: IRAM and LERMA-LRA
Manpower: 26 months in total
- **J. Pety**: 6 months;
- N. Rodriguez-Fernandez: 4 months;
- M. Gerin: 4 months;
- ANR post-doc (during the 2nd year of the project): 12 months;
- External contributor: P.Hily-Blant.

Timescale: From month 13 to month 24
Deliverables:
- After 18 months: First data acquired and reduced. These data will help to constrain the geometry and the kinematics of pillars.
- After 24 months: First publication.

3.4. CALENDRIER DES TACHES, LIVRABLES ET JALONS / PLANNING OF TASKS, DELIVERABLES AND MILESTONES

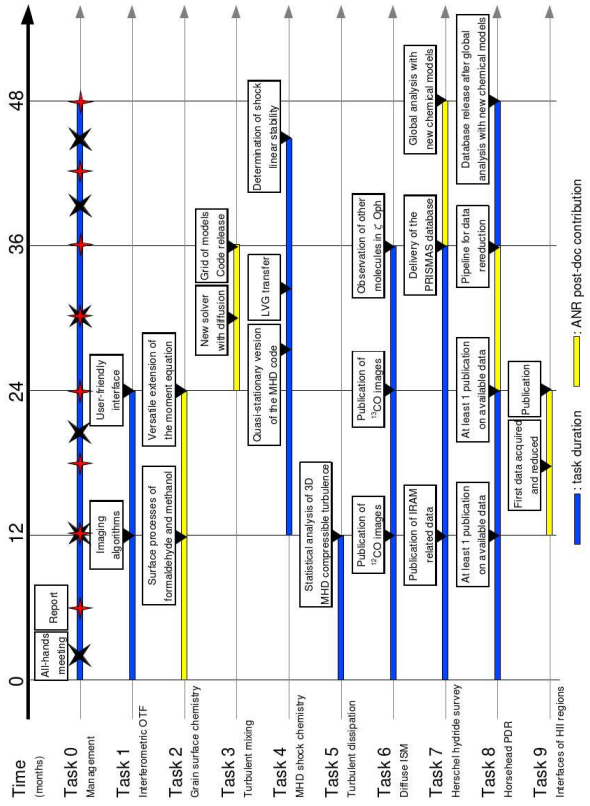

Figure 3: Time table of the different tasks of the SCHISM project.

The list of deliverable (and partner in charge in parenthesis) is:
- Task 0 (IRAM/LERMA-LRA/LUTH-ISM): Management
  - After 3 months: 1st all-hands meeting to set up the consortium agreement;
  - One all-hands teleconference every month;
  - One all-hands face-to-face meeting every 9 months;
  - After 42 months: Project report #7;
  - After 45 months: Last all-hands meeting;
  - After 48 months: Final report.
- Task 1 (IRAM): Commissioning the interferometric on-the-fly observing mode
  - After 12 months: First version of the deconvolution and imaging algorithms;
  - After 24 months: Science verification and design of a user-friendly interface.
- Task 2 (LUTH-ISM): Coupling gas-phase and solid-state chemistry in the Meudon PDR code
  - After 12 months: Inclusion of grain surface processes of formaldehyde and methanol in the PDR code using the formalism of the moment equation. First publication.
  - After 24 months: Introduction of the first and second moments of the probabilities of presence of adsorbed species, enabling a versatile extension of the moment equation formalism. Application to deuteration processes on dust surfaces. Second publication.
- Task 3 (LUTH-ISM and LERMA-LRA): Including the turbulent mixing formalism in the Meudon PDR code
  - After 30 months: 1st version of the PDR code with a new solver to include diffusion.
  - After 36 months: Grid of models.
- Task 4 (LERMA-LRA): Time-dependent MHD shocks and chemistry
  - After 27 months: Delivery of a quasi-stationary version of the MHD code from Lesaffre et al (2004a).
  - After 33 months: LVG radiative transfer post-processing.
  - After 45 months: Delivery of a code to determine the linear stability of the above shocks.
- Task 5 (LERMA-LRA): Dissipative structures of turbulence and chemistry
  - After 12 months: Implementation of the statistical analysis of the simulations of 3D MHD compressible turbulence to improve the description of the turbulent medium.
- Task 6 (IRAM): Imaging experiment 1: Connecting the chemistry of diffuse gas with its dynamics
  - After 12 months: Initial publication of CO images of mm-wave absorption-line host clouds;
  - After 24 months: Acquisition, data reduction and publication of ^{13}CO emission maps and observation of C^{18}O and HCO$^+$ emission at the peak of the ^{13}CO maps;
  - After 36 months: Higher resolution ARO observations of CO and other species in the ç Oph cloud.
- Task 7 (LERMA-LRA and LUTH-ISM): Legacy survey 1: An extensive study of hydrides as part of the Herschel guaranteed time key project PRISMAS
  - After 12 months: Publication of IRAM related data;
  - Probably after 36 months (i.e. 18 months after reception of the first data set from Herschel): Delivery of the PRISMAS database.
  - After 48 months: Global analysis with the new chemical models developed in tasks 2 to 5.
- Task 8 (IRAM, LERMA-LRA and LUTH-ISM): Legacy survey 2: Establishing the Horsehead mane PDR as an observational benchmark to chemical models
  - After 12 months: At least 1 publication on available data;
  - After 24 months: At least 1 publication on available data;
  - After 36 months: Set up of a pipeline for consistent recalibration;
  - After 48 months: Global analysis with the new dynamical models before the release of the published data.
- Task 9 (IRAM and LERMA-LRA): Imaging experiment 2: Is the Horsehead nebula a typical pillar?

  - After 18 months: First data acquired and reduced. These data will help to constrain the geometry and the kinematics of pillars;
  - After 24 months: First publication.

4. STRATEGIE DE VALORISATION DES RESULTATS ET MODE DE PROTECTION ET D'EXPLOITATION DES RESULTATS / DATA MANAGEMENT, DATA SHARING, INTELLECTUAL PROPERTY AND RESULTS EXPLOITATION

The interferometric On-The-Fly observing mode will be released to the community of Plateau de Bure Interferometer users in the GILDAS software suite (see http://www.iram.fr/IRAMFR/GILDAS). The algorithms developed will also be transferred to ALMA in the framework of the FP6 "ALMA Enhancement" program. All the algorithmic work will be published so that any other (sub-)millimeter interferometer in the world (Carma, SMA, …) can benefit from this work. As a result, we expect that interferometric On-The-Fly will considerably increase the wide-field imaging capabilities of both the current and future generation of (sub-)millimeter interferometers in the world.

The Meudon PDR code is available to the community at http://aristote.obspm.fr/MIS. It is documented and maintained by the ISM team at LUTH/Observatoire de Paris (E. Roueff, J. Le Bourlot, F. Le Petit). New versions will be available in the same way after the corresponding publications are accepted. The snapshot algorithm of a MHD shock will be distributed to the community through a similar web interface after acceptance of the corresponding publication. For several years, the LUTH-ISM partner has participated to the definition of the standards in the VO-Theory group at IVOA (International Virtual Observatory Alliance). In this context, tools and methods have first been developed to provide online access to the Meudon PDR code through the astrogrid infrastructure. Moreover, in the framework of the Astronet STARFORMAT grant, a VO compatible database of model simulations is now developed. On the long term, these VO facilities will be maintained by the VO-Paris Datacentre at Paris Observatory. The SCHISM ANR project will use this extensive expertise to provide most of its modeling tools and results in a VO compatible way.

The Herschel key program teams have been required by ESA to provide the processed data and all related scientific outcome to the community. To comply with this demand, the reduced data from the PRISMAS legacy survey will be put on the web by the LERMA-LRA partner. We have prepared a web-accessible database, which will contain all information about our program. Herschel data, together with preparatory work from ground-based observations, will be made available through this tool (http://astro.ens.fr/hifi-abs). The database will also provide documentation on how the data were observed and processed. The database is currently password protected, but we will enable public access when the data are ready to be distributed. The reduced data from the Horsehead legacy survey will be put on the web by the IRAM partner in a similar manner.

The other tools and data which will be developed in the framework of this project but which are not foreseen for public release will stay the property of their developers/principal investigators. In the publications related to this project and in other publications, which would

make use of the legacy tools and data, we will request an acknowledgment of the ANR funding support.

5. ORGANISATION DU PARTENARIAT / CONSORTIUM ORGANISATION AND DESCRIPTION

5.1. DESCRIPTION, ADÉQUATION ET COMPLÉMENTARITÉ DES PARTENAIRES / RELEVANCE AND COMPLEMENTARITY OF THE PARTNERS WITHIN THE CONSORTIUM

Partner 1: IRAM
IRAM is currently the world's best millimeter radio-astronomy facility with leading instruments both in single-dish (30m) and in interferometry (Plateau de Bure interferometer). IRAM hardware and software expertise is recognized in Europe as it is a major ESO partner in the construction of ALMA, the next generation of sub-millimeter interferometer. For instance, in the software area, IRAM has been granted two positions (one engineer and one astronomer from 2006 to 2010) to commission the OTF technique for the ALMA interferometer, in the framework of the European FP6 "ALMA Enhancement" project. A natural continuation is to make the additional efforts to propose this observing mode in a user-friendly way at Plateau de Bure interferometer so that IRAM keeps its cutting-edge position in millimeter interferometry. Moreover, CLASS, the IRAM software tools dedicated to the reduction of the single-dish spectra, is used in many observatories in the world (CSO, JCMT, APEX, SOFIA…) and it is considered for use on Herschel/HIFI datasets. Being involved in the scientific analysis of the legacy project PRISMAS as proposed in this project will be a powerful driver for the needed tools in CLASS. In the same spirit, the expertise of the IRAM member of the SCHISM project has been used to devise successful and directly applicable observations of the dense and diffuse interstellar medium (see e.g. our data already acquired on the Horsehead PDR mane). As all the observations proposed in this project, the Horsehead PDR mane has already been and will continue to be the birth place of innovative data-processing software, which is then delivered to the community: For instance, the IRAM/GILDAS software suite is currently the only one which is routinely considered for the processing of an interferometric mosaic with the associated short-spacings coming from a single-dish.

Partner 2: LERMA-LRA
The launch of the Herschel Space Observatory in October 2008, and the construction of the giant sub-millimeter interferometer ALMA are two major steps forward that the LERMA-LRA has been preparing for many years. For instance, M. Gerin and E. Falgarone are co-Investigators of the Herschel/HIFI instruments. M Gerin has led the preparation of the scientific programmes on the interstellar medium within the HIFI consortium and she is the PI of the PRISMAS program. Other LERMA-LRA members have been closely involved in the calibration and software activities for HIFI.
One of the main research areas of the team is the study of structure and chemistry of the interstellar medium, combining detailed observations at high spatial and spectral resolution with sophisticated modeling. Research at LRA makes extensive use of current facilities, both on the ground and in space (IRAM, CSO, Spitzer). In the last five years, with the award to Pr. S.Balbus of a Chaire d'excellence by the French Ministry of Research, the theme of fluid simulations has developed considerably. In particular, the LERMA-LRA is the coordinator partner of the ANR grant MAGNET, which supports the development of compressible MHD codes (RAMSES and PARODY) in collaboration with the CEA. While this effort brings the expertise of dynamical codes at LERMA-LRA, the team proposing this new ANR project is only partially involved in the MAGNET project. Finally, the LERMA-LRA partner is coordinating the ASTRONET project STARFOMATT (PI: P. Hennebelle). This project is done in collaboration with the LUTH-ISM, the University and the Max Planck Institute in Heidelberg and the Hamburg Observatory. The main goal of this project is to provide the community with state of the art simulations of the formation of molecular clouds. It will include synthetic observations of the simulation results. The extension of the Meudon PDR code to 2D geometry will be funded within this project.

Partner 3: LUTH-ISM
The LUTH-ISM team is an interdisciplinary team combining expertise in atomic and molecular physics and modelling of chemical and physical processes in interstellar environments. The Meudon PDR code is developed, improved and maintained by this team. It has been a long standing effort, starting with the studies of the H/H_2 transition in Abgrall et al. 1992, C^+/C/CO interface in Le Bourlot et al. 1993, D/HD conversion by Le Petit et al. 2002. Numerous applications to FUSE (Far Ultra Violet Spectroscopic Explorer) observational data have then been undertaken. These studies have revealed the need to improve the treatment of the UV radiative transfer where considerable efforts both on theoretical and numerical aspects, have been realized in a collaboration between LERMA –LRA and LUTH-ISM teams (Goicoechea & Le Bourlot 2007). The Herschel perspective has prompted us to include explicitly H_2O cooling and emission as a specific milestone within the Molecular Universe FP6 network. The whole rotational structure of H_2O has been introduced which implied to develop an exact IR-submillimeter radiative transfer to take into account radiative pumping by lines and dust continuum emission (Gonzalez-Garcia et al. 2008). The forthcoming challenges, in perfect accordance to the present ANR project, are improvements of the physics and chemistry of grains and inclusion of dynamical effects in the Meudon PDR code. Some ways are investigated such as solving surface chemistry with moment equations approach (in collaboration with O. Biham from Jerusalem university – Foreign ministry contract) and coupling the grain code from IAS (Desert et al. 1990) and the Meudon PDR code.

5.2. QUALIFICATION DU COORDINATEUR DU PROJET / QUALIFICATION OF THE PROJECT COORDINATOR

The SCHISM project coordinator will be Jérôme Pety from IRAM. Jérôme Pety is a 38 year-old astronomer at Observatoire de Paris, detached to IRAM/Grenoble. Since 2003, he has been in charge of the GILDAS software, which is used to reduce the data produced by the IRAM instruments. In this task, he coordinates the activity of about 10 persons (engineers and astronomers). Since the beginning of 2008, he has been in addition appointed director of the Action Spécifique ALMA from INSU, which is charged with coordinating ALMA scientific activities in France.

5.3. QUALIFICATION, ROLE ET IMPLICATION DES PARTICIPANTS / CONTRIBUTION AND QUALIFICATION OF EACH PROJECT PARTICPANT

The project is based on three groups of researchers, i.e. eight permanent researchers and a software engineer. Moreover, there is one PhD student and two astronomers on a non-permanent contract, who are directly working with the permanent researchers. Two foreign close collaborators will complete our team (H. Liszt and J. R. Goicoechea, see 1.7.2). This set of collaborators constitutes the main task force of the project.

Additional external collaborators are: Pierre Hily-Blant (LAOG, France), Guillaume Pineau des Forêts (IAS, France), David Teyssier (ESA, Spain), Robert Lucas (ALMA, Chili).

Partenaire IRAM	Nom	Prénom	Emploi actuel	Personne. mois	Rôle/Responsabilité dans le projet 4 lignes max
Coordinateur/responsable	PETY	Jérôme	Astronome-adjoint	24	Establishing the Horsehead mane PDR as an observational benchmark for chemical models
Autres membres	REYNIER	Emmanuel	Ingénieur logiciel	12	Maintenance of the infrastructure of the GILDAS software in which the interferometric OTF algorithms are developed
	RODRIGUEZ-FERNANDEZ	Nemesio	Post-doc	12	Development of the imaging algorithms of the interferometric OTF observing mode

	LISZT	Harvey	NRAO astronomer	12	Observation and analysis of data from the diffuse interstellar medium

Partenaire LERMA-LRA	Nom	Prénom	Emploi actuel	Personne. mois	Rôle/Responsabilité dans le projet 4 lignes max
Coordinateur/responsable	GERIN	Maryvonne	Directrice de recherche CNRS	24	PI of the Herschel guaranteed time PRISMAS key project
Autres membres	FALGARONE	Edith	Directrice de recherche CNRS	12	Modelling the chemistry in the dissipative structures of interstellar turbulence
	LESAFFRE	Pierre	Chargé de recherche CNRS	12	Development of time-dependent MHD shock and turbulent mixing models
	GOICOECHEA	Javier	Spain Ramon Y Cajal Fellow	12	Radiative transfer at millimeter and far infra-red wavelengths
	DE LUCA	Massimo	Post-doc	16	Data reduction, scientific analysis and database publication of the Herschel guaranteed time PRISMAS project
	GODARD	Benjamin	PhD student	6	Comparison of models of turbulent dissipation regions with observations of the diffuse interstellar medium
	CABRIT	Sylvie	Astronome	4	Validation of shock models. Line radiative transfer in shocks

Partenaire LUTH-ISM	Nom	Prénom	Emploi actuel	Personne. mois	Rôle/Responsabilité dans le projet 4 lignes max
Coordinateur/responsable	LE PETIT	Franck	Astronome-adjoint	16	Implementation of the turbulent mixing formalism in the Meudon PDR code
Autres membres	ROUEFF	Evelyne	Astronome	16	Coupling of the gas-phase and grain-surface chemistry in the Meudon PDR code
	LE BOURLOT	Jacques	Professeur	8	Architecture of the Meudon PDR code

6. JUSTIFICATION SCIENTIFIQUE DES MOYENS DEMANDES / SCIENTIFIC JUSTIFICATION OF REQUESTED BUDGET

6.1. PARTNER 1 : IRAM

- *Staff: A 2 year post-doc is requested*

We wish to hire a post-doc during two years to support the activities at IRAM. First, the post-doc will be in charge of developing the observation strategy of the pillar environments, including answers to calls for proposals, data acquisition, data reduction, data analysis and publication (task 9). This kind of object is ideal to test the On-The-Fly interferometric mode which is being commissioned at IRAM. In this context, the post-doc will have to work on the user interface (including documentation) of this new observing mode to make its use intuitive. Several risks (no data acquired yet and a new observing mode in development) are associated with this particular task of the project. As an alternative to this task, the post-doc may be associated with the data acquisition, reduction and analysis of the emission maps of the diffuse interstellar medium (tasks 3,5,6). In both alternatives, the expected time required is an additional 1 year.

Second, the post-doc will be in charge of data reduction, analysis and publication of unpublished Horsehead data (task 8). He/she will have to ensure the consistency of the data reduction of all the

already-acquired data before their release in the public domain, which includes the documentation and the setup of the web site. Depending on the condition of the numerical tasks (2 & 3) of the project, he/she will have the possibility to reinterpret the whole data sets with the new tools before the public release. This work will be done in close collaboration between the IRAM, LERMA-LRA and LUTH-ISM partners. The expected time required is about 1 year.

- *Missions / Missions*

There will be four persons (including the permanent, the non-permanents and the additional post-doc we plan to hire) at IRAM working on this project. One of them will be active during 4 years and the 3 others will be active 2 years. For a good circulation of the information between the Paris and Grenoble partners (including the all-hands meetings) as well as a good dissemination of the results in national and international conferences, it is necessary to provide the project members with adequate travel funding. The estimated cost is on average 400 €, 600 € and 1200 € for a 3 to 5 days travel respectively within France, Europe and oversea. An average support of 1 k€ per member and per year of activity is felt adequate. Therefore we believe that 4+3*2=10 trips are well-justified which leads to a total amount of 10 k€. This amount is divided between tasks in proportion of the manpower associated to the tasks.

In addition, H.S.Liszt is a world known expert of the structure and chemistry of the diffuse interstellar medium. His expertise of the chemical and physical processes at work in the diffuse interstellar medium will be instrumental in the project. Face-to-face 10-day working sessions are needed to ensure a good inclusion of task 6 in the whole project. We estimate the cost per stay to be 2000 €. During the project lifetime, two such stays would happen in Paris and two others in Grenoble, leading to a total of 8000 €.

We therefore ask for a grand total of 18000 € in travel funds for the IRAM partner.

- *Autres dépenses de fonctionnement / Other expenses*

In the same way, it is essential for the efficient execution of the project to cover expenses of at least 1 k€ per year of activity and per person for small equipment and software licenses. This includes laptop, desktop, and external disk to store data.

This amounts to another 10 k€ in 4 years for partner 1.

6.2. PARTNER 2 : LERMA-LRA

- *Staff: A 2 year post-doc is requested*

Note that while the PRISMAS project has been accepted for observation, the Herschel project is not delivering any manpower help to quickly reduce the data and the CNES resources for scientific manpower is very limited.

Within the PRISMAS project, the LERMA-LRA team is in charge of the overall coordination and communication of the scientific results, the ground-based preparatory spectroscopy program and the analysis of the carbon and nitrogen hydrides. The post-doc will join the team when the program will be actively going on. He will be in charge of the continuation of the data processing and archiving, as well as the preparation and coordination of follow up projects based on the first Herschel results. He/she will work in close connection with the scientists responsible for studying the other families of molecules, to exchange information on the data-processing, line-identification and line-fitting tools. The second focus of his/her activity will be the scientific analysis of the data, especially the comparison of the measured hydride properties with the predictions from sophisticated model tools developed in parallel within the SCHISM project. The post-doc will be a key person in the delicate

comparison of observations and models as we foresee that model results will be used as templates in the data analysis. The required time to complete this task is estimated to be one year.

Conversely, new measurements will drive model improvements. It is therefore expected that the post-doc will also contribute to the development of the theoretical models. The comparison with models will be done in collaboration with the LUTH-ISM partner. The theoretical activity will be focused on the implementation of turbulent mixing in the Meudon-PDR code (task 3). For this purpose, the structure of the solver of the Meudon PDR code must replaced, either with a shooting/fitting-at-midpoint method or a relaxation scheme. Given the present structure of the Meudon PDR code, this task can be completed in one year.

The candidate should have good skills in numerical analysis and good knowledge in physical processes at play in the interstellar medium. Previous experience with millimeter or submillimeter spectroscopy of the interstellar medium would be appreciated.

- *Travel*

There will be 7 persons at LERMA-LRA (including the permanent, the non-permanents and the additional post-doc we plan to hire) working on this project. 4 of them will work 4 years on the project, 2 of them 2 years and 1 of them 1 year. The same computation as for partner 1 implies 4*4+2*2+1*1=21 k€ in travel expenses during the project lifetime. This amount is divided between tasks in proportion of the manpower associated to the tasks.

In addition, J.R.Goicoechea is the member of the project who has the most expertise in radiative transfer at millimeter and far infra-red wavelengths. In the last years he has been modelling the mm line emission from the Horsehead by coupling the Meudon PDR code abundance predictions with consistent radiative transfer simulations. This expertise will be instrumental in the analysis of the acquired data to bridge the gap between observed spectra and modeled column densities and temperatures. He also coordinates the Herschel/PACS (57-210 µm) observations in the PRISMAS project. Regular 5-day face-to-face meetings both in Paris and Grenoble are needed to ensure that this expertise is well spread over the project team. We estimate the cost per stay of 5 working days to be 200 € for the airfare, 325 € in Grenoble and 550 € in Paris for the hotel and 250 € for the daily expenses, which make a total of 775 € for one Grenoble stay and 1000 € for one Paris stay. During the project lifetime, four such stays would happen in Paris and four others in Grenoble, leading to a total of 7100 €.

We therefore ask for a grand total of 28100 € in travel funds for the LERMA-LRA partner.

- *Other expenses: Small equipment*

The same computation as for partner 1 ends up into 21 k€ in small equipment in 4 years for partner 2.

6.3. PARTNER 3: LUTH-ISM

- *Manpower: A 2 year post-doc is requested*

The post-doc will introduce the surface reactions network involving formaldehyde and methanol resulting from the diagrammatic approach of Barzel and Biham (2007) within the moment formalism in the Meudon PDR code. This will require to extend the present efforts developped for H2, HD and D2 in collaboration with Biham and Barzel. Two different techniques can be used: the matrix describing the coupling between the zero, first and second order moments of the adsorbed species may be written explicitely for specific networks, as it is done presently for H2, HD and D2. This can be done within one year together with a specific application to the Horsehead nebula. A more challenging procedure would be to introduce the different moments as "pseudo-chemical species" which could then be coupled by the pseudo reactions directly written in a data file. This would allow the extension

of more complex cases more straightforwardly, once the various coupling matrix elements have been determined. Such a development requires that the post-doc is already familiar with the code and could be undertaken after several months of experience. The foreseen applications are probing the role of surface reactions on deuteration and including surface reactions of hydrocarbons and aggregation of carbon containing molecules via surface reactions. The expected increase of complexity implies indeed an automated procedure of handling surface reactions, such as the one described previously.

The candidate should have good skills in numerical analysis and enjoy multidisciplinary and novel approaches. Physical and chemical background will be most useful and welcome.

- *Travel*

There will be 4 persons at LUTH-ISM (including the permanents and the additional post-doc we plan to hire) working on this project. 3 of them will be active during 4 years and 1 will be active 2 years. The same computation as for partner 1 yields 3*4+1*2=14 k€ in travel expenses during the project lifetime. This amount is divided between the two main tasks the partner is responsible for.

- *Other expenses: Small equipment*

The same computation as for partner 1 ends up into 14 k€ in small equipment in 4 years for partner 3.

7. ANNEXES

7.1. REFERENCES BIBLIOGRAPHIQUES / REFERENCES

- Abergel, A., et al. 2003, *A&A*, 410, 577
- Aikawa, Y., Nomura, H., 2008, Physica scripta, 130, Proceeding of the Nobel symposium 135
- André, P., Ward-Thompson, D., Barsony, M 2000, Protostars and Planets IV, 59.
- André M. K., Le Petit F., Sonnentrucker P., et al., 2004, A&A
- Barzel B., Biham O., 2007, AJ 658, L37
- Barzel B., Biham O., 2007, J. Chem. Phys. 127, 4703
- Bergin, E., Tafalla, M., 2007, ARAA, 45, 339
- Biham, O., Furman, I., Pirronello, V., Vidali, G., 2001, ApJ, 553, 595
- Boisssé P., Le Petit F., Rollinde E., et al., 2005, A&A
- Brown, Paul D., Charnley, S. B 1990, MNRAS, 244, .432.
- Chièze et al. 1998, MNRAS, 295, 672.
- Compiègne, M. et al. 2007, *A&A*, 471, 205
- Cuppen et al. 2005, MNRAS, 361, 565.
- Cuppen et al. 2006, MNRAS, 376, 1757
- De Luca M, Giannini T., Lorenzettti D., 2007, A&A 474, 863
- Dionatos O, Nisini B, Garcia Lopez R, Giannini T, Davis CJ, Smith M, Ray TP, De Luca M, 2008, ApJ in press
- Douglas & Herzberg 1941, ApJ, 94, 381
- Dutrey, A., Guilloteau, S., Ho, P., 2007, Protostars and Planets V
- Ekers, R. & Rots, A., "Short Spacing Synthesis from a Primary Beam Scanned Interferometer » in Image Formation from Coherence Functions in Astronomy, Proceedings of IAU Colloq. 49, held in Groningen, Netherlands, August 10-12, 1978. Edited by C. van Schooeveld, C. D. Reidel Publishing Co. (Astrophysics and Space Science Library. Volume 76), 1979, p.61
- Elia D., Massi F., Strafella F., De Luca M., et al., 2007, ApJ 655, 316
- Falgarone *et al*. 1994, ApJ, 438, 728.
- Falgarone E., Phillips T.G. & Pearson, J., 2005, ApJ, 634, L149
- Falgarone, E., Pineau des Forêts G., Hily-Blant P. & Schilke, P., 2006, A&A, 452, 511
- Falgarone, E., Troland, T. H., Crutcher, R. M. et al., 2008, A&A, 481, 367
- E. Falgarone, J. Pety, P. Hily-Blant, in preparation (2008)
- Flower, Pineau des Forêts, Hartquist, 1985, MNRAS, 216, 775

- Garrod, R. T. & Herbst, E 2006, A&A, 457, 927
- Garrod, R. T., et al., 2008, ApJ, 682, 283
- Gerin M., Lis D. C., Philipp S., Güsten R., Roueff E., Reveret V., 2006, A&A 454, L63
- Gerin, M., et al. 2008, *A&A,* in press.
- Giannini T, Lorenzetti D., De Luca M, et al, 2007, ApJ 671, 470
- Godard, B, Falgarone, E., et al., 2008, A&A, in press
- J.R. Goicoechea, J. Cernicharo, 2002, ApJ, 576, L77
- Goicoechea J, Rodriguez-Fernandez NJ, Cernicharo J, 2004, ApJ 600, 214-233
- J.R. Goicoechea, J. Pety, M.Gerin, E. Roueff, D. Teyssier, P. Hily-Blant, S. Baek, 2006, A&A, 456, 565
- Goicoechea J. R. & Le Bourlot 2007, A&A, 467, 1
- J.R. Goicoechea, O. Berné, M. Gerin. C. Joblin, D. Teyssier, 2008, ApJ, 680, 466
- Goicoechea, J.R., et al. 2009, in prep.
- Gonzales-Garcia M., Le Bourlot J., Le Petit F., Roueff E., 2008, A&A, 485, 127
- C. Gry, F. Boulanger, C. Nehmé, G. Pineau des Forêts, E. Habart, E. Falgarone, A&A, 391, 675 (2002)
- Habart et al. 2004, A&A, 414, 531
- Habart, E., et al. 2005, *A&A*, 437, 177
- Herbst, E., J. Phys. Chem., 2005, A 109, 4017
- Hidaka, H., Watanabe, N, Shiraki, T., et al., 2004, ApJ, 614, 1124
- Hidaka, H., Miyauchi, N., Kouchi, A., Watanabe, N., 2008, Chem. Phys. Lett, 456, 36
- Hily-Blant P. & Falgarone E., 2007, A&A, 469, 173
- Hily-Blant, P., Falgarone, E., Pety, J., 2008, A&A, 474, 923
- Hiraoka, K, Miyagoshi, T. Takayama, T, et al., 1998, ApJ, 498, 710
- Joulain, K., Falgarone, E., Pineau Des Forêts, G., Flower, D. 1998, A&A, 340, 241
- Le Bourlot J. Pineau des forêts G., Roueff E., Flower D., 1993, A&A 267, 233
- Le Petit F., Roueff E., Le Bourlot J., 2002, A&A 390, 369
- Le Petit F., Roueff E., Herbst E., 2004, A&A 417, 993
- Le Petit F., Nehme C., Le Bourlot J. Roueff E., 2006, ApJS 164, 506
- Lesaffre et al. 2004a, A&A, 427, 147
- Lesaffre et al. 2004b, A&A, 427, 157
- Lesaffre, P., Belloche, A., Chièze, J.-P., André, P. 2005, A&A 443, 961
- Lesaffre, P. 2006 Geoph. & Astroph. Fluid Dyn. 100, 265
- Lesaffre, Gerin, Hennebelle, 2007, A&A, 469, 949
- Levrier F., Falgarone E. & Viallefond F., 2006, A&A, 456, 205
- Lipshtat A. & Biham O., 2003, A&A 400, 585
- H.S. Liszt, R. Lucas, A&A, 391, 693 (2002).
- Liszt & Lucas, 1996, A&A, 307, 237
- 1998, A&A, 339, 561
- 2000, A&A, 355, 333L
- 2002, A&A, 384. 1054
- H.S. Liszt, R. Lucas, 2002, A&A, 391, 693
- H. Liszt, 2003, A&A, 398, p.621-634
- H. Liszt, 2006, RSPTA, 364, p. 3049-3062
- H. S. Liszt, R. Lucas and J. Pety, 2006, *A&A,* 448, 253
- H. Liszt, 2007, A&A, 461, p. 205-214
- H. Liszt, 2007, A&A, 476, p. 291-304
- H. Liszt, J. Pety & R. Lucas, 2008, A&A, 486, p. 493-496
- Marcelino, N., Cernicharo, J., Agundez, M., Roueff, E., Gerin, M., Martin-Pintado, J., Mauersberger, R., Thum, C., 2007, ApJ 665, L127
- Maret, S., Bergin, E., 2007, ApJ, 664, 956
- Massi F., De Luca M., Elia D. et al., 2007 A&A 466, 1013
- D. Neufeld et al., ApJ, 580, 278 (2002).
- Neufeld, D. A., Lepp, S., Melnick, G.J. 1995 ApJS, 100, 132
- Oberg, K. et al., 2007, ApJ, 662, L23
- G. Olofsson et al., in preparation (2008).
- Perets H.B. et al. 2007, ApJ 661, L163

- J. Pety, D. Teyssier, D. Fossé, M. Gerin, E. Roueff, A. Abergel, E. Habart, and J. Cernicharo, 2005, A&A 435, 885
- J. Pety, F. Gueth, S. Guilloteau, A. Dutrey, 2006, A&A, 458, 841
- Pety, J., et al. 2007a, *A&A*, 464, L41
- Pety, J., et al. 2007b, Molecules in Space and Laboratory, 13.
- Pety, Liszt & Lucas, 2008, A&A, 489, 219
- Rodriguez-Fernandez NJ, Martin-Pintado J, Fuente A, Wilson TL, Huttemeister S, 2004, A&A 427, 217-229
- Rodriguez-Fernandez NJ, Martin-Pintado J, 2005, A&A 429, 923-938
- Rodriguez-Fernandez NJ, Braine J, Brouillet N, Combes F, 2006, A&A 453, 77-82
- Rodriguez-Fernandez NJ, Combes F, Martin-Pintado J, Wilson T.L., Apponi A. 2006, A&A 455, 963-969
- Röllig et al. 2007, A&A, 467, 187
- E. Roueff, D. Lis, F.F.S. van der Tak, M. Gerin, P.F. Goldsmith, 2005, Astron. Astrophys. 438, 585
- Roueff E., Dartois E., Geballe T. R., Gerin M., 2006, A&A 447, 963
- E. Roueff, E. Herbst, D.C. Lis, T.G. Philips, 2007, Astrophys. J. Letters 661, L159
- E. Roueff, B. Parise, E. Herbst, 2007, Astron. Astrophys. 464, 245
- Scalo & Elmegreen, 2004, ARAA, 42, 275
- Schlegel *et al*. 1998, ApJ, 500, 525.
- Solomon, P. M & Vanden Bout, P.A, 2005, ARAA, 43, 677
- Stantcheva, T., Herbst, E., 2003, MNRAS, 340, 983
- Swings & Rosenfeld, 1937, ApJ, 86, 483.
- Tachihara *et al*. 2000, PASJ, 52, 1147
- Teyssier, D., et al. 2004, *A&A*, 417, 135
- Teyssier, D., et al. 2009, in prep.
- Vasyunin, A. I, Semenov, D. A., 2008, astro-ph 0810.1591
- Wolfire, M. G., Hollenbach, D., McKee, C. F., Tielens, A. G. G., Bakes, E. L. O .1995, ApJ, 443, 152.

7.2. BIOGRAPHIES / CV, RESUME

Partenaire 1 : IRAM

PETY, Jérôme, 6 months/year

- → 38 ans, astronome-adjoint à l'Observatoire de Paris, détaché à l'IRAM/Grenoble.
- → 2008(-2012) : Directeur de l'Action Spécifique ALMA de l'INSU.
- → 2003-présent : Responsable des logiciels de réduction de l'IRAM :
  - Suivi global des projets, des relations avec la direction et avec les utilisateurs.
  - Coordination de l'activité d'une dizaine de personnes : ingénieurs, post-doctorants et chercheurs permanents.
  - Encadrement direct de
    - Deux ingénieurs : E. Reynier et S. Bardeau depuis fin 2006.
    - Un post-doctorant : N. Rodriguez-Fernandez depuis septembre 2006.
  - Encadrement passé de deux post-docs
    - 2005-2007 : P. Hily-Blant, Maître de conférence à Grenoble depuis janvier 2008.
    - 2006-2007 : V. Piétu, CDI à l'IRAM depuis décembre 2007.
- → 2001-2002 : Post-doctorant à l'IRAM/Grenoble, responsable des simulations qui ont contribué à la décision de la construction de l'Attacama Compact Array (12 antennes submillimétriques de 7m plus 4 antennes submillimétriques de 12m), partie de la participation japonaise à ALMA.
- → 2000 : ATER à l'Université Pierre et Marie Curie (Paris VI).
- → 1996-1999 : Thèse sur les structures dissipatives de la turbulence interstellaire.
- → 1994-1996 : Coopérant scientifique au Caltech Submillimeter Observatory (Pasadena, USA).
- → 5 publications significatives sur 18 durant les 5 dernières années (25 publications au total):

- "Imaging Galactic diffuse gas: Bright, turbulent CO surrounding the line-of-sight to NRAO150", J. Pety, R. Lucas, H. S. Liszt, *A&A,* 489, 217.
- "Deuterium fractionation in the Horsehead edge", J. Pety, J. R. Goicoechea, P. Hily-Blant, M. Gerin and D. Teyssier, 2007, *A&A,* 464, L41.
- "Plateau de Bure interferometer observations of the disk and outflow of HH 30", J. Pety, F. Gueth, S. Guilloteau, A. Dutrey, 2006, *A&A,* 458, 841.
- "Comparative chemistry of diffuse clouds. V. Ammonia and formaldehyde", H. S. Liszt, R. Lucas and J. Pety, 2006, *A&A,* 448, 253.
- "Are PAHs precursors of small hydrocarbons in photo-dissociation regions? The Horsehead case", J. Pety, D. Teyssier, D. Fossé, M. Gerin, E. Roueff, A. Abergel, E. Habart, and J. Cernicharo, 2005, *A&A,* 435, 885.

Rodriguez-Fernandez, Nemesio, 6 months/year

- → 34 ans, astronome chargé du développement des algorithmes d'imagerie et de déconvolution de données On-The-Fly interférométriques.
- → 9/2006-présent : Astronome à l'IRAM (Contrat d'usage sur un projet européen financé jusque 2012).
- → 9/2005-8/2006 : ATER à l'Université de Bordeaux I / Observatoire de Bordeaux.
- → 9/2004-8/2005 : ATER à l'Université Paris VII / Observatoire de Paris.
- → 10/2002-9/2004 : Chercheur Marie Curie à l'Observatoire de Paris.
- → 10/1998-9/2002 : Thèse à l'Observatorio Astronomico Nacional et à l'Universidad Complutense de Madrid (Espagne).
- → 4/1997-9/1998 : Master à l'Observatorio Astronomico Nacional.
- → 5 publications significatives durant les 5 dernières années (19 publications au total).
  - "Coupling the dynamics and the molecular chemistry in the Galactic center", Rodriguez-Fernandez NJ, Combes F, Martin-Pintado J, Wilson T.L., Apponi A. 2006, A&A 455, 963-969.
  - "C^+ emission and star formation in the spiral arms of M31", Rodriguez-Fernandez NJ, Braine J, Brouillet N, Combes F, 2006, A&A 453, 77-82.
  - "ISO observations of the Galactic center interstellar medium: ionized gas" Rodriguez-Fernandez NJ, Martin-Pintado J, 2005, A&A, 429, 923-938.
  - "ISO observations of the Galactic center interstellar medium: neutral gas and dust", Rodriguez-Fernandez NJ, Martin-Pintado J, Fuente A, Wilson TL, Huttemeister S, 2004, A&A, 427, 217-229.
  - "The Far-Infrared Spectrum of the Sagittarius B2 Region: Extended Molecular Absorption, Photodissociation, and Photoionization", Goicoechea J, Rodriguez-Fernandez NJ, Cernicharo J, 2004, ApJ 600, 214-233.

Reynier, Emannuel, 6 months/year

- → 43 ans, ingénieur développement, en charge de l'infrastructure des logiciels de réduction de l'IRAM.
- → 2007-présent : Contrat à durée indéterminé à l'IRAM.
- → 1993-2006 : Ingénieur développement chez un éditeur logiciel de FAO (Fabrication Assistée par Ordinateur) : la société ALMA .
- → 1991-1992 : Post-doctorant à l'Université de Grenoble sur des projet européens Speech Maps et Multiworks : traitement et visualisation de la voix et d'image.
- → 1988-1990 : Thèse à l'Institut National Polytechnique de Grenoble : Analyseurs linguistiques pour la compréhension de la parole.

Liszt, Harvey, 3 months/year

- → 62 ans, Scientist (titularisé) National Radio Astronomy Observatory (USA).
- → 2003-présent: NRAO Spectrum Manager:

- → 1995-1998: Project Scientist, Green Bank Telescope
- → 1980-présent:, Scientist, National Radio Astronomy Observatory (USA)
- → 1974: Thèse « CO in HII Regions », Princeton U. (USA)
- → 5 publications significatives durant les 5 dernières années (109 publications au total):
  - "Limits on chemical complexity in diffuse clouds…", H. Liszt, J. Pety & R. Lucas, 2008, A&A, 486, p. 493-496.
  - "Formation, fractionation, and excitation of carbon monoxide in diffuse clouds", H. Liszt., 2007, A&A, 476, p. 291-3004.
  - "Time-dependent H_2 formation and protonation in diffuse clouds", H. Liszt,,2007, A&A, 461, p. 205-214.
  - "$H3^+$ in the diffuse interstellar medium", H. Liszt,, 2006, RSPTA, 364, p. 3049-3062.
  - "Gas-phase recombination, grain neutralization and cosmic-ray ionization in diffuse gas,", H. Liszt, 2003, A&A, 398, p.621-6304.

Partenaire 2 : Obs. de Paris, LERMA-LRA

Gerin, Maryvonne, 6 months/year

- → 48 ans, directrice de recherche deuxième classe CNRS, LERMA/Observatoire de Paris.
- → 2008-present: Head of the LERMA-LRA team.
- → 2007-present: Deputy director of the CNRS interdisciplinary program: Origins of planets and life.
- → 2004-2007: Director of Action Spécifique ALMA
- → 1998-present: co-I of the Herschel/HIFI instrument and PI of the PRISMAS guaranteed time key project.
- → 1995-1996: Visiting associate at the Caltech Submillimeter Observatory.
- → 5 Publications (out of 96):
  - *"Discovery of Interstellar Propylene (CH2CHCH3): Missing Links in Interstellar Gas-Phase Chemistry"*, Marcelino, N., Cernicharo, J., Agundez, M., Roueff, E., Gerin, M., Martin-Pintado, J., Mauersberger, R., Thum, C., 2007, ApJ 665, L127.
  - "*The distribution of ND2H in LDN 1689N*", 2006, Gerin M., Lis D. C., Philipp S., Güsten R., Roueff E., Reveret V., 2006, A&A 454, L63.
  - *"Infrared detection of gas phase formaldehyde towards the high mass protostar W33A*", Roueff E., Dartois E., Geballe T. R., Gerin M., 2006, A&A 447, 963.
  - *"Effects of turbulent diffusion on the chemistry of diffuse cloud"*, Lesaffre P., Gerin M., Hennebelle P. 2007, A&A, 469, 949.
  - *"Low sulfur depletion in the Horsehead PDR"*, Goicoechea J. R., Pety J., Gerin M., Teyssier D., Roueff E., Hily-Blant P., Baek S., 2006, A&A 456, 565.

Lesaffre, Pierre, 3 months/year

- → 33 ans, chargé de recherche deuxième classe au CNRS, travaillant au LERMA-LRA & l'Observatoire de Paris.
- → 2008-2009: Visiting scientist at Institute of Astronomy (Cambridge, UK).
- → 2005-2007: Postdoc at ENS/LRA. MHD in accretion disks.
- → 2002-2005: Postdoc at Cambridge (IoA) and Oxford (Dept. of Physics). From late stellar evolution phases to the ignition conditions of type IA supernovae: the convective Urca process.
- → 1999-2002: PhD thesis at CEA/SAp with J.-P. Chièze. « Aspects dymaniques du milieu interstellaire ».
- → 5 Publications (out of 16):
  - *"Effects of turbulent diffusion on the chemistry of diffuse clouds"*, Lesaffre P., Gerin M., Hennebelle P. 2007, A&A 469, 949.

- *"Temporal evolution of magnetised molecular shocks I. Moving grid simulations"*, Lesaffre, P., Chièze, J.-P., Cabrit, S., Pineau des Forêts, G. 2004, A&A 427, 147.
- *"Time-dependent analytical solutions of quasi-steady shocks with cooling"*, Lesaffre, P. 2006 Geoph. & Astroph. Fluid Dyn. 100, 265.
- *"The dynamical importance of cooling in the envelope of prestellar and protostellar cores*", Lesaffre, P., Belloche, A., Chièze, J.-P., André, P. 2005, A&A 443, 961.
- "*Temporal evolution of magnetised molecular shocks II. Analytics of the steady state and semi-analytical construction of intermediate age*", Lesaffre, P., Chièze, J.-P., Cabrit, S., Pineau des Forêts, G. 2004, A&A 427, 157.

Falgarone, Edith, 3 months/year

- → 60 ans, Directeur de Recherche 1ere classe CNRS at LERMA-LRA.
- → Astronomy Co-I of Herschel/HIFI, Co-I of several HIFI key-projects (GT & OT)
- → 2007-present: Scientific adviser, Agency for research & higher education assessment
- → 1987-90: Visiting associate, Caltech Submillimeter Observatory (USA)
- → 1979 : Thèse d'Etat on "Contagious star formation"
- → 5 Publications (out of 99):
  - *"Dissipative structures of diffuse molecular gas: III Small-scale intermittency of intense velocity shears"*, Hily-Blant, P., Falgarone E. & Pety J. 2008, A&A, in press (2008arXiv:0802.0758).
  - *"Dissipative structures of diffuse molecular gas: II The translucent environment of a dense core"*, Hily-Blant P. & Falgarone E., 2007, A&A, 469, 173.
  - *"Fourier analysis in radio-interferometry"*, Levrier F., Falgarone E. & Viallefond F., 2006, A&A, 456, 205.
  - *"Dissipative structures of diffuse molecular gas: I - Broad HCO+ (J=1-0) emission"*, Falgarone, E., Pineau des Forêts G., Hily-Blant P. & Schilke, P., 2006, A&A, 452, 511.
  - *"First detection of $^{13}CH^+$ (1-0)"*, Falgarone E., Phillips T.G. & Pearson, J., 2005, ApJ, 634, L149.

Goicoechea, Javier R., 3 months/year

- → 31 yrs old, Researcher at Universidad Complutense de Madrid and LAM-CAB/CSIC-INTA Espagne).
- → Responsabilities:
  - 2008-present: One of the two SAFARI's (SPICA Far-IR Instrument) Project Scientists. SPICA is the JAXAS/ESA next generation Far-IR space telescope.
  - Associated member in several Herschel Guaranteed-Time Key Programs (GT-KPs). In particular, coordinator of the "PACS spectral surveys" section within the PRISMAS-GT-KP.
- → 2008-2013: *"Ramon y Cajal"* researcher in Madrid (Spain).
- → 2005-2007: Marie Curie contract at LRA/École Normale Supériure and Observatoire de Paris.
- → 2004-2005: Postdoctoral contract *Ministère délégué à la recherche et nouvelles technologies* at LRA/École Normale Supérieure and Observatoire de Paris.
- → 2003-2004:Postdoctoral contract "*ALMA y HERSCHEL*", at DAMIR/IEM-CSIC (Madrid).
- → 1999-2003:PhD thesis at DAMIR/IEM-CSIC (Madrid) supervised by Prof. José Cernicharo: *"Far-IR Molecular Astrophysics: Interstellar and Circumstellar clouds"*.
- → 5 publications (out of 25):
  - "*Star Formation near PDRs: Detection of a peculiar protostar towards Ced201*" J.R. Goicoechea, O. Berné, M. Gerin. C. Joblin, D. Teyssier, 2008, ApJ, 680, 466.
  - "*The penetration of FUV radiation in molecular clouds*", J.R. Goicoechea, J. Le Bourlot, 2007, A&A, 467, 1.

- "*Low sulfur depletion in the Horsehead PDR*", J.R. Goicoechea, J. Pety, M.Gerin, E. Roueff, D. Teyssier, P. Hily-Blant, S. Baek, 2006, A&A, 456, 565.
- "*The Far-Infrared Spectrum of the Sagittarius B2 Region: Extended Molecular Absorption, Photodissociation, and Photoionization*", J.R. Goicoechea, N.J. Rodriguez-Fernandez, J. Cernicharo, 2004, ApJ 600, 214.
- "*Far-Infrared OH Fluorescent Emission in Sagittarius B2*", J.R. Goicoechea, J. Cernicharo, 2002, ApJ, 576, L77.

Godard, Benjamin, 6 months/year during 1 year.

- → 24 ans, PhD student.
- → 2006-present: PhD thesis at Laboratoire de Radioastronomie (LERMA-LRA) with Edith Falgarone and Guillaume Pineau des Forêts. "Dissipative structures of the interstellar medium: Observations and modelisations".
- → Publication: "" Godard B., Falgarone E., Pineau des Forêts F., 2008, A&A submitted.

De Luca, Massimo, 8 months/year during 2 years.

- → 33 years, post-doctorate researcher at LERMA-LRA.
- → 2007-2008: Indiana University Cyclotron resonance facility.
- → 2004-2007: PhD thesis, at Tor Vergata University « Optical fiber spectroscopy in the near infrared : innovative techniques for the sky background subtraction ».
- → 5 publications out of 8:
  - *"Atomic Jets from Class O sources detected by Spitzer: the case of L1448C "* Dionatos O, Nisini B, Garcia Lopez R, Giannini T, Davis CJ, Smith M, Ray TP, De Luca M, 2008, ApJ in press.
  - " *Spitzer MIPS survey of the young stellar content in the Vela Molecular Ridge-D "* Giannini T, Lorenzetti D., De Luca M. et al, 2007, ApJ 671, 470.
  - *" Near and Far infrared counterparts of Millimeter dust cores in the Vela Molecular ridge D"*, De Luca M, Giannini T., Lorenzettti D.: 2007, A&A 474, 863.
  - *" Star formation in the Vela Molecular Ridge : Large scale mapping of cloud D in the millimeter continuum"*, Massi F., De Luca M., Elia D. et al., 2007 A&A 466, 1013.
  - *"Mapping molecular emission in the Vela Molecular Ridge cloud D : "* Elia D., Massi F., Strafella F., De Luca M., et al., 2007, ApJ 655, 316.

Partenaire 3 : Obs. de Paris, LUTH-ISM

Franck Le Petit, 3 months/year

- → 33 ans, astronome adjoint à l'Observatoire de Paris/LUTH-ISM.
- → Member of the VO-Theory interest group of the IVOA. In this framework, it works on standards to deliver simulation codes and simulation results to the community with the VO standards.
- → 2002-2005: Post-doc at Onsala Space Observatory/ Chalmers University with Pr John Black.
- → 2001-2002: ATER at University of Cergy / LERMA. Research subject: Laboratory experiments to determine H2 formation rate on ISM like dusts.
- → 1998-2001: PhD thesis at LUTH-ISM/Observatoire de Paris with Evelyne Roueff – « HD in the Interstellar Medium »
- → Five Publications (out of 11):
  - 2008 – « Line radiative transfer revisited – Application to PDRs », A&A, 485, 127, Gonzales-Garcia M., Le Bourlot J., Le Petit F., Roueff E.
  - 2006 – *« A model for atomic and molecular interstellar gas: The Meudon PDR code »*, ApJ Supp., Le Petit F., Nehmé C., Le Bourlot J., Roueff E.

- 2005 – « *A far UV study of intersellar gas towards HD 34078: High excitation H2 and small scale structure* », A&A, Boisssé P., Le Petit F., Rollinde E., et al.
- 2004 – « *Tiny-Scale molecular structures in the Magellanic Clouds. I. FUSE, HST and VLT observations* », A&A – André M. K., Le Petit F., Sonnentrucker P., et al.
- 2004 – « *H3+ and other species in the diffuse cloud towards zeta Persei : A new detailed model* », A&A - Le Petit, F, Roueff, E. Herbst, E.

Evelyne Roueff, 3 months/year

→ 66 ans, Astronome Classe exceptionnelle, 1er échelon depuis jan. 2004, Observatoire de Paris/LUTH-ISM.

→ Responsabilities:

- 1996-2004: Chair of the Programme National «Physique et Chimie du Milieu Interstellaire (PCMI) ».
- 1971-1975 and 1995-1999: Elected member of the "Comité National des Universités" (CNU).
- 1981-1985 and 2004-2008: Elected member A of the Comité National du Centre National de la Recherche Scientifique (CNRS).
- 1999-2002 and 2004-2007: Elected member of the "Conseil Scientifique de l'Observatoire de Paris".
- 2004-2008: Member of the board of the european network "The Molecular Universe" of the FP6 program.
- 1998-2002: Member of the board of the FP4 european network "Astrochemistry".
- 2006: Chair of the International Conference "ICAMDATA" (International Conference on Atomic and Molecular DAta And Their Applications), Meudon.
- 2002: Chair of the International Conference "Deuterium in the Universe", Meudon.

→ Prix DESLANDRES 1999 de l'Académie des Sciences (avec G. Pineau des Forêts).

→ 5 publications significatives récentes (sur environ 160 au total) :

- "H_3^+ and other species in the diffuse cloud towards ζ Persei: A new detailed model", Le Petit F., Roueff E. , Herbst E., 2004, *A&A* **417**, 993.
- "Are PAHs precursors of small hydrocarbons in photo-dissociation regions? The Horsehead case", J. Pety, D. Teyssier, D. Fossé, M. Gerin, E. Roueff, A. Abergel, E. Habart, and J. Cernicharo, 2005, *A&A* **435**, 885
- "Interstellar deuterated ammonia : from NH_3 to ND_3", E. Roueff, D. Lis, F.F.S. van der Tak, M. Gerin, P.F. Goldsmith, *Astron. Astrophys.* **438**, 585 (2005)
- "The effect of an increased D/H ratio on deuterium fractionation in the cold interstellar medium", E. Roueff, E. Herbst, D.C. Lis, T.G. Philips, *Astrophys. J. Letters* **661**, L159 (2007)
- "Deuterium fractionation in warm dense interstellar clumps" E. Roueff, B. Parise, E. Herbst, *Astron. Astrophys.* **464**, 245 (2007)

7.3. IMPLICATION DES PERSONNES DANS D'AUTRES CONTRATS / INVOLVEMENT OF PROJECT PARTICIPANTS TO OTHER GRANTS, CONTRACTS, ETC ...

Partenaire	Nom de la personne participant au projet	Personne. Mois	Intitulé de l'appel à projets Source de financement Montant attribué	Titre du projet	Nom du coordinateur	Date début - Date fin
N°1	N.Rodriguez-Fernandez	30	European FP 6	ALMA Enhancement	T. L. Wilson	01/01/2006-31/12/2010
N°1	E. Reynier	60	European FP 6	ALMA Enhancement	T. L. Wilson	01/01/2006-31/12/2010

Partenaire	Nom de la personne participant au projet	Personne. Mois	Intitulé de l'appel à projets Source de financement Montant attribué	Titre du projet	Nom du coordinateur	Date début - Date fin
N°2	P. Lesaffre	9	ANR programme blanc 2006	Magnetohydrodynamique en astrophysique et geophysique numerique et theorique	E. Dormy	01/09/2006-31/08/2010
N°2	E.Falgarone	24	ANR programme blanc 2006	Magnetohydrodynamique en astrophysique et geophysique numerique et theorique	E. Dormy	01/09/2006-31/08/2010
N°2	E. Falgarone	6	ASTRONET 1st joint call	Star formation models and tools: a theoretical database	P. Hennebelle	01/01/2009-31/12/2010

Partenaire	Nom de la personne participant au projet	Personne. Mois	Intitulé de l'appel à projets Source de financement Montant attribué	Titre du projet	Nom du coordinateur	Date début - Date fin
N°3	F. Le Petit	6	ASTRONET 1st joint call	Star formation models and tools: A theoretical database	P. Hennebelle	01/01/2009-31/12/2010
N°3	J. Le Bourlot	6	ASTRONET 1st joint call	Star formation models and tools: A theoretical database	P. Hennebelle	01/01/2009-31/12/2010
N°3	F. Le Petit	9	ANR programme blanc 2009	OEDIPE	A. Dutrey	
N°3	J. Le Bourlot	6	ANR programme blanc 2009	OEDIPE	A. Dutrey	
N°3	E. Roueff	9	ANR programme blanc 2008	OEDIPE	A. Dutrey	

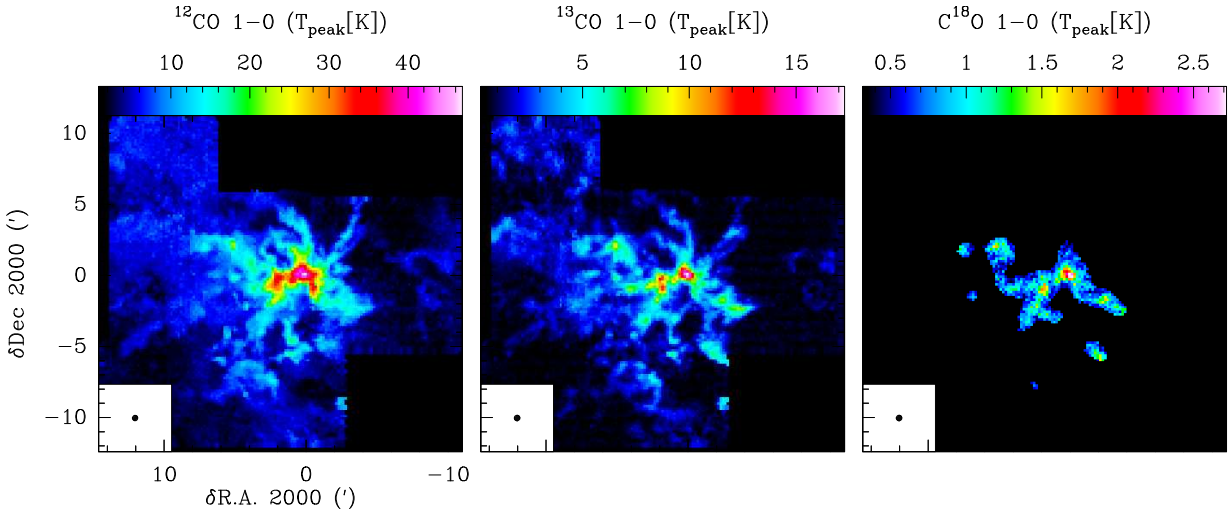

Copyright: Jérôme Pety (IRAM/30m)

Chapitre 7

Spectro-imagerie grand-champ en radio-astronomie (sub)-millimétrique

Les questions scientifiques posées ci-dessus requièrent des observations fiables sur des champs de vue suffisamment larges à la meilleure résolution angulaire possible. Les notions de champs de vue et de résolution dépendent fortement du type d'instrument employé : un télescope unique tel que le 30m de l'IRAM à Pico Veleta près de Grenade ou un interféromètre comme celui du Plateau de Bure.

7.1 Mode télescope unique

Un télescope comme l'IRAM-30m a une résolution angulaire typique de $11''$ à $1\,\mathrm{mm}$ de longueur d'onde. L'instrumentation actuelle permet d'imager $1^{\circ 2}$ en 50 heures avec une sensibilité typique d'environ 0.5 K (T_{A}^{*}) dans des canaux de 0.25 $\mathrm{km\,s^{-1}}$. Pour obtenir ce résultat, il faut acquérir environ 10^6 spectres bruts qui donnent après réduction un cube d'environ 200 000 spectres (si on suppose un échantillonnage critique, c.-à-d. un spectre toutes les $5''$). Chaque spectre a 512 canaux correspondant typiquement soit à une bande passante de 1 GHz ($\sim 1300\,\mathrm{km\,s^{-1}}$ à $1\,\mathrm{mm}$) avec une résolution spectrale de $2\,\mathrm{MHz}$ ($\sim 2.6\,\mathrm{km\,s^{-1}}$ à $1\,\mathrm{mm}$), soit à une bande passante de $10\,\mathrm{MHz}$ à $20\,\mathrm{kHz}$ de résolution.

L'imagerie grand-champ a fait des progrès spectaculaires sur les antennes uniques grâce à deux révolutions successives. A la fin des années 1990, nous sommes passés d'une technique d'observation dite "raster mapping", où les données sont acquises en posant indépendamment sur chaque position indépendante du champ de vue à observer, à la technique d'observation dite "On-The-Fly" (OTF), où les données sont acquises de manière continue en même temps que

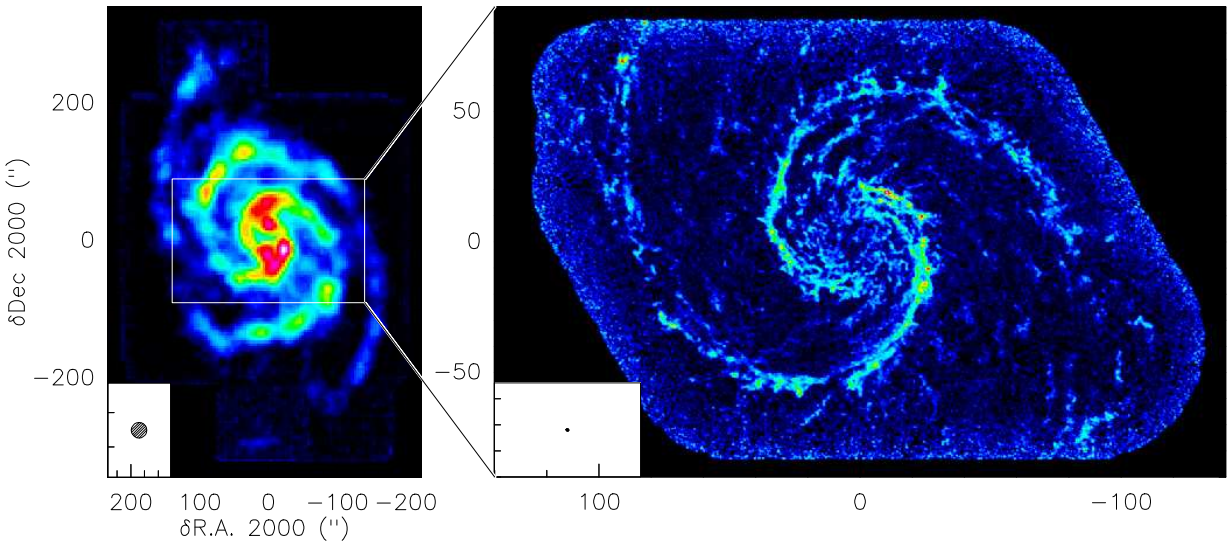

FIG. 7.1 – La célèbre galaxie du tourbillon (M51) observée grâce à l'émission de la raie de ^{12}CO J=1–0 avec l'antenne du 30m à gauche et l'interféromètre du Plateau de Bure à droite. L'image interférométrique a été obtenue dans le cadre d'un grand projet IRAM, nommé PdBI Arcsecond Whirlpool Survey [C6]. Les $8\,\mathrm{kpc}$ centraux sont imagés avec une résolution exceptionnelle de $45\,\mathrm{pc}$ ($\sim 1''$), équivalente à la résolution d'un télescope de 700 m de diamètre ! Le facteur de zoom entre les deux images est environ 25.

l'antenne se déplace sur le ciel. La deuxième révolution a eu lieu dans les années 2002–2003 avec l'arrivée d'HERA à l'IRAM-30m, un récepteur hétérodyne de 18 pixels échantillonnant le plan focal du télescope.

Ces deux révolutions ont conduit à une augmentation du nombre de spectres à traiter d'environ 3 ordres de grandeur en moins de 10 ans. Pour répondre à ce défi, j'ai entrepris à partir de 2003, avec S. Guilloteau (Obs. de Bordeaux/LAB), P. Hily-Blant (post-doc à l'IRAM puis maître de conférence à l'IPAG) et S. Bardeau (ingénieur logiciel à l'IRAM), une refonte complète de la réduction des données d'imagerie à l'IRAM [M1, M7, M13], allant du format de données aux algorithmes de réduction en passant par la visualisation des données brutes et réduites avec l'introduction de nouveaux concepts dans la gestion des données : tables de contenus, sélection fine d'un sous-ensemble de données, outils interactifs de visualisation, etc... Cet effort soutenu a permis de donner une deuxième jeunesse à `CLASS` qui continue aujourd'hui à être le logiciel leader pour la réduction et l'analyse des données spectroscopiques en radio-astronomie : des astronomes du monde entier l'utilisent pour traiter des données d'Herschel/HIFI, de SOFIA/GREAT, d'APEX, de NANTEN, du CSO, du JCMT, du GBT, d'Effelsberg...

7.2 Mode interférométrique

De nombreux objectifs scientifiques[1] requièrent à la fois une haute résolution angulaire (mieux que $1''$), que seuls les interféromètres peuvent fournir aujourd'hui, et un champ de vue

[1]Par exemple, la mesure du contraste bras/interbras dans les galaxies proches, la turbulence du milieu interstellaire, la formation des enveloppes proto-stellaires, les flots moléculaires des objets stellaires jeunes, etc...

suffisemment large, au moins quelques minutes d'arc au carré. La figure 7.1 montre un exemple récent spectaculaire, à savoir l'imagerie avec l'interféromètre du Plateau de Bure d'une surface de $5' \times 3'$ au centre de la célèbre galaxie spirale M51 à une résolution typique de $1''$ [C6]. Or, les antennes de 12m de l'interféromètre d'ALMA donnent un champ de vue instantané relativement petit : $27''$ à $230\,\mathrm{GHz}$ et $9''$ à $690\,\mathrm{GHz}$. L'interférométrie grand-champ est donc un enjeu essentiel pour ALMA.

Historiquement, les interféromètres (sub)-millimétriques actuels (PdBI, CARMA, SMA) ont été construits pour démontrer la viabilité et la nécessité scientifique de l'interférométrie (sub)-millimétrique. L'importance de leurs résultats a conduit à la réalisation du projet ALMA. En contre-partie, l'imagerie grand-champ n'a été un objectif important qu'une dizaine d'années après leur mise en service. A l'inverse, l'imagerie grand-champ a été un objectif prioritaire d'ALMA dès sa phase de conception. Durant les années 2001 et 2002, j'ai étudié l'ajout au concept initial (50 antennes de 12m) d'un réseau 12 antennes de 7m (dit ACA, Atacama Compact Array) pour améliorer des performances d'imagerie grand-champ de l'instrument [M20, M21, M22]. En effet, comme tout interféromètre multiplicatif, ALMA filtre les fréquences spatiales inférieures à environ 1.5 fois le diamètre des antennes (ici 18m) et l'utilisation des antennes en mode puissance totale (auto-corrélation) ne permet de récupérer que la fréquence spatiale à 0m. L'objectif du réseau ACA est de combler le manque de mesures des fréquences spatiales aux alentours de 10m. Ces études réalisées en collaboration avec F. Gueth (IRAM) et S. Guilloteau (alors "Project Scientist" d'ALMA) ont été essentielles dans la décision de l'ajout d'ACA au projet de base pour un coût estimé entre 100 et 150 Meuros. Les outils que nous avons développés ont été par la suite utilisés par nos collègues japonais pour affiner le design d'ACA [M14].

Par ailleurs, l'imagerie grand-champ en interférométrie millimétrique est aujourd'hui obtenue avec une technique classique, dite "stop-and-go mosaicing". Cette technique est comparable au "raster mapping" avec une antenne unique. Bien qu'elle permette de faire de l'imagerie grand-champ, cette technique limite à la fois l'efficacité[2] et le champ de vue observable. L'imagerie grand-champ est ainsi aujourd'hui au même point en mode interférométrique qu'elle l'était en mode télescope unique au début des années 1990. Nous sommes donc potentiellement à la veille d'une révolution dans ce domaine avec l'introduction du mode d'observation OTF en interférométrie. Hormis les problèmes techniques (synchronisation d'antennes en mouvement simultané, augmentation importante du débit de données, etc...), l'absence d'algorithmes d'imagerie et de déconvolution dédiés est une des raisons principales pour lesquelles le mode d'observation OTF n'a, à notre connaissance, jamais été utilisé auparavant sur un interféromètre millimétrique. Dans le traitement d'observations classiques ("stop-and-go mosaicing"), les visibilités sont imagées indépendamment champ par champ avant que les images produites ne soient combinées linéairement. La quantité de données produites par les observations OTF exclut une telle approche. Je propose avec N. Rodriguez-Fernandez un traitement dans lequel les visibilités observées sur diverses positions du ciel sont rééchantillonnées sur une grille régulière à la fois dans le plan du ciel et dans le plan uv[3] avant d'être imagées et déconvoluées [A7]. Cette inversion des opérations permet de traiter le problème par une réduction de la quantité de données d'au moins un ordre de grandeur. Plus fondamentalement, nous montrons qu'elle introduit aussi un changement conceptuel important dans la manière de penser l'imagerie grand-champ en interférométrie millimétrique.

[2]Car le signal n'est pas intégré lorsque les antennes passent d'une position à une autre.

[3]Le plan uv est l'espace où sont mesurées les visibilités interférométriques. Ce plan est lié au plan de Fourier.

Ce travail a été réalisé dans le cadre d'un contrat européen (6ème PCRD) "ALMA Enhancement" conduit par l'ESO de 2006 à 2011, contrat dans lequel l'IRAM était responsable (pour un budget de 900 keuros) du commissionning du mode d'observation OTF à l'interféromètre du Plateau de Bure avant de transférer l'expertise au projet ALMA. En 2011, l'équipe comprenait deux ingénieurs logiciels (M. Lonjaret, J.C. Roche), un post-doc (N. Rodriguez-Fernandez) et deux astronomes (F. Gueth et moi-même). Dans ce projet de recherche, deux objectifs sur trois ont été réalisés : 1) la réalisation d'observations OTF au Plateau de Bure, et 2) la livraison au projet ALMA d'un nouvel algorithme d'imagerie [M2]. Il reste la mise au point d'un algorithme de déconvolution adapté que l'IRAM va continuer de développer sous ma direction au-delà du contrat initial pour ses propres besoins.

7.3 Le futur de la radio-astronomie (sub-)millimétrique

Conscient du potentiel des récepteurs multi-pixels pour l'imagerie grand-champ, l'IRAM a une politique de recherche et développement offensive dans ce domaine depuis plus de 10 ans. Cela a conduit à la réalisation d'HERA à l'IRAM-30m. Des programmes de R&D sont aujourd'hui en cours tant au niveau des récepteurs pour miniaturiser les mélangeurs (FP7 AMSTAR+) qu'au niveau des spectromètres pour obtenir de grandes résolutions spectrales sur l'ensemble des bandes passantes délivrées par les récepteurs.

Ces projets vont déboucher dans les 5 ans à venir par une nouvelle génération de récepteurs multi-pixels à l'IRAM-30m : un récepteur de 50 pixels à 3 mm (les éléments de base étant soit des mélangeurs SIS soit des amplificateurs HEMT) et un successeur d'HERA de 98 pixels à 1 mm (à base de mélangeurs SIS). Le remplacement des auto-corrélateurs par des spectromètres à transformée de Fourier a permis de gagner un ordre de grandeur sur le nombre de canaux par spectre permettant de couvrir soit 16 GHz pour les récepteurs monopixels (EMIR) soit 1 GHz pour HERA de bande passante par pixel à 200 kHz de résolution. Ces développements conduisent à un nouvel accroissement de la quantité de données par un facteur environ 50, auquel l'équipe des développeurs de `CLASS` fait face par de nouvelles modifications en profondeur du logiciel.

En ce qui concerne le Plateau de Bure, la priorité dans les 5 prochaines années va au projet NOEMA, qui consiste à

- doubler le nombre d'antennes de 15 m (de 6 à 12, impliquant un doublement de la surface collectrice) ;
- doubler la plus grande ligne de base (de 800 à 1600 m), et donc à doubler la résolution angulaire actuelle ;
- utiliser une instrumentation innovante, en particulier une nouvelle génération de récepteurs qui quadruple la bande passante totale (de 8 GHz à 32 GHz), impliquant une sensibilité 4 fois plus grande en continuum et la possibilité d'observer simultanément 4 fois plus de raies.

L'imagerie grand-champ bénéficiera directement de ces améliorations grâce au quadruplement du nombre de lignes de base, ce qui permettra une bien meilleure qualité d'images à temps d'observation égal. Le budget acquis en ce moment (33 Meuros) permet de financer 4 antennes supplémentaires, le remplacement de tous les récepteurs et un corrélateurs pour 12 antennes. L'addition de 2 antennes supplémentaires ainsi que le doublement de la plus grande ligne de base sont soumises à la contribution d'un partenaire exterieur aux pays fondateurs de l'IRAM.

Dans ce projet, j'ai été nommé mi-2011 responsable de l'ensemble des logiciels scientifiques[4].

La réalisation de récepteurs multi-pixels pour l'interféromètre du Plateau de Bure sera une suite logique au projet NOEMA que les actions de R&D entreprises aujourd'hui permettront de mener à bien, d'autant plus que la loi de Moore permet de gagner un ordre de grandeur tous les 6 ans dans la corrélation numérique des signaux. De plus, la taille des cabines des antennes de Bure permet d'abriter à la fois des récepteurs mono-pixels, multi-fréquences, et un récepteur multi-pixel, mono-fréquence, donnant une flexibilité scientifique similaire à celle de l'IRAM-30m d'aujourd'hui. Au niveau algorithmique, les développements actuels que nous menons pour mettre en œuvre le mode d'observation interférométrique grand-champ, dit On-The-Fly, sont un préalable à l'utilisation de récepteurs multi-pixels en interférométrie. Un autre défi algorithmique sera le développement des méthodes de calibration en amplitude et en phase de ces récepteurs multi-pixels.

[4]Le projet NOEMA est divisé en 8 packages : 1) suivi logistique, 2) construction des antennes, 3) récepteurs, 4) corrélateur, 5) logiciels de contrôle, 6) logiciels scientifiques (acquisition, réduction, analyse), 7) commissioning, 8) réseaux et archivage.

IRAM Memo 2005-1

CLASS evolution: I. Improved OTF support

P. Hily-Blant[1], J. Pety[1,2], S. Guilloteau[3]

1. IRAM (Grenoble)
2. LERMA, Observatoire de Paris
3. L3AB, Observatoire de Bordeaux

Dec, 20th 2005
Version 1.0

Change Record

Revision	Date	Section/ Page affected	Remarks
1	2005-12-20	All	Initial version

Contents

1 CLASS internal data format **4**
1.1 Pointed observation . . . 4
1.2 On–The–Fly observation . . . 4

2 Limitations, ease of use and efficiency **6**
2.1 Philosophy . . . 6
2.2 Implications . . . 6
2.2.1 New OTF data format . . . 6
2.2.2 Memory limitations . . . 6
2.3 Warning . . . 7

3 Large dataset processing **7**
3.1 Basic idea . . . 7
3.2 Listing and Table of Content . . . 7
3.3 Index consistency . . . 9
3.4 Visualization . . . 9
3.5 Sorting . . . 10
3.6 Baseline fitting . . . 10
3.7 Interactive data exploration . . . 12

4 Miscellaneous changes **15**
4.1 New defaults . . . 15
4.2 Command names . . . 15
4.3 Griding and spectra cube visualization . . . 15
4.4 `PLAIT` algorithm . . . 16

5 CLASS90 for beta testers **16**

Abstract

CLASS is a **GILDAS**[1] software for reduction and analysis of (sub)–millimeter spectroscopic data. It is daily used to reduce spectra acquired with the IRAM 30m telescope. **CLASS** is currently used in many other facilities (*e.g.* CSO, HHT, Effelsberg) and it is considered for use by Herschel/HIFI. **CLASS** history started in 1983. As a consequence, it was written in FORTRAN 77 and tailored to reduce pointed observations. On–The–Fly support was added in the 90s but it showed limitation as the quantity of OTF data increased quickly. One year ago, we decided to fully rewrite **CLASS** in FORTRAN 90 with the 3 following goals: 1) clarifying satisfying features with backward compatibility in mind, 2) improving code readability to simplify maintenance and 3) easing reduction of large OTF data sets. This memo is describing the *current* state of affair with a particular emphasis on changes in the program behavior. Future foreseen changes (linked to the increase of receiver instantaneous bandwidth like an improved conversion from frequency to velocity axis) will be described in a future memo.

1 CLASS internal data format

Observations with a single dish telescope may be divided in two categories:

1. Pointed observation: The telescope beam is pointed toward a fixed position of the source during the signal integration. In its simplest form, the scan is composed of a spectrum whose intensity is accumulated during the scan duration. Nothing prevents more complex scan definitions, *e.g.* a scan composed of several shorter integrations, all at the same position on the sky.

2. On-The-Fly (OTF) observation: The telescope beam continuously drifts on source during the integration to make a map of the source. The scan is then composed of set of spectra regularly dumped (typically every 1 second) during a contiguous portion of time (typically 10 minutes). Each dumped spectra corresponds to a different position on the sky.

1.1 Pointed observation

Only two minor changes happened into the data format of a scan containing a single spectra. The data is stored as a header (divided in independent sections) and the data. We have added: 1) the three parameters associated to the descriptive coordinate system (2 parameters for the system center + the system position angle) to be able to go from this descriptive coordinate system to a standard (*e.g.* equatorial) coordinate system and 2) a subscan number. This subscan number is foreseen to always be greater than 1. There is one exception: when **CLASS90** read data in old format, the subscan number is zero and a warning is issued.

1.2 On–The–Fly observation

In **CLASS77**, an OTF scan is stored as a header and a 2 dimensional array containing the intensities of dumped spectra as a function of time plus a given number of columns (named DAPS for Data Associated Parameters) containing header parameters whose values vary during the scan (*e.g.* the position on the sky, date from beginning of scan). Therefore, all the dumped spectra share the same header in **CLASS77**.

In **CLASS90**, each dumped spectra of an OTF scan is stored as a pointed observation with its own header and data. The concept of scan is kept, as all dumped spectra inside an OTF scan share the same scan number. They are tagged by a subscan number whose value is incremented for each new OTF line (both to enable easy selection of a single line inside one OTF scan, and to ensure consistency with the 30m numbering). The dumped spectra are also tagged by a unique observation number. This new OTF data format has several advantages:

[1] `http://www.iram.fr/GILDAS`

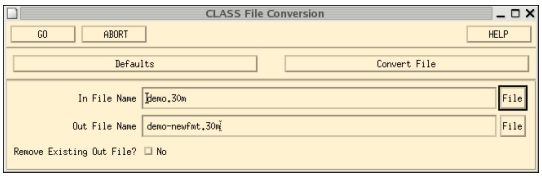

Figure 1: File conversion tool to convert from **CLASS77** to **CLASS90** data format. The action of this widget is equivalent to "`go class-convert infilename outfilename`" command at prompt level.

- It considerably simplifies the source code, as operations on OTF scan are not a special case anymore. While some operations need the information that a dumped spectra is part of an OTF scan, OTF scans may be seen as a collection of independent spectra for many basic operations.
- The granularity of operations is much finer. For instance, access and work on any dumped spectra is now obvious. Moreover, it is obvious in this framework to store the windows used for baseline fitting for every dumped spectra.
- The scan/subscan organization can be generalized to other kind of observation (rasters, cross scans, ...)

For backward compatibility, **CLASS90** will be able to read the old OTF data format. Nevertheless, it will then stubbornly refuse to do anything else with it than to rewrite the data in the new OTF data format. This is easily done with the following commands:

```
LAS90> file in  12co21-oldfmt.30m
LAS90> file out 12co21-newfmt.30m new
LAS90> set line 12co(2-1)
LAS90> find
LAS90> for ientry 1 to found
LAS90>    get n
LAS90>    write
LAS90> next
```

For the user's convenience, **CLASS90** proposes a widget that implements this conversion with several additional safeguards (as avoiding to convert again data already written in new format). Fig. 1 shows this widget available in the main **CLASS90** menu. This widget is just a front-end to a procedure launched by the "`go class-convert infilename outfilename`" command. This procedure can be used in scripts to automate conversion.

Since the advent of the New Control System (NCS) of the 30m in fall 2005, the reading of raw data and the chopper calibration is done by **MIRA** (developed by H. Wiesemeyer) which directly writes data in the **CLASS90** format. For data acquired previously (with the Old Control System), the conversion step is mandatory. Indeed, the reading of raw data format and the chopper calibration were done by **OTFCAL** (maintained by A. Sievers), which still writes OTF scans using the **CLASS77** data format.

2 Limitations, ease of use and efficiency

2.1 Philosophy

Several qualities are desirable for a reduction software: portability, stability, ease of maintenance, ease of use, short learning curve, good documentation, time and storage efficiency, best functionalities, no arbitrary limitations and last but not least backward compatibility. As we are manpower limited, it is impossible to get the perfect software. We thus have to make some compromises to get the closest possible to perfect. For instance, we rewrote **CLASS** in FORTRAN 90 although this may bring short-term instability because this clarifies the program structure and it thus eases future maintenance (key to long term stability). We also favor functionalities over efficiency with the idea that **CLASS** users will be happier to be able to do something a bit inefficiently than to be stuck. Obviously, we always keep storage and time efficiency in mind and we are willing to improve the situation when a widely used feature is too inefficient. Finally, if we make all our effort to have a 100% backward compatibility in data format so that users will be able to do something useful even with even very old data, we can not ensure full backward compatibility on defaults and command names. The easiest way to implement new features (required by improved instrumentation) is sometimes to change defaults and command names though we try to refrain from making those kind of changes without good reasons.

2.2 Implications

2.2.1 New OTF data format

One of the major change in **CLASS90** is the new way OTF data are stored. While advantages have already been described, the main inconvenient is an increase of the size of the data on disk and RAM memory by at most 20-30%, due to the new individual headers (Note that this increase becomes negligible for spectra with a large number of channels).

Data access time is less problematic as the data has always been buffered by **CLASS**. In fact, we choose this OTF data format to have a much more user-friendly approach to OTF processing. Indeed, it maybe (but still has to be proven...) that the CPU time will be a bit larger with **CLASS90** than with **CLASS77** for perfect data. However, our main goal is to decrease the human time spent on data reduction to deal with the unavailable problems.

2.2.2 Memory limitations

Almost all processing steps are available spectrum per spectrum because this is a very powerful way to work around the limitation of your computer RAM memory. There are two main exceptions:

- When opening a file, **CLASS** is buffering information (source name, line name, telescope name, scan number, offset, etc...) on each observations of the file to speed next `find` commands. This buffer has a fixed sized to avoid code complexity. This limits the number of observations that **CLASS90** can read/write during one session. The default maximum number of observations is currently set to 100 000 which amounts to about 5 MB of RAM memory. This number can be set to a larger value through the `CLASS_IDX_SIZE` logical variable in your `$HOME/.gag.dico` configuration file as it is probable that the default value is too small with the largest maps observed today.
- In **CLASS90**, it is also possible to load a whole index as a single 2D array for further visualization and processing (see below). There is no limitation on the number of dumped spectra loadable, apart from the previous limitation and the RAM memory of your computer.

Except from the index buffer, all other **CLASS90** buffers are now dynamically allocated, in particular the buffer R & T containing the spectra data. This means that the number of channels of a spectrum is now unlimited which is a useful feature for line surveys.

2.3 Warning

When processing a small number of spectra, **CLASS90** will be quick on whatever kind of computer. Now, if **CLASS90** users needs to process 300 000 dumped spectra, they should then be prepared to use a powerful computer (with lot's of RAM to avoid swapping) and to wait during processing, whichever software (in particular whichever version of **CLASS**) they are using.

Moreover, flexibility is favored in **CLASS90**. This means that the same things may be done in many different, more or less efficient ways. It will take time to the **CLASS90** community to learn what should be or not be done to ensure efficiency. For instance, loading 300 000 with the `LOAD` command (see below) on a laptop is probably going to take a while (if possible at all due to limitation in RAM memory). However, this possibility does not even exist within **CLASS77**.

3 Large dataset processing

It is today possible with the IRAM–30 m to map a square degree field in ^{12}CO (J=2–1). As an order of magnitude, this gives a final spectra cube of about 10^6 spectra with a slight oversampling of $4''$.

3.1 Basic idea

An observer who has just spent a few hours doing OTF observation of the same source may want to visualize all the dumped spectra at once even though they do not belong to the same scan. This was impossible in **CLASS77**. In **CLASS90**, it is now possible to load all the individual spectra currently in the index as a 2D array for future work, in particular visualization.

3.2 Listing and Table of Content

Before visualizing, the user needs to know what kind of data is available. The `LIST` command is commonly used to easily see the content of the current index. However, this command outputs one line per observation in **CLASS90** which is useless when dealing with thousands of observations. The `LIST /SCAN` command reintroduces the **CLASS77** way of listing an index, *i.e.* one line per scan and setup (*i.e.* unique combination of source, line and telescope names). `LIST /SCAN /BRIEF` lists the scan with the number of associated observations. These three possibilities respectively give

```
LAS90> list
I-LISTE, Current index:
 197; 3 B0355+508    12CO(1-0)    30M-V01-A100   -109.1   -100.0 Eq  9608; 1
 198; 3 B0355+508    12CO(1-0)    30M-V01-A100   -106.1   -100.0 Eq  9608; 1
 199; 3 B0355+508    12CO(1-0)    30M-V01-A100   -103.0   -100.0 Eq  9608; 1
 200; 3 B0355+508    12CO(1-0)    30M-V01-A100   -100.5   -100.0 Eq  9608; 1
 201; 3 B0355+508    12CO(1-0)    30M-V01-A100    -97.5   -100.0 Eq  9608; 1
 ...
 270; 3 B0355+508    12CO(1-0)    30M-V02-B100   -109.1   -100.0 Eq  9608; 1
 271; 3 B0355+508    12CO(1-0)    30M-V02-B100   -106.1   -100.0 Eq  9608; 1
 272; 3 B0355+508    12CO(1-0)    30M-V02-B100   -103.0   -100.0 Eq  9608; 1
 273; 3 B0355+508    12CO(1-0)    30M-V02-B100   -100.5   -100.0 Eq  9608; 1
 274; 3 B0355+508    12CO(1-0)    30M-V02-B100    -97.5   -100.0 Eq  9608; 1
 ...
 343; 3 B0355+508    12CO(2-1)    30M-V03-A230   -109.1   -100.0 Eq  9608; 1
 344; 3 B0355+508    12CO(2-1)    30M-V03-A230   -106.1   -100.0 Eq  9608; 1
 345; 3 B0355+508    12CO(2-1)    30M-V03-A230   -103.0   -100.0 Eq  9608; 1
 346; 3 B0355+508    12CO(2-1)    30M-V03-A230   -100.5   -100.0 Eq  9608; 1
 347; 3 B0355+508    12CO(2-1)    30M-V03-A230    -97.5   -100.0 Eq  9608; 1
```

```
...
416; 3 B0355+508    12CO(2-1)    30M-V04-B230   -109.1   -100.0 Eq  9608; 1
417; 3 B0355+508    12CO(2-1)    30M-V04-B230   -106.1   -100.0 Eq  9608; 1
418; 3 B0355+508    12CO(2-1)    30M-V04-B230   -103.0   -100.0 Eq  9608; 1
419; 3 B0355+508    12CO(2-1)    30M-V04-B230   -100.5   -100.0 Eq  9608; 1
420; 3 B0355+508    12CO(2-1)    30M-V04-B230    -97.5   -100.0 Eq  9608; 1
...
661; 3 B0355+508    12CO(1-0)    30M-V01-A100   -109.8    -90.0 Eq  9609; 1
662; 3 B0355+508    12CO(1-0)    30M-V01-A100   -106.7    -90.0 Eq  9609; 1
663; 3 B0355+508    12CO(1-0)    30M-V01-A100   -103.6    -90.0 Eq  9609; 1
664; 3 B0355+508    12CO(1-0)    30M-V01-A100   -101.2    -90.0 Eq  9609; 1
665; 3 B0355+508    12CO(1-0)    30M-V01-A100    -98.1    -90.0 Eq  9609; 1
...
734; 3 B0355+508    12CO(1-0)    30M-V02-B100   -109.8    -90.0 Eq  9609; 1
735; 3 B0355+508    12CO(1-0)    30M-V02-B100   -106.7    -90.0 Eq  9609; 1
736; 3 B0355+508    12CO(1-0)    30M-V02-B100   -103.6    -90.0 Eq  9609; 1
737; 3 B0355+508    12CO(1-0)    30M-V02-B100   -101.2    -90.0 Eq  9609; 1
738; 3 B0355+508    12CO(1-0)    30M-V02-B100    -98.1    -90.0 Eq  9609; 1
...
807; 3 B0355+508    12CO(2-1)    30M-V03-A230   -109.8    -90.0 Eq  9609; 1
808; 3 B0355+508    12CO(2-1)    30M-V03-A230   -106.7    -90.0 Eq  9609; 1
809; 3 B0355+508    12CO(2-1)    30M-V03-A230   -103.6    -90.0 Eq  9609; 1
810; 3 B0355+508    12CO(2-1)    30M-V03-A230   -101.2    -90.0 Eq  9609; 1
811; 3 B0355+508    12CO(2-1)    30M-V03-A230    -98.1    -90.0 Eq  9609; 1
...
880; 3 B0355+508    12CO(2-1)    30M-V04-B230   -109.8    -90.0 Eq  9609; 1
881; 3 B0355+508    12CO(2-1)    30M-V04-B230   -106.7    -90.0 Eq  9609; 1
882; 3 B0355+508    12CO(2-1)    30M-V04-B230   -103.6    -90.0 Eq  9609; 1
883; 3 B0355+508    12CO(2-1)    30M-V04-B230   -101.2    -90.0 Eq  9609; 1
884; 3 B0355+508    12CO(2-1)    30M-V04-B230    -98.1    -90.0 Eq  9609; 1
LAS90> list /scan
I-LISTE, Current index:
 B0355+508    12CO(1-0)    30M-V01-A100   -109.1:+108.2   -100.0 Eq  9608; 73
 B0355+508    12CO(1-0)    30M-V02-B100   -109.1:+108.2   -100.0 Eq  9608; 55
 B0355+508    12CO(2-1)    30M-V03-A230   -109.1:+108.2   -100.0 Eq  9608; 73
 B0355+508    12CO(2-1)    30M-V04-B230   -109.1:+108.2   -100.0 Eq  9608; 73
 B0355+508    12CO(1-0)    30M-V01-A100   -109.8:+107.5    -90.0 Eq  9609; 73
 B0355+508    12CO(1-0)    30M-V02-B100   -109.8:+107.5    -90.0 Eq  9609; 73
 B0355+508    12CO(2-1)    30M-V03-A230   -109.8:+107.5    -90.0 Eq  9609; 73
 B0355+508    12CO(2-1)    30M-V04-B230   -109.8:+107.5    -90.0 Eq  9609; 73
LAS90> list /scan /brief
I-LISTE, Current index:
 9608; 274   9609; 292
```

It is also useful to get all the available setups of a file at a glance. This is available through the "`list in /toc`" command

```
LAS90> file in 12co21-newfmt.30m
LAS90> list in /toc
I-LIST, Input index:
 Number of sources......   1
     B0355+508          17210
 Number of Lines........   2
```


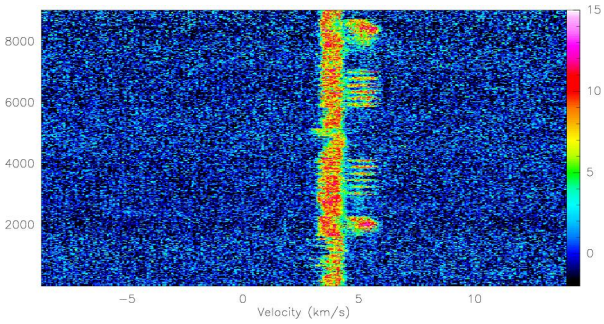

Figure 2: Time series of the intensity as a function of velocity of 9000 dumped spectra part of 200 OTF scans. Only 7 commands are needed to obtain this result, 4 of which are mandatory and 2 of which just there to improve the visual aspect.

```
    12CO(1-0)          8596
    12CO(2-1)          8614
Number of backends.....   4
    30M-V01-A100       4307
    30M-V02-B100       4289
    30M-V03-A230       4307
    30M-V04-B230       4307
Number of setups.......   4
    B0355+508    12CO(1-0)    30M-V01-A100       4307
    B0355+508    12CO(1-0)    30M-V02-B100       4289
    B0355+508    12CO(2-1)    30M-V03-A230       4307
    B0355+508    12CO(2-1)    30M-V04-B230       4307
```

3.3 Index consistency

Loading a whole index as a 2D array implies that all the spectra are consistent (basically the same coordinate system and the same frequency axis) to obtain meaningful results. A new command, named `LAS\CONSISTENCY`, was introduced to check the consistency of all the spectra of the current index. The source name, the source position, the line name and the frequency axis are checked by default. It is possible to avoid one or several of those checks with the `NOCHECK` option. The commands which work on the whole index (*e.g.* `LOAD` or `TABLE`) automatically trigger the check of the index consistency, if this check was not already done previously.

3.4 Visualization

The following list of commands is all you need to plot as a single image (see Fig. 2) 9000 dumped spectra part of 200 OTF scans observed in ∼ 4 hours.


```
LAS90> lut rainbow3
LAS90> file in 12co21-newfmt.30m
LAS90> find
LAS90> load
LAS90> set mode y -2 15
LAS90> plot /index
```

3.5 Sorting

In the previous visualization, the dumped spectra were order according to their observation number, which most often corresponds to the observing time sequence. However, it often happens that two sequential OTF scans belongs to 2 far-away part of the same source. It is thus desirable to be able to sort dumped spectra in the index by coordinates. In **CLASS90**, the "`set sort keyword`" command defines the sorting that will be applied when the index will be built by the next `find` command. In particular, the `keyword` may be `lambda` or `beta`. Fig. 3 shows the results of the following commands

```
LAS90> set mode y 0 8
LAS90> set angle second
LAS90> set sort beta
LAS90> for ilambda -470 to -260 by 30
LAS90>    find /range 'ilambda' 'ilambda+10' * *
LAS90>    if (found.ne.0) then
LAS90>       load
LAS90>       plot /index
LAS90>       g\draw text 0 1 'ilambda'"' < lambda < "'ilambda+10'"'" 5 /char 8
LAS90>       list
LAS90>       pause
LAS90>    endif
LAS90> next
```

which enables to view the dumped spectra with a good continuity in intensity.

3.6 Baseline fitting

Other operations than visualization may benefit from the definition of the 2D array. The first coming in mind is baseline fitting. It is well known that this requires the separation of the spectrum channels between signal and baseline, in other words the definition of baseline windows. When dealing with a small number of spectra, the windows are often defined separately on each spectrum. When dealing with thousands of spectra, we still need to define windows adapted to each individual spectrum as large velocity gradients (*e.g.* in galaxies) may quickly move in frequency the separation between signal and baseline from one spectrum to another. However, defining windows on each individual spectrum is both impractical and inefficient as this does not take into account spatial homogeneity (really useful in case of moderately weak lines). We thus enable the definition of spectral windows directly on the 2D plot with polygons.

The following set of commands are used to define the polygon and to fit the baselines

```
LAS90> file out 12co21-newfmt-base.30m new
LAS90> plot /index
LAS90> set window /polygon
LAS90> for iobs 1 to found
LAS90>    get next
LAS90>    base
LAS90>    write
LAS90> next
```


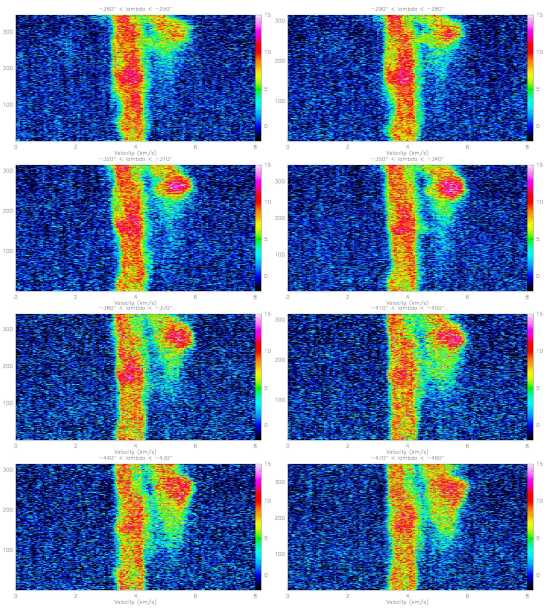

Figure 3: Beta sorted series of dumped spectra intensities as a function of the velocity. For each panel, only the spectra with a lambda offset belonging to the same spatial resolution bin is shown. This is the way to ensure the best possible intensity continuity from one to another dumped spectra.

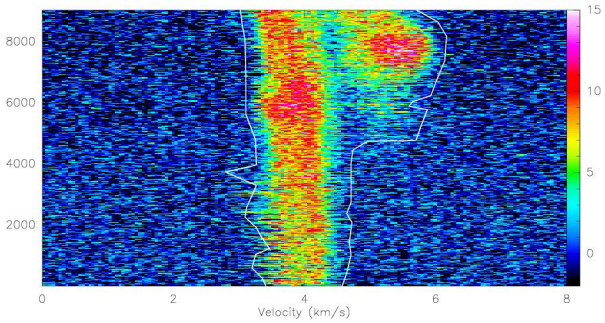

Figure 4: Beta sorted series of dumped spectra intensities as a function of the velocity. All the lambda offsets are shown here, implying the presence of horizontal stripes in the image. This representation of the data nevertheless enable a very quick (even though not optimal) first data reduction by the definition of baseline windows through a polygon drawing.

Up to 21 independent polygons may be defined. The polygon boundaries are directly converted to individual windows for each dumped spectra. Those windows are stored in the **set%window SIC** array which is then used by the **base** and **write** commands. In the end, each spectrum will have its own baseline window stored in its header. Each polygon is also stored in a separate file for the user's convenience.

3.7 Interactive data exploration

Scripting is important for memory and/or for automating data processing. However, repeatedly typing the same commands quickly becomes cumbersome in particular when discovering new data. Interactive exploration of data is now available through the following set of commands

```
LAS90> file in 12co21-newfmt-base.30m
LAS90> set source YOUR-SOURCE
LAS90> set line 12CO(2-1)
LAS90> set tele 30M-V03-A230
LAS90> go explore
```

"**go explore**" enables loop visualization of data scan by scan or by offset range (as in section 3.5). It is possible to visualize a 2D image or the average of the observations. Zoom are easily accessible as well as popups of spectra and drifts. An up-to-date summary of the possibility is available by typing **input explore**. "**go explore**" is best used in conjunction with the possibility to easily select a consistent setup. To do this (*i.e.* exploring a subset of its input data file), the user must select this setup through the **set** command because the "**go explore**" script issues many intermediate **find** commands. Both functionalities (selection and exploration) are merged in the **Explore Data File** widget of the **CLASS90** main menu. Examples are given in Figs. 5 to 7.

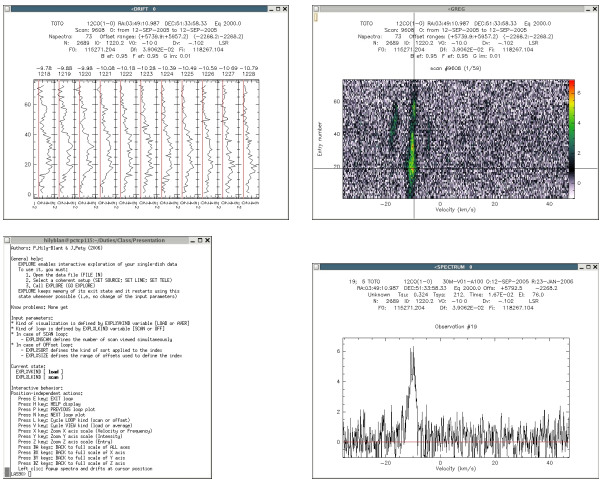

Figure 5: Data exploration by selecting **Explore Data File** from the **CLASS90** main menu or by typing **go explore** at the **CLASS90** prompt. Upper right: The 73 dumped spectra of scan 9608. Upper left: Intensity as a function of entry number, in ten contiguous velocity channels centered on the channel shown as the vertical line of the upper right panel. Bottom right: Spectrum corresponding to entry number 19 defined as the horizontal line of the upper right panel. Bottom left: On-line documentation of this interactive tool.

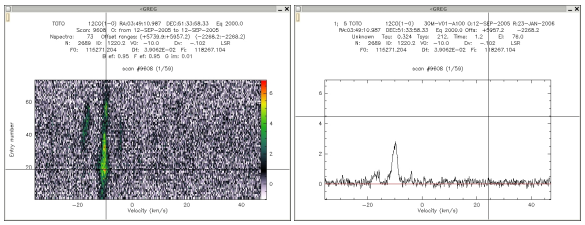

Figure 6: Data exploration by scan. Left: 2D image of all dumped spectra of the scan. Right: Averaged spectrum computed on all dumped spectra of the scan.

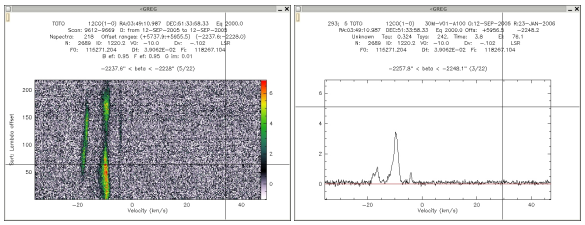

Figure 7: Same as Fig 6 except that the displayed data belong to a beta offset range.

4 Miscellaneous changes

4.1 New defaults

A few defaults has been changed **CLASS77** and **CLASS90**. They are summarized in Table 1. We are

Default kind	Old names	New names
Extension	.bur	.30m
Angular unit	arcminute	arcsecond
Epoch	1950.00	2000.00

Table 1: Correspondence between changed defaults in **CLASS77** and **CLASS90**.

distribution a **CLASS** procedure named `old-set-defaults.class` which reset the **set** default in the **CLASS77** way.

4.2 Command names

Due to its long history, **CLASS77** command name were sometimes awkward, *e.g.* the **GAUSS** command which was launching a fit even though the fitting function was not Gaussian! We made the minimum number of changed to avoid disturbing too much long standing habits of **CLASS** users. We are also furnishing a **CLASS** procedure named `old-command-names.class` which aliases new and old names through the use of **GILDAS** symbols. This is distributed for maximum backward compatibility, *e.g.* to enable use of **CLASS77** within **CLASS90** (this is not foolproof though). However, it is clear that old command names are obsolete and *we advise users against the use of the aliases*. In particular, users' new procedures should use new command names. Table 2 displays an exhaustive list of correspondence between old and new names. The fit–related commands have been gathered into a separate language named **FIT**. The **GAUSS** and **FIT** commands have been replaced by the more explicit **MINIMIZE** and **VISUALIZE** names. For logical reasons, **SUM** has been replaced by the **AVERAGE**. Due to the new way of dealing with OTF data, the **RECORD** command is now obsolete and will disappear soon. The **GRID** command is also obsolete as its functionalities have been redistributed and extended in the **TABLE** and **XY_MAP** commands (cf. section 4.3). Finally, the **CFITS** language has been replaced by a single **LAS\FITS** command. Indeed, most of the **CFITS** commands were customized for tapes which are an obsolescent storage medium.

Old names	New names
ANALYSE\GRID	Obsolete (replaced by ANALYSE\TABLE and MAP\XY_MAP)
ANALYSE\DISPLAY	FIT\DISPLAY
ANALYSE\FIT	FIT\VISUALIZE
ANALYSE\GAUSS	FIT\MINIMIZE
ANALYSE\ITERATE	FIT\ITERATE
ANALYSE\KEEP	FIT\KEEP
ANALYSE\LINES	FIT\LINES
ANALYSE\METHOD	FIT\METHOD
ANALYSE\RESIDUAL	FIT\RESIDUAL
LAS\SUM	LAS\AVERAGE
LAS\RECORD	Obsolete (not useful anymore)

Table 2: Correspondence between command names in **CLASS77** and **CLASS90**.

4.3 Griding and spectra cube visualization

The functionalities of the old **ANALYSE\GRID** command has been redistributed and extended in several commands:

- `ANALYSE\TABLE` creates a table containing the offsets, weights and intensities of all the dumped spectra. A check of the consistency of the observations in the current index is performed at this step, if not already done before.
- `MAP\XY_MAP` grids the dumped spectra from the table to an lmv cube. An image of the associated weights is also produced for further processing like optimal combination of several data cubes.
- Moreover, all the plotting capabilities of **GREG** program has been imported inside **CLASS** so that the user can directly visualize the data cube of the gridded spectra. For instance, Fig. 8 has been obtained with the following sequence of commands:

```
LAS90> file in 12co21-newfmt.30m
LAS90> find
LAS90> table 12co21 new
LAS90> xy_map 12co21
LAS90> let name 12co21
LAS90> let type lmv
LAS90> go view
```

The "`go view`" scripts enables interactive visualization of a spectra cube. Channel maps may be produced through the `go bit` command and position-velocity diagrams through the `go xv` and `go vy` commands.

4.4 `PLAIT` algorithm

The `PLAIT` algorithm "combine" two spectra cubes resulting from OTF observation with orthogonal scanning directions into a single spectra cube. It works in the Fourier plane and it reduces the striping due to receiver and atmospheric instabilities which inevitably show up in OTF maps. A version of this algorithm has been implemented as a **GILDAS** task named `PLAIT` from a previous version by C.Nieten (itself elaborated on original ideas from the NOD2 package).

5 CLASS90 for beta testers

The current default version of **CLASS** is **CLASS77**. Soon enough, the default version will swap to **CLASS90**, *i.e.* users will have access directly to **CLASS90** when calling **CLASS** from the shell prompt. There will be a warning that this is a new **CLASS** with modified features and that the old **CLASS** is still available through the **CLASS77** name in case of a problem with **CLASS90**. **CLASS77** will stay about one year after the swap to ensure good stability of **CLASS90**. However, *no* support will be given anymore to **CLASS77**.

Before the swap happens, you can become beta testers of **CLASS90** if you are interested by the new features. Beta testers should be able to quickly get bug fixes in their version. We thus recommend they use anonymous CVS in the following way:

```
1 shell-prompt> export CVSROOT=:pserver:anonymous@netsrv1.iram.fr:/CVS/GILDAS
2 shell-prompt> cvs co -r feb06 -d gildas-src-feb06 gildas
3 shell-prompt> cd gildas-src-feb06
4 shell-prompt> source admin/gildas-env.sh
5 shell-prompt> make
6 shell-prompt> make install
7 shell-prompt> cd packages/class90
8 shell-prompt> cvs up -r class90-stable
9 shell-prompt> make clean
```


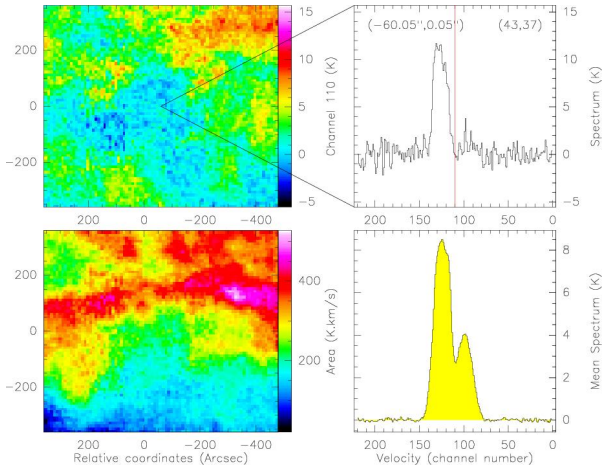

Figure 8: Screen-shot of result of the `go view` command. The top,left panel is the channel map corresponding to velocity shown as a vertical red line in the top,right panel. The top,right panel displays the spectrum at the position localized on the top,right panel. The bottom,left panel shows the line emission integrated over the velocity range appearing in yellow on the bottom,right panel. This last panel displays the spectrum averaged over the whole map. `go view` is an interactive command with many more features. Please, type `h` to display the complete help.


```
10 shell-prompt> make
11 shell-prompt> make install
```

Line 1 and 2 create a directory name `gildas-src-feb06` with the feb06 "stable" monthly release. Lines 3 to 6 are the standard way to install **GILDAS**. As **CLASS90** is evolving quickly, the **CLASS90** version shipped in a **GILDAS** monthly release may be unstable. We thus recommend that you go to the **CLASS90** directory (line 7), update it to a "stable" version (line 8), compile and install it (lines 9 to 11).

Beta testers also refer to the manual which is being fully updated. Bug reports and suggestions of improvements should be send to `gildas@iram.fr`. We will try to fix bugs quickly. We will consider the feasibility of all suggestions on longer timescales. When a bug is fixed, here are the steps to update **CLASS90**:

```
1 shell-prompt> export CVSROOT=:pserver:anonymous@netsrv1.iram.fr:/CVS/GILDAS
2 shell-prompt> cd gildas-src-feb06
3 shell-prompt> source admin/gildas-env.sh
4 shell-prompt> cd packages/class90
5 shell-prompt> cvs up -r class90-stable
6 shell-prompt> make
7 shell-prompt> make install
```

Line 5 is the line which will update the class90 directory. Be sure to type it only in the `gildas-src-feb06/packages/class90` directory to ensure that only **CLASS90** is updated because nothing ensure that other parts of **GILDAS** are "stable" between 2 monthly releases.

Have fun!

A&A 526, A47 (2011)
DOI: 10.1051/0004-6361/201015487
© ESO 2010

Astronomy & Astrophysics

Weeds: a CLASS extension for the analysis of millimeter and sub-millimeter spectral surveys

S. Maret[1], P. Hily-Blant[1], J. Pety[2,3], S. Bardeau[2], and E. Reynier[2]

[1] Laboratoire d'Astrophysique de Grenoble, Observatoire de Grenoble, Université Joseph Fourier, CNRS, UMR 571 Grenoble, France
e-mail: sebastien.maret@obs.ujf-grenoble.fr
[2] Institut de Radioastronomie Millimétrique, 300 rue de la Piscine, 38406 Saint Martin d'Hères, France
[3] LERMA, UMR 8112, CNRS and Observatoire de Paris, 61 avenue de l'Observatoire, 75014 Paris, France

Received 28 July 2010 / Accepted 6 December 2010

ABSTRACT

The advent of large instantaneous bandwidth receivers and high spectral resolution spectrometers on (sub-)millimeter telescopes has opened up the possibilities for unbiased spectral surveys. Because of the large amount of data they contain, any analysis of these surveys requires dedicated software tools. Here we present an extension of the widely used CLASS software that we developed to that purpose. This extension, named Weeds, allows for searches in atomic and molecular lines databases (e.g. JPL or CDMS) that may be accessed over the internet using a virtual observatory (VO) compliant protocol. The package permits a quick navigation across a spectral survey to search for lines of a given species. Weeds is also capable of modeling a spectrum, as often needed for line identification. We expect that Weeds will be useful for analyzing and interpreting the spectral surveys that will be done with the HIFI instrument onboard *Herschel*, but also observations carried-out with ground based millimeter and sub-millimeter telescopes and interferometers, such as IRAM-30 m and Plateau de Bure, CARMA, SMA, eVLA, and ALMA.

Key words. ISM: molecules – ISM: lines and bands – line: identification – methods: data analysis – virtual observatory tools

1. Introduction

A spectral survey consists in a series of spectra covering a significant spectral domain. At (sub-)millimeter wavelengths, a spectral survey typically covers several tens of GHz. Spectral surveys are generally referred to as unbiased if they provide a complete coverage with a uniform sensitivity. As such, they allow for a complete census of the species emitting in that band, and sometimes for discovery of new interstellar species. In addition, because a given band often contains many transitions of the same species, the simultaneous analysis of all these lines provides stringent constraints on the physical conditions in the emitting gas, such as the density and temperature. Therefore spectral surveys are very useful for characterizing both the chemical composition and physical condition in the observed objects.

Ever since the pioneering work of Johansson et al. (1984), who carried-out an unbiased spectral survey of the Orion KL star-forming region and IRC +10216 carbon-rich star between 72 and 91 GHz with the Onsala telescope, many spectral surveys have been carried-out at millimeter and sub-millimeter wavelengths using ground-based telescopes (see Herbst & van Dishoeck 2009, for a review). Because of the limited sensitivity of the instruments available at that time, early spectral surveys were targeted at bright star-forming regions, such as Orion KL and Sgr B2 in the millimeter range. Thanks to the increasing sensitivity of heterodyne receivers and the availability of sub-millimeter telescopes, these surveys were later extended to higher frequencies (e.g. Schilke et al. 1997, 2001; Comito et al. 2005) and carried-out towards fainter young stellar objects (e.g. NGC 1333 IRAS4 or IRAS16292-2422; Blake et al. 1994; van Dishoeck et al. 1995; Blake et al. 1995). A few spectral surveys have been carried with millimeter and sub-millimeter interferometers, such as OVRO or the SMA (e.g. Blake et al. 1996; Beuther et al. 2006). The HIFI instrument (de Graauw et al. 2010) onboard the *Herschel* space observatory (Pilbratt et al. 2010) now allows for a complete coverage of the almost unexplored 480–1250 and 1410–1910 GHz frequency bands. Its large spectral coverage – up to 4 GHz instantaneous bandwidth – and unprecedented sensitivity in this frequency range enable astronomers to carry-out spectral surveys over almost 1.5 THz down to the line confusion limit in a few tens of hours. The first spectral surveys with this instrument have already given spectacular results (Bergin et al. 2010; Ceccarelli et al. 2010). Among these, we can cite the richness of the Orion BN-KL spectrum observed at THz frequencies (see Fig. 2, Bergin et al. 2010) or the discovery of ND in IRAS16293-2422 (Bacmann et al. 2010).

Current developments in (sub-)millimeter instruments include an increase in the instantaneous bandwidth of the detection devices. During the past decade, the instantaneous bandwidth of tunable heterodyne receivers has increased by more than an order of magnitude, now routinely reaching ~10 GHz. Other technologies (e.g. HEMT, FCRAO and IRAM) have already provided several tens of GHz, although it is still unclear whether the sensitivity of these receivers can match that of SIS receivers. This increase in bandwidth has been accomplished in parallel with the advent of digital spectrometers (autocorrelators, fast Fourier transform), the versatility of which allow the coverage of such bandwidth with a spectral resolution down to a few hundred kHz. As a result, unbiased spectral surveys of the 3 mm atmospheric window (ν = 80–117 GHz) can be done with the IRAM-30 m telescope in ~10 h, with a 2 mK noise at 1σ in 2 MHz (~6 km s^{-1}) spectral channels. The ALMA interferometer will also permits coverage of large frequency windows, providing spectral cubes with up to 8 GHz bandwidth (Wootten 2008).

Thanks to its sensitivity, this instrument will allow, in its compact configuration, line surveys to be carried-out down to the confusion limit toward a large number of sources. Spectral surveys are thus still in their infancy and will very likely become routine observing modes in the coming years.

Spectral surveys covering large frequency bands require specific tools to be analyzed efficiently. In this article, we present a software that is intended for the analysis of spectral surveys. In Sect. 2, we briefly describe how such surveys are analyzed. In Sect. 3 we detail how our software was designed and implemented to carried-out such an analysis. Finally Sect. 4 concludes this article and discuss future developments.

2. Spectral surveys analysis

The analysis of a spectral survey usually consists in identifying the various lines and in deriving the physical and chemical properties of the emitting gas (density, temperature and column densities of the observed species). The main difficulty in such identification is that large molecules may have hundreds of lines in the (sub-)millimeter range. These species – such as methanol, methyl formate or dimethyl ether – are often named *weeds* by spectroscopists. If the lines are too broad, they may overlap and blend together, which makes the identification of weaker lines difficult. This is the *line confusion limit* (Schilke et al. 1997): line identification is not limited by the signal-to-noise of the observations, but by the line blending.

Because of this problem, extreme care must be taken when identifying species from a spectral survey. Herbst & van Dishoeck (2009) summarize the criteria for a firm detection as follows: "*(i)* rest frequencies are accurately known to $1{:}10^7$, either from direct laboratory measurements or from a high-precision Hamiltonian model; *(ii)* observed frequencies of clean, nonblended lines agree with rest frequencies for a single well-determined velocity of the source; if a source has a systematic velocity field as determined from simple molecules, any velocity gradient found for lines of a new complex molecule cannot be a random function of transition frequency; *(iii)* all predicted lines of a molecule based on an LTE spectrum at a well-defined rotational temperature and appropriately corrected for beam dilution are present in the observed spectrum at roughly their predicted relative intensities. A single anticoincidence (that is, a predicted line missing in the observational data) is a much stronger criterion for rejection than hundreds of coincidences are for identification. This last criterion is one of the strongest arguments for complete line surveys rather than targeted line searches".

The rest frequencies needed to fulfill criterion *(i)* are usually taken from spectral lines catalogs, such as the Cologne Database for Molecular Spectroscopy (CDMS, Müller et al. 2001) or the JPL Molecular Spectroscopy catalog (Pickett et al. 1998). For criterion *(ii)*, we need to compare the consistency of the centroid velocities of all the line candidates. Finally criterion *(iii)* requires to perform a model of the predicted emission of the given species so that it can be compared with the observations. The traditional technique for this consist in building a rotational diagram (Goldsmith & Langer 1999) to see if all detected lines agree with a single rotational temperature and column density. Alternatively, one can compute synthetic spectrum and compare it directly with the observations – a technique called *forward fitting* (Comito et al. 2005). This approach is also extremely useful when one wants to search for weak lines of a specie among hundreds from various weeds: a synthetic spectrum of the emission of the weeds can be constructed to fit the observed transitions in an iterative fashion. Once the brightest lines have been modeled, one can compare the synthetic spectrum to the observed one to look for lines from less abundant species (see Belloche et al. 2008, for an example of this technique). Of course, this also allows the physical and chemical properties of the emitting gas to be derived.

Since spectral surveys may contain thousands of lines, they require specific tools to be efficiently analyzed. Two packages have been developed for that purpose. The first of them, XCLASS (Schilke et al. 2001), is an extension of the widely used CLASS data reduction software, which is part of Gildas. XCLASS contains a spectral line database which is built from the CDMS and JPL catalogs. Technically, it uses the MySQL database server which must be installed on the user computer. This database may be updated manually, by replacing the database file by the one provided by the program authors. XCLASS allows the user to look for lines corresponding to a given frequency in its catalog, but also to make a model at the LTE of the observed spectra. XCLASS has been successfully used to reduce several spectral surveys obtained with the CSO and the IRAM-30 m (Schilke et al. 2001; Comito et al. 2005; Belloche et al. 2008). However, XCLASS is based on an obsolete version of CLASS, which is not maintained anymore. Indeed, the CLASS internal structures was largely rewritten in 2005–2006 to adapt to the challenges of data reductions coming with the recent generation of receivers (Hily-Blant et al. 2005). The second package, CASSIS, has been developed primarily to analyze *Herschel*-HIFI spectral surveys, although it can be used to analyze surveys from ground based telescopes as well. CASSIS itself does not have data reduction capabilities; therefore data must first be reduced in another software such as CLASS or HIPE (Ott et al., in prep.) before analysis in CASSIS. CASSIS uses a database which is built from the CDMS and the JPL catalog; in recent CASSIS versions, this database (SQLite) is embedded in the program so that an external database server is no longer required. Like XCLASS, CASSIS allows the forward-fitting of a spectrum, but also the search for the various transitions of a given specie.

3. Weeds design and implementation

3.1. General design

Weeds has been designed specifically to analyze spectral surveys, following the approach presented in Sect. 2. Although its development was inspired by the XCLASS and CASSIS packages, it is different in several aspects. Weeds is an extension of the current version of the CLASS software, and is mostly written in Python language, except for a few command written in the Gildas command interpreter (SIC) language. To do this, Weeds uses the new possibility offered by GILDAS to interleave Python and SIC in the same session (Bardeau et al. 2010). In particular, the variable contents are shared between Python and SIC. Python has several advantages over other languages for developing such extensions. It benefits from a large library of modules that allow complex tasks – such as making a query in a VO-compliant database, see Sect. 3.2 – to be done relatively easily. Although it is interpreted, it is still computationally efficient, because critical modules (e.g. the module for array computations that we use for the spectra modeling, see Sect. 3.4) are written in compiled languages such as C or Fortran. Weeds is distributed with Gildas since April 2010. The source code is freely available from the IRAM website[1]. A user manual is also available on that page.

[1] http://iram.fr/IRAMFR/GILDAS/

Because Weeds is an extension of CLASS, it can be used to analyze any data format that CLASS supports. In practice, the CLASS data format is used by many ground-based telescopes (e.g. IRAM-30 m, CSO and APEX). Data from other telescopes can be converted to FITS format and imported into CLASS as well. For example, *Herschel*-HIFI can be imported into CLASS through the FITS filler delivered by the HIPE data reduction software (Delforge et al., in prep.). In order to analyze data in Weeds, the data must have been calibrated and reduced first. The reduction usually consists in flagging the bad channels, averaging the scan covering the same frequency range together, and removing a polynomial baseline. If the data were obtained with double sideband (DSB) receiver, sideband deconvolution might be needed in order to produce a SSB spectrum. This requires a special observing technique, i.e. a number of overlapping spectra with shifted local oscillator frequency. Deconvolution can then be performed in CLASS using the algorithm developed by Comito & Schilke (2002). Thus data reduction and analysis can be done within the same environment.

3.2. Spectral line catalogs queries

As mentioned above, line identification requires repeated queries to spectral lines catalogs, such as the CDMS or the JPL. Unlike XCLASS and CASSIS – who require a custom catalog installed on the user's computer – Weeds performs queries in spectral line databases through the Internet[2]. This has the advantage of not requiring any update of a custom catalog: changes in the database, such as species addition or line frequency corrections or updates, are readily available in Weeds. In order to make queries in spectral lines catalogs, we have implemented the VO-compliant *Simple Line Access Protocol* (SLAP, Salgado et al. 2009) in Weeds. This protocol allows spectral line databases queries to be made in a standardized way; any database that implements the protocol can be accessed by Weeds. Because it is a VO standard, it is likely that more and more spectral line database will use it in the future. Nonetheless, as of this writing only the CDMS is accessible using that protocol, through an interface at the Paris VO Observatory (Moreau et al. 2008). Therefore, in order to access the JPL catalog from Weeds, we have implemented queries in the specific protocol which is used by this database. The CDMS can be accessed through its own protocol as well.

For the moment, only one database can be used at a time; it is not possible to combine the catalogs, i.e. to use species some out the JPL and some out the CDMS. In the future, the VAMDC project[3] will provide a single, unified database, including state-of-art spectroscopic data from both the CDMS and the JPL catalogs. We plan on implementing an access to this database from Weeds as soon as it it released.

From the user point of view, Weeds provides a command to search for lines corresponding to a given frequency range in a spectral line catalog. The user can select a region on the spectrum displayed in CLASS, and the command prints all the lines from the catalog around the region selected. The lines can be filtered out on the basis of the species they belong to, their Einstein coefficient, or their upper level energy. For double sideband spectra, a command option allows the search for lines from the image band.

[2] However, Weeds can make a cache of part or an entire catalog, so that it can be used later with no Internet connection.

[3] http://www.vamdc.org/

3.3. Lines browsing/identification

To secure the detection of a species in a spectral survey, one needs, according to criterion *(ii)* to search for all the transitions of that species in the entire frequency range covered by the survey. One also needs to measure the velocity of each line to check that they correspond to a single velocity. Weeds allows the user to browse through a survey rapidly. For this, Weeds has a command to search for all the lines of a given specie that fall in the frequency range covered by the survey. The command prints the lines in the terminal, but also builds an internal index containing all these lines, that we can order either by increasing frequency or increasing upper level energy. Another command allow the user to examine each of the line candidate one by one, to see if the line is detected or not. This command makes a zoom on a small frequency region around the (expected) line, and also sets the velocity scale with respect to the rest frequency of the line. A vertical mark is also drawn on the displayed spectrum at the source velocity, so that we can easily determine if the line is detected or not. A Gaussian fit of the observed line may be performed to determine the velocity of each line.

3.4. Spectra modeling

Once several transitions of a given specie have been found, one needs to check if the relative intensities of these components agree with a single excitation temperature (criterion *(iii)*). In addition, one needs to make sure that non-detected lines are consistent with the excitation temperature derived from other species – or in other words, that no lines are "missing". For this Weeds allows the user to compute a synthetic spectrum that can be compared directly with the observations (forward-fitting). Following the approach used in XCLASS and described in Comito et al. (2005) the synthetic spectrum is computed assuming that the emission arises from one or several components at the LTE. Although this approximation is simplistic – it is well known that in the interstellar medium species are often out of local thermodynamic equilibrium, and many sources are known to have density and temperature gradients – yet such a zeroth-order approach is often extremely useful to identify lines, as mentioned above. Once the lines have been identified, a more realistic modeling, taking into account non-LTE excitation effects as well as the source structure, can be carried-out.

Under these assumptions, and after baseline subtraction, the brightness temperature of a given species as a function of the rest frequency ν is given by:

$$T_{\mathrm{B}}(\nu) = \eta\left[J_\nu(T_{\mathrm{ex}}) - J_\nu\left(T_{\mathrm{bg}}\right)\right]\left(1 - \mathrm{e}^{-\tau(\nu)}\right) \quad (1)$$

where η is beam dilution factor, which, for a source with a Gaussian brightness profile and a Gaussian beam, is equal to:

$$\eta = \frac{\theta_{\mathrm{s}}^2}{\theta_{\mathrm{s}}^2 + \theta_{\mathrm{t}}^2} \quad (2)$$

where θ_{s} and θ_{t} the source and telescope beam *FWHM* sizes, respectively. For a sake of simplicity, the latter is assumed to be given by the diffraction limit[4]

$$\theta_{\mathrm{t}} = 1.22\frac{c}{\nu D} \quad (3)$$

[4] (Sub-)millimeter telescopes usually have tapers that limit the power received in side-lobes. Because of this, the telescope beam size may be different that of a purely diffraction limited antenna of the same diameter. However, the difference between the two is usually small: at 100 GHz, the measured *FWHM* of the IRAM-30 m is 24.6″, while Eq. (3) gives 25.2″.

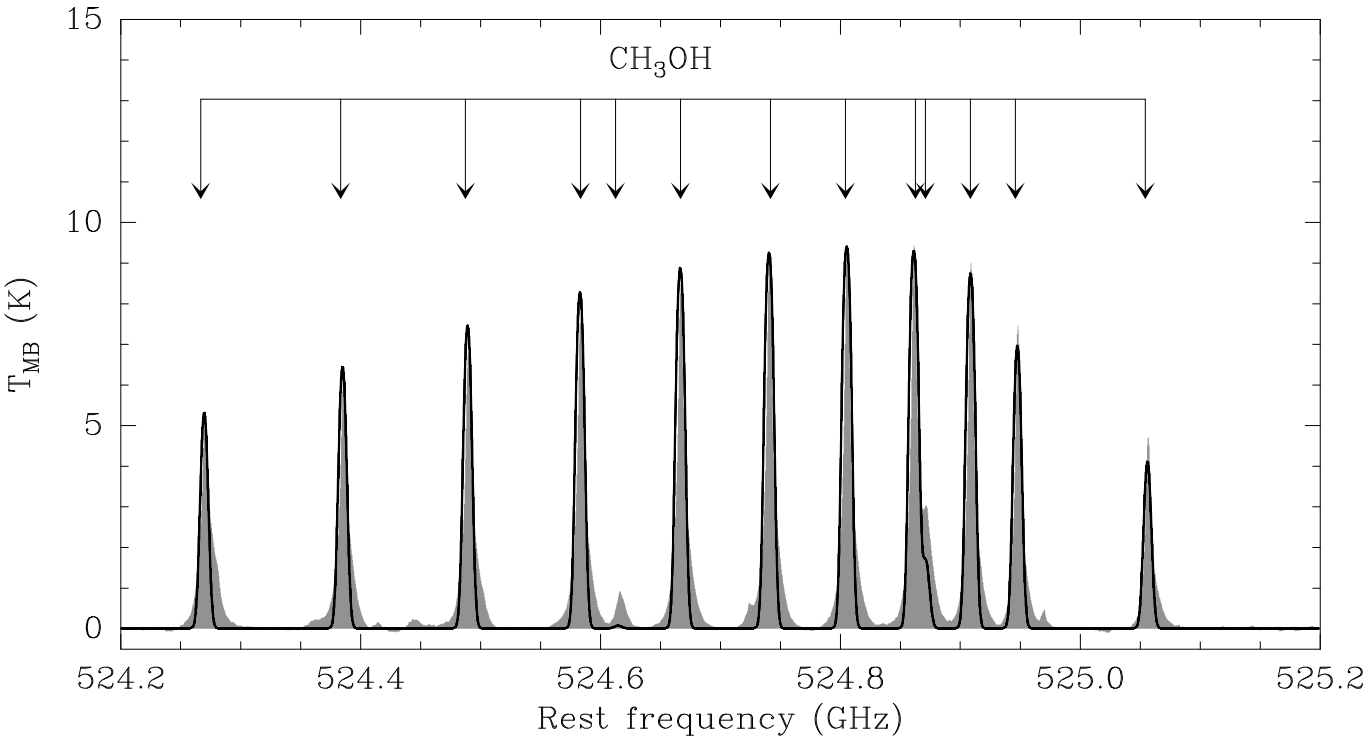

Fig. 1. Spectra between 524.2 and 525.5 GHz observed towards Orion-KL with *Herschel-HIFI* (filled histogram) and LTE model produced with Weeds (continuous black line). The rest frequencies of several detected methanol lines are indicated.

where c is the light speed and D is the diameter of the telescope. $T_{\rm bg}$ is the brightness temperature of the background emission, i.e. the physical temperature that would have a black body producing the same background continuum emission (e.g. 2.73 K for the cosmic microwave background). $T_{\rm ex}$ is the excitation temperature, and the opacity $\tau(\nu)$ is:

$$\tau(\nu) = \frac{c^2}{8\pi\nu^2}\frac{N_{\rm tot}}{Q(T_{\rm ex})}\sum_i A^i\, g_u^i\, {\rm e}^{-E_u^i/kT_{\rm ex}}\left({\rm e}^{h\nu_0^i/kT_{\rm ex}}-1\right)\phi^i \quad (4)$$

where the summation is over each line of the considered species. Here $N_{\rm tot}$ is the total column density of the species considered, $Q(T_{\rm ex})$ is the partition function, A^i is the Einstein coefficient of the i line, g_u^i and E_u are the upper level degeneracy and energy of the i line, and ϕ^i is the i line profile function. The latter is given by:

$$\phi^i = \frac{1}{\sigma\sqrt{2\pi}}{\rm e}^{-(\nu-\nu_0^i)^2/2\sigma^2} \quad (5)$$

where ν_0^i the is i line rest frequency and σ the line width in frequency units at $1/e$. σ can be expressed as a function of the line *FWHM* in velocity units ΔV as follows:

$$\sigma = \frac{\nu_0^i}{c\sqrt{8\ln 2}}\Delta V. \quad (6)$$

Note that some of the model parameters may be degenerate in certain cases. In the optically thick or thin limits, the source size and temperature or the size and column density are degenerate, respectively (see Eqs. (1) and (3)). This degeneracy can be usually lifted if both thick and thin lines are present in the survey, or if lines from an rare isotopologue are detected together with the main one (e.g. $^{13}CH_3OH$ and CH_3OH). The source size may also be constrained from interferometric observations.

Several components with e.g. different kinetic temperature or column density can be included in the computation. For this, we assume that the various components are not coupled radiatively – that is a photon from one component can not be absorbed by a another, foreground component – in which case the emerging spectrum is simply the sum of the brightness temperature of each components given by Eq. (1). Each of these component can be Doppler-shifted with respect to each other, which is useful when modeling sources with several components at different velocities. It is also possible to compute the spectra from several species; this is done by a summation of Eq. (1) over each specie.

The column densities, kinetic temperatures, Doppler width and source sizes for each species and components are read from a text file. Einstein coefficients, upper level degeneracy and energies as well as the partition functions are taken from spectral line catalogs. Because these catalogs usually give the partition functions at a few temperatures only, the partition function at the user temperature is computed from a linear interpolation (or extrapolation if the user given temperature is outside the range of temperature provided in the catalog). When computing the synthetic spectrum, a frequency sampling corresponding to the minimum ΔV divided by 10 is taken (or a frequency sampling equal to that of the observed spectra, if it smaller than the minimum ΔV divided by 10). This ensures that the sampling at all frequencies and for all species and components is sufficient. At the end of the computation, the synthetic spectrum is re-sampled to the same channel spacing than the observed spectrum in order to take the channel dilution factor into account. This allows for a direct comparison between the synthetic and observed spectra.

In Fig. 1, we show an example of such a modeling. The figure shows a spectrum between 524.2 and 525.2 GHz observed towards Orion-KL with *Herschel-HIFI* as part of the HEXOS guaranteed time key program (Bergin et al. 2010). These data have been already presented by Wang et al. (2010). Several

methanol lines are detected. On this figure we show model predictions computed with a Weeds for a single component source with $N(CH_3OH) = 2 \times 10^{17}$ cm^{-2}, $\theta_S = 18''$, $T = 80$ K and $\Delta V = 4$ km s^{-1}, and using the JPL database. Overall, the model predictions are in good agreement with the observations – in particular, we reproduce successfully the relative intensity of the brightest lines. On the other hand, this simple model underestimates the small line at 524 620 MHz and the shoulder at 524 880 MHz, maybe suggesting several emitting components and/or non-LTE excitation. Note that for the given parameters the emission is predicted to be optically thin, so that the column density and source size can not be constrained independently. A complete analysis of the methanol emission in this source is clearly beyond the scope of this paper; however this example demonstrates how a simple LTE model is useful to identify lines in a spectral survey. Finally, we have crossed-checked these model predictions with CASSIS and two packages were found to be in excellent agreement.

4. Conclusions and prospects

We have presented an extension of the CLASS data reduction software for analyzing spectral surveys. This extension allows the user to make queries in spectral line databases using a VO compliant protocol. It also allows the user to quickly search for the various transitions of a given specie. Finally it can compute model predictions at the LTE, as often needed to identify lines in spectra close to the confusion limit. Weeds has already been successfully used to analyze part of the IRAS 16293-2422 survey obtained with *Herschel-HIFI* (Bacmann et al. 2010; Hily-Blant et al. 2010), and we expect that it will be useful for future spectral surveys with this instrument as well. We think that it will become a standard tool for analyzing spectral surveys obtained with single dish ground based telescopes such as the IRAM-30 m. Yet, Weeds is not limited to the analysis of single dish observations. It may be used to analyze spectral surveys obtained with interferometers as well, such as the IRAM Plateau de Bure, CARMA, the SMA, and the upcoming ALMA and eVLA interferometers. In fact, since Weeds is written in Python, it could be used from the Python based CASA software, that will be used by the eVLA and ALMA. However, analyzing ALMA data will be challenging, because these data will consist in large spectral cubes, i.e. essentially a spectral survey on large number of pixels. In fact, doing such an analysis by hand, i.e. identifying the various lines/species on each spectrum of map is probably impossible; this will require some automatic fitting tools to extract the relevant information (column densities and excitation temperature of the various species) as a function of position. Such tools require efficient minimization algorithms to fit a model with a large number of free parameters to the data. The development of such tools is already in progress (e.g. in XCLASS using the MAGIX minimization framework), and implementing these automatic fitting tools in Weeds would be desirable in the future.

Acknowledgements. The authors would like to thank Peter Schilke and Emmanuel Caux for fruitful discussions on the analysis of spectral surveys. We are also grateful to Charlotte Vastel for helping us testing the LTE modeling done in Weeds against CASSIS, and to Shyia Wang for providing us the Orion-KL spectrum prior to publication. Finally, we wish to thank the persons in charge of maintaining and the CDMS, JPL and Paris VO databases; without their continuous efforts, the development of analysis software such as Weeds would not be possible. We are especially grateful to Holger Müller, Brian Drouin and Nicolas Moreau for their help in implementing access to these databases in Weeds.

References

Bacmann, A., Caux, E., Hily-Blant, P., et al. 2010, A&A, 521, L42
Bardeau, S., Reynier, E., Pety, J., & Guilloteau, S. 2010, PYGILDAS: Interleaving Python and GILDAS, Tech. Rep., IRAM
Belloche, A., Menten, K. M., Comito, C., et al. 2008, A&A, 482, 179
Bergin, E., Phillips, T., Comito, C., et al. 2010, A&A, 521, L20
Beuther, H., Zhang, Q., Reid, M. J., et al. 2006, ApJ, 636, 323
Blake, G. A., van Dishoek, E. F., Jansen, D. J., Groesbeck, T. D., & Mundy, L. G. 1994, ApJ, 428, 680
Blake, G. A., Sandell, G., van Dishoeck, E. F., et al. 1995, ApJ, 441, 689
Blake, G. A., Mundy, L. G., Carlstrom, J. E., et al. 1996, ApJ, 472, L49
Ceccarelli, C., Bacmann, A., Boogert, A., et al. 2010, A&A, 521, L22
Comito, C., & Schilke, P. 2002, A&A, 395, 357
Comito, C., Schilke, P., Phillips, T. G., et al. 2005, ApJS, 156, 127
de Graauw, T., Helmich, F., Phillips, T., et al. 2010, A&A, 518, L6
Goldsmith, P. F., & Langer, W. D. 1999, ApJ, 517, 209
Herbst, E., & van Dishoeck, E. F. 2009, ARA&A, 47, 427
Hily-Blant, P., Pety, J., & Guilloteau, S. 2005, CLASS Evolution: I. Improved OFT support, Tech. Rep., IRAM
Hily-Blant, P., Walmsley, M., Pineau Des forêts, G., & Flower, D. 2010, A&A, 513, A41
Johansson, L. E. B., Andersson, C., Ellder, J., et al. 1984, A&A, 130, 227
Müller, H. S. P., Thorwirth, S., Roth, D. A., & Winnewisser, G. 2001, A&A, 370, L49
Moreau, N., Dubernet, M. L., & Müller, H. 2008, in Astronomical Spectroscopy and Virtual Observatory, ed. M. Guainazzi, & P. Osuna, 195
Pickett, H. M., Poynter, R. L., Cohen, E. A., et al. 1998, JQSRT, 60, 830
Pilbratt, G. L., Riedinger, J. R., Passvogel, T., et al. 2010, A&A, 518, L1
Salgado, J., Osuna, P., Osuna, M., et al. 2009, Simple Line Access Protocol, Tech. Rep., International Virtual Observatory Alliance
Schilke, P., Groesbeck, T. D., Blake, G. A., & Phillips, T. G. 1997, ApJS, 108, 301
Schilke, P., Benford, D. J., Hunter, T. R., Lis, D. C., & Phillips, T. G. 2001, ApJS, 132, 281
van Dishoeck, E. F., Blake, G. A., Jansen, D. J., & Groesbeck, T. D. 1995, ApJ, 447, 760
Wang, S., Bergin, E., Crockett, N., et al. 2010, A&A, submitted
Wootten, A. 2008, Ap&SS, 313, 9

IRAM Memo 2009-1

IRAM-30m EMIR time/sensitivity estimator

J. Pety[1,2], S. Bardeau[1], E. Reynier[1]

1. IRAM (Grenoble)
2. Observatoire de Paris

Feb, 18th 2010
Version 1.1

Abstract

This memo describes the equations used in the IRAM-30m EMIR time/sensitivity estimator available in the `GILDAS/ASTRO` program. A large part of the memo aims at deriving sensitivity estimate for the case of On-The-Fly observations, which is not clearly documented elsewhere (to our knowledge). Numerical values of the different parameters used in the time/sensitivity estimator are grouped in appendix A.

History:

Version 1.0 (Feb, 04th 2009).

Version 1.1 (Feb, 18th 2010) Simplified.

Contents

1 Generalities **3**
1.1 The radiometer equation . . . 3
1.2 System temperature . . . 3
1.3 Elapsed telescope time . . . 3
1.4 The number of polarizations . . . 4
1.5 Switching modes and observation kinds . . . 4

2 Tracked observations **4**
2.1 Frequency switched . . . 4
2.2 Position switched . . . 5
2.3 Comparison . . . 5

3 On-The-Fly observations **5**
3.1 Additional notions and notations . . . 5
3.2 Frequency switched . . . 6
3.3 Position switched . . . 6
3.3.1 Two key points: 1) Sharing OFF among many ONs and 2) system stability timescale 6
3.3.2 Relation between $t_{\rm onoff}$ and $t_{\rm sig}^{\rm beam}$ . . . 7
3.3.3 Time/Sensitivity estimation . . . 8
3.4 Comparison . . . 9

4 Acknowledgement **10**

A Numerical values **11**
A.1 Overheads . . . 11
A.2 Atmosphere . . . 11
A.3 Telescope . . . 11
A.4 Frontends . . . 11
A.5 Backends . . . 11
A.6 On-The-Fly . . . 12

B Optimal number of ON per OFF measurements **13**

1 Generalities

1.1 The radiometer equation

The radiometer equation for a total power measurement reads

$$\sigma = \frac{T_{\rm sys}}{\eta_{\rm bpec}\sqrt{d\nu\, t}}, \tag{1}$$

where σ is the rms noise obtained by integration during t in a frequency resolution $d\nu$ with a system whose system temperature is given by $T_{\rm sys}$ and spectrometer efficiency is $\eta_{\rm bpec}$. However, total power measurement includes other contributions (*e.g.* the atmosphere emission) in addition to the astronomical signal. The usual way to remove most of the unwanted contributions is to switch, *i.e.* to measure alternatively on-source and off-source and then to subtract the off-source from the on-source measurements. It is easy to show that the rms noise of the obtained measurement is

$$\sigma = \sqrt{\sigma_{\rm on}^2 + \sigma_{\rm off}^2} = \frac{T_{\rm sys}}{\eta_{\rm bpec}\sqrt{d\nu\, t_{\rm sig}}} \quad \text{with} \quad t_{\rm sig} = \frac{t_{\rm on}\, t_{\rm off}}{t_{\rm on} + t_{\rm off}}, \tag{2}$$

where $\sigma_{\rm on}$ and $\sigma_{\rm off}$ are the noise of the on and off measurement observed respectively during the $t_{\rm on}$ and $t_{\rm off}$ integration time. $t_{\rm sig}$ is just a useful intermediate quantity.

1.2 System temperature

The system temperature is a summary of the noise added by the system. This noise comes from 1) the receiver and the optics, 2) the emission of the sky, and 3) the emission picked up by the secondary side lobes of the telescope. It is usual to approximate it (in the T_a^* scale) with

$$T_{\rm sys} = \frac{(1+G_{\rm im})\exp\{\tau_{\rm s}\, A\}}{F_{\rm eff}}\left[F_{\rm eff}\, T_{\rm atm}\, (1-\exp\{-\tau_{\rm s}\, A\}) + (1-F_{\rm eff})\, T_{\rm cab} + T_{\rm rec}\right], \tag{3}$$

where $G_{\rm im}$ is the receiver image gain, $F_{\rm eff}$ the telescope forward efficiency, $A = 1/\sin(\text{elevation})$ the airmass, $\tau_{\rm s}$ the atmospheric opacity in the signal band, $T_{\rm atm}$ the mean physical atmospheric temperature, $T_{\rm cab}$ the ambient temperature in the receiver cabine and $T_{\rm rec}$ the noise equivalent temperature of the receiver and the optics. All those parameters are easily measured, except $\tau_{\rm s}$, which is depends on the amount of water vapor in the atmosphere and which is estimated by complex atmospheric models.

1.3 Elapsed telescope time

The goal of a time estimator is to find the elapsed telescope time ($t_{\rm tel}$) needed to obtain a given rms noise, while a sensitivity estimator aims at finding the rms noise obtained when observing during $t_{\rm tel}$. If $t_{\rm onoff}$ is the total integration time spent both on the on-source and off-source observations, then

$$t_{\rm onoff} = \eta_{\rm tel}\, t_{\rm tel}, \tag{4}$$

where $\eta_{\rm tel}$ is the efficiency of the observing mode, *i.e.* the time needed 1) to do calibrations (*e.g.* pointing, focus, temperature scale calibration), and 2) to slew the telescope between useful integrations.

The tuning of the receivers is not proportional to the total integration time but it should be added to the elapsed telescope time. A time estimator can hardly anticipate the total tuning time for a project. Indeed, one project (*e.g.* faint line detection) can request only one tuning to be used during many hours and another (*e.g.* line survey) can request a tuning every few minutes. In our case, we thus request that the estimator user add by hand the tuning time to the elapsed telescope time estimation.

1.4 The number of polarizations

Heterodyne mixers are coupled to a single linear polarization of the signal. Hence, heterodyne receivers have at least two mixers, each one sensitive to one of the two linear polarization of the incoming signal. Both mixers are looking at the same sky position. This implies that we have to distinguish between the time spent on a given position of sky and the human elapsed time. Indeed, we will use the time spent on a given position of the sky when estimating the sensitivity, while we will give human elapsed time for the telescope and the on and off times.

If the mixers are tuned at the same frequency, the times spent on and off in the same direction of the sky will be twice the human elapsed time. We thus have to introduce the number of polarization simultaneously tuned at the same frequency, $n_{\rm pol}$, which can be set to 1 or 2. It happens that for EMIR, the two polarizations are always tuned at the same frequency, *i.e.* $n_{\rm pol} = 2$. The simplest way to take into account the distinction between human time and sky time is to slightly modify the radiometer equation to take into account the number of polarization

$$\sigma = \frac{T_{\rm sys}}{\eta_{\rm spec}\sqrt{d\nu\, n_{\rm pol}\, t_{\rm sig}}} \quad \text{with} \quad t_{\rm sig} = \frac{t_{\rm on}\, t_{\rm off}}{t_{\rm on} + t_{\rm off}}. \tag{5}$$

This equation implies that $t_{\rm on}$, $t_{\rm off}$, $t_{\rm onoff}$ and $t_{\rm tel}$ will be human times.

1.5 Switching modes and observation kinds

Switching is done in two main ways.

Position switch where the off-measurement is done on a close-by sky position devoid of signal. Wobbler switching is a particular case.

Frequency switch where the telescope always points towards the the source and the switching is done in the frequency (velocity) space.

Moreover, there are two main observation kinds.

Tracked observations where the telescope track the source, *i.e.* it always observes the same position in the source referential. The result is a single spectra.

On-The-Fly observations where the telescope continuously slew through the source with time to map it. The result is a cube of spectra.

In the following, we will work out the equations needed by the time/sensitivity estimator for each combination.

2 Tracked observations

2.1 Frequency switched

In this case, all the time is spent in the direction of the source. However, the frequency switching also implies that all this times can be counted as on-source and off-source times. Thus

$$t_{\rm onoff} = t_{\rm on} = t_{\rm off}, \tag{6}$$

$$t_{\rm sig} = \frac{t_{\rm on}}{2} = \frac{t_{\rm off}}{2} = \frac{t_{\rm onoff}}{2}, \tag{7}$$

and

$$\sigma_{\rm fsw} = \frac{\sqrt{2}\,T_{\rm sys}}{\eta_{\rm spec}\sqrt{d\nu\, n_{\rm pol}\, \eta_{\rm tel}\, t_{\rm tel}}}. \tag{8}$$

2.2 Position switched

In this case, only half of the time is spent in the direction of the source. Thus

$$t_{\rm on} = t_{\rm off} = \frac{t_{\rm onoff}}{2}, \tag{9}$$

$$t_{\rm sig} = \frac{t_{\rm on}}{2} = \frac{t_{\rm off}}{2} = \frac{t_{\rm onoff}}{4}, \tag{10}$$

and

$$\sigma_{\rm psw} = \frac{2\,T_{\rm sys}}{\eta_{\rm spec}\sqrt{d\nu\, n_{\rm pol}\, \eta_{\rm tel}\, t_{\rm tel}}}. \tag{11}$$

2.3 Comparison

For tracked observations, position switched observations results in a noise rms $\sqrt{2}$ larger than frequency switched observations for the same elapsed telescope time. In other words, frequency switched observations are twice as efficient in time to reach the same rms noise than position switched observations.

However, time efficiency is not the only criteria of choice. Indeed, with the current generation of receivers (before march 2009), the IF bandpass is much cleaner in position switched than in frequency switched observations. Frequency switched is thus really useful only when the lines are narrow so that the IF bandpass can be easily cleaned out through baselining with low order polynomials.

3 On-The-Fly observations

3.1 Additional notions and notations

The On-The-Fly (OTF) observing mode is used to map a given region of the sky. The time/sensitivity estimator will have to link the elapsed telescope time to cover the whole mapped region to the sensitivity in each independent resolution element. To do this, we need to introduce

- $A_{\rm map}$ and $A_{\rm beam}$, which are respectively the area of the map and the area of the resolution element. The map area is a user input while the resolution area is linked to the telescope full width at half maximum (θ) by
$$A_{\rm beam} = \frac{\eta_{\rm grid}\,\pi\,\theta^2}{4\,\ln(2)} \tag{12}$$
where $\eta_{\rm grid}$ comes from the fact that the OTF data is gridded by convolution. When the convolution kernel is a Gaussian of FWHM equal to $\theta/3$ (the default inside the `GILDAS/CLASS` software), it is easy to show that
$$\eta_{\rm grid} = 1 + \frac{1}{9} \simeq 1.11. \tag{13}$$
- The number of independent measurement ($n_{\rm beam}$) in the final map which is given by
$$n_{\rm beam} = \frac{A_{\rm map}}{A_{\rm beam}}. \tag{14}$$
- The on and off time spent per independent measurement, $t_{\rm on}^{\rm beam}$ and $t_{\rm off}^{\rm beam}$. The associated $t_{\rm sig}^{\rm beam}$ can then be written
$$t_{\rm sig}^{\rm beam} = \frac{t_{\rm on}^{\rm beam}\, t_{\rm off}^{\rm beam}}{t_{\rm on}^{\rm beam} + t_{\rm off}^{\rm beam}} \tag{15}$$
- The on and off time spent to map the whole map, $t_{\rm on}^{\rm tot}$ and $t_{\rm off}^{\rm tot}$. $t_{\rm onoff}$ is deduced from $t_{\rm on}^{\rm tot}$ and $t_{\rm off}^{\rm tot}$ in a way which depends on the switching scheme.

In addition, we must ensure that the user does not try to scan faster than the telescope can slew. To do this, we need to introduce

- The linear scanning speed, $v_{\rm linear}$, and its maximum value, $v_{\rm linear}^{\rm max}$.
- The area scanning speed, $v_{\rm area}$, and its maximum value, $v_{\rm area}^{\rm max}$. When the scanning pattern is linear, then $v_{\rm area}$ and $v_{\rm linear}$ are linked through
$$v_{\rm area} = v_{\rm linear}\,\Delta\theta, \tag{16}$$
where $\Delta\theta$ is the separation between consecutive rows. To avoid nasty signal and noise aliasing problems, we must ensure a Nyquist sampling, *i.e.*
$$\Delta\theta = \frac{\theta}{2.5}. \tag{17}$$

3.2 Frequency switched

In frequency switched observations, the switching happens as the telescope is slewed. This is correct as long as the switching time is much smaller than the time needed to slew a significant fraction of the telescope beam.

It is easy to understand that

$$t_{\rm onoff} = t_{\rm on}^{\rm tot} = t_{\rm off}^{\rm tot}, \tag{18}$$

$$t_{\rm on}^{\rm beam} = t_{\rm off}^{\rm beam} = \frac{t_{\rm onoff}}{n_{\rm beam}}, \tag{19}$$

$$t_{\rm sig}^{\rm beam} = \frac{t_{\rm on}^{\rm beam}}{2} = \frac{t_{\rm off}^{\rm beam}}{2} = \frac{t_{\rm onoff}}{2n_{\rm beam}}, \tag{20}$$

and

$$\sigma_{\rm fsw} = \frac{\sqrt{2\,n_{\rm beam}}\,T_{\rm sys}}{\eta_{\rm spec}\sqrt{d\nu\, n_{\rm pol}\, \eta_{\rm tel}\, t_{\rm tel}}}. \tag{21}$$

The velocity check can then be written as

$$\frac{A_{\rm map}}{t_{\rm onoff}} \leq v_{\rm area}^{\rm max}. \tag{22}$$

3.3 Position switched

3.3.1 Two key points: 1) Sharing OFF among many ONs and 2) system stability timescale

When the stability of the system is long enough, we can share the same off for several *independent* on-positions measured in a row (*e.g.* ON-ON-ON-OFF-ON-ON-ON-OFF...). The first key point here is the fact that the on-positions must be independent. The OTF is an observing mode where the sharing of the off can be used because the goal is to map a given region of the sky made of independent positions or resolution elements. When sharing the off-position between several on, Ball (1976) showed that the optimal off integration time is

$$t_{\rm off}^{\rm optimal} = \sqrt{n_{\rm on/off}}\,t_{\rm on} \tag{23}$$

where $n_{\rm on/off}$ is the number of on measurements per off. Replacing $t_{\rm off}$ by its optimal value in eq. 5, we obtain

$$t_{\rm sig} = \frac{t_{\rm on}}{1 + \frac{1}{\sqrt{n_{\rm on/off}}}} \quad \text{and} \quad \sigma = \frac{T_{\rm sys}}{\eta_{\rm spec}\sqrt{d\nu\, n_{\rm pol}\, t_{\rm on}}}\sqrt{1 + \frac{1}{\sqrt{n_{\rm on/off}}}}. \tag{24}$$

We thus see that the rms noise decreases when the number of independent on per off increases. It seems tempting to have only one off for all the on positions of the OTF map. However, the second key point of the method is that the system must be stable between the first and last on measurement. To take this point into account we must introduce

- The concept of submap, which is a part of a map observed between two successive off measurements.
- $A_{\rm submap}$, which is the area covered by the telescope in each submap.
- $n_{\rm submap}$ the number of such submaps needed to cover the whole map area.
- $t_{\rm stable}$, the typical time where the system is stable. This time will be the maximum time between two off measurements, which is noted $t_{\rm submap}$.
- $n_{\rm cover}$, the number of coverages needed either to reach a given sensitivity or to exhaust the acquisition time.
- $t_{\rm on}^{\rm cover}$ and $t_{\rm off}^{\rm cover}$ are the times spent respectively on and off per independent measurement and per coverage.

We note that the number of on per off ($n_{\rm on/off}$) is a purely geometrical quantity. This implies that the time spent off is linked to the time spent on by Eq. 23 both in each individual coverage and when averaging all the coverages.

3.3.2 Relation between $t_{\rm onoff}$ and $t_{\rm sig}^{\rm beam}$

By construction

- The number of submaps is the area of the map divided by the area of a submap
$$n_{\rm submap} = \frac{A_{\rm map}}{A_{\rm submap}}. \tag{25}$$
- The number of on per off is the number of independent resolution elements in each submap
$$n_{\rm on/off} = \frac{A_{\rm submap}}{A_{\rm beam}}. \tag{26}$$
- The number of independent resolution elements in the map is the product of number of submaps by the number of on per off
$$n_{\rm beam} = n_{\rm submap}\, n_{\rm on/off}. \tag{27}$$
- The submap area is the product of the area velocity by the time to cover it
$$A_{\rm submap} = v_{\rm area}\, t_{\rm submap}. \tag{28}$$
- The time to scan a submap is the sum of the $n_{\rm on/off}$ independent on integration time
$$t_{\rm submap} = n_{\rm on/off}\, t_{\rm on}^{\rm cover}. \tag{29}$$
- The relations between times per coverage and times integrated over all the coverages are
$$t_{\rm on}^{\rm beam} = n_{\rm cover}\, t_{\rm on}^{\rm cover} \quad \text{and} \quad t_{\rm off}^{\rm beam} = n_{\rm cover}\, t_{\rm off}^{\rm cover} \quad \text{with} \quad t_{\rm off}^{\rm cover} = \sqrt{n_{\rm on/off}}\, t_{\rm on}^{\rm cover}. \tag{30}$$
- Using the last two points, it is easy to derive
$$t_{\rm sig}^{\rm beam} = n_{\rm cover}\, t_{\rm sig}^{\rm cover} = \frac{n_{\rm cover}\, t_{\rm submap}}{n_{\rm on/off} + \sqrt{n_{\rm on/off}}}. \tag{31}$$

- Finally, the total time spent on and off is given by

$$t_{\rm onoff} = n_{\rm cover}\, n_{\rm submap}\, (n_{\rm on/off}\, t_{\rm on}^{\rm cover} + t_{\rm off}^{\rm cover}). \quad (32)$$

Using Eqs. 23 and 29, we derive

$$t_{\rm onoff} = n_{\rm cover}\, t_{\rm submap}\, n_{\rm submap}\, \left(1 + \frac{1}{\sqrt{n_{\rm on/off}}}\right). \quad (33)$$

Both $t_{\rm sig}^{\rm beam}$ and $t_{\rm onoff}$ are proportional to $n_{\rm cover}\, t_{\rm submap}$ (cf. Eqs. 31 and 33). It is thus easy to derive that

$$t_{\rm onoff} = t_{\rm sig}^{\rm beam}\, n_{\rm submap}\, \left(1 + \sqrt{n_{\rm on/off}}\right)^2. \quad (34)$$

Using Eq. 27, we can replace $n_{\rm on/off}$ and obtain

$$t_{\rm onoff} = t_{\rm sig}^{\rm beam}\, \left(\sqrt{n_{\rm submap}} + \sqrt{n_{\rm beam}}\right)^2. \quad (35)$$

Using Eqs. 5, 4 and 35, we obtain

$$\sigma_{\rm psw} = \frac{\left(\sqrt{n_{\rm beam}} + \sqrt{n_{\rm submap}}\right)\, T_{\rm sys}}{\eta_{\rm spec}\, \sqrt{d\nu\, n_{\rm pol}\, \eta_{\rm tel}\, t_{\rm tel}}}. \quad (36)$$

The last equation in theory enables us to find the rms noise as a function of the elasped telescope time (sensitivity estimation) and vice-versa (time estimation). However, it is not fully straightforward because we must enforce that $n_{\rm cover}$ and $n_{\rm submap}$ have an integer value.

3.3.3 Time/Sensitivity estimation

This paragraph describes the algorithm to do a time/sensitivity estimation for a position-switched On-The-Fly observation.

Step #1: Computation of $n_{\rm beam}$ and $n_{\rm submap}$
$n_{\rm beam}$ is just computed as the ratio $A_{\rm map}/A_{\rm beam}$. Using Eqs. 28 and 25, we obtain

$$n_{\rm submap} = \frac{A_{\rm map}}{v_{\rm area}\, t_{\rm submap}}. \quad (37)$$

Using this equation, we start to compute $n_{\rm submap}$ for $t_{\rm submap} = t_{\rm stable}$ and $v_{\rm area} = v_{\rm area}^{\rm max}$. We want to enforce the integer character of $n_{\rm submap}$ in a way which decreases the product $t_{\rm submap}\, v_{\rm area}$. To do this, we use

$$n_{\rm submap} = 1 + \texttt{int}(n_{\rm submap}). \quad (38)$$

Eq. 38 ensures that $t_{\rm submap}\, v_{\rm area} < t_{\rm stable}\, v_{\rm area}^{\rm max}$. The value of $v_{\rm area}$ must be decreased so that Eq. 37 is enforced.

Step #2: Computation of $t_{\rm tel}$ or σ We use the following equations in descending order to compute the elapsed telescope time and in ascending order to compute the rms noise level:

1. $t_{\rm sig}^{\rm beam} = \dfrac{T_{\rm sys}^2}{\eta_{\rm spec}^2\, \sigma^2\, d\nu\, n_{\rm pol}}$, (39)
2. $t_{\rm onoff} = t_{\rm sig}^{\rm beam}\, \left(\sqrt{n_{\rm submap}} + \sqrt{n_{\rm beam}}\right)^2$, (40)
3. $\eta_{\rm tel}\, t_{\rm tel} = t_{\rm onoff}$. (41)

Step #3: Computation of derived quantities

1. $n_{\rm on/off} = \dfrac{n_{\rm beam}}{n_{\rm submap}}$, (42)
2. $n_{\rm cover} = \dfrac{t_{\rm sig}^{\rm beam}}{t_{\rm submap}}\, \left(n_{\rm on/off} + \sqrt{n_{\rm on/off}}\right)$, (43)
3. $t_{\rm on}^{\rm beam} = \dfrac{n_{\rm cover}\, t_{\rm submap}}{n_{\rm on/off}}$ (44)
3. $t_{\rm off}^{\rm beam} = t_{\rm on}^{\rm beam}\, \sqrt{n_{\rm on/off}}$. (45)

Step #4: Is $n_{\rm cover}$ an integer number? The interpretation of the above equation to compute $n_{\rm cover}$ has two cases.

1. $n_{\rm cover} < 1$. This means that either the user tries to cover a too large sky area in the given telescope elasped time (sensitivity estimation) or the telescope need a minimum time to cover $A_{\rm map}$ at the maximum velocity possible with the telescope and this minimum time implies a more sensitive observation than requested by the user (time estimation).
2. $n_{\rm cover} \geq 1$. $n_{\rm cover}$ will generally not be an integer, we can think to decrease $t_{\rm submap}$ from $t_{\rm stable}$ to obtain an integer value. However, this must be done at constant $A_{\rm submap} (= v_{\rm area}\, t_{\rm submap})$. Decreasing $t_{\rm submap}$ thus implies increasing $v_{\rm area}$. It is not clear that this is possible because of the constraint $v_{\rm area} < v_{\rm area}^{\rm max}$. Another way to deal with this is to keep $t_{\rm submap}$ to its maximum value and to adjust $t_{\rm tel}$ (sensitivity estimation) or $t_{\rm sig}$ and thus σ (time estimation) to obtain an integer value of $n_{\rm cover}$. However, this implies a change in the wishes of the user. The program can not make such a decision alone and we will only warn the user. Indeed, the worst case is when $n_{\rm cover}$ is changing from 1 to 2 because this can decrease the sensitivity by a factor 1.4 (sensitivity estimation) or double the elapsed telescope time (time estimation). The larger the value of $n_{\rm cover}$ the less harm it is to enforce the integer character of $n_{\rm cover}$.

3.4 Comparison

Contrary to tracked observations, the position switched observing mode can be more efficient than the frequency switched observing mode. Indeed, in frequency switch, the same time is spent in the on and off spectrum. When subtracting them, the off brings as much noise as the on. In position switch, the same off can be shared between many ons, in which case the optimal integration time on the off is much larger than on each independent on spectrum. Hence, the noise brought by the off spectrum can be much smaller than the noise brought by the on spectrum.

For frequency switched observations,

$$\sigma_{\rm fsw} = \frac{\sqrt{2\, n_{\rm beam}}\, T_{\rm sys}}{\eta_{\rm spec} \sqrt{d\nu\, n_{\rm pol}\, \eta_{\rm tel}\, t_{\rm tel}}}, \quad (46)$$

while for position switched observations,

$$\sigma_{\rm psw} = \frac{\left(\sqrt{n_{\rm beam}} + \sqrt{n_{\rm submap}}\right)\, T_{\rm sys}}{\eta_{\rm spec}\, \sqrt{d\nu\, n_{\rm pol}\, \eta_{\rm tel}\, t_{\rm tel}}}. \quad (47)$$

We thus have

$$\frac{\sigma_{\rm psw}}{\sigma_{\rm fsw}} = \frac{1}{\sqrt{2}}\, \left(1 + \sqrt{\frac{n_{\rm submap}}{n_{\rm beam}}}\right). \quad (48)$$

Position switched OTF is more efficient than frequency switched OTF for

$$\frac{n_{\rm beam}}{n_{\rm submap}} = n_{\rm on/off} \geq \frac{1}{3 - 2\sqrt{2}} \sim 6. \quad (49)$$

Moreover, $\sigma_{\rm psw}/\sigma_{\rm fsw} \simeq 0.84$ for $n_{\rm on/off} = 30$, and $\simeq 0.78$ for $n_{\rm on/off} = 100$. Using eqs. 28 and 26, we see that the limit on the maximum number of on per off is set by

$$n_{\rm on/off} = \frac{t_{\rm stable}}{A_{\rm beam}/v_{\rm area}^{\rm max}}, \quad (50)$$

i.e. the ratio of the maximum system stability time by the minimum time required to map a telescope beam.

As for tracked observations, there are other considerations to be taken into account. For extra-galactic observations, the lines are large which excludes the use of frequency switched observations. For Galactic observations, the intrinsic sensitivity of the receivers may make it difficult to find a closeby position devoid of signal. We can still use the position switched OTF observing mode. But we then have to observe the off position in frequency switched track observing mode long enough to be able to add back the off astronomical signal.

4 Acknowledgement

The author thanks M. Guélin, S. Guilloteau, C. Kramer and C. Thum for useful discussions.

References

Ball, J. A., in Meth. Exper. Phys., Vol. 12, Part C, Astrophysics: Radio Observations, Chap. 4.3, p. 46, ed. M. L. Meeks

A Numerical values

This appendix groups all the numerical values used in the time/sensitivity estimator. We made conservative choices for two reasons: 1) time/sensitivity estimators tend to be too optimistics and 2) EMIR is a new generation of receivers which had not yet been tested at the telescope.

A.1 Overheads

- $\eta_{\rm tel} = 0.5$.
- After estimating the number of tunings needed to complete the project, the user has to add to the telescope time 30 minutes per tuning (this includes the observation of a line calibrator).

A.2 Atmosphere

- $T_{\rm atm} = 250$ K.
- The opacities at signal frequencies are computed with a recent version of the ATM program (maintained by J.R. Pardo).
- They are computed for 3 different amount of water vapor per season (1, 2 and 4 mm for the winter season and 2, 4 and 7 mm for the summer season).

A.3 Telescope

- $T_{\rm cab} = 290$ K.
- $F_{\rm eff} = 0.95$ at 3 mm, 0.93 at 2 mm, 0.91 at 1 mm and 0.88 at 0.8 mm.

A.4 Frontends

Warning: Please do not quote these values in your papers. You should refer to the publications which fully describe the receivers.

- The receiver temperature is the sum of
  - The mixer temperature: Typically 50 K below 260 GHz and 70 K above;
  - The mirror losses: Typically 10 K;
  - The dichroic losses: Typically 15 K. Nota Bene: Dichroics enable dual frequency observation by frequency separation of the sky signal.

  We end up with $T_{\rm rec} = 75$ K below 260 GHz and $Trec = 95$ K above 260 GHz.
- $G_{\rm im} = 0.1$.

A.5 Backends

- $\eta_{\rm spec} = 0.87$ because of the 2 bit quantization at the input of the correlators.
- The noise equivalent bandwidth of our correlators is almost equal to the channel spacing. So we do not take this into account in our estimation.

A.6 On-The-Fly

- $t_{\rm stable} = 2$ minutes.
- $\theta = \frac{2460''}{\nu\,\mathrm{GHz}}$.
- The maximum linear velocity is limited by the maximum dumping rate of $f_{\rm dump} = 2$ Hz. We know that in order to avoid beam elongation along the scanning direction, we need to sample at least 4 points per beam in the scanning direction. We thus end up with

$$v_{\rm linear}^{\rm max} = f_{\rm dump}\,\frac{\theta}{4}\,\mathrm{arcsec/s} \tag{51}$$

and

$$v_{\rm area}^{\rm max} = f_{\rm dump}\,\frac{\theta}{2.5}\,\frac{\theta}{4}\,\mathrm{arcsec^2/s} \quad \text{or} \quad v_{\rm area}^{\rm max} = f_{\rm dump}\,\frac{\theta^2}{10}\,\mathrm{arcsec^2/s} \tag{52}$$

B Optimal number of ON per OFF measurements

This section is just a reformulation of the original demonstration by Ball (1976).

Let's assume that we are measuring $n_{\rm on/off}$ *independent* on-positions for a single off. The same integration time ($t_{\rm on}$) is spent on each on-position and the off integration time is

$$t_{\rm off} = \alpha\, t_{\rm on}, \tag{53}$$

where α can be varied. Using eq. 2 and $t_{\rm onoff} = n_{\rm on/off} t_{\rm on} + t_{\rm off} = (n_{\rm on/off} + \alpha)\, t_{\rm on}$, it can be shown than

$$t_{\rm onoff} = \frac{T_{\rm sys}^2}{\eta_{\rm spec}^2\,\sigma^2\,d\nu}\left(1 + n_{\rm on/off} + \alpha + \frac{n_{\rm on/off}}{\alpha}\right). \tag{54}$$

Differenciating with respect to α, we obtain

$$\frac{dt_{\rm onoff}}{d\alpha} \propto 1 - \frac{n_{\rm on/off}}{\alpha^2} \tag{55}$$

Setting the result to zero then gives that the minimum elapsed time to reach a given rms noise is obtained for

$$\alpha = \sqrt{n_{\rm on/off}} \quad \text{or} \quad t_{\rm off}^{\rm optimal} = \sqrt{n_{\rm on/off}}\, t_{\rm on}. \tag{56}$$

IRAM-30m HERA time/sensitivity estimator

J. Pety[1,2], M. González[3], S. Bardeau[1], E. Reynier[1]

1. IRAM (Grenoble)
2. Observatoire de Paris
3. IRAM (Granada)

Feb., 18th 2010
Version 1.0

Abstract

This memo describes the equations used in the IRAM-30m HERA time/sensitivity estimator available on the IRAM-30m web page. A large part of the memo aims at describing the peculiarities of time/sensitivity estimation of the On-The-Fly observing mode with a multi-pixel like HERA. It explains how to generalize the equations of the single pixel case, so that the same code can be used in both cases (single and multi-pixel).

1 Summary of the formulas for a single pixel receiver

We summarize here the relations between the rms noise (σ) and the elapsed telescope time ($t_{\rm tel}$) derived by Pety et al. (2009) in the case of a single-pixel heterodyne receiver. The results depends on a combination of

- The observation kind:

  Tracked observations where the telescope track the source, *i.e.* it always observes the same position in the source referential. The result is a single spectra.

  On-The-Fly observations where the telescope continuously slew through the source with time to map it. The result is a cube of spectra.

- and of the switching mode:

  Position switch where the off-measurement is done on a close-by sky position devoid of signal. Wobbler switching is a particular case.

  Frequency switch where the telescope always points towards the the source and the switching is done in the frequency (velocity) space. In this case,

The formulas are

- for tracked observations

$$\sigma^{\rm track}_{\rm psw} = \frac{2\,T_{\rm sys}}{\eta_{\rm spec}\sqrt{d\nu\,n_{\rm pol}\,\eta_{\rm tel}\,t_{\rm tel}}}, \quad \text{and} \quad \sigma^{\rm track}_{\rm fsw} = \frac{\sqrt{2}\,T_{\rm sys}}{\eta_{\rm spec}\sqrt{d\nu\,n_{\rm pol}\,\eta_{\rm tel}\,t_{\rm tel}}}. \tag{1}$$

- for OTF observations

$$\sigma^{\rm otf}_{\rm psw} = \frac{\left(\sqrt{n_{\rm beam}}+\sqrt{n_{\rm submap}}\right)\,T_{\rm sys}}{\eta_{\rm spec}\sqrt{d\nu\,n_{\rm pol}\,\eta_{\rm tel}\,t_{\rm tel}}}, \quad \text{and} \quad \sigma^{\rm otf}_{\rm fsw} = \frac{\sqrt{2\,n_{\rm beam}}\,T_{\rm sys}}{\eta_{\rm spec}\sqrt{d\nu\,n_{\rm pol}\,\eta_{\rm tel}\,t_{\rm tel}}}. \tag{2}$$

In these formulas

- $\eta_{\rm tel}$ is the efficiency of the telescope. It includes the time needed 1) to do calibrations (*e.g.* pointing, focus, temperature scale calibration), and 2) to slew the telescope between useful integrations, etc... Its value is decided by IRAM: It should *not* be changed by the PI.
- $\eta_{\rm spec}$ is the spectrometer efficiency.
- $d\nu$ is the frequency resolution.
- $n_{\rm pol}$ is the number of polarizations tuned at the same frequency (1 or 2).
- $T_{\rm sys}$ is the system temperature, which is a summary of the noise added by the system. It is usual to approximate it (in the T_a^* scale) with

$$T_{\rm sys} = \frac{(1+G_{\rm im})\exp\{\tau_{\rm s}\,A\}}{F_{\rm eff}}\left[F_{\rm eff}\,T_{\rm atm}\,(1-\exp\{-\tau_{\rm s}\,A\})+(1-F_{\rm eff})\,T_{\rm cab}+T_{\rm rec}\right], \tag{3}$$

  where $G_{\rm im}$ is the receiver image gain, $F_{\rm eff}$ the telescope forward efficiency, $A=1/\sin(\text{elevation})$ the airmass, $\tau_{\rm s}$ the atmospheric opacity in the signal band, $T_{\rm atm}$ the mean physical atmospheric temperature, $T_{\rm cab}$ the ambient temperature in the receiver cabine and $T_{\rm rec}$ the noise equivalent temperature of the receiver and the optics.
- $n_{\rm beam}$ is the number of independent measurement in the map observed in the OTF mode. It is given by

$$n_{\rm beam} = \frac{A_{\rm map}}{A_{\rm beam}} \quad \text{with} \quad A_{\rm beam} = \frac{\eta_{\rm grid}\,\pi\,\theta^2}{4\,\ln(2)}. \tag{4}$$

  where $A_{\rm map}$ is the map area, $A_{\rm beam}$ is the area of the resolution element in the map, $\eta_{\rm grid}$ is the smoothing factor due to gridding and θ is the telescope full width at half maximum.
- $n_{\rm submap}$ the number of submaps needed to cover the whole map area, a submap being the area covered between two successive off measurements. $n_{\rm submap}$ is computed with

$$n_{\rm submap} = \frac{A_{\rm map}}{A_{\rm submap}} \quad \text{with} \quad A_{\rm submap} = \frac{\theta}{2.5}\,v_{\rm linear}\,t_{\rm stable} \tag{5}$$

  where $v_{\rm linear}$ is the telescope scanning speed and $t_{\rm stable}$ is the typical timescale of stability of the observing system.

The demonstrations and additional subtleties for the OTF case are fully described in Pety et al. (2009).

2 Generalization to a multi-pixel receiver

2.1 Description of HERA, the IRAM-30m multi-pixels

HERA is a multi-pixel receiver working at 1 mm of wavelength. Each pixel is an heterodyne mixer using a SIS junction. There are nine pixels per polarization. The pixels of one polarization follow a 3×3 square pattern, the distance between two pixels being $\Delta = 24''$. Both polarizations are aligned. Hence, HERA has 18 pixels in total looking at 9 different sky position simultaneously. The polarizations of HERA can simultaneously be tuned at two different frequencies.

The number of used polarization, $n_{\rm pol}$ can thus be set to 1 or 2 and the number of pixels per polarization is $n_{\rm pix} = 9$.

2.2 An average pixel

The scatter of the mixer performances, which translate into a scatter of receiver temperatures, is the first thing to deal with. Instead of computing the sensitivity associated with each mixer, we introduce an average pixel, which will represent all the other ones. In Eqs. 1 and 2, the caracteristics of the mixers are hidden into the system temparature, $T_{\rm sys}$. We will thus define an average system temperature, $\overline{T}_{\rm sys}$, which will represent the receiver average pixel.

Among the different ways to define such an average system temperature, we priviledge the one which will give the right sensitivity in the case where the same point of the sky is seen by all the different pixels. This choice is made because 1) the same point of the sky is at least seen by two pixels (one per polarization) and 2) it is a good idea when mapping to try to cover the mapped area as many time as possible with sligthly different observing configuration of HERA (*e.g.* rotations by 90deg) to homogenize the noise distribution and to ensure that bad pixels see different part of the mapped area.

It is well-known that the optimal way to combine (*e.g.* to average or to grid) spectra is to weight them by $w = 1/\sigma^2$ before combination, where σ is their rms noise. In this case, it can be shown that the weight of the combination is the linear sum of the weights. From this, it is easy to define $\overline{T}_{\rm sys}$ as

$$\frac{n_{\rm pol}\,n_{\rm pix}}{\overline{T}^2_{\rm sys}} = \sum_{i=1,n_{\rm pol},j=1,n_{\rm pix}} \frac{1}{T^2_{{\rm sys}_{i,j}}}. \tag{6}$$

2.3 Impact on tracked observations

During tracked observations, each pixel of one polarization will look at a different position of the sky, but always the same position with time. We thus simply have to change $T_{\rm sys}$ by $\overline{T}_{\rm sys}$ in Eqs. 1, *i.e.*

$$\sigma^{\rm track}_{\rm psw} = \frac{2\,\overline{T}_{\rm sys}}{\eta_{\rm spec}\sqrt{d\nu\,n_{\rm pol}\,\eta_{\rm tel}\,t_{\rm tel}}}, \quad \text{and} \quad \sigma^{\rm track}_{\rm fsw} = \frac{\sqrt{2}\,\overline{T}_{\rm sys}}{\eta_{\rm spec}\sqrt{d\nu\,n_{\rm pol}\,\eta_{\rm tel}\,t_{\rm tel}}}. \tag{7}$$

2.4 Imaging with HERA

HERA has a derotator, which ensures that the pixels do not rotate on the sky. The sky can thus be mapped by scanning along *e.g.* the right ascension or the declination axis in equatorial coordinates. We aim at obtaining a fully sampled map, implying a distance between the rows of $\Delta = \theta/2.5$, where θ is the beam full width at half maximum: At 1 mm, this corresponds typically to $4''$. However, the pixels are typically separated by $\Delta \simeq 2\theta$. We thus have to find the best scanning strategy which will fill the hole of the instantaneous footprint of the multi-pixel. To do this, we will use a property of the deroratator, *i.e.* it can be configured so that one of the main axes of the multi-pixel is rotated by an angle (α) from the scanning direction. Indeed, we can ask what is the value of α needed so that the distance between the rows of two adjacent pixels is exactly Δ. For a receiver of $\sqrt{n_{\rm pix}}\times\sqrt{n_{\rm pix}}$ pixels, we end up with $\sqrt{n_{\rm pix}}$ groups of lines, the distance between two group of lines being noted δ'. A bit of geometry gives

$$\delta = \Delta\,\sin\alpha \quad \text{and} \quad \delta' = \Delta\,\cos\alpha. \tag{8}$$

If we now impose that

$$\delta' = n_{\rm subscan}\,\sqrt{n_{\rm pix}}\,\delta, \tag{9}$$

we obtain

$$\tan\alpha = \frac{1}{n_{\rm subscan}\,\sqrt{n_{\rm pix}}}. \tag{10}$$

We can fully sample without redundancy a given fraction of the sky in a single subscan ($n_{\rm subscan}=1$) or in two parallel subscans (zigzag, $n_{\rm subscan}=2$).

For HERA, $\sqrt{n_{\rm pix}}=3$ and the Δ value is fixed to $4''$ by the observing wavelenght ~ 1 mm. $n_{\rm subscan}=1$ gives $\alpha = 18.4°$, $\Delta \sim 12''$ and $n_{\rm subscan}=2$ gives $\alpha = 9.5°$, $\Delta \sim 24''$. Current optical design implies a minimum distance between the pixels which is only compatible with the $n_{\rm subscan}=2$ solution.

In summary, by setting an angle of 9.5° between one of the main axes of a 3×3 multi-pixels and the scanning direction, we can sweep in a fully sampled mode a given portion of the sky with two parallel scans separated by $3\delta = 12''$. The region of the sky fully sampled will then be rectangular: the length of the rectangular side perpendicular to the scanning direction is then $d_\perp = n_{\rm subscan} n_{\rm pix} \delta$, while the length of the rectangular size parallel to the scanning direction, $d_\parallel$, will depend on the observing strategy. However, there is an edge effect, due to the rotation of the array from the scanning direction. Indeed, the edges of the maps are not fully sampled: Thus must thus be considered as overheads. The area of the scanned sky must thus be larger than the targeted area, which must be fully sampled. Let's assume that the targeted area ($A_{\rm target}$) is swept as a succession of $n_\perp$ rectangles of size $d_\perp \times d_\parallel$. We get

$$A_{\rm target} = n_\perp \, d_\perp \, d_\parallel. \tag{11}$$

The area swept in the under-sampled edges ($A_{\rm edge}$) is just the area of the rectangle whose side sizes are $n_\perp \, d_\perp$ and the scanning size of multi-pixel rotated by α, *i.e.*

$$d_{\rm edge} = (\sqrt{n_{\rm pix}} - 1) \, \Delta \, (\cos\alpha + \sin\alpha) \tag{12}$$

Indeed, the geometry of the edges show that half this area is covered on each size of the targeted area. Using Eqs. 8 and 9, we obtain

$$d_{\rm edge} = (\sqrt{n_{\rm pix}} - 1) \, (1 + n_{\rm subscan} \sqrt{n_{\rm pix}}) \delta \tag{13}$$

We now define the mapping efficiency $\eta_{\rm edge}$ as

$$\eta_{\rm edge} = \frac{A_{\rm target}}{A_{\rm target} + A_{\rm edge}}, \quad \text{with} \quad A_{\rm edge} = n_\perp \, d_\perp \, d_{\rm edge}. \tag{14}$$

Replacing $A_{\rm target}$ and $A_{\rm edge}$ by their expressions 11 and 14, we derive

$$\eta_{\rm edge} = \frac{1}{1 + \frac{d_{\rm edge}}{d_\parallel}} = \frac{1}{1 + \frac{d_{\rm edge}}{a \, n_\perp \, d_\perp}}. \tag{15}$$

This expression indicates that the most efficient mapping strategy is to observe very wide scans. However, avoiding the edge overheads is only one aspect of wide-field mapping with a multi-pixels. In particular, we aim at having the most homogeneous map as possible. To achieve this, we need to scan as fast as possible so that the observing conditions are as comparable as possible on the whole map. We can then repeat the map as many time as possible so that the data affected by technical problems or bad weather happening during one coverage can just be discarded. In any case, at least two coverages obtained in perpendicular scanning direction is always advise to be able to use destriping algorithms (*e.g.* plait algorithms). Stripes happen because the system stability (weather, telescope, receiver and backend) evolves from one row to the other. Getting stripes is all the more probable than the time to scan a row is long. So this argues against making very wide scans, which are at the same time required to decrease the relative time spent in the edge overheads. A compromise is thus to map area chunks which are as close as possible to squares. A way to parametrize this is to introduce the map aspect ratio, defined as

$$a = \frac{d_\parallel}{n_\perp \, d_\perp} \quad \text{with} \quad a > 1 \quad \text{and} \quad n_\perp \text{ integer}. \tag{16}$$

A given area $A_{\rm map}$ will be mapped in chunks whose area ($A_{\rm chunk}$) is defined by the linear scanning speed and the time of stability of the system ($t_{\rm chunk}$). This gives

$$n_\perp \, d_\perp \, (d_\parallel + d_{\rm edge}) = A_{\rm chunk} \quad \text{with} \quad A_{\rm chunk} = v_{\rm linear} \, d_\perp \, t_{\rm chunk}. \tag{17}$$

Using 16 to replace $d_\parallel$ by $a \, n_\perp \, d_\perp$, we yield

$$n_\perp^2 + n_\perp \, \frac{d_{\rm edge}}{a \, d_\perp} - \frac{A_{\rm chunk}}{a \, d_\perp^2} = 0. \tag{18}$$

Table 1: Mapping strategy to minimize edge effects.

$t_{\rm chunk}$ min.	$n_\perp$	a	$\eta_{\rm edge}$
1	1	3.7	0.83
2	2	1.9	0.83
5	4	1.2	0.86
10	6	1.1	0.90

This equation of the 2nd order has only one physical solution

$$n_\perp = \frac{1}{2} \, \frac{d_{\rm edge}}{a \, d_\perp} \left[\sqrt{1 + \frac{4a \, A_{\rm chunk}}{d_{\rm edge}^2}} - 1 \right]. \tag{19}$$

We note that this yields

$$\eta_{\rm edge} = \frac{1}{1 + \frac{2}{\sqrt{1 + \frac{4a \, A_{\rm chunk}}{d_{\rm edge}^2}} - 1}} \tag{20}$$

$$\text{with} \quad \frac{a \, A_{\rm chunk}}{d_{\rm edge}^2} = \frac{\theta}{4\delta} \, \frac{a \, f_{\rm dump} t_{\rm chunk}}{\left[\left(\sqrt{n_{\rm subscan} \, n_{\rm pix}} - \frac{1}{\sqrt{n_{\rm subscan} \, n_{\rm pix}}} \right) - \left(\sqrt{n_{\rm subscan}} - \frac{1}{\sqrt{n_{\rm subscan}}} \right) \right]^2}. \tag{21}$$

This expression can be used to understand how to get the highest mapping effiency ($\eta_{\rm edge}$). This implies to get the largest value of the $(a \, A_{\rm chunk})/d_{\rm edge}^2$ ratio. We see that the larger the multi-pixel array, the smaller this ratio. Increasing the chunk area, either by increasing the linear velocity (*i.e.* increasing the dump rate, $f_{\rm dump}$) or by increasing the stability time ($t_{\rm chunk}$) will increase the efficiency. The dump rate is fixed by the peak data rate, which gives typically $f_{\rm dump} = 2$ Hz. The stability time depends on the switching mode: It is the time between two off measurements in position switch (typically 1 or 2 minutes) and the time between two calibrations in frequency switch (typically 10 to 15 minutes).

Previous equations give the impression that the aspect ratio is a free parameter. This is not fully true because, $n_\perp$ must be an integer. The following algorithm ensures that we get an integer value for $n_\perp$ with the value of $a > 1$ and closest to 1. Starting with $a = 1$, Eq. 18 gives a value of $n_\perp$. We enforce the integer nature of $n_\perp$ with

$$n_\perp = \text{floor}(n_\perp), \tag{22}$$

and we recompute the associated aspect ratio with

$$a = \frac{A_{\rm chunk}}{(n_\perp \, d_\perp)^2} - \frac{d_{\rm edge}}{n_\perp \, d_\perp}. \tag{23}$$

Table 1 gives the resulting values of $n_\perp$, a and $\eta_{\rm edge}$ as a function of the stability time ($t_{\rm chunk}$). We see that edge efficiencies are quite high. However, it is easier to have square chunks when the stability time is larger.

In summary, the time spent in edges is counted as overheads. It translates into a multiplicative efficiency ($\eta_{\rm edge}$) because we enforce a mapping pattern through rectangular chunks. Although it is not intuitive (edge sizes are in general unrelated to area), this is not a big assumption because the use of a square multi-pixel anyway enforces mapping in rectangular chunks. We now summarize the algorithm to compute $\eta_{\rm edge}$:

Step #1: Computation of input quantities

$$d_\perp = n_{\rm subscan} \, n_{\rm pix} \, \delta, \tag{24}$$

$$d_{\rm edge} = (\sqrt{n_{\rm pix}} - 1) \, (1 + n_{\rm subscan} \sqrt{n_{\rm pix}}) \delta, \tag{25}$$

$$t_{\rm chunk}^{\rm psw} = 2 \text{ minutes} \quad \text{and} \quad t_{\rm chunk}^{\rm fsw} = 10 \text{ minutes}. \tag{26}$$

$$A_{\rm chunk} = \frac{\theta}{4} \, f_{\rm dump} \, \frac{d_\perp}{n_{\rm subscan}} \, t_{\rm chunk}. \tag{27}$$

Step #2: Computation of $n_\perp$ and a

Case $A_{\rm target} < \eta_{\rm edge}^{\rm min} \, A_{\rm chunk}$ with $\eta_{\rm edge}^{\rm min} = 0.8$

1. $n_\perp = \text{floor} \left[\frac{\sqrt{A_{\rm target}}}{d_\perp} \right]$, (28)
2. if $n_\perp = 0$, then send an error message: "Area too small, use raster mapping.", (29)
3. $a = \frac{A_{\rm target}}{(n_\perp \, d_\perp)^2}$. (30)

Case $A_{\rm target} \geq \eta_{\rm edge}^{\rm min} \, A_{\rm chunk}$

1. $n_\perp = \text{floor} \left\{ \frac{1}{2} \, \frac{d_{\rm edge}}{d_\perp} \left[\sqrt{1 + \frac{4 A_{\rm chunk}}{d_{\rm edge}^2}} - 1 \right] \right\}$, (31)
2. if $n_\perp = 0$, then send an error message: "Area too small, use raster mapping.", (32)
3. $a = \frac{A_{\rm chunk}}{(n_\perp \, d_\perp)^2} - \frac{d_{\rm edge}}{n_\perp \, d_\perp}$. (33)

Step #3: Computation of $\eta_{\rm edge}$

$$\eta_{\rm edge} = \frac{1}{1 + \frac{d_{\rm edge}}{a \, n_\perp \, d_\perp}}. \tag{34}$$

Step #4: Recomputation of $A_{\rm chunk}$ and $t_{\rm chunk}$ when $A_{\rm target} < \eta_{\rm edge}^{\rm min} \, A_{\rm chunk}$

1. $A_{\rm chunk}^{\rm new} = \frac{A_{\rm target}}{\eta_{\rm edge}}$, (35)
2. $t_{\rm chunk}^{\rm new} = t_{\rm chunk} \, \frac{A_{\rm chunk}^{\rm new}}{A_{\rm chunk}}$, (36)
3. $A_{\rm chunk} = A_{\rm chunk}^{\rm new}$ and $t_{\rm chunk} = t_{\rm chunk}^{\rm new}$. (37)

If $t_{\rm chunk} < 1$ minute, the targeted area is too small and the PI should use raster mapping instead of OTF mapping.

2.5 Impact on OTF observations

For OTF observations, there are several effects to take into account.

1. We will use the average system temperature to take into account the different mixer performances.
2. Edges result in inhomogeneous noise, which depends on the exact observing setup. We here try to estimate a single noise value for the whole map. The area swept in edges are thus considered as overheads. If the total targeted area is $A_{\rm map}$, the receiver will then have to map $A_{\rm map} + A_{\rm edge}$. As discussed above, we can write the previous sum as a product of the targeted area times an efficiency factor, *i.e.*

$$\eta_{\rm edge} \, (A_{\rm map} + A_{\rm edge}) = A_{\rm map}. \tag{38}$$

We thus have to remplace $A_{\rm map}$ by $A_{\rm map}/\eta_{\rm edge}$ in Eqs 4 and 5 to compute $n_{\rm beam}$ and $n_{\rm submap}$. Now, if edge area is considered overheads when estimating the sensitivity, the spectra acquired in the edges will nevertheless be used to form the final image. We must thus ensure that enough time is observed on the off position when estimating the sensitivity in the position switch mode. This comes naturally if we consider the edge area as part of the submap between two off positions. This implies that the change on the total mapped area, expressed above, is the only one needed in the equations to take the edges into account.

3. A multi-pixel can cover $n_{\rm pix}$ times as fast the same area of the sky with the same sensitivity as a single-pixel of similar $\overline{T}_{\rm sys}$. Another way to look at this, is to assume that each identical (average) pixel will cover an independent part of the sky during a given observing time (*i.e.* $\eta_{\rm tel} \, t_{\rm tel}$). This implies that the area seen by each pixel will be

$$A_{\rm map}^{\rm pix} = \frac{A_{\rm map}/\eta_{\rm edge}}{n_{\rm pix}}. \tag{39}$$

This finally gives

$$\sigma_{\rm psw}^{\rm otf} = \frac{\left(\sqrt{n_{\rm beam}^{\rm pix}} + \sqrt{n_{\rm submap}^{\rm pix}} \right) \overline{T}_{\rm sys}}{\eta_{\rm spec} \sqrt{d\nu \, n_{\rm pol} \, \eta_{\rm tel} \, t_{\rm tel}}}, \quad \text{and} \quad \sigma_{\rm fsw}^{\rm otf} = \frac{\sqrt{2 \, n_{\rm beam}^{\rm pix}} \, \overline{T}_{\rm sys}}{\eta_{\rm spec} \sqrt{d\nu \, n_{\rm pol} \, \eta_{\rm tel} \, t_{\rm tel}}}, \tag{40}$$

where $n_{\rm beam}^{\rm pix}$ and $n_{\rm submap}^{\rm pix}$ are computed with

$$n_{\rm beam}^{\rm pix} = \frac{A_{\rm map}}{\eta_{\rm edge} \, n_{\rm pix} \, A_{\rm beam}} \quad \text{and} \quad n_{\rm submap}^{\rm pix} = \frac{A_{\rm map}}{\eta_{\rm edge} \, n_{\rm pix} \, A_{\rm submap}^{\rm pix}} \tag{41}$$

$$\text{with} \quad A_{\rm submap}^{\rm pix} = v_{\rm area}^{\rm pix} \, t_{\rm stable} \quad \text{and} \quad v_{\rm area}^{\rm pix} = \delta \, v_{\rm linear}. \tag{42}$$

The times spent on and off and in the edges per pixel are then

$$t_{\rm onoff}^{\rm pix} = \eta_{\rm edge} \, \eta_{\rm tel} \, t_{\rm tel} \quad \text{and} \quad t_{\rm edge}^{\rm pix} = (1 - \eta_{\rm edge}) \, \eta_{\rm tel} \, t_{\rm tel}. \tag{43}$$

The algorithm to derive the time/sensitivity estimation in the case of OTF can thus be applied with the following modifications in the input parameters : $t_{\rm onoff}$, $v_{\rm area}$, $n_{\rm submap}$, $n_{\rm beam}$ must be replaced by $t_{\rm onoff}^{\rm pix}$, $v_{\rm area}^{\rm pix}$, $n_{\rm submap}^{\rm pix}$, $n_{\rm beam}^{\rm pix}$.

References

Pety, J., Bardeau, S. and Reynier, E., 2009, IRAM-30m EMIR time/sensitivity estimator, IRAM Memo 2009-1

ALMA Memo 398

Impact of ACA on the Wide-Field Imaging Capabilities of ALMA

Jérôme PETY, Frédéric GUETH, Stéphane GUILLOTEAU

IRAM, Institut de Radio Astronomie Millimétrique
300 rue de la Piscine, F-38406 Saint Martin d'Hères

November 18, 2001

Abstract

This document presents the imaging simulations performed at IRAM to study the importance of the ALMA Compact Array (ACA) on the wide field imaging performances of ALMA. The simulations are based on a fast, approximate but sufficiently accurate method. The image reconstruction is based on two new CLEAN-based deconvolution methods for mosaics. The effects of *i)* pointing errors, *ii)* amplitude calibration errors and *iii)* atmospheric phase noise have been systematically studied. The effect of a poor knowledge of the primary beams has also been studied. Finally we investigated the impact of variations of the deconvolution parameters.

A large number of simulations have been performed, using several test images. This allowed us to disentangle artifacts due to particular random sampling of the errors from the genuine, average impact of these errors on all images. We find that adding ACA observations improves the image quality of ALMA in some types of images. More importantly, ACA provides robust results, when ALMA fails in presence of some type of errors, or on some images. One of the two new deconvolution techniques requires only a very moderate increase in computing time to include the ACA data.

Contents

1 Introduction **3**

2 Simulator Overview **3**
2.1 The Simulation Process . . . 4
2.2 The Simulator Interface . . . 5
2.3 The Simulation Pipeline and Archive . . . 8
2.4 Environment of Development and Performances . . . 8

3 Toward Realistic Simulations: Including Errors **8**
3.1 Pointing Errors . . . 9
3.1.1 Error Models . . . 9
3.1.2 Simulations of the Corrupted Visibilities . . . 9
3.2 Phase Errors . . . 10
3.2.1 Atmospheric Phase Screen . . . 10
3.2.2 Phase Calibration . . . 10

3.2.3 Dynamic Refraction . . . 12
3.3 Amplitude Errors . . . 13
3.3.1 Interferometer Model . . . 13
3.3.2 Single-Dish Model . . . 13
3.4 Thermal Noise . . . 14

4 Mosaic Deconvolution Techniques **14**
4.1 Data from an Homogeneous Array (ALMA-only or ACA-only) . . . 14
4.2 Using Single-Dish Data . . . 15
4.2.1 ALMA and Single-Dish . . . 15
4.2.2 ACA and Single-Dish . . . 15
4.3 Data from an Heterogeneous Array (ALMA and ACA together) . . . 16
4.3.1 Joint Deconvolution . . . 16
4.3.2 *uv* Plane Hybridization Technique . . . 17
4.4 Relative Weight of Data . . . 18
4.4.1 Single-Dish versus Interferometer . . . 18
4.4.2 ALMA versus ACA . . . 18

5 Understanding Fidelities **18**
5.1 Image Plane . . . 18
5.2 *uv* Plane . . . 20
5.3 Summary Plots . . . 21

6 Simulation Description **22**
6.1 The Image Library . . . 22
6.2 Default Conditions . . . 24
6.2.1 Array Layout . . . 24
6.2.2 Atmosphere . . . 24
6.2.3 Observing Cycle . . . 25
6.2.4 Range of Errors . . . 25
6.3 Compared Methods . . . 25

7 Simulation Results **26**
7.1 Error Free Case . . . 26
7.2 Pointing Errors . . . 26
7.3 Amplitude Errors . . . 29
7.4 Phase Errors . . . 32
7.5 Combined Errors in Typical Conditions . . . 33
7.6 Other Tests . . . 34
7.6.1 Primary Beam Errors . . . 34
7.6.2 Mosaic Oversampling . . . 34
7.6.3 Other Combined Deconvolutions . . . 34

8 Comparison with Other Work **35**

9 Conclusions **35**

1 Introduction

With the prospect of Japan joining the ALMA project in a 3-way partnership, it is necessary to explore what are the best scientific options for the possible extensions of the baseline ALMA proposal. These include a compact array of smaller antennas (the ALMA Compact Array – ACA), which would hopefully provide enhanced wide-field imaging capabilities by measuring the short spacings poorly or not sampled by ALMA.

In theory, all *uv* spacings can be measured by an homogeneous array like the ALMA baseline (64 12m–antennas), provided single-dish data is added and mosaicing is used. However, in practice, deconvolution methods do not necessarily recover the proper visibilities on intermediate baselines between 6 and 15 m. Moreover, pointing errors translate into phase errors proportional to the *uv* distance from the closest measured visibilities. Those phase errors are thus greatest around 9 m.

An array of small antennas, e.g. 7m–dishes, could measure directly these visibilities and be less sensitive to the pointing errors. Initial simulations (Pety et al. 2001 [5, 6], Yun 2001 [9], Morita 2001 [4]) showed that this is indeed the case. However, measured visibilities are also affected by other type of errors, like atmospheric phase noise and errors of amplitude calibration. No complete simulation including realistic values for these errors has yet been performed. Thus, it is not yet known whether the advantage provided by the ACA addition about the pointing errors remains significant in practical observing conditions.

This document presents in a comprehensive way the software developed at IRAM to do such simulations, and the results that have been obtained. In particular, it addresses the following problems:

- Can the short spacing information be recovered properly?
- Is the data obtained with ACA more immune to errors than data obtained with ALMA only?
- What happens when pointing errors induced by anomalous refraction are considered in a coherent way with the atmospheric phase errors?
- Are these results independent of the types of scientific problems?

Sections 2–4 presents the details of the methods used for the simulations. The readers interested in the results only may skip these sections and proceed directly to Sections 5–8, or even to the conclusions (Section 9).

2 Simulator Overview

Our goal is to compare wide–field imaging capabilities of ALMA with or without the use of ACA data. This section gives an overview of the steps taken to do this. In short, we need to simulate *i)* interferometric observations with ALMA and ACA and *ii)* single-dish observations with a limited number of 12m-antennas. To make these simulations realistic, different type of errors are introduced (a thorough description is given in Section 3). The different simulated observations must then be merged and deconvolved to produce the simulated images (cf. Section 4). A comparison between those simulated images and the input model finally allows us to evaluate the contribution of ACA to the image quality.

2.1 The Simulation Process

The simulator includes the following steps:

Interferometer simulation

The same routines are used to simulate ALMA or ACA observations (only the input parameters differ). For simplicity sake, simulation is made in 3 steps: amplitude and phase errors are first encapsulated as complex gains; ideal visibilities are then computed from the input model image; error gains are finally applied to the ideal visibilities.

1. *uv* coverage
   The *uv* coverage is generated from the array configuration, source declination, and observing time. A short timescale *uv* table corresponding to the baselines sampled every second is generated. It initially contains perfect gains (Amplitude 1, Phase 0).
2. Instrumental gain.
   Gains are then corrupted by the phase errors due to the atmospheric phase screen, and by the amplitude errors. For convenience, effects resulting from phase calibration are included in this step, i.e. the final gains contained in the *uv* coverage table are **calibrated** gains. A table of pointing errors induced by anomalous refraction is also computed at this step.
3. Time average.
   The gain table is then time-averaged according to the selected integration time (dictated either by the Nyquist rate, or the observing sequence). Correction for decorrelation is applied at this step.
4. Model visibilities.
   Generation of the model visibilities, including pointing errors, is made only on the integration–time basis. Hence, the pointing errors tables (induced by anomalous refraction and/or from a model including thermal or wind effect) are first time averaged. Visibilities are then computed for each integration period using the effective pointing centers for each antenna. Pointing errors induced by anomalous refraction can be taken into account.
   Mosaics are simulated by adding the field offsets to the pointing error at the beginning of this step. The output *uv* table is sorted to produce one *uv* table per field. Note that the procedure assumes that the fields are observed in a loop (i.e. in a snapshot mode), each visibility dump corresponding to another position in the sky. The total integration time is truncated so that an integer number of cycles is observed.
5. Corrupted visibilities.
   The visibilities computed in the previous step are multiplied by the gain table obtained in step 3 to account for phase and amplitude errors.

Single-Dish simulation

1. Single-Dish observations.
   The model image is convolved by the antenna lobe and the intensity is then estimated at *(i)* the position of the mosaic fields (for merging with ALMA visibilities), and *(ii)* on an extended grid (for merging with ACA visibilities), with typically 3 pixels per beam. If the required position does not coincide with a pixel center, a bilinear interpolation from the neighbor pixels is performed.

   Pointing errors can be included by estimating the intensity at the position corrupted by the pointing offset. Thermal noise can then be added to the data and the corresponding weight is stored. Finally, an error of amplitude calibration can be simulated.
2. Extracting Single-Dish pseudo-visibilities.
   If the Single-Dish data are to be merged with the ACA data, then "pseudo-visibilities" are computed from the Single-Dish map (see Section 4.2.2 for a detailed description of the algorithm).

Imaging

1. Merging interferometric and Single-Dish visibilities.
   The merging of the two datasets is done for each field. The relative weight between the two datasets is an adjustable parameter (see Section 4.4.1).
2. Mosaic reconstruction.
   Dirty images are produced for each mosaic field, and are then linearly combined to produce the dirty mosaic (cf. Section 4.1).
3. Deconvolution.
   The mosaics are deconvolved with the appropriate algorithm (see Section 4). Depending on the initial setup of the simulator, six images can possibly be produced: ALMA-only, ACA-only, ALMA+SD, ACA+SD, ALMA+ACA, ALMA & ACA+SD.
4. Hybridization.
   If required, two images can be combined in the *uv* plane to produce the **hybrid** deconvolved image (see Section 4.3.2). This is done in practice with ACA+SD and ALMA+SD.

Comparison between model and simulation

For each of the 7 possible simulated images, a comparison is performed with the original image, convolved with the appropriate CLEAN beam. A **fidelity** (see Section 5) image is computed. The comparison is performed both in the image and the *uv* plane.

2.2 The Simulator Interface

In order to perform the various steps involved in the simulation, flexible procedures as well as a window interface were written. The top part of Fig. 1 shows the control window of the simulator. The user has to define 3 global parameters: the input model image, the output directory, and the type of simulation. 7 different types of simulations can be made: ALMA only, ACA only, ALMA+ACA, ALMA+SD, ACA+SD, **all** (= ALMA & ACA+SD), and **hybrid** (*uv* plane hybridization). All results are stored in the same output directory, so that a simulation requiring results from another one shares the same files when needed.

A simulation actually consists in 3 different steps, each with its own associated button: `COMPUTE` the observation results, `COMPARE` with the original data, and `DISPLAY` the comparison. The `COMPUTE` step can be replaced by a `LOAD` step if results from a previous simulation exist. In addition an `EXPERT` button allows access to individual steps in the computations (not recommended, but useful for debugging new features).

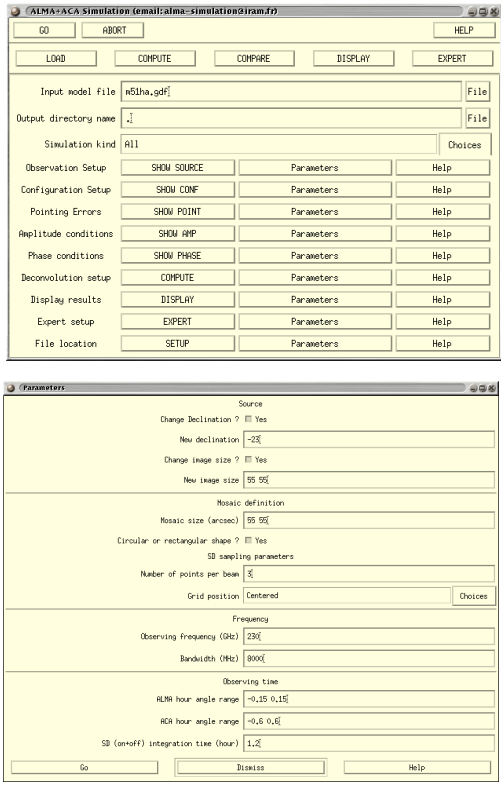

Figure 1: Top: Control window of the simulation package. Bottom: Window obtained by clicking on the "parameter" button in the main window, allowing one to modify the default parameters (here, of the `Observation Setup`).

The control window includes definition buttons, which allow one to setup simulation parameters (through pop-up windows as shown on the bottom part of Fig. 1):

`SHOW SOURCE` defines the source related observation parameters: source declination, image size, mosaic size and shape, parameters of the single-dish map, observing frequency and bandwidth, hour angle range for ALMA and ACA, and single-dish integration time.

`SHOW CONF` defines the array configuration parameters, of ALMA (style and size of the array configuration), ACA (size of antennas, style and size of the array configuration), and Single-Dish (number and size of antennas used for single dish).

`SHOW POINT` defines the pointing errors. For each sub-array (ALMA, ACA or SD), it specifies the error model, the rms value of the error, and a filename in case of table-driven errors.

`SHOW AMP` defines the amplitude conditions: errors and noise. Noise is derived from specified receiver temperature and zenith opacity. Amplitude errors are specified by the rms value, drift value and drift time constant.

`SHOW PHASE` defines the atmospheric phase conditions. They are specified by the phase screens for ALMA and ACA, the phase noise at 300 m, wind speed and direction, the screen altitude, the calibrator position, the integration time on source and calibrator, the parameters of the Water Vapor Radiometry, and the calibration method. In addition, a parameter indicates whether anomalous refraction should be computed and added to the pointing errors.

`COMPUTE` activates the simulation. This button has a number of parameters to specify the details of imaging and deconvolution: the Single-Dish weight, the primary beam truncation level for the mosaic, the number of CLEAN components, the CLEAN loop gain. When hybridizing different simulated images in the *uv* plane, the images and the *uv* transition radius to be used can also be selected here.

`DISPLAY` displays the results. Several displays are possible:

- The fields position;
- The single-dish image;
- The *uv* weights;
- The synthesized beam(s);
- The flux convergence, i.e. the cumulative flux as function of CLEAN component number;
- The image plane comparison: the model, simulated, difference, and fidelity images are plotted; it also presents the cumulative histogram of the fidelity;
- The *uv* plane comparison: the visibility amplitudes are plotted for the model and the difference; the fidelity directly computed in the *uv* plane as well as a radial average of the fidelity are also shown;
- Two different types of summary plots presenting a combination of the previous ones;
- The phase calibration results when available.

`EXPERT` toggles some controls to allow "experts" to force performing some simulation steps. This should only be used for debugging or special simulations.

`SETUP` specifies the location of the model images, pointing error tables, and phase screens.

The input parameters of the simulation and the intermediate results are stored in files, thus allowing one to re-run part of the simulation using previously computed data, i.e. without starting from the very beginning. Only the incomplete simulation steps are re-done when needed.

2.3 The Simulation Pipeline and Archive

On top of the GILDAS simulator, a pipeline was written to run automatically all the procedures and save the results. This allows us to run a large number of simulations to assess the impact of the different input parameters (e.g. short spacings addition, noise level, pointing errors, etc.) on the image quality.

The pipeline maintains a database of results, which can be browsed through GILDAS procedures to select and display part of it. More than 2000 different simulations were performed in the course of the ACA study, leading to more than 100 GBytes of results.

2.4 Environment of Development and Performances

The simulation package was developed and implemented in the GILDAS environment, used for the data reduction softwares of the IRAM instruments. As the whole GILDAS environment, the simulator runs under HPUX, Linux (RedHat), or MS-Windows. The simulator uses the MAPPING subpart of GILDAS. Starting from the existing tools, a number of new algorithms were developed and implemented, as e.g. the simulation of single-dish measurements, pointing errors models, the estimation of visibilities in presence of pointing errors, or the deconvolution of data taken with an heterogeneous array. In addition, several existing tasks were improved to be more flexible, and/or to save some memory space, and/or to speed up the computation time. For that purpose, part of the MAPPING software code was translated from FORTRAN-77 to FORTRAN-90, which allows an easier implementation of mathematical algorithms.

The amount of time needed to perform a simulation depends on the size of the problem. On a 1 GHz AMD Athlon PC with 756 Mbytes of memory, the simulation of a 7–fields mosaic observed with ALMA takes only a few minutes. The simulation of ALMA & ACA+SD is somewhat longer, ∼15–20 minutes, because the deconvolution of an heterogeneous array is rather slow. As a rule, the imaging part (Fourier Transform and deconvolution) is always the time-consuming step of the simulation.

3 Toward Realistic Simulations: Including Errors

The simulation engine has been designed to handle pointing, phase and amplitude errors. Speed was the major design goal. Accordingly, the simulations have limited accuracy; in the absence of error, the relative precision of the simulation is about 1 part in a thousand. However, as shown below, the inclusion of typical error values completely dominates the image quality. The relative inaccuracy of our modeling is thus not a problem.

3.1 Pointing Errors

3.1.1 Error Models

Pointing errors include:

- Systematic offset: a global mispointing of the mosaic.
- Random offsets per antenna: such offsets can result for example from measurement errors in the last pointing calibration.
- Wind induced effects: a randomly variable component, with a range of direction and magnitude, and a correlation coefficient between antennas. The timescale of variation is of order 1 second.
- Thermally induced effects: a drift with time, with slowly varying direction and a large correlation coefficient between antennas. This large correlation is used to reflect the common deformation mode of the antennas due to solar illumination. The timescale for variation is of order 10 to 30 minutes.
- The so-called "*anomalous*" or rather *Dynamic* refraction. The *anomalous* refraction is due to time variations of the refractive index of the wet air along the line of sight. This is a perfectly "normal" and unavoidable process, so we prefer to call it *Dynamic* refration, by opposition to the *Static* refraction due to the static part of the atmosphere.

The derivation of dynamic refraction is described in Section 3.2.3. The other terms are computed for each antenna on a 1 second timescale basis, and stored in a pointing error table. Time averaging is then applied to derive the mean pointing error on the integration timescale. Several tables of pointing errors have been generated. The use of a pre-calculated pointing error table allows us to apply the same errors to the ALMA and ALMA+ACA simulations, and hence compare intrinsic differences rather than effects due to different generation of random numbers.

3.1.2 Simulations of the Corrupted Visibilities

For a single field, the observed visibility is the Fourier Transform of the multiplication of the sky brightness distribution by the primary beam of the antenna (i.e. the convolution of the Fourier Transform of the sky brightness by the antenna transfer function, which is simply the Fourier Transform of the antenna beam). For rapidly varying pointing errors, as this is the case in our simulations, this quantity has to be computed for each integration time or dump. Rather than computing this convolution by a multiplication in the image plane followed by Fourier transform (which would be needed for each integration time), we perform it directly in the *uv* plane. The visibilities are estimated by the convolution of the (gridded) FFT of the sky brightness distribution by an analytic form of the antenna transfer function. We use a truncated Gaussian illumination, with 11.5 dB edge taper[1]. Pointing errors are simply handled by applying the appropriate phase term to the antenna illumination pattern. Furthermore, the convolution is approximated by a weighted sum of the neighbor points. Since the illumination pattern has an outer radius equal to the antenna diameter, this is a local operation in the *uv* plane, to be performed at each required *uv* position.

[1] The transfer function is the autocorrelation of the antenna illumination.

3.2 Phase Errors

Phase errors are directly proportional to pathlength errors. Phase errors can thus be introduced into the simulation, using a pre-calculated table of pathlength errors. Only pathlength errors due to the atmosphere are used in this memo, although introduction of other types of pathlength errors would be possible (e.g. baseline errors).

3.2.1 Atmospheric Phase Screen

To compute the atmospheric phase errors, we generate a 2-D phase screen on a grid with sufficient spatial resolution to sample the antenna diameter (typically 4-m pixels for ALMA, and 2-m pixels for ACA). The phase screen is generated in the Fourier plane with the constraint that its 2nd order structure function is a combination of 3 power laws in 3 different spatial ranges. The resulting phase screen is averaged over the effective dish diameter. Because of the size limitation imposed by the FFT, very long phase screen are built as a linear combination of independently generated screens. This is correct since atmospheric pathlength variations are completely uncorrelated at large distances.

Observations through the phase screen are simulated in a realistic way. The observing direction through the screen is computed every second for the source as well as for the calibrator. Moreover, the phase screen is assumed to move with a given wind speed along one direction. For simplicity sake, the wind direction is assumed to be constant in time. This simplification should only have a small effect on the phase error since the phase screen is isotropic (see however the dynamic refraction paragraph). The free parameters are: the rms phase on the 300-m baselines, the angular distance between source and calibrator, the direction of the wind with respect to the source-calibrator vector, and the wind speed and altitude of the phase screen above the ground.

The use of the 2-D approximation prohibits exact handling of the elevation dependence of the phase function. We instead used a simple prescription in which the phase error scales with the square root of the elevation. An example of a phase screen and its gradients is given in Fig. 2.

3.2.2 Phase Calibration

Since source and calibrator are observed through the same phase screen, standard phase calibration techniques can also be applied to the simulated data. 4 different calibration methods have been implemented:

1. Standard calibration: a continuous curve (polynomial or smoothing spline) is fitted through the time sequence of calibrator phases , and removed from the source phases.
2. Fast switching: a linear interpolation of the phase is performed between two consecutive calibrator measurements, and removed from the source phases.
3. Water Vapor Radiometry: a WVR might be used to correct the atmospheric phases in real time. We modeled the corrected phase as

$$P_{\rm WVR}(t) = P(0) + \chi(P(t) - P(0)) + N(t) \quad (1)$$

where $P(t)$ is the original atmospheric phase, and $t = 0$ is the beginning of the observing sequence. χ is the precision of the radiometer: $\chi = 0$ represents a perfect correction, $\chi = 1$ no correction. $N(t)$ is the phase noise introduced by the WVR. In our model, we assume the WVR is not able to follow the atmospheric phase when slewing from the calibrator to the source ("*non-connecting*" WVR), and thus reset

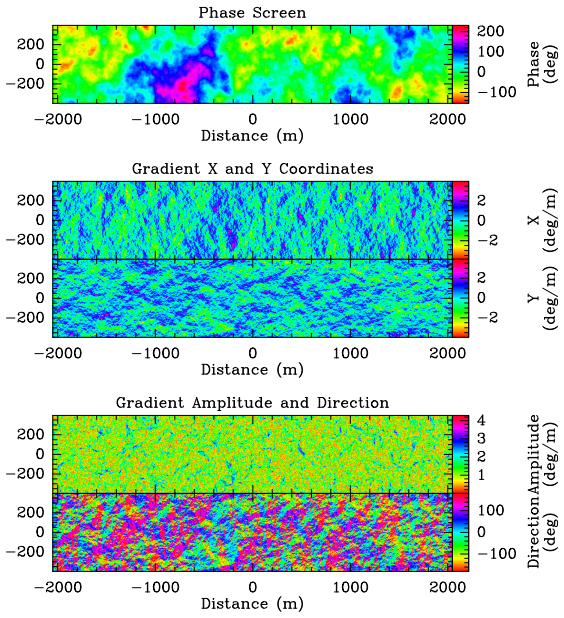

Figure 2: Example of a phase screen with its associated phase gradients, also shown as magnitude and direction.

$t = 0$ at each change between source and calibrator. A subsequent phase calibration is thus required.

4. Combined WVR and Fast Switching: in this mode, the WVR is used to correct the short term phase fluctuations, and the phase on the last calibration $P_{\rm cal}$ is subtracted from $P_{\rm WVR}(t)$. This is an optimum scheme for "*non-connecting*" WVR.

Fig. 3 shows the phase structure function before and after phase calibration for Option 2 and 4. Option 4 gives the best result on baselines longer than about 80-m. However, there still is a residual phase error after calibration even with a perfect WVR ($\chi = 0$ and $N(t) = 0$). This is due to the angular distance between the source and calibrator, and the limited antenna speed which imposes a time delay between the source and calibrator

measurements. Only a *connecting* WVR, which allow (partial) pathlength correction even when slewing from source to calibrator, would possibly give better results. Option 4 gives better result than Option 3 (not shown here) because the time delay is half the switching period in Option 3, while it is only the slew time in Option 4.

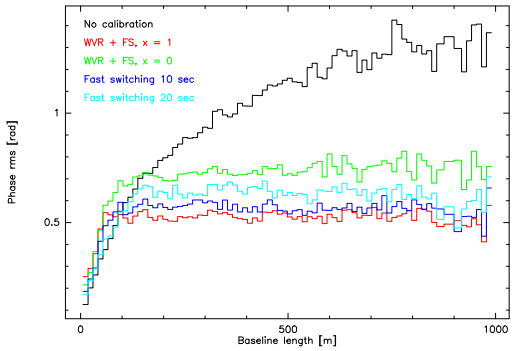

Figure 3: Residual rms phase errors as function of baseline length after application of different calibration methods. The calibrator was 2 degrees away from the source, and the phase screen was 1000-m above the site, moving at a wind speed of 10 m/s.

Note also that calibration **increases** the phase noise on short baselines. Moreover, the shorter the calibration timescale, the larger the phase noise on short baselines increases. This indicates that a better calibration strategy for ACA, whose baselines always are shorter than 60 m, would be to use Option 3 with a long calibration timescale.

3.2.3 Dynamic Refraction

Dynamic (anomalous) refraction is directly proportional to the phase gradient. We thus compute the phase gradient associated to the phase screen, in order to obtain a coherent derivation of the dynamic refraction term. As the phase screen, the phase gradient is averaged over the effective dish diameter.

In practice, we did not compute the effect of the resulting pointing error every second, and average the visibilities afterward, but rather compute the mean pointing error on each integration time. This procedure is justified because the theoretical (error free) visibilities are not changing significantly within each integration time (since we sample better than the Nyquist rate).

Computing the mean pointing error in each integration time is equivalent to averaging the phase gradients in an anisotropic way, i.e. convolving them with a function elongated along the wind direction. It can be seen from Fig. 2 that after such an anisotropic smoothing, one of the (smoothed) gradient components will be smaller than the other, since each gradient has a different preferential direction . The resulting gradient is larger across than along the wind direction, implying that dynamic (anomalous) refraction has a privileged direction, related to the wind. As surprising as it looks, this is an intrinsic property of the gradients of turbulent fields.

In actual conditions, this anisotropy may be small because the wind direction has some random variations. Moreover, it would be difficult to observe because other pointing errors will also have preferential directions with respect to the wind (such as the errors induced by wind pressure on the antenna).

3.3 Amplitude Errors

Amplitude errors mostly originate from *i)* uncertainties and variations in the atmospheric transmission, and *ii)* slow antenna gain variations due to dish distortion and defocus, especially at high frequencies. Receiver gain fluctuations and drifts should remain at a much lower level than the two previous, unavoidable, effects.

3.3.1 Interferometer Model

The error on the amplitude gain is modeled as the sum of an offset and a drift with time. The offset and drift values are randomly reset at each calibration for each antennas. The typical amplitude calibration timescale has been set to 15 minutes. So far, no correlation coefficient between the amplitude errors of the various antennas has been used, although some of the effects will have a common mode (e.g. it is likely that thermal deformation of the dishes are similar in all antennas).

It is assumed that the amplitude drop due to decorrelation (due to the phase fluctuations during the integration time) is completely calibrated out. Failure to do so results in systematic under-scalings of the visibilities, but has no significant influence on the morphology, since the phase noise is essentially constant as function of baseline length after calibration (see Fig. 3).

3.3.2 Single-Dish Model

As for the interferometer, the error on the amplitude gain is modeled as the sum of an offset and a drift with time, whose values are randomly reset every 15 minutes for each antenna. In addition, an offset common to all the antennas can also be added to the amplitude gain.

For the single-dish data, the effects of errors on flux densities highly depends on the observing strategy. How many antennas are used, do they scan the source or do they point on a few observing direction, what are the possible scanning directions, what averaging is performed become a required knowledge to derive the final resulting error on the single-dish image. In the absence of a prescription for the Single-Dish observing strategy, we implemented the two simplest approaches depending on the kind of interferometric data that Single-Dish will complement.

Combination with ACA data A single-dish map is here useful to provide the short spacing information (see Section 4.2.1). We thus assume that a single-dish map is obtained for each antenna by scanning the appropriate region as slowly as allowed by the available observing time. At each second, the 4 used antennas look at the same direction. The 4 maps obtained with the 4 antennas are later averaged together. For example, for a 7 field mosaic, each single-dish map is made of 21×21 points sampled at $1/3^{\rm rd}$ of the beamwidth. Obviously, obtaining the maps by scanning as fast as possible, and crossing the scanning

direction between antennas at each second would result in more homogeneous maps. Hence, the selected method somewhat maximizes the distortion one may expect from amplitude errors.

Combination with ALMA data When combining with ALMA data, only the total flux for each field can be used (see Section 4.2.2). We thus assume that each field center is observed at least once per independent amplitude calibration sample (e.g. every 15 minutes in our typical simulation). For example, for a 7 field mosaic, only 7 directions on the sky are observed. Compared to the previous map, the amplitude error is thus smaller by a factor of $\sim \sqrt{21 \times 21/7} \sim 8$ in the typical simulation. Care is also taken that exactly the same amplitude errors are applied to these single-dish fluxes than to the single-dish map. Hence, for the 7 field mosaic, each of the 7 pointing directions is observed 63 times to use the same 441 error values as used for the single-dish map required for ACA. Further reduction of the amplitude error will result from the averaging over the 4 Single-Dish antennas, because of the uncorrelated part of the amplitude errors.

Comparison of the two observing strategies The simulation thus somewhat disadvantages the ACA observations (which rely on a Single-Dish map) with respect to ALMA observations. The opposite is perhaps more likely to happen in reality. Indeed, assuming that we can actually directly measure the flux density for each field center requires an observing method such as wobbler switching to a blank field. In many circumstances, such blank fields will not exist, and Single-Dish flux densities for the mosaic fields may have to be derived by interpolation from a fully sampled On–The–Fly map, rather than from direct observations of the field centers. Even with full sampling, the interpolation errors could easily be of order 2-3 %.

3.4 Thermal Noise

Thermal noise can be accounted for in our simulation. The thermal noise is derived from $T_{\rm sys}$ (taking into account the variation with elevation), the integration time, and the bandwidth. This is done for Single-Dish data as well as for interferometric observations. The simulation process also allows us to add random phase noise to the visibilities. Such phase noise is expected, especially when using a WVR.

4 Mosaic Deconvolution Techniques

Deconvolution of the raw images obtained with ALMA and ACA is required to provide correct comparison between the initial image and the simulation results. We used CLEAN-based deconvolution methods, which we summarize in this section.

4.1 Data from an Homogeneous Array (ALMA-only or ACA-only)

The deconvolution of a mosaic observed from an homogeneous interferometer (i.e. all array antennas have the same diameter) is done using a CLEAN-based method developed for the IRAM Plateau de Bure interferometer (see e.g. the chapter on mosaicing in the proceedings of IRAM millimeter interferometry summer school). In short: the dirty mosaic is reconstructed as a linear combination of all dirty maps,

$$J = \left(\sum_i \frac{B_i}{\sigma_i^2} F_i \right) \Big/ \left(\sum_i \frac{B_i^2}{\sigma_i^2} \right) , \qquad (2)$$

where F_i, B_i and σ_i respectively are the dirty map, the primary beam and the rms noise of each field. The mosaic is thus homogeneous to the sky brightness distribution, but the noise level is not uniform and strongly increases at the edges of the field of view. As a consequence, using the classical CLEAN method can be dangerous, as noise peaks might be selected as CLEAN components. The method used for the Plateau de Bure data consists in selecting the CLEAN components on a modified mosaic: the initial mosaic is normalized by the noise level distribution. Hence, this modified mosaic is homogeneous to the signal-to-noise ratio.

Truncated primary beams B_i are used instead of the theoretical beam to avoid propagation of errors at beam edges. The truncation threshold is one free parameter in the method. The algorithm turns out to give excellent results, both in terms of image quality and computation time. It has been used during the last few years to deconvolve the mosaics observed with the Plateau de Bure interferometer.

4.2 Using Single-Dish Data

In the presence of extended structure, the previous algorithm cannot recover all structures[2]. Inclusion of the short spacing information is required.

4.2.1 ALMA and Single-Dish

In this case of an homogeneous array, the short spacings are measured with the same antennas as the interferometric data. As the measured visibilities results from the convolution of the Fourier Transform of the model with the antenna transfer function (i.e. a local average, cf. Section 3.1.2), single dish measurements can only give the *zero spacing* in this case. This is done by inserting for each field the *zero spacing flux* (as measured in single-dish mode) prior to the imaging. The mosaic deconvolution then proceeds as before. The method provides good convergence properties.

4.2.2 ACA and Single-Dish

When complementing ACA interferometric data, the short spacings will come from the ALMA antennas. It is then possible to take advantage of the larger diameter (D) of the ALMA antennas to derive short spacing informations for the small antennas of diameter d up to distance $D - d$ in the uv plane (where the convolution to compute the visibility makes sense). This is done by the following operations:

1. The Single-Dish measurements are re-gridded and then FFTed into the uv domain.
2. The data are corrected for the single-dish beam by division by its Fourier Transform (truncated to the antenna diameter).
3. The data are FFTed back to the image plane where the ACA primary beam is applied (by multiplication).
4. The visibilities are then interpolated from a regular grid after yet another FFT.
5. In the case of a mosaic, the two last operations are performed for each pointing center.

Visibilities up to $D - d$ are finally extracted and merged with the ACA data before proceeding to the mosaic stage as in Section 4.1.

[2] In theory, with an infinite size mosaic, short spacings can be recovered, but the zero spacing is recovered only with zero weight...

4.3 Data from an Heterogeneous Array (ALMA and ACA together)

When using data from the ALMA and ACA arrays, the imaging problem becomes more complex, since two different types of primary beams now exist. We have developed two imaging methods with can handle such situation, provided no correlations between small and large antennas are performed. In the first method, the deconvolution operates at the same time on both types of data. In the second method, ALMA and ACA mosaics are separately deconvolved and then combined in the *uv* plane. This second method has a very small computation overhead compared to the deconvolution of the ALMA mosaic alone.

4.3.1 Joint Deconvolution

Description Starting from two *uv* tables corresponding to the observations of the same source with two arrays, the following operations are performed:

1. Fourier Transform of the data, and reconstruction of two separate mosaics (the ALMA and ACA ones). Although the field positions do not need to coincide in the observations performed by the two arrays, this is the case with the current version of the simulator.
2. Major cycles are performed, in which CLEAN components are identified in the residual image with the highest signal-to-noise ratio. A very satisfying method (in terms of image quality and convergence speed) is to use the Clark method [1] if the components are to be found on the ALMA image, and the Steer-Dewdney-Ito approach [8] if they are to be found on the ACA image.
3. The components found in each major cycle are subtracted from both residual images. If they were identified on the ALMA image, a compression allows us to re-sample them on the ACA grid. However, the components found on the ACA image need a more complex processing to make sure that the same quantity is subtracted from both residual images (otherwise the method would diverge). We first derive from each ACA component a set of contiguous positions on the ALMA grid, such that they cover exactly the area of the pixel of the ACA grid; these components are then subtracted from the ALMA residual image; they are also compressed (via FFT) back to the ACA grid, to be subtracted from the ACA residual image. This back-and-forth method allows us to get rid of the ambiguities (interpolation errors, aliasing) that would occur if the ACA components would have been directly interpolated on the ALMA grid.
4. Finally, all CLEAN components identified by the algorithm are convolved by the ALMA clean beam (highest angular resolution), and the weighted residual images are added.

Short spacing information can also be introduced in this method, either in the ALMA data as before (see Section 4.2.1), or (more logically) in the ACA data (Section 4.2.2), or even in both. In practice, we incorporated the short spacings in the ACA data. As with the more simple homogeneous problems, the relative weight of Single-Dish data compared to interferometric data is a key parameter in the convergence speed. A poorly adjusted weight can slow down considerably the deconvolution. In this work, we always used the weights imposed by the noise level for this purpose (see Section 4.4.1).

Convergence Properties The convergence properties of this method are more complex (and less satisfying) than those of standard CLEAN. The algorithm usually quickly recovers the total flux, but then often needs a large number of components to locate the fine structures. Flux overshoot during the deconvolution process can sometimes occur, especially when the Single-Dish weight is too high. This non-monotonic flux convergence property can be understood as a result of the competition between the need to determine to first order all the flux (measured only with ACA), and then to locate precisely point sources (located only with ALMA).

To illustrate this problem, consider a set of 5 points sources at the corners and center of a square. Depending on the size of the square, the joint deconvolution may be fast or slow. For a square much larger than the ACA synthesized beam, the sources will be identified as point sources by ALMA, and quickly removed. For a square similar to the ACA synthesized beam, it is possible that the SNR (Signal to Noise Ratio) in the ACA data (where it looks like a point source) is larger than in the ALMA data (where each source is separated from the others). In this case, a mean flux will first be removed, and details of the structure within the square will require a larger number of CLEAN components than in the other case.

Conclusion This CLEAN-based algorithm adapted to heterogeneous arrays proved to be quite valuable and able to handle a wide variety of images. It can still be improved in several ways: e.g. by constraining the number of components to be found in each image, or by using a smoother kernel to derive the ALMA components from the ACA components, etc...

4.3.2 *uv* Plane Hybridization Technique

The method consists in combining two images, e.g. the deconvolved ALMA+SD image and the deconvolved ACA+SD image, in the *uv* plane. The FFT of the two clean images are computed, and linearly combined by selecting one image for *uv* distances shorter than e.g. 15 m, and the other for larger *uv* distances. The result is FFTed back to the image plane to produce the final image. The method has the following free parameters: the transition radius, the detailed shape of that transition, and the images to actually be combined. To avoid discontinuity, the transition shape is chosen to be reasonably smooth. The transition radius was chosen as 15 m, since beyond that ALMA data usually has better SNR than ACA data.

Another possibility is to combine clean images from ALMA+SD and ALMA & ACA+SD. By doing this, one can combine the advantages of several deconvolution methods and produce an optimum result. For example, because of the slow convergence of the joint ALMA & ACA+SD deconvolution, the deconvolved ALMA+SD image often better reproduces the long *uv* ranges, while the ALMA & ACA+SD image better reproduces the large scale structures, i.e. the short *uv* spacings. Provided the transition radius is well chosen, the hybrid image is thus better than any of these two.

In practice, the differences between both type of combinations were usually limited. The chosen combination (ALMA+SD and ACA+SD) has two significant advantages: *i*) it requires only very limited computation in addition to the deconvolution of ALMA+SD (the deconvolution of ACA+SD is much faster than ALMA+SD because of the smaller number of pixels) and *ii*) although we actually use a deconvolved ACA+SD image, the sampling of the *uv* plane up to 15 m is complete, so a linear combination of the initial visibilities could in principle be made. Noise amplification due to deconvolution should thus be very limited (see Schwarz 1978 [7]).

4.4 Relative Weight of Data

4.4.1 Single-Dish versus Interferometer

In all cases involving short spacings, the relative weight of the single dish data to interferometer data is critical. Within the restrictions imposed by the noise level, this weight is a free parameter. The usual approach is to match (as far as possible) the Single-Dish and interferometric densities of weights in the *uv* plane. This is what is required to provide a complete Gaussian beam from a truncated Gaussian weight distribution in the *uv* plane. This approach is optimal in terms of noise, since the restoring beam is usually Gaussian.

The weight distribution of the ALMA compact configuration is not yet completely decided, but is likely to have some over density of weights at the shortest spacings (15 to 25 m). Hence, when doing the single-dish weight matching, it may be better to consider the average weight density in the 25 to 50-m spacing range. For ACA, which only has 12 antennas in our study, the weight distribution is very uneven, and matching the weight density of single-dish is more problematic. The optimum result may depend on the image being restored.

4.4.2 ALMA versus ACA

Similarly, the relative weights of ALMA and ACA data can be derived from weight density in the *uv* plane. The optimal relative weights directly determine the relative integration times of each data set (ALMA, ACA and Single-Dish). In practice, a good result is obtained with ACA and the 4 12-m antennas observing 4 times longer than ALMA. Another possible approach is related to signal to noise considerations. Since there is much more flux at short spacings than on longer baselines, and since these are affected by calibration errors anyhow, it may be worth relaxing the noise level at the shortest baselines, hence diminishing the integration times with ACA. This obviously would depend on the image.

5 Understanding Fidelities

Estimating the quality of the simulated image as compared to the original model is not an easy task: the actual criteria to estimate the observation quality depends on the science that is to be done! Despite this caveat, and in order to provide a quantitative evaluation of the methods, we chose to present the results in terms of **fidelity**. Fidelity is the inverse of the relative error. A fidelity of 100 is equivalent to a 1% relative error.

Fidelities can be computed either in the image plane or directly in the *uv* plane. While the latter tell us which space scales are well reproduced, the former quantifies the visual impression coming from the comparison of the model image with the simulated one. A thorough investigation of the imaging capabilities of the instrument must take into account those two pieces of information.

5.1 Image Plane

In the image plane, the fidelity is defined as

$$\text{Fidelity}(i,j) = \frac{\text{abs}(\text{Model}(i,j))}{\text{abs}(\text{Model}(i,j) - \text{Simulated}(i,j))} \quad (3)$$

In practice, the very high fidelity points due to value coincidence between the model and simulation have to be flagged out, because they do not reflect the mean accuracy of the

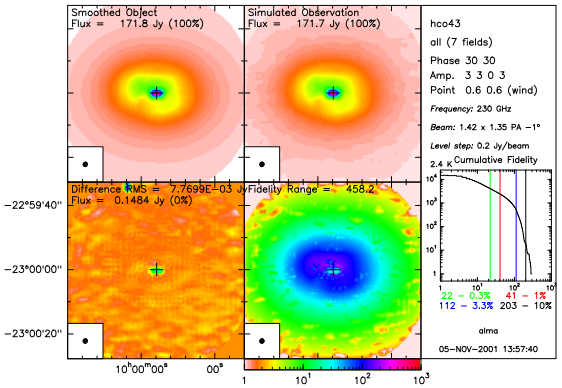

Figure 4: Image plane display of the fidelity.

simulation. For that purpose, the lowest values of the difference image are truncated, and the fidelity image is thus computed as:

$$\text{Fidelity}(i,j) = \frac{\text{abs}(\text{Model}(i,j))}{\max(\text{abs}(\text{Difference}(i,j)), 0.7 \times \text{rms}(\text{Difference}))} \quad (4)$$

The `DISPLAY` task plots the fidelity image as well as a cumulative histogram of the fidelity values, i.e. the number of pixels whose values are larger than a given fidelity. It also computes the median fidelities, taking into account only the pixels whose intensity in the initial model image is higher than 0.3, 1, 3 or 10% of the peak. Using the statistical properties of *median* values, *median* relative errors can be computed by just taking the inverse of these fidelities. Fig. 4 displays the summary of the fidelity in the image plane. It is a composite display containing:

- Top Left: the model image convolved with the CLEAN beam;
- Top Right: the simulated, deconvolved image produced by the observations;
- Bottom Left: the difference image;
- Bottom Right: the fidelity image;
- Right Insert: the cumulative histogram of the fidelity image, with median fidelity values for pixels above 4 thresholds (as fraction of the original image peak).

Those 4 median fidelities are convenient when doing a large number of simulations: they allow a global estimate of the effect of one of the parameters (e.g. pointing errors) on the simulation results. We also compute the "fidelity range" defined by L.Kogan:

$$\text{Fidelity range} = \frac{\max(\text{abs}(\text{Model}))}{\text{rms}(\text{Difference})} \quad (5)$$

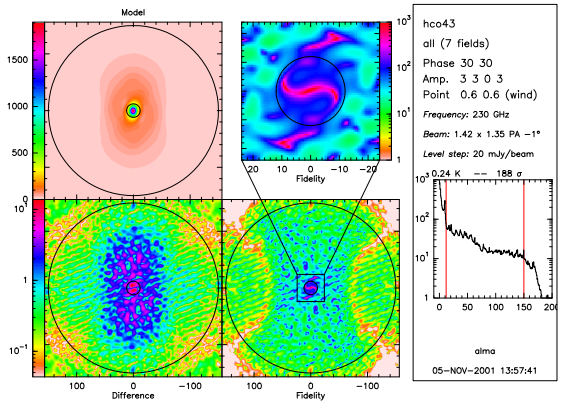

Figure 5: *uv* plane display of the fidelity.

This estimator converges toward the image dynamic range for images dominated by a single point source, and toward the median fidelity for images dominated by extended structure. In the present study, we found more convenient to use the 4 median values rather than the fidelity range to quantify the simulation results. The fidelity range is thus not used anymore in the remaining part of this memo.

5.2 *uv* Plane

The fidelity can also be analyzed in the *uv* plane. This is convenient to see which space scales are well represented, and which are most affected by errors. Typical output is shown in Fig. 5. It includes:

- Top Left: the amplitude of the FFT of the model image (convolved with the CLEAN beam);
- Bottom Left: the amplitude of the FFT of the difference between the model image and the simulated image;
- Bottom Right: the fidelity distribution in the *uv* plane, defined as the model divided by the difference; note that this is **not** the Fourier transform of the Image plane fidelity;
- Top Right: A zoom of the fidelity over the inner 20-m square of the *uv* plane;
- Insert: the azimuthal average (not median) of the fidelity as function of *uv* radius.

This type of plot is particularly useful to compare the different methods since all expected differences should only occur in the 0-15 m *uv* range. In addition, fidelity drops at longer baselines is a diagnostic of insufficient convergence of the CLEAN algorithm.

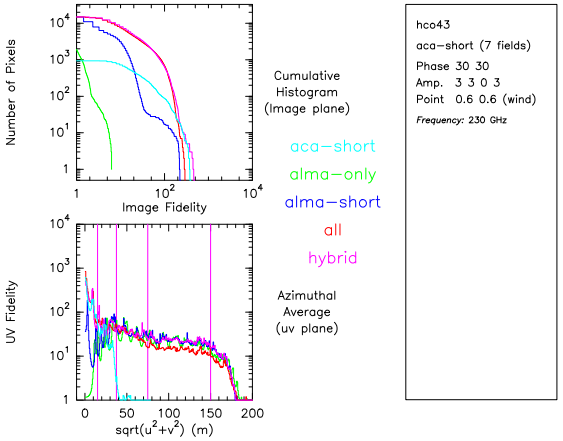

Figure 6: Overlay of the Image and *uv* plane summary displays of the fidelity for 5 different observation and deconvolution methods.

As above, fidelity medians can be computed in 4 different range of *uv* distance (0–15 m, 15–37.5 m, 37.5–75 m, 75–150 m) to allow easy estimation of trend when varying one parameter of the simulation. Some artifacts are sometimes visible in the *uv* plane fidelity, like a centered cross, and/or ring-like structures. These artifacts are related neither to the simulation nor to the deconvolution but to the presentation process: they are due to the sharp edges of the mosaic. It is possible to reduce these artifacts by applying a shallower mask. We simply chose to forget about these artifacts, since they play a minor role on the median fidelities.

5.3 Summary Plots

Comparison between the results provided by the various observation and deconvolution methods (for a same set of observing conditions) can be summarized with the two "summary" plots presented as the inserts in the image and *uv* fidelity displays. This is shown in Fig. 6.

6 Simulation Description

6.1 The Image Library

A set of test images has been used to evaluate the performances of the various observation and deconvolution methods. The images are:

- An Hα image of the M51 galaxy, with high angular resolution. The original image is 1024×1024 pixels. It contains a large number of point sources, spread over a wide area, which simulate extended emission when observed with low angular resolution. Its dynamic range exceeds 10^4. The image was provided by D.Thilker.
- An image of an HII region in M31, with complex extended structure. The image size is 128×128, and its dynamic range about 3000. The image was provided by M.Holdaway.
- A model of the HCO^+(4-3) line emission in a protostellar envelope. The image size is 256×256, and the dynamic range about 200. The image was provided by M.Hogerheijde.
- A model of a protostellar cluster, with a dozen of protostellar condensations. The image size is 512×512 pixels. The dynamic range exceeds 10^4. The image was provided by K.Tatematsu.
- A model of turbulent cloud. The image size is 512×512 pixels, and the dynamic range about 100. The power spectrum of this distribution is known. The image was provided by J.Pety.
- A model of a dusty disk around a young star, with tidal gaps created by proto-planets. The image was provided by L.Mundy.

These images have obviously different properties: spatial dynamic range from 50 to 500, intensity dynamic range from 100 to several thousands, filamentary structures in some of them, core dominated structures in others, etc... They are expected to represent a reasonable sample of the scientific problems requiring short spacing information.

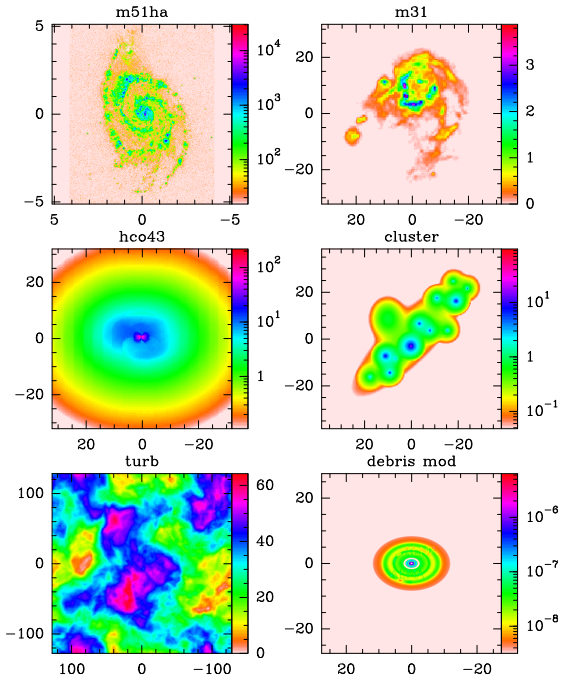

Figure 7: Images used to test the imaging properties of ALMA and ACA. Image sizes and amplitude scales are arbitrary.

6.2 Default Conditions

6.2.1 Array Layout

The array configurations used for the simulations are shown in Fig. 8. The ACA array consists of 12 7m–antennas used as an interferometer; 4 12m–antennas are simultaneously used for Single-Dish measurements. It is assumed that these 12+4 antennas are correlated together for calibration operations (Guilloteau 2001 [2]). No particular optimization process has yet been done to select the ACA configuration: it was manually selected among several randomly generated configurations. Optimization of the sidelobes level may yield better results. Note that there is a slight inconsistency between the number of ALMA antennas involved in this study (64) and the number which should actually be cross-correlated if ACA is used (60). This should however have negligible impact on the results.

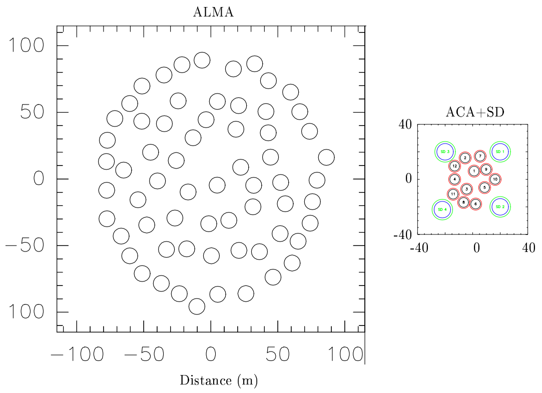

Figure 8: Selected ALMA and ACA configurations. The ALMA compact configuration was designed by M.Yun, and include 64 12-m antennas. The ACA is made of 12 7-m antennas, with close packing limited to 1.25 times the diameter, with 4 12-m antennas used as single-dish.

6.2.2 Atmosphere

We used a calibrator 2 degrees away from the source on a direction perpendicular to the wind. The phase screen was assumed to be at 1000 m above ground level, moving at 10 m s^{-1}. A "*non-connecting*" perfect WVR was assumed to be used for phase calibration, with phase referencing on the previous calibrator (Option 4 in Section 3.2.2). Note that, as shown in Fig. 3 this scheme **increases** the residual phase noise on the shortest baselines (< 30 m).

The specification of the statistical properties of the used phase screen are based on the results of the site survey. It provided a scaling exponent and a mean value on the 300-m projected baselines for the square root of the 2nd order structure function of the phase. Values to be applied to real observations depend on the observing strategy. Following Holdaway et al. (2001 [3]), we used an exponent of 0.62 on all baselines for our simulations: This may overestimate the phase noise and especially the dynamic refraction on the shortest baselines.

Using a strategy where the observing frequency is selected according to the atmospheric phase stability would result in a typical rms phase between 30 and 45 degrees at zenith. It will scale approximately as square root of the number of airmass. Other observing strategy (e.g. selecting frequency according to the atmospheric transparency) will usually result in **higher** phase noise, especially at high frequencies. However, for low frequency observations, it will still be possible to pick up observing conditions where the rms phase noise is lower than those typical numbers.

6.2.3 Observing Cycle

We simulated short observations (but not a snapshot): ALMA observes for 18 minutes, and ACA and the 4 Single-Dish 12-m antennas observe for 4 times longer (i.e. 72 minutes). The basic observing cycle was 26 seconds long: 2 seconds on calibrator, 2 seconds dead time, 20 seconds on source, 2 seconds dead time. All observations are centered around transit with sources transiting at zenith. ALMA and ACA observe the same field centers, i.e. the ACA mosaic is oversampled. For a 7 field mosaic, each field is observed 6 times with ALMA, and 23 times with ACA. Some azimuthal smoothing of the instantaneous synthesized beam thus occurs, compared to snapshot observations.

6.2.4 Range of Errors

We made computations scanning "likely" ranges of errors: 0–18 % relative pointing error (compared to the 12-m primary beam width), 0–10 % relative amplitude error, 0–60° phase errors. With 4 pointing errors, 4 amplitude errors, 4 phase errors, 6 sources, this represents 384 different simulations. We also performed simulations with one type of errors only to evaluate the effect of different error models: e.g. another set of 282 simulations were made to test 9 different sets of pointing errors. We finally made computations in "typical" high frequency observing conditions, defined as: pointing error 6 or 12% of the 12-m primary beam, amplitude error 3% (and drift 6% per hour), phase error 30°. In total, more than 700 simulations were performed.

6.3 Compared Methods

We made computations for 4 different methods:

1. **alma-only** which includes only ALMA interferometric data;
2. **alma-short** where single-dish flux has been added to the ALMA interferometric data (mosaic deconvolution of ALMA+SD);
3. **all** which results from the joint deconvolution of the ALMA and ACA+SD dirty mosaics (see Section 4.3.1);
4. **hybrid** which results from the *uv* plane hybridization of the ALMA+SD and ACA+SD clean mosaics (see Section 4.3.2).

	Intensity threshold (in % of peak intensity) 0.3%				1%				3%				10%			
m51ha	1	4	23	28	1	23	72	90	2	32	104	128	4	56	162	189
HCO43	1	3	83	46	1	5	132	66	1	14	260	112	1	14	506	148
turb	1	3	32	20	1	3	32	20	1	3	33	20	1	3	33	20
m31	1	139	92	119	2	160	112	145	2	186	141	175	2	223	175	211
cluster	1	103	141	145	2	141	191	179	2	178	249	213	4	268	377	286
debris	3	185	153	183	4	196	200	196	4	186	220	191	22	195	161	193

Table 1: Comparison of the median fidelities measured in the image plane for different observing modes and/or deconvolution algorithms: observation with ALMA only (**alma-only**, first columns); observations with ALMA and the 4 Single Dish antennas (**alma-short**, second columns); observations with ALMA, ACA and the 4 Single Dish and with a joint deconvolution (**all**, third columns) or with a separate deconvolution (**hybrid**, fourth columns). The median fidelities are measured for 4 different intensity thresholds. Observations simulated here are **ideal** (i.e. without noise or errors). Note that for the first 3 images, using the ACA data considerably improves the median fidelities.

	uv range 0–15m				15–37.5m				37.5–75m				75–150m			
m51ha	2	39	376	309	138	384	463	546	192	578	335	820	118	392	134	505
HCO43	2	15	468	545	56	104	307	145	67	151	244	213	30	59	71	73
turb	1	2	29	38	4	6	18	16	6	10	9	20	4	5	4	5
m31	2	827	496	501	23	1396	328	1265	50	1683	307	1696	29	752	103	803
cluster	2	491	484	523	94	1788	736	1833	118	1558	385	1455	65	898	153	763
debris	4	326	1545	1568	249	2315	1273	3011	663	3459	1751	5325	505	2164	995	2910

Table 2: Idem as Table 1 except that fidelities are here directly measured in the Fourier plane between 4 *uv* ranges. Note that for the first 3 images the use of ACA data improves the 0-15 m median fidelities by at least one order of magnitude (in the present **ideal** case).

7 Simulation Results

7.1 Error Free Case

The error free case is a useful limit *i)* to figure out the properties and precision of the simulation and deconvolution methods, and *ii)* to provide a reference. A summary is given in Tables 1–2.

A striking result is that some images are better deconvolved with ACA, others without. However, in all cases, using ACA produces a good result, while some catastrophic failures occur without it. An extreme example is the `turb` image, which is only well reconstructed with the **all** method; this image has very little power in small scale structures, and CLEAN has real difficulties in handling it. A second result is that all the differences indeed come from the 0-15 m range, which usually dominates the image plane fidelity. Extremely high fidelities can be obtained, showing that the approximations made in the simulation process are small enough for our purpose.

7.2 Pointing Errors

Simulations were made to assess the effects of pointing errors. Three different models of pointing errors were used: wind induced pointing errors (`Wind` model), thermally induced pointing errors (`Thermal` model), or both together (`Both` model). Sample results are given in Fig. 9–10 for two sources, `HCO43` and `cluster`. These results do not include anomalous refraction, which has negligible effect (see Section 7.4).

The results properties are best understood by looking at the *uv* plane fidelities. **all** always give better fidelity in the 0–15 m *uv* range, but sometimes lower fidelities than either **alma-short** or even **alma-only** at the longest baselines. When pointing errors approach 10% of the beamwidth, the three methods give essentially similar fidelities in the *uv* plane

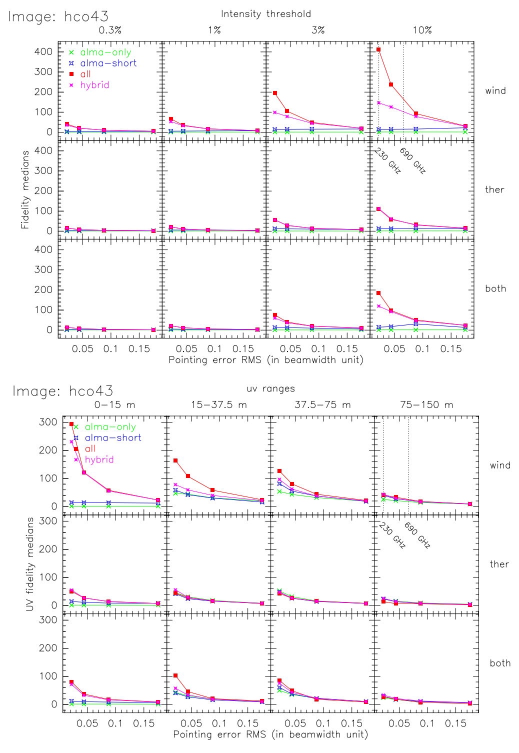

Figure 9: Median fidelities computed in the image plane (top) and the *uv* plane (bottom) as function of pointing errors. The model image is here `HCO43`.

ranges above 15 m. **all** continues to give better results in the range 0–15 m. The **hybrid** method, which was used with a transition radius of 15 m, basically combines the best of both worlds. It is only marginally worse than **all** for `HCO43` because the 15–30 m *uv* range is still poorly represented by **alma-short** in this image. In the image plane, **alma-short**, **all**

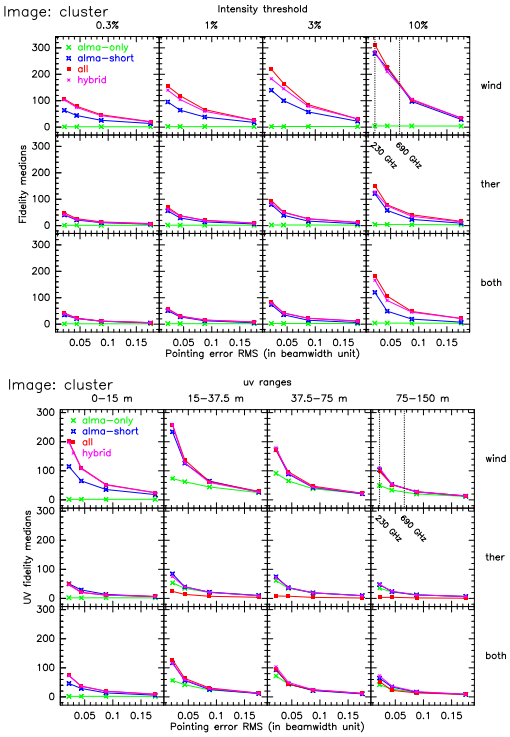

Figure 10: Same as Fig. 9 except for the model image, which is here `cluster`.

and **hybrid** converge to very similar results for large pointing errors, but **all** and **hybrid** remain superior in practically all cases.

The effect of pointing errors should be understood in a statistical sense. Because the observing duration is short, the results for any particular simulation may depend on the exact values of the generated pointing errors. In some circumstances, a pointing error may actually lead to increased image fidelity for part of an image where the deconvolution

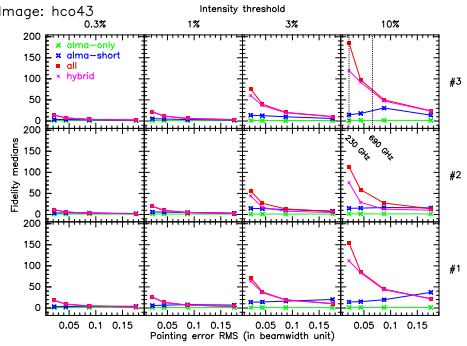

Figure 11: Image plane median fidelities for `HCO43` for 3 different samples of pointing errors.

method fails in the absence of error. The median fidelity for the brightest pixels of `HCO43` is particularly likely to suffer from such coincidences, because this image has only one bright peak and thus few pixels above 10% of the peak intensity. Effects of different pointing samples with the same rms value are shown in Fig. 11. It is seen that fidelities from **alma-short** occasionally improves for some particular pointing error, while the behavior of either **all** or **hybrid** is quite smooth and monotonic.

7.3 Amplitude Errors

Fig. 12 and 13 shows image plane and *uv* plane fidelities as function of amplitude errors. Amplitude errors have only been applied to Single-Dish data in Fig. 12, and to both Single-Dish and interferometric data in Fig. 13.

Even small amplitude errors on the Single-Dish data (2 %) can have dramatic effects on the fidelities in the 0–15 m range but, as expected, little or no impact at all on the fidelities at longer baselines (see Fig. 12). When amplitude errors are also applied to the interferometer data, the fidelity (in the image or the *uv* plane) drops smoothly with increasing error (see Fig. 13). Similarly to pointing errors, a single example is not sufficient to evaluate the effect of amplitude errors, and the image plane fidelities can get spuriously high in some cases.

Although the adopted observing strategy for the Single-Dish favors the **alma-short** method in presence of amplitude errors (see Section 3.3), we here find that **all** and **hybrid** remain superior to **alma-short** in all circumstances, especially in the 0–15 m range. Also note that the effect of amplitude errors on interferometric data is relatively limited if they remain below 3 %.

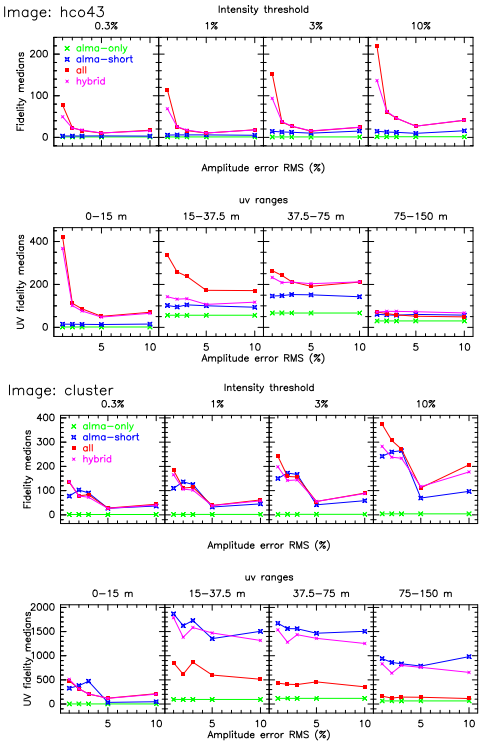

Figure 12: From top to bottom: Image and *uv* plane median fidelities as function of amplitude errors for `HCO43`, and then for `cluster`. Amplitude errors have only been applied to Single-Dish data (i.e. interferometric data is error free).

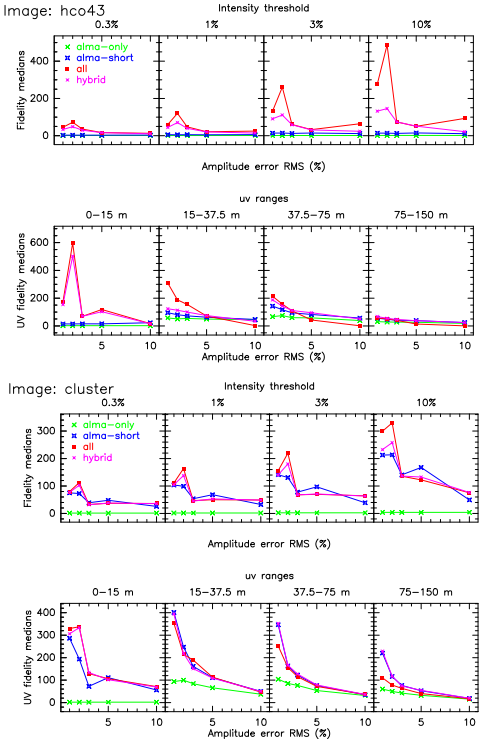

Figure 13: Same as Fig. 12 except that amplitude errors have been applied to both Single-Dish and interferometric data.

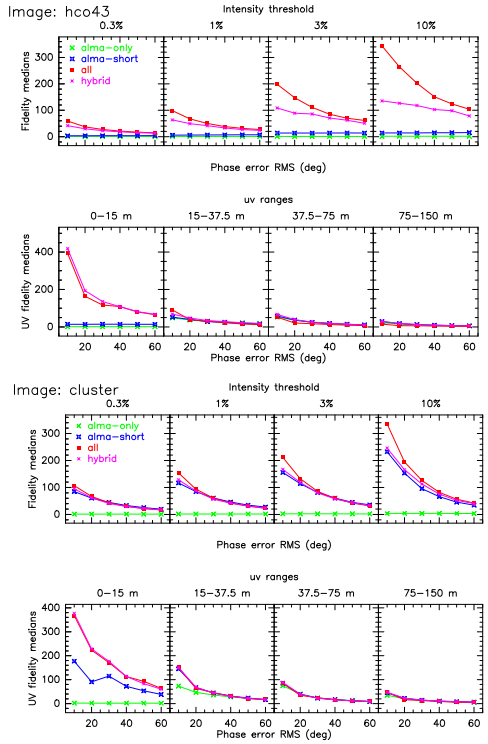

Figure 14: From top to bottom: Image and *uv* plane median fidelities as function of phase errors for `HCO43`, and then for `cluster`.

7.4 Phase Errors

Phase errors only affect the interferometer data.

Fig. 14 shows image plane and *uv* plane fidelities as function of phase errors (expressed as the value of the rms phase noise for 300 m–baselines) for two images. There is smooth

errors, 3% beamwidth fractional pointing error (0.6″ in each direction at 230 GHz), and 30° phase noise on 300-m baseline, with a 0.62 scaling exponent. The pointing error was assumed to follow our "Wind" error model (indeed high frequency mosaic observations could be done at night where thermal effects are negligible). The results are presented for all images in Tables 3–4. An interesting property of these results is that, despite the large differences between the images in the absence of errors, image plane fidelities become quite similar with these typical errors. Image plane fidelities of 30 to 50 are found for the 0.3 to 3% intensity thresholds. Amplitude errors are negligible in this result, while pointing and phase errors have similar importance.

Note also that in the presence of these errors, the **hybrid** method basically gives the best results on all images, even if **all** was significantly better in the absence of errors. The **hybrid** method also gains an advantage over **alma-short** for all images.

7.6 Other Tests

7.6.1 Primary Beam Errors

Our model of the primary beam assumes a truncated Gaussian in the *uv* plane (i.e. a Gaussian illumination distribution up to the antenna radius) and a perfect Gaussian (with matched beamwidth) in the image plane. While this is inconsistent from a theoretical point of view, this corresponds reasonably well to what is occurring in real-life, where a more detailed model of the primary beam might be difficult to implement.

We also performed (though accidentally...) a series of computation where the primary beam was truncated to its 10 % level in the image plane. While this may be a rather large error on the knowledge of the primary beam, these computations allowed us to find out that the **all** or **hybrid** methods are much less sensitive to errors on the primary beam than **alma-short**.

This should be kept in mind when considering high frequency mosaics, where the wavelength is closer to the precision of the surface accuracy (i.e. the primary beam will only approximately be known because of surface errors and varying shape of the antenna dish). A systematic (although simple) investigation of errors on the primary beam could be made with our package, which offers a scaling parameter for the beamsize.

7.6.2 Mosaic Oversampling

We tried oversampling the ALMA mosaics by factors 1.49 and 1.73. The corresponding mosaics had 13 and 23 fields respectively, and covered a somewhat larger region than the original 7 fields mosaic. We did not find any significant improvement in the **alma-short** results when doing so. There was some improvement in the **all** results for long baselines, presumably because oversampling effectively gives measured visibilities at more *uv* points. It however did not improve at all the recovery of short spacings.

7.6.3 Other Combined Deconvolutions

We tried a joint deconvolution of ALMA+SD with ACA+SD, rather than ALMA-Only with ACA+SD as in the **all** method. This produced significantly worse results.

On the other hand, combining the results of **alma-short** with those of **all** to obtain the **hybrid** results improved the image fidelity on the most difficult cases (the `HCO43` image). However, it was also necessary to increase the transition radius to obtain this improvement. We believe that our original hybrid (ALMA+SD and ACA+SD) provides the advantage of much faster computation, and a robust default value for the (a priory adjustable) transition radius.

	Intensity threshold (in % of peak intensity)															
	0.3%				1%				3%				10%			
m51ha	1	5	6	6	1	20	21	21	2	30	39	41	3	60	77	83
HCO43	1	4	22	19	1	7	41	34	1	15	112	75	1	15	203	111
turb	1	2	29	16	1	2	29	16	1	2	29	16	1	2	29	16
m31	1	39	33	36	1	47	40	46	2	60	52	58	2	75	66	72
cluster	1	40	47	43	2	56	69	60	2	77	96	81	4	96	126	101
debris	3	29	51	55	3	32	69	77	4	35	94	95	14	56	56	70

Table 3: Same as Table 1 except that errors are set at their typical values.

	uv range															
	0–15m				15–37.5m				37.5–75m				75–150m			
m51ha	2	39	56	48	35	41	44	43	30	30	29	30	21	21	21	21
HCO43	2	15	175	183	21	41	46	52	29	33	33	33	20	22	15	23
turb	1	2	39	17	4	5	14	14	6	9	8	19	4	5	4	6
m31	2	68	85	103	30	52	41	49	28	28	29	28	21	21	16	21
cluster	2	85	142	167	54	67	66	65	36	35	37	35	23	24	23	24
debris	3	36	221	191	54	60	45	62	37	37	46	37	26	26	27	26

Table 4: Same as Table 2 except that errors are set at their typical values.

(almost monotonic) degradation of the fidelities with increasing phase error. For most images (like `cluster`), all methods converge toward the same (rather poor) result at the largest error values. **all** and **hybrid** remain however superior in all circumstances, especially in the 0–15 m range.

Contrary to pointing and amplitude errors, the average effect of phase errors is well represented by a single simulation because there are many random phase errors generated in a single observation (one random number per antenna per integration time, or about 4000 numbers for one observation).

We also checked the effect of dynamic (anomalous) refraction associated with the simulated phase screen. We found that the effect of the associated pointing error was small compared to the direct effect of the phase. Moreover, it is even possible that the scaling exponent value (0.62) used for the phase structure function actually overestimates phase errors on short baselines, where one would expect 3-D turbulence to dominate and lead to a steeper exponent (0.83). Accordingly, anomalous refraction needs only to be considered through its effect on pointing calibration on one hand, and on single-dish observations on the other hand. The impact of anomalous refraction on single-dish data will depend on the array layout (through the relative location of the Single-Dish antennas), and on the observing strategy.

7.5 Combined Errors in Typical Conditions

In real life, all types of errors are present. From the ALMA specification, we may expect a typical amplitude calibration error of no more than 3%. For pointing errors, the specification is 0.6″ which translates into 1 to 10% of the beam width for frequencies between 100 and 900 GHz. However, anomalous refraction, whose value typically ranges from 0.5 to 2″ may add up as a measurement error to this value. Atmospheric phase noise has a typical value of 30–45° on a 300-m baseline, if observing frequency is matched to the phase conditions.

We thus made a set of simulations assuming the following "typical" errors: 3% amplitude

8 Comparison with Other Work

The computations presented here represent the most extensive set of imaging simulations performed for ALMA. Only part of the results have been presented in this document, but the complete set can be accessed from the ALMA Web site at IRAM[3].

We only used CLEAN-based deconvolution methods. However, M.Holdaway (NRAO) and K-I.Morita (NAOJ) performed similar, though less extensive, simulations using MEM-based deconvolutions (Maximum Entropy Method). They also use a different method to derive visibilities. Their simulation process is more accurate in the absence of errors, because of the handling of the pointing problem. But both simulations give very similar results in the presence of errors. In particular, it appears that the difference in behavior between the various images is not related to the use of a particular deconvolution tool, but rather is an intrinsic property of the image.

K-I.Morita also performed simulations including thermal noise, and found that the behavior depends in a rather complex way on the noise level. Basically, MEM requires a SNR of at least 5 on ACA visibilities to perform properly, and can catastrophically fail otherwise. We have not yet performed simulations with a varying noise level. However, in our **hybrid** process, the operations performed to recover the short spacings are essentially linear (because the *uv* coverage is complete, see Schwarz 1978 [7]). We thus expect this method to be stable with respect to noise. On the other hand, it is possible that the **all** method be less stable in this respect.

M.Holdaway suggested that adding a "guard band" of fields around the useful mosaiced region significantly improves MEM imaging in the **alma-short** case. This may be understood when the emission falls to zero at the image edge, since it would provide a reference value for MEM. Whether this result also applies to CLEAN remains to be studied. Moreover, it is unclear that this improvement also occurs in a complex area where emission extends well beyond the mosaic edge.

9 Conclusions

In summary, we found that:

1. The homogeneous array, even with the inclusion of zero spacing (ALMA+SD), fails to produce reliable results on some type of images. This failure is not so much related to unavoidable observational errors (phase noise, pointing or amplitude errors), but rather to the amount of smooth extended structure present in the image.

2. The addition of data from a compact array of 12 7m–antennas (ACA) allows one to obtain reliable results in all circumstances. Although the newly developed joint deconvolution (ALMA & ACA+SD) sometimes produces the most accurate image, in presence of typical observational errors, the simpler and much faster *uv* hybridization method (ALMA+SD with ACA+SD) gave similar or even better results on all test images.

3. The inclusion of ACA data allows one to produce images which are much less sensitive to primary beam errors than ALMA+SD. Although we did not quantify this advantage, it should not be forgotten since primary beams may actually not be well known, especially at the highest frequencies.

[3] http://iram.fr/~alma

4. We found that the effect of pointing errors due to anomalous refraction is much less significant than the direct effect of phase errors on the visibilities when standard (i.e. observed) parameters of the atmospheric model are used.

5. The data processing remains simple, and does not require any significant additional computing power.

Although the above results are based on CLEAN-based deconvolution techniques, it is important to stress that independent work based on MEM deconvolution have confirmed the main conclusions.

We thus conclude that the addition of the ACA brings a significant advantage to ALMA in typical observing conditions, and provides the following improvements to the ALMA project:

1. A more robust imaging process.

2. Results more immune to pointing and primary beam errors.

3. A practical advantage for the short spacing measurements: since only 4 12-m antennas are used, it may be easier to equip these antennas with optimized hardware for single-dish. This can include wobbling subreflectors, receiver optimized for stability, specific hardware for anomalous refraction correction such as a scanning water vapor radiometer, etc... It may also be possible to select the best 4 antennas among the 64 available ones.

In addition to these basic improvements, the ACA provides an array available in a compact configuration at any time for high frequency work, whereas the 12-m antennas of ALMA may be spread in long baseline configurations when observing conditions suitable to high frequency work occur. Indeed, at 900 GHz, ACA provides an angular resolution of $1.5''$, quite comparable to that provided by the compact configuration of ALMA at 230 GHz.

Additional remark ACA certainly results in additional complexity in the operations, since it basically represents another array with its own observing program. It also induces some more complexity for construction and maintenance, by introducing a different type of antenna and receivers. Using the same antenna mount and the same focal ratio will limit, but not suppress the differences.

Future work Although fairly realistic, our simulations are amenable to several extensions and improvements:

1. The effects of thermal noise should be checked.

2. The indirect effect of dynamic refraction on pointing error measurements could be accounted for more accurately. The properties of the phase structure function imply some correlation between the pointing errors introduced by dynamic refraction on the various antennas. The amount of correlation depend on the power spectrum of the phase, and also on the array layout.

3. The effects of primary beam errors could be incorporated and studied.

4. Single-Dish observations could be simulated in a more realistic way. This would likely improve results based on the ACA+SD mosaic (the **hybrid** and **all** method), and degrade results of the **alma-short** method.

Because of the robustness of the results obtained with ACA, we do not believe any of these additional tests will result in a significant change of our conclusions.

Finally, the simulator developed in the course of this project may play a role in the future of ALMA by helping astronomers to evaluate ALMA performance on their data. Its speed (about 10 minutes per image on today's computers) makes it amenable to extensive use, and it can readily be converted into a fully automated pipeline, taking a model FITS image as input, producing a "likely" output image and estimating expected image fidelity. Such a tool could be important to help astronomers select the best observing strategy.

Acknowledgements

We thank M.Holdaway for his critical screening of our simulation results, all ACA "tiger" team members for their comments, F.Viallefond for his nice ideas about the atmospheric phase screens and H.Wiesemeyer and V.Pietu for efficient help during some parts of this study.

References

[1] B. G. Clark. An efficient implementation of the algorithm 'CLEAN'. *A&A*, 89(3):377–378, 1980.

[2] S. Guilloteau. Single-Dish and short baselines. ALMA Memo XXX, IRAM, 2001. In preparation.

[3] M. A. Holdaway and J. Mangum. Relative pointing sensitivity at 30 and 90 ghz for the ALMA test interferometer. ALMA Memo 373, NRAO, 2001.

[4] K.-I. Morita. Wide field imagings with the Atacama large millimeter/submillimeter array. ALMA Memo 374, NAOJ, 2001.

[5] J. Pety, F. Gueth, and S. Guilloteau. ALMA+ACA simulation results. ALMA Memo 387, IRAM, 2001.

[6] J. Pety, F. Gueth, and S. Guilloteau. ALMA+ACA simulation tools. ALMA Memo 386, IRAM, 2001.

[7] U. J. Schwarz. Mathematical-statistical description of the iterative beam removing technique (method CLEAN). *A&A*, 65:345–356, 1978.

[8] D. G. Steer, P. E. Dewdney, and M. R. Ito. Enhancements to the deconvolution algorithm 'CLEAN'. *A&A*, 137(2):159–165, 1984.

[9] M. Yun. An imaging study for ACA. ALMA Memo 368, NRAO, 2001.

ALMA Memo No. 488.1
Wide-Field Imaging of ALMA with the Atacama Compact Array: Imaging Simulations

Takahiro Tsutsumi[1], Koh-Ichiro Morita[2], Tetsuo Hasegawa[1],
and
Jérôme Pety[3,4]

[1] *National Astronomical Observatory of Japan (NAO-J), 2-21-1 Osawa, Mitaka, Tokyo 181-8588, Japan*
tsutsumi@alma.mtk.nao.ac.jp, tetsuo.hasegawa@nao.ac.jp

[2] *Nobeyama Radio Observatory, NAO-J, Nobeyama, Minamimaki, Minamisaku, Nagano 384-1305, Japan*
morita@nro.nao.ac.jp

[3] *IRAM, 300 rue de la Piscine, 38406 Grenoble Cedex, France*
pety@iram.fr

[4] *LERMA, Obs. de Paris*

May 11, 2004

Abstract

We examined the significance of the Atacama Compact Array (ACA) in wide-field imaging of ALMA through imaging simulations. The purpose of the simulations are to i) demonstrate importance of ACA in wide-field imaging with ALMA and ii) identify which component of errors has more significant influence than others on quality of final images obtained with ALMA+ACA using realistic parameters as to give feedback on designing and specifications of the ACA system. We particularly focused on the following aspects: difference on the ACA configuration design and effects of pointing errors, amplitude errors, and atmospheric phase errors. The simulations indicate that how densely packed the ACA configuration is an important factor for good imaging performance. The pointing errors at submm waves seriously degrade fidelity of an image. The atmospheric phase fluctuation also plays a major role. As indicated by previous works, our study indicates that ACA can boost the quality of wide-field imaging with ALMA by a factor of two or more for many cases, while dependency on structures of model images exists. In presence of all the errors, the projected goal of the imaging fidelity of 20 or better for ALMA when ACA is included, can be achieved if the current specifications are met.

1 Introduction

The Atacama Compact Array (ACA) system which is being proposed by Japan to use jointly with the ALMA 64-element array to enhance the wide-field imaging capability of ALMA. The ACA system consists of an array with twelve 7-m antennas in closely packed configuration and four 12-m antennas as single dishes for total power measurement and calibration. ACA recovers the shorter baseline information that is missing from the data taken by the ALMA 64-element array alone by directly sampling short *uv*-spacing. As the field of view for the ALMA 12m 64-element array, which is $18''$ at 345 GHz and $7''$ at 850 GHz, are relatively small, it is anticipated that wide-field imaging by mosaic has a large demand in scientific observations using ALMA, particularly at sub-millimeter wavelengths. In the recent report of the ALMA Design Reference Science Plan (DRSP) of Version 1

(van Dishoeck, Wootten, & Guilloteau 2003), the scientific projects that proposed to include ACA amount to about 41 % of total hours requested in the DRSP.

The homogeneous 64-element array alone is not sufficient to produce high quality mosaic images. However, high fidelity wide-field imaging with ALMA will be made possible by adding the ACA system with its smaller high precision antennas providing short spacing information as well as its dedicated single-dish telescopes for zero spacing information.

Several imaging simulation studies for the impact of ACA in the wide-field imaging capability of ALMA have been conducted. Yun (2001) and Morita (2001) used maximum entropy methods for deconvolution of a mosaic image. The basic ACA configuration was studied by Yun and further analysis including pointing error effect were conducted by Morita. Pety, Gueth and Guilloteau (2001a, 2001b, 2001c) using CLEAN-based deconvolution for mosaicing, investigated imaging capability of ACA under various errors. All the authors concluded the importance of the ACA system in high quality wide-field imaging.

As the detailed design of ACA is taking shapes now, it is very important to re-investigate these simulations to test specific parameters and reflect these results in the design of the ACA system. For our simulations, we adopted tools used by Pety et al and following similar paths as they did. In this memo, we report our investigation of two important aspects which might influence imaging quality: array characteristics (configuration, a ratio of close packing, etc) and the imaging capability under various errors. For the later, we studied the effects of pointing, amplitude, and atmospheric phase errors. We focused on imaging performance in realistic error conditions so as to give feedback in determination of optimal error budget for the system.

2 Simulation Procedures

We used the GILDAS ALMA+ACA simulation tools for our investigation. The simulator was developed in the GILDAS data reduction software environment by the IRAM group (Pety et al. 2001a, 2001b, 2001c) to study wide-field imaging performance of ALMA by adding the ACA observations to the ALMA 64-element array observations. For detailed description of the simulator, one should refer to Pety et al (2001c). Here we describe the basic procedures of the simulator.

The simulator simulates observing sequences and generates the simulated visibility data for the 64-element and ACA arrays (In this memo, we often referred the 7-m array of ACA as ACAi) based on given input parameters. For single dish (SD) data, a pointed observation at the center of each field is simulated when it is combined with the 64-element array visibilities to produce ALMA+SD data. The on-the-fly mapping is simulated to derive short spacing information up to the distance of 5m (difference in the dish diameters of the SD and ACAi element) in *uv*-plane when it is combined with ACAi visibilities to produce ACAi+SD data. Using these data, the mosaic dirty images are created. In the GILDAS simulator, two types of imaging method for the heterogeneous array are provided. In the *uv*-plane hybridization method, the ALMA+SD and ACAi+SD images are separately created and deconvolved. Then the two images are Fourier transformed to *uv* domain and linearly combined in the *uv*-plane, then the combined visibility data are transformed back to the image. The other method is a CLEAN-based joint-deconvolution method which simultaneously use the ALMA and ACA dirty mosaic-ed images in the CLEAN process to generate a single combined image. In our simulations, the joint-deconvolution method occasionally gave unreasonable results, which may require more fine tuning of the parameters. Therefore, for our current purpose, we adopted the hybrid method which is more straight forward and gives more uniform reliable results than the true-joint deconvolution method. This also significantly reduces CPU time for simulations. The GILDAS with the ALMA simulator tools was installed on the Intel Pentium 4 and dual CPU Xeon based PCs running RedHat Linux. Nearly two thousand sets of simulations were performed.

2.1 Simulation parameters

Some of common parameters used in the simulation results presented here are summarized in Table 1. For the simulations to study the influence of the ACA configuration characteristics without errors (Section 3), 230 GHz is used as an observing frequency. For the simulations including errors (Section 4), two observing frequencies, 230 and 850 GHz, are considered. We assume durations of observations to be relatively short with the hour angle ranges of ± 0.15 hr and ± 0.6 hr for the 64-element array and ACAi, respectively. For the 64-element array, the most compact configuration, C1 is used. The configuration data currently available to us is based on 60 elements. Thus we adopt this data to represent the 64-element configuration.

The number of fields for mosaic is 19. We found that higher image fidelity was obtained for 19-field mosaics than for the 7-field ones as were used by Pety et al (2001c) (typically, the fidelity increases by 10-20%). We used four model images (M51Hα, M31, cluster, HCO^+(4-3)) as used in Pety et al. Figure 1 and 2 list models scaled for the 230 GHz case ($70'' \times 70''$) in image- and *uv*-planes. For all the model images, the declination of -23 degree is used. As we stated earlier, *uv*-plane hybridization method is used for mosaic imaging for the ALMA+ACA data. The deconvolved ALMA+SD and ACAi+SD images are combined in the *uv* domain by selecting the ACA data up to a transition radius and the ALMA data for longer *uv* distances than the transition radius (an exponential function is used to ensure smooth transition around the transition radius). The transition radius is set to 15 m as the *uv* response of ACA quickly diminishes beyond this distance (Morita & Holdaway 2004).

Array configuration of ALMA 64-element array	c1	
no. mosaic field	19	
Observing frequency	230GHz	850GHz
image size	$70''$x$70''$(230GHz)	$19''$x$19''$(850GHz)
model	M51Hα, cluster, M31, HCO43(HCO^+(4-3))	
source declination	-23 deg.	
observing hour angle range [hr]	ALMA -0.15 to 0.15; ACA -0.6 to 0.6	

Table 1: Common parameters

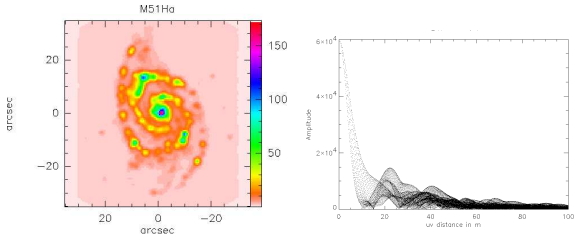

(a) M51Hα: image (b) M51Hα: uv distribution

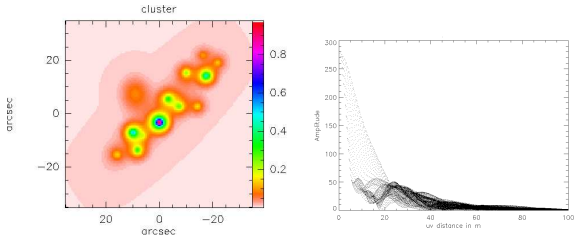

(c) cluster: image (d) cluster: uv distribution

Figure 1: Input models (at 230 GHz). The images are smoothed with the ALMA beam. In the *uv* distribution plots, only the data with the uv distance < 100m are shown.

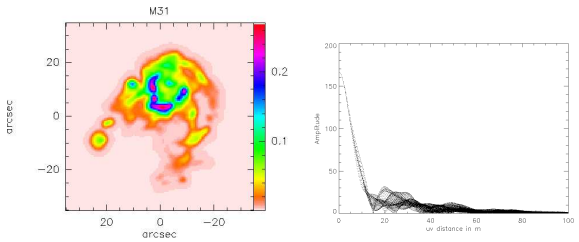

(a) M31: image (b) M31: uv distribution

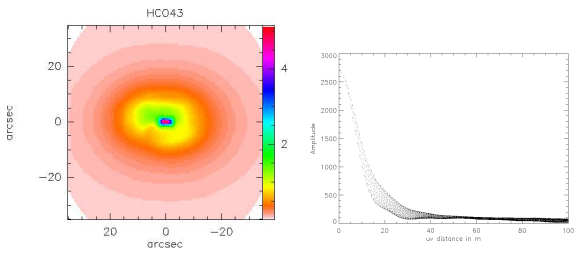

(c) HCO43: image (d) HCO43: uv distribution

Figure 2: Input Models (continued)

2.2 Analysis

In the GILDAS simulator, a primary indicator to assess the quality of simulated images is fidelity. The image fidelity is computed at each pixel on the image following its definition (Pety et al 2001c):

$$Fidelity(i,j) = \frac{abs(Model(i,j))}{abs(Model(i,j) - Simulated(i,j))} \quad (1)$$

Actual calculations of fidelity in the simulator involve exclusion of the extremely high fidelity points (Eqn. 4. in Pety et al) to ensure that the determined fidelities reflect mean image quality. The median image fidelities at the four different pixel intensity cutoff (0.3, 1, 3, 10% of the peak intensity of the original image) are computed from the fidelity map. Also, the fidelity in the *uv* plane is obtained. The model and difference images are Fourier-transformed to the *uv* domain and then the *uv* fidelities are computed by dividing the model by the difference. The median fidelities at the four levels of *uv* range (0-15m, 15-37.5m, 37.5-75m, 75-150m) are evaluated.

3 Effects of ACA Array Configuration Characteristics on Imaging

Here we study the effects of different ACA configurations in imaging performance. Types of the array configuration for 12 7-m element ACA array used in these simulations are as shown in Figure 3. The configuration labeled as 'iram' is the one used by Pety et al (2001c) in their simulations and is generated randomly. The one labeled as 'mw2003' is from Wright (2003), which is generated by two nested Reuleaux triangles with optimizations using the code developed by Boone (2001). No optimizations were performed for the other two configurations that we generated. The observing frequency of 230 GHz is assumed for this part of simulations. The simulations were performed without errors.

3.1 Configuration Types

The four types of the configuration for ACA array are compared for the image fidelity in Table2. It lists the median image fidelity determined from the pixels with their intensity above the threshold value given in percentage of peak intensity of original images.

It is clear that the addition of ACA array greatly improves the imaging performance in general except for M31. The ratio of fidelities of ALMA+ACAi+SD over those of ALMA+SD (hereinafter referred as "fidelity gain") is typically 2 or greater for the other three models. Difference among the four types of configurations depends on source structure. For the M51Hα and HCO43 models, the ring performs poorly while for the rest of the configurations, the difference is not significant. Now, if we focus on the results for the fidelity medians that determined with the intensity threshold of 1% of peak intensity, the iram and spiral types have good overall performance for all the models.

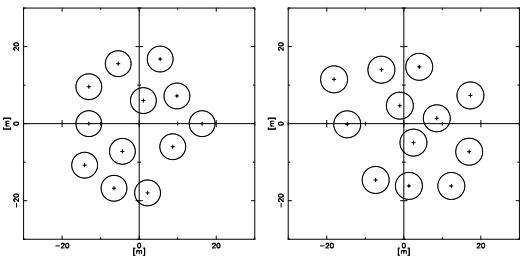

(a) IRAM-type (b) MW2003

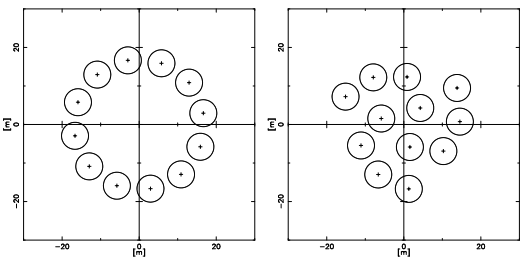

(c) ring (d) spiral

Figure 3: ACA configuration types tested. All the configurations shown here are set to have a close packing ratio of 1.25.

modd	ACA config.	Intensity threshold 0.30% ALMA+SD	0.30% all	0.30% fidelity gain	1% ALMA+SD	1% all	1% fidelity gain	3% ALMA+SD	3% all	3% fidelity gain	10% ALMA+SD	10% all	10% fidelity gain
HCO43	iram	6	66	10.9	8	110	14.6	21	156	7.3	20	168	8.3
	ring	6	13	2.1	8	17	2.3	21	42	2.0	20	52	2.6
	spiral	6	62	10.1	8	105	14.0	21	164	7.6	20	180	8.9
	mw2003	6	44	7.3	8	73	9.7	21	107	5.0	20	113	5.6
M51Hα	iram	5	54	11.0	28	148	5.3	51	206	4.0	102	300	2.9
	ring	5	15	3.0	28	44	1.6	51	85	1.7	102	180	1.8
	spiral	5	53	10.8	28	151	5.4	51	213	4.2	102	296	2.9
	mw2003	5	53	10.8	28	127	4.5	51	171	3.4	102	269	2.6
cluster	iram	46	195	4.3	65	250	3.9	95	300	3.2	186	408	2.2
	ring	46	161	3.5	65	224	3.5	95	292	3.1	186	403	2.2
	spiral	46	207	4.5	65	267	4.1	95	311	3.3	186	416	2.2
	mw2003	46	186	4.1	65	235	3.6	95	285	3.0	186	379	2.0
M31	iram	85	184	2.2	99	221	2.2	117	273	2.3	138	338	2.5
	ring	85	180	2.1	99	219	2.2	117	264	2.3	138	333	2.4
	spiral	85	184	2.2	99	220	2.2	117	278	2.4	138	331	2.4
	mw2003	85	183	2.2	99	221	2.2	117	276	2.4	138	333	2.4

Table 2: Comparison of median image fidelities with different ACA configurations (close packing ratio = 1.25), 19-field mosaic, no error case. ALMA+SD= ALMA 64 element array + single-dish, all= the 64-dment array with the ACA system using the hybrid method. The fidelity gain is defined as $\frac{all}{ALMA+SD}$.

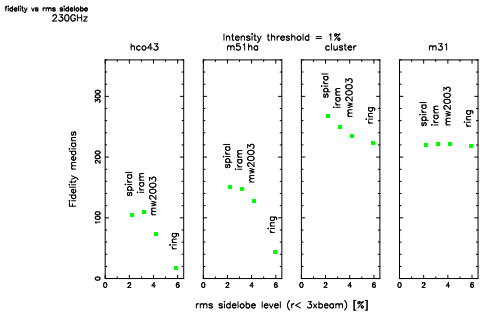

Figure 5: Relationship between image fidelity and the rms sidelobe levels inside a radius of 3 x ACA beam.

These differences may be attributed to how compactly packed the array is. Figure 4 shows that the image median fidelity is in fact correlated with the number of visibility within the *uv* distance of 15m for the different type of the ACA array configuration. In comparison with sidelobes of the four types of the ACA configuration, the spiral and iram-types have lower rms sidelobe levels which are evaluated within a radius of three times the beam size. Figure 5 shows that comparison between the fidelities and sidelobe levels of the ACA beams.

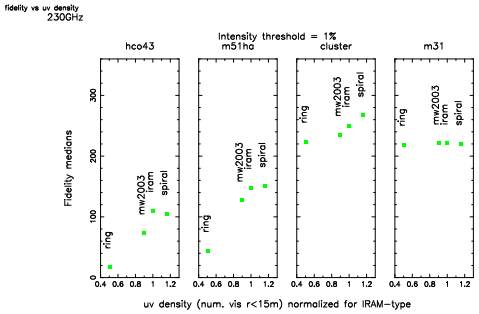

Figure 4: Relationship between image fidelity and the number of visibility within *uv* distance of 15m. The uv density were normalized to that of the iram-type configuration.

3.2 Close Packing

We also examined the dependency of fidelity on ratios of close packing (minimum baseline/antenna diameter). The ACA configurations with different close packing ratios are generated by scaling a given configuration type. Figure 6 shows that *uv* fidelity medians in the *uv* range of 0-15m as the close packing ratio are varied between 1.15 to 1.35 for a spiral configuration. The fidelities in this *uv* range are essentially contribution from the ACAi+SD data. The red lines indicate the fidelities of ALMA+SD only. In all models, the smaller close packing ratio results in higher image fidelity. For the HCO43 and M51Hα models, the fidelity medians decline sharply for the close packing ratio greater than 1.30. Since the array is scaled as whole, the observed dependency is not only caused by variation in minimum baseline but also it is related to how densely packed.

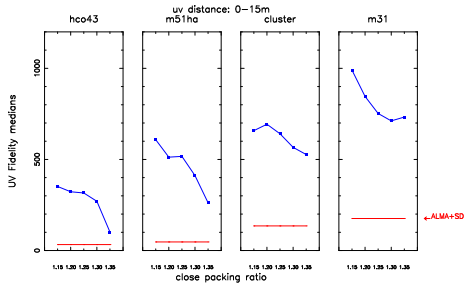

Figure 6: Comparison of fidelities in different close packing ratio of the spiral-type ACA configuration. ALMA+ACAi+SD cases are shown in blue lines. For reference, the fidelities of ALMA+SD cases are indicated in red lines.

3.3 Summary of Sec.3

We examined different array configuration characteristics. The number of visibility within certain *uv* radius (in this study, r_{uv}=15m) and close packing ratio are related to how the array is densely packed, or *compactness* of the array. While there are some variations among the source models, it is generally true that an array with higher degree of compactness (higher concentration of elements

toward the array center and the higher close packing ratio) gives better imaging performance.

One word of caution is that for the results presented above we used the most compact configuration (C1) for the 64-element array. Thus the *uv* response of the 64-element array extends short-ward of uv distances and the "*uv* gap" in the visibilities of the 64-element array filled by those of ACA is least. In actual operations, the 64-element array will be in C1 only in a relatively brief duration in the whole configuration cycle of the 64-element array and the ACA data is anticipated to combine with the data taken with the 64-element array in continuous reconfiguration, probably, up to an 1-km array. The contribution of ACA in such cases would be greater since sampling of spatial frequency <30m would be predominantly from ACA. In such cases, the compactness of the ACA array investigated here may not apply, or at least, the criteria of compactness could be different. Simulations with ALMA 64-element array's sparser configurations are needed before an optimal design of ACA array configuration is decided.

4 Simulations Including Systematic Errors

An investigation on which error has more influence on quality of final images obtained with the ALMA+ACAi+SD mode than others is important since it will, in turn, give feedback on the design of the ACA system. By addressing error budget that influence image quality of ALMA+ACA, it can help shape optimal designs to bring the most out of the ACA system. We consider here pointing, amplitude gain, and atmospheric phase errors.

For the simulation results reported in this section, a spiral-type with a close packing ratio of 1.25 was used for the ACA configuration. To represent both millimeter and submillimeter wavelengths condition, two observing frequencies, 230 and 850 GHz were used. Common parameters listed in Table 1 of Section 2 were used again for the simulations presented in this section.

For the rest of discussions in this section, we focus on the median fidelities determined from pixels with the intensity greater or equal to 1% of the peak intensity in the original image assuming that these represent average behaviors of imaging quality.

Treatments of various errors in the simulator are described in Pety et al (2001c). We give some comments on how we made particular choices of models of errors for our simulations in the following sections of individual errors. Some relevant ALMA 64-element array and ACA specifications which we make comparison with are listed in Table 3.

Pointing errors (offset) (ALMA&ACA)	$0.6''$
Close packing ratio of ACA	1.25
Amplitude error (ALMA& ACA)	1% for $\nu < 300$ GHz, 3% for $\nu > 300$ GHz

Table 3: ALMA specifications

4.1 Pointing Errors

In high fidelity wide-field imaging, good pointing accuracy is critical as pointed out by Cornwell, Holdaway, & Uson (1993) and Holdaway (1997). Pety et al (2001c) and Morita (2001) showed that the addition of ACA improves the situation.

The pointing errors are assumed to be residual random offsets per antenna after pointing calibration and set independently for each elements of the 64-element and ACA arrays and single dish (SD). More sophisticated models considering time variable wind- and thermally-induced effects were done by Pety et al (2001c). We assumed that systematic errors including the thermally induced effect can be corrected by calibration. The wind-induced pointing errors are randomly varying with short time scale and some coupling among antennas are expected. The effect can also be different between

the ACA 7-m and ALMA 12-m antennas under different observing parameters and conditions (i.e. observing frequency, observation by night or daytime, etc.) and they add more parameter space to explore for simulations. Therefore for our purpose, only random errors is considered assuming that the net effect in the image fidelity is reasonably represented with these errors. Note that as we described in Section 2, the single dish data for ALMA+SD and ALMA+ACAi+SD are treated differently. The former is from pointed observations and later is from on-the-fly mapping. Therefore, it could produce systematic difference between ALMA+SD and ALMA+ACAi+SD in the effect of pointing errors.

The ALMA specification for a pointing error of the 12-m dish stated in the ALMA Project Book is $0.6''$. We consider rms pointing error of $0.6''$ as an ideal case and $1.2''$ to represent a poor pointing accuracy condition and tested all combinations of these two values of pointing errors among ALMA, ACAi and SD. The simulations with the same set of the parameters were ran 10 times to obtain averaged values of fidelities. While it is difficult to quote the uncertainties of the determined fidelity, the uncertainties estimated from the scatters in median fidelities (with 1% intensity threshold) among the 10 simulations are 5-10%.

Table 4 and 5 show the image fidelity medians with pixel intensity threshold of 1% at 230 and 850 GHz, respectively. The *fidelity gain*, a factor of the median fidelity improved by adding ACA, is given in the last columns. Figure 7 summarizes these tables for "all" case (ALMA+ACAi+SD). The influence of pointing errors is significant for 850 GHz cases as the fidelity gain quickly declined as the pointing errors increase. Even with a pointing error of 0.6 $''$, which is the current ALMA specification, at 850 GHz it corresponds to ∼9% and ∼5% of beams (FWHM) of the 12-m and 7-m antennas, respectively. As shown in Figure 7, when pointing errors of the 12-m antennas of ALMA (the 64-element array) and SD are $0.6''$ (green solid lines),pointing errors of ACA 7-m also significantly influence the image quality. However, in the case for a pointing error of the ALMA 12-m is $1.2''$, the pointing errors of ACA 7-m and SD 12-m do have a little influence and the fidelity is below 20 for most of the cases at 850 GHz. So for pointing errors, the errors of the 64-element array have most impact in imaging while the errors of ACA have less impact. However, to achieve high fidelity imaging at good conditions, the pointing accuracy specification of the ACA 7-m antenna should not be relaxed since it also contribute to degrading of the fidelity. Behavior of the fidelity also depends on the structure of the source model. The HCO43 model which has a relatively simple structure as shown in image and *uv* distribution in Figure 2, is showing greater improvement with ACA than other models.

230GHz

	median fidelity				
	pointing error		(intensity threshold 1%)		
model	ALMA	ACA7m, SD	*ALMA + SD*	*all*	*fidelity gain*
HCO43		no err.	8	105	14.0
	$0.6''$	$0.6''$, $0.6''$	8	87	11.3
		$1.2''$, $0.6''$	8	72	9.5
		$0.6''$, $1.2''$	8	68	8.6
		$1.2''$, $1.2''$	8	65	8.2
	$1.2''$	$0.6''$, $0.6''$	8	72	9.3
		$1.2''$, $0.6''$	8	67	8.4
		$0.6''$, $1.2''$	8	57	7.1
		$1.2''$, $1.2''$	8	58	7.0
M51Hα		no err.	28	151	5.4
	$0.6''$	$0.6''$, $0.6''$	29	111	3.9
		$1.2''$, $0.6''$	28	106	3.8
		$0.6''$, $1.2''$	32	97	3.0
		$1.2''$, $1.2''$	32	93	2.9
	$1.2''$	$0.6''$, $0.6''$	28	75	2.7
		$1.2''$, $0.6''$	27	75	2.7
		$0.6''$, $1.2''$	29	72	2.5
		$1.2''$, $1.2''$	30	70	2.4
cluster		no err.	65	267	4.1
	$0.6''$	$0.6''$, $0.6''$	60	168	2.8
		$1.2''$, $0.6''$	63	137	2.2
		$0.6''$, $1.2''$	49	133	2.7
		$1.2''$, $1.2''$	53	136	2.6
	$1.2''$	$0.6''$, $0.6''$	45	110	2.4
		$1.2''$, $0.6''$	50	106	2.1
		$0.6''$, $1.2''$	43	114	2.6
		$1.2''$, $1.2''$	47	98	2.1
M31		no err.	99	220	2.2
	$0.6''$	$0.6''$, $0.6''$	85	144	1.7
		$1.2''$, $0.6''$	83	119	1.4
		$0.6''$, $1.2''$	71	105	1.5
		$1.2''$, $1.2''$	72	102	1.4
	$1.2''$	$0.6''$, $0.6''$	68	109	1.6
		$1.2''$, $0.6''$	66	99	1.5
		$0.6''$, $1.2''$	59	98	1.7
		$1.2''$, $1.2''$	59	90	1.5

Table 4: Image fidelity medians for different combinations of pointing errors at 230GHz.

850GHz

	median fidelity				
	pointing error		(intensity threshold 1%)		
model	ALMA	ACA7m, SD	*ALMA + SD*	*all*	*fidelity gain*
HCO43		no err.	8	105	14.0
	$0.6''$	$0.6''$, $0.6''$	9	31	3.6
		$1.2''$, $0.6''$	9	22	2.4
		$0.6''$, $1.2''$	10	14	1.4
		$1.2''$, $1.2''$	11	13	1.3
	$1.2''$	$0.6''$, $0.6''$	10	22	2.3
		$1.2''$, $0.6''$	10	19	1.8
		$0.6''$, $1.2''$	13	12	0.9
		$1.2''$, $1.2''$	13	13	1.0
M51Hα		no err.	29	156	5.4
	$0.6''$	$0.6''$, $0.6''$	27	36	1.3
		$1.2''$, $0.6''$	28	30	1.1
		$0.6''$, $1.2''$	14	18	1.2
		$1.2''$, $1.2''$	14	17	1.2
	$1.2''$	$0.6''$, $0.6''$	12	14	1.2
		$1.2''$, $0.6''$	12	14	1.2
		$0.6''$, $1.2''$	11	13	1.1
		$1.2''$, $1.2''$	11	13	1.1
cluster		no err.	63	255	4.1
	$0.6''$	$0.6''$, $0.6''$	24	44	1.9
		$1.2''$, $0.6''$	25	34	1.3
		$0.6''$, $1.2''$	11	22	1.9
		$1.2''$, $1.2''$	12	16	1.4
	$1.2''$	$0.6''$, $0.6''$	12	18	1.5
		$1.2''$, $0.6''$	12	18	1.5
		$0.6''$, $1.2''$	9	17	1.9
		$1.2''$, $1.2''$	9	15	1.7
M31		no err.	99	222	2.2
	$0.6''$	$0.6''$, $0.6''$	26	35	1.3
		$1.2''$, $0.6''$	26	24	0.9
		$0.6''$, $1.2''$	11	16	1.5
		$1.2''$, $1.2''$	11	14	1.3
	$1.2''$	$0.6''$, $0.6''$	12	16	1.4
		$1.2''$, 0.6"	12	15	1.2
		$0.6''$, $1.2''$	9	12	1.3
		$1.2''$, $1.2''$	9	13	1.4

Table 5: Same as Table 4 but at 850GHz.

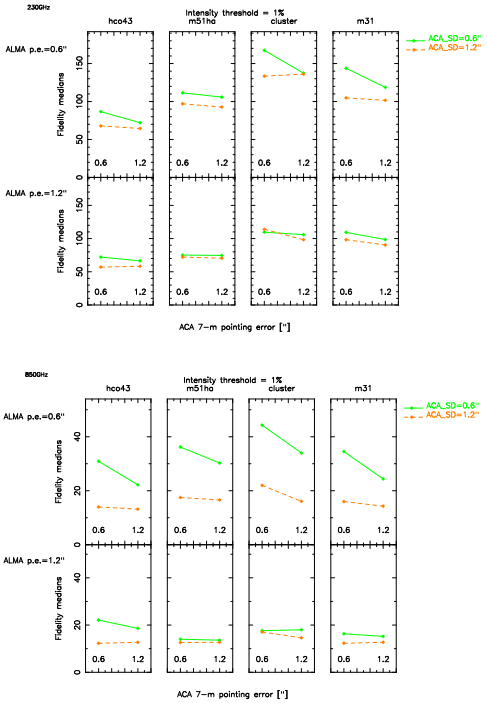

Figure 7: Image fidelity medians as a function of the ACA-7m pointing errors in presence of the ALMA pointing error of 0.6″(*upper panel*) and of 1.2″(*lower panel*) at 230 (*top*) and 850 GHz (*bottom*). The green solid line: for the ACA-12m single dish pointing error of 0.6″; the orange dashed line: for the ACA 12-m pointing error of 1.2″.

850GHz	offset term only			
	amplitude	median fidelity		
	gain error	(Intensity threshold 1%)		
model	[%]	*ALMA + SD*	*all*	*fidelity gain*
HCO43	0	8	105	14.0
	3	8	56	7.5
	10	8	21	2.6
M51Hα	0	29	156	5.4
	3	30	75	2.5
	10	26	24	0.9
cluster	0	63	255	4.1
	3	57	95	1.7
	10	34	38	1.1
M31	0	99	222	2.2
	3	109	100	0.9
	10	47	42	0.9

Table 7: Image fidelity medians at 850GHz as a function of amplitude gain errors given by (time-independent) random offsets.

850GHz	drift term only			
	amplitude	median fidelity		
	gain error	(Intensity threshold 1%)		
model	[%]	*ALMA + SD*	*all*	*fidelity gain*
HCO43	0	8	105	14.0
	3	8	83	10.8
	10	8	50	6.2
M51Hα	0	29	156	5.4
	3	27	138	5.1
	10	26	97	3.8
cluster	0	63	255	4.1
	3	80	221	2.8
	10	86	106	1.2
M31	0	99	222	2.2
	3	127	197	1.6
	10	175	106	0.6

Table 8: Image fidelity medians at 850GHz as a function of amplitude gain errors given by time dependent drift term.

4.2 Amplitude Gain Errors

Amplitude gain errors are simulated by considering two terms: offset which is constant in time, and drift which varies with time. Main sources of amplitude gain error are variations of atmospheric transmission, antenna gain variations caused by defocus and dish distortion, and receiver gain fluctuation and drift. Both terms are considered to be random residual errors after amplitude calibration done every 15 minutes. The values were reset randomly for each antennas. Equal rms values of amplitude errors were entered on each of the 64-element and ACA arrays, and SD. At 230 GHz, slow variation of antenna gain and receiver gain drift are assumed to be negligible and thus no drift term is considered. At 850 GHz, we assume that the two terms have equal weight.

Degradation of the fidelity with amplitude gain errors of 0, 1, 3, and 10% rms at 230 GHz is shown in Table 6 and Figure 8. Each fidelity is an averaged value of 10 simulations performed with the same set of parameters. For all the models, amplitude gain errors of 3% result in degradation of the fidelity by a roughly factor of two. In Figure 9, the case of offset amplitude errors at 850 GHz is shown. The trend is similar to those at 230 GHz but slightly stronger effect as the errors increase. The drift term has less effect on fidelity as shown in Figure 10. It is shown that if the amplitude gain errors are at the ALMA specification, 1% and 3% or less at 230 and 850 GHz, respectively, the fidelity improves by factor of two or greater for most of the cases by adding ACAi. While the fidelity for ALMA+ACAi+SD is generally a smooth function of amplitude gain errors, for ALMA+SD, it occasionally show spurious values that are higher than those in the absence of error as seen in M31 and cluster cases. These effects could partly be caused when the deconvolution fails for part of an image in the absence of error (Pety et al. 2001c).

230GHz				
	amplitude	median fidelity		
	gain error	(Intensity threshold 1%)		
model	[%]	*ALMA + SD*	*all*	*fidelity gain*
HCO43	0	8	105	14.0
	1	7	95	12.9
	3	8	57	7.6
	10	8	18	2.3
M51Hα	0	28	151	5.4
	1	28	120	4.2
	3	28	75	2.7
	10	21	23	1.1
cluster	0	65	267	4.1
	1	68	189	2.8
	3	50	124	2.5
	10	32	36	1.1
M31	0	99	220	2.2
	1	95	156	1.7
	3	98	89	0.9
	10	40	33	0.8

Table 6: Image fidelity medians at 230GHz as a function of amplitude gain errors. The amplitude gain errors here are modelled as random offsets.

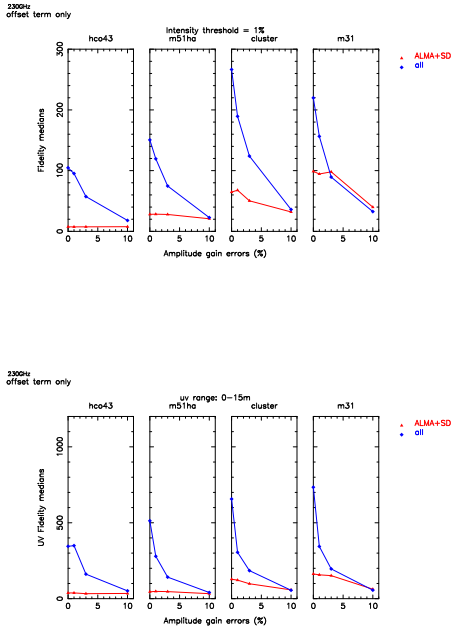

Figure 8: Degradation of fidelity by amplitude gain errors considering offset term only at 230 GHz. *upper panel:* Image fidelity medians as a function of amplitude gain errors in percent. *lower panel:* *uv*-domain fidelity in the *uv* range of 0-15m. The red lines: ALMA+SD; the blue lines: ALMA+ACAi+SD by the hybrid method.

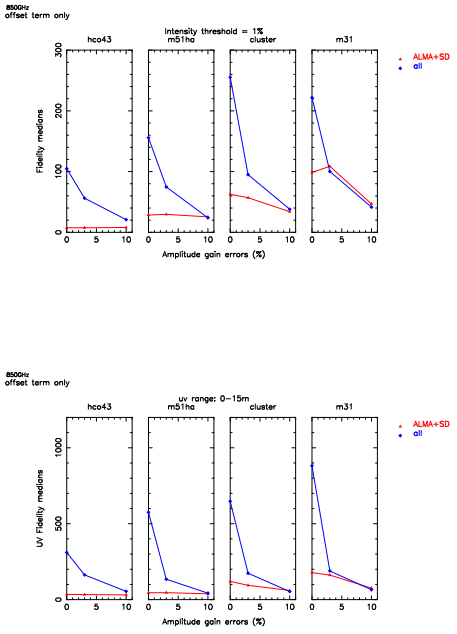

Figure 9: Degradation of fidelity by amplitude gain errors considering offset term only at 850 GHz. *upper panel:* Image fidelity medians as a function of amplitude gain errors in percent. *lower panel: uv*-domain fidelity in the *uv* range of 0-15m. The red lines: ALMA+SD; the blue lines: ALMA+ACAi+SD by the hybrid method.

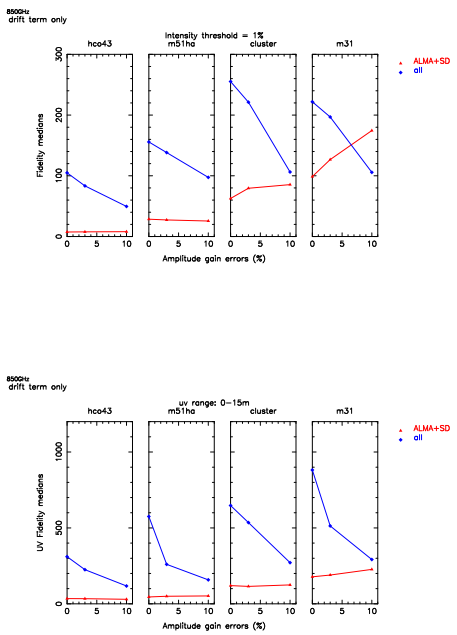

Figure 10: Same as Figure 8 but considering drift term only at 850 GHz. *upper panel:* Image fidelity medians as a function of amplitude gain errors in percent. *lower panel: uv*-domain fidelity in the *uv* range of 0-15m. The red lines: ALMA+SD; the blue lines: ALMA+ACAi+SD by hybrid method.

4.3 Atmospheric Phase Errors

Atmospheric phase errors are simulated using a 2-D phase screen model generated with a 2nd order structure function. For our simulations, we assumed that the power of the 2nd order structure function to be 0.61, wind velocity of 10m/s at altitude of 1000m. The angular separation between a calibrator and a target source were taken to be 2 degrees. The standard calibration is employed by intervening the calibrator and target source (2sec on the calibrator and 20sec on the target) in 26-second cycles. Calibration by water vapor radiometry (WVR) is also applied. Due to the current design of the simulator, these calibrations are applied to both the 64-element and ACA arrays. For ACA, these calibration schemes do not help to improve imaging quality and even add some noises introduced by calibration errors. The fast switching method does not work for ACA since all the ACA baselines are much less than 100m and the phase pattern passes by above the array in less time than the fast switching cycle. The current WVR is not sensitive enough to correct phase degradation for the ACA baselines. For the baselines less than 60m, there is a little difference in phase noises between after applying different calibration methods (WVR calibration, fast switching, or combination of both) and without any calibration as shown in Figure 3 of Pety et al (2001c). In test simulations that we ran for the cases with no phase calibration at all, *uv* fidelities of ALMA+ACAi+SD in the 0-15m range actually improved sometimes by a factor of two for the case with both fast switching and wvr calibrations being applied.

The simulations were performed by varying the phase noise of the phase screen model with the fixed power. Table 9 lists the simulation results in terms of phase conditions in percentile at 230 and 850 GHz determined from the site data at Chajnantor (Holdaway 2003, private communication). The set of percentiles represents good and poor (but still doable) observing conditions at millimeter and submillimeter wavelengths. Image fidelity and *uv*-plane fidelity as a function of phase noise at 100m are plotted in Figure 11. For "good" phase conditions (25% and 5% for 230 and 850 GHz, respectively), the fidelity improved by a factor of two or more by adding ACA except M31 model. For the case of "poor" conditions, the improvement is limited. Since the phase calibrations of ACAi data may in fact lead to degrading of fidelity, these results should be considered to be lower limits.

model	site condition		median fidelity (intensity threshold 1%)		
	230GHz	850GHz	*ALMA + SD*	*all*	*fidelity gain*
HCO43	0% (no err.)		8	105	14.0
	25%	5%	8	67	8.6
	50%	10%	8	39	4.8
M51Hα	0% (no err.)		28	151	5.4
	25%	5%	24	57	2.3
	50%	10%	18	28	1.5
cluster	0% (no err.)		65	267	4.1
	25%	5%	52	97	1.9
	50%	10%	37	50	1.3
M31	0%(no err.)		99	220	2.2
	25%	5%	66	84	1.3
	50%	10%	41	41	1.0

Table 9: Image fidelity medians as a function of atmospheric condition at the site given in percentiles.

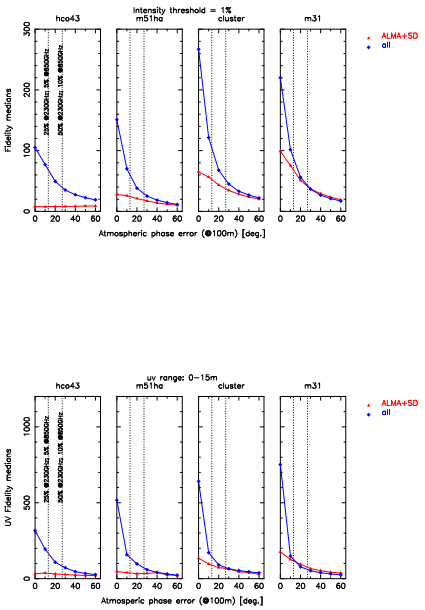

Figure 11: *upper panel:* Image fidelity medians as a function of atmospheric phase error (rms) at 100-m baseline. *lower panel: uv*-domain fidelity medians in *uv* range of 0-15m. The red lines: ALMA+SD; the blue lines: ALMA+ACA+SD by hybrid method. The dashed lines indicate 25% (at 230 GHz) or 5% (at 850 GHz), and 50% (230 GHz) or 10% (850 GHz)

4.4 Simulations Including All the Errors

In the previous sections, we simulated by selecting one component of errors at a time. To reflect more realistic situations, we also performed the simulations including all the errors. To represent typical observing conditions, the parameters were chosen based on the ALMA specifications, which are 0.6″ rms for pointing errors, 1% (offset term) at 230 GHz and 3% (offset and drift terms combined) at 850 GHz for amplitude errors. The simulations were ran for the two cases of atmospheric condition as in Section 4.3.

Figure 12 and 13 show the image and *uv* fidelities (averaged values of 10 simulations with identical parameters) in terms of the atmospheric condition. The fidelities that are free of any errors are plotted as 0% of the atmospheric condition. As similar to what Pety et al (2001) found in their simulations including all typical errors, the general trend is that introduction of errors greatly reduces the fidelity and its variation among the four tested models are less significant than the error free case. For HCO43 model, the rate of degrading is less as compared with the other models at both frequencies. The sharper drops in fidelity for 850-GHz case (from error free case to 5-percentile) than 230-GHz case are mainly caused by a larger fraction of pointing errors with respect to the beams. The relative contribution of ACA can be seen better in terms of the fidelity gain ($\frac{all}{ALMA+SD}$) listed in Table 10 and 11. For the HCO43 model, a factor of two or better improvement is seen by the inclusion of ACA under good and poor observing conditions at both frequencies. For the M51Hα and cluster models, some improvements are seen at good observing conditions. In the case of M31, the contribution of ACA is much less even at best observing conditions at these particular frequencies.

230GHz				
model	site condition	median fidelity (intensity threshold 1%)		
		$ALMA+SD$	all	$fidelity\ gain$
HCO43	0% (no err.)	8	105	14.0
	25%	9	43	5.1
	50%	9	33	3.7
M51Hα	0% (no err.)	28	151	5.4
	25%	22	44	2.0
	50%	17	25	1.5
cluster	0% (no err.)	65	267	4.1
	25%	61	85	1.4
	50%	41	47	1.1
M31	0% (no err.)	99	220	2.2
	25%	85	73	0.9
	50%	47	39	0.8

Table 10: Image fidelity medians at intensity threshold of 1% and "fidelity gain" ($\frac{all}{ALMA+SD}$) at 230GHz.

850GHz				
model	site condition	median fidelity (intensity threshold 1%)		
		$ALMA+SD$	all	$fidelity\ gain$
HCO43	0% (no err.)	8	105	14.0
	5%	10	31	3.0
	10%	11	22	2.1
M51Hα	0% (no err.)	29	156	5.4
	5%	22	28	1.3
	10%	17	20	1.2
cluster	0% (no err.)	63	255	4.1
	5%	24	38	1.6
	10%	20	32	1.6
M31	0% (no err.)	99	222	2.2
	5%	27	32	1.2
	10%	23	28	1.2

Table 11: Same as Table 10 but at 850GHz

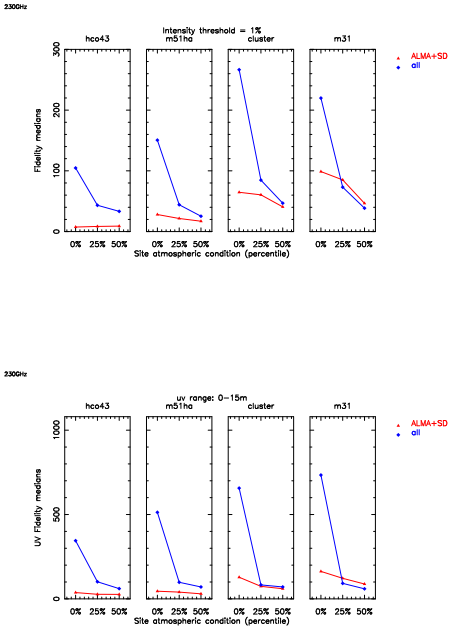

Figure 12: 230 GHz fidelity versus the atmospheric condition. *upper panel:* Image fidelity medians including all the errors. *lower panel: uv*-domain fidelity medians in *uv* range of 0-15m. The red lines: ALMA+SD; the blue lines: ALMA+ACA+SD by the hybrid method

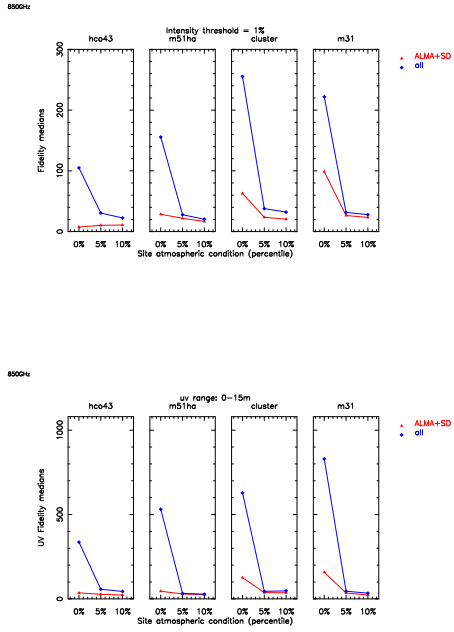

Figure 13: 850 GHz fidelity versus the atmospheric condition. *upper panel:* Image fidelity medians including all the errors. *lower panel: uv*-domain fidelity medians in *uv* range of 0-15m. The red lines: ALMA+SD; the blue lines: ALMA+ACA+SD by the hybrid method

4.5 Summary of Sec. 4

We examined relative contribution of each component of pointing, amplitude gain, and atmospheric phase errors in degrading the image quality in the ALMA 64-element array+ACA system.

- At 230 GHz, relative contributions of pointing and amplitude gain errors in image quality are about the same. Having pointing errors of $0.6''$ (or $1.2''$) results in similar fidelity as the case of having amplitude gain errors of 1% (or 3%). In such cases, atmospheric phase errors are the dominant factor.
- At 850 GHz, pointing errors have the dominant effect followed by atmospheric phase errors. The effect of amplitude gain errors is relatively small as long as these errors remain near the ALMA specification.
- For the simulations with atmospheric phase errors, fidelity of data including ACA could be improved by different calibration scheme or applying no calibration at all while in the current scheme the calibration method is globally set for both ALMA and ACA arrays.

For significant influence of atmospheric phase errors at the both frequencies indicated by these simulations, the calibration by fast switching or WVR are ineffective in the current specifications of these techniques. The calibration methods specific to ACA remain to be a subject for studies.

In addition to the last point described above, the array configuration combination used here (C1 for ALMA and a spiral for ACA) probably gives a lower limit of the fidelity gain produced by the ACA system as we stated in the Section 3.

The science requirements in the Project Description of Atacama Compact Array System states that ALMA 64-element array with the ACA system should routinely achieve a median fidelity >20 in average observing condition at ν <345 GHz, and the similar level of fidelity in favorable condition at ν >345 GHz. Our simulations support that these requirements are reasonably met providing that both the 64-element array and ACA system comply with their specifications.

5 Conclusions and Future Works

In summary:

1 **From the simulations with different ACA array characteristics, we found that an array densely packed toward the center generally gives good imaging performance. The antenna close packing ratio of 1.25 in the ALMA specification should also apply to ACA.**

2 **For the simulations with a variety of errors assumed, the atmospheric phase errors are a dominant factor at millimeter wavelengths in limiting the quality of the wide-field imaging with ALMA including the ACA system. The effects of the pointing errors and amplitude gain errors have similar, but secondary, contribution. At submillimeter wavelengths, the effect of the pointing errors become dominant factor to limit the imaging quality with the atmospheric phase errors being second.**

3 **To maximize the merit of ACA in the wide-field imaging capability of ALMA, accurate pointing of the ACA 7-m antenna is important. The absolute value of pointing errors should be as good as that of the 12-m antenna of the 64-element array.**

There are other parameters to be explored in simulations that is left to future works. The following is a list of such items.

- Simulations at different source declinations to study shadowing effect. In the current simulations, the durations of observations in our simulations were short and the observations were assumed to be made near zenith, and the effect of shadowing were not explored.
- Simulations with sparser 64-element array configurations are needed since in the current simulations we combined ACA only with the most compact configuration of the 64-element array (C1).
- For more thorough imaging study in the presence of pointing errors, one should also include effect of dynamic refraction which is not included in the present simulations.
- The effects of instrumental phase errors are not included in the present simulations. To do that one needs to generate some error models which reflect the sources of the errors.
- Simulations including thermal noise. Morita (2001) performed the imaging simulations including thermal noise using the MEM. It would be interesting to compare if there is any difference by the deconvolution method used.

References

Boone, F. 2001, "Interferometric array design: Optimizing the locations of the antenna pads", A&A, 377 , 368.

Cornwell, T.J., Holdaway, M.A., and Uson, J.M. 1993, "Radio-interferometric imaging of very large objects: implications for array design", A&A, 271, 687.

Holdaway, M. 1997, ALMA Memo 178, "Effects of Pointing Errors on Mosaic Images with 8m, 12m, and 15m Dishes"

Morita, K.-I. 2001, ALMA Memo 374, "Wide Field Imagings with the Atacama Large Millimeter/Submillimeter Array"

Morita, K.-I, and Holdaway, M. A. 2004, ALMA Memo in preparation.

Pety, J., Gueth, F., and Guilloteau, S. 2001a, ALMA Memo 396, "ALMA+ACA Simulation Tool"

Pety, J., Gueth, F., and Guilloteau, S. 2001b, ALMA Memo 397, "ALMA+ACA Simulation Results"

Pety, J., Gueth, F., and Guilloteau, S. 2001c, ALMA Memo 398, "Impact of ACA on the Wide-Field Imaging Capabilities of ALMA"

van Dishoeck E.F., Wootten, A., and Guilloteau, S. 2003, "The ALMA Design Reference Science Plan Version 1.0" (http://www.strw.leidenuniv.nl/ joergens/alma/)

Wright, M.C.H. 2003, ALMA Memo 450, "Heterogeneous Imaging with the ALMA Compact Array"

Yun, M. S. 2001, ALMA Memo 368, "An Imaging Study for ACA"

A&A 517, A12 (2010)
DOI: 10.1051/0004-6361/200912873
© ESO 2010

Astronomy & Astrophysics

Revisiting the theory of interferometric wide-field synthesis

J. Pety[1,2] and N. Rodríguez-Fernández[1]

[1] IRAM, 300 rue de la Piscine, 38406 Grenoble Cedex, France
e-mail: [pety;rodriguez@iram.fr]
[2] LERMA, UMR 8112, CNRS and Observatoire de Paris, 61 avenue de l'Observatoire, 75014 Paris, France

Received 13 July 2009 / Accepted 16 March 2010

ABSTRACT

Context. After several generations of interferometers in radioastronomy, wide-field imaging at high angular resolution is today a major goal for trying to match optical wide-field performances.
Aims. All the radio-interferometric, wide-field imaging methods currently belong to the mosaicking family. Based on a 30 years old, original idea from Ekers & Rots, we aim at proposing an alternate formalism.
Methods. Starting from their ideal case, we successively evaluate the impact of the standard ingredients of interferometric imaging, i.e. the sampling function, the visibility gridding, the data weighting, and the processing of the short spacings either from single-dish antennas or from heterogeneous arrays. After a comparison with standard nonlinear mosaicking, we assess the compatibility of the proposed processing with 1) a method of dealing with the effect of celestial projection and 2) the elongation of the primary beam along the scanning direction when using the on-the-fly observing mode.
Results. The dirty image resulting from the proposed scheme can be expressed as a convolution of the sky brightness distribution with a set of wide-field dirty beams varying with the sky coordinates. The wide-field dirty beams are locally shift-invariant as they do not depend strongly on position on the sky: their shapes vary on angular scales typically larger or equal to the primary beamwidth. A comparison with standard nonlinear mosaicking shows that both processing schemes are not mathematically equivalent, though they both recover the sky brightness. In particular, the weighting scheme is very different in both methods. Moreover, the proposed scheme naturally processes the short spacings from both single-dish antennas and heterogeneous arrays. Finally, the sky gridding of the measured visibilities, required by the proposed scheme, may potentially save large amounts of hard-disk space and cpu processing power over mosaicking when handling data sets acquired with the on-the-fly observing mode.
Conclusions. We propose to call this promising family of imaging methods *wide-field synthesis* because it explicitly synthesizes visibilities at a much finer spatial frequency resolution than the one set by the diameter of the interferometer antennas.

Key words. methods: analytical – techniques: interferometric – methods: data analysis – techniques: image processing

1. Introduction

The instantaneous field of view of an interferometer is naturally limited by the primary beam size of the individual antennas. For the ALMA 12 m-antennas, this field of view is ∼9″ at 690 GHz and ∼27″ at 230 GHz. The astrophysical sources in the (sub)-millimeter domain are often much larger than this, but still structured on much smaller angular scales. Interferometric wide-field techniques enable us to fully image these sources at high angular resolution. These techniques first require an observing mode that in one way or another scans the sky on spatial scales larger than the primary beam. The most common observing mode in use today, known as stop-and-go mosaicking, consists in repeatedly observing sky positions typically separated by half the primary beam size. The improvement of the tracking behavior of modern antennas now leads astronomers to consider on-the-fly observations, with the antennas slewing continuously across the sky. The improvements in correlator and receiver technologies are also leading to techniques that could potentially sample the antenna focal planes with multi-beam receivers instead of the single-pixel receivers installed on current interferometers.

The ideal measurement equation of interferometric wide-field imaging is

$$V\left(u_\mathrm{p},\alpha_\mathrm{s}\right) = \int_{\alpha_\mathrm{p}} B\left(\alpha_\mathrm{p}-\alpha_\mathrm{s}\right) I\left(\alpha_\mathrm{p}\right) \mathrm{e}^{-\mathrm{i}2\pi\alpha_\mathrm{p}u_\mathrm{p}}\,\mathrm{d}\alpha_\mathrm{p}, \quad (1)$$

where V is the visibility function of 1) u_p (the spatial frequency with respect to the fixed phase center) and 2) α_s (the scanned sky angle), I is the sky brightness, and B the antenna power pattern or primary beam of an antenna of the interferometer (Thompson et al. 1986, Chap. 2). For simplicity, 1) we assume that the primary beam is independent of azimuth and elevation, and 2) we use one-dimensional notation without loss of generality. We do not deal with polarimetry (see e.g. Hamaker et al. 1996; Sault et al. 1996a, 1999) because it adds another level of complexity over our first goal here, i.e. wide-field considerations. Several aspects make Eq. (1) peculiar with respect to the ideal measurement equation for single-field observations. First, the visibility is a function not only of the *uv* spatial frequency (u_p) but also of the scanned sky coordinate (α_s). Second, Eq. (1) is a mix between a Fourier transform and a convolution equation. It can be regarded, for example, as the Fourier transform along the α_p dimension of the function, $B(\alpha_\mathrm{p}-\alpha_\mathrm{s})\,I(\alpha_\mathrm{p})$, of the $(\alpha_\mathrm{p},\,\alpha_\mathrm{s})$ variables. But Eq. (1) can also be written as the convolution:

$$V\left(u_\mathrm{p},\alpha_\mathrm{s}\right) = \int_{\alpha_\mathrm{p}} \mathcal{B}\left(\alpha_\mathrm{s}-\alpha_\mathrm{p}\right)\,\mathcal{I}\left(\alpha_\mathrm{p},u_\mathrm{p}\right)\,\mathrm{d}\alpha_\mathrm{p}, \quad (2)$$

where

$$\mathcal{B}\left(\alpha_\mathrm{s}-\alpha_\mathrm{p}\right) \equiv B\left(\alpha_\mathrm{p}-\alpha_\mathrm{s}\right) \quad (3)$$

and

$$\mathcal{I}\left(\alpha_\mathrm{p},u_\mathrm{p}\right) \equiv I\left(\alpha_\mathrm{p}\right)\,\mathrm{e}^{-\mathrm{i}2\pi\alpha_\mathrm{p}u_\mathrm{p}}. \quad (4)$$

For each u_p kept constant, $V(u_p, \alpha_s)$ is the convolution of $\mathcal{B}$ and $\mathcal{I}$. Indeed, $\mathcal{I}(\alpha_p, u_p = 0) = I(\alpha_p)$, so we derive

$$V\left(u_p = 0, \alpha_s\right) = \int_{\alpha_p} \mathcal{B}(\alpha_s - \alpha_p)\, I(\alpha_p)\, \mathrm{d}\alpha_p, \tag{5}$$

i.e., the convolution equation for single-dish observations.

Ekers & Rots (1979) were the first to show that the measurement equation (Eq. (1)) enables us to recover spatial frequencies of the sky brightness at a much finer *uv* resolution than the *uv* resolution set by the diameter of the interferometer antennas. Interestingly enough, the goal of Ekers & Rots (1979) was "just" to find a way to produce the missing short spacings of a multiplying interferometer. However, Cornwell (1988) realized that Ekers & Rots' scheme has a much stronger impact, because it explains why an interferometer is able to do wide-field imaging. Cornwell (1988) also demonstrated that on-the-fly scanning is not absolutely necessary to interferometric wide-field imaging. Indeed, the large-scale information can be retrieved in mosaics of single-field observations, provided that the sampling of the single fields follows the sky-plane Nyquist sampling theorem.

As a result, all the information about the sky brightness is coded in the visibility function. From a data-processing viewpoint, all the current radio-interferometric wide-field imaging methods (see, e.g., Gueth et al. 1995; Sault et al. 1996b; Cornwell et al. 1993; Bhatnagar & Cornwell 2004; Bhatnagar et al. 2008; Cotton & Uson 2008) belong to the mosaicking family[1] pioneered by Cornwell (1988). In this family, the processing starts with Fourier transforming $V(u_p, \alpha_s)$ along the u_p dimension (i.e. at constant α_s) to produce a set of single-field dirty images before linearly combining them and forming a wide-field dirty image. In this paper, we propose an alternate processing, which starts with a Fourier transform of $V(u_p, \alpha_s)$ along the α_s dimension (i.e. at constant u_p). We show how this explicitely synthesizes the spatial frequencies needed to do wide-field imaging, which are linearly combined to form a "wide-field *uv* plane", i.e., one *uv*-plane containing all the spatial frequency information measured during the wide-field observation. Inverse Fourier transform will produce a dirty image, which can then be deconvolved using standard methods. The existence of two different ways to extract the wide-field information from the visibility function raises several questions: are they equivalent? What are their relative merits?

We thus aim at revisiting the mathematical foundations of wide-field imaging and deconvolution. Sections 2 to 7 propose the new algorithm, which we call wide-field synthesis: Sect. 2 first defines the notations and it then lays out the basic concepts used throughout the paper. Section 3 states the steps needed to go beyond the Ekers & Rots scheme and explores the consequences of incomplete sampling of both the *uv* and sky planes. Section 4 discusses the effects of gridding by convolution and regular resampling. Section 5 describes how to influence the dirty beam shapes and thus the deconvolution. Section 6 states how to introduce short spacings measured either from a single-dish antenna or from heterogeneous interferometers. Section 7 compares the proposed wide-field synthesis algorithm with standard nonlinear mosaicking. Some detailed demonstrations are factored out in Appendix A to enable an easier reading of the main paper, while ensuring that interested readers can follow the demonstrations. Appendices B and C then explain how the wide-field synthesis algorithm can cope with non-ideal effects: Appendix B discusses how at least one standard way to cope with sky projection problems is compatible with the wide-field synthesis algorithm. Appendix C explores the consequences of using the on-the-fly observing mode. Finally, we assume good familiarity with single-field imaging in various places. We refer the reader to well-known references: e.g. Chap. 6 of Thompson et al. (1986) and Sramek & Schwab (1989).

[1] In the rest of this paper, stop-and-go mosaicking refer to the observing mode, while mosaicking alone refer to the imaging family.

2. Notations and basic concepts

2.1. Notations

In this paper, we use the Bracewell (2000)'s notation to display the relationship between a function $I(\alpha)$ and its direct Fourier transform $\overline{I}(u)$, i.e.,

$$I(\alpha) \supset \overline{I}(u), \tag{6}$$

where (α, u) is the couple of Fourier conjugate variables. We also use the following sign conventions for the direct and inverse Fourier transforms

$$\overline{I}(u) \equiv \int_{\alpha} I(\alpha)\, \mathrm{e}^{-\mathrm{i}2\pi\alpha u}\, \mathrm{d}\alpha \tag{7}$$

and

$$I(\alpha) \equiv \int_{u} \overline{I}(u)\, \mathrm{e}^{+\mathrm{i}2\pi u\alpha}\, \mathrm{d}u. \tag{8}$$

As V is a function of two independent quantities (u_p and α_s), the Fourier transform may be applied independently on each dimension, while the other dimension stays constant. Several additional conventions are used to express this. First, we introduce a specific notation to state that either the first or the second dimension stays constant:

$$V_{u_p}(\alpha_s) \equiv V\left(u_p = \text{const.}, \alpha_s\right), \tag{9}$$

and

$$V^{\alpha_s}\left(u_p\right) \equiv V\left(u_p, \alpha_s = \text{const.}\right). \tag{10}$$

Second, we use a bottom/top line to derive the notation of the Fourier transform along the first/second dimension from the notation of the original function. Third, on the Fourier transform sign (i.e. $\supset$), we explicitly state the dimension along which the Fourier transform is computed. For instance, if D is a function of (α_p, α_s), then the Fourier transform of D along the first dimension is expressed as

$$D\left(\alpha_p, \alpha_s\right) \underset{u_p}{\overset{\alpha_p}{\supset}} \underline{D}\left(u_p, \alpha_s\right), \tag{11}$$

while the Fourier transform of D along the second dimension is expressed as

$$D\left(\alpha_p, \alpha_s\right) \underset{u_s}{\overset{\alpha_s}{\supset}} \overline{D}\left(\alpha_p, u_s\right). \tag{12}$$

We also use a more compact notation when doing the Fourier transform on both dimensions simultaneously, i.e.,

$$D\left(\alpha_p, \alpha_s\right) \underset{(u_p, u_s)}{\overset{(\alpha_p, \alpha_s)}{\supset}} \overline{\underline{D}}\left(u_p, u_s\right). \tag{13}$$

Finally, the convolution of two functions G and V is noted and defined as

$$\{G \star V\}(u) \equiv \int_{v} G(u - v)\, V(v)\, \mathrm{d}v. \tag{14}$$

Table 1. Definition of the symbols used to expose the wide-field synthesis formalism.

Symbol	& Definition	Plane(s)[a]
α_s	Scanned angle	sky
u_s	Scanned spatial frequency	uv
α_p	Phased angle	sky
u_p	Phased spatial frequency	uv
I	Sky brightness	sky
B	Primary beam	sky
V	Visibility function	uv & sky
S	Sampling function	uv & sky
Δ	Set of single-field dirty beams	sky & sky
D	Set of wide-field dirty beams	sky & sky
Ω	Sky-plane weighting function	sky & sky
W	uv-plane weighting function ($\Omega \supset W$)	uv & uv
$\mathcal{G}$	Gridding function ($=g\,\gamma$)	uv & sky
g	uv-plane gridding function	uv
γ	Sky-plane gridding function	sky
$I_{\rm dirty}$	Wide-field dirty image	sky

Notes. [(a)] Planes of definition of the associated symbols.

Table 2. Definition of the uv and sky scales relevant to wide-field interferometric imaging.

Symbol	Definition
$[\lambda$, rad$]^a$	Conjugate uv and angular scale
$d_{\rm max}, \theta_{\rm syn}$	Maximum baseline length & Synthesized beam
$d_{\rm prim}, \theta_{\rm prim}$	Antenna diameter & Primary beamwidth
$d_{\rm alias}, \theta_{\rm alias}$	Minimum image size for tolerable aliasing
$d_{\rm field}, \theta_{\rm field}$	Targeted field of view
$d_{\rm image}, \theta_{\rm image}$	Final image size

Notes. [(a)] The chosen units (radians for θ and wavelength for d) imply that the conjugate scales are linked through $\theta = 1/d$, instead of the usual $\theta = \lambda/d$.

For reference, Table 1 summarizes the definitions of the symbols used most throughout the paper. With the one-dimensional notation used throughout the paper, the number of planes quoted directly gives the number of associated dimensions of the symbols. Generalization to images would require a doubling of the number of planes/dimensions. Table 2 defines the uv and angular scales that are relevant to wide-field interferometric imaging, and Fig. 1 sketches the different angular scales. Each angular scale (θ) is related to a uv scale (d) through $\theta = 1/d$, where θ and d are measured in radians and in units of λ (the wavelength of the observation). In the rest of the paper, we explicitely distinguish between $\theta_{\rm prim} \equiv 1/d_{\rm prim}$, the angular scale associated to the diameter of the interferometer antennas, and $\theta_{\rm fwhm}$, the full width at half maximum of the primary beam. The relation between $\theta_{\rm prim}$ and $\theta_{\rm fwhm}$ depends on the illumination of the receiver feed by the antenna optics. In radio astronomy, we typically have $\theta_{\rm fwhm} \sim 1.2\,\theta_{\rm prim}$ (see e.g. Goldsmith 1998, Chap. 6). Finally, the notion of anti-aliasing scale ($\theta_{\rm alias}$) is introduced and discussed in Sect. 4.2.

2.2. Basic concepts

Figure 2 illustrates the principles underlying 1) the setup to get interferometric wide-field observations and 2) our proposition to process them. For simplicity, we display the minimum possible

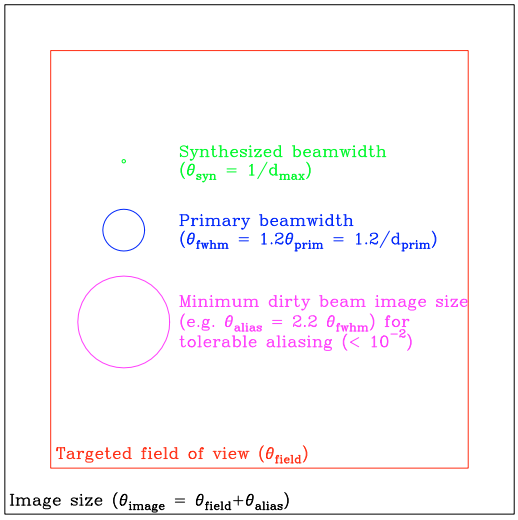

Fig. 1. Visualization of the different angular scales relevant to wide-field interferometric imaging. The notion of anti-aliasing scale ($\theta_{\rm alias}$) is introduced and discussed in Sect. 4.2.

complexity without loss of generality. The top row displays the sky plane. The middle row represents the 4-dimensional measurement space at different stages of the processing. As it is difficult to display a 4-dimensional space on a sheet of paper, the bottom row shows 2-dimensional cuts of the measurement space at the same processing stages.

2.2.1. Observation setup and measurement space

Panel a) displays the sky region for which we aim for estimating the sky brigthness, $I(\alpha)$. The field of view of an interferometer observing in a given direction of the sky has a typical size set by the primary beam shape. In our example, this is illustrated by any of the circles whose diameter is $\theta_{\rm prim}$. As we aim at observing a wider field of view, e.g. $\theta_{\rm field}$, the interferometer needs to scan the targeted sky field. We assume that we scan through stop-and-go mosaicking, ending up with a 7-field mosaic.

After calibration, the output of the interferometer is a visibility function, $V(u_p, \alpha_s)$, whose relation to the sky brightness is given by the measurement equation (Eq. (1)). Panel b.1) shows the measurement space as a mosaic of single-field uv planes: the uv plane coverage of each single-field observation is displayed as a blue sub-panel at the sky position where it has been measured and which is featured by the red axes. We assume 1) that the interferometer has only 3 antennas and 2) that only a single integration is observed per sky position. This implies only 6 visibilities per single-field uv plane. In panel b.2), the uv planes at constant α_s are displayed as the blue vertical lines. The measured spatial frequencies belong to the $[-d_{\rm max}, -d_{\rm min}]$ and $[+d_{\rm min}, +d_{\rm max}]$ ranges, where $d_{\rm min}$ and $d_{\rm max}$ are respectively the shortest and longest measured baseline length. $d_{\rm min}$ is related to the minimum tolerable distance between two antennas to avoid collision. Here, we chose $d_{\rm min} \sim 1.5\,d_{\rm prim}$. The grey zone between $-d_{\rm min}$, and $+d_{\rm min}$ displays the missing short spacings.

2.2.2. Processing by explicit synthesis of the wide-field spatial frequencies

All the information about the sky brightness, $I(\alpha)$, is somehow coded in the visibility function, $V(u_p, \alpha_s)$. The high spatial

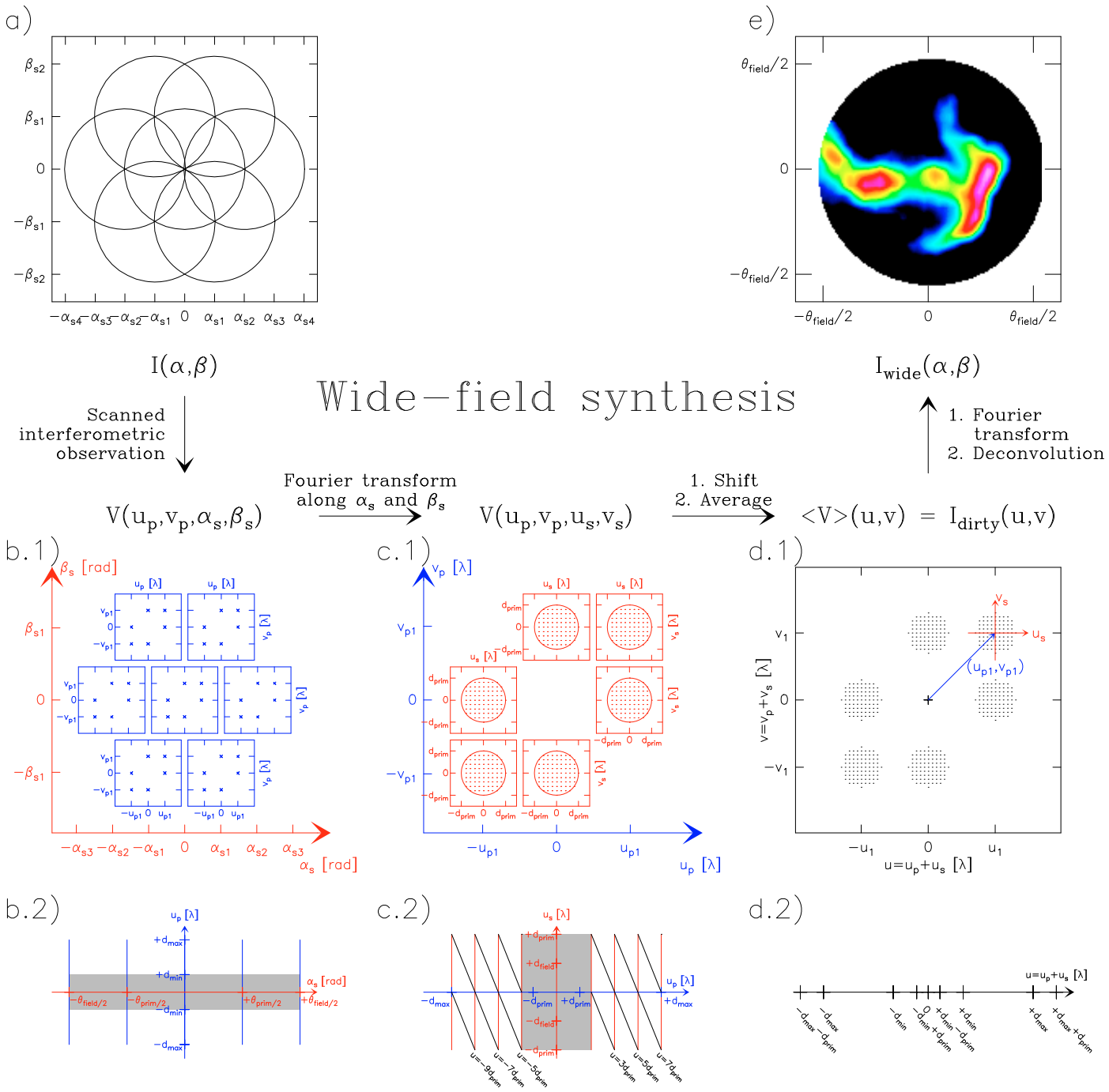

Fig. 2. Illustration of the principles of wide-field synthesis, which enables us to image wide-field interferometric observations. *The top row* displays the sky plane. *The middle row* displays the 4-dimensional visibility space and *the bottom row* shows 2-dimensional cuts of this space at different stages of the processing. In panels **b)** to **d)**, the scanned dimensions (α_s and u_s) are displayed in blue while the phased spatial scale dimensions (u_p) are displayed in red and the spatial scale dimensions (u) of the final wide-field *uv* plane are displayed in black. The grey zones of panels **b.2)** and **c.2)** show the regions of the visibility space without measurements (missing short-spacings). In detail, panel **a)** shows a possible scanning strategy of the sky to measure the unknown brightness distribution at high angular resolution: for simplicity it is here just a 7-field mosaic. Panels **b.1)** and **b.2)** sketch the space of measured visibilities: the *uv* plane at each of the 7 measured sky positions is displayed as a blue square box in panel **b.1)** and a blue vertical line in panel **b.2)**. For simplicity, only 6 visibilities are plotted in panel **b.1)**. Panels **c.1)** and **c.2)** sketch the space of synthesized visibilities after Fourier transform of the measured visibilities along the scanned coordinate (α_s): at each measured spatial frequency u_p (displayed on the blue axes) is associated one space of synthesized wide-field spatial frequencies displayed as one of the red squares in panel **c.1)** and the red vertical lines in panel **c.2)**. The wide-field spatial scales are synthesized 1) on a grid whose cell size is related to the total field of view of the observation and 2) only inside circles whose radius is the primary diameter of the interferometer antennas. Panels **d.1)** and **d.2)** display the final, wide-field *uv* plane. This plane is built by application of the shift-and-average operator along the black lines on panel **c.2)**, lines that display the region of constant u spatial frequency in the (u_p, u_s) space. Standard inverse Fourier transform and deconvolution methods then produce a wide-field distribution of sky brightnesses as shown in panel **e)**.

frequencies (from $d_{\rm min}$ to $d_{\rm max}$) are clearly coded along the $u_{\rm p}$ dimension. The uncertainty relation between Fourier conjugate quantities also implies that the typical spatial frequency resolution along the $u_{\rm p}$ dimension is only $d_{\rm prim}$ because the field of view of a single pointing has a typical size of $\theta_{\rm prim}$. However, wide-field imaging implies measuring all the spatial frequencies with a finer resolution, $d_{\rm field} = 1/\theta_{\rm field}$. The missing information must then be hidden in the $\alpha_{\rm s}$ dimension.

In Sect. 3, we show that Fourier transforming the measured visibilities along the $\alpha_{\rm s}$ dimension (i.e. at constant $u_{\rm p}$) can synthesize the missing spatial frequencies, because the $\alpha_{\rm s}$ dimension is sampled from $-\theta_{\rm field}/2$ to $+\theta_{\rm field}/2$, implying a typical spatial-frequency resolution of the $u_{\rm s}$ dimension equal to $d_{\rm field}$. Conversely, the $\alpha_{\rm s}$ dimension is probed by the primary beams with a typical angular resolution of $\theta_{\rm prim}$, implying that the $u_{\rm s}$ spatial frequencies will only be synthesized inside the $[-d_{\rm prim}, +d_{\rm prim}]$ range. Panels c.1) and c.2) illustrate the effects of the Fourier transform of $V(u_{\rm p}, u_{\rm s})$ along the $\alpha_{\rm s}$ dimension, in 4 and 2 dimensions, respectively. The red subpanels or vertical lines display the $u_{\rm s}$ spatial frequencies around each constant $u_{\rm p}$ spatial frequency.

In panels d.1) and d.2) (i.e. after the Fourier transform along the $\alpha_{\rm s}$ dimension), $\overline{V}(u_{\rm p}, u_{\rm s})$ contains all the measured information about the sky brightness in a spatial frequency space. However, the information is ordered in a strange and redundant way. Indeed, we show that $\overline{V}(u_{\rm p}, u_{\rm s})$ is linearly related to $\overline{I}(u_{\rm p}+ u_{\rm s})$. To first order, the information about a given spatial frequency u is stored in all the values of $\overline{V}(u_{\rm p}, u_{\rm s})$ which verifies $u = u_{\rm p} + u_{\rm s}$ (black lines on panel c.2).

A shift operation will reorder the spatial scale information and averaging will compress the redundancy (illustrated by the halving of the number of the space dimensions). The use of a shift-and-average operator thus produces a final *uv* plane containing all the spatial scale information to image a wide field in an intuitive form. We thus call this space the *wide-field uv plane*. Panels d.1) and d.2) display this space, where the minimum relevant spatial frequency is related to the total field of view, while the maximum one is related to the interferometer resolution.

Sections 3 and 4 show that applying the shift-and-average operator to $\overline{V}$ produces the Fourier transform of a dirty image, which is a local convolution of the sky brightness by a slowly varying dirty beam. As a result, inverse Fourier transform of $\langle\overline{V}\rangle$ and deconvolution methods will produce a wide-field distribution of sky brightness as shown in panel e) at the top right of Fig. 2.

3. Beyond the Ekers & Rots scheme

In the real world, the visibility function is not only sampled, but this sampling is incomplete for two main reasons. 1) The instrument has a finite spatial resolution, and the scanning of the sky is limited, implying that the sampling in both planes has a finite support. 2) The *uv* coverage and the sky-scanning coverage can have holes caused either by intrinsic limitations (e.g. lack of short spacings or small number of baselines) or by acquisition problems (implying data flagging). The incomplete sampling makes the mathematics on the general case complex. We thus start with the ideal case where we assume that the visibility function is continuously sampled along the $u_{\rm p}$ and $\alpha_{\rm s}$ dimension. We then look at the general case.

3.1. Ideal case: infinite, continuous sampling

Starting from the measurement Eq. (1), Ekers & Rots (1979) first demonstrated (see Sect. A.1) that[2]

$$\forall \left(u_{\rm p}, u_{\rm s}\right), \quad \overline{V}_{u_{\rm p}}(u_{\rm s}) = \overline{B}(-u_{\rm s})\, \overline{I}\left(u_{\rm p} + u_{\rm s}\right). \tag{15}$$

For each constant $u_{\rm p}$ spatial frequency, the Fourier transform thus synthesizes a function, $\overline{V}_{u_{\rm p}}(u_{\rm s})$, which is simply related to $\overline{I}(u_{\rm p}+ u_{\rm s})$, the Fourier components of the sky brightness around $u_{\rm p}$. $\overline{V}(u_{\rm p}, u_{\rm s})$ is only defined in the $[-d_{\rm prim}, +d_{\rm prim}]$ interval along the $u_{\rm s}$ dimension because $\overline{B}(-u_{\rm s})$ is itself only defined inside this interval, since $\overline{B}(-u_{\rm s})$ is the autocorrelation of the antenna illumination.

We search to derive a single estimate of the Fourier components $\overline{I}(u)$ of the sky brightness. Equation (15) indicates that the fraction $\overline{V}(u_{\rm p}, u_{\rm s})/\overline{B}(-u_{\rm s})$ gives us an estimate of $\overline{I}(u)$ for each couple $(u_{\rm p}, u_{\rm s})$ that satisfies $u = u_{\rm p} + u_{\rm s}$. However, the information about $\overline{I}$ is strangely ordered. There are two possible ways to look at this ordering. 1) Starting from the measurement space, the Ekers & Rots scheme synthesizes frequencies around each $u_{\rm p}$ measure inside the interval $[u_{\rm p} - d_{\rm prim}, u_{\rm p} + d_{\rm prim}]$ at the $d_{\rm field}$ spatial frequency resolution. 2) Starting from our goal, we want to estimate $\overline{I}$ at a given spatial frequency u with a $d_{\rm field}$ spatial frequency resolution. We thus search for all the couples $(u_{\rm p}, u_{\rm s})$ satisfying $u = u_{\rm p} + u_{\rm s}$, which are displayed in panel c.2) of Fig. 2 as the diagonal black lines. It immediately results that 1) there are several estimates of $\overline{I}$ for each spatial frequency u and 2) the number of estimates varies with u. We can average them to get a better estimate of $\overline{I}(u)$.

This last viewpoint thus suggests averaging in the $(u_{\rm p}, u_{\rm s})$ space along linepaths defined by $u = u_{\rm p} + u_{\rm s}$. Such an operator can mathematically be defined as

$$\langle F\rangle(u) \equiv \iint_{u_{\rm p}u_{\rm s}} \delta\left[u - (u_{\rm p} + u_{\rm s})\right] W\left(u_{\rm p}, u_{\rm s}\right)\, F\left(u_{\rm p}, u_{\rm s}\right)\, {\rm d}u_{\rm p}{\rm d}u_{\rm s}, \tag{16}$$

where F is the function to be averaged and W is a normalized weighting function. Using the properties of the Dirac function, we can reduce the double integral to

$$\langle F\rangle(u) = \int_{u_{\rm p}} W\left(u_{\rm p}, u - u_{\rm p}\right)\, F\left(u_{\rm p}, u - u_{\rm p}\right)\, {\rm d}u_{\rm p}. \tag{17}$$

In this equation, we easily recognize a *shift-and-average operator*. The normalized weighting function plays a critical role in the following formalism, and we propose clever ways to define W in Sect. 5. In the ideal case studied here, W can be defined as

$$W(u_{\rm p}, u_{\rm s}) \equiv 1/(2\sqrt{2}\, d_{\rm prim}) \ \text{ for } u_{\rm s} \text{ in } [-d_{\rm prim}, +d_{\rm prim}],$$
$$W(u_{\rm p}, u_{\rm s}) \equiv 0 \ \text{ for other values of } u_{\rm s}.$$

In other words, we have just normalized the integral by the constant length $(2\sqrt{2}\, d_{\rm prim})$ of the averaging linepath.

[2] The convolution theorem, which states that the Fourier transform of the convolution of two functions is the product of the Fourier transform of both individual functions, is a special case for Eq. (15): it can be recovered by setting $u_{\rm p} = 0$. Indeed, as already mentioned in the introduction, the ideal measurement Eq. (1) can be interpreted as a convolution with an additional phase term. By Fourier transforming along the $\alpha_{\rm s}$ dimension, the convolution translates into a product of Fourier transforms $\overline{B}$ and $\overline{I}$, while the phase term translates into a shift of coordinates: $u_{\rm p} + u_{\rm s}$.

3.1.1. Wide-field dirty image, dirty beam and image-plane measurement equation

Section 3.2 shows that the incomplete sky and *uv* sampling forbid us to apply the shift-and-average operator to the $\overline{V}(u_\mathrm{p}, u_\mathrm{s})/\overline{B}(-u_\mathrm{s})$ function. To guide us in this general case, we thus explore the consequences of applying this operator to $\overline{V}$ in the ideal case. It is easy to demonstrate that the result is the Fourier transform of a dirty image, i.e.,

$$\overline{I}_\mathrm{dirty}(u) = \left\langle \overline{V} \right\rangle (u). \tag{18}$$

Indeed, substituting $\langle \overline{V} \rangle(u)$ with the help of Eqs. (17) and (15) and taking the inverse Fourier transform, we get

$$\overline{I}_\mathrm{dirty}(u) = \overline{D}(u)\, \overline{I}(u), \tag{19}$$

with

$$\overline{D}(u) \equiv \int_{u_\mathrm{p}} W\left(u_\mathrm{p}, u - u_\mathrm{p}\right) \overline{B}\left(u_\mathrm{p} - u\right) \mathrm{d}u_\mathrm{p}. \tag{20}$$

Here, I_dirty conforms to the usual idea of dirty image, i.e., the convolution of a dirty beam by the sky brightness:

$$I_\mathrm{dirty}(\alpha) = \{D \star I\}(\alpha)\,. \tag{21}$$

In contrast to the usual situation for single-field observations, the mix between a Fourier transform and a convolution of Eq. (1), associated with the specific processing[3] changes the image-plane measurement equation from a convolution of a dirty beam with the product $B\,I$ to a convolution of a dirty beam with I. *The dependency on the primary beam is still there. It is just transferred from a product of the sky brightness distribution into the definition of the dirty beam.*

3.1.2. Summary and interpretation

In summary, a theoretical implementation of wide-field synthesis implies

1. the possibility of Fourier transforming the visibility function along the α_s dimension (i.e. at constant u_p), which gives us a set of synthesized *uv* planes;
2. the possibility of shifting-and-averaging these synthesized *uv* planes to build the final, wide-field *uv* plane containing all the available information.

Using those tools, we are able to write the wide-field image-plane measurement equation as a convolution of a wide-field dirty beam (D) by the sky brightness (I), i.e.,

$$I_\mathrm{dirty}(\alpha) = \int_{\alpha'} D\left(\alpha - \alpha'\right)\, I\left(\alpha'\right)\, \mathrm{d}\alpha'. \tag{22}$$

We can write a convolution equation in this ideal case because the wide-field response of the instrument is shift-invariant; i.e., D only depends on differences of the sky coordinates.

It is well-known that for a single-field observation, the dirty beam is the inverse Fourier transform of the sampling function. The shape of this sampling function is due to the combination of aperture synthesis (the interferometer antennas give a limited number of independent baselines) and Earth-rotation synthesis (the rotation of the Earth changes the projection of the physical baselines onto the plane perpendicular to the instantaneous line of sight). By analyzing via a Fourier transform, the evolution of the visibility function with the sky position, the Ekers & Rots scheme synthesizes visibilities at spatial frequencies needed to image a larger field of view than the interferometer primary beam. We thus propose to call this specific processing: *wide-field synthesis*.

[3] I.e. direct Fourier transform along the α_s dimension, shift-and-average to define a final wide-field *uv* plane, and inverse Fourier transform.

3.2. General case: incomplete sampling

Reality imposes limitations on the synthesis of spatial frequencies. Indeed, we have already stated that the visibility function is incompletely sampled both in the *uv* and sky planes. To take the sampling effects into account, we introduce the sampling function $S\,(u_\mathrm{p},\, \alpha_\mathrm{s})$, which is a sum of Dirac functions at measured positions[4]. The sampling function cannot be factored into the product of two functions, each only acting on one plane. Indeed, the Earth rotation happening during the source scanning implies a coupling of both dimensions of the sampling function. In other words, the *uv* coverage will vary with the scanned sky coordinate. This leads us to a shift-dependent situation, precluding us from writing the wide-field image-plane measurement equation as a true convolution. We nevertheless search for a wide-field image-plane measurement equation as close as possible to a convolution because all the inversion methods devised in the past three decades in radioastronomy are tuned to deconvolve images. The simplest mathematical way to generalize Eq. (22) to a shift-dependent situation is to write it as

$$I_\mathrm{dirty}(\alpha) = \int_{\alpha'} D\left(\alpha - \alpha', \alpha\right)\, I\left(\alpha'\right)\, \mathrm{d}\alpha'. \tag{23}$$

In this section, we show how the *linear character of the imaging process* allows us to do this. Section 3.2.1 derives the impact of incomplete sampling on the Ekers & Rots equation, and Sect. 3.2.2 derives the wide-field measurement equation in the *uv* plane. Section 3.2.3 interprets these results.

3.2.1. Effect on the Ekers & Rots equation

The sampled visibility function, $S\,V$, is defined as the product of S and V and $\overline{S\,V}$ its Fourier transform along α_s, i.e.,

$$S\,V\left(u_\mathrm{p}, \alpha_\mathrm{s}\right) \equiv S\,\left(u_\mathrm{p}, \alpha_\mathrm{s}\right)\, V\left(u_\mathrm{p}, \alpha_\mathrm{s}\right), \tag{24}$$

and

$$S\,V\left(u_\mathrm{p}, \alpha_\mathrm{s}\right) \underset{u_\mathrm{s}}{\overset{\alpha_\mathrm{s}}{\supset}} \overline{S\,V}\left(u_\mathrm{p}, u_\mathrm{s}\right). \tag{25}$$

Because $S\,V_{u_\mathrm{p}}$ is the product of two functions of α_s, we can use the convolution theorem to show that $\overline{S\,V}_{u_\mathrm{p}}$ is the convolution of $\overline{S}_{u_\mathrm{p}}$ by $\overline{V}_{u_\mathrm{p}}$, i.e.,

$$\overline{S\,V}_{u_\mathrm{p}}\,(u_\mathrm{s}) = \int_{u'_\mathrm{s}} \overline{S}_{u_\mathrm{p}}(u_\mathrm{s} - u'_\mathrm{s})\, \overline{V}_{u_\mathrm{p}}(u'_\mathrm{s})\, \mathrm{d}u'_\mathrm{s}. \tag{26}$$

By replacing $\overline{V}_{u_\mathrm{p}}$ with the help of the Ekers & Rots relation (Eq. (15)), we derive

$$\overline{S\,V}_{u_\mathrm{p}}\,(u_\mathrm{s}) = \int_{u'_\mathrm{s}} \overline{S}_{u_\mathrm{p}}\,(u_\mathrm{s} - u'_\mathrm{s})\, \overline{B}\,(-u'_\mathrm{s})\, \overline{I}\left(u_\mathrm{p} + u'_\mathrm{s}\right)\, \mathrm{d}u'_\mathrm{s}. \tag{27}$$

[4] Loosely speaking, the sampling function can be thought as a function whose value is 1 where there is a measure and 0 elsewhere.

As $\overline{B}$ is bounded inside the $[-d_{\rm prim}, +d_{\rm prim}]$ interval, $\overline{SV}_{u_{\rm p}}(u_{\rm s})$ is a *local* average, weighted by $\overline{S}_{u_{\rm p}}(u_{\rm s}-u'_{\rm s})\,\overline{B}(-u'_{\rm s})$, of $\overline{I}(u_{\rm p}+u'_{\rm s})$ around the $u_{\rm p}$ spatial frequency.

As expected, we recover Eq. (15) for the ideal case (i.e., infinite, continuous visibility function) because then $\overline{S}_{u_{\rm p}}(u_{\rm s}-u'_{\rm s}) = \delta(u_{\rm s}-u'_{\rm s})$. A more interesting case arises when the visibility function is continuously sampled over a limited sky field of view, i.e.,

$$\forall u_{\rm p}, \qquad S\left(u_{\rm p},\alpha_{\rm s}\right) = 1 \quad \text{if} \quad |\alpha_{\rm s}| \leq \theta_{\rm field}/2, \tag{28}$$

$$\forall u_{\rm p}, \qquad S\left(u_{\rm p},\alpha_{\rm s}\right) = 0 \quad \text{if} \quad |\alpha_{\rm s}| > \theta_{\rm field}/2. \tag{29}$$

After Fourier transform this gives

$$\forall u_{\rm p}, \quad \overline{S}\left(u_{\rm p},u_{\rm s}\right) = \frac{1}{d_{\rm field}}\,\mathrm{sinc}\left(\frac{u_{\rm s}}{d_{\rm field}}\right). \tag{30}$$

In this case, the local average of the sky brightness Fourier components happens on a typical uv scale equal to $d_{\rm field}$. However, the sinc function is known to decay only slowly. Some observing strategy (e.g. quickly observing outside the edges of the targeted field of view to provide a bandguard) could be considered to apodize the sky-plane dependence of the sampling function, resulting in faster decaying $\overline{S}$ functions, hence in less mixing of the wide-field spatial frequencies.

3.2.2. uv-plane wide-field measurement equation

Because we aim at estimating the Fourier component of $\overline{I}$, we introduce the following change of variables $u' \equiv u_{\rm p} + u'_{\rm s}$ and $\mathrm{d}u' = \mathrm{d}u'_{\rm s}$, to derive

$$\overline{SV}_{u_{\rm p}}(u_{\rm s}) = \int_{u'} \overline{S}_{u_{\rm p}}\left(u_{\rm p}+u_{\rm s}-u'\right)\,\overline{B}\left(u_{\rm p}-u'\right)\,\overline{I}\left(u'\right)\,\mathrm{d}u'. \tag{31}$$

We then shift-and-average $\overline{SV}(u_{\rm p},u_{\rm s})$ to build the Fourier transform of a wide-field dirty image

$$\overline{I}_{\rm dirty}(u) \equiv \left\langle \overline{SV} \right\rangle (u), \quad \text{with} \quad u = u_{\rm p}+u_{\rm s}. \tag{32}$$

Substituting the shift-and-average operator by its definition and using Eq. (31) to replace $\overline{SV}_{u_{\rm p}}(u_{\rm s})$, we derive

$$\overline{I}_{\rm dirty}(u) = \iint_{u_{\rm p}u'} W\left(u_{\rm p},u-u_{\rm p}\right)\,\overline{S}\left(u_{\rm p},u-u'\right)\,\overline{B}\left(u_{\rm p}-u'\right)\,\overline{I}\left(u'\right)\,\mathrm{d}u_{\rm p}\mathrm{d}u'. \tag{33}$$

This uv-plane wide-field measurement equation can be written as

$$\overline{I}_{\rm dirty}(u) = \int_{u'} \underline{\overline{D}}\left(u',u-u'\right)\,\overline{I}\left(u'\right)\,\mathrm{d}u', \tag{34}$$

if we enforce the following equality

$$\underline{\overline{D}}\left(u',u-u'\right) \equiv \int_{u_{\rm p}} W\left(u_{\rm p},u-u_{\rm p}\right)\overline{S}\left(u_{\rm p},u-u'\right)\overline{B}\left(u_{\rm p}-u'\right)\,\mathrm{d}u_{\rm p}. \tag{35}$$

This is one way to define $\underline{\overline{D}}$, which is convenient though unusual. It is implicit in this definition that we need to make a change of variable ($u'' = u-u'$) to derive

$$\underline{\overline{D}}\left(u',u''\right) \equiv \int_{u_{\rm p}} W\left(u_{\rm p},u'+u''-u_{\rm p}\right)\overline{S}\left(u_{\rm p},u''\right)\overline{B}\left(u_{\rm p}-u'\right)\,\mathrm{d}u_{\rm p}. \tag{36}$$

In the following, we use either one or the other definition of $\underline{\overline{D}}$, depending on convenience.

3.2.3. Interpretation

Appendix A.2 demonstrates that the image and uv-plane wide-field measurement equations (Eqs. (23) and (34)) are equivalent if

$$D\left(\alpha_{\rm p},\alpha_{\rm s}\right) \overset{(\alpha_{\rm p},\alpha_{\rm s})}{\underset{(u_{\rm p},u_{\rm s})}{\supset}} \underline{\overline{D}}\left(u_{\rm p},u_{\rm s}\right). \tag{37}$$

The image-plane wide-field measurement equation (Eq. (23)) can be written as

$$I_{\rm dirty}(\alpha) = \{D^{\alpha} \star I\}(\alpha). \tag{38}$$

Its interpretation is straightforward: the sky brightness distribution is convolved with a dirty beam, $D(\alpha',\alpha'')$, which varies with the sky coordinate α''. This raises the question of the rate of change of the dirty beam with the sky coordinate. This question is addressed in Sects. 4.2 and 5.

4. Gridding by convolution and regular resampling

We want to Fourier transform the raw visibilities along the sky dimension ($\alpha_{\rm s}$) at some constant value in the $u_{\rm p}$ dimension. The raw data, however, is sampled on an irregular grid in both the uv and sky planes. We need to grid the measured visibilities in both the uv and the sky planes before Fourier transformation for different reasons. First, the gridding in the uv plane will handle the variation in the spatial frequency as the sky is scanned, i.e., the difficulty and perhaps the impossibility of Fourier-transforming at a completely constant $u_{\rm p}$ value. Second, the gridding along the sky dimension allows the use of Fast Fourier Transforms. As usual, we grid through convolution and regular resampling.

4.1. Convolution

4.1.1. Definitions

We first define a gridding kernel that depends on both dimensions, $\mathcal{G}(u,\alpha_{\rm s})$. This gridding kernel can be chosen as the product of two functions, simplifying the following demonstrations:

$$\mathcal{G}\left(u_{\rm p},\alpha_{\rm s}\right) \equiv g\left(u_{\rm p}\right)\,\gamma\left(\alpha_{\rm s}\right). \tag{39}$$

We then define the sampled visibility function gridded in both the uv and sky planes as

$$SV^{\mathcal{G}}\left(u_{\rm p},\alpha_{\rm s}\right) \equiv \{\mathcal{G}\star SV\}\left(u_{\rm p},\alpha_{\rm s}\right) \tag{40}$$

$$= \iint_{u'_{\rm p}\alpha'_{\rm s}} g\left(u_{\rm p}-u'_{\rm p}\right)\,\gamma\left(\alpha_{\rm s}-\alpha'_{\rm s}\right)\,SV\left(u'_{\rm p},\alpha'_{\rm s}\right)\,\mathrm{d}u'_{\rm p}\mathrm{d}\alpha'_{\rm s}. \tag{41}$$

Finally, when assessing the impact of the gridding on the measurement Eq. (34), a new function,

$$\Sigma\left(u_{\rm p},\alpha_{\rm s},\alpha''_{\rm s}\right) \equiv S\left(u_{\rm p},\alpha_{\rm s}\right)\,B\left(\alpha''_{\rm s}-\alpha_{\rm s}\right), \tag{42}$$

and its Fourier transforms naturally appear in the equations. Defining the following Fourier transform relationships

$$\Sigma\left(u_{\rm p},\alpha_{\rm s},\alpha''_{\rm s}\right) \overset{\alpha_{\rm s}}{\underset{u_{\rm s}}{\supset}} \overline{\Sigma}\left(u_{\rm p},u_{\rm s},\alpha''_{\rm s}\right), \tag{43}$$

and

$$\overline{\Sigma}\left(u_{\rm p},u_{\rm s},\alpha''_{\rm s}\right) \overset{\alpha''_{\rm s}}{\underset{u''_{\rm s}}{\supset}} \underline{\overline{\Sigma}}\left(u_{\rm p},u_{\rm s},u''_{\rm s}\right), \tag{44}$$

we easily derive

$$\overline{\Sigma}\left(u_\mathrm{p}, \alpha_\mathrm{s}, u''_\mathrm{s}\right) = S\left(u_\mathrm{p}, \alpha_\mathrm{s}\right) \overline{B}\left(u''_\mathrm{s}\right) \mathrm{e}^{-\mathrm{i}2\pi u''_\mathrm{s}\alpha_\mathrm{s}}, \quad (45)$$

and

$$\underline{\overline{\Sigma}}\left(u_\mathrm{p}, u_\mathrm{s}, u''_\mathrm{s}\right) = \overline{S}\left(u_\mathrm{p}, u_\mathrm{s} + u''_\mathrm{s}\right) \overline{B}\left(u''_\mathrm{s}\right). \quad (46)$$

Using these notations, we have before gridding,

$$S\,V\left(u_\mathrm{p}, \alpha_\mathrm{s}\right) = \int_{\alpha_\mathrm{p}} \Sigma\left(u_\mathrm{p}, \alpha_\mathrm{s}, \alpha_\mathrm{p}\right) I\left(\alpha_\mathrm{p}\right) \mathrm{e}^{-\mathrm{i}2\pi\alpha_\mathrm{p}u_\mathrm{p}}\,\mathrm{d}\alpha_\mathrm{p}, \quad (47)$$

and

$$\underline{\overline{D}}\left(u', u-u'\right) = \int_{u_\mathrm{p}} W\left(u_\mathrm{p}, u-u_\mathrm{p}\right) \underline{\overline{\Sigma}}\left(u_\mathrm{p}, u-u_\mathrm{p}, u_\mathrm{p}-u'\right) \mathrm{d}u_\mathrm{p}. \quad (48)$$

4.1.2. Conservation of the wide-field measurement equation

Appendix A.3 demonstrates that the wide-field dirty image is here again the convolution of the sky brightness I by a wide-field dirty beam D^α or, in the Fourier plane,

$$\overline{I}^{\mathcal{G}}_{\mathrm{dirty}}\left(u\right) \equiv \left\langle \overline{S\,V}^{\mathcal{G}} \right\rangle (u) = \int_{u'} \underline{\overline{D}}^{\mathcal{G}}\left(u', u-u'\right) \overline{I}\left(u'\right) \mathrm{d}u' \quad (49)$$

with

$$\underline{\overline{D}}^{\mathcal{G}}\left(u', u-u'\right) \equiv \int_{u_\mathrm{p}} W\left(u_\mathrm{p}, u-u_\mathrm{p}\right) \underline{\overline{\Sigma}}^{\mathcal{G}}\left(u_\mathrm{p}, u-u_\mathrm{p}, u'\right) \mathrm{d}u_\mathrm{p}, \quad (50)$$

where

$$\overline{\Sigma}^{\mathcal{G}}\left(u_\mathrm{p}, \alpha_\mathrm{s}, u'\right) \equiv$$

$$\iint_{u'_\mathrm{p}\alpha'_\mathrm{s}} g\left(u_\mathrm{p}-u'_\mathrm{p}\right) \gamma\left(\alpha_\mathrm{s}-\alpha'_\mathrm{s}\right) \overline{\Sigma}\left(u'_\mathrm{p}, \alpha'_\mathrm{s}, u'_\mathrm{p}-u'\right) \mathrm{d}u'_\mathrm{p}\mathrm{d}\alpha'_\mathrm{s}. \quad (51)$$

We thus have equations that resemble those containing the sampling function alone, except for 1) the replacement of the generalized sampling function $\overline{\Sigma}$ by its gridded version $\overline{\Sigma}^{\mathcal{G}}$ and 2) the way the variables are linked together both in the gridding of $\overline{\Sigma}$ (i.e., Eq. (51)) and in the averaging of $\underline{\overline{\Sigma}}^{\mathcal{G}}$ (i.e., Eq. (50)).

4.2. Regular resampling

It is well known that too low a resampling rate in one space implies power aliasing in the conjugate space (see e.g. Bracewell 2000; Press et al. 1992). Aliasing must be avoided as much as possible because it folds power outside the imaged region back into it. Table 3 defines the intervals of definition of the different functions we are dealing with (i.e., visibilities, primary beam, dirty image, and dirty beam), as well as the associated sampling rates needed to enforce Nyquist sampling. The boundary values of the definition intervals ($|u|_\mathrm{max}$ and $|\alpha|_\mathrm{max}$) are related to the sampling rates ($\partial\alpha$ and ∂u, respectively) through

$$|u|_\mathrm{max} \cdot \partial\alpha = |\alpha|_\mathrm{max} \cdot \partial u = \frac{1}{n_\mathrm{samp}}, \quad (52)$$

where n_samp is an integer characterizing the sampling. Nyquist sampling implies $n_\mathrm{samp} = 2$. However, slight oversampling (e.g. $n_\mathrm{samp} = 3$) is often recommended because the measures suffer from errors and the deconvolution is a nonlinear process. In this section, we examine the properties of the different functions to define their associated sampling rates.

Table 3. Interval ranges of definition and associated sampling rates for the used functions.

Functions	Intervals	Samplings
Visibilities	$\lvert u_\mathrm{p}\rvert \le d_\mathrm{max}$	$\partial u_\mathrm{p} = 2\,d_\mathrm{alias}/n_\mathrm{samp}$
	$\lvert\alpha_\mathrm{p}\rvert \le \theta_\mathrm{alias}/2$	$\partial\alpha_\mathrm{p} = \theta_\mathrm{syn}/n_\mathrm{samp}$
	$\lvert u_\mathrm{s}\rvert \le d_\mathrm{prim}$	$\partial u_\mathrm{s} = 2\,d_\mathrm{image}/n_\mathrm{samp}$
	$\lvert\alpha_\mathrm{s}\rvert \le \theta_\mathrm{image}/2$	$\partial\alpha_\mathrm{s} = \theta_\mathrm{prim}/n_\mathrm{samp}$
Primary beam	$\lvert u'_\mathrm{s}\rvert \le d_\mathrm{prim}$	$\partial u'_\mathrm{s} = 2\,d_\mathrm{alias}/n_\mathrm{samp}$
	$\lvert\alpha'_\mathrm{s}\rvert \le \theta_\mathrm{alias}/2$	$\partial\alpha'_\mathrm{s} = \theta_\mathrm{prim}/n_\mathrm{samp}$
	$\lvert u''_\mathrm{s}\rvert \le d_\mathrm{prim}$	$\partial u''_\mathrm{s} = 2\,d_\mathrm{alias}/n_\mathrm{samp}$
	$\lvert\alpha''_\mathrm{s}\rvert \le \theta_\mathrm{alias}/2$	$\partial\alpha''_\mathrm{s} = \theta_\mathrm{prim}/n_\mathrm{samp}$
Dirty image	$\lvert u\rvert \le d_\mathrm{max}$	$\partial u = 2\,d_\mathrm{image}/n_\mathrm{samp}$
	$\lvert\alpha\rvert \le \theta_\mathrm{image}/2$	$\partial\alpha = \theta_\mathrm{syn}/n_\mathrm{samp}$
Dirty beam	$\lvert u'\rvert \le d_\mathrm{max}$	$\partial u' = 2\,d_\mathrm{image}/n_\mathrm{samp}$
	$\lvert\alpha'\rvert \le \theta_\mathrm{image}/2$	$\partial\alpha' = \theta_\mathrm{syn}/n_\mathrm{samp}$
	$\lvert u''\rvert \le d_\mathrm{prim}$	$\partial u'' = 2\,d_\mathrm{image}/n_\mathrm{samp}$
	$\lvert\alpha''\rvert \le \theta_\mathrm{image}/2$	$\partial\alpha'' = \theta_\mathrm{prim}/n_\mathrm{samp}$

4.2.1. The α_s sampling rate of the visibility function

When Fourier transforming the measurement Eq. (1) along the α_s axis, we derive the Ekers & Rots Eq. (15). This equation implies that $\overline{V}(u_\mathrm{p}, u_\mathrm{s})$ is bounded inside the $[-d_\mathrm{prim}, +d_\mathrm{prim}]$ spatial frequency interval along the u_s axis. As a result, the visibility function needs to be regularly resampled at a rate of only $0.5/d_\mathrm{prim}$ to satisfy the Nyquist theorem. This was first pointed out by Cornwell (1988). This sampling rate is equal to $\theta_\mathrm{prim}/2$ or $\sim\theta_\mathrm{fwhm}/2.4$. The "usual, wrong" habit of sampling at $\theta_\mathrm{fwhm}/2$ is indeed undersampling with aliasing as a consequence. Mangum et al. (2007) discuss the consequences of undersampling in-depth in the framework of single-dish imaging.

4.2.2. The U_p sampling rate of the visibility function

Now, the Fourier transform of the measurement Eq. (1) along the u_p axis gives

$$\underset{\sim}{V}\left(\alpha_\mathrm{p}, \alpha_\mathrm{s}\right) = B\left(\alpha_\mathrm{p}-\alpha_\mathrm{s}\right) I\left(\alpha_\mathrm{p}\right), \quad (53)$$

where

$$\underset{\sim}{V}\left(\alpha_\mathrm{p}, \alpha_\mathrm{s}\right) \overset{\alpha_\mathrm{p}}{\underset{u_\mathrm{p}}{\supset}} V\left(u_\mathrm{p}, \alpha_\mathrm{s}\right). \quad (54)$$

We use the tilde sign under V to denote the inverse Fourier transform of V along its first dimension. A well-known Fourier transform property implies that B has infinite support because $\overline{B}$ is bounded. The resampling rate along the u_p axis therefore depends on the properties of the product of $B(\alpha_\mathrm{p}-\alpha_\mathrm{s})$ times $I(\alpha_\mathrm{p})$ as a function of α_p. While no unique answer exists, three facts help us to find the right sampling rate: 1) B falls off relatively quickly; 2) the result depends on the spatial distribution of the sky brightness and in particular on the dynamic range in brightness needed to accurately image it; 3) the measure of $\underset{\sim}{V}(\alpha_\mathrm{p}, \alpha_\mathrm{s})$ has a limited accuracy owing to thermal noise, phase noise, and other possible systematics (e.g. pointing errors). For simplicity, we quantify the measurement accuracy by a single number, namely the maximum instrumental fidelity measured in the image plane as defined in Pety et al. (2001). There are two cases:

1. the maximum instrumental fidelity limits the dynamic range in brightness. For instance, Pety et al. (2001) showed that the

Table 4. Minimum sizes of the dirty beam images to get an image fidelity or a dynamic range greater than a given value.

Minimum fidelity or dynamic range	$\theta_{\rm alias}/\theta_{\rm fwhm}$ [a] ($f_{\rm b}=0$) [b]	($f_{\rm b}=0.0625$)	($f_{\rm b}=0.1$)
10^2	2.2	2.2	2.2
10^3	3.5	3.7	6.6
10^4	8.4	13.4	13.7
10^5	19.8	>20.0	>20.0

Notes. [(a)] The image sizes are expressed in units of the primary beam full width at half maxium. [(b)] The computation is done for 3 different ratios of the secondary-to-primary diameters (i.e. $f_{\rm b}$, the antenna blockage factors). The values are derived from the modeling of the antenna power patterns shown in Fig. 3.

fidelity of interferometric imaging at (sub)-millimeter wavelengths will be limited to a few hundred. In this case, $\tilde{V}(\alpha_{\rm p}, \alpha_{\rm s})$ aliasing can be tolerated when the amplitude of B is less than a fraction of the inverse of the maximum instrumental fidelity;

2. the maximum instrumental fidelity is much greater than the image fidelity, as can be the case at centimeter wavelengths. In this case, $\tilde{V}(\alpha_{\rm p}, \alpha_{\rm s})$ aliasing can only be tolerated when the amplitude of B is less than a fraction of the inverse of the dynamic range of the image.

The criterion derived in each case gives a typical image size ($\theta_{\rm alias}$), which can be converted into the desired $u_{\rm p}$ sampling rate. To be more quantitative, Fig. 3 models the normalized antenna power patterns of an antenna illuminated by a Gaussian beam of 12.5 dB edge taper and with a given blockage factor (ratio of the secondary-to-primary diameters). The top panel presents an ideal case without secondary miror, while the middle and bottom panels present simple models of the ALMA and PdBI antennas. The largest angular sizes at which the power patterns are less than a given value, $\mathcal{P}_0$, is a first-order estimate of $\theta_{\rm alias}/2$ to get a fidelity or dynamic range higher than $1/\mathcal{P}_0$. Table 4 gives the values of $\theta_{\rm alias}/\theta_{\rm fwhm}$ as a function of the searched fidelity or dynamic range. This condition is sufficient but not necessary. Indeed, the aliasing properties also depend on the brightness distribution of the source.

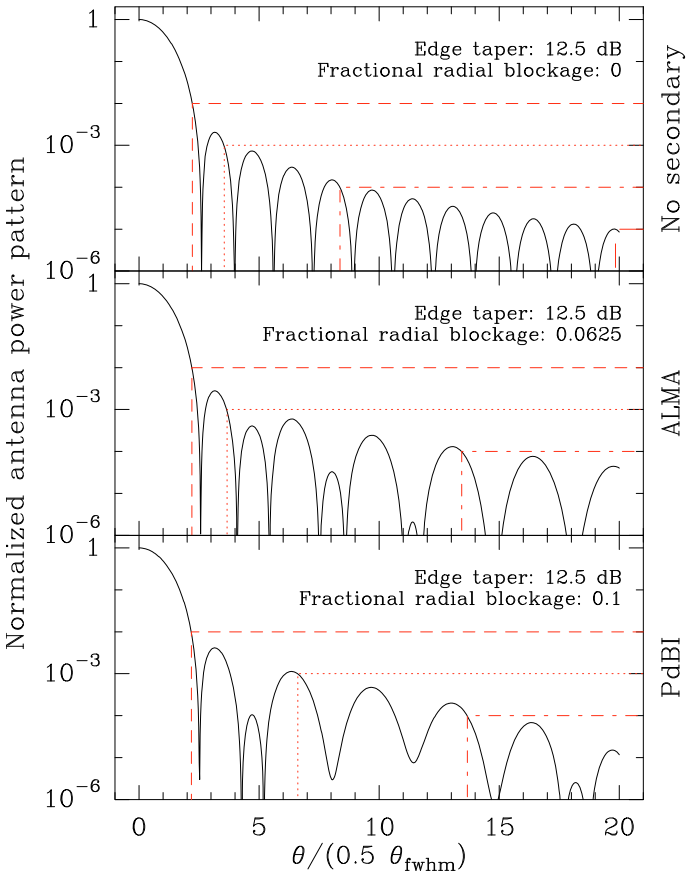

Fig. 3. Simple models of the antenna power patterns as a function of the sky angle in units of half the primary beam FWHM ($\theta_{\rm fwhm}$). In the 3 cases shown, the illumination is Gaussian with an edge taper of 12.5 dB but 3 different ratios of the secondary-to-primary diameters (i.e. $f_{\rm b}$, the antenna blockage factors) are considered (see e.g. Goldsmith 1998, Chap. 6). *The middle and bottom panels* respectively model ALMA and PdBI antennas. The red lines define the minimum angular sizes for which the antenna power pattern is less than a given fraction.

4.2.3. The u sampling rate of $\bar{\rm I}_{\rm dirty}(u)$

We have no garantee that the sky outside the targeted field of view is devoid of signal, so the only way to ensure a given dynamic range inside the targeted field of view is to choose the image size large enough so that the aliasing of potential outside sources is negligible. This means that the dirty image size must be equal to the field-of-view size plus the tolerable aliasing size

$$\theta_{\rm image} = \theta_{\rm field} + \theta_{\rm alias}. \quad (55)$$

The conjugate uv distance and associated uv sampling then are

$$d_{\rm image} = \frac{d_{\rm field}}{1+\frac{d_{\rm field}}{d_{\rm alias}}} \quad \text{and} \quad \partial u = \frac{d_{\rm image}}{n_{\rm samp}}. \quad (56)$$

4.2.4. The u' and u'' sampling rates of $\overline{D}(u',u'')$

The u'' axis must thus be sampled at the same rate as the second dimension of the definition space of $\overline{S}$, i.e., as $u_{\rm s}$. Moreover, u' has in this equation a behavior ($u' = u_{\rm p} + u''_{\rm s}$) similar to u ($=u_{\rm p}+u_{\rm s}$). It must thus have the same sampling behavior as u. This sampling rate ($\partial u' = d_{\rm image}/n_{\rm samp}$) is quite high. Some deconvolution methods (see below) allow us to relax this sampling rate.

4.3. Absence of gridding "correction"

Imaging of single-field observations goes through the following steps: 1) convolution by a gridding kernel; 2) regular resampling; 3) fast Fourier transform; and 4) gridding "correction". The so-called gridding "correction" is a division of the dirty beam and dirty image by the Fourier transform of the gridding kernel used in the initial convolution. This step is mandatory when imaging single-field observations to keep the image-plane measurement equation as a simple convolution equation (see e.g. Sramek & Schwab 1989). When imaging wide-field observations, as proposed here, the Fourier transform along the $\alpha_{\rm s}$ dimension, followed by the shift-and-average operation, freeze the convolution kernel into the dirty beam of the wide-field measurement equation. This is why the gridding "correction" step is irrelevant here.

5. Dirty beams, weighting, and deconvolution

In radioastronomy, the dirty beam is the response of the interferometer to a point source. In the wide-field synthesis framework, the response of the interferometer to a point source, D, a priori depends on the source position on the sky. $D(\alpha', \alpha'')$ can thus be interpreted as a set of dirty beams, with each dirty beam referred to by its fixed α'' sky coordinate. These simple facts raise several questions. What are the properties of the convolution kernel? Is it possible to modify these properties? How do we deconvolve the dirty image?

5.1. A set of wide-field dirty beams

With the wide-field synthesis framework proposed here, Appendix A.6 shows that

$$D(\alpha', \alpha'') = \iint_{\alpha_p \alpha_s} B(\alpha'' - \alpha' - \alpha_s)\, \Omega\left(\alpha' - \alpha_p, \alpha'' - \alpha_s\right) \Delta\left(\alpha_p, \alpha_s\right) \mathrm{d}\alpha_p \mathrm{d}\alpha_s, \quad (57)$$

where

$$\Delta\left(\alpha_p, \alpha_s\right) \overset{\alpha_p}{\underset{u_p}{\supset}} S\left(u_p, \alpha_s\right), \quad (58)$$

and

$$\Omega(\alpha', \alpha'') \overset{(\alpha', \alpha'')}{\underset{(u', u'')}{\supset}} W(u', u''). \quad (59)$$

$\Delta(\alpha_p, \alpha_s)$ is the single-field dirty beam, associated with the uv sampling at the sky coordinate α_s. And $\Omega(\alpha', \alpha'')$ will be called the image plane weighting function, while $W(u', u'')$ is the uv plane weighting function. The set of wide-field dirty beams D is then the double convolution of the image plane weighting function and the single-field dirty beams, apodized by the primary beam at the current sky position α_s.

While the shape of the single-field dirty beam is directly given by the Fourier transform of the sampling function, the shape of the wide-field dirty beam depends, directly or through Fourier transforms, on the sampling function (S), the primary beam shape (B), and the weighting function (W). Moreover, the wide-field dirty beam shape a priori varies slowly with the sky position, since it is basically constant over the primary beamwidth as stated in Sect. 4.2. It nevertheless varies, implying, for instance, a "slow" variation of the synthesized resolution over the whole field of view.

While the single-field and wide-field dirty beam expressions seem very different, they share the same property of expressing the way the interferometer is used to synthesize a telescope of larger diameter in the image plane. In other words, the sampling function for single-field imaging and $\underline{\overline{D}}$ for wide-field imaging express the sensitivity of the interferometer to a given spatial frequency. These uv space functions are called the transfer functions of the interferometer (Thompson et al. 1986, Chap. 5). Modifying the transfer function has a direct impact on the measured quantity. Once the interferometer is designed and the observations are done, the only way to change this transfer function is data weighting.

An ideal set of wide-field dirty beams, $D(\alpha', \alpha'')$, would have the following properties. All the wide-field dirty beams should be identical (i.e., independent of the α'' sky coordinate) and equal to a narrow Gaussian (its FWHM giving the image resolution). *This would give the product of a wide Gaussian of u' by a Dirac function of u'', as the ideal wide-field transfer function, $\underline{\overline{D}}(u', u'')$.*

5.2. Dirty beam shapes and weighting

When imaging single-field observations, giving a multiplicative weight to each visibility sample is an easy way to modify the shape of the dirty beam and thus the properties of the dirty and deconvolved images. Natural weighting (which maximizes signal-to-noise ratio), robust weighting (which maximizes resolution), and tapering (which enhances brightness sensitivity at the cost of a lower resolution) are the most popular weighting techniques (see e.g. Sramek & Schwab 1989).

In the case of wide-field synthesis, a multiplicative weight can also be attributed to each visibility sample before any processing. However, the weighting is also at the heart of the wide-field synthesis because it is an essential part of the shift-and-average operation. No constraint has been set on the weighting function up to this point, which indicates that the weighting function (W) gives us a degree of freedom in the imaging process. We look in turn at both kinds of weighting. In both cases, an obvious issue is the definition of the optimum weighting functions. As in the case of single-field imaging, there is no single answer to this question. It depends on the conditions of the observation and on the imaging goals.

5.2.1. Weighting the measured visibilities

Natural weighting consists of slightly changing the definition of the sampling function. It is now set to a normalized natural weight where there is a measure and 0 elsewhere. The natural weight is usually defined as the inverse of the thermal noise variance, computed from the radiometric equation, i.e., from the system temperature, the frequency resolution, and the integration time. Using this weighting scheme before computing the first Fourier transform along the α_s sky dimension makes sense because the observing conditions (and thus the noise) vary from visibility to visibility.

We propose to generalize this weighting scheme to other observing conditions than just the system noise. Indeed, critical limitations of interferometric wide-field imaging are pointing errors, tracking errors, atmospheric phase noise (in the (sub)-millimeter domain), etc. While techniques exist for coping with these problems (e.g., water vapor radiometer, direction-dependent gains: Bhatnagar et al. 2008), they are not perfect. The usual way to deal with the remaining problems is to flag the source data based on a priori knowledge of the problems, e.g., pointing measurement, tracking errors, rms phase noise on calibrators, etc. However, flagging involves the definition of thresholds, while reality is never black and white. It can thus be asked whether some weighting scheme could be devised to minimize the effect of pointing errors, tracking errors or phase noise on the resulting image. We propose to modulate natural weighting based on the a priori knowledge of the observing conditions.

5.2.2. Weighting the synthesized visibilities

Robust weighting or tapering the *measured* visibilities do not make sense in wide-field synthesis because the dirty image is made from the synthesized visibilities after the first Fourier transform along the α_s sky dimension. A weighting function W then appears naturally as part of the shift-and-average operator. Its optimum value depends on the properties of the measured sampling function. Here are a few examples.

Infinite, continuous sampling. This is the ideal case studied in Sect. 3.1. Knowing that the Ekers & Rots Eq. (15) links the

quantity we want to estimate, i.e., $\overline{I}$, to many noisy[5] measurements, $\overline{V}(u_\mathrm{p}, u_\mathrm{s})$, via a product by $\overline{B}$ (assumed to be perfectly defined), we can invoke a simple least-squares argument (see e.g. Bevington & Robinson 2003) to demonstrate that the optimum weighting function is

$$W\left(u_\mathrm{p}, u-u_\mathrm{p}\right) = \frac{w\left(u_\mathrm{p}, u-u_\mathrm{p}\right)\,\overline{B}\left(u_\mathrm{p}-u\right)}{\int_{u_\mathrm{p}} w\left(u_\mathrm{p}, u-u_\mathrm{p}\right)\,\overline{B}^2\left(u_\mathrm{p}-u\right)\,\mathrm{d}u_\mathrm{p}}, \qquad (60)$$

with $w(u_\mathrm{p}, u_\mathrm{s})$ the weight computed from the inverse of the noise variance of $\overline{V}(u_\mathrm{p}, u_\mathrm{s})$. Using Eq. (20), it is then easy to demonstrate that $\overline{D}(u) = 1$, and then $I_\mathrm{dirty}(\alpha) = I(\alpha)$. The dirty image is a direct estimate of the sky brightness; i.e., deconvolution is superfluous.

Complete sampling. The signal is Nyquist-sampled, but it has a finite support in both the *uv* and sky planes, implying a finite synthesized resolution and a finite field of view. In contrast to the previous case, this one may have practical applications, e.g., observations done with ALMA in its compact configuration. Indeed, the large number of independent baselines coupled to the design of the ALMA compact configuration ensure a complete, almost Gaussian, sampling for each snapshot. In this case, the best choice may be to choose the weighting function so that all the dirty beams are identical to the same Gaussian function. In this case, the deconvolution would also be superfluous.

Incomplete sampling. This is the more general case studied in Sect. 3.2. The signal not only has a finite support but it also is undersampled (at least in the *uv* plane). The deconvolution is mandatory. The choice of the weighting function thus will depend on imaging goals.

If the user needs the best signal-to-noise ratio, some kind of natural weighting will be needed. It is tempting to use Eq. (60) as a natural weighting scheme. However, the main condition for derivation of this weighting function, i.e., the Ekers & Rots Eq. (15), is not valid anymore, as the noisy measured quantity $(\overline{SV})$ is now linked to the quantity we want to estimate $(\overline{I})$ by a local average (see Eq. (31)). This is why it was more appropriate to try to get a Gaussian dirty beam shape in the complete sampling case.

If the signal-to-noise ratio is high enough, the user has two choices. Either he/she wants to maximize angular resolution power and needs some kind of robust weighting, or he/she wants to get the more homogeneous dirty beam shape over the whole field of view. This requirement cannot always be fully met. The Ekers & Rots scheme enables us to recover unmeasured spatial frequencies only in regions near to measured ones, because $\overline{B}$ has a finite support.

5.3. Deconvolution

Writing the image-plane measurement equation in a convolution-like way is very interesting because all the deconvolution methods developed in the past 30 years are optimized to treat deconvolution problems (see e.g. Högbom 1974; Clark 1980; Schwab 1984; Narayan & Nityananda 1986). For instance, it should be possible to deconvolve Eq. (23) with just slight modifications to the standard CLEAN algorithms. Indeed, Eq. (23) can be interpreted as the convolution of the sky brightness by a set of dirty beams, so that the only change, once a CLEAN component is found, would be the need to find the right dirty beam in this set in order to remove the CLEAN component from the residual image.

Following Clark (1980) and Schwab (1984), most algorithms today deconvolve in alternate minor and major cycles. During a minor cycle, a solution of the deconvolution is sought with a simplified (hence approximate) dirty beam. During a major cycle, the current solution is subtracted either from the original dirty image using the exact dirty beam or from the measured visibilities, implying a new gridding step. In both cases, the major cycles result in greater accuracy. The iteration of minor and major cycles enables one to find an accurate solution with better computing efficiency. In our case, the approximate dirty beams used in the minor cycle could be 1) dirty beams of a much smaller size than the image; or 2) a reduced set of dirty beams (i.e., guessing that the typical variation sizescale of the dirty beams with the sky coordinate is much larger than the primary beamwidth); or 3) both simultaneously. The model would be subtracted from the original visibilities before re-imaging at each major cycle. The trade-off is between the memory space needed to store a full set of accurate dirty beams and the time needed to image the data at each major step. Some quantitative analysis is needed to know how far the dirty beams can be approximated in the minor cycle.

It is worth noting that the accuracy of the deconvolved image will be affected by edge effects. Indeed, the dirty brightness at the edges of the observed field of view is attenuated by the primary beam shape. When deconvolving these edges, the deconvolved brightness will be less precise, because the primary beam has a low amplitude there. This only affects the edges, because inside the field of view, every sky position should be observed a fraction of the time with a primary beam amplitude between 0.5 and 1. This edge effect is nevertheless expected to be much less troublesome than the inhomogeneous noise level resulting from standard mosaicking imaging (see Sect. 7.1).

6. Short spacings

6.1. The missing flux problem

Radio interferometers are bandpass instruments; i.e., they filter out not only the spacings longer than the largest baseline length but also the spacings shorter than the shortest baseline length, which is typically comparable to the diameter of the interferometer antennas. In particular, radio interferometers do *not* measure the visibility at the center of the *uv* plane (the so-called "zero spacing"), which is the total flux of the source in the measured field of view.

The lack of short baselines or *short spacings* has strong effects as soon as the size of the source is more than about 1/3 to 1/2 of the interferometer primary beam. Indeed, when the size of the source is small compared to the primary beam of the interferometer, the deconvolution algorithms use, in one way or another, the information of the flux at the lowest *measured* spatial frequencies for extrapolating the total flux of the source. The extreme case is a point source at the phase center for which the amplitude of all the visibilities is constant and equal to the total flux of the source: extrapolation is then exact. However, the larger the size of the source, the worse the extrapolation, which then underestimates the total source flux. This is the well-known problem of the missing flux that observers sometimes note when comparing a source flux measured by a mm interferometer with the flux observed with a single-dish antenna.

[5] The noise is assumed to have a Gaussian probability distribution function.

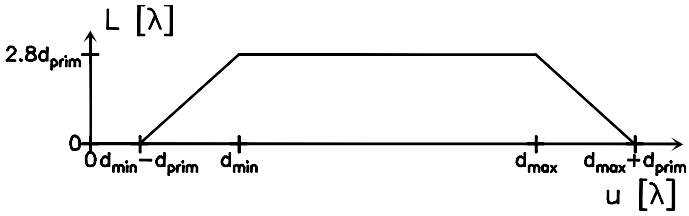

Fig. 4. Length of the averaging linepaths displayed as black lines in panel c.2) of Fig. 2, as a function of the spatial scale in the final, wide-field *uv* plane. In the case of a continuous sampling of u_p between d_{min} and d_{max}, these quantities can be interpreted as the number of measures that contribute to the estimate of $\overline{I}(u)$.

Wide-field synthesis does *not* recover the full short spacings. Let us assume that the visibility function is continuously sampled from d_{min} to d_{max}, with $d_{min} \sim 1.5\, d_{prim}$. The length of the averaging linepath[6]), $L(u)$, can be interpreted as the number of measures that contribute to the estimation of $\overline{I}(u)$. Figure 4 shows the variations of $L(u)$ function when starting from a visibility function continuously defined in the $[d_{min}, d_{max}]$ interval along the u_p dimension. We can expect to recover $\overline{I}(u)$ only inside the $[d_{min} - d_{prim}, d_{max} + d_{prim}]$ interval. In particular, information on short spacings lower than $d_{min} - d_{prim}$ (e.g. the crucial zero spacing) cannot be recovered when using a homegeneous interferometer, and the short spacings in the interval $[d_{min} - d_{prim}, d_{min}]$ are recovered with increasing accuracy from $d_{min} - d_{prim}$ to d_{min}. Both effects imply the need for complementary instruments to accurately measure the missing short-spacings.

6.2. Usual hardware and software solutions

To derive the correct result for larger source sizes, it is necessary to complement the interferometer data with additional data, which contain the missing short-spacing information. The IRAM-30 m single-dish telescope is used to complement the Plateau de Bure Interferometer. Short-spacing information can also be in part recovered with a secondary array of smaller antennas and shorter baselines (e.g. the CARMA interferometer). In the ALMA project, the short-spacing information will be derived by a combination of four 12 m-single-dish antennas and an interferometer of 12 antennas of 7 m called ACA (Atacama Compact Array).

From the software point-of-view, two main families of algorithms exist in the standard processing of mosaics. Either the short-spacing information is combined on the deconvolved image (i.e., the interferometer data is imaged and deconvolved separately) through a *hybridization* in the Fourier plane (see e.g. Pety et al. 2001), or the long and short-spacing information is imaged and/or deconvolved jointly. In this category, we find the *pseudo-visibility* technique, which produces interferometric-like visibilities from single-dish maps (see e.g. Pety et al. 2001; Rodríguez-Fernández et al. 2008, and references therein), and the multi-resolution deconvolution algorithms, which work on images containing different spatial frequency ranges.

In the next two sections, we show how wide-field synthesis naturally processes the short-spacing information either from single-dish or from heterogeneous arrays.

[6] The notion of averaging linepath has been introduced in Sect. 3.1 (see in particular Eq. (16)).

6.3. Processing short spacings from single-dish measurements

The single-dish measurement equation can be written as

$$I_{sd}(\alpha) = S_{sd}(\alpha) \int_{\alpha'} B_{sd}(\alpha' - \alpha)\, I(\alpha')\, d\alpha', \tag{61}$$

where I_{sd} is the measured single-dish intensity, S_{sd} the single-dish sampling function, and B_{sd} the single-dish antenna power pattern. As already stated in the introduction, the above integral is identical to the ideal measurement equation of interferometric wide-field imaging taken in $u_p = 0$. If we define a single-dish visibility function as

$$V_{sd}\left(u_p = 0, \alpha\right) \equiv \int_{\alpha'} B_{sd}(\alpha' - \alpha)\, I(\alpha')\, d\alpha', \tag{62}$$

we can thus write the measured single-dish intensity as

$$I_{sd}(\alpha) = S_{sd}(\alpha)\; V_{sd}\left(u_p = 0, \alpha\right). \tag{63}$$

The recognition that the single-dish measurement equation is a particular case of the interferometric wide-field measurement equation opens the way to treating both the single-dish and interferometric data sets through exactly the same processing steps. We just have to define a hybrid sampling function, S_{hyb}, as

$$S_{hyb}\left(u_p \neq 0, \alpha\right) = S\left(u_p, \alpha\right) \tag{64}$$

$$S_{hyb}\left(u_p = 0, \alpha\right) = S_{sd}(\alpha), \tag{65}$$

the Fourier transform of the hybrid primary beam, $\overline{B}_{hyb}$, as

$$\overline{B}_{hyb}\left(u_p \neq 0, u'\right) = \overline{B}\left(u_p - u'\right) \tag{66}$$

$$\overline{B}_{hyb}\left(u_p = 0, u'\right) = \overline{B}_{sd}(-u'), \tag{67}$$

and a hybrid weighting function, W_{hyb}, as

$$W_{hyb}\left(u_p \neq 0, u' + u'' - u_p\right) = W_{hyb}\left(u_p, u' + u'' - u_p\right), \tag{68}$$

$$W_{hyb}\left(u_p = 0, u' + u''\right) = W_{sd}(u' + u''). \tag{69}$$

All the processing steps described in the previous sections (including a potential gridding step of single-dish, on-the-fly data) can then be directly applied to the hybrid data set. Using the wide-field synthesis formalism, we can easily write

$$\overline{I}_{hyb}(u) = \int_{u'} \underline{\overline{D}}_{hyb}(u', u - u')\, \overline{I}(u')\, du', \tag{70}$$

with

$$\overline{I}_{hyb}(u) = \overline{I}_{dirty}(u) + W_{sd}(u)\, \overline{I}_{sd}(u) \tag{71}$$

and

$$\underline{\overline{D}}_{hyb}(u', u'') = \underline{\overline{D}}(u', u'') + W_{sd}(u' + u'')\, \overline{S}_{sd}(u'')\, \overline{B}_{sd}(-u'). \tag{72}$$

We thus see that $\overline{I}_{hyb}$ is a linear combination of the information measured by the single-dish ($\overline{I}_{sd}$) and by the interferometer ($\overline{I}_{dirty}$). There, $W_{sd}(u)$ plays a particular role for two reasons. First, its dependency on the spatial frequency (u) enables us to filter out the highest spatial frequencies that are measured by the single-dish antenna with low accuracy. Second, it is well-known that the relative weight of the single-dish to interferometric data is a critical parameter in the processing of the short spacings from single-dish data (see e.g. Rodríguez-Fernández et al. 2008).

Table 5. Definition of the symbols used to expose the processing of the short spacings.

Symbol	& Definition	Plane(s)
$I_{\rm sd}$	Measured single-dish intensity	sky
$B_{\rm sd}$	Single-dish antenna power pattern	sky
$S_{\rm sd}$	Single-dish sampling function	sky
$V_{\rm sd}$	Single-dish visibility function	sky
$W_{\rm sd}$	Single-dish uv-plane weighting function	uv
b_i	Voltage pattern of antenna i	sky
B_{ij}	Power pattern of antenna i and j $(=b_i\, b_j^\star)$	sky
V_{ij}	Visibility between antenna i and j	uv & sky
$I_{\rm hyb}$	Hybrid dirty image	sky
$B_{\rm hyb}$	Hybrid antenna power pattern	sky
$S_{\rm hyb}$	Hybrid sampling function	uv & sky
$W_{\rm hyb}$	Hybrid uv-plane weighting function	uv & uv
$D_{\rm hyb}$	Set of hybrid dirty beams	sky & sky

Notes. This table uses similar conventions as Table 1. The top part defines symbols related to single-dish measurements. The middle part defines symbols related to heterogeneous-array measurements. The bottom part defines hybrid symbols, which results from combinations of single-dish and heterogeneous-array measurements.

This relative weight is a free parameter within the restrictions set by the noise level (i.e., we want the single-dish data to bring information and not just noise to the interferometric data), and a criterion must therefore be defined to adjust it to an optimal value. We refer the reader to the discussion of Sect. 5, which also applies here.

6.4. Processing short spacings from heterogeneous arrays

A heterogeneous array is an interferometer composed with antennas of different diameters. ALMA and CARMA are two such examples. The measurement equation for a heterogeneous array is

$$V_{ij}\left(u_{\rm p},\alpha_{\rm s}\right) = \int_{\alpha_{\rm p}} b_i\left(\alpha_{\rm p}-\alpha_{\rm s}\right) b_j^\star\left(\alpha_{\rm p}-\alpha_{\rm s}\right) I\left(\alpha_{\rm p}\right)\, {\rm e}^{-{\rm i}2\pi\alpha_{\rm p}u_{\rm p}}\, {\rm d}\alpha_{\rm p}, \quad (73)$$

where b_i and b_j are the voltage reception patterns of the antenna pair that forms the ij baseline and the asterisk denotes the complex conjugate (Thompson et al. 1986, Chap. 3). The formalism developed in the previous sections holds as long as we redefine

$$B_{ij}\left(\alpha\right) \equiv b_i\left(\alpha\right)\, b_j^\star\left(\alpha\right). \quad (74)$$

A simple application of the correlation theorem implies that

$$\overline{B}_{ij}\left(u\right) = \int_{u'} \overline{b}_i\left(u+u'\right)\, \overline{b}_j\left(u'\right)\, {\rm d}u'. \quad (75)$$

The use of the baseline indices ij must be generalized throughout the equations because the knowledge of the antenna type must be attached to each individual data point (visibility). As a result, the wide-field synthesis formalism can be easily adapted to heterogeneous arrays at the price of additional bookkeeping.

6.5. Two textbook cases: IRAM-30 m + PdBI and ALMA + ACA

Figure 5 sketches why wide-field synthesis naturally handles the short spacings in two textbook cases. In the ideal case, the Fourier transform along the $\alpha_{\rm s}$ dimension produces visibilities, which are related to the wide-field spatial frequencies of the source brightness weighted by the transfer function of the interferometer. In this sense, Fig. 5 displays the natural weighting of the synthesized wide-field visibilities at the position of each measured visibility. Handling visibilities from antenna of different sizes just implies that the natural weighting function of the synthesized visibilities will have a different shape.

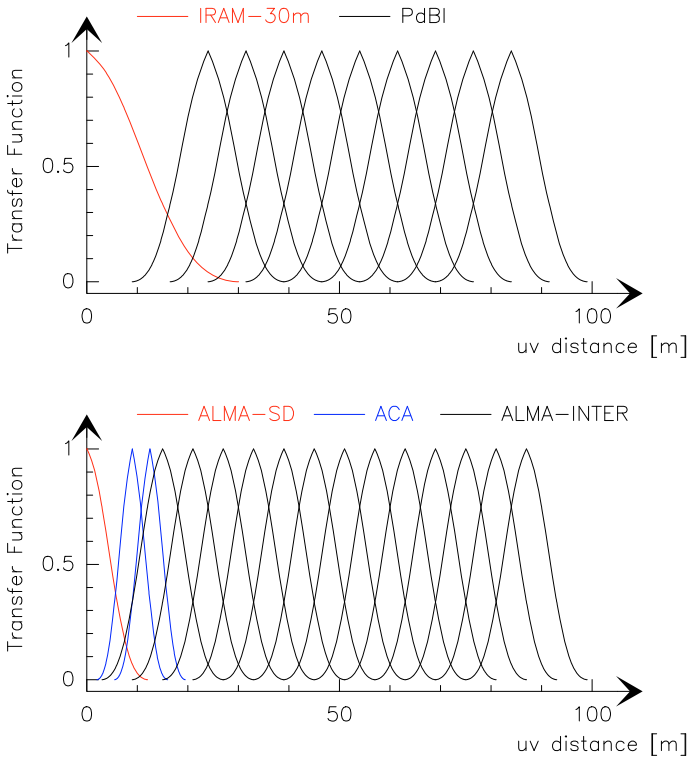

Fig. 5. Sketches of the natural weighting of the synthesized wide-field visibilities. Each measured spatial frequency will produce wide-field spatial frequencies apodized by the transfer function ($\overline{B}$) centered on the measured spatial frequency. The used transfer function depends on the telescopes used, explaining why wide-synthesis naturally handles the short spacing either from a single-dish antenna or from a heterogeneous array. The synthesized visibilities in the overlapping regions will then be averaged. Two textbook examples are illustrated: 1) the combination of data from the IRAM-30 m single-dish (red transfer function) and from the Plateau de Bure Interferometer (black transfer functions) at the top; and 2) the combination of data from ALMA 12 m-antennas used either in single-dish mode (red transfer function), in interferometric mode (black transfer functions) and of data from the ACA 7 m-antennas (blue transfer functions) at the bottom. The minimum uv distances measured by each interferometer were set from the minimum possible distance between antennas (24 m for PdBI, 15 m for ALMA and 9 m for ACA).

The top panel of Fig. 5 displays how the IRAM-30 m single-dish is used to complement the Plateau de Bure interferometer visibilities. The bottom panel displays how ACA is used to produce the short spacing information for ALMA. The four 12 m-antennas will provide the single-dish information, while the 12 additional 7 m-antennas will form with ALMA a heterogeneous array. In the first design, ACA and ALMA form two independent interferometers; i.e., they are not cross-correlated. The single-dish antennas, ACA and ALMA, thus appear as three different instruments. It is thus possible to decompose the hybrid set of wide-field dirty beams obtained by processing the 3 sets of data together in 3 different sets of dirty beams

$$\underline{\overline{D}}_{\rm hyb}\left(u',u''\right) = \underline{\overline{D}}_{\rm 12\,m}\left(u',u''\right) + \underline{\overline{D}}_{\rm 7\,m}\left(u',u''\right) + \underline{\overline{D}}_{\rm sd}\left(u',u''\right), \quad (76)$$

with

$$\overline{D}_{\rm hyb}\left(u',u''\right) \equiv \int_{u_{\rm p}} W_{\rm hyb}\left(u_{\rm p},u'+u''-u_{\rm p}\right)\,\overline{S}_{\rm hyb}\left(u_{\rm p},u''\right)\,\overline{B}_{\rm hyb}\left(u_{\rm p},u'\right)\,{\rm d}u_{\rm p}. \quad (77)$$

For a multiplying interferometer,

$$\forall\left|u_{\rm p}\right| < d_{\rm prim}, \quad S\left(u_{\rm p},\alpha_{\rm s}\right) = 0 \quad \text{and} \quad \overline{S}\left(u_{\rm p},u_{\rm s}\right) = 0. \quad (78)$$

This implies that $\overline{D}_{\rm sd}$ contributes at $u_{\rm p} = 0$ in the sum over $u_{\rm p}$ in Eq. (77), $\overline{D}_{7\ {\rm m}}$ contributes for 9 m $< u_{\rm p} \lesssim$ 40 m and $\overline{D}_{12\ {\rm m}}(u', u'')$ contributes for 15 m $< u_{\rm p} <$ 150 m in the most compact configuration of ALMA.

7. Comparison with standard nonlinear mosaicking

7.1. Mosaicking in a nutshell

Several excellent descriptions of the mosaicking imaging and deconvolution algorithms can be found (see e.g. Cornwell 1988; Cornwell et al. 1993; Sault et al. 1996b). Here, we summarize the approach implemented in the GILDAS/MAPPING software used to image and deconvolve the data from the Plateau de Bure Interferometer. This approach is based on original ideas by F. Viallefond in the early 90s (Gueth et al. 1995).

The basic ideas of nonlinear mosaicking are 1) imaging the different fields of the mosaic independently; 2) linearly adding the single-field dirty images into a dirty mosaic; and 3) jointly deconvolving the dirty mosaic.

7.1.1. Single-field imaging

For simplicity, we skip the gridding convolution in the following equations because the gridding step does not change the nature of the equations. Imaging the fields individually means that we will work at constant $\alpha_{\rm s}$. We first define the single-field dirty image of the $\alpha_{\rm s}$-field as

$$I_{\rm sfd}\left(\alpha_{\rm p},\alpha_{\rm s}\right) \overset{\alpha_{\rm p}}{\underset{u_{\rm p}}{\supset}} \overline{I}_{\rm sfd}\left(u_{\rm p},\alpha_{\rm s}\right), \quad (79)$$

where the Fourier transform of the single-field dirty image is the product of the sampling function $S(u_{\rm p}, \alpha_{\rm s})$ and the visibility function $V(u_{\rm p}, \alpha_{\rm s})$:

$$\overline{I}_{\rm sfd}\left(u_{\rm p},\alpha_{\rm s}\right) \equiv S\,V\left(u_{\rm p},\alpha_{\rm s}\right). \quad (80)$$

From the previous equations, it is easily demonstrated that

$$I_{\rm sfd}\left(\alpha_{\rm p},\alpha_{\rm s}\right) = \int_{\alpha'_{\rm p}} \Delta\left(\alpha_{\rm p}-\alpha'_{\rm p},\alpha_{\rm s}\right)\left[B\left(\alpha'_{\rm p}-\alpha_{\rm s}\right)I\left(\alpha'_{\rm p}\right)\right]{\rm d}\alpha'_{\rm p}, \quad (81)$$

where the single-field dirty beam is defined as

$$\Delta\left(\alpha_{\rm p},\alpha_{\rm s}\right) \overset{\alpha_{\rm p}}{\underset{u_{\rm p}}{\supset}} S\left(u_{\rm p},\alpha_{\rm s}\right). \quad (82)$$

We can rewrite the previous equation as

$$I^{\alpha_{\rm s}}_{\rm sfd}\left(\alpha_{\rm p}\right) = \left\{\Delta^{\alpha_{\rm s}} \star \left(B^{\alpha_{\rm s}} I\right)\right\}\left(\alpha_{\rm p}\right), \quad (83)$$

meaning that the single-field dirty images can be written as a local convolution of $B^{\alpha_{\rm s}} I$ and $\Delta^{\alpha_{\rm s}}$, the single-field dirty beam associated to the currently imaged field.

7.1.2. Mosaicking the dirty images

In GILDAS/MAPPING[7], the single-field dirty images are formed on the same grid (in particular the same pixel size and the same image size covering about twice the mosaic field of view). These single-field dirty images are then linearly averaged as

$$I_{\rm mos}\left(\alpha_{\rm p}\right) \equiv \int_{\alpha_{\rm s}} \Omega_{\rm mos}\left(\alpha_{\rm p},\alpha_{\rm s}\right)\,I_{\rm sfd}\left(\alpha_{\rm p},\alpha_{\rm s}\right)\,{\rm d}\alpha_{\rm s}, \quad (84)$$

where

$$\Omega_{\rm mos}\left(\alpha_{\rm p},\alpha_{\rm s}\right) \equiv \frac{w\left(\alpha_{\rm s}\right)\,B\left(\alpha_{\rm p}-\alpha_{\rm s}\right)}{\int_{\alpha_{\rm s}} w\left(\alpha_{\rm s}\right)\,B^2\left(\alpha_{\rm p}-\alpha_{\rm s}\right)\,{\rm d}\alpha_{\rm s}} \quad (85)$$

and $w(\alpha_{\rm s})$ is the sky plane weighting function, i.e.,

$$w\left(\alpha_{\rm s}\right) = \sum_i \delta\left(\alpha_{\rm s}-\alpha_i\right)\frac{1}{\sigma_i^2}\cdot \quad (86)$$

In the previous equation, the α_i are the positions of each sky-plane measurement, and σ_i is the rms noise associated with $I^{\alpha_i}_{\rm sfd}$. Cornwell et al. (1993) demonstrates that the noise in the mosaic image naturally varies across the field as

$$N_{\rm mos}\left(\alpha_{\rm p}\right) = \frac{1}{\sqrt{\int_{\alpha_{\rm s}} w\left(\alpha_{\rm s}\right)\,B^2\left(\alpha_{\rm p}-\alpha_{\rm s}\right)\,{\rm d}\alpha_{\rm s}}}\cdot \quad (87)$$

In particular, it rises sharply at the edges of the mosaic.

7.1.3. Joint deconvolution

Standard algorithms of single-field deconvolution must be adapted to the mosaicking case because both the dirty beam and the noise vary across the mosaic field of view. We describe here the adaptations made in GILDAS/MAPPING of the simplest CLEAN deconvolution method, described in Högbom (1974). Adaptations of more evolved CLEAN deconvolution methods are also implemented following the same basic rules.

1. We first initialize the residual and signal-to-noise maps from the dirty and noise maps

$$R_0\left(\alpha_{\rm p}\right) = I_{\rm mos}\left(\alpha_{\rm p}\right) \quad (88)$$

and

$${\rm SNR}_0\left(\alpha_{\rm p}\right) = \frac{I_{\rm mos}\left(\alpha_{\rm p}\right)}{N_{\rm mos}\left(\alpha_{\rm p}\right)}\cdot \quad (89)$$

2. The kth CLEAN component is sought on the ${\rm SNR}_{k-1}$ map instead of the R_{k-1} map to ensure that noise peaks at the edges of the mosaic are not confused with the true signal of the same magnitude.
3. Using that the kth CLEAN component is a point source of intensity I_k at position α_k, the residual and signal-to-noise maps are then upgraded as follows:

$$R_k\left(\alpha_{\rm p}\right) = R_{k-1}\left(\alpha_{\rm p}\right) - \gamma I_k \int_{\alpha_{\rm s}} \Omega_{\rm mos}\left(\alpha_{\rm p},\alpha_{\rm s}\right)\,\Delta\left(\alpha_{\rm p}-\alpha_k,\alpha_{\rm s}\right)\,B\left(\alpha_k-\alpha_{\rm s}\right)\,{\rm d}\alpha_{\rm s}, \quad (90)$$

[7] See http://www.iram.fr/IRAMFR/GILDAS for more information about the GILDAS software.

and

$$\mathrm{SNR}_k\left(\alpha_\mathrm{p}\right) = \frac{R_k\left(\alpha_\mathrm{p}\right)}{N_\mathrm{mos}\left(\alpha_\mathrm{p}\right)}\,. \tag{91}$$

Here $\gamma(\sim 0.2)$ is the usual loop gain that ensures convergence of the CLEAN algorithms.

4. Steps 2 and 3 are iterated as long as the stopping criterion is not met.

7.1.4. Wide-field measurement equation

To help the comparison between mosaicking and wide-field synthesis, we now go one step further than is usually done in the description of mosaicking; i.e., we write the image-plane measurement equation as a wide-field measurement equation of the same kind as Eq. (23). Substituting Eq. (81) into Eq. (84) and reordering the terms after inverting the order of the sum over α_s and α_p, one obtains

$$I_\mathrm{mos}\left(\alpha_\mathrm{p}\right) = \int_{\alpha'_\mathrm{p}} D_\mathrm{mos}\left(\alpha_\mathrm{p} - \alpha'_\mathrm{p}, \alpha_\mathrm{p}\right) I\left(\alpha'_\mathrm{p}\right) \mathrm{d}\alpha'_\mathrm{p}, \tag{92}$$

with

$$D_\mathrm{mos}\left(\alpha', \alpha''\right) = \int_{\alpha_\mathrm{s}} B\left(\alpha'' - \alpha' - \alpha_\mathrm{s}\right)\, \Omega_\mathrm{mos}\left(\alpha'', \alpha_\mathrm{s}\right)\, \Delta\left(\alpha', \alpha_\mathrm{s}\right)\, \mathrm{d}\alpha_\mathrm{s}. \tag{93}$$

Taking the inverse Fourier transforms of D_mos, we get the mosaicking transfer function

$$\overline{D}_\mathrm{mos}\left(u', u - u'\right) = \iint_{u_\mathrm{p} u_\mathrm{s}} W_\mathrm{mos}\left(u - u_\mathrm{p}, u_\mathrm{s} - u'\right) \overline{S}\left(u_\mathrm{p}, u_\mathrm{p} - u_\mathrm{s}\right) \overline{B}\left(u_\mathrm{p} - u'\right) \mathrm{d}u_\mathrm{p} \mathrm{d}u_\mathrm{s}, \tag{94}$$

with

$$\Omega_\mathrm{mos}\left(\alpha', \alpha''\right) \overset{(\alpha', \alpha'')}{\underset{(u', u'')}{\supset}} W_\mathrm{mos}\left(u', u''\right). \tag{95}$$

7.2. Comparison

While both mosaicking and wide-field synthesis produce image-plane measurement equations of the same kind (see Eqs. (23) and (92)), the comparison of the dirty beams (Eqs. (57) and (93)) and of the transfer functions (Eqs. (35) and (94)) immediately shows the different dependencies on the primary beams (B), the single-field dirty beams (Δ), the image-plane weighting functions (Ω), and their respective Fourier transforms ($\overline{B}$, $\overline{S}$ and W). This means that mosaicking is not mathematically equivalent to wide-field synthesis, though both methods recover the sky brightness. These differences come directly from the differences in the processing. If we momentarily forget the gridding steps, mosaicking starts with a Fourier transform along the u_p dimension of the visibility function, and most of the processing thus happens in the sky plane, while wide-field synthesis starts with a Fourier transform along the α_s dimension, and most of the processing thus happens in the uv plane.

Moreover, both methods are irreducible to each other. Wide-field synthesis gives a more complex dirty beam formulation in the image plane, which could give the impression that it is a generalization of mosaicking. Indeed, the wide-field image-plane weighting function can be chosen as the product of a Dirac function of α' times a function ω of α'',

$$\text{i.e.,}\quad \Omega\left(\alpha', \alpha''\right) = \delta(\alpha')\, \omega\left(\alpha''\right). \tag{96}$$

This implies a wide-field uv-plane weighting function independent of u'; i.e., $W(u', u'') = \overline{\omega}(u'')$. This choice is a clear limitation because it enables us to influence the transfer function only locally (around each measured u_p spatial frequency), while weighting is generally intended to globally influence the transfer function (see Sect. 5). Eitherway, in this case, the wide-field dirty beam can easily be simplified to

$$D\left(\alpha', \alpha''\right) = \int_{\alpha_\mathrm{s}} B\left(\alpha'' - \alpha' - \alpha_\mathrm{s}\right) \omega\left(\alpha'' - \alpha_\mathrm{s}\right) \Delta\left(\alpha', \alpha_\mathrm{s}\right)\, \mathrm{d}\alpha_\mathrm{s}. \tag{97}$$

While this simplified formulation of the wide-field dirty beam is closer to the mosaicking formulation, they still differ in a major way: $\omega(\alpha'' - \alpha_\mathrm{s})$ is a shift-invariant function contrary to $\Omega_\mathrm{mos}(\alpha'', \alpha_\mathrm{s})$. This is the shift-dependent property of $\Omega_\mathrm{mos}(\alpha'', \alpha_\mathrm{s})$, which implies the additional complexity (integral over u_s in addition to the integral over u_p) of the mosaicking transfer function (Eq. (94)) over the wide-field one (Eq. (35)).

One main difference between the two processing methods is that standard mosaicking prescribes a precise weighting function, while we argue that the wide-field weighting function should be defined according to the context (see Sect. 5). Another important difference is the treatment of the short spacings, which are naturally processed in the wide-field synthesis methods, but which needs a very specific treatment in mosaicking (see Sect. 6 and references therein). Finally, while mosaicking implies a gridding only of u_p dimension of the measured visibilities, wide-field synthesis naturally requires a gridding of both the u_p and α_s dimensions. As the Nyquist sampling along the α_s dimension is only $0.5/d_\mathrm{prim}$, the gridding of the sky plane can result in a large reduction of the data storage space and cpu processing cost when processing on-the-fly and/or multi-beam observations.

8. Summary

Interferometric wide-field imaging implies scanning the sky in one way or another (e.g. stop-and-go mosaicking, on-the-fly scanning, sampling of the focal plane by multi-beams). This produces sampled visibilities SV, which depends both on the uv-plane and sky coordinates (e.g., u_p and α_s).

Based on a basic idea by Ekers & Rots (1979), we proposed a new way to image the interferometric wide-field sampled visibilities: $SV(u_\mathrm{p}, \alpha_\mathrm{s})$. After gridding the measured visibilities both in the uv and sky planes, the gridded visibilities $SV^\mathcal{G}$ are Fourier-transformed along the α_s sky dimension, yielding synthesized visibilities $\overline{SV}^\mathcal{G}$ sampled on a uv grid whose cell size is related to the total field of view; i.e., it is much finer than the diameter of the interferometer antennas. We thus proposed calling this processing scheme "wide-field synthesis".

The Fourier transform is performed for each constant u_p value. As many independent estimates of the uv plane are produced as independent values of u_p measured. A shift-and-average operator is then used to build a final, wide-field uv plane, which translates into a wide-field dirty image after inverse Fourier transform, i.e.,

$$\overline{I}^\mathcal{G}_\mathrm{dirty}\left(u\right) \equiv \int_{u_\mathrm{p}} W\left(u_\mathrm{p}, u - u_\mathrm{p}\right) \overline{SV}^\mathcal{G}\left(u_\mathrm{p}, u - u_\mathrm{p}\right) \mathrm{d}u_\mathrm{p}, \tag{98}$$

where W is a normalized weighting function. Using these tools, we demonstrated that:

1. The dirty image ($I^{\mathcal{G}}_{\rm dirty}$) is a convolution of the sky brightness distribution (I) with a set of wide-field dirty beams ($D^{\mathcal{G}}$) varying with the sky coordinate α, i.e.,
$$I^{\mathcal{G}}_{\rm dirty}(\alpha) = \int_{\alpha'} D^{\mathcal{G}}(\alpha - \alpha', \alpha)\, I(\alpha')\, {\rm d}\alpha'. \quad (99)$$
Compared to single-field imaging, the dependency on the primary beam is transferred from a product of the sky brightness distribution into the definition of the set of wide-field dirty beams.
2. The set of gridded dirty beams ($D^{\mathcal{G}}$) can be computed from the ungridded sampling function (S), the transfer function ($\overline{B}$, the inverse Fourier transform of the primary beam), and the gridding convolution kernel (see Eqs. (42), (50) and (51)).
3. The dependence of the wide-field dirty beams on the sky position is slowly-varying, with their shape varying on an angular scale typically larger than or equal to the primary beamwidth.

Adaptations of the existing deconvolution algorithms should be straightforward.

A comparison with standard nonlinear mosaicking shows that it is not mathematically equivalent to the wide-field synthesis proposed here, though both methods do recover the sky brightness. The main advantages of wide-field synthesis over standard nonlinear mosaicking are

1. Weighting is at the heart of the wide-field synthesis because it is an essential part of the shift-and-average operation. Indeed, not only can a multiplicative weight be attributed to each visibility sample before any processing, but the uv-plane weighting function (W, see Eq. (98)) is also a degree of freedom, which should be set according to the conditions of the observation and the imaging goals, e.g. highest signal-to-noise ratio, highest resolution, or most uniform resolution over the field of view. The W weighting function thus enables us to modify the wide-field response of the instrument. On the other hand, mosaicking requires a precise weighting function in the image plane, which freezes the wide-field response of the interferometer.
2. Wide-field synthesis naturally processes the short spacings from both single-dish antennas and heterogeneous arrays along with the long spacings. Both of them can then be jointly deconvolved.
3. The gridding of the sky plane dimension of the measured visibilities, required by the wide-field synthesis, may potentially save large amounts of hard-disk space and cpu processing power relative to mosaicking when handling data sets acquired with the on-the-fly observing mode. Wide-field synthesis could thus be particularly well suited to process on-the-fly observations.

The wide-field synthesis algorithm is compatible with the uvw-unfaceting technique devised by Sault et al. (1996a) to deal with the celestial projection effect, known as non-coplanar baselines (see Appendix B). Finally, on-the-fly observations imply an elongation of the primary beam along the scanning direction. These effects can be decreased by an increase in the primary beam sampling rate. However, it may limit the dynamic range of the image brightness if the primary beam sampling rate is too coarse (see Appendix C).

Acknowledgements. This work has mainly been funded by the European FP6 "ALMA enhancement" grant. This work was also funded by grant ANR-09-BLAN-0231-01 from the French *Agence Nationale de la Recherche* as part of the SCHISM project. The authors thank F. Gueth for the management of the on-the-fly working package of the "ALMA enhancement" project. They also thank S. Guilloteau, R. Lucas and J. Uson for useful comments at various stages of the manuscript and D. Downes for editing their English. They finally thank the referee, B. Sault, for his insightful comments, which challenged us to try to write a better paper.

Appendix A: Demonstrations

A.1. Ekers & Rots scheme

Fourier-transforming the visibility function along the $\alpha_{\rm s}$ dimension at constant $u_{\rm p}$, we derive with simple replacements

$$\overline{V}_{u_{\rm p}}(u_{\rm s}) = \int_{\alpha_{\rm s}} V_{u_{\rm p}}(\alpha_{\rm s})\, {\rm e}^{-{\rm i}2\pi\alpha_{\rm s}u_{\rm s}}\, {\rm d}\alpha_{\rm s} \quad (A.1)$$
$$= \iint_{\alpha_{\rm s}\alpha_{\rm p}} B\left(\alpha_{\rm p} - \alpha_{\rm s}\right) I\left(\alpha_{\rm p}\right) {\rm e}^{-{\rm i}2\pi\left(\alpha_{\rm p}u_{\rm p} + \alpha_{\rm s}u_{\rm s}\right)}\, {\rm d}\alpha_{\rm s}{\rm d}\alpha_{\rm p}. \quad (A.2)$$

We then use the following change of variables $\beta \equiv \alpha_{\rm p} - \alpha_{\rm s}$ and ${\rm d}\beta = -{\rm d}\alpha_{\rm s}$, to get

$$\overline{V}_{u_{\rm p}}(u_{\rm s}) = \iint_{\alpha_{\rm p}\beta} B(\beta)\, I\left(\alpha_{\rm p}\right) {\rm e}^{-{\rm i}2\pi\left[\alpha_{\rm p}\left(u_{\rm p}+u_{\rm s}\right) - \beta u_{\rm s}\right]}\, {\rm d}\alpha_{\rm p}{\rm d}\beta \quad (A.3)$$
$$= \left[\int_{\beta} B(\beta)\, {\rm e}^{-{\rm i}2\pi\beta(-u_{\rm s})}\, {\rm d}\beta\right]\left[\int_{\alpha_{\rm p}} I\left(\alpha_{\rm p}\right) {\rm e}^{-{\rm i}2\pi\alpha_{\rm p}\left(u_{\rm p}+u_{\rm s}\right)}\, {\rm d}\alpha_{\rm p}\right] \quad (A.4)$$
$$= \overline{B}(-u_{\rm s})\, \overline{I}\left(u_{\rm p} + u_{\rm s}\right). \quad (A.5)$$

A.2. Incomplete sampling

We here demonstrate that Eqs. (23) and (34) are equivalent. To do this, we take the direct Fourier transform of $I_{\rm dirty}(\alpha)$

$$\overline{I}_{\rm dirty}(u) = \iint_{\alpha\alpha'} D(\alpha - \alpha', \alpha)\, I(\alpha')\, {\rm e}^{-{\rm i}2\pi\alpha u}\, {\rm d}\alpha{\rm d}\alpha', \quad (A.6)$$

and we replace $I(\alpha')$ by its formulation as a function of its Fourier transform

$$I(\alpha') = \int_{u'} \overline{I}(u')\, {\rm e}^{+{\rm i}2\pi u'\alpha'}\, {\rm d}u'. \quad (A.7)$$

We thus derive

$$\overline{I}_{\rm dirty}(u) = \int_{u'}\left[\iint_{\alpha\alpha'} D(\alpha - \alpha', \alpha)\, {\rm e}^{-{\rm i}2\pi(\alpha u - \alpha' u')}\, {\rm d}\alpha{\rm d}\alpha'\right]\overline{I}(u')\, {\rm d}u'. \quad (A.8)$$

Using the following change of variables $\alpha'' \equiv \alpha - \alpha'$, $\alpha' = \alpha - \alpha''$ and ${\rm d}\alpha'' = -{\rm d}\alpha'$, the innermost integral can be written as

$$\iint_{\alpha\alpha'} D(\alpha - \alpha', \alpha)\, {\rm e}^{-{\rm i}2\pi(\alpha u - \alpha' u')}\, {\rm d}\alpha{\rm d}\alpha' =$$
$$\int_{\alpha}\left[\int_{\alpha''} D(\alpha'', \alpha)\, {\rm e}^{-{\rm i}2\pi\alpha'' u'}\, {\rm d}\alpha''\right] {\rm e}^{-{\rm i}2\pi\alpha(u-u')}\, {\rm d}\alpha \quad (A.9)$$
$$= \int_{\alpha} \underline{D}(u', \alpha)\, {\rm e}^{-{\rm i}2\pi\alpha(u-u')}\, {\rm d}\alpha \quad (A.10)$$
$$= \overline{\underline{D}}(u', u - u'). \quad (A.11)$$

In the last two steps, we have simply recognized two different steps of Fourier transforms of D. Finally,

$$\overline{I}_{\rm dirty}(u) = \int_{u'} \overline{\underline{D}}(u', u - u')\, \overline{I}(u')\, {\rm d}u'. \quad (A.12)$$

A.3. Gridding

The gridding kernel can be defined as the product of two functions, each one operating in its own dimension. We use this to study separately the effect of gridding in the *uv* and sky planes. We then use the intermediate results to get the effect of gridding simultaneously in both planes.

A.4. Gridding in the uv plane

We define the sampled visibility function gridded in the *uv* plane as

$$SV^g\left(u_\mathrm{p},\alpha_\mathrm{s}\right) \equiv \{g \star SV^{\alpha_\mathrm{s}}\}\left(u_\mathrm{p}\right) = \int_{u'_\mathrm{p}} g(u_\mathrm{p}-u'_\mathrm{p})\, SV^{\alpha_\mathrm{s}}(u'_\mathrm{p})\,\mathrm{d}u'_\mathrm{p}. \quad (A.13)$$

Using that the gridding is here applied on the u_p dimension, while the Fourier transform is applied on the α_s dimension, it is easy to show that the gridding and Fourier-transform operations commute:

$$\overline{SV}^g_{u_\mathrm{p}}(u_\mathrm{s}) = \iint_{\alpha_\mathrm{s}u'_\mathrm{p}} g\left(u_\mathrm{p}-u'_\mathrm{p}\right) S\left(u'_\mathrm{p},\alpha_\mathrm{s}\right) V\left(u'_\mathrm{p},\alpha_\mathrm{s}\right) \mathrm{e}^{-\mathrm{i}2\pi\alpha_\mathrm{s}u_\mathrm{s}}\,\mathrm{d}\alpha_\mathrm{s}\mathrm{d}u'_\mathrm{p} \quad (A.14)$$

$$= \int_{u'_\mathrm{p}} g\left(u_\mathrm{p}-u'_\mathrm{p}\right) \overline{SV}_{u'_\mathrm{p}}(u_\mathrm{s})\,\mathrm{d}u'_\mathrm{p}. \quad (A.15)$$

Defining the Fourier transform of the *uv* gridded dirty image, we derive

$$\overline{I}^g_\mathrm{dirty}(u) \equiv \left\langle \overline{SV}^g \right\rangle(u) \quad (A.16)$$

$$= \iint_{u_\mathrm{p}u'_\mathrm{p}} W\left(u_\mathrm{p},u-u_\mathrm{p}\right) g\left(u_\mathrm{p}-u'_\mathrm{p}\right) \overline{SV}_{u'_\mathrm{p}}\left(u-u_\mathrm{p}\right)\mathrm{d}u_\mathrm{p}\mathrm{d}u'_\mathrm{p}. \quad (A.17)$$

Using Eq. (31) to replace $\overline{SV}_{u'_\mathrm{p}}(u-u_\mathrm{p})$, we can write the Fourier transform of the *uv* gridded dirty image as

$$\overline{I}^g_\mathrm{dirty}(u) = \int_{u'} \underline{\overline{D}}^g(u',u-u')\,\overline{I}(u')\,\mathrm{d}u', \quad (A.18)$$

with

$$\underline{\overline{D}}^g(u',u-u') \equiv \int_{u_\mathrm{p}} W\left(u_\mathrm{p},u-u_\mathrm{p}\right) \underline{\overline{\Sigma}}^g\left(u_\mathrm{p},u-u_\mathrm{p},u'\right)\mathrm{d}u_\mathrm{p} \quad (A.19)$$

and

$$\underline{\overline{\Sigma}}^g\left(u_\mathrm{p},u_\mathrm{s},u'\right) \equiv \int_{u'_\mathrm{p}} g\left(u_\mathrm{p}-u'_\mathrm{p}\right) \overline{S}\left(u'_\mathrm{p},u_\mathrm{s}-u'+u'_\mathrm{p}\right) \overline{B}\left(u'_\mathrm{p}-u'\right)\mathrm{d}u'_\mathrm{p}. \quad (A.20)$$

Using

$$\overline{S}\left(u'_\mathrm{p},u_\mathrm{s}-u'+u'_\mathrm{p}\right) = \left[\int_{\alpha_\mathrm{s}} S_{u'_\mathrm{p}}(\alpha_\mathrm{s})\,\mathrm{e}^{-\mathrm{i}2\pi\alpha_\mathrm{s}u_\mathrm{s}}\,\mathrm{d}\alpha_\mathrm{s}\right]\mathrm{e}^{-\mathrm{i}2\pi\left(u'_\mathrm{p}-u'\right)\alpha_\mathrm{s}}, \quad (A.21)$$

and

$$\overline{\Sigma}^g\left(u_\mathrm{p},\alpha_\mathrm{s},u'\right) \overset{\alpha_\mathrm{s}}{\underset{u_\mathrm{s}}{\supset}} \overline{\underline{\Sigma}}^g\left(u_\mathrm{p},u_\mathrm{s},u'\right), \quad (A.22)$$

we derive

$$\overline{\Sigma}^g\left(u_\mathrm{p},\alpha_\mathrm{s},u'\right) = \int_{u'_\mathrm{p}} g(u_\mathrm{p}-u'_\mathrm{p})\, S\left(u'_\mathrm{p},\alpha_\mathrm{s}\right) \overline{B}\left(u'_\mathrm{p}-u'\right)\mathrm{e}^{-\mathrm{i}2\pi\left(u'_\mathrm{p}-u'\right)\alpha_\mathrm{s}}\,\mathrm{d}u'_\mathrm{p}, \quad (A.23)$$

or

$$\overline{\Sigma}^g\left(u_\mathrm{p},\alpha_\mathrm{s},u'\right) = \int_{u'_\mathrm{p}} g\left(u_\mathrm{p}-u'_\mathrm{p}\right) \overline{\Sigma}\left(u'_\mathrm{p},\alpha_\mathrm{s},u'_\mathrm{p}-u'\right)\mathrm{d}u'_\mathrm{p}. \quad (A.24)$$

Thus, $\overline{\Sigma}^g$ is the *uv* gridded version of the generalized sampling function $\overline{\Sigma}$.

A.4.1. Gridding in the sky plane

We define the sampled visibility function gridded in the sky plane as

$$SV^\gamma\left(u_\mathrm{p},\alpha_\mathrm{s}\right) \equiv \left\{\gamma \star SV_{u_\mathrm{p}}\right\}(\alpha_\mathrm{s}) \quad (A.25)$$

$$= \int_{\alpha'_\mathrm{s}} \gamma(\alpha_\mathrm{s}-\alpha'_\mathrm{s})\, SV_{u_\mathrm{p}}(\alpha'_\mathrm{s})\,\mathrm{d}\alpha'_\mathrm{s}. \quad (A.26)$$

Applying the convolution theorem on the Fourier transform along the α_s dimension, we derive

$$\overline{SV}^\gamma_{u_\mathrm{p}}(u_\mathrm{s}) = \overline{\gamma}(u_\mathrm{s})\,\overline{SV}_{u_\mathrm{p}}(u_\mathrm{s}). \quad (A.27)$$

Defining the Fourier transform of the sky-gridded dirty image, we derive

$$\overline{I}^\gamma_\mathrm{dirty}(u) \equiv \left\langle \overline{SV}^\gamma \right\rangle(u) \quad (A.28)$$

$$= \int_{u_\mathrm{p}} W\left(u_\mathrm{p},u-u_\mathrm{p}\right)\overline{\gamma}\left(u-u_\mathrm{p}\right)\overline{SV}_{u_\mathrm{p}}\left(u-u_\mathrm{p}\right)\mathrm{d}u_\mathrm{p}. \quad (A.29)$$

Using Eq. (31) to replace $\overline{SV}_{u_\mathrm{p}}(u-u_\mathrm{p})$, we can write the Fourier transform of the sky-gridded dirty image as

$$\overline{I}^\gamma_\mathrm{dirty}(u) = \int_{u'} \underline{\overline{D}}^\gamma(u',u-u')\,\overline{I}(u')\,\mathrm{d}u' \quad (A.30)$$

with

$$\underline{\overline{D}}^\gamma(u',u-u') \equiv \int_{u_\mathrm{p}} W\left(u_\mathrm{p},u-u_\mathrm{p}\right) \underline{\overline{\Sigma}}^\gamma\left(u_\mathrm{p},u-u_\mathrm{p},u_\mathrm{p}-u'\right)\mathrm{d}u_\mathrm{p} \quad (A.31)$$

and

$$\underline{\overline{\Sigma}}^\gamma\left(u_\mathrm{p},u_\mathrm{s},u''_\mathrm{s}\right) \equiv \overline{\gamma}(u_\mathrm{s})\,\overline{S}\left(u_\mathrm{p},u_\mathrm{s}+u''_\mathrm{s}\right)\overline{B}(u''_\mathrm{s}), \quad (A.32)$$

or, with the definition of $\overline{\underline{\Sigma}}$ (i.e., Eq. (45)),

$$\underline{\overline{\Sigma}}^\gamma\left(u_\mathrm{p},u_\mathrm{s},u''_\mathrm{s}\right) \equiv \overline{\gamma}(u_\mathrm{s})\,\overline{\underline{\Sigma}}\left(u_\mathrm{p},u_\mathrm{s},u''_\mathrm{s}\right). \quad (A.33)$$

Using

$$\overline{\Sigma}^\gamma\left(u_\mathrm{p},\alpha_\mathrm{s},u''_\mathrm{s}\right) \overset{\alpha_\mathrm{s}}{\underset{u_\mathrm{s}}{\supset}} \underline{\overline{\Sigma}}^\gamma\left(u_\mathrm{p},u_\mathrm{s},u''_\mathrm{s}\right), \quad (A.34)$$

and the convolution theorem when taking the inverse Fourier transform of $\underline{\overline{\Sigma}}^\gamma$, we derive

$$\overline{\Sigma}^\gamma\left(u_\mathrm{p},\alpha_\mathrm{s},u''_\mathrm{s}\right) = \int_{\alpha'_\mathrm{s}} \gamma\left(\alpha_\mathrm{s}-\alpha'_\mathrm{s}\right)\overline{\Sigma}\left(u_\mathrm{p},\alpha'_\mathrm{s},u''_\mathrm{s}\right)\mathrm{d}\alpha'_\mathrm{s}. \quad (A.35)$$

Thus, $\overline{\Sigma}^\gamma$ is the sky gridded version of the generalized sampling function $\overline{\Sigma}$.

A.5. Gridding in both planes

Starting from the definition of $SV^{\mathcal{G}}$ (Eq. (41)), we Fourier-transform it along the sky dimension at constant u_p. Using that the gridding along the u_p dimension can be factored out of the Fourier transform, we derive

$$\overline{SV}^{\mathcal{G}}_{u_\mathrm{p}}(u_\mathrm{s}) = \int_{u'_\mathrm{p}} g\left(u_\mathrm{p} - u'_\mathrm{p}\right) \overline{SV}^{\gamma}_{u'_\mathrm{p}}(u_\mathrm{s})\, \mathrm{d}u'_\mathrm{p}. \tag{A.36}$$

Using Eq. (A.27), we now replace $\overline{SV}^{\gamma}_{u'_\mathrm{p}}(u_\mathrm{s})$ in the previous equation to get

$$\overline{SV}^{\mathcal{G}}_{u_\mathrm{p}}(u_\mathrm{s}) = \overline{\gamma}(u_\mathrm{s}) \int_{u'_\mathrm{p}} g\left(u_\mathrm{p} - u'_\mathrm{p}\right) \overline{SV}_{u'_\mathrm{p}}(u_\mathrm{s})\, \mathrm{d}u'_\mathrm{p}, \tag{A.37}$$

or

$$\overline{SV}^{\mathcal{G}}_{u_\mathrm{p}}(u_\mathrm{s}) = \overline{\gamma}(u_\mathrm{s})\, \overline{SV}^{g}_{u_\mathrm{p}}(u_\mathrm{s}). \tag{A.38}$$

From this relation, it is easy to deduce that

$$\overline{\Sigma}^{\mathcal{G}}\left(u_\mathrm{p}, u_\mathrm{s}, u'\right) = \overline{\gamma}(u_\mathrm{s})\, \overline{\Sigma}^{g}\left(u_\mathrm{p}, u_\mathrm{s}, u'\right). \tag{A.39}$$

Using the convolution theorem when taking the inverse Fourier transform of $\overline{\Sigma}^{\mathcal{G}}$ along the u_s dimension and replacing $\overline{\Sigma}^{g}(u_\mathrm{p}, \alpha'_\mathrm{s}, u')$ with Eq. (A.24), we finally derive

$$\overline{\Sigma}^{\mathcal{G}}\left(u_\mathrm{p}, \alpha_\mathrm{s}, u'\right) \equiv \iint_{u'_\mathrm{p}\alpha'_\mathrm{s}} g\left(u_\mathrm{p} - u'_\mathrm{p}\right) \gamma\left(\alpha_\mathrm{s} - \alpha'_\mathrm{s}\right) \overline{\Sigma}\left(u'_\mathrm{p}, \alpha'_\mathrm{s}, u'_\mathrm{p} - u'\right) \mathrm{d}u'_\mathrm{p}\mathrm{d}\alpha'_\mathrm{s}. \tag{A.40}$$

A.6. Wide-field vs. single-field dirty beams

The notation (59) yields $W(u', u'') = \underline{\Omega}(u', u'')$. Using this in Eq. (35) gives

$$\overline{D}(u', u'') = \int_{u_\mathrm{p}} \underline{\Omega}\left(u_\mathrm{p}, u' + u'' - u_\mathrm{p}\right) \overline{S}\left(u_\mathrm{p}, u''\right) \overline{B}\left(u_\mathrm{p} - u'\right) \mathrm{d}u_\mathrm{p}. \tag{A.41}$$

Taking the inverse Fourier transform along the u'' axis of Eq. (A.41) and reordering the integral to factor out the term independent of u'', we can write

$$\underline{D}(u', \alpha'') = \int_{u_\mathrm{p}} \overline{B}\left(u_\mathrm{p} - u'\right) \mathrm{FT}_1(u_\mathrm{p}, u', \alpha'')\, \mathrm{d}u_\mathrm{p}, \tag{A.42}$$

where

$$\mathrm{FT}_1(u_\mathrm{p}, u', \alpha'') \equiv \int_{u''} \underline{\Omega}\left(u_\mathrm{p}, u' + u'' - u_\mathrm{p}\right) \overline{S}\left(u_\mathrm{p}, u''\right) \mathrm{e}^{+\mathrm{i}2\pi u''\alpha''}\, \mathrm{d}u''. \tag{A.43}$$

We now introduce the following definition

$$\overline{S}\left(u_\mathrm{p}, u''\right) \equiv \int_{\alpha_\mathrm{s}} S\left(u_\mathrm{p}, \alpha_\mathrm{s}\right) \mathrm{e}^{-\mathrm{i}2\pi\alpha_\mathrm{s}u''}\, \mathrm{d}\alpha_\mathrm{s}, \tag{A.44}$$

to derive

$$\mathrm{FT}_1(u_\mathrm{p}, u', \alpha'') = \int_{\alpha_\mathrm{s}} S\left(u_\mathrm{p}, \alpha_\mathrm{s}\right) \left[\int_{u''} \underline{\Omega}\left(u_\mathrm{p}, u' + u'' - u_\mathrm{p}\right) \mathrm{e}^{+\mathrm{i}2\pi u''(\alpha'' - \alpha_\mathrm{s})}\, \mathrm{d}u''\right] \mathrm{d}\alpha_\mathrm{s}.$$

Using the following change of variables $v \equiv u'' + u' - u_\mathrm{p}$, $u'' = v - u' + u_\mathrm{p}$ and $\mathrm{d}v = \mathrm{d}u''$ on the innermost integral, we get

$$\mathrm{FT}_1(u_\mathrm{p}, u', \alpha'') = \int_{\alpha_\mathrm{s}} S\left(u_\mathrm{p}, \alpha_\mathrm{s}\right) \underline{\Omega}\left(u_\mathrm{p}, \alpha'' - \alpha_\mathrm{s}\right) \mathrm{e}^{+\mathrm{i}2\pi\left(u_\mathrm{p} - u'\right)\left(\alpha'' - \alpha_\mathrm{s}\right)}\, \mathrm{d}\alpha_\mathrm{s}.$$

Substituting this result into Eq. (A.42) and taking the inverse Fourier transform along the u' axis, we can write

$$D(\alpha', \alpha'') = \iint_{u_\mathrm{p}\alpha_\mathrm{s}} \underline{\Omega}\left(u_\mathrm{p}, \alpha'' - \alpha_\mathrm{s}\right) S\left(u_\mathrm{p}, \alpha_\mathrm{s}\right) \mathrm{FT}_2(u_\mathrm{p}, \alpha_\mathrm{s}, \alpha', \alpha'')\, \mathrm{d}u_\mathrm{p}\mathrm{d}\alpha_\mathrm{s}, \tag{A.45}$$

where

$$\mathrm{FT}_2(u_\mathrm{p}, \alpha_\mathrm{s}, \alpha', \alpha'') \equiv \int_{u'} \overline{B}(u_\mathrm{p} - u')\, \mathrm{e}^{+\mathrm{i}2\pi u_\mathrm{p}(\alpha'' - \alpha_\mathrm{s})}\, \mathrm{e}^{+\mathrm{i}2\pi u'(\alpha' - \alpha'' + \alpha_\mathrm{s})}\, \mathrm{d}u'.$$

Using the following change of variables $v \equiv u_\mathrm{p} - u'$, $u' = u_\mathrm{p} - v$ and $\mathrm{d}v = \mathrm{d}u'$, we get

$$\mathrm{FT}_2(u_\mathrm{p}, \alpha_\mathrm{s}, \alpha', \alpha'') = B\left(\alpha'' - \alpha' - \alpha_\mathrm{s}\right) \mathrm{e}^{+\mathrm{i}2\pi u_\mathrm{p}\alpha'}. \tag{A.46}$$

Substituting this result into Eq. (A.45) and re-ordering the terms, we can write

$$D(\alpha', \alpha'') = \int_{\alpha_\mathrm{s}} B\left(\alpha'' - \alpha' - \alpha_\mathrm{s}\right) \mathrm{FT}_3(\alpha_\mathrm{s}, \alpha', \alpha'')\, \mathrm{d}\alpha_\mathrm{s}, \tag{A.47}$$

where

$$\mathrm{FT}_3(\alpha_\mathrm{s}, \alpha', \alpha'') \equiv \int_{u_\mathrm{p}} \underline{\Omega}\left(u_\mathrm{p}, \alpha'' - \alpha_\mathrm{s}\right) S\left(u_\mathrm{p}, \alpha_\mathrm{s}\right) \mathrm{e}^{+\mathrm{i}2\pi u_\mathrm{p}\alpha'}\, \mathrm{d}u_\mathrm{p}.$$

A simple application of the convolution theorem gives

$$\mathrm{FT}_3(\alpha_\mathrm{s}, \alpha', \alpha'') \equiv \int_{\alpha_\mathrm{p}} \Omega\left(\alpha' - \alpha_\mathrm{p}, \alpha'' - \alpha_\mathrm{s}\right) \Delta\left(\alpha_\mathrm{p}, \alpha_\mathrm{s}\right) \mathrm{d}\alpha_\mathrm{p},$$

where

$$\Delta\left(\alpha_\mathrm{p}, \alpha_\mathrm{s}\right) \overset{\alpha_\mathrm{p}}{\underset{u_\mathrm{p}}{\supset}} S\left(u_\mathrm{p}, \alpha_\mathrm{s}\right). \tag{A.48}$$

Substituting this result into Eq. (A.47), we finally derive the desired expression, i.e., Eq. (57).

Appendix B: From the celestial sphere onto a single tangent plane

Equation (1) neglects projection effects, known as non-coplanar baselines. Any method which deals with interferometric wide-field imaging must take this problem into account. After a short introduction to the problem, we show how wide-field synthesis is compatible with at least one method, namely the *uvw*-unfaceting of Sault et al. (1996b). This method tries to build a final wide-field *uv* plane from different pieces, just as our wide-field synthesis approach does. Another promising method is the *w*-projection, based on original ideas of Frater & Docherty (1980) and first successfully implemented by Cornwell et al. (2008). We did not look yet at its compatibility with wide-field synthesis.

B.1. w-axis distortion

When projection effects are taken into account, the measurement equation reads

$$V\left(w, u_\mathrm{p}, \alpha_\mathrm{s}\right) = \int_{\alpha_\mathrm{p}} B\left(\alpha_\mathrm{p} - \alpha_\mathrm{s}\right) \frac{I\left(\alpha_\mathrm{p}\right)}{\sqrt{1-\alpha_\mathrm{p}^2}} \mathrm{e}^{-\mathrm{i}2\pi\left[\alpha_\mathrm{p} u_\mathrm{p} + w\left(\sqrt{1-\alpha_\mathrm{p}^2}-1\right)\right]} \mathrm{d}\alpha_\mathrm{p}. \quad \text{(B.1)}$$

In this equation, we continue to work in 1 dimension for the sky cosine direction (α_p), but we explicitly introduce the dependence along the direction perpendicular to the sky plane. This dependence appears in two ways, which is handled in very different ways. First, the factor $\sqrt{1-\alpha_\mathrm{p}^2}$ can be absorbed into a generalized sky brightness function

$$\mathcal{I}\left(\alpha_\mathrm{p}\right) \equiv \frac{I\left(\alpha_\mathrm{p}\right)}{\sqrt{1-\alpha_\mathrm{p}^2}}\cdot \quad \text{(B.2)}$$

After imaging and deconvolution, $I(\alpha_\mathrm{p})$ can be easily restored from the deconvolved $\mathcal{I}(\alpha_\mathrm{p})$ image. The second dependence appears as an additional phase, which is written as

$$P\left(\alpha_\mathrm{p}, w\right) \equiv \mathrm{e}^{-\mathrm{i}2\pi w\left(\sqrt{1-\alpha_\mathrm{p}^2}-1\right)}. \quad \text{(B.3)}$$

Thompson et al. (1986, Chap. 4) shows that this additional phase can be neglected only if[8]

$$\frac{\pi}{4}\frac{\theta_\mathrm{field}^2}{\theta_\mathrm{syn}} \ll 1 \quad \text{or} \quad \pi\frac{\lambda d_\mathrm{max}}{d_\mathrm{field}^2} \ll 1. \quad \text{(B.4)}$$

The first form of the criterion indicates that the approximation gets worse at high spatial dynamic range (i.e., $\theta_\mathrm{field}/\theta_\mathrm{syn} \ll 1$) while the second form indicates that the approximation gets worse at long wavelengths.

B.2. uvw-facetting

For stop-and-go mosaicking, it is usual to delay-track at the center of the primary beam for each pointing/field of the mosaic. This phase center is also the natural center of projection of each pointing/field. Stop-and-go mosaicking thus naturally paves the celestial sphere with as many tangent planes as there are pointings/fields; i.e., this observing scheme is somehow enforcing a *uvw*-faceting scheme. In the framework of on-the-fly observations with ALMA, D'Addario & Emerson (2000) indicate that the phase center will be modified between each on-the-fly scan while it will stay constant during each on-the-fly scan. This is a compromise between loss of coherence and technical possibilities of the phase-locked loop. Using this hypothesis, the maximum sky area covered by the on-the-fly scan must take into account the maximum tolerable *w*-axis distortion.

The easiest way to deal with such data is to image each pointing/field around its phase center and then to reproject this image onto the mosaic tangent plane as displayed in Fig. 5 of Sault et al. (1996b). These authors point out that this scheme implies a typical *w*-axis distortion ϵ less than

$$\epsilon \leq \left(1-\cos\theta_\mathrm{alias}\right)\sin\theta_\mathrm{center} \sim \frac{1}{2}\theta_\mathrm{center}\,\theta_\mathrm{alias}^2, \quad \text{(B.5)}$$

where θ_center is the angle from the pointing/field center and θ_alias is the anti-aliasing scale defined in Sect. 4.2. In particular, ϵ is 0 at the phase center of each pointing/field. In other words, this scheme limits the magnitude of the *w*-axis distortion to its magnitude on a size equal to the anti-aliasing scale (i.e., a few time the primary beamwidth) instead of a size equal to the total mosaic field of view. This scheme thus solves the projection effect as long as the *w*-axis distortion is negligible at sizes smaller than or equal to the anti-aliasing scale. A natural name for this processing scheme is *uvw*-unfaceting because it is the combination of a faceting observing mode (i.e., regular change of phase center) and a linear transform of the *uv* coordinates to derive a single sine projection for the whole field of view.

Sault et al. (1996b) also demonstrate that the reprojection may be done much more easily and quickly in the *uvw* space before imaging the visibilities because it is then just a simple transformation of the *uv* coordinates, followed by a multiplication of the visibilities by a phase term. Finally, Sault et al. (1996b) note that it is the linear character of this *uv* coordinate transform which preserves the measurement Eq. (1). As the change of coordinates happens before any other processing, it also conserves all the equations derived in the previous sections to implement the wide-field synthesis.

[8] In contrast to the convention used in this paper, the d_max and d_field unit is meter instead of unit of λ in the second form of the criterion, in order to explicitely show the dependence on the wavelength.

Appendix C: On-the-fly observing mode and effective primary beam

Usual interferometric observing modes (including stop-and-go mosaicking) implies that the interferometer antennas observe a fixed point of the sky during the integration time. Conversely, the on-the-fly observing mode implies that the antennas slew on the sky during the integration time. This implies that the measurement Eq. (1) must be written as (Holdaway & Foster 1994; Rodríguez-Fernández et al. 2009):

$$V\left(\hat{u}_\mathrm{p}, \hat{\alpha}_\mathrm{s}\right) = \frac{1}{\delta t}\int_{t_0-\delta t/2}^{t_0+\delta t/2}\left[\int_{\alpha_\mathrm{p}} B\left\{\alpha_\mathrm{p}-\alpha_\mathrm{s}(t)\right\} I\left(\alpha_\mathrm{p}\right)\mathrm{e}^{-\mathrm{i}2\pi\alpha_\mathrm{p}u_\mathrm{p}(t)}\,\mathrm{d}\alpha_\mathrm{p}\right]\mathrm{d}t, \quad \text{(C.1)}$$

where δt is the integration time and $\hat{u}_\mathrm{p}$ and $\hat{\alpha}_\mathrm{s}$ are the mean spatial frequency and direction cosine, defined as

$$\hat{u}_\mathrm{p} \equiv \frac{1}{\delta t}\int_{t_0-\delta t/2}^{t_0+\delta t/2} u_\mathrm{p}(t)\,\mathrm{d}t \quad \text{and} \quad \hat{\alpha}_\mathrm{s} \equiv \frac{1}{\delta t}\int_{t_0-\delta t/2}^{t_0+\delta t/2} \alpha_\mathrm{s}(t)\,\mathrm{d}t. \quad \text{(C.2)}$$

In this section, we analyze the consequences of the antenna slewing on the accuracy of the wide-field synthesis.

C.1. Time averaging

In all interferometric observing modes, it is usual to adjust the integration time so that $u_\mathrm{p}(t)$ can be approximated as $\hat{u}_\mathrm{p}$. To do this, it is enough to ensure that $u_\mathrm{p}(t)$ always varies less than the *uv* distance associated with tolerable aliasing (d_alias, see Sect. 4.2) during the integration time (δt)

$$\delta t \ll \frac{d_\mathrm{alias}}{d_\mathrm{max}\,\omega_\mathrm{earth}} \quad \text{or} \quad \frac{\mathrm{d}t}{1\ \mathrm{s}} \ll \frac{6900}{\theta_\mathrm{alias}/\theta_\mathrm{syn}}, \quad \text{(C.3)}$$

where d_max is the maximum baseline length, ω_earth is the angular velocity of a spatial frequency due to the Earth rotation (7.27×10^{-5} rad s^{-1}), θ_alias and θ_syn are respectively the minimum field of view giving a tolerable aliasing and the synthesized beam angular values.

Table C.1. Definition of the symbols used to explore the influence of on-the-fly scanning on the measurement equation.

Symbol	& Definition
δt	Integration time
$\hat{\alpha}_\mathrm{s}$	Scanned angle averaged during δt
$\hat{u}_\mathrm{p}$	Spatial frequency averaged during δt
$\delta\alpha_\mathrm{s}$	Angular distance scanned during δt
v_slew	Slew angular velocity of the telescope
A	Primary beam apodizing function
B_eff	Effective primary beam resulting from OTF scanning: $B_\mathrm{eff}(\alpha) = \{B \star A\}(\alpha)$
ω_earth	Angular velocity of a spatial frequency due to Earth rotation

C.2. Effective primary beam

Assuming that condition (C.3) is ensured, we can write Eq. (C.1) with the same form as Eq. (1) by the introduction of an effective primary beam (B_eff); i.e.,

$$V\left(\hat{u}_\mathrm{p}, \hat{\alpha}_\mathrm{s}\right) = \int_{\alpha_\mathrm{p}} B_\mathrm{eff}\left(\alpha_\mathrm{p} - \hat{\alpha}_\mathrm{s}\right) I\left(\alpha_\mathrm{p}\right) \mathrm{e}^{-\mathrm{i}2\pi\alpha_\mathrm{p}\hat{u}_\mathrm{p}}\,\mathrm{d}\alpha_\mathrm{p}, \tag{C.4}$$

where

$$B_\mathrm{eff}\left(\alpha_\mathrm{p} - \hat{\alpha}_\mathrm{s}\right) \equiv \frac{1}{\delta t}\int_{t_0-\delta t/2}^{t_0+\delta t/2} B\Big\{\alpha_\mathrm{p} - \alpha_\mathrm{s}(t)\Big\}\,\mathrm{d}t. \tag{C.5}$$

Using the following change of variables

$$\beta \equiv \alpha_\mathrm{s}(t) - \hat{\alpha}_\mathrm{s}, \quad \mathrm{d}\beta = \frac{\mathrm{d}\alpha_\mathrm{s}(t)}{\mathrm{d}t}\mathrm{d}t \quad \text{or} \quad \mathrm{d}t = \frac{\mathrm{d}\beta}{v_\mathrm{slew}\,(\beta)}, \tag{C.6}$$

we derive

$$B_\mathrm{eff}\left(\alpha_\mathrm{p} - \hat{\alpha}_\mathrm{s}\right) = \int_\beta B\left\{\left(\alpha_\mathrm{p} - \hat{\alpha}_\mathrm{s}\right) - \beta\right\} A\,(\beta)\,\mathrm{d}\beta \tag{C.7}$$

with

$$A\,(\beta) \equiv \frac{1}{v_\mathrm{slew}\,(\beta)\;\delta t}\,\Pi\left(\frac{\beta}{\delta\alpha_\mathrm{s}}\right) \tag{C.8}$$

and

$$\delta\alpha_\mathrm{s} \equiv \int_{t_0-\delta t/2}^{t_0+\delta t/2} v_\mathrm{slew}(t)\,\mathrm{d}t. \tag{C.9}$$

In these equations, $v_\mathrm{slew}(\beta)$ is the slew angular velocity of the telescope as a function of the sky position, $\delta\alpha_\mathrm{s}$ is the angular distance covered during δt, A is an apodizing function, and $\Pi(\beta)$ is the usual rectangle function, which reproduces the finite character of the time integration.

C.3. Interpretation

The form of the measurement equation is conserved when averaging the visibility function over a finite integration time, as long as the true primary beam is replaced by an effective primary beam, which is the convolution of the true primary beam by an apodizing function. To go further, it is important to return to the two dimensional case. Indeed, the convolution must be done along the slewing direction, resulting in an effective primary beam elongated in a particular direction.

In principle, the equations derived in Sect. 3 can be accommodated just by replacing the true primary beam by its effective associate. In practice, the probability to take into account the effective primary beam is low because its shape varies with time. Indeed, it is often assumed that the sky is slewed along a straight line at constant angular velocity. Even in this simplest case, it is advisable to slew along at least two perpendicular directions to average systematic errors, implying two different effective primary beams. However, practical reasons may/will lead to complex scanning patterns: 1) the limitation of the acceleration when trying to image a square region leads to spiral or Lissajous scanning patterns; 2) the probable absence of derotators in future multi-beam receivers (B. Lazareff, private communication) implies the need to take into account the Earth rotation in the scanning patterns of the off-axis pixels.

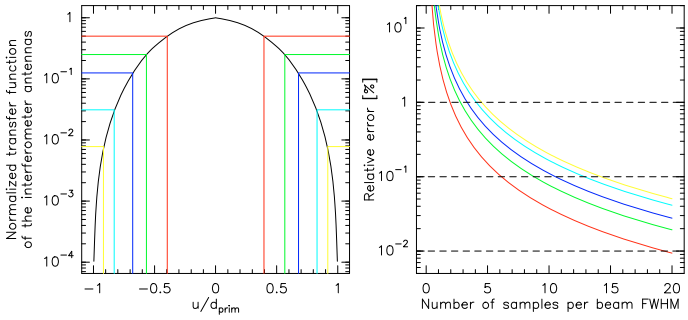

Fig. C.1. Assessement of the relative error implied by the use of the true primary beam instead of the effective primary beam when analyzing interferometric on-the-fly data sets. *Left*: inverse Fourier transform of interferometer primary beam, $\overline{B}$ (i.e. the autocorrelation of the antenna illumination). *Right*: relative error as a function of sampling rate of the primary beam. The curves of different colors show the results at different normalized uv distances (u/d_prim) from the center of $\overline{B}$.

C.4. Approximation accuracy

In the following, we thus ask what is the trade-off accuracy of using the true primary beam instead of the effective primary beam. The first point to mention is that using different scanning patterns somehow helps because the averaging process then makes the bias less systematic. Following Holdaway & Foster (1994), we quantify the accuracy lost in the Fourier plane. Indeed, the Ekers & Rots scheme tries to estimate missing sky brightness Fourier components from their measurements apodized by the Fourier transform of the primary beam. In the Fourier space, the above convolution just translates into a product. The Fourier transform of the apodizing function thus degrades the sensitivity of the measured visibility, $V(u_\mathrm{p}, \alpha_\mathrm{s})$, to spatial frequencies at the edges of the interval $[u_\mathrm{p} - d_\mathrm{prim}, u_\mathrm{p} + d_\mathrm{prim}]$. To guide us in our quantification of the accuracy lost, we now explore the simplest case of linear scanning at constant velocity, where $v_\mathrm{slew}(\beta)$ is constant and $\delta\alpha_\mathrm{s} = v_\mathrm{slew}\,\delta t$. The Fourier transform of the apodizing function is then a sinc function:

$$\overline{A}\,(u) = \mathrm{sinc}\,(u\,\delta\alpha_\mathrm{s})\,. \tag{C.10}$$

The relative error implied by the use of the true primary beam instead of the effective primary beam is then

$$\frac{\overline{B}_\mathrm{eff}\,(u) - \overline{B}\,(u)}{\overline{B}_\mathrm{eff}\,(u)} = 1 - \frac{1}{\overline{A}\,(u)} = 1 - \frac{1}{\mathrm{sinc}\,(u\,\delta\alpha_\mathrm{s})}\,\cdot \tag{C.11}$$

Figure C.1 shows this relative error as a function of the number of samples per primary beam FWHM in the image plane (i.e.,

$\theta_{\rm fwhm}/\delta\alpha_{\rm s}$) for different uv distances (in units of $d_{\rm prim}$). We see that we derive a 1% accuracy at all u when we sample the image plane at a rate of 5 dumps per primary beam. However getting a 0.1% accuracy needs quite high sampling rates (about 15). This must be compared with the accuracy of knowledge of $\overline{B}$.

We note that if a better accuracy is needed than the one achievable with the highest sampling rate, it is in theory possible to replace in the correlator software the rectangle apodizing function by another function which falls more smoothly. To avoid the loss of sensitivity inherent to the use of such an apodizing function (by throwing away data at the edges of the time interval of integration), would require, for instance, to half-overlap the integration intervals. This would imply more book-keeping in the correlator software and some noise correlation between the measured visibilities.

References

Bevington, P. R., & Robinson, D. K. 2003, Data Reduction and Error Analysis For the Physical Sciences, 3rd edn. (McGraw-Hill)

Bhatnagar, S., & Cornwell, T. J. 2004, A&A, 426, 747

Bhatnagar, S., Cornwell, T. J., Golap, K., & Uson, J. M. 2008, A&A, 487, 419

Bracewell, R. N. 2000, The Fourier Transform and its Applications, 3rd edn. (McGraw-Hill)

Clark, B. G. 1980, A&A, 89, 377

Cornwell, T. J. 1988, A&A, 202, 316

Cornwell, T. J., Holdaway, M. A., & Uson, J. M. 1993, A&A, 271, 697

Cornwell, T. J., Golap, K., & Bhatnagar, S. 2008, IEEE Journal of Selected Topics in Signal Processing, 2, 647

Cotton, W. D., & Uson, J. M. 2008, A&A, 490, 455

D'Addario, L. R., & Emerson, D. T. 2000, On-The-Fly Fringe Tracking, ALMA memo, 331

Ekers, R. D., & Rots, A. H. 1979, in Image Formation from Coherence Fucntions in Astronomy, ed. C. van Schoonedveld (D. Reidel), IAU Proc., 49, 61

Frater, R. H., & Docherty, I. S. 1980, A&A, 84, 75

Goldsmith, P. F. 1998, Gaussian Beam, Quasioptical Propagation and Applications (IEEE Press)

Gueth, F., Guilloteau, S., & Viallefond, F. 1995, in The XXVIIth Young European Radio Astronomers Conference, ed. D. A. Green, & W. Steffen, 8

Hamaker, J. P., Bregman, J. D., & Sault, R. J. 1996, A&AS, 117, 137

Högbom, J. A. 1974, A&AS, 15, 417

Holdaway, M. A., & Foster, S. M. 1994, On-The-Fly Mosaicing, ALMA memo, 122

Mangum, J. G., Emerson, D. T., & Greisen, E. W. 2007, A&A, 474, 679

Narayan, R., & Nityananda, R. 1986, ARA&A, 24, 127

Pety, J., Gueth, F., & Guilloteau, S. 2001, Impact of ACA on the Wide-Field Imaging Capabilities of ALMA, ALMA memo, 398

Press, W. H., Teukolsky, S. A., Vetterling, W. T., & Flannery, B. P. 1992, Numerical Recipes in C, 2nd edn. (Cambridge University Press)

Rodríguez-Fernández, N. J., Pety, J., & Gueth, F. 2008, Single-dish observation and processing to produce the short-spacing information for a millimeter interferometer, IRAM memo, 2008-2

Rodríguez-Fernández, N. J., Pety, J., & Gueth, F. 2009, Imaging of interferometric On-The-Fly observations: Context and discussion of possible methods, IRAM memo, 2009-2

Sault, R. J., Hamaker, J. P., & Bregman, J. D. 1996a, A&AS, 117, 149

Sault, R. J., Staveley-Smith, L., & Brouw, W. N. 1996b, A&AS, 120, 375

Sault, R. J., Bock, D. C.-J., & Duncan, A. R. 1999, A&AS, 139, 387

Schwab, F. R. 1984, AJ, 89, 1076

Sramek, R. A., & Schwab, F. R. 1989, Synthesis Imaging in Radio Astronomy, Conf. Ser. (ASP), 117

Thompson, A. R., Moran, J. M., & Swenson, G. W. J. 1986, Interferometry and Synthesis in Radio Astronomy (John Wiley & Sons)

IRAM Memo 2011-2

WIFISYN: The GILDAS implementation of a new wide-field synthesis algorithm*

J. Pety[1,2], N. Rodriguez-Fernandez[1]
1. IRAM (Grenoble)
2. Observatoire de Paris

Jan, 19th 2011
Version 0.1

Abstract

The usual way to image wide-field interferometric observations is known as mosaicking. Different variants of mosaicking exist (*e.g.* Cornwell, 1988; Sault et al., 1996), including an interesting recent implementation of mosaicking in the *uv* plane (golap et al., priv. comm.). Pety & Rodríguez-Fernández (2010) revisited the theory of wide-field imaging to propose a different algorithm to image interferometric wide-field observations, based on the well-known Ekers & Rots' scheme. This algorithm is named wide-field synthesis because it *explicitely* synthesizes the wide-field spatial frequencies throughout the *uv* plane. This memo describes the current state of the implementation of this algorithm in a new package, named WIFISYN, of the GILDAS software suit.

*This work was mainly funded by the European FP6 "ALMA enhancement" grant. It was also partially funded by the grant ANR-09-BLAN-0231-01 from the French *Agence Nationale de la Recherche* as part of the SCHISM project.

Contents

1 Introduction **3**

2 Theory **3**
2.1 Observation setup and measurement space . . . 3
2.2 Processing by explicit synthesis of the wide-field spatial frequencies . . . 5

3 Practice **5**
3.1 Simulating a wide-field observation . . . 5
3.2 Fourier transform along α_s and β_s . . . 7
3.2.1 Gridding . . . 7
3.2.2 Reordering . . . 8
3.2.3 Wide-field synthesis . . . 9
3.3 Shifting and averaging . . . 11
3.4 Getting the dirty image through inverse Fourier transform . . . 11

4 Conclusion **12**

A Implementation plan **14**

B WIFISYN Language Internal Help **17**
B.1 Language . . . 17
B.2 COMPLEX . . . 17
B.3 FFT . . . 17
B.4 LOAD . . . 18
B.5 READ . . . 18
B.6 SETUP . . . 18
B.7 UVBEAM . . . 18
B.8 UVGRID . . . 18
B.9 UVMAP . . . 18
B.10 UVSYMMETRY . . . 19
B.11 VARIABLE . . . 19
B.12 WIFI2VISI . . . 19
B.13 WRITE . . . 19

1 Introduction

The usual way to image wide-field interferometric observations is known as mosaicking. Different variants of mosaicking exist (*e.g.* Cornwell, 1988; Sault et al., 1996), including an interesting recent implementation of mosaicking in the *uv* plane (golap et al., priv. comm.). Pety & Rodríguez-Fernández (2010) revisited the theory of wide-field imaging to propose a different algorithm to image interferometric wide-field observations, based on the well-known Ekers & Rots' scheme. This algorithm is named wide-field synthesis because it *explicitely* synthesizes the wide-field spatial frequencies throughout the *uv* plane. This memo describes the current state of the implementation of this algorithm in a new package, named WIFISYN, of the GILDAS software suit. The first section summarizes the ideas underlying the proposed algorithm. The second section demonstrates the different steps taken to implement the algorithm (*i.e.* simulation, gridding, Fourier transform along the scanned sky coordinates to synthesize the wide-field visibilities, application of a shift-and-average operator to obtain the wide-field *uv* plane and inverse Fourier transform to yield the dirty image). We conclude on the additional needed steps to use this new algorithm on a daily basis. Appendix A includes the implementation plan written before coding WIFISYN. Appendix B includes the document of the current user interface of the WIFISYN package.

2 Theory

Figure 1 illustrates the principles underlying 1) the setup to get interferometric wide-field observations and 2) our proposition to process them. For simplicity, we display the minimum possible complexity without loss of generality. The top row displays the sky plane. The middle row represents the 4-dimensional measurement space at different stages of the processing.

2.1 Observation setup and measurement space

Panel a) displays the sky region for which we aim for estimating the sky brigthness, $I(\alpha)$. The field of view of an interferometer observing in a given direction of the sky has a typical size set by the primary beam shape. In our example, this is illustrated by any of the circles whose diameter is $\theta_{\rm prim}$. As we aim at observing a wider field of view, *e.g.* $\theta_{\rm field}$, the interferometer needs to scan the targeted sky field. We assume that we scan through stop-and-go mosaicking, ending up with a 7-field mosaic.

After calibration, the output of the interferometer is a visibility function, $V(u_p,\alpha_s)$, whose relation to the sky brightness is given by the measurement equation

$$V(u_p,\alpha_s) = \int_{\alpha_p} B(\alpha_p-\alpha_s)\, I(\alpha_p)\, {\rm e}^{-i2\pi\alpha_p u_p}\, {\rm d}\alpha_p, \quad (1)$$

where V is the visibility function of 1) u_p (the spatial frequency with respect to the fixed phase center) and 2) α_s (the scanned sky angle), I is the sky brightness, and B the antenna power pattern or primary beam of an antenna of the interferometer. Panel b.1) shows the measurement space as a mosaic of single-field *uv* planes: The *uv* plane coverage of each single-field observation is displayed as a blue sub-panel at the sky position where it has been measured and which is featured by the red axes. We assume 1) that the interferometer has only 3 antennas and 2) that only a single integration is observed per sky position. This implies only 6 visibilities per single-field *uv* plane.

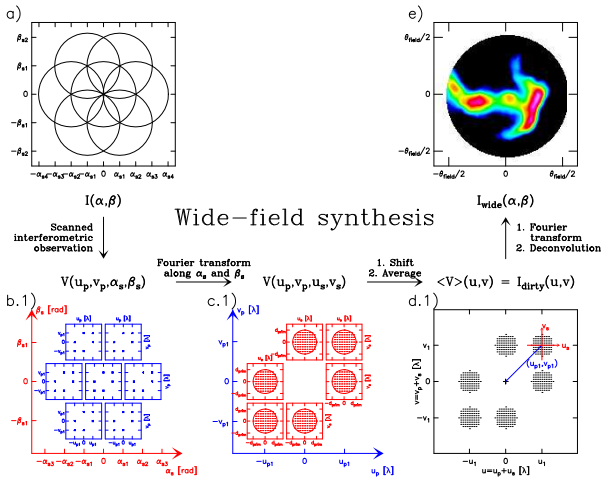

Figure 1: Illustration of the principles of wide-field synthesis, which enables us to image wide-field interferometric observations. The top row displays the sky plane. The bottom row displays the 4-dimensional visibility space at different stages of the processing. In panels b) to d), the scanned dimensions (α_s and u_s) are displayed in blue while the phased spatial scale dimensions (u_p) are displayed in red and the spatial scale dimensions (u) of the final wide-field uv plane are displayed in black. In detail, panel a) shows a possible scanning strategy of the sky to measure the unknown brightness distribution at high angular resolution: For simplicity it is here just a 7-field mosaic. Panel b.1) and b.2) sketch the space of measured visibilities: The uv plane at each of the 7 measured sky positions is displayed as a blue square box in panel b.1) and a blue vertical line in panel b.2). For simplicity, only 6 visibilities are plotted in panel b.1). Panels c.1) and c.2) sketch the space of synthesized visibilities after Fourier transform of the measured visibilities along the scanned coordinate (α_s): At each measured spatial frequency u_p (displayed on the blue axes) is associated one space of synthesized wide-field spatial frequencies displayed as one of the red squares in panel c.1) and the red vertical lines in panel c.2). The wide-field spatial scales are synthesized 1) on a grid whose cell size is related to the total field of view of the observation and 2) only inside circles whose radius is the primary diameter of the interferometer antennas. Panels d.1) and d.2) display the final, wide-field uv plane. This plane is built by application of a shift-and-average operator. Inverse Fourier transform and deconvolution methods then produce a wide-field distribution of sky brightnesses as shown in panel e).

2.2 Processing by explicit synthesis of the wide-field spatial frequencies

All the information about the sky brightness, $I(\alpha)$, is somehow coded in the visibility function, $V(u_p,\alpha_s)$. The high spatial frequencies (from $d_{\rm min}$ to $d_{\rm max}$) are clearly coded along the u_p dimension. The uncertainty relation between Fourier conjugate quantities also implies that the typical spatial frequency resolution along the u_p dimension is only $d_{\rm prim}$ because the field of view of a single pointing has a typical size of $\theta_{\rm prim}$. However, wide-field imaging implies measuring all the spatial frequencies with a finer resolution, $d_{\rm field} = 1/\theta_{\rm field}$. The missing information must then be hidden in the α_s dimension.

Pety & Rodríguez-Fernández (2010) show that Fourier transforming the measured visibilities along the α_s dimension (*i.e.* at constant u_p) can synthesize the missing spatial frequencies, because the α_s dimension is sampled from $-\theta_{\rm field}/2$ to $+\theta_{\rm field}/2$, implying a typical spatial-frequency resolution of the u_s dimension equal to $d_{\rm field}$. Conversely, the α_s dimension is probed by the primary beams with a typical angular resolution of $\theta_{\rm prim}$, implying that the u_s spatial frequencies will only be synthesized inside the $[-d_{\rm prim},+d_{\rm prim}]$ range. Panel c) illustrates the effects of the Fourier transform of $V(u_p,u_s)$ along the α_s dimension. The red subpanels display the u_s spatial frequencies around each constant u_p spatial frequency.

In panel d) (*i.e.* after the Fourier transform along the α_s dimension), $\overline{V}(u_p,u_s)$ contains all the measured information about the sky brightness in a spatial frequency space. However, the information is ordered in a strange and redundant way. Indeed, we show that $\overline{V}(u_p,u_s)$ is linearly related to $\overline{I}(u_p+u_s)$. To first order, the information about a given spatial frequency u is stored in all the values of $\overline{V}(u_p,u_s)$ which verifies $u = u_p + u_s$.

A shift operation will reorder the spatial scale information and averaging will compress the redundancy (illustrated by the halving of the number of the space dimensions). The use of a shift-and-average operator thus produces a final uv plane containing all the spatial scale information to image a wide field in an intuitive form. We thus call this space the *wide-field uv plane*. Panel d) displays this space, where the minimum relevant spatial frequency is related to the total field of view, while the maximum one is related to the interferometer resolution.

Applying the shift-and-average operator to $\overline{V}$ produces the Fourier transform of a dirty image, which is a local convolution of the sky brightness by a slowly varying dirty beam (Pety & Rodríguez-Fernández, 2010). As a result, inverse Fourier transform of $\langle\overline{V}\rangle$ and deconvolution methods will produce a wide-field distribution of sky brightness as shown in panel e) at the top right of Fig. 1.

3 Practice

In the real world, the visibility function is not only sampled, but this sampling is incomplete for two main reasons. 1) The instrument has a finite spatial resolution, and the scanning of the sky is limited, implying that the sampling in both planes has a finite support. 2) The uv coverage and the sky-scanning coverage can have holes caused either by intrinsic limitations (*e.g.* lack of short spacings or small number of baselines) or by acquisition problems (implying data flagging).

3.1 Simulating a wide-field observation

In order to test the implementation, we need a controlled data set. We simulated the simplest meaningful case, *i.e.*, a point source at the phase center (at the position of the famous Horsehead

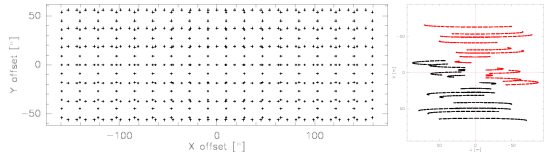

Figure 2: Sky and uv coverage of a simulated interferometric on-the-fly observation with the Plateau de Bure interferometer. **Left:** Each cross display the average sky position attributed to a set of visibilities recorded during one integration time. The center of the coordinate system is the phase center. **Right:** Each cross display the uv position of a measured visibilities whatever the associated sky position. The black crosses are measured. The red ones are deduced from the Hermitian symmetry of the visibilities.

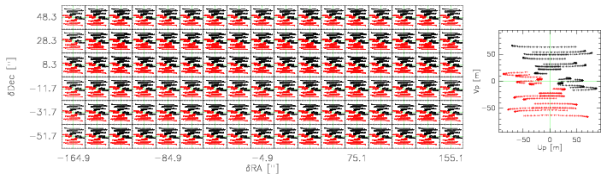

Figure 3: Chessboard display of the uv planes. **Left:** Each panel display the uv coverage of all the visibilities whose position on the sky falls in a 20″-range around the displayed sky coordinate. **Right:** Typical zoom of one of the uv coverages displayed left.

nebula in the Orion molecular cloud). We choose to simulate observations with the Plateau de Bure Interferometer because it allows us to clearly test the effect of incomplete instantaneous uv sampling due to the limited number of available antennas. The most compact configuration (D-configuration) was selected offering baseline length up to about 120 m. We simulated observations at the frequency of the ^{13}CO (J=1–0) line, *i.e.* 110.201 GHz or 2.72 mm. At this frequency, the primary beamwidth of 15m-antenna is 44.9″.

We simulated On-The-Fly observations covering a total field of view of 300″ × 100″, which converts into the observation of about 17 independent fields. The field of view is rectangular to explore the effect of non-square pixels in the uv planes. We scanned the source along two perpendicular direction, named hereafter lambda and beta. The distance between two consecutive rows ensures Nyquist sampling, *i.e.*, $\lambda/D = 18.7''$. We sampled along the scanning direction at 5 points per primary beamwidth along the scanning direction to decrease the effect of beam elongation. We dumps at a rate of 0.5 Hz, *i.e.*, one dump every two seconds. These two last considerations implies a scanning velocity of 4.5″ per second. We observed one full track, *i.e.*,

during 9 consecutive hours alterning beta and lambda coverage in a loop with 5 minutes calibration measurements intersperse every 20 minutes. Each lambda or beta coverage lasts about 16 minutes. There were thus 47 coverages observed in total. Taking into account various overheads (*e.g.*, slew time between rows) and shadowing (about 13% of the visibilities lost), we estimate the observing efficiency to be about 60%, *i.e.* 60% of the time is spent on-source. We end up with a data set of 148 147 visibilities. If the data was imaged through standard mosaicking, it would imply between 500 and 10 000 actual fields depending on the acquisition system. Indeed, it is difficult to ensure that each scanning line always starts at exactly the same position on-sky for each coverage as it is ideally assumed in this simulation.

Fig. 2 separately displays the sky and uv coverage, each cross representing one measure. In reality, the uv coverage *a priori* depends on the position of the sky because of the Earth rotation. Fig. 3 thus display the uv coverage as a function of the position on the sky through a chessboard display. Each case of the chessboard displays the all the uv measures which falls in a 20″-range around the marked sky coordinate. The uv coverage is qualitatively similar over the full field of view as a result of the observing strategy. The left panel of Fig. 3 is a zoom of one of the uv coverages shown on the chessboard. The uv coverage displayed on Fig. 2 is much densely populated than any of the individual uv coverages.

3.2 Fourier transform along α_s and β_s

We want to Fourier transform the raw visibilities along the sky dimension (α_s and β_s) at some constant value of u_p and v_p. The raw data, however, is sampled on an irregular grid in both the uv and sky planes. We need to grid the measured visibilities in both the uv and the sky planes before Fourier transformation for different reasons. First, the gridding in the uv plane will handle the variation in the spatial frequency as the sky is scanned, *i.e.*, the difficulty and perhaps the impossibility of Fourier-transforming at a completely constant (u_p,v_p) values. Second, the gridding along the sky dimension enables the use of Fast Fourier Transforms.

3.2.1 Gridding

As usual, we grid through convolution and regular resampling. The visibilities must be convolved in 4 dimensions (α_s, β_s, u_p and v_p). For simplicity sake's, the convolution kernel is just the product of 4 one-dimensional functions along each convolution dimension. We used the standard spheroidal functions (cf. Fig. 4), whose Fourier transforms die off as quickly as themselves. This is a desirable mathematical property in processing interferometry data because it limits aliasing.

Fig. 5 displays the amplitude of the grided 4D visibility cube using a chessboard display, *i.e.* a set of uv images positionned at their right place in the (δRA,δDec) sky coordinate system. The first obvious visual impression when the color scale is linear is that the visibility amplitude decreases isotropically as the distance from the point source position (at the center of the coordinate system) increases. Indeed, the decrease in amplitude mimic the primary beam shape which was used to similate the visibilities, *i.e.* a Gaussian of 44.9″-beamwidth. The same chessboard is also displayed with a logarithmic color scale to emphasize edge effects. The gridded visibilities "abruptly" go to zero following an almost rectangular pattern. This is just the consequence of gridding along rectangular axes a limited field of view (the observed one) while the Gaussian primary beam has an unlimited support.

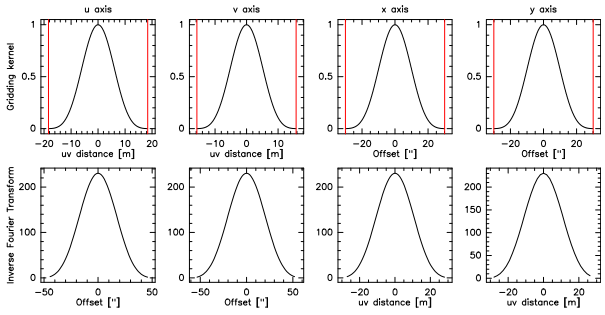

Figure 4: Convolution kernels used to grid the visibilities along the u_p (first column), v_p (second column), α_s (third column) and β_s (fourth column) dimension. The top row displays the used kernels while the bottom row displays their Fourier transform. The vertical red lines show the size of the support over which the kernels are computed and used.

The left panel is a zoom of the image displayed at the point source position on the chessboard. The visibility amplitude results here from the combination of the true visibility function (*i.e.*, a Gaussian for a point source at the phase center) and of the density and quality of the measurements at the considered position on the sky (because we grid the weighted visibilities, uV, and not just the visibilities themselves, V). The images on the chessboard ressembles each other to first order because the uv coverage is similar over the whole field of view.

3.2.2 Reordering

The chessboards in Fig. 5 display the u_p and v_p visibility planes at constant values of α_s and β_s. However, we want to Fourier transform the grided visibilities along the sky dimensions (α_s and β_s) at constant value of u_p and v_p. We thus reorder in Fig. 6 the chessboards so that they display the α_s and β_s visibility planes at constant values of u_p and v_p. Nothing is actually done on the visibility cube itself, it is just a change in the way it is displayed. We note that we now recognize on the chessboard display the footprint of the uv plane sampling. Each image of the chessboards looks like the two zooms, which clearly show the Gaussian shape of the beam centered on the point source position. In particular, the images of the chessboards here are rectangular[1] (to keep the ratio aspect of the $\alpha_s\beta_s$ planes).

[1]This is better seen on the chessboard with a logarithmic color scale.

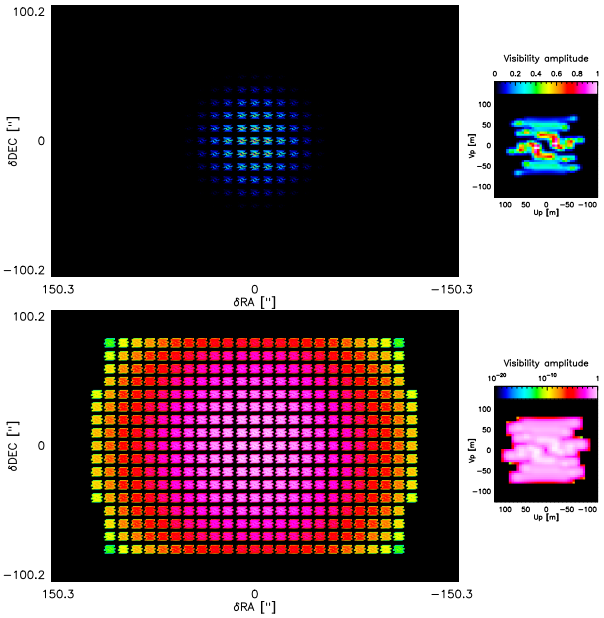

Figure 5: Chessboard display of the visibility amplitudes after the 4-dimensional gridding. The amplitudes were arbitrarily normalized to get a maximum value of 1 because this allows the reader to easily quantify the dynamic at which potential artifacts arise. **Left:** Each panel display the image of the visibility amplitude at constant value of the sky coordinates (α_s,β_s) and as a function of the uv coordinates (u_p,v_p). **Right:** Typical zoom of one of visibility amplitude images. **Top:** The color scale is linear. **Bottom:** The color scale is logarithmic.

3.2.3 Wide-field synthesis

The chessboards in Fig. 9 display the visibility amplitude after Fourier transform along the (α_s,β_s) dimensions at constant (u_p,v_p). We thus obtain a chessboards of (u_s,v_s) planes at their positions

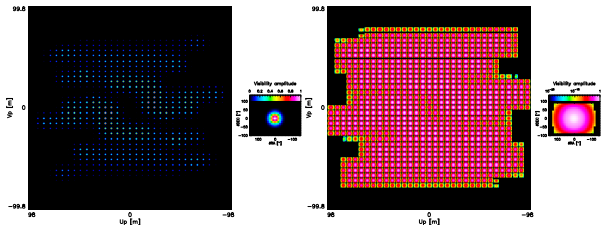

Figure 6: Same as Fig. 5 after reordering of the axes, *i.e.* each panel display the image of the visibility amplitude at constant value of the uv coordinates (u_p,v_p) and as a function of the sky coordinates (α_s,β_s).

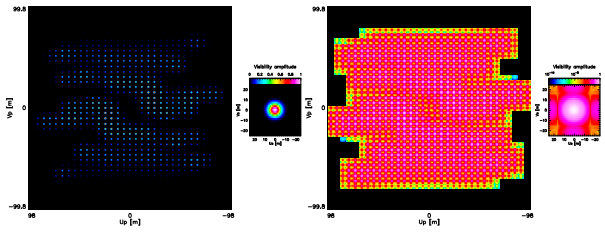

Figure 7: Chessboard display of the amplitudes of the synthesized wide-field visibilities after direct Fourier transform along the α_s and β_s axes at constant (u_p,v_p) values. The amplitudes were arbitrarily normalized to get a maximum value of 1. **Left:** Each panel display the image of the visibility amplitude at constant value of the wide scale uv coordinates (u_s,v_s) and as a function of the narrow scale uv coordinates (u_p,v_p). **Right:** Typical zoom of one of visibility amplitude images. **Top:** The color scale is linear. **Bottom:** The color scale is logarithmic.

in the (u_p,v_p) plane. The Fourier transform of a Gaussian is a Gaussian. The zoom panels thus display to first order a Gaussian shape of full width at half maximum of about 15 m (*i.e.* the bure antenna diameter). The zoom panel using a logarithmic color scale clearly shows departure from the Gaussian shapes at the edges of the image because of the presence of "abrupt" edges in Fig. 6. This is at this step that the wide-field visibility are synthesized, although they are ordered in an unnatural way.

3.3 Shifting and averaging

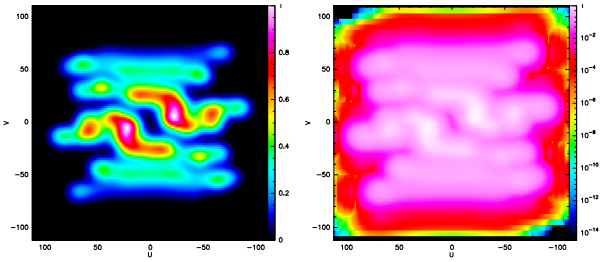

Figure 8: Wide-field 2D uv plane after shifting-and-averaging the wide-field 4D uv plane displayed in Fig. 7. The amplitudes were arbitrarily normalized to get a maximum value of 1. **Right:** The color scale is linear. **Left:** The color scale is logarithmic.

After the wide-field synthesis step, we obtain a 4D wide-field visibility cube for which each final uv spatial frequency (u,v) is measured for every (u_p,v_p,u_s,v_s) such that $u = u_p + u_s$ and $v = v_p + v_s$. The use of a shift-and-average operator allows us to get an intuitive wide-field uv plane because this first reorders the spatial frequencies at their right place and this then compresses them.

Fig. 8 display the wide-field uv plane, which results from this operation. It can be shown that the properties of the measurement equations imply that this wide-field uv plane must comply with the Hermitian symmetry, *i.e.* $V(u,v) = V^\star(-u,-v)$. This is equivalent to state that the dirty image must be real. However, this Hermitian symmetry is only approximately enforced when the shift-and-average operator is used blindly over the 4D wide-field visibility cube, probably due to rounding errors. We thus enforces the Hermitian symmetry through 1) computation of only half of the wide-field uv plane (the one with negative values of v) and 2) deduction of the other half using the Hermitian symmetry.

3.4 Getting the dirty image through inverse Fourier transform

Once the wide-field uv plane is available, the dirty image is obtained by taking the real part of the 2D Fourier transform of this plane. The top panel of Fig. 9 displays this dirty image, which clearly shows a point source at the phase center. As this image is the response of the wide-field synthesized interferometer to a point source located at the phase center, it can be interpreted at the dirty beam at the phase center. In this framework, the side-lobes peaks at about 10% and there is a negative bowl surrounding it because of the missing zero-spacing. The bottom panel shows the absolute value of the dirty image with a logarithmic color scale to display the levels at which appear different kind of artefacts. Aliasing replications appear between 10^{-2} and 10^{-5}

of the peak (yellow-red replications of the main blob along the two main axes) and they become pronounced between 10^{-5} and 10^{-7} of the peak (green strips).

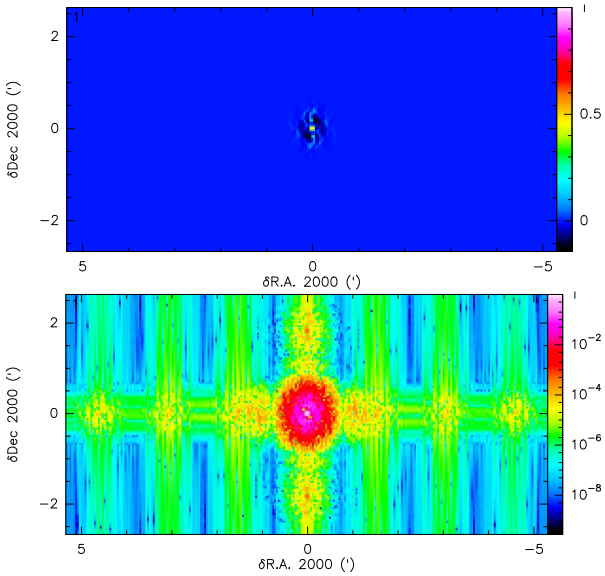

Figure 9: Dirty image after inverse Fourier transform of the wide-field 2D *uv* plane displayed in Fig. 8. The images were arbitrarily normalized to get a maximum value of 1. **Top:** The dirty image is displayed with a linear color scale. **Bottom:** The absolute value for the dirty image is displayed with a logarithmic color scale.

4 Conclusion

This memo describes the first implementation in the GILDAS software suit of the wide-field synthesis imaging algorithm, proposed in Pety & Rodríguez-Fernández (2010). It shows good promise

to process the large datasets produced by the on-the-fly interferometric observing mode. The current implementation does not yet include deconvolution, a mandatory step to get clean images compatible with the sky brightness distribution of the observed source. As a first step in this direction, we computed the sets of wide-field dirty beams associated with the observation. Indeed, the dirty beam slowly varies with the position of the sky because of the shift-variant nature of interferometric wide-field observations. Using these dirty beams, standard CLEAN deconvolution algorithms will be adapted to our imaging algorithm.

Acknowledgments. The authors thank S. Guilloteau for useful discussions at early stages of the WIFISYN implementation.

References

Cornwell, T. J. 1988, A&A, 202, 316

Pety, J. & Rodríguez-Fernández, N. 2010, A&A, 517, A12+

Sault, R. J., Staveley-Smith, L., & Brouw, W. N. 1996, A&AS, 120, 375

A Implementation plan

This appendix displays the implementation plan written when the GILDAS prototype was started.

```
* Step #1: Reading the uv and the xy (short-spacings) tables
    - Substeps (READ OTF)
        + Read uv if available, results:
            o Measured uv and sky positions (4 columns: up,vp,as,bs)
            o Measured weights (nf columns)
            o Measured visibilities (2*nf columns)
        + Read xy if available, results:
            o Measured sky positions (2 real columns: as,bs
                                      2 virtual columns: up=0,vp=0)
            o Measured weights (nf columns)
            o Measured brightness (2*nf columns)
        + If uv and xy available then
            o Check consistency (spatial and frequency coordinates)
              of UV and XY tables
            o Crop XY table to a reasonable size
            o Convert XY into jansky
            o Merge both tables (The origin of the data must be kept as
              additional columns)
    - Results
        + Measured uv and sky positions (4 columns: up,vp,as,bs)
        + Measured weights (nf columns)
        + Measured visibilities (2*nf columns)
    - Comments
        + We probably want to read several uv table coming from different
          instruments (e.g. ALMA + ACA). The difficulty is not so much in
          reading and merging the tables but in assigning the correct
          transfer function to the correct visibilities.

* Step #2: Analysis of the data and definition of the tasks
    - Substeps:
        + Sorting the visibilities in 3D if not already done
        + Definition of the grid axes
        + Definition of the kernels
    - Results:
        + Sorted uv table
        + Grided uv and sky axes (4 axes: upg,vpg,asg,bsg)
        + Gridding Kernels (spheroidals)
    - Comments:
        + The gridding function should depend on the kind of antennas

* Step #3: Gridding
    - Substeps:
```



```
        + Convolution of weighted visibilities
        + Convolution of weights
    - Results:
        + Grided weights (5D cube: upg,vpg,asg,bsg,nu)
        + Grided visibilities (5D cube: upg,vpg,asg,bsg,nu)
    - Comments:
        + No gridding correction

* Step #4: 2D DFFT along sky dimensions
    - Substeps:
        + 2D DFFT of grided visibilities
        + Transformed weights (Hyp: independent weights before 2D FFT)
    - Results:
        + Synthesized visibilities (5D cube: upg,vpg,usg,vsg,nu)
        + Transformed weights (5D cube: upg,vpg,usg,vsg,nu)

* Step #5: Shift-and-average
    - Substeps:
        + Definition of the weighting function (using the transformed
          weights, 5D cube: upg,vpg,usg,vsg,nu)
        + Shift-and-average data
    - Results:
        + Wide-field visibilities (3D cube: u,v,nu)

* Step #6: 2D IFFT
    - Substeps:
        + 2D IFFT of wide-field visibilities
    - Results:
        + Dirty image   (3D cube: a,b,nu)

* Step #7: Computation of the dirty beams
    - Substeps:
        + Computation of the transfer functions of the single-dish and
          interferometer antennas
        + Computation of a uv table corresponding to point sources at
          position where the dirty beams must be computed
            Sft(up,vp,as,bs,us",vs",nu) = S(up,vp,as,bs,nu).T(us",vs",nu).exp-(i.2.pi.us".as)
          Results: A set of uv tables
        + Loop over steps 3 to 6 on each table and store the dirty beams
        + Fit of clean beams on the dirty beams
    - Results:
        + Set of dirty beams (5D cube: a',b',a",b",nu)
        + Set of clean beams (4D cube: (major,minor,angle),a",b",nu)
    - Comments:
        + If only the width of the beam and not its shape varies with
          the frequency, then we can apply a dilatation of the coordinates
```

as a function of frequency, implying the computation of a single dirty beam for all the frequencies.

B WIFISYN Language Internal Help

This appendix describes the user interface of the WIFISYN package.

B.1 Language

```
COMPLEX    : Transfer complex internal buffers into SIC real images and
             vice-versa
FFT        : Compute direct or inverse FFT of internal buffers
LOAD       : Load an internal buffer into a SIC variable
READ       : Read the input files in internal buffers
SETUP      : Setup and display the imaging parameters for the internal
             uvxy table
UVBEAM     : Compute the dirty beams associated to the internal uvxy
             table
UVGRID     : Grid the internal uvxy table
UVMAP      : Compute the dirty image associated to the internal uvxy
             table
UVSHIFT    : Shift the phase center of the internal uvxy table
             (Not working yet)
UVSORT     : Sort the internal uvxy table
             (Not working yet)
UVSWAP     : Swap the UVT and UVR buffers
             (Not working yet)
UVSYMMETRY : Check the Hermitian symmetry of the internal buffers
VARIABLE   : Map the imaging internal parameters onto the WIFI% SIC
             structure
WIFI2VISI  : Shift-and-average the wide-field hypercube to get a
             ''standard'' visibility plane
WRITE      : Write internal buffers into output files
```

B.2 COMPLEX

[WIFISYN\]COMPLEX VISICUBE|WIFICUBE TO|FROM AMPLITUDE|PHASE|REAL|IMAGINARY

Transfer complex internal buffers (visicube or wificube) into SIC real images for display. The inverse operation is possible to set or to modify the complex internal buffers.

B.3 FFT

[WIFISYN\]FFT VISICUBE|WIFICUBE /DIRECT|INVERSE /UV|XY

Compute the direct or inverse 2D Fast Fourier Transform of internal complex buffers (visicube or wificube). When the FFT is applied to the wificube buffer, the 2D FFT can be applied along either the uv or the xy

axes.

B.4 LOAD

[WIFISYN\] LOAD Buffer Varname

Load the specified internal buffer (VISI, WEIGHT, BEAM, DIRTY) into the specified SIC variable (Varname).

B.5 READ

[WIFISYN\]READ Buffer File [/PLANE First Last]

Read the specified internal buffer (UV, BEAM, DIRTY) from the specified input File. Default extensions are respectively .tuv, .beam, .lmv. A range of channels can be specified using the /PLANE option.

B.6 SETUP

[WIFISYN\]SETUP

Setup and display the imaging parameters for the internal uvxy table.

B.7 UVBEAM

[WIFISYN\]UVBEAM

Compute the dirty beams associated to the internal uvxy table.

B.8 UVGRID

[WIFISYN\]UVGRID [/NOCONV]

Grid the internal uvxy table into a wificube. The /NOCONV option creates the wificube of the right dimension and initializes it so that the user can fill it through the COMPLEX command.

B.9 UVMAP

[WIFISYN\]UVMAP

Compute the dirty image associated to the internal uvxy table. This command is equivalent to the following sequence: SETUP, UVGRID, FFT WIFI /DIRECT /XY, WIFI2VISI, FFT VISI /INVERSE, COMPLEX VISI TO REAL.

B.10 UVSYMMETRY

[WIFISYN\]UVSYMMETRY

Check the Hermitian symmetry of the wificube (or visicube???) buffer.

B.11 VARIABLE

[WIFISYN\]VARIABLE

Map the imaging internal parameters onto the WIFI% SIC structure.

B.12 WIFI2VISI

[WIFISYN\]WIFI2VISI

Shift-and-average the wide-field hypercube to get a ''standard'' visibility UV plane, which can then be FFTed to get the dirty image.

B.13 WRITE

[WIFISYN\]WRITE Buffer File [/PLANE First Last]

Write the specified output File from the specified internal buffer (UV, BEAM, DIRTY). Default extensions are respectively .tuv, .beam, .lmv. A range of channels can be specified using the /PLANE option.

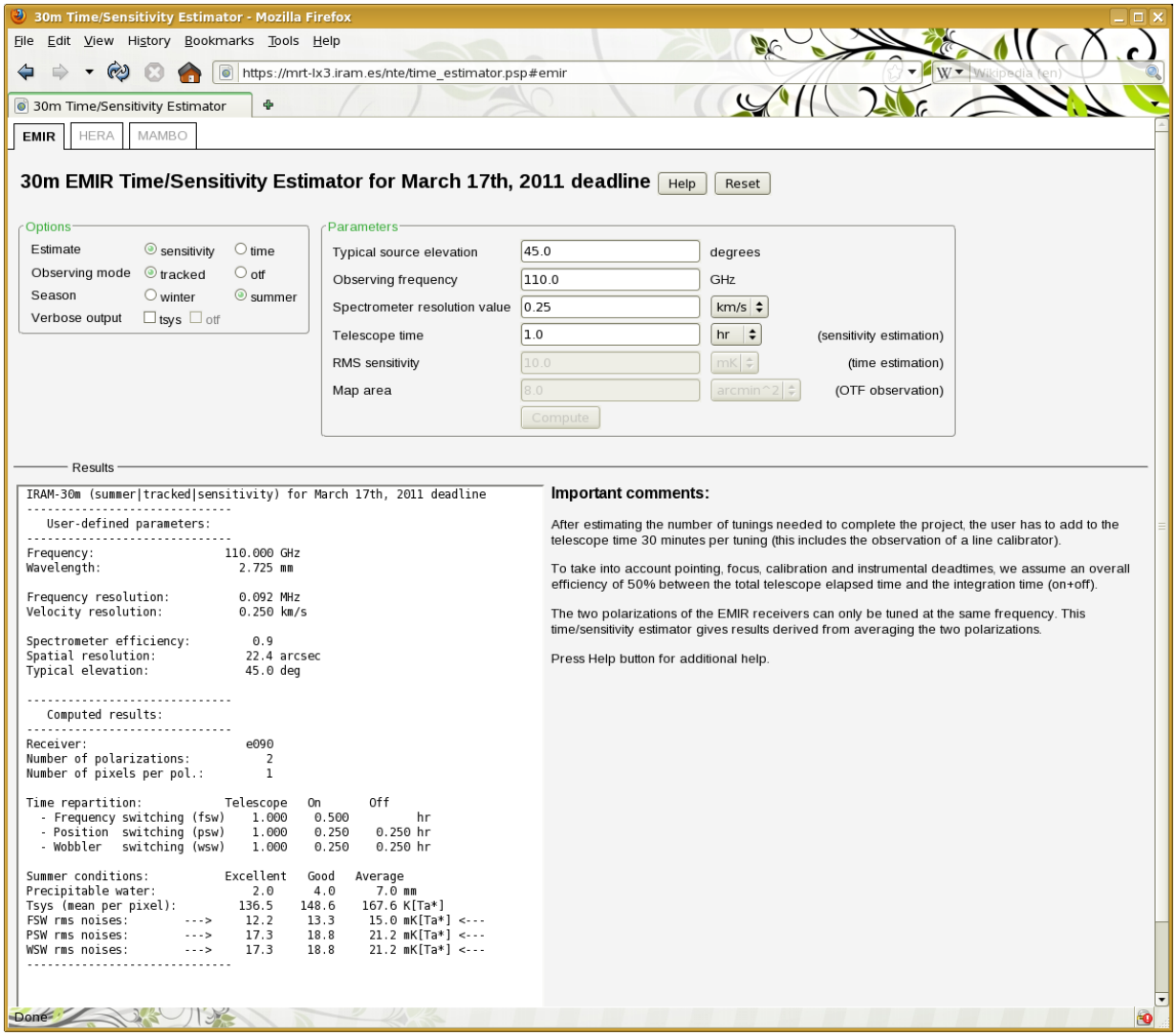

Copyright: IRAM/GILDAS

Chapitre 8

Gestion des logiciels GILDAS

8.1 Présentation et contexte

GILDAS (http ://www.iram.fr/IRAMFR/GILDAS) est un ensemble de logiciels (state-of-the-art) orientés vers la réduction de données de radioastronomie (sub)-millimétrique, qu'elles proviennent d'une antenne unique ou d'un interféromètre. GILDAS comprend environ 425 000 lignes de code exécutable (c.-à-d. hors commentaires ou documentation) et il est structuré en deux parties : 1) un cœur, nommé GREG, qui délivre 1) les services communs tels qu'une bibliothèque graphique et 2) les logiciels astronomiques proprement dit : ASTRO, CLASS, CLIC,

MAPPING... GILDAS est disponible pour de nombreux systèmes allant de Linux à Windows en passant par Mac/OSX. Il est ainsi possible de l'utiliser sur un portable ou sur des stations de travail puissantes suivant les besoins. Il comprend des outils avancés, comme une réduction facile des données d'imagerie grand-champ provenant d'une antenne unique ou d'un interféromètre.

L'histoire de GILDAS a commencé en 1983 dans le Groupe d'Astrophysique de Grenoble. Aujourd'hui, c'est une partie essentielle des instruments de l'IRAM puisque c'est la suite de logiciels utilisée pour réduire les données provenant du télescope de 30m de l'IRAM et de l'interféromètre du Plateau de Bure. En conséquence, GILDAS est aujourd'hui principalement maintenu par des personnels IRAM avec des contributions de Grenoble/IPAG, de Bordeaux/LAB et de Paris/LERMA[1].

Par ailleurs, des parties de GILDAS sont utilisées ou considérées dans beaucoup d'autres contextes :

- CLASS (le logiciel utilisé pour réduire les données spectroscopiques de télescopes uniques) est utilisé de manière courante dans d'autres observatoires (Herschel, SOFIA, APEX, CSO, JCMT, NANTEN, ARO, Effelsberg, etc...).
- Le simulateur ALMA, construit en 2000-2001 pendant la phase de conception (voir la section précédente), est toujours utilisé par de nombreux scientifiques pour simuler la faisabilité d'observations ALMA à partir de diverses simulations de sources astrophysiques.
- Une large partie de l'analyse des caractéristiques des prototypes d'antennes d'ALMA (par exemple, la qualité de la surface des antennes par holographie ou la qualité du pointage) a été réalisée dans GILDAS. Aujourd'hui encore, les holographies des antennes sont réalisées sur le site (Atacama) dans GILDAS.

Une contrainte importante est ainsi que toute évolution de GILDAS pour servir les besoins de l'IRAM doit être pensée en gardant tous les autres utilisateurs à l'esprit.

La longue histoire de GILDAS prouve la robustesse de son design. Elle implique aussi une impressionnante accumulation d'expertise en radio-astronomie millimétrique, qui se traduit par une excellente adéquation entre les services offerts et les besoins des utilisateurs. Les développeurs historiques de GILDAS (P. Valiron, R. Lucas, S. Guilloteau, G. Duvert,...) se sont en grande partie tournés vers d'autres tâches au début des années 2000. Cela signifie que 1) l'expertise est transférée dans de nouveaux contextes et/ou instruments tels qu'ALMA (par exemple R. Lucas est aujourd'hui un des acteurs clés du commissioning d'ALMA) et 2) qu'il a fallu renouveler les développeurs GILDAS.

8.2 Assurer la continuité et la professionnalisation

J'ai ainsi eu deux objectifs principaux depuis que j'ai pris en main l'organisation de GILDAS fin 2002 : il s'est agi, en embauchant et en formant graduellement une nouvelle génération de développeurs, 1) d'assurer la continuité de GILDAS et 2) de professionnaliser le développement. C'est dans cette perspective que j'ai encadré les post-doctorats de P. Hily-Blant (actuellement

[1]En détail, l'équipe GILDAS est aujourd'hui composée de deux ingénieurs IRAM à temps plein (S. Bardeau et E. Reynier), deux ingénieurs IRAM à temps partiel (J.-C. Roche et M. Lonjaret), d'un ingénieur LERMA à temps partiel (B. Delforge à 10% jusque fin 2010) et de nombreux astronomes à temps partiel affiliés soit à l'IRAM (J. Pety, R. Zylka, H. Ungerechts, A. Sievers, V. Pietu, F. Gueth, A. Castro-Carrizo) soit à d'autres laboratoires (ESO, Chili : R. Lucas, LAB : S. Guilloteau, IPAG : S. Maret et P. Hily-Blant, Max Planck à Bonn : H. Wiesemeyer).

maître de conférence à Grenoble), V. Piétu (actuellement en CDI à l'IRAM pour s'occuper du logiciel de calibration des données interférométriques) et que j'encadre aujourd'hui le travail de quatre ingénieurs de niveau recherche (S. Bardeau J.-C. Roche, M. Lonjaret et E. Reynier, en contrat avec l'IRAM).

Parmi les activités vitales et consommatrices de temps bien qu'essentiellement invisibles de l'extérieur, nous avons 1) introduit l'usage d'outils de développement collaboratifs (par exemple CVS), 2) remis à plat la distribution de `GILDAS` (par exemple le système de compilation) et 3) maintenu ou réécrit les librairies communes pour les porter vers de nouveaux OS (par exemple Mac OSX), pour supporter de nouveaux standards (par exemple Fortran 2003, POSIX), pour introduire de nouvelles technologies (par exemple, le multi-threading). L'aide aux utilisateurs est une autre activité consommatrice de temps. Cela comprend l'écriture de documentation (toujours à compléter), le maintien de la page web (`http ://www.iram.fr/IRAMFR/GILDAS`) et les réponses à `gildas@iram.fr` où sont traités les commentaires, les questions et les rapports de bug (les temps médians de première et dernière réponse à une requête sont par exemple 11 et 32 heures). La section NEWS de la page web de `GILDAS` indique les changements intervenus dans chaque distribution mensuelle (3110 lignes entre la distribution de `nov03` et celle de `jan12`). Elle montre en particulier un renouvellement régulier des différentes parties de `GILDAS`.

Enfin, outre l'organisation du travail d'équipe et ma participation à la maintenance et à l'aide aux utilisateurs, je représente `GILDAS` tant à l'intérieur de l'IRAM (présentations à la direction, au Scientific Advisory Committee de l'IRAM) qu'à l'extérieur (présentations et démonstrations à des écoles ou des ateliers). Cela représente 50% de mon activité. La recherche sur les algorithmes d'imagerie grand-champ en interférométrie (cf. partie 7) a représenté une activité supplémentaire de 20% au cours des 5 dernières années.

8.3 Perspectives

La radio-astronomie millimétrique continue de connaître un développement instrumental considérable. Les sensibilités théoriques limites sont presque atteintes. Les bandes passantes instantanées se mesurent aujourd'hui en GHz et demain en dizaines de GHz. Les plans focaux commencent à être échantillonnés sur plusieurs minutes d'arc. Les surfaces collectrices augmentent fortement et les techniques radio sont de plus en plus utilisées à petite longueur d'onde. Dans ce contexte, les logiciels de réduction doivent se réinventer en permanence, mais pas forcément de zéro. L'expertise acquise et la compatibilité arrière sont des atouts considérables qu'il faut savoir faire fructifier. Avec l'avènement d'Herschel et d'ALMA, la question de l'avenir de `GILDAS` est souvent posée. Plutôt que de choisir un environnement logiciel produit pour un autre instrument, la politique actuelle de l'IRAM est de maintenir des logiciels de haute qualité pour ses instruments, tout en restant ouvert au monde extérieur. Cela se traduit par exemple par des développements précis mais si possible génériques, par la possibilité d'échanger les données avec d'autres environnements logiciels à travers l'utilisation de formats standards et l'adaptation de l'interface à des usages modernes (par exemple la possibilité d'interagir avec `GILDAS` à travers `python`).

IRAM Memo 2011-1

Preparing GILDAS for large datasets
I - GREG 2011*

S. Bardeau[1], E. Reynier[1], J. Pety[1,2]

1. IRAM (Grenoble)
2. Observatoire de Paris

06-apr-2011
version 1.3

Abstract

The size of the datasets produced by the IRAM instruments experience a tremendeous increase (because of multi-beam receivers, wide bandwidth receivers, spectrometers with thousands of channels, and/or new observing mode like the interferometric on-the-fly). Visualizing these datasets in a fluent way is a challenge, which requires the best use of the available hardware and operating systems (multi-cores processors and multi-window environments). This prompted a large rewriting of the part of the GILDAS kernel (known as GTV) in charge of the interface between the plotting facilities and the system. The main guidelines of this rewriting were 1) the backward compatibility when possible, 2) the use of modern standards as the multi-threading or the GTK+ toolkit, 3) the factorization of the source code for different OS (Linux, Mac OSX and MS Windows), 4) the implementation of new facilities like a PNG output or an interactive lens. This document thoroughly describes the improvements for the end-users and the programmers.

Keywords: multithreading, multiwindowing, the GIMP ToolKit (GTK+), Portable Network Graphics (PNG)
Related documents: *GreG documentation*, *Programming in GILDAS*

*This work was partially funded by the grant ANR-09-BLAN-0231-01 from the *French Agence Nationale de la Recherche* as part of the SCHISM project.

Contents

1 Why a new implementation of the GTV library? 3

2 The new cool things for the enthousiastic users 3

3 Requirements 4
3.1 Widget and graphic library . . . 4
3.2 Fortran compilers . . . 5

4 Changes for end-users 5
4.1 Behavior . . . 5
4.1.1 Removed . . . 5
4.1.2 Changed . . . 6
4.1.3 New . . . 6
4.2 Commands, variables, SIC logicals and symbols . . . 7

5 Changes for programmers 11
5.1 The new GTV overview . . . 11
5.2 Entry points . . . 12
5.2.1 Removed . . . 12
5.2.2 New . . . 13

A Exhaustive description of the changes in GTV 14
A.1 Commands . . . 14
A.1.1 Removed . . . 14
A.1.2 Changed . . . 16
A.1.3 New . . . 17
A.2 Variables . . . 18
A.2.1 Removed . . . 18
A.2.2 Changed . . . 19
A.2.3 New . . . 19
A.3 SIC logicals . . . 19
A.3.1 Removed . . . 19
A.3.2 New . . . 19
A.4 Symbols . . . 20
A.4.1 Removed . . . 20

1 Why a new implementation of the GTV library?

The `GreG` program lies on the so-called `GTV` library, a low level segment library. This library was written two decades ago, and not updated for several years. This was resulting in old-fashion graphical aesthetics for nowadays users, with some annoying constraints from other ages, e.g. windows which where not refreshed as often as the user would like.

For the maintainers point of view, the lack of experts of the source code was a big problem to fix bugs or improve any feature, especially with an old-fashion source code. Finally the status was usual rule in such a case: *"If you don't touch it you don't break it"*.

It was decided in 2007 to act before reaching the non-return point. In particular it was time to cut the dependency with the old widget library `Motif` (and its various implementations giving more or less satisfying results). The choice was made to use GTK instead, a well-known widget library for Linux users (but also supported on MS Windows and Mac OSX), and actively developed by the community. This was a first part of the work.

Another key piece is that GTV could only do one action at a time. By *action* one have to understand: storing a new plot coming from a user command, or drawing in one window, or plotting an hardcopy, etc. In particular this explains why the windows could not all be refreshed when desired. From the developers point of view, it was due to the fact that a large amount of the drawings were performed with global variables (some of them were internal to the library, but some others were the user property!). Thanks to modern Fortran features (namely derived types and pointers), the majority of the variables are not global anymore, but are passed to the drawing routines through a small number of structures describing the plot and its destination.

Finally, thanks to the above point, it was possible to implement GTV as a multi-threaded library: the user can work on its data while all its X windows are automatically refreshed or updated.

In this new context, the field is open for new and modern graphical tools. For example, a *lens* is already available: a popup window can be opened to zoom and browse a plotting window with the cursor. And more tools are already considered for the future.

2 The new cool things for the enthousiastic users

Will your life change with the new GTV? Well, not exactly, but consider these points:

- the GTV is now **multithreaded**: this means basically that the drawings and the flow of commands (including the data processing) are done in two different *threads*. With the efficient rewriting of the code and your multi-core machine, you will experience much more fluid graphics: the drawing events won't be slowed or postponed by the data processing, and vice-versa.
- **GTK+** is now used as the widget library. No more old-fashion windows, forms, or file browsing popups, they will look like what you are used to.
- **multi-windowing** is more user friendly: you can have several plots in several windows, all are refreshed in real time. No more `ZOOM REFRESH`: windows are always up-to-date. You

can also define the windows size and position with much more flexibility. The first window is not anymore forced to open in the top right corner of your screen: now YOU decide if your windows should open or not at a specific position.

- **zooming** is now easier and more interactive: a lens is now available at any time when center-clicking in any plotting window, and zooming/unzooming is done with the mouse wheel.
- tired of PostScript captures, rotations, and even color conversions? Now you can convert (hardcopy) your plot natively to the **PNG image format**. In particular, the background transparency is supported for an enhanced cosmetic of your presentations.

There also other things which will ease your life:

- **Encapsulated PostScripts** of landscape-oriented plots are not rotated anymore to portrait orientation. It is assumed that you will include it in another document (Latex source, presentation, etc): you will not have do derotate it back to landscape orientation.
- the **Look-Up-Table dynamics** has been increased from 128 to 65536 levels. You will not see anymore staircasing effects on smoothly-varying images.
- the so-called ***static* Look-Up Table mode** works now: you can use one Look-Up Table per image in a single window.
- the **GTV variables** have been merged under a few SIC structures: this avoids diluting your own variables into a large number of program variables.
- some **command and options** have been renamed for clarity, and to get rid of obsolete nomenclature. Among other things, you will not have anymore to figure out which one of the nine `CLEAR` flavors you need. For a smooth transition, GTV will recognize the old syntax commands and let you know what they should be replaced with. Some **variables, SIC logicals, and synbols** have also changed for the same reasons: you will find a summary of all the changes in the tables 2, 3, 4 and 5.
- N^2 **algorithms** in the source code are fixed. You think that `GO SPECTRUM` or `GO BIT` are taking ages on a big data cube, slowing down at a point you feel they will never finish? Try again now!
- no more **weird error messages** like *"Not enough colors"* or *"Too many images plotted"*: the internal limitations have been removed and you are now only limited by the physical memory of your computer.

And more will come in the future!

3 Requirements

3.1 Widget and graphic library

The GIMP ToolKit (GTK+) is now used as the widget library, while the GIMP Drawing Kit (GDK) is used as the graphic library. This choice ensures portable code and similar rendering on the three major sytems Gildas supports: Linux, Mac OSX, MS Windows. GTK+ and GDK are thus now a requirement in order to compile the Gildas kernel. They are provided together

on the system repositories as a unique package. Its presence on your system can be checked with the following command:

```
pkg-config --exists gtk+-2.0; echo $?
```

If a 0 is returned (i.e. no error), then you will be able to compile the new Gildas kernel. If another value is returned, you will need first to install the package.

The GTK+/GDK package has been tested between versions 2.10 and 2.22. Beyond this range, you can encounter GTK warnings or errors. Please report these to `gildas@iram.fr`, with your GTK version which you can find in the file `gtk/gtkversion.h` installed on your system.

In addition, the support for the old widget library `Xforms` is removed. Its support was still present but was not tested for years. The support for the `MOTIF` library (the default used with the previous kernel) is obsolete and is considered for complete removal soon.

3.2 Fortran compilers

At the time this documentation is written (14-dec-2010), here is the status of the various Fortran compilers supported by Gildas:

- Intel Fortran Compiler (ifort): versions 9.0 and 11.1 have been tested. As far as we know it seems fine to compile the new kernel with ifort. There is no bug directly related to the new kernel, but remember there can be problems in old version of ifort (e.g. a memory leak with ifort 9.0).
- g95: none of the stable versions of g95 (i.e. up to 0.92) is now able to run correctly the new Gildas kernel. The Fortran runtime libraries it provides do not seem to be thread-safe, i.e. there are conflictual access to its internal routines. With the implementation of the Fortran co-arrays, the current development version of g95 (0.93) should be thread-safe. The problem is that this version is not stable enough to compile the Gildas kernel, and developments seem frozen since August 2010.
- the GNU Fortran Compiler (gfortran): recent versions of gfortran are able to compile and run correctly the new Gildas kernel. The lower limit 4.3.0 required for the gfortran version and introduced 2 years ago is kept unchanged. The annoying bug which enforce the user to type `RETURN` after clicking in a widget is **not** related to the new kernel. A patch for this bug has been submitted to the development versions of gfortran, and it will be part of the releases 4.4.6, 4.5.2 and 4.6.0.

4 Changes for end-users

All the obsolete, changed or new concepts are exhaustively described in this section and in the appendix A.

4.1 Behavior

4.1.1 Removed

There is a number of *devices* officially supported by GTV which have been removed. In the GTV context, a *device* is a destination for the plot stored in the GTV tree (e.g. X-Windows or PostScripts). The following ones have been removed, mostly because they are just obsolete:

- `HPGL`
- `REGIS`
- `TEKTRO`

This includes all the variants which were available in the Gildas `kernel/etc/` sources, but not compiled by default in the standard Terminal Definition File.

The device `SVG INTERACTIVE` is also disabled, at least as long as its need is not clearly required. The device `SVG [LOCAL]` is kept for hardcopies.

4.1.2 Changed

- The EPS (Encapsulated PostScript) hardcopies are not automatically rotated anymore. The reason is that we assume now that EPS are intended to be included in another document rather than being printed. The new option `/FITPAGE` for command `HARDCOPY` enables automatic rotation and scaling (i.e. the historical behavior). The option `/PRINT` (formerly `/PLOT`) implicitely activates `/FITPAGE`. Finally, the standard (non-encapsulated) PostScripts have not been changed. The table 1 summarizes the former and new rotation rules.
- The default Look-Up Table (LUT) is now a continuous variation of colors, from black to white. It is similar to the LUT which can be loaded from the file `rainbow3.lut`, probably the most popular LUT in GTV. It can be reloaded at any time with the command `LUT DEFAULT`. The previous default LUT was also a continuous variation of colors (circular hue value), but from red to red, resulting in confusing low and high levels. It still can be loaded with the command `LUT COLOR`.
- The so-called "LUT static" mode has been fixed and works correctly now. "LUT static" mode can be used to define one LUT per GreG image. See `HELP GTVL\CHANGE LUT` for details.
- Now the pen is a global atribute, e.g.:

```
GREG\PEN 0  ! Black
CREATE DIRECTORY SUB
CHANGE DIRECTORY SUB
GREG\PEN 1  ! Red
CHANGE DIRECTORY ..
```

With the above sequence of commands, the next segments created in the first directory would have been black, since there was a memory of the last pen in use when leaving the directory. Now, the pen used *everywhere* is the last pen defined *anywhere*.

4.1.3 New

- An interactive "lens" tool: browsing and zooming in your figures is now enhanced thanks to a new tool: i) open the lens with a center-click on any plotting window, ii) zoom in or out with the mouse wheel, iii) enlarge or reduce the lens with CTRL+wheel, iv) close the lens with center-click again.

Table 1: How the PostScripts and Encapsulated PostScripts are rotated or not depending on the GTV version and the plotting page. *Condition1*: Yes if the X range of the drawings is larger than its Y range, else No. This table reflects how the printers or the Latex inclusions behave. It does not reflect how some viewers can display the PostScript, in particular *ghostview*.

	Old		New			
Kind	EPS	PS	EPS	PS	EPS /FITPAGE	PS /FITPAGE
Landscape	Yes	Yes	No	Yes	Condition1	Yes
Portrait	No	No	No	No	Condition1	No

- PNG hardcopies: in the context of modern use of figures (e.g. digital presentations, webpages, etc), Greg plots can now be transfered natively to PNG images. See `HELP GTVL\HARDCOPY` for details. In particular, these images support background transparency

4.2 Commands, variables, SIC logicals and symbols

There has been an important effort to clarify the names of the various GTV *objects*, to fix or improve their behavior, and to clean out the obsolete ones. This can imply here and there an action from the user to make its procedures compatible with the new GTV. The new GTV knows about the old commands: it will detect these and suggest to the user what they should be replaced with. It can run in 2 modes, tolerant or strict, which can be toggled with the SIC variable `GTV%STRICT2011`. All the changes regarding these objects are exhaustively described in the appendix A. The tables 2, 3, 4 and 5 summarize these changes.

Table 2: Old GTV and GREG commands which are removed or modified, their purpose, and their equivalent with the new GTV syntax. Refer to section A.1 for a detailed description.

Old command	Behavior	Equivalent
CLEAR	perform a CLEAR PLOT	see CLEAR PLOT
CLEAR ALPHA	bring the plotting window in front	not yet defined
CLEAR GRAPHIC	bring the terminal in front	none
CLEAR PLOT	perform a CLEAR WHOLE, or perform a CLEAR TREE	DESTROY ALL, or CHANGE DIRECTORY + CLEAR DIRECTORY
CLEAR TREE	destroy the current tree	CHANGE DIRECTORY + CLEAR DIRECTORY
CLEAR WHOLE	destroy all the trees	DESTROY ALL
CLEAR WINDOW [Num]	close the active/numbered window	DESTROY WINDOW [Dir [Num]]
CHANGE CLEAR TREE|WHOLE	set the behavior of CLEAR PLOT	none
CHANGE DRAW ON|OFF	toggle the drawing state to active or sleeping	none
CHANGE ZOOM NEW|CURRENT	toggle the default behavior of ZOOM	none
CREATE DIRECTORY /PIXEL	set the window size of a new top directory	CREATE DIRECTORY /GEOMETRY
CREATE DIRECTORY /SIZE	set the plot page of a new top directory	CREATE DIRECTORY /PLOT_PAGE
DISPLAY CLEAR	show the CLEAR PLOT behavior	none
HARDCOPY /PLOT	send the hardcopy to the printer	HARDCOPY /PRINT
ZOOM REFRESH	force the redraw of the active window	none
ZOOM /REGION	define the zoom area with the cursor	none
ZOOM /CURRENT	zoom is performed in the current window	none
ZOOM /NEW	zoom is performed in a new window	ZOOM without argument
GREG1\SET DRAW ON|OFF	toggle the drawing state to active or sleeping	none
GREG1\SHOW DRAW	display the drawing state	none

Table 3: GTV and GREG variables which are removed, modified, or added. Their read-write status is indicated in the third column. Refer to section A.2 for a detailed description.

Old name	New name	Read-Write	Usage
GTV%SLEEP	none	RO	the active/sleeping drawing state
GTV%IMAGES[4,15]	none	RO	internal values associated to the first 15 images
GTV%IDENT	none	RW	the number of the device currently in use
LUT	none	RO	the hue values of the current LUT in use
REXTR	none	RO	the extrema of the last segment created
REXTR_D	none	RO	the extrema of the current working directory
none	GTV%PWD	RO	the current working directory
GTV%LUT_STATIC	LUT%STATIC	RO	the dynamic/static LUT state
LUT_SIZE	LUT%SIZE	RO	the number of levels of the current LUT
LUT_MODE	LUT%MODE	RW	the HSV or RGB mode for the user-defined LUT
HUE	LUT%HUE	RW	the hue values of the current LUT (input/output)
SATURATION	LUT%SATURATION	RW	same for the saturation values
VALUE	LUT%VALUE	RW	same for the intensity values
RED	LUT%RED	RW	same for the red intensity values
GREEN	LUT%GREEN	RW	same for the green intensity values
BLUE	LUT%BLUE	RW	same for the blue intensity values
B_HUE	LUT%BLANKING%HUE	RW	the hue value of the blanking color (input/output)
B_SATURATION	LUT%BLANKING%SATURATION	RW	same for the saturation value
B_VALUE	LUT%BLANKING%VALUE	RW	same for the intensity value
B_RED	LUT%BLANKING%RED	RW	same for the red intensity value
B_GREEN	LUT%BLANKING%GREEN	RW	same for the green intensity value
B_BLUE	LUT%BLANKING%BLUE	RW	same for the blue intensity value
P_HUE	LUT%PEN%HUE	RW	the hue values of the user-defined pens (input/output)
P_SATURATION	LUT%PEN%SATURATION	RW	same for the saturation values
P_VALUE	LUT%PEN%VALUE	RW	same for the intensity values
P_RED	LUT%PEN%RED	RW	same for the red intensity values
P_GREEN	LUT%PEN%GREEN	RW	same for the green intensity values
P_BLUE	LUT%PEN%BLUE	RW	same for the blue intensity values
LCUT	CURIMA%SCALE[1]	RO	low cut for last image PLOT'ted
HCUT	CURIMA%SCALE[2]	RO	high cut for last image PLOT'ted
SCALING	CURIMA%SCALING	RO	scaling mode for last image PLOT'ted
EQUAL_NLEV	CURIMA%EQUAL%NLEV	RO	number of levels in EQUAL mode
EQUAL_LEV	CURIMA%EQUAL%LEV	RO	levels in EQUAL mode
EQUAL_HIST	CURIMA%EQUAL%HIST	RO	values per level in EQUAL mode

Table 4: SIC logicals in GTV which are modified or added. Refer to section A.3 for a detailed description.

Old name	Equivalent name	Usage
LUT_DIR:	LUT#DIR:	where the LUT files should be searched in
none	WINDOW_GEOMETRY	the default geometry of new windows
none	WINDOW_POSITION	the position on screen of the first window

Table 5: Old GTV symbols which are removed, and the command which can be used to define them in user's ∼/.gag.dico . Refer to section A.4 for a detailed description.

Old symbol	Equivalent
CD	SYMBOL CD "GTVL\CHANGE DIRECTORY"
PWD	SYMBOL PWD "GTVL\DISPLAY DIRECTORY"
MKDIR	SYMBOL MKDIR "GTVL\CREATE DIRECTORY"

5 Changes for programmers

5.1 The new GTV overview

In the previous version of the GTV, the metacode describing the plots was stored in several chunks of memory. The current chunk was contiguously filled with all the incoming data: directory descriptors, segments descriptors, segment data, or image descriptors. When the current chunk was (nearly) full, it was copied to a newly allocated chunk, and reset for new use. This had 3 major limitations:

- it was a permanent worry to make sure that the incoming data will fit in the remaining place of the current chunk,
- the tree size and the numbers of images in the tree were limited by hard coded parameters in the source code,
- the various links in the tree between the directories, the segments, and their data, were remembering the chunk number and the position in the chunk. Deleting an object and freeing its associated memory was just a nightmare: links could not be updated easily.

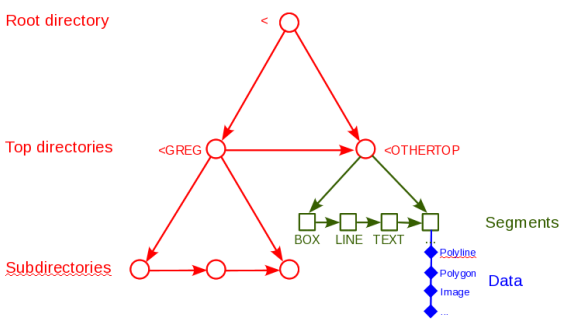

Figure 1: The tree and linked lists structure of the metacode storing the plots in the GTV, with a basic example of top directories, subdirectories, and segments. The relationship presented here between the various elements is not exhaustive.

Given these limitations, the choice was made to fully rewrite the way the metacode data is stored in memory. Appropriate Fortran derived types were defined: they describe the various links an object can have with others in the tree. Figure 1 shows an example of the various kind

of data which can be encountered in the metacode.

All the links are made with allocatable pointers, which are allocated in real time, on-demand. The tree is thus now growing dynamically in memory. Deleting an object is just as easy as deallocating a pointer to it, after having taken care that the surrounding elements in the tree are correctly updated. Furthermore, deallocation can be delayed (i.e. put in the event stack) after all the events which need it are done, without altering the normal life of the tree (as ruled by the commands executed).

5.2 Entry points

5.2.1 Removed

The so-called "immediate pen" support and associated entry points are removed:

- `gti_where`
- `gti_pen`
- `gti_out`
- `gti_draw`
- `gti_reloc`

The "immediate pen" was used to plot lines directly on the default window, without storing them in the metacode. This was an unsatisfying mechanism since: i) these drawings (probably useful) were lost as soon as the window was redrawn, ii) the window manager could ask for a window redraw at any time.

The `Sleep` and `Wake_Up` modes for `gtview` are removed. They were intended to delay the drawing of new segments being added to the metacode. This behavior has been removed because i) the drawing is performed in another thread i.e. it does not slow down the main thread execution, ii) the drawing routines were speed up to avoid re-reading the whole tree in order to search for undrawn segments, iii) user always wants to see the segments being added as soon as possible. As a consequence the following entry points are removed:

- `gtstat` (it was returning the sleeping status of the `GTV`)
- `gtview('Sleep')` and `gtview('Wake_Up')` (they were setting the sleeping status of the `GTV`).

The following obsolete entry points are removed:

- `gtpaus`
- `gtg_charsiz`
- `gtg_open`

5.2.2 New

Any segment opened with `gr_segm` must now be closed with the following new entry point after all the data it contains has been sent to the metacode:

- `gr_segm_close(error)`

The following conditions applies:

- at close time (`gr_segm_close`), a segment is implicitely drawn by `GTV`,
- attempting to send segment data to the metacode while there is no segment currently opened is an error,
- attempting to open (`gr_segm`) a new segment while the previous one is not closed (`gr_segm_close`) is an error,
- attempting to close (`gr_segm_close`) twice a segment is an error.

Given the first point above, the necessity for an `Append` mode for `gtview` is severely reduced. Basically, what you will probably have to do is to replace all the statements `gtview('Append')` by `gr_segm_close(error)`. The only purpose to call `gtview('Append')` is now when you are filling a unique segment, and want the user to see in real-time this segment being filled (e.g. a curve showing the convergence of a computation, or an interactive drawing with the cursor, ...).

Instead of calling `gr_exec('CLEAR SEGMENT FOO')`, programmers can invoke the public subroutine `gt_clear_segment(name,present,error)` where `name` is the segment(s) name to be destroyed (e.g. if `name` is `FOO` it will destroy all the segments named `FOO:*`), `present` is a logical indicating if an error should be raised if no segment with such a name is found, and `error` is an `inout` logical error flag (i.e. it keeps its entering value if no error occurs).

A Exhaustive description of the changes in GTV

A.1 Commands

A choice has been made to clarify the various commands. In particular, there were some keywords which were refering to some obsolete devices (e.g. `CLEAR ALPHA` and `CLEAR GRAPHIC`).

There was a also a confusion with the behavior command `CLEAR`. The rule is now: `CLEAR FOO` erases the content of the object designated by `FOO`, while the new command `DESTROY` kills this object.

A.1.1 Removed

- `CHANGE CLEAR TREE|WHOLE, DISPLAY CLEAR`
  - commands were controling and displaying the behavior of `CLEAR PLOT`
  - reason: associated `CLEAR TREE` and `CLEAR WHOLE` are removed.
- `CHANGE ZOOM NEW|CURRENT`
  - command was controling the default behavior of `ZOOM`, i.e. if the zoom should be performed in the main or in a new window.
  - `CHANGE ZOOM` is removed since the zoom is now always performed in a new window.
- `CHANGE DRAW ON|OFF`, and `GREG1\SET DRAW ON|OFF`
  - commands were both disabling (`OFF`) the real-time drawing of the new segments being added to the metacode, and drawing them (`ON`) later on.
  - reason: associed mode is removed in the Fortran API (see comments on `gtview` at section 5.2.1.
- `CLEAR GRAPHIC`
  - command was supposed to bring to front (or focus) the terminal (`CLEAR GRAPHIC` means *hide the graphic window*).
  - reason: not supported on any known modern window managers + too many keywords accepted by `CLEAR` + keywords have no meaning for those who did not know the old devices like Tektro.
- `CLEAR PLOT`
  - reason: there was a confusion between plot clearing and windows destruction.
  - in the simplest case, you have one window, and you are working in the top directory (probably `<GREG`): just type `CLEAR` to erase the content of the current directory and clear the window.
  - if you have several windows: i) if you want to *clear* one window, type `CLEAR TopDir` where `TopDir` is the directory associated to the window you want to clear, ii) but if you want to *kill* one directory and its associated window, type `DESTROY TopDir`
  - finally if you want to reset all your plots i.e. get back the startup status, type `DESTROY ALL`.

- `CLEAR TREE`
  - reason: too many keywords associated to the command `CLEAR`, can be replaced in the new GTV context
  - use `CLEAR DIRECTORY TopDir` instead, or `CHANGE DIRECTORY` (with no argument, it goes to the top directory) + `CLEAR DIRECTORY` (with no argument, it erases the content of the current directory).
- `CLEAR WHOLE`
  - reason: too many keywords associated to the command `CLEAR`, command unused
  - use `CLEAR` without argument instead
- `CLEAR WINDOW [Num]`
  - reason: name is ambiguous, too many keywords associated to the `CLEAR` command
  - use `DESTROY WINDOW [Dir [Num]]` instead. No way to destroy (from the command line) the current window only. For the old `CLEAR WINDOW ZOOM`, use `ZOOM OFF` instead.
- `CREATE DIRECTORY|WINDOW /PIXEL`
  - option `/PIXEL Nx Ny` is removed. It was overiding the default size of the new window opened by the command.
  - reason: new option `/GEOMETRY` does the same and more (see detailed description hereafter)
  - use `CREATE DIRECTORY|WINDOW /GEOMETRY Nx Ny` for an identical result.
- `CREATE DIRECTORY /SIZE`
  - option `/SIZE` is renamed `/PLOT_PAGE` for symmetry with command `GREG\SET PLOT_PAGE`) which does the same afterwards. These commands define the physical size of the plotting area of a top directory.
- `HARDCOPY /PLOT`
  - option `/PLOT` for command `HARDCOPY` is renamed `/PRINT`.
  - reason: nowadays we use printers, not plotters.
- `GREG1\SHOW DRAW`
  - command was displaying the current real-time or delayed drawing status.
  - reason: associated command `GREG1\SET DRAW ON|OFF` is removed.
- `ZOOM REFRESH`
  - reason: unnecessary
- `ZOOM /NEW|/CURRENT`
  - options were indicating if the zoom had to be performed in the main or in a new window

  - these options are removed since it not possible anymore to zoom in the main window (i.e. /NEW is implicit now)

- ZOOM /REGION
  - reason: not available on MS Windows, unused, duplicate of the new lens.
- ZOOM buttons
  - "A" (Clear alphanumeric screen) is removed
  - reason: same as CLEAR ALPHA

A.1.2 Changed

- CHANGE WINDOW WinNum
  - change the active window to the given window number. The active window is the one in which the interactive cursor will appear when it is invoked.
  - window numbering starts now from 1 (Fortran like) instead of 0 (C like). So in most of the cases the main window of the current directory has now number 1, and the zoom window (if any) has number 2.
- CLEAR
  - was performing a CLEAR PLOT
  - now performs a CLEAR ALL (see after).
- CLEAR ALPHA
  - commands is renamed (new name to be defined). It is supposed to bring to front (or focus) the graphic window (CLEAR ALPHA means *hide the alphanumeric terminal*).
  - reason: too many keywords accepted by CLEAR + keywords have no meaning for those who did not know the old devices like Tektro.
  - remark: this feature is poorly supported on Linux window managers (too many applications must have excessively used this, so that the window managers are very restrictive now).
- CLEAR DIRECTORY [DirName]
  - the old behavior was to make the directory and its content invisible for later destruction by COMPRESS.
  - command behaves differently: CLEAR DIRECTORY DirName empties the directory named DirName. As a consequence, this clears the windows seeing this directory. Without argument the content of the current working directory is removed. Segments are now really deleted.
  - reason: need a command which clears the content of a window i.e. of a top directory (usually). Need also to minimize the number of keywords accepted by CLEAR for clarity.
  - the old behavior (destruction of the directory) is ensured by the new command DESTROY DIRECTORY DirName.

- CLEAR SEGMENT
  - without argument, command was deleting the last segment created *in the metacode*.
  - without argument, command behaves slightly differently: it deletes the last created segment *in the current working directory*, which can be different from the old behavior.
  - reason: the metacode is now growing dynamically and the segments have lost their "temporality". Actually the new behavior seems better than the previous one.
  - no way to mimic exactly the old behavior
  - NB: CLEAR SEGMENT Name behaves as before, except it really deletes the segment now (in the past it could have only made the segment invisble for later deletion by COMPRESS).
- METACODE IMPORT|EXPORT
  - Backward compatibility is broken.

A.1.3 New

- CHANGE POSITION
  - support for Offx[Unitx] Offy[Unity] is added. See CREATE WINDOW /POSITION above for the syntax.
- CLEAR ALL
  - clear the content of all the top directories, which clears the content of their windows. Top windows are not destroyed.
- CREATE WINDOW [/GEOMETRY] [/POSITION]
  - new options /GEOMETRY and /POSITION are added:

```
CREATE WINDOW [/GEOMETRY Sx[u] Sy[u]]
              [/POSITION Offx[u] Offy[u]]
```

    where Sx and Sy are the window size, Offx and Offy the offset on the screen. "u" (unit) can be "p" for pixels, "%" for percent of the screen, or "r" for the aspect ratio in unit of the other dimension. Default unit is pixel.
  - if /GEOMETRY is omitted, the values are read from the logical WINDOW_GEOMETRY defined in user's ~/.gag.dico with the same syntax as above. If the logical WINDOW_GEOMETRY is not defined, internal defaults are used for the window size.
  - if /POSITION is omitted, the choice of the window position is let to the window manager. "r" unit is a non-sense and is forbidden for this option.
- CREATE DIRECTORY [/GEOMETRY] [/POSITION]
  - new options /GEOMETRY and /POSITION are added: they apply to the creation of the window of a new top-directory. See CREATE WINDOW above for the syntax.
- DESTROY DIRECTORY DirName

  - destroys the input directory and its windows attached. Destroying <GREG is allowed (as long as user has moved before to another directory).
- DESTROY WINDOW [DirName [WinNum]]
  - destroys all the windows attached to the directory DirName, i.e. should be all the windows named DirName Number. Destroys all the windows of the current working directory by default. If a window number is given, only this window is destroyed.
- DESTROY ALL
  - destroys all the top directories and their windows
  - since the user can not be in the root directory (<) and can not create segments in it, he would have to create right after a new top directory. A first top directory is thus created implicitely.
  - As a consequence of these two points, the command resets the tree and windows to the startup status.
- HARDCOPY /DIRECTORY DirName
  - this new option allows to plot the given GTV directory. Default remains the current working directory.
- HARDCOPY /FITPAGE
  - this new option allows to adjust at best the plot on the hardcopy physical size. This is suited for EPS harcopies which are not automatically rotated and scaled anymore.
  - this option is exclusive with the historical option /EXACT (which disables the automatic scaling).
- LUT Name /REVERT
  - the look-up-table Name is loaded and reverted on the fly.
- GREG1\PEN [Ipen] /DASH 8
  - an 8th dashing style is added. It contains regular dashes, shorter than the 2nd style dashes, and larger than the 3rd (dot) style. Execute @ gag_demo:demo5.greg for an overview of all the pen attributes.

A.2 Variables

A.2.1 Removed

The following GTV variables are removed:

- GTV%SLEEP: the real-time or delayed drawing status, but this functionality is removed.
- GTV%IMAGES[2,15]: size and memory address of the images stored in the metacode, for debugging purpose.
- GTV%IDENT: the number in Terminal Definition File of the device currently in use.

- the LUT array is removed: it was describing the hue values of the current Look-Up Table in use. But since the hue is not enough to describe a LUT (saturation and value are also needed), the two triplets (LUT%RED, LUT%GREEN, LUT%BLUE) or (LUT%HUE, LUT%SATURATION, LUT%VALUE) should now be used to get and set the Look-Up Table values.
- REXTR: the extrema (in plot_page units) of the last segment created in the metacode.
- REXTR_D: the extrema (in plot_page units) of the current working directory.

A.2.2 Changed

The look-up table related variables are merged in a new structure named LUT%. See table 3 for details. This structure has three major groups of variables related to the images look-up table (under LUT%), to the blanking color (under LUT%BLANKING%) and to the pen look-up table (under LUT%PEN%).

The variables describing the current RG image plotted by the command GREG2\PLOT are merged under the structure CURIMA%. The equalization mode, if in use, is described under the substructure CURIMA%EQUAL%. See table 3 for details.

A.2.3 New

- GTV%PWD: this new variable contains the current working GTV directory as a character string. It is aimed to help writing plotting procedures which can work in the directory they are started in without altering the other plots (trees) already created by the user.
- GTV%STRICT2011: this new variable will be available *temporarily* to rule how the interpreter should behave when encountering an old GTV command. If its values is "yes", an error is raised. If "no", it is only a warning. In both cases an explanatory message is displayed. Default value is "yes". This variable is present to help the users and programmers to speed up the transition, but without breaking abruptly their procedures and programs.

A.3 SIC logicals

A.3.1 Removed

- LUT_DIR:
  - logical is removed. It was controlling the directory where the LUT files have to be searched in.
  - reason: new logical LUT#DIR: is better.

A.3.2 New

- GAG_LUT:, LUT#DIR:
  - new logical GAG_LUT: is the path to the internal LUT files. User should not change it.
  - new logical LUT#DIR: is *a collection* of paths where the LUT files should be searched in. User can customize it as its will. Default value is ./;GAG_LUT:;.
- WINDOW_GEOMETRY, WINDOW_POSITION

  - if defined, these new logicals control respectively the size of any new window, and the position on the screen of the first window when the device is opened.
  - user can define (one of) them in its ~/.gag.dico for all its sessions, or later during a session.
  - the option /GEOMETRY of the command CREATE DIRECTORY|WINDOW override the values in WINDOW_GEOMETRY.
  - see CREATE DIRECTORY|WINDOW above for the syntax to be used.

A.4 Symbols

A.4.1 Removed

- CD
  - reason: should not be provided by GREG
  - use CHANGE DIRECTORY or define the same symbol instead
- PWD
  - reason: unused / should not be provided by GREG
  - use DISPLAY DIRECTORY or define the same symbol instead
- MKDIR
  - reason: should not be provided by GREG
  - use CREATE DIRECTORY or define the same symbol instead

Copyright: Stéphane Guisard (Los Cielos de America)

Chapitre 9

Action Spécifique ALMA (administration de la recherche)

9.1 Statut du projet ALMA

Les deux prochaines années vont voir la mise en service scientifique d'ALMA. Sur le site à 5000 m d'altitude, les premières franges à deux antennes ont été obtenues fin octobre 2009 et les clôtures d'amplitude et de phase à 3 antennes ont été obtenues début 2010, les premières observations scientifiques (cycle 0 de la période dite "early science") réalisées à partir d'octobre 2011 et il y a actuellement une vingtaine d'antennes en fonctionnement. Dans le calendrier actuel, la date limite pour le deuxième appel à observations scientifiques aura lieu début juillet et la fin de la construction d'ALMA est prévue pour 2013. Le passage de la phase de construction à la phase d'exploitation scientifique d'un observatoire tel qu'ALMA pose de nombreuses questions. Comment préparer au mieux la phase scientifique d'un instrument extrêmement compétitif car unique et ouvrant de nouveaux espaces de paramètres (très haute résolution angulaire, longueurs d'onde sub-millimétriques) ? Comment s'assurer que l'expertise technique (matérielle et logicielle) utilisée lors de la construction soit conservée pour permettre de faire d'ALMA un instrument évolutif ? Quel est l'avenir des observatoires actuels de radio-astronomie sub-millimétrique ?

9.2 Objectifs de l'action spécifique

J.-M. Hameury m'a nommé directeur de l'Action Spécifique ALMA (`http ://www.graal.univ-mo`
depuis janvier 2008 avec un conseil scientifique entièrement renouvelé[1] pour aider à répondre à

[1]Il comprend des spécialistes (F. Boone remplacé en 2009 par P. Salomé du LERMA, P.-A. Duc du CEA/Saclay, E. Josselin du GRAAL, V. Piétu de l'IRAM, F. Selsis du LAB et A. Walters du CESR), des membres des programmes nationaux (S. Charlot pour le PNCG, E. Dartois pour PCMI, L. Jorda remplacé en 2010 par N. Biver pour le PNP, F. Ménard pour le PNPS et M. Tallon remplacé en 2011 par O. Chesneau pour l'ASHRA) ainsi que trois membres invités (F. Gueth, membre de l'ALMA Science Advisory Committee, F. Pajot, chargé de mission à l'INSU

ces questions. Notre premier objectif est d'animer et de structurer la communauté scientifique nationale en vue de l'exploitation d'ALMA. Il s'agit en effet d'assurer que le retour scientifique français soit à la hauteur des efforts financiers importants de la France dans le domaine (sub)-millimétrique tant pour construire ALMA que pour gérer l'IRAM.

En particulier, l'ASA est active pour sensibiliser la communauté au sens large aux premiers appels d'offre et à la compétition accrue sur ALMA. Obtenir du temps sur l'interféromètre du Plateau de Bure est déjà difficile. L'effet est amplifié avec ALMA car il s'agit d'un instrument unique, impliquant une compétition mondiale d'autant plus accrue que le comité de sélection des propositions est unifié et qu'ALMA devra servir une communauté bien plus grande que la communauté radio. Par ailleurs, la sensibilité accrue d'ALMA par rapport à l'interféromètre du Plateau de Bure actuel (d'environ un facteur 10) compensera tout juste la difficulté des observations demandées sur ALMA dans le submillimétrique et à très haute résolution angulaire. Ainsi, lors de l'appel à proposition dit « Early Science Cycle 0 », seule 1 proposition sur 9 a été acceptée et le nombre de propositions acceptées (112 projets pour la 1ère année) sur ALMA a été du même ordre de grandeur que le nombre de propositions acceptées aujourd'hui au Plateau de Bure (environ 150 projets par an). Nous essayons donc de promouvoir une structuration scientifique de la communauté française : 1) en identifiant les thématiques astrophysiques où la France peut jouer un rôle de premier plan au sein des programmes nationaux de l'INSU ; et 2) en développant l'approche multi-longueurs d'onde. Cette structuration est d'autant plus importante qu'il n'y a pas de temps garanti sur ALMA, et que les études multi-longueurs d'ondes vont sans aucun doute jouer un rôle crucial dans l'analyse des données d'ALMA. Le retour scientifique pour le permier appel est bon : 256 français ont répondu en tant que PI ou co-Is ; 7 propositions acceptées ont un PI français et 34 autres ont au moins un co-I français[2].

9.3 Activités 2008-2011

Après une période de présentation du projet ALMA en 2008 (séminaires à l'IAS, à l'IAP, au GRAAL/LUPM, au CESR/IRAP et au CEA/Saclay ainsi qu'une présentation à la semaine de la SF2A), nous avons organisé début avril 2009 les journées ASA à Grenoble (co-organisation avec l'IRAM et le LAOG/IPAG). Durant ces journées, toute la communauté (une centaine de personnes présentes) a été invitée à discuter de la manière dont elle souhaitait s'organiser scientifiquement. Suite à ces journées, l'ASA a proposé dans un appel d'offre joint 2009-2010 de soutenir financièrement des groupes dont l'objectif à terme est d'obtenir du temps avec ALMA. Cette action a été reconduite dans l'appel d'offre 2011. C'est au total neuf groupes qui auront été soutenus entre 2009 et 2011[3].

---

et L. Vigroux, président du conseil de l'ESO).

[2]En tout 40% des propositions acceptées ont au moins un co-I français, alors que le retour « théorique » attendu est 6% (= 18% part de la France dans l'ESO × 33% part de l'ESO dans ALMA).

[3]Les coordinateurs et les thèmes de ces groupes sont : 1) P. André, phases précoces de la formation des étoiles de toute masse ; D. Bockelée-Morvan, planétologie avec ALMA - Préparation Early Science ; O. Chesneau, enveloppe commune et disques autour des étoiles évoluées ; J. Braine, formation stellaire et milieu interstellaire : de la Galaxie aux galaxies ; J.-F .Gonzalez, disques protoplanétaires dans le (sub)-millimétrique : paver la route vers ALMA ; S. Guilloteau et A. Dutrey, Mass and Ages of Young Stars and Chemistry in Disks ; E. Josselin, Etoiles évoluées avec ALMA : études chimiques et polarimétriques ; J.-P. Kneib, Distant dusty galaxies lensed by massive clusters at millimeter wavelength ; B. Rocca-Volmerange, Radio galaxies lointaines du catalogue HzRG avec ALMA.

En 2009, l'ASA s'est aussi investie dans l'effort de prospective INSU. Nous avons eu deux actions. Nous avons d'abord répondu aux questionnaires du groupe moyen[4] et du groupe de réflexion sur les services d'observation à propos du service SO3/ALMA. Puis, nous avons donné un avis sur les problèmatiques de la prospective en lien direct avec l'ASA dans un document[5] où nous avons entre autres défendu la complémentarité entre ALMA et le projet NOEMA d'extension de l'interféromètre millimétrique du Plateau de Bure.

En 2010, l'ASA a en plus soutenu les deux évènements organisés par le nœud de l'ARC à l'IRAM : 1) l'école bi-annuelle d'interférométrie millimétrique en octobre et 2) un atelier décrivant les capacités (sensibilité, résolution spatiale, réglages des récepteurs et des spectromètres) et les outils "early science" (estimateurs de temps, soumission de proposition, réduction de données) en décembre 2010.

En 2011, nous avons organisé de nouvelles journées ASA intitulées « ALMA early science cycle 0 : et après ? ». Ces journées ont commencé par une présentation de la situation actuelle : montée en puissance des capacités ALMA, statut de l'ARC européen et de son nœud à l'IRAM, complémentarité avec le projet NOEMA, bilan et perspectives de l'ASA. Puis, nous avons mis en place des échanges nouveaux qui découlent naturellement des progrès instrumentaux en radioastronomie (sub)-millimétrique : comment transférer l'expertise de la communauté galactique vers la communauté extragalactique pour bénéficier à plein de l'augmentation de résolution angulaire ? comment la communauté galactique peut profiter des environnements nouveaux offerts par la recherche extragalactique (régime sous-métallique, starbursts) pour raffiner les modèles ? quels sont les besoins en données spectroscopiques et de micro-physique pour les études du système solaire, des systèmes extrasolaires, des étoiles en formation, du milieu interstellaire (cette partie a été organisée en coordination avec le GDR spectroscopie).

En s'appuyant sur les recommandations du groupe de réflexion sur les services d'observation dans l'exercice de prospective, l'ASA a exprimé fin 2010 les besoins en services d'observation ALMA pour la période 2011-2014. Dans ce document[6], trois types de besoins différents sont recensés : 1) le prêt (par mission longue, mise à disposition ou détachement) de personnels qualifiés au projet ALMA pour participer à l'effort commissioning ; 2) la participation au support face-à-face dans le cadre du nœud de l'ARC à l'IRAM et 3) le développement d'outils experts (polarimétrie, imagerie on-the-fly, pipeline alternatif, ...). Parmi ces 3 besoins, le support face-à-face est particulier. Une de ces difficultés est de se tenir au courant du projet (par exemple quelles sont les évolutions du projet ALMA, que s'est-il réellement passé lors des observations, quelles sont les limitations du logiciel de réduction et comment les contourner ?). Pour réussir cela, il faut une équipe soudée qui s'occupe uniquement d'ALMA une large fraction de son temps. C'est pour cela que l'ASA a jugé nécessaire de localiser l'ensemble du support face-à-face uniquement à Grenoble. Ce document a été largement diffusé à la communauté, ce qui a amené à une (re)définition des tâches de service par l'Observatoire de Grenoble[7] et de Bordeaux[8] Les prochaines étapes sont l'obtention d'un accord formel entre l'IRAM et l'Observatoire de Grenoble ainsi que la labellisation de la tâche par la commission spécialisée astrophysique et

[4] A propos de la 2nde génération d'instruments pour ALMA et du nœud de l'ALMA Régional Center en cours de constitution à l'IRAM (`http ://www.iram.fr/IRAMFR/ARC/`).

[5] Voir `http ://paa09.cesr.fr/pub/Main/InfosPubliquesG2/priorites_asa.pdf`.

[6] cf. `http ://www.graal.univ-montp2.fr/hosted/alma/asa-so.pdf`.

[7] cf. `http ://www-laog.obs.ujf-grenoble.fr/Laog/Servobs/so_alma.html`.

[8] cf. `http ://www.oasu.u-bordeaux1.fr/index.php ?pg=alma&lg=fr`.

astronomie de l'INSU.

Enfin, je maintiens depuis 4 ans une liste d'emails (asa-news@iram.fr) dont le but est d'informer la communauté sur le statut du projet ALMA et les actions de l'ASA. Par ailleurs, j'ai géré pendant 4 ans pour l'INSU l'accueil annuel de 2 étudiants chiliens pour commencer à les former à la radioastronomie (sub)millimétrique, avec l'idée de favoriser la coopération scientifique France-Chili. Durant la première semaine, ils participaient à l'école de radioastronomie de l'IRAM. Puis, ils passaient leur deuxième semaine dans un laboratoire français pour travailler sur des données de radioastronomie (sub)-millimétrique, aux frais de l'INSU. Les 8 étudiants chiliens accueillis ainsi que les équipes françaises accueillantes ont tous donné un compte-rendu positif de ces expériences. Cette coopération fructueuse a été l'un des éléments qui ont permis la réalisation d'une Unité Mixte Internationale au Chili dans la deuxième moitié de 2011.

9.4 Quel avenir pour l'ASA ?

Le mandat actuel de l'ASA se termine fin 2012. L'ASA aura alors existé pendant 8 ans. La question de son renouvellement et de ses objectifs se pose donc. Comme la phase de construction d'ALMA devrait s'achever en 2013, les prochaines années seront essentielles pour le positionnement de la communauté française dans la compétition scientifique internationale. Garder une action spécifique dédiée à ALMA durant ces années pour accompagner la transition de la phase de construction à la phase d'exploitation semble indispensable. Cela permettrait aussi de transmettre correctement l'organisation scientifique autour d'ALMA aux différents programmes concernés.

Cependant, le conseil scientifique de l'ASA souhaite éviter d'installer une routine de financement récurrent de quelques groupes demandant du temps d'observation d'ALMA. La demande de renouvellement doit donc s'accompagner d'objectifs clairs si possible en lien avec une liste d'actions concrètes pour au moins 2013 et 2014. Parmi les actions passées, deux ont particulièrement permis de former et de structurer la communauté française. Il s'agit des financements pour aider à la participation aux écoles d'interféromètrie et des journées de discussion regroupant diverses communautés (entre autres modélisateurs, observateurs, fournisseurs de données micro-physiques).

Le conseil scientifique a enfin pris note que le projet NOEMA d'agrandissement de l'interféromètre du Plateau de Bure est sur le point d'être mis en œuvre. Il sera important de mobiliser la communauté française pour qu'elle exploite au mieux la complémentarité ALMA/NOEMA. Cela pourra faire partie des nouveaux objectifs de l'ASA.

Contribution de l'Action Spécifique ALMA à l'exercice de prospective 2009

J. Pety pour le conseil scientifique de l'ASA

10 Juin 2009

Les cinq prochaines années vont voir la mise en service scientifique d'ALMA. Dans le calendrier actuel, la phase de "commissioning and science verification" commencera sur le site fin 2009, les premières observations scientifiques ("early science") auront lieu mi-2011 et la fin de la construction d'ALMA est prévue pour 2013. Le passage de la phase de construction à la phase d'exploitation scientifique d'un observatoire tel qu'ALMA pose de nombreuses questions. Comment préparer au mieux la phase scientifique d'un instrument extrêmement compétitif car unique et ouvrant de nouveaux espaces de paramètres (très haute résolution angulaire, longueurs d'onde sub-millimétriques) ? Comment s'assurer que l'expertise technique (matérielle et logicielle) utilisée lors de la construction soit conservée pour permettre de faire d'ALMA un instrument évolutif ? Quel est l'avenir des observatoires actuels de radio-astronomie sub-millimétrique ?

1 Aspects organisationnels

1.1 ALMA : le premier observatoire mondialisé au sol

La pratique de la radio-astronomie évolue d'une pratique individuelle à une pratique collective. A l'IRAM, parmi les propositions ordinaires, les signataires d'une seule proposition sont souvent nombreux. Cet effet est amplifié du fait que l'IRAM propose depuis 1 an un appel à observation spécifique grands projets (plus de 100 heures par semestre sur 2 ans, les données étant rendues publiques 18 mois après la fin des observations). Une raison sous-jacente à ce changement de pratique est que la radio-astronomie millimétrique est devenue mature : de constatations "simples" sur quelques objets pas toujours résolus, on est passé soit à des modèles complexes sur des objets très bien observés, soit à des statistiques sur un grand nombre d'objets. Ce que l'on pouvait faire seul sur un ou deux spectres demande maintenant des expertises très poussées et complémentaires (traitement des données, transfert de rayonnement, modélisation chimique et/ou mhd, etc...) sur une grande quantité de données.

L'effet sera amplifié avec ALMA car il s'agit d'un instrument unique, signifiant une compétition mondiale d'autant plus accrue que le comité de sélection des propositions sera unique et qu'ALMA devra servir

Tab. 1 – Sensibilité en brillance à 1mm en fonction de la résolution angulaire et du temps d'intégration pour l'interféromètre du Plateau de Bure (PdBI) et ALMA. A même résolution angulaire, ALMA est beaucoup plus rapide que PdBI. Par contre, une augmentation de la résolution angulaire d'un facteur 10 à même sensibilité en brillance demande une fraction significative d'une année pour un interféromère comme ALMA. Un compromis soit sur la sensibilité soit sur la résolution angulaire est nécessaire pour diminuer les temps d'intégration.

Instrument	Résolution	Sensibilité	Temps d'intégration	Commentaire
PdBI 2009	$1''$	0.3 K	2 hrs	
ALMA 2013	$1''$	0.3 K	3.5 min	Même raie, beaucoup d'objets
ALMA 2013	$0.1''$	0.3 K	575 hrs	6.5% d'une année!
ALMA 2013	$0.1''$	5 K	2 hrs	Compromis en sensibilité
ALMA 2013	$0.4''$	0.3 K	2 hrs	Compromis en résolution

une communauté bien plus grande que la communauté radio. Par ailleurs, la sensibilité accrue d'ALMA par rapport à l'interféromètre du Plateau de Bure actuel (environ un facteur 10) compensera tout juste la difficulté des observations demandées sur ALMA dans le submillimétrique et à très haute résolution angulaire (cf. table 1). Le nombre de propositions acceptées sur ALMA devrait être du même ordre de grandeur que le nombre de propositions acceptées aujourd'hui au Plateau de Bure (environ 150 projets par an). Une conséquence directe est que la qualité formelle (pédagogie, clarté des objectifs, compétences de l'équipe, etc...) des propositions d'observation devra être irréprochable pour être acceptée par le comité des programmes.

L'Action Spécifique ALMA est active pour sensibiliser la communauté au sens large à la compétition accrue sur ALMA et à l'imminence des premiers appels d'offre. Le bilan des journées ASA[1] indique clairement que la communauté française a des cartes à jouer dans de nombreux domaines : cosmologie, formation et évolution des galaxies, formation stellaire, disques circumstellaires et protoplanétaires, étoiles évoluées et matière circumstellaire, physique et chimie du milieu interstellaire, système solaire, etc... Bien que la France soit en pointe sur les thématiques scientifiques au coeur d'ALMA, l'internationalisation nécessaire (et déjà visible sur les demandes IRAM) des équipes risque de diluer la visibilité française. **Il est donc important que la communauté française se structure au niveau national pour assurer le leadership français de propositions internationales ambitieuses sur ALMA.** Cette structuration est d'autant plus importante qu'il n'y a pas de temps garanti sur ALMA, et que les études multi-longueurs d'ondes vont sans aucun doute jouer un rôle crucial dans l'analyse des données de ALMA.

1.2 Rôle des ALMA Regional Center dans l'obtention et la réduction des données

L'ARC (ALMA Regional Center) est la structure qui sert d'interface entre ALMA et la communauté scientifique, avant les observations (call for proposals, phase 1, phase 2) et une fois que les données ont été obtenues (accès à l'archive, support aux utilisateurs, etc). En Europe, l'ARC est organisé sous la forme d'un réseau. Le noeud central à l'ESO/Garching est en charge de la gestion des demandes de temps et des observations, de l'archive, et de la distribution des données de ALMA. Les six noeuds additionnels sont en charge de la formation des utilisateurs en amont, de l'aide directe fournie aux utilisateurs pour la préparation des projets et la réduction des données (support face-à-face), ainsi que du développement de techniques et d'algorithmes de traitement de données innovants.

L'ARC est une structure essentielle pour assurer le succès de ALMA : dans une compétition mondiale extrêmement forte, il est nécessaire d'avoir des centres d'expertise pouvant fournir un support efficace et rapide à la communauté, notamment pour la réduction des données. Les ARC nord-américains et asiatiques sont localisés à un seul endroit. Le modèle européen consistant à impliquer plusieurs laboratoires est justifié par le manque d'expertise disponible à l'ESO, mais comporte un risque très fort de dispersion des efforts.

La communauté française est dans ce contexte avantagée, car elle possède déjà une expertise indéniable en interférométrie millimétrique, grâce notamment à l'IRAM, qui est l'un des noeuds de l'ARC. L'expérience du Plateau de Bure montre qu'un support efficace nécessite des personnes impliquées pour une large fraction de leur temps (au moins 30%), ainsi qu'une masse critique permettant de couvrir toutes les problématiques (instrumentales, logicielles, scientifiques). **La communauté française doit soutenir le développement du noeud de l'ARC européen à l'IRAM, qui sera un atout essentiel dans l'exploitation d'ALMA.**

1.3 Besoins spécifiques à l'analyse scientifique des données

La communauté s'étonne de la faiblesse des moyens consacrés à l'utilisation scientifique de nouveaux instruments en regard de leur coûts de construction et de fonctionnement. Pour obtenir un retour scientifique complet d'un instrument tel qu'ALMA, il faut un grand nombre de compétences très pointues, incluant entre autres :

- les développements instrumentaux ;
- le développement et la maintenance de logiciels de traitement des données ;

[1] Voir `http ://www.graal.univ-montp2.fr/hosted/alma/programme.html` et `http ://www.graal.univ-montp2.fr/hosted/alma/cs2009a.html`.

- la fourniture de données de micro-physique ;
- le développements et la maintenance d'outils d'analyse des données (par exemple transfert de rayonnement) ;
- le développement et la maintenance d'outils de modélisation (modèles physico-chimiques génériques, modèles magnéto-hydrodynamiques génériques, etc...) ;

Un souci particulier se situe aux interfaces comme la fourniture de données micro-physiques fiables. Il s'agit de services essentiels pour la communauté astrophysique, mais insuffisemment valorisés (cités) et soutenus sur le long terme. En outre, le dialogue entre communautés de culture très différente est le seul moyen d'obtenir une bonne adéquation entre les besoins astrophysiques et l'expertise disponible. C'est d'autant plus crucial que les problèmes astrophysiques sont plus difficiles et plus nombreux à traiter. **Un soutien pérenne à ces différentes communautés et à leur dialogue est donc une priorité.**

Par ailleurs, la possibilité de mobiliser rapidement des post-docs une fois le temps d'observation obtenu sera également un aspect clé du succès de l'utilisation d'un instrument comme ALMA, et l'ASA s'inquiète des possibilités restreintes existantes en France. **L'Action Spécifique ALMA soutient une idée récurrente avancée pour améliorer la situation : l'attribution à ces tâches d'un pourcentage du coût de construction d'instruments de classe mondiale.**

1.4 Ressources humaines

La mise en service d'ALMA s'accompagne de besoins assez différents en ressources humaines. ALMA devant servir une communauté bien plus large que la communauté des radio-astronomes, il faut encourager les actions de formation des autres communautés. Cela passe par l'organisation d'écoles (par exemple les écoles de radio-astronomie et d'interférométrie de l'IRAM) mais aussi par la formation d'étudiants sur des thématiques scientifiques à cheval sur plusieurs longueurs d'ondes. En outre, l'accueil d'étudiants chiliens est un moyen particulièrement efficace de commencer des collaborations avec le Chili, qui dispose de 10% du temps ALMA. Il est aussi important d'encourager des personnes à passer du temps au Chili comme astronome résident mis à la disposition de l'ESO pour ALMA. C'est certainement la meilleure manière d'assurer une très bonne connaissance de l'instrument et de la diffuser dans la communauté française.

Le noeud de l'ARC à l'IRAM est un projet qui s'inscrit dans le long terme, puisqu'il devra accompagner la montée en puissance de ALMA avant sa phase de fonctionnement. L'ASA aura donc une action pour que le noeud de l'ARC à l'IRAM soit cité dans la catégorie AA-SO5 : « Centres de traitement et d'archivage de données ». En plus des besoins précédents, le succès scientifique d'ALMA dépend d'un grand nombre d'activités qui sont autant de services à la communauté (cf. section 1.3). Une difficulté dans la définition des tâches de service ALMA est que le projet reconnaît difficilement les contributions qu'il ne finance pas. Pour prendre ces différents aspects en compte et pour s'assurer que l'ensemble de la communauté soit pleinement associée à la définition des tâches de service ALMA, l'ASA propose donc de lancer un appel à idées, les réponses étant classées par l'ASA puis transmises à la CSA pour une demande de labellisation.

2 Aspects instrumentaux

2.1 L'évolution d'ALMA au-delà de 2013

Dans le calendrier actuel, la construction d'ALMA se terminera en 2013. Dans le budget de fonctionnement d'ALMA (environ 65 M$), 10 M$ sont envisagés annuellement à partir de 2015 pour faire évoluer ALMA jusqu'à l'horizon 2020. A l'heure actuelle, des discussions préliminaires ont lieu, essentiellement dans le cadre du Science Advisory Committee d'ALMA. Or il est difficile d'envisager dès aujourd'hui l'impact scientifique de ces possibles améliorations puisqu'il faudra plusieurs années pour ressentir pleinement l'impact d'ALMA dans sa configuration actuelle. Parmi les options envisagées, on trouve :

- une amélioration de certains aspects d'ALMA (par exemple, la possibilité de faire du VLBI ou des observations solaires) ;
- la complétion de la couverture spectrale d'ALMA par la construction des bandes de fréquence actuellement manquantes (B11 au-delà du THz, B5 de 163 à 211 GHz, B2 de 67 à 90 GHz, B1 de 31 à 45 GHz) ;
- une augmentation significative du nombre d'antennes (par exemple de 50 à 64).

Les budgets et les calendriers associés à ces projets sont très différents et parfois mal déterminés car ils peuvent demander une phase de recherche et développement importante.

Bien que les projets soient en cours de définition, il est néanmoins important de rappeler qu'ALMA a vocation à évoluer de manière significative après sa construction. Dans ce cadre, la France doit encourager les laboratoires français et l'IRAM à conserver leur importante expertise matérielle et logicielle en radio-astronomie millimétrique. En effet, il est important pour la communauté française d'anticiper sur des bases scientifiques et techniques l'évolution d'ALMA. Ceci permettra d'avoir un rôle moteur dans cette évolution, ce que l'expertise française a déjà permis pour les phases de conception et de construction d'ALMA[2]. Ceci est d'autant plus essentiel que pour la première fois dans le projet ALMA, la notion de temps garanti pourrait éventuellement être associée aux appels d'offres générés par les évolutions d'ALMA après 2013 (possibilité mentionnée par L.Testi, European Project Scientist, lors des journées ASA à Grenoble).

2.2 Le projet NOEMA d'extension de l'interféromètre du Plateau de Bure

ALMA sera un instrument unique de par ses possibilités *submillimétriques* et de *très grande résolution angulaire* (la plus grande ligne de base faisant 14 km). Il est prévu qu'ALMA passera au maximum 25% de son temps d'observation (cad 3 mois par an) dans le domaine millimétrique (longueur d'onde entre 3 et 1mm) et dans des configurations « compactes » (cad ayant une ligne de base maximum inférieure à 1.6 km)[3]. En considérant la fraction française d'ALMA (environ 6%), on obtient 1.5% ou 6 jours par an pour faire de la science millimétrique à résolution angulaire « moyenne » (entre 0.2" et 2"). Une fraction majeure du coût d'ALMA ainsi que son plus fort potentiel de découverte scientifique vient principalement de ses capacités submillimétriques (site à très haute altitude, très grande qualité de surface d'antenne) et de ses capacités de très haute résolution angulaire. Cela conduit à penser que les estimations de temps ci-dessus sont des limites largement supérieures car elles extrapolent la science faite aujourd'hui avec des instruments principalement millimétriques aux résolutions angulaires limitées.

Le domaine millimétrique est scientifiquement crucial car il contient notamment la plupart des transitions fondamentales des molécules observées dans le milieu interstellaire froid (e.g. disques protoplanétaires, coeurs pré-stellaires, nuages moléculaires dans les galaxies, etc...). Le domaine millimétrique est aussi essentiel pour la découverte et l'étude des sources à grand redshift, en continuum de par l'effet de la correction K inverse, et en raies de par le redshift. Par ailleurs, il n'y a pas pour l'instant de provision pour des « legacy surveys » sur ALMA parce que l'ensemble des thématiques scientifiques doivent pouvoir bénéficier dès le début de l'opération du changement de domaine de paramètre exploitable par ALMA (résolution, longueur d'onde). Ces arguments soulignent la nécessité d'avoir, en complémentarité avec ALMA, un instrument dédié aux études systématiques dans le domaine millimétrique avec une sensibilité similaire à celle d'ALMA.

L'interféromètre du Plateau de Bure (PdBI) est aujourd'hui le meilleur interféromètre millimétrique au monde. Améliorer un interféromètre peut se faire de quatre façons différentes : 1) augmenter le nombre d'antennes, 2) augmenter la longueur de la plus grande ligne de base, 3) augmenter la bande passante totale des récepteurs, 4) passer de récepteurs mono-pixels à des récepteurs multi-pixels. Le projet NOEMA vise à faire de PdBI un instrument complémentaire à ALMA en jouant simultanément sur les trois premières possibilités :

- doubler le nombre d'antennes de 15 m (de 6 à 12, impliquant un doublement de la surface collectrice et meilleure qualité d'imagerie par quadruplement du nombre de lignes de base) ;
- doubler la plus grande ligne de base (de 800 à 1600 m) et donc de doubler la résolution angulaire actuelle ;

[2] Au contraire de NRAO, l'ESO a peu de connaissance en radio-astronomie (sub)-millimétrique. L'essentiel de la construction d'ALMA en Europe est donc sous-contracté par l'ESO à des instituts spécialisés en radio-astronomie. En France, il s'agit de l'IRAM/Grenoble, du LERMA/Paris et du LAB/Bordeaux

[3] Le « Design Science Reference Plan » indique en effet qu'ALMA passera environ 55% du temps d'observation à faire des observations millimétriques (cf. `http://www.eso.org/sci/publications/messenger/archive/no.131-mar08/messenger-no131-46.pdf`). Par ailleurs, les 28 configurations d'ALMA (dont 14 configurations « compactes ») tourneront avec une périodicité de 18 mois au rythme typique d'un changement d'antenne par jour. Il est donc possible d'estimer qu'ALMA passera au plus 50% de son temps dans des configurations « compactes ». En multipliant les deux pourcentages, on obtient 27.5%

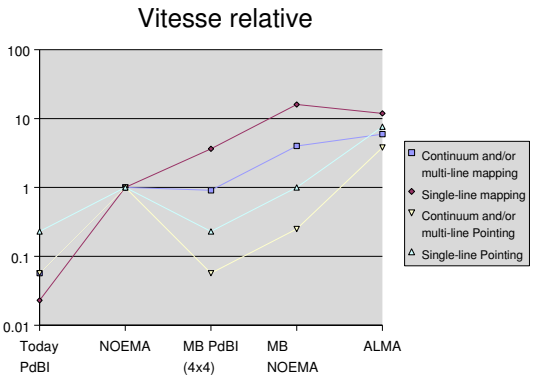

FIG. 1 – Vitesses relatives de différents instruments dont les caractéristiques sont définies dans le tableau ci-dessous, où D est le diamètre des antennes, $N_{\rm ant}$ le nombre d'antennes, $N_{\rm bas}$ le nombre de lignes de base, $N_{\rm pix}$ le nombre de pixels et B la bande passante totale disponible. La vitesse relative est définie comme l'inverse du temps qu'il faut pour atteindre la même sensibilité par point observé du ciel ; en mode pointé, elle est proportionnelle à $B\,N_{\rm bas}\,D^4$; en mode d'imagerie grand champ, elle est proportionnelle à $B\,N_{\rm pix}\,N_{\rm bas}\,D^2$. Les vitesses ont été normalisées par les performances de NOEMA.

	Single beam			Multi beams	
	Today PdBI	NOEMA	ALMA	PdBI (4 × 4)	NOEMA (4 × 4)
D [m]	15	15	12	15	15
$N_{\rm ant}$	6	12	50	6	12
$N_{\rm bas}$	15	66	1225	15	66
$N_{\rm pix}$	1	1	1	16	16
B [GHz]	8	32	16	8	8

- d'utiliser une instrumentation innovante, en particulier une nouvelle génération de récepteurs qui quadruple la bande passante totale (de 8 GHz à 32 GHz), impliquant une sensibilité 4 fois plus grande en continuum et la possibilité d'observer simultanément 4 fois plus de raies.

Ces options sont techniquement réalistes : en particulier, des prototypes de tels récepteurs existent déjà aujourd'hui à l'IRAM. NOEMA et ses possibles améliorations sont dans la continuité des développements technologiques qui ont conduit l'IRAM à installer 3 générations de récepteurs et 4 générations de corrélateurs à Bure depuis 1990. Le coût total du projet NOEMA est 43 Meuros dont entre 8 et 16 Meuros financés par la France (suivant le résultat de la campagne actuellement en cours pour obtenir des fonds privés), cad un coût moindre que le budget de fonctionnement d'ALMA pour une seule année.

Pour des raisons de design et de site, NOEMA sera dédié à l'étude du domaine de longueur d'onde millimétrique (3mm, 2mm et 1 mm) à des résolutions angulaires comprises entre 0.2" et 2" avec une rotation rapide entre configurations (de l'ordre de 6 mois). En mode pointé et en continuum, la sensibilité de NOEMA sera la moitié de celle d'ALMA, ce qui implique qu'ALMA sera 4 fois plus rapide (cf. figure 1).

En raie, la sensibilité de NOEMA sera 36% de celle d'ALMA, ce qui implique qu'ALMA sera 8 fois plus rapide pour des raies individuelles. Cependant, pour les surveys de raies, ALMA sera seulement 4 fois plus rapide parce que la bande passante de NOEMA sera 2 fois plus large que celle d'ALMA et contiendra donc 2 fois plus de raies. Compte tenu de la fraction de temps maximum (25%) passée par ALMA en millimétrique à résolution « moyenne », NOEMA aura donc une production annuelle *au moins* comparable dans ce domaine de paramètres. En pratique, NOEMA sera ainsi l'instrument de choix pour des études systématiques (de type "surveys") dans les bandes millimétriques (3, 2 et 1 mm). On peut citer par exemple : la détection et l'étude de populations de galaxies « normales » à grand redshift, la détection et l'étude la fonction de masse des proto-naines brunes (origine de l'IMF), l'étude des cycles de la matière (gaz et poussière) dans différents environnements (turbulents, chocs, PDRs, ...).

En résumé, le projet NOEMA offre donc à la communauté un instrument indispensable, dédié aux longueurs d'onde millimétriques à des résolutions intermédiaires entre une antenne unique (du type IRAM-30m) et ALMA. Par contraste, ALMA est un instrument très flexible (8 bandes de récepteurs, 28 configurations), devant servir une communauté pratiquement mondiale, et dont le potentiel de découverte est d'abord déterminé par ses aspects uniques, à savoir le submillimétrique et la très haute résolution angulaire. La sensibilité de NOEMA est proche de celle d'ALMA, donnant à la communauté française une puissance d'observation millimétrique au moins égale (dans l'hémisphère nord) à résolutions angulaires comprises entre 0.2" et 2". NOEMA est donc un projet qui est un complément idéal de l'EVLA aux longueurs d'onde centimétriques et d'ALMA aux longueurs d'onde submillimétriques. Enfin, c'est un projet qui permet à la communauté française de garder une expertise matérielle, logicielle et scientifique, mondialement reconnue aujourd'hui comme l'indique son implication importante dans la construction d'ALMA.

Appendice

A Des multi-pixels à Bure : une suite logique au projet NOEMA

La vitesse d'imagerie grand-champ de NOEMA (définie comme l'inverse du temps qu'il faut pour atteindre la même sensibilité par point observé du ciel) est aussi commensurable avec celle d'ALMA (cf. figure 1). Pour atteindre la même vitesse d'imagerie grand-champ sans changer le nombre d'antennes à Bure, il faut remplacer les récepteurs mono-pixels par des récepteurs d'au moins 16 pixels dans le plan focal des antennes de l'interféromètre. Outre le fait qu'un multi-pixel n'augmente que la vitesse d'imagerie grand-champ et non la vitesse d'imagerie en mode pointé, la définition de vitesse d'imagerie grand-champ donnée ci-dessus oublie un aspect essentiel en interférométrie, à savoir la qualité d'imagerie obtenue. Celle-ci est directement liée à la couverture du plan *uv*. La figure 2 compare la couverture du plan *uv* obtenue en configuration compacte pour le Plateau de Bure actuel (6 antennes) et pour NOEMA (12 antennes) en 12 heures d'observation. Le quadruplement du nombre de lignes de base permet à NOEMA d'obtenir une résolution angulaire deux fois plus fine avec une couverture du plan *uv* bien plus complète.

Conscient du potentiel des récepteurs multi-pixels pour l'imagerie grand-champ, l'IRAM a une politique de recherche et développement offensive dans ce domaine depuis plus de 10 ans. Cela a conduit à la réalisation d'HERA (récepteur de 18 pixels installé à l'IRAM-30m). Et cela se traduit aujourd'hui par des programmes de R&D en cours tant au niveau matériel pour miniaturiser les mélangeurs (FP7 AMSTAR+) qu'au niveau algorithmique pour mettre en oeuvre le mode d'observation interférométrique grand-champ, dit On-The-Fly (FP6 ALMA Enhancement). Par ailleurs, la taille des cabines des antennes de Bure permet d'abriter à la fois des récepteurs mono-pixels, multi-fréquences, et un récepteur multi-pixel, mono-fréquence, donnant une flexibilité scientifique similaire à celle de l'IRAM-30m d'aujourd'hui. Enfin, le transport du signal et le corrélateur de NOEMA, représentant une fraction majeure du coût de tout projet interféromètre, permettent de traiter soit 32 GHz de bande passante pour un mono-pixel, soit 32/N GHz de band passante pour un récepteur de N pixels.

Le projet NOEMA permet donc de gagner un facteur 16 en vitesse d'observation par rapport au PdBI d'aujourd'hui (cad l'équivalent d'un récepteur de 16 pixels). Le projet NOEMA fournit *en plus* un gain en sensibilité en mode pointé *et* en qualité d'imagerie (couverture du plan *uv*). Tout cela pour un coût environ 2 fois plus grand que le coût estimé (environ 20 Meuros) de l'installation d'un récepteur de 16 pixels et du corrélateur associé sur les 6 antennes déjà existantes à Bure. La réalisation de multi-pixels est une suite logique au projet NOEMA que les actions de R&D entreprises aujourd'hui permettront de mener à bien à terme, d'autant plus que la loi de Moore permet de gagner un ordre de grandeur tous les 6 ans dans la corrélation numérique des signaux.

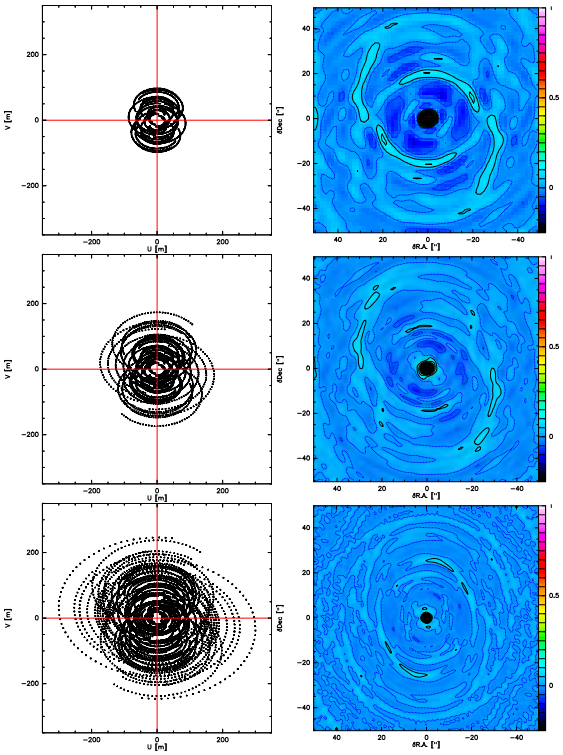

FIG. 2 – Couverture *uv* (colonne gauche) et lobe sale associé (colonne droite) pour une source à 45 degrés de déclinaison et pour la configuration D de PdBI (haut, 12 heures d'intégration), l'association des configurations CD de PdBI (milieu, 24 heures d'intégration) et la configuration D de NOEMA (bas, 12 heures d'intégration). Le quadruplement du nombre de lignes de base entre PdBI et NOEMA permet d'augmenter la résolution d'environ un facteur 2 tout en obtenant un lobe sale de bien meilleure qualité. La qualité d'imagerie de NOEMA est même meilleure que la combinaison des configurations C et D de PdBI, combinaison qui requiert un doublement du temps d'intégration.

Besoins en services d'observation ALMA pour la période 2011-2014

Le conseil scientifique de l'ASA
J. Pety, S. Charlot, E. Dartois, P. A. Duc, F. Gueth, L. Jorda,
E. Josselin, F. Ménard, F. Pajot, V. Piétu, P. Salomé, F. Selsis,
M. Tallon, L. Vigroux, A. Walters

26 octobre 2010

Résumé

La période 2011-2014 verra la montée en puissance scientifique du projet ALMA. Ce document décrit la redéfinition des besoins en services d'observation ALMA qu'implique le passage de la phase de construction à la phase d'exploitation scientifique. Etant donné l'importance d'ALMA pour la radioastronomie (sub)-millimétrique dans la décennie à venir, l'ASA recommande d'augmenter le nombre de personnes affectés au service d'observation ALMA de 50%, c'est-à-dire de passer de 11 à 17 chercheurs sur la période 2011-2014 : 2 chercheurs supplémentaires seraient affectées au commissionning au Chili, 2 chercheurs supplémentaires au soutien face-à-face de la communauté au sein de l'ARC européen, et 2 chercheurs supplémentaires à la mise au point d'outils experts.

1 Introduction

Les prochaines années vont voir la mise en service scientifique d'ALMA. La phase de « commissioning and science verification » a commencé sur le site fin 2009, les premières observations scientifiques (« early science ») auront lieu fin-2011 et la fin de la construction d'ALMA est prévue pour 2013. Le passage de la phase de construction à la phase d'exploitation scientifique d'un observatoire tel qu'ALMA nécessite une redéfinition des besoins en services d'observation ALMA.

Au moins onze chercheurs (6 CNAP, 3 CNRS, 2 post-docs) travaillaient pour le service d'observation ALMA lors du recensement fait par le groupe ad-hoc de l'exercice de prospective astronomie et astrophysique 2009-2010. Etant donné l'importance d'ALMA pour la radioastronomie (sub)-millimétrique dans la décennie à venir, l'ASA recommande d'augmenter le nombre de chercheurs affectés au service d'observation ALMA de 50%, c'est-à-dire de passer de 11 à 17 chercheurs sur la période 2011-2014.

2 Contexte

2.1 Quelques rappels sur les services d'observation

Les services d'observation concernent l'ensemble des personnels CNAP. Il s'agit donc ici de voir quels sont les besoins engendrés par le projet ALMA. Satisfaire ces besoins passe aussi bien par *la réaffectation de personnels* que par le recrutement.

Les services d'observation sont des projets d'envergure. Il n'est pas possible de saupoudrer les ressources sur l'ensemble de la France car cela entraine un besoin de personnel supplémentaire pour coordonner le travail, et donc une perte d'efficacité.

La labellisation est un processus 1) qui passe devant le comité scientifique de l'INSU et 2) qui engage les personnels sur de nombreuses années. C'est pourquoi les demandes de labellisation doivent proposer des cadres génériques de travail plutôt que se perdre dans des descriptions précises de travail à effectuer à court terme (par exemple dans les 6 prochains mois). En pratique, les services seront labellisés pour une période prédéfinie (typiquement 4 ans), renouvelables plusieurs fois.

Il faut bien séparer les activités de recherche des activités de service. Par exemple, la recherche en instrumentation est considérée comme une activité de recherche (débouchant sur la notion de chercheur instrumentaliste) alors que la construction (design inclus) d'un instrument résultant de cette recherche est une activité de service. Et ceci même s'il est probable que ce seront en grande partie les mêmes personnes qui s'occuperont de ces deux aspects.

2.2 Rôle de l'ASA dans la définition des services d'observation ALMA

L'ASA ne peut se substituer aux observatoires qui ont la prérogative d'affecter du personnel et des moyens sur des services d'observation. Par ailleurs, si l'IRAM, un des acteurs dans les services d'observation ALMA, n'est pas un observatoire au sens administratif français du terme, une partie de ses personnels sont détachés d'observatoires français.

Par contre, l'ASA est aujourd'hui consulté tous les ans par le président de la section du CNAP pour les priorités des services d'observation ALMA. Il n'y a pas eu de demande de labellisation de tâche de service ALMA dans les deux dernières années mais l'ASA a été contacté lors de l'exercice de prospective INSU 2009 par le groupe de réflexion sur les services d'observation pour faire un bilan (y compris humain) des services d'observation ALMA.

L'ASA a donc clairement un rôle de correspondant national au niveau des services ALMA. C'est à ce titre que le conseil scientifique de l'ASA définit dans ce document, en tant qu'expert, les *besoins* nationaux en services d'observation ALMA.

2.3 Le projet ALMA et le rôle des « ALMA Regional Centers »

Contrairement aux instruments optiques, ALMA est un projet sans contribution en nature (pour l'instant), ce qui signifie qu'un chercheur recruté en France n'a de statut aux yeux du projet ALMA qu'à condition qu'il participe à un contrat financé par ALMA.

Par ailleurs, l'ARC (ALMA Regional Center) est la structure qui sert d'interface entre ALMA et la communauté scientifique, avant les observations (appels à proposition, phase 1, phase 2) et une fois que les données ont été obtenues (accès à l'archive, soutien aux utilisateurs, etc). L'ARC américain est intégré dans l'ensemble des activités ALMA de NRAO, incluant la construction et la maintenance d'ALMA.

En Europe, l'ARC est organisé sous la forme d'un réseau. Le noeud central à l'ESO/Garching est en charge de la gestion des demandes de temps et des observations, de l'archive, et de la distribution des données de ALMA. Les sept noeuds additionnels sont en charge de la formation des utilisateurs en amont, ainsi que de l'aide directe fournie aux utilisateurs pour la préparation des projets et la réduction des données (soutien face-à-face).

Ainsi le soutien ALMA sera très différent du soutien actuel aux utilisateurs de l'interferomètre du plateau de Bure (PdBI). En effet, les astronomes assurant le soutien aux utilisateurs du PdBI assurent le développement de l'instrument ainsi que le suivi des observations et la responsabilité des logiciels de réduction de données. Ceci n'est pas le cas des astronomes travaillant dans les noeuds de l'ARC européen, ce qui pose la question d'un transfert efficace des informations[1] du projet ALMA à ces noeuds de l'ARC européen. Les besoins en tâches de service ALMA doivent prendre en compte cette difficulté et permettre d'établir des liens privilégiés avec l'observatoire lui-même au Chili et les équipes (presque exclusivement à NRAO, USA) chargées du développement des logiciels de réduction de données.

3 Relation avec les services d'observation IRAM

Les services d'observation ALMA et IRAM sont liés. Une très large fraction des personnes affiliées à l'un ou l'autre des services travaillent consécutivement ou simultanément dans les deux services. Cela est dû à la similitude et à la très grande technicité des instruments et logiciels employés. Il faut des années pour monter des équipes à la pointe dans ces domaines.

[1] Comment avoir plus d'information sur tel problème technique intervenu lors des observations ? Comment se tenir au courant des derniers développements dans les logiciels de réductions presqu'exclusivement développés à NRAO ?

4 Besoins en services ALMA

Le classement d'ALMA dans les services SO2 (instrumentation) et SO3 (soutien aux observatoires) est suffisant pour englober les besoins ci-dessous.

4.1 Participation au commissioning d'ALMA

Cette tâche est primordiale pour avoir un contact direct avec l'instrument et les personnes qui le construisent et en assurent le fonctionnement. Il s'agit pour l'instant de séjours de 3 à 6 mois sur place pour lequel l'ESO ne paie que les frais de mission (le salaire reste donc à la charge de l'Observatoire de rattachement). L'ESO souhaite des personnels expérimentés car leur but n'est pas de former des gens mais d'aider à la construction d'ALMA. Pour information, l'IRAM envoie en 2010/2011 deux personnes pour un séjour de 3 mois.

L'ASA encourage les observatoires français à envoyer des astronomes au Chili, astronomes mis à la disposition de l'ESO pour ALMA. L'ASA recommande d'assurer la présence de 2 français au Chili sur toute la période de commissionning. C'est certainement la meilleure manière d'assurer une bonne connaissance de l'instrument et de la diffuser dans la communauté française pour la préparer à une utilisation optimale d'ALMA.

4.2 Soutien face à face

L'ARC est une structure essentielle pour assurer le succès de la communauté française dans son utilisation d'ALMA : dans une compétition mondiale extrêmement forte, il est nécessaire d'avoir des centres d'expertise pouvant fournir un soutien efficace et rapide à la communauté, notamment pour la réduction des données. Les ARC nord-américains et asiatiques sont localisés à un seul endroit. Le modèle européen consistant à impliquer plusieurs laboratoires est justifié par le manque d'expertise disponible à l'ESO, mais comporte un risque très fort de dispersion des efforts.

Pour éviter l'émiettement des ressources françaises et pour couvrir toutes les problématiques (instrumentales, logicielles, scientifiques) en un même lieu, l'ASA défend l'idée que le soutien face à face doit se faire exclusivement à Grenoble dans le cadre du noeud de l'ARC européen qui s'y développe. Quel que soit le montage administratif retenu, il est important de souligner que pour qu'une petite équipe réussisse à offrir un soutien face-à-face de qualité dans un environnement aussi complexe (car mondialisé) qu'ALMA, il faut un investissement des membres de l'équipe supérieur aux 30% de tâches de service habituel d'un personnel CNAP. L'ASA recommande l'affectation de 2 postes supplémentaires à cette tâche sur la période 2011-2014.

4.3 Mise au point d'outils experts

Il s'agit par exemple d'outils de visualisation de données, d'estimation de la qualité de la calibration, d'imagerie avancée, de polarimétrie, etc... Dans un premier temps (au moins pendant la période dite « Early Science »), ALMA va produire des données brutes sans pipeline (sans réduction automatique). La réduction et l'analyse manuelle des données se fera à l'aide du logiciel CASA qui est en très grande partie développé par NRAO. L'existence d'outils experts permettra durant cette période d'identifier et/ou de résoudre plus rapidement les problèmes qui ne manqueront pas d'arriver. Ces outils auront pour but d'ajouter une meilleure interactivité avec les données et/ou des algorithmes d'étalonnage ou d'imagerie non-standards. A plus long terme, les outils experts devraient permettre de tirer au mieux parti du télescope dans ses limites non-couvertes par le pipeline. En effet, assurer le développement et le suivi d'outils experts donnera à la communauté française un avantage dans l'obtention de temps sur cet observatoire unique au monde et donc très compétitif. L'ASA recommande ici aussi l'affectation de 2 postes supplémentaires à cette tâche sur la période 2011-2014.

5 Besoins en services annexes, bénéfiques entre autres à ALMA

Tirer le meilleur parti scientifique d'ALMA implique d'autres types de besoins qui ne sont pas spécifiques à ALMA. L'ASA souligne ces besoins pour encourager les observatoires à y répondre.

5.1 Mise à disposition de données de micro-physique fiables

Il s'agit d'efforts essentiels pour la communauté astrophysique, mais insuffisamment valorisés (cités) et soutenus sur le long terme. En outre, le dialogue entre communautés de cultures très différentes est le seul moyen d'obtenir une bonne adéquation entre les besoins astrophysiques et l'expertise disponible. C'est d'autant plus crucial que les problèmes astrophysiques sont plus difficiles et plus nombreux à traiter. La partie service concerne ici la mise à disposition de données souhaitées par la communauté ALMA. Cela englobe 1) la définition de ces besoins, 2) la standardisation des données, 3) l'évaluation de la qualité et de la zone de validité des données disponibles et 4) la mise en service, la documentation et la maintenance de bases de données de façon à pérenniser les données. En particulier, il faut soutenir les actions ayant une audience mesurable suffisamment grande.

5.2 Mise à disposition d'outils d'analyse

Les outils d'analyse tels que les codes de transfert de rayonnement, codes de chimie, codes de MHD, etc... sont des objets de recherches qui s'améliorent sans cesse. Néanmoins, certains d'entre eux ont atteint un degré de maturité qui en font des outils trop complexes pour être facilement réécrits tout en répondant à des problèmes précis suffisamment utiles à une communauté d'utilisateurs. La partie service englobe ici la mise en place de benchmarks, la documentation (en particulier la description de leurs conditions de fonctionnement normal), la mise à disposition (e.g. interface VO) et le soutien aux utilisateurs.

Articles publiés dans des revues à comité de lecture

[A1] H. S. Liszt and **Pety**. Imaging diffuse clouds : Bright and dark gas mapped in CO. *A&A*, 2012. Accepté.

[A2] V. Guzmán, J. **Pety**, J. R. Goicoechea, M. Gerin, and E. Roueff. H_2CO in the Horsehead PDR : photo-desorption of dust grain ice mantles. *A&A*, 534 :A49, October 2011.

[A3] V. Piétu, F. Gueth, P. Hily-Blant, K.-F. Schuster, and J. **Pety**. High resolution imaging of the GG Tauri system at 267 GHz. *A&A*, 528 :A81, April 2011.

[A4] S. Maret, P. Hily-Blant, J. **Pety**, S. Bardeau, and E. Reynier. Weeds : a CLASS extension for the analysis of millimeter and sub-millimeter spectral surveys. *A&A*, 526 :A47+, February 2011.

[A5] A. Fuente, O. Berné, J. Cernicharo, J. R. Rizzo, M. González-García, J. R. Goicoechea, P. Pilleri, V. Ossenkopf, M. Gerin, R. Güsten, M. Akyilmaz, A. O. Benz, F. Boulanger, S. Bruderer, C. Dedes, K. France, S. García-Burillo, A. Harris, C. Joblin, T. Klein, C. Kramer, F. Le Petit, S. D. Lord, P. G. Martin, J. Martín-Pintado, B. Mookerjea, D. A. Neufeld, Y. Okada, J. **Pety**, T. G. Phillips, M. Röllig, R. Simon, J. Stutzki, F. van der Tak, D. Teyssier, A. Usero, H. Yorke, K. Schuster, M. Melchior, A. Lorenzani, R. Szczerba, M. Fich, C. McCoey, J. Pearson, and P. Dieleman. Herschel observations in the ultracompact HII region Mon R2. Water in dense photon-dominated regions (PDRs). *A&A*, 521 :L23+, October 2010.

[A6] H. S. Liszt, J. **Pety**, and R. Lucas. The CO luminosity and CO-H_2 conversion factor of diffuse ISM : does CO emission trace dense molecular gas ? *A&A*, 518 :A45+, July 2010.

[A7] J. **Pety** and N. Rodríguez-Fernández. Revisiting the theory of interferometric wide-field synthesis. *A&A*, 517 :A12+, July 2010.

[A8] S. Leurini, B. Parise, P. Schilke, J. **Pety**, and R. Rolffs. H_2CO and CH_3OH maps of the Orion Bar photodissociation region. *A&A*, 511 :A82+, February 2010.

[A9] E. Falgarone, J. **Pety**, and P. Hily-Blant. Intermittency of interstellar turbulence : extreme velocity-shears and CO emission on milliparsec scale. *A&A*, 507 :355–368, November 2009.

[A10] P. Boissé, E. Rollinde, P. Hily-Blant, J. **Pety**, S. R. Federman, Y. Sheffer, G. Pineau Des Forêts, E. Roueff, B.-G. Andersson, and G. Hébrard. CO emission and variable CH and CH^+ absorption towards HD 34078 : evidence for a nascent bow shock ? *A&A*, 501 :221–237, July 2009.

[A11] H. S. Liszt, J. **Pety**, and K. Tachihara. Imaging galactic diffuse clouds : CO emission, reddening and turbulent flow in the gas around ζ Ophiuchi. *A&A*, 499 :503–513, May 2009.

[A12] J. R. Goicoechea, J. **Pety**, M. Gerin, P. Hily-Blant, and J. Le Bourlot. The ionization fraction gradient across the Horsehead edge : an archetype for molecular clouds. *A&A*, 498 :771–783, May 2009.

[A13] M. Gerin, J. R. Goicoechea, J. **Pety**, and P. Hily-Blant. HCO mapping of the Horsehead : tracing the illuminated dense molecular cloud surfaces. *A&A*, 494 :977–985, February 2009.

[A14] K. Schreyer, S. Guilloteau, D. Semenov, A. Bacmann, E. Chapillon, A. Dutrey, F. Gueth, T. Henning, F. Hersant, R. Launhardt, J. **Pety**, and V. Piétu. Chemistry in disks. II. Poor molecular content of the AB Aurigae disk. *A&A*, 491 :821–827, December 2008.

[A15] J. **Pety**, R. Lucas, and H. S. Liszt. Imaging galactic diffuse gas : bright, turbulent CO surrounding the line of sight to NRAO150. *A&A*, 489 :217–228, October 2008.

[A16] H. S. Liszt, J. **Pety**, and R. Lucas. Limits on chemical complexity in diffuse clouds : search for CH_3OH and HC5N absorption. *A&A*, 486 :493–496, August 2008.

[A17] P. Salomé, Y. Revaz, F. Combes, J. **Pety**, D. Downes, A. C. Edge, and A. C. Fabian. Observations of CO in the eastern filaments of NGC 1275. *A&A*, 483 :793–799, June 2008.

[A18] P. Hily-Blant, E. Falgarone, and J. **Pety**. Dissipative structures of diffuse molecular gas. III. Small-scale intermittency of intense velocity-shears. *A&A*, 481 :367–380, April 2008.

[A19] S. Guilloteau, A. Dutrey, J. **Pety**, and F. Gueth. Resolving the circumbinary dust disk surrounding HH 30. *A&A*, 478 :L31–L34, February 2008.

[A20] J. M. Winters, T. Le Bertre, J. **Pety**, and R. Neri. Mass loss from dusty, low outflow-velocity AGB stars. II. The multiple wind of EP Aquarii. *A&A*, 475 :559–568, November 2007.

[A21] J. **Pety**, J. R. Goicoechea, P. Hily-Blant, M. Gerin, and D. Teyssier. Deuterium fractionation in the Horsehead edge. *A&A*, 464 :L41–L44, March 2007.

[A22] A. Dutrey, T. Henning, S. Guilloteau, D. Semenov, V. Piétu, K. Schreyer, A. Bacmann, R. Launhardt, J. **Pety**, and F. Gueth. Chemistry in disks. I. Deep search for N_2H^+ in the protoplanetary disks around LkCa 15, MWC 480, and DM Tauri. *A&A*, 464 :615–623, March 2007.

[A23] V. Piétu, A. Dutrey, S. Guilloteau, E. Chapillon, and J. **Pety**. Resolving the inner dust disks surrounding LkCa 15 and MWC 480 at mm wavelengths. *A&A*, 460 :L43–L47, December 2006.

[A24] J. **Pety**, F. Gueth, S. Guilloteau, and A. Dutrey. Plateau de Bure interferometer observations of the disk and outflow of HH 30. *A&A*, 458 :841–854, November 2006.

[A25] J. R. Goicoechea, J. **Pety**, M. Gerin, D. Teyssier, E. Roueff, P. Hily-Blant, and S. Baek. Low sulfur depletion in the Horsehead PDR. *A&A*, 456 :565–580, September 2006.

[A26] S. Cabrit, J. **Pety**, N. Pesenti, and C. Dougados. Tidal stripping and disk kinematics in the RW Aurigae system. *A&A*, 452 :897–906, June 2006.

[A27] H. S. Liszt, R. Lucas, and J. **Pety**. Comparative chemistry of diffuse clouds. V. Ammonia and formaldehyde. *A&A*, 448 :253–259, March 2006.

[A28] E. Habart, A. Abergel, C. M. Walmsley, D. Teyssier, and J. **Pety**. Density structure of the Horsehead nebula photo-dissociation region. *A&A*, 437 :177–188, July 2005.

[A29] J. **Pety**, D. Teyssier, D. Fossé, M. Gerin, E. Roueff, A. Abergel, E. Habart, and J. Cernicharo. Are PAHs precursors of small hydrocarbons in photo-dissociation regions ? The Horsehead case. *A&A*, 435 :885–899, June 2005.

[A30] J. **Pety**, A. Beelen, P. Cox, D. Downes, A. Omont, F. Bertoldi, and C. L. Carilli. Atomic carbon in PSS 2322+1944, a quasar at redshift 4.12. *A&A*, 428 :L21–L24, December 2004.

[A31] A. Beelen, P. Cox, J. **Pety**, C. L. Carilli, F. Bertoldi, E. Momjian, A. Omont, P. Petitjean, and A. O. Petric. Starburst activity in the host galaxy of the z =2.58 quasar J1409+5628. *A&A*, 423 :441–447, August 2004.

[A32] D. Teyssier, D. Fossé, M. Gerin, J. **Pety**, A. Abergel, and E. Roueff. Carbon budget and carbon chemistry in Photon Dominated Regions. *A&A*, 417 :135–149, April 2004.

[A33] J. **Pety** and E. Falgarone. Non-Gaussian velocity shears in the environment of low mass dense cores. *A&A*, 412 :417–430, December 2003.

[A34] P. Cox, A. Omont, S. G. Djorgovski, F. Bertoldi, J. **Pety**, C. L. Carilli, K. G. Isaak, A. Beelen, R. G. McMahon, and S. Castro. CO and Dust in PSS 2322+1944 at a redshift of 4.12. *A&A*, 387 :406–411, May 2002.

[A35] E. Falgarone, J. **Pety**, and T. G. Phillips. Filamentary Structure and Helical Magnetic Fields in the Environment of a Starless Dense Core. *ApJ*, 555 :178–190, July 2001.

[A36] J. **Pety** and É. Falgarone. The elusive structure of the diffuse molecular gas : shocks or vortices in compressible turbulence ? *A&A*, 356 :279–286, April 2000.

[A37] J. W. Kooi, J. Pety, B. Bumble, C. K. Walker, H. G. Leduc, P. L. Schaffer, and T. G. Phillips. A 850-GHz waveguide receiver employing a niobium SIS junction fabricated on a 1-μm Si/sub 3/N/sub 4/ membrane. *IEEE Transactions on Microwave Theory Techniques*, 46 :151–161, February 1998.

[A38] D. C. Lis, J. Keene, Y. Li, T. G. Phillips, and J. **Pety**. Statistical Properties of Line Centroid Velocity Increments in the rho Ophiuchi Cloud. *ApJ*, 504 :889–+, September 1998.

[A39] D. C. Lis, J. **Pety**, T. G. Phillips, and E. Falgarone. Statistical Properties of Line Centroid Velocities and Centroid Velocity Increments in Compressible Turbulence. *ApJ*, 463 :623–+, June 1996.

[A40] J.-C. Maréchal, J. **Pety**, Y. Simon, and M. David. Analytical comparison of different types of pulse tubes refrigerators. *Cryogenics*, 34 :163–166, 1994.

Mémos IRAM et ALMA

[M1] S. Bardeau, J. **Pety**, and S. Guilloteau. CLASS user section. Technical report, 2011. IRAM Memo 2011-3.

[M2] J. **Pety** and N. Rodriguez-Fernandez. WIFISYN : The GILDAS implementation of a new wide-field synthesis algorithm. Technical report, 2011. IRAM Memo 2011-2.

[M3] S. Bardeau, E. Reynier, and J. **Pety**. Preparing gildas for large datasets. i - greg 2011. Technical report, 2011. IRAM Memo 2011-1.

[M4] J. **Pety**, M. Gonzalez, S. Bardeau, and E. Reynier. Iram-30m hera time/sensitivity estimator. Technical report, 2010. IRAM Memo 2010-2.

[M5] J. **Pety**, G. Quintana-Lacaci, R. Zylka, S. Bardeau, and E. Reynier. Iram-30m mambo time/sensitivity estimator. Technical report, 2010. IRAM Memo 2010-1.

[M6] J. **Pety**, S. Bardeau, and E. Reynier. Comparison of atm versions : Impact on the calibration of iram instruments. Technical report, 2009. IRAM Memo 2009-5.

[M7] S. Bardeau and J. **Pety**. Averaging spectra with class. Technical report, 2009. IRAM Memo 2009-4.

[M8] N. Rodriguez-Fernandez, F. Gueth, and J. **Pety**. A simulator of interferometric on-the-fly observations. Technical report, 2009. IRAM Memo 2009-3.

[M9] N. Rodriguez-Fernandez, J. **Pety**, and F. Gueth. Imaging of interferometric on-the-fly observations : (1) context and discussion of possible methods. Technical report, 2009. IRAM Memo 2009-2.

[M10] J. **Pety**, S. Bardeau, and E. Reynier. Iram-30m emir time/sensitivity estimator. Technical report, 2009. IRAM Memo 2009-1.

[M11] N. Rodriguez-Fernandez, J. **Pety**, and F. Gueth. Single-dish observation and processing to produce the short-spacing information for a millimeter interferometer. Technical report, 2008. IRAM Memo 2008-2.

[M12] J. **Pety**, N. Rodriguez-Fernandez, and S. Guilloteau. Mapping. Technical report, 2007. A GILDAS software documentation.

[M13] P. Hily-Blant, J. **Pety**, and S. Guilloteau. Class evolution : I. improved oft support. Technical report, 2005. IRAM Memo 2005-1.

[M14] T. Tsutsumi, K.-I. Morita, T. Hasegawa, and J. **Pety**. Wide-field imaging of alma with the atacama compact array : Imaging simulations. Technical report, 2004. ALMA Memo 488.

[M15] J. **Pety**, A. Baker, A. Coulais, F. Gueth, D. Shepherd, L. Testi, and C. Wilson. AIPS++ reuse analysis test : Report on phase II. Technical report, 2003. ALMA Memo 473.

[M16] J. **Pety**, F. Gueth, S. Guilloteau, P. J. Teuben, and M. C. H. Wright. Case for interoperability as alma off–line. Technical report, 2003. ALMA Memo 465 & IRAM Memo 2003-4.

[M17] J. **Pety**, F. Gueth, S. Guilloteau, P. J. Teuben, and M. C. H. Wright. Complementarity of the AIPS++, gildas and miriad packages as seen from evaluations for alma off-line data processing. Technical report, 2003. ALMA Memo 464 & IRAM Memo 2003-3.

[M18] F. Gueth, S. Guilloteau, R. Lucas, J. **Pety**, and M. C. H. Wright. Evaluation of the gildas package for alma off-line data processing. Technical report, 2003. BIMA Memo 96 & IRAM Memo 2003-2.

[M19] M. C. H. Wright, P. J. Teuben, and J. **Pety**. Evaluation of the miriad package for alma off-line data processing. Technical report, 2003. BIMA Memo 95 & IRAM Memo 2003-1.

[M20] J. **Pety**, F. Gueth, and S. Guilloteau. Impact of aca on the wide-field imaging capabilities of alma. Alma memo 398, IRAM, 2001.

[M21] J. **Pety**, F. Gueth, and S. Guilloteau. Alma+aca simulation results. Alma memo 387, IRAM, 2001.

[M22] J. **Pety**, F. Gueth, and S. Guilloteau. Alma+aca simulation tools. Alma memo 386, IRAM, 2001.

Actes de colloques nationaux et internationaux

[C1] J. **Pety**, H. S. Liszt, and R. Lucas. The CO-H_2 conversion factor of diffuse ISM : Bright ^{12}CO emission also traces diffuse gas. In M. Röllig, R. Simon, V. Ossenkopf, & J. Stutzki, editor, *EAS Publications Series*, volume 52 of *EAS Publications Series*, pages 151–155, November 2011.

[C2] P. Pilleri, C. Joblin, M. Gerin, J. Pety, J. Montillaud, F. Boulanger, and A. Fuente. Production of small hydrocarbons in photo-dissociation regions. In *IAU Symposium*, volume 280 of *IAU Symposium*, page 300P, May 2011.

[C3] V. Guzman, J. Pety, J. R. Goicoechea, M. Gerin, and E. Roueff. H_2CO in the Horsehead nebula. In *IAU Symposium*, volume 280 of *IAU Symposium*, page 187P, May 2011.

[C4] P. Gratier, J. Pety, M. Gerin, J. Montillaud, V. Guzman, and J. R. Goicoechea. The Horsehead Nebula : a template for extragalactic high density tracers studies ? In *IAU Symposium*, volume 280 of *IAU Symposium*, page 182P, May 2011.

[C5] J. **Pety**, H. S. Liszt, and R. Lucas. Bright ^{12}CO emission traces both dense and diffuse gas. *Memorie della Societa Astronomica Italiana*, 82 :872, 2011.

[C6] E. Schinnerer, A. Leroy, J. **Pety**, G. Dumas, S. Meidt, D. Colombo, S. Garcia-Burillo, A. Hughes, C. Kramer, H. Rix, K. Schuster, T. Thompson, A. Weiss, S. Aalto, and N. Scoville. The Molecular Gas in the Whirlpool Galaxy. In *Bulletin of the American Astronomical Society*, volume 43 of *Bulletin of the American Astronomical Society*, pages 24611–+, January 2011.

[C7] J. R. Goicoechea, J. **Pety**, M. Gerin, P. Hily-Blant, D. Teyssier, and E. Roueff. Simple Organic Chemistry in the Horsehead Nebula. In K. J. Meech, J. V. Keane, M. J. Mumma, J. L. Siefert, & D. J. Werthimer , editor, *Astronomical Society of the Pacific Conference Series*, volume 420 of *Astronomical Society of the Pacific Conference Series*, pages 43–+, December 2009.

[C8] E. Falgarone, P. Hily-Blant, and J. **Pety**. Small-scale Intermittency of the Dissipation of Interstellar Turbulence. In D. C. Lis, J. E. Vaillancourt, P. F. Goldsmith, T. A. Bell, N. Z. Scoville, & J. Zmuidzinas, editor, *Astronomical Society of the Pacific Conference*

Series, volume 417 of *Astronomical Society of the Pacific Conference Series*, pages 243–+, December 2009.

[C9] P. Boissé, E. Rollinde, G. Hébrard, P. Hily-Blant, J. **Pety**, S. R. Federman, Y. Sheffer, B. G. Andersson, G. Marmin, G. P. Des Forêts, and E. Roueff. A Multiwavelength Study of the Close Environment of HD 34078. In M. E. van Steenberg, G. Sonneborn, H. W. Moos, & W. P. Blair , editor, *American Institute of Physics Conference Series*, volume 1135 of *American Institute of Physics Conference Series*, pages 107–109, May 2009.

[C10] J. **Pety**, J. R. Goicoechea, and M. Gerin. Two prototypical Galactic PDRs : The Orion bar and the Horsehead mane. In C. Kramer, S. Aalto, & R. Simon, editor, *EAS Publications Series*, volume 31 of *EAS Publications Series*, pages 35–41, 2008.

[C11] E. Falgarone, P. Hily-Blant, J. **Pety**, and G. Pineau Des Forets. Dissipation of turbulence in a dense core environment : chemical signatures. In *Molecules in Space and Laboratory*, December 2007.

[C12] J. **Pety**, J. R. Goicoechea, M. Gerin, P. Hily-Blant, D. Teyssier, E. Roueff, E. Habart, and A. Abergel. The Horsehead mane : Toward an observational benchmark for chemical models. In *Molecules in Space and Laboratory*, December 2007.

[C13] M. Gerin, P. Lesaffre, J. R. Goicoechea, P. Hennebelle, J. **Pety**, J. Le Bourlot, and F. Le Petit. Molecules in the diffuse and dense interstellar gas. In *Molecules in Space and Laboratory*, December 2007.

[C14] E. Falgarone, P. Hily-Blant, J. **Pety**, and G. Pineau Desforêts. Small-Scale Dissipative Structures of Diffuse ISM Turbulence : II – Chemical Diagnostics. In M. Haverkorn & W. M. Goss, editor, *SINS - Small Ionized and Neutral Structures in the Diffuse Interstellar Medium*, volume 365 of *Astronomical Society of the Pacific Conference Series*, pages 190–+, July 2007.

[C15] P. Hily-Blant, J. **Pety**, and E. Falgarone. Small-Scale Dissipative Structures of Diffuse ISM Turbulence : I – CO Diagnostics. In M. Haverkorn & W. M. Goss, editor, *SINS - Small Ionized and Neutral Structures in the Diffuse Interstellar Medium*, volume 365 of *Astronomical Society of the Pacific Conference Series*, pages 184–+, July 2007.

[C16] E. Falgarone, P. Hily-Blant, J. **Pety**, and G. Pineau Des Forêts. The turbulent environment of low-mass dense cores. In B. G. Elmegreen & J. Palous, editor, *IAU Symposium*, volume 237 of *IAU Symposium*, pages 24–30, 2007.

[C17] J. **Pety**, J. R. Goicoechea, M. Gerin, P. Hily-Blant, D. Teyssier, E. Roueff, E. Habart, and A. Abergel. Benchmarking PDR models against the Horsehead edge. In D. Barret, F. Casoli, G. Lagache, A. Lecavelier, & L. Pagani , editor, *SF2A-2006 : Semaine de l'Astrophysique Francaise*, pages 247–+, June 2006.

[C18] P. Hily-Blant, J. **Pety**, and E. Falgarone. Small-scale dissipative structures of the diffuse ISM : CO diagnostics. In D. Barret, F. Casoli, G. Lagache, A. Lecavelier, & L. Pagani , editor, *SF2A-2006 : Semaine de l'Astrophysique Francaise*, pages 239–+, June 2006.

[C19] J. R. Goicoechea, J. **Pety**, M. Gerin, D. Teyssier, E. Roueff, and P. Hily-Blant. Low Sulfur Depletion in Photodissociation Regions. In D. Barret, F. Casoli, G. Lagache, A. Lecavelier, & L. Pagani , editor, *SF2A-2006 : Semaine de l'Astrophysique Francaise*, pages 229–+, June 2006.

[C20] J. **Pety**. Successes of and Challenges to GILDAS, a State-of-the-Art Radioastronomy Toolkit. In F. Casoli, T. Contini, J. M. Hameury, & L. Pagani, editor, *SF2A-2005 : Semaine de l'Astrophysique Francaise*, pages 721–+, December 2005.

[C21] E. Falgarone, P. Hily-Blant, J. **Pety**, and G. Pineau Des Forêts. Intermittency of interstellar turbulence : observational signatures in diffuse molecular gas. In E. M. de Gouveia dal Pino, G. Lugones, & A. Lazarian, editor, *Magnetic Fields in the Universe : From Laboratory and Stars to Primordial Structures.*, volume 784 of *American Institute of Physics Conference Series*, pages 299–307, September 2005.

[C22] H. Liszt, R. Lucas, and J. **Pety**. Millimeter-wave Observations of Polyatomic Molecules in Diffuse Clouds. In D. C. Lis, G. A. Blake, & E. Herbst, editor, *Astrochemistry : Recent Successes and Current Challenges*, volume 231 of *IAU Symposium*, pages 187–196, August 2005.

[C23] M. Gerin, E. Roueff, J. Le Bourlot, J. **Pety**, J. R. Goicoechea, D. Teyssier, C. Joblin, A. Abergel, and D. Fossé. Carbon Chemistry in Photodissociation Regions. In D. C. Lis, G. A. Blake, & E. Herbst, editor, *Astrochemistry : Recent Successes and Current Challenges*, volume 231 of *IAU Symposium*, pages 153–162, August 2005.

[C24] D. Teyssier, P. Hily-Blant, M. Gerin, J. Cernicharo, E. Roueff, and J. **Pety**. Variation of the C_3H_2 cyclic/linear abundance ratio across the Horsehead nebula Photo-Dominated Region. In A. Wilson, editor, *ESA Special Publication*, volume 577 of *ESA Special Publication*, pages 423–424, January 2005.

[C25] S. Cabrit, J. **Pety**, N. Pesenti, and C. Dougados. Disk Kinematics and Tidal Stripping in the RW Aur System. In *Protostars and Planets V*, page 8103, 2005.

[C26] J. R. Goicoechea, J. **Pety**, M. Gerin, E. Roueff, D. Teyssier, A. Abergel, E. Habart, and C. Joblin. Sulfur chemistry in the Horsehead PDR : deriving the S abundance from CS. In *IAU Symposium*, volume 235 of *IAU Symposium*, pages 75P–+, 2005.

[C27] P. Hily-Blant, E. Falgarone, J. **Pety**, and G. Pineau Des Forêts. The spatial distribution of optically thin ^{12}CO(1 - 0) in diffuse molecular clouds. In *IAU Symposium*, volume 235 of *IAU Symposium*, pages 61P–+, 2005.

[C28] E. Falgarone, P. Hily–Blant, and J. **Pety**. Intermittent Dissipation of Interstellar Turbulence : Observational Signatures. In D. Johnstone, F. C. Adams, D. N. C. Lin, D. A. Neufeeld, & E. C. Ostriker , editor, *Star Formation in the Interstellar Medium : In Honor of David Hollenbach*, volume 323 of *Astronomical Society of the Pacific Conference Series*, pages 185–+, December 2004.

[C29] J. **Pety**, F. Gueth, S. Guilloteau, R. Lucas, P. J. Teuben, and M. C. H. Wright. Interoperating GILDAS and MIRIAD. In F. Ochsenbein, M. G. Allen, & D. Egret, editor, *Astronomical Data Analysis Software and Systems (ADASS) XIII*, volume 314 of *Astronomical Society of the Pacific Conference Series*, pages 416–+, July 2004.

[C30] J. **Pety**, F. Gueth, A. Dutrey, and S. Guilloteau. Millimeter Properties of the Protoplanetary Disk Surrounding HH 30. In S. Pfalzner, C. Kramer, C. Staubmeier, & A. Heithausen, editor, *The Dense Interstellar Medium in Galaxies*, pages 649–+, 2004.

[C31] D. Teyssier, J. **Pety**, M. Gerin, D. Fosse, A. Abergel, E. Roueff, and C. Joblin. Small Carbon Chains and Rings in Photo-Dominated Regions. In S. Pfalzner, C. Kramer, C. Staub-

meier, & A. Heithausen, editor, *The Dense Interstellar Medium in Galaxies*, pages 521–+, 2004.

[C32] D. Teyssier, D. Fossé, M. Gerin, J. **Pety**, A. Abergel, and E. Habart. Connection Between PAHs and Small Hydrocarbons in the Horsehead Nebula PhotoDissociation Region. In C. L. Curry & M. Fich, editor, *SFChem 2002 : Chemistry as a Diagnostic of Star Formation*, pages 422–+, 2003.

[C33] E. Falgarone, G. Pineau Des Forêts, P. Hily-Blant, P. Schilke, and J. **Pety**. Non-equilibrium Chemistry in the Dissipative Structures of Interstellar Turbulence. In C. L. Curry & M. Fich, editor, *SFChem 2002 : Chemistry as a Diagnostic of Star Formation*, pages 291–+, 2003.

[C34] J. **Pety**, F. Gueth, S. Guilloteau, and A. Dutrey. The stellar mass of HH30. In F. Combes & D. Barret, editor, *SF2A-2002 : Semaine de l'Astrophysique Francaise*, pages 481–+, June 2002.

[C35] J. **Pety**, F. Gueth, and S. Guilloteau. Simulating the wide-field imaging capabilities of ALMA. In F. Combes, D. Barret, & F. Thévenin, editor, *SF2A-2001 : Semaine de l'Astrophysique Francaise*, pages 569–+, May 2001.

[C36] E. Falgarone and J. **Pety**. Turbulence in the Environment of two Starless Dense Cores. In T. Montmerle & P. André, editor, *From Darkness to Light : Origin and Evolution of Young Stellar Clusters*, volume 243 of *Astronomical Society of the Pacific Conference Series*, pages 53–+, 2001.

[C37] J. **Pety** and É. Falgarone. The structure of the cold neutral matter : shocks or vortices ? In *Young European Radio Astronomers' Conference (YERAC)*, 2000.

[C38] J. **Pety** and É. Falgarone. Kinematic localization of the dissipative structures of interstellar turbulence. In *Young European Radio Astronomers' Conference (YERAC)*, 2000.

[C39] D. C. Lis, T. G. Phillips, M. Gerin, J. Keene, Y. Li, J. **Pety**, and E. Falgarone. Centroid Velocity Increments as a Probe of the Turbulent Velocity Field in Interstellar Molecular Clouds. In J. Franco & A. Carraminana, editor, *Interstellar Turbulence*, pages 203–+, 1999.

[C40] D. C. Lis, J. **Pety**, T. G. Phillips, and E. Falgarone. PDFs of centroid velocities and centroid velocity increments in supersonic compressible turbulence. In W. B. Latter, S. J. E. Radford, P. R. Jewell, J. G. Mangum, & J. Bally, editor, *IAU Symposium*, volume 170 of *IAU Symposium*, pages 433–+, 1997.

[C41] J. W. Kooi, J. **Pety**, P. L. Schaffer, T. G. Phillips, B. Bumble, H. G. Leduc, and C. K. Walker. A 850 GHz SIS Receiver Employing Silicon Micro-Machining Technology. In E. J. Rolfe & G. Pilbratt, editor, *Submillimetre and Far-Infrared Space Instrumentation*, volume 388 of *ESA Special Publication*, pages 163–+, December 1996.

Caractériser le milieu interstellaire : un clé pour comprendre l'Univers

Qu'ont en commun la détection de carbone atomique à un redshift de 4, la cartographie à 1" de résolution de l'émission ^{12}CO J=1–0 de la galaxie du tourbillon (M51), l'étude des avant-plans galactiques de Planck, et l'étude de la cinématique du disque et du flot moléculaire de la proto-étoile HH30 ? Au-delà du fait qu'elles sont réalisées dans le domaine (sub-)millimétrique, ces observations sont liées aux processus physiques et chimiques du milieu interstellaire. Caractériser ces processus permet de comprendre les objets les plus divers de l'univers, des plus proches au plus lointains, des plus petits au plus grands. Je décris ici une décennie de travail consacrée à la compréhension du milieu interstellaire. Je commence par présenter deux des approches scientifiques que j'ai prises. La première concerne la caractérisition d'une des transitions les moins bien comprises du gaz dans son chemin vers la formation des étoiles, à savoir la transition HI vers H_2. Je montre comment l'interprétation de l'émission ^{12}CO J=1–0 pointe tout autant vers le milieu dense et froid que vers le milieu diffus et tiède. Dans un 2ème temps, je décris la nécessité et la mise en place d'une référence observationnelle (la chevelure de la nébuleuse de la Tête de Cheval) pour les modéles photochimiques, eux-mêmes utilisés dans tous les contextes évoqués ci-dessus.

La décennie qui vient sera aussi féconde grâce à plusieurs événements. Tout d'abord, la communauté qui étudie le milieu interstellaire se structure rapidement autour de grands projets. A mon niveau, e suis porteur du contrat ANR « Structure and CHemistry of the Inter-Stellar Medium » (SCHISM) qui réunit observateurs, numériciens et théoréticiens de l'IRAM et de l'Observatoire de Paris. Par ailleurs, l'instrumentation radio fait des progrès spectaculaires qui vont déboucher sur la spectro-imagerie grand champ à haute résolution angulaire et spectrale. L'IRAM a un rôle prépondérant dans cette aventure et j'y contribue au niveau logiciel et algorithmique. Enfin, je participe à la maturation des nouveaux instruments comme les caméras grand-champs pour les antennes uniques et les projets ALMA et NOEMA en interférométrie (sub-)millimétrique. La conjonction de ces facteurs contribuera à percer à jour l'origine des galaxies, des étoiles, des systèmes planétaires et des molécules prébiotiques.

Mots-clefs : Milieu interstellaire, Radio-astronomie, Spectro-imagerie grand champ, Interféromètrie.

Characterizing the interstellar medium: A key to understand the Universe

What is there in common between the detection of atomic carbon at a redshift of 4, 1"-mapping of the ^{12}CO J=1–0 of the whirpool galaxy (M51), the study of the Galactic foreground emission in Planck data, and the kinematic study of the molecular disk and outflow of the HH30 proto-star? Beyond the fact that all these observations are done at (sub-)millimeter wavelengths, they are linked through the physical and chemical processes of the interstellar medium. Characterizing these processes permits us to understand the most diverse objects of the universe near and far and from smallest to largest. I describe here one decade of work directed toward understanding of the interstellar medium. I start with the description of two of the approaches I took. The first concerns the characterization of one of the less well-understood step in the gas on its way to form stars, the transition from HI to H_2. I show how the interpretation of the ^{12}CO J=1–0 emission relates to cold dense gas as well as warm diffuse gas. Second, I present the need for and the making of an observational benchmark (the Horsehead Mane) for complex photo-chemical models, which are subsequently used in the contexts mentioned above.

The decade to come promises to be as fruitful as the last one, for several reasons. The community studying the interstellar medium increasingly organizes itself around large projects. On my own part, I am the PI of the SCHISM ANR grant (Structure and CHemistry of the InterStellar Medium) that brings together observers, numerical specialists and theoreticians mainly from IRAM and the Observatoire de Paris. Moreover, radio instrumentation is making spectacular progress regarding high angular and spectral resolution spectro-imaging. IRAM has a preponderant role in these challenges to which I contribute software development and algorithms. Finally, I participate in the maturation of new instruments such as single-dish wide-field cameras and the ALMA and NOEMA interferometers. The conjonction of the factors will contribute to bring to light the origins of the galaxies, stars, planetary systems and pre-biotic molecules.

Keywords: Interstellar medium, Radio-astronomy, Wide-field spectro-imaging, Interferometry.